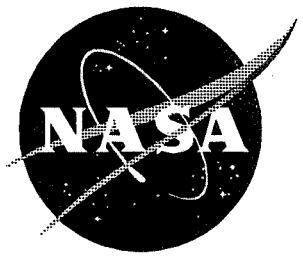

NASA Conference Publication 3335

1995 NASA High-Speed Research Program Sonic Boom Workshop

Volume I

Edited by
Daniel G. Baize

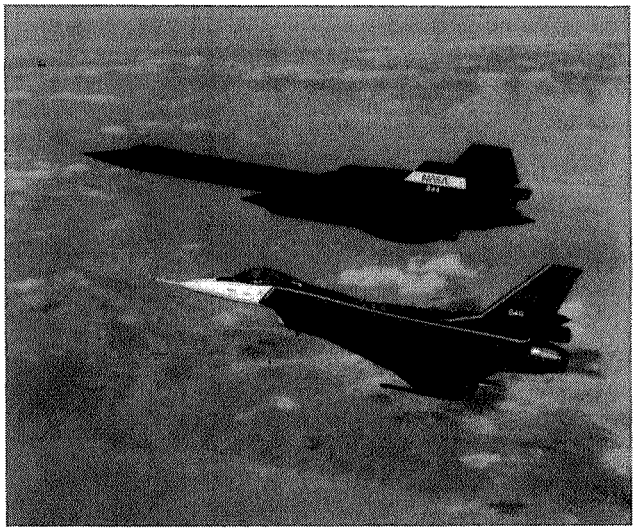

Proceedings of a workshop held at
Langley Research Center
Hampton, Virginia
September 12–13, 1995

July 1996

NASA Conference Publication 3335

1995 NASA High-Speed Research Program Sonic Boom Workshop

Volume I

Edited by
Daniel G. Baize
Langley Research Center • Hampton, Virginia

Proceedings of a workshop held at
Langley Research Center
Hampton, Virginia
September 12–13, 1995

National Aeronautics and Space Administration
Langley Research Center • Hampton, Virginia 23681-0001

July 1996

This publication is available from the following sources:

NASA Center for AeroSpace Information
800 Elkridge Landing Road
Linthicum Heights, MD 21090-2934
(301) 621-0390

National Technical Information Service (NTIS)
5285 Port Royal Road
Springfield, VA 22161-2171
(703) 487-4650

PREFACE

The High-Speed Research Program and NASA Langley Research Center sponsored the NASA High-Speed Research Program Sonic Boom Workshop on September 11-13, 1995. The workshop was designed to bring together NASA's scientists and engineers and their counterparts in industry, other Government agencies, and academia working in the sonic boom element of NASA's High-Speed Research Program. Specific objectives of this workshop were to: (1) report the progress and status of research in sonic boom propagation, acceptability, and design; (2) promote and disseminate this technology within the appropriate technical communities; (3) help promote synergy among the scientists working in the Program; and (4) identify technology pacing the development of viable reduced-boom High-Speed Civil Transport concepts.

The Workshop was organized in three sessions as follows:

Session I	Sonic Boom Propagation (Theoretical)
Session II	Sonic Boom Propagation (Experimental)
Session III	Acceptability Studies - Human and Animal

Conference Chairman — Daniel G. Baize, NASA Langley Research Center

ATTENDEES

Daniel G. Baize
NASA Langley Research Center
Mail Stop 248
Hampton, VA 23681-0001

Catherine M. Bahm
NASA Dryden Flight Research Center
MS D-4840, P. O. Box 273
Edwards, CA 93523-0273

Gene G. Bergmeier
Aerospace & Mechanical Engineering Dept.
The University of Arizona
Tucson, AZ 85721

David T. Blackstock
Applied Research Labs.
University of Texas
P. O. Box 8029
Austin, TX 78713-8029

Percy J. Bobbitt
Eagle Aeronautics, Inc.
12388 Warwick Blvd, Suite 301
Newport News, VA 23606-3850

Ann E. Bowles
Hubbs - Sea World Research Institute
2595 Ingraham Street
San Diego, CA 92122

James P. Chambers
National Center for Physical Acoustics
University of Mississippi
Coliseum Drive
University, MS 38677

Aditi Chattopadhyay
Mechanical & Aerospace Engineering Dept.
Arizona State University
Tempe, AZ 85287-6106

Hsien K. Cheng
Department of Aerospace Engineering
University of Southern California
Los Angeles, CA 90089-1191

Samson H. Cheung
McDonnell Douglas
Mail Code 71-35
Box 22608
Long Beach, CA 90801-5608

Robin O. Cleveland
Applied Research Laboratories
The University of Texas at Austin
P. O. Box 8029
Austin, TX 78713-8029

Steven C. Crow
Aerospace and Mechanical Engineering Dept.
The University of Arizona
Tucson, AZ 85721

J. Ray Dagenhart
NASA Langley Research Center
Mail Stop 170
Hampton, VA 23681-0001

Christine M. Darden
NASA Langley Research Center
Mail Stop 119
Hampton, VA 23681-0001

J. Micah Downing
USAF Armstrong Laboratory
AL/OEBN; 2610 Seventh Street
Wright-Patterson Air Force Base,
OH 45433-7901

L. Jack Ehernberger
NASA Dryden Flight Research Center
MS D-2033, P. O. Box 273
Edwards, CA 93523-0273

Sanford Fidell
BBN Systems and Technologies
21120 Vanowen Street
Canoga Park, CA 91303

Kamran Fouladi
Lockheed Engineering and Sciences Co.
Mail Stop 248
NASA Langley Research Center
Hampton, VA 23681-0001

Joe Garrelick
Cambridge Acoustical Associates, Inc.
200 Boston Avenue, Suite 2500
Medford, MA 02155-4243

Edward A. Haering, Jr.
Aerodynamics Branch
Mail Stop D-2033
P. O. Box 273
NASA Dryden Flight Research Center
Edwards, CA 93523-0273

Mohamed M. Hafez
Department of Mechanical and
Aerospace Engineering
University of California, Davis
Davis, CA 95616

George T. Haglund
Boeing Commercial Airplane Group
P. O. Box 3707
Seattle, WA 98124-2207

Munson A. Kwok
The Aerospace Corporation
P. O. Box 92957, M5-753
Los Angeles, CA 90009-2957

Robert J. Mack
NASA Langley Research Center
Mail Stop 248
Hampton, VA 23681-0001

Domenic J. Maglieri
Eagle Aeronautics, Inc.
12388 Warwick Blvd., Suite 301
Newport News, VA 23606-3850

David A. McCurdy
NASA Langley Research Center
Mail Stop 463
Hampton, VA 23681-0001

John M. Morgenstern
McDonnell Douglas Aerospace
2401 E. Wardlow Road
Long Beach, CA 90807-4418

Johnny R. Narayan
Aerospace Research Center
Arizona State University
Tempe, AZ 85287-8006

Stephen R. Norris
6939 Wildridge Road
Indianapolis, IN 46256

Allan D. Pierce
Boston University
110 Cummington Street
Boston, MA 02215

Kenneth J. Plotkin
Wyle Laboratories
2001 Jefferson Davis Highway, Suite 701
Arlington, VA 22202

Hugh W. Poling
Boeing Commercial Airplane Group
P. O. Box 3707, MS 6H-FR
Seattle, WA 98124-2207

Robert G. Rackl
Boeing Company
P. O. Box 3707, MS 6H-FR
Renton, VA 98124-2207

Richard Raspet
National Center for Physical Acoustics
University of Mississippi
Coliseum Drive
University, MS 38677

Judith L. Rochat
Graduate Program in Acoustics
The Pennsylvania State University
P. O. Box 30
State College, PA 16804

A. Richard Seebass
Aerospace Engineering Sciences
Campus Box 420
Boulder, CO 80309-0429

Kevin Shepherd
NASA Langley Research Center
Mail Stop 463
Hampton, VA 23681-0001

Michael J. Siclari
Northrop Grumman
Mail Stop K01-14
Bethpage, NY 11714

Norbert F. Smith
McDonnell Douglas Aerospace
22 enterprise Parkway, Suite 120
Hampton, VA 23666

Victor W. Sparrow
Graduate Program in Acoustics
157 Hammond Building
The Pennsylvania State University
University Park, PA 16802

Phillip T. Snyder
NASA Ames Research Center
MS 237-2
Moffett Field, CA 94035-1000

Brenda M. Sullivan
Lockheed Martin Engineering and
Sciences Co.
NASA Langley Research Center
Mail Stop 463
Hampton, VA 23681-0001

Louis C. Sutherland
Consultant in Acoustics
27803 Longhill Drive
Rancho Palos Verdes, CA 90275

Eugene L. Tu
NASA Ames Research Center
MS 258-1
Moffett Field, CA 94035

Leonard M. Weinstein
NASA Langley Research Center
Mail Stop 493
Hampton, VA 23681-0001

Alan R. Wenzel
Virginia Consortium of Engineering
and Science Universities
303 Butler Farm Road, Suite 101
Hampton, VA 23666

CONTENTS

VOLUME I

SESSION I

SESSION II

SESSION III

TURBULENCE SCALES, RISE TIMES, CAUSTICS, AND THE SIMULATION OF SONIC BOOM PROPAGATION

Allan D. Pierce
Boston University
Department of Aerospace and Mechanical Engineering
Boston, MA 02215

Work supported by NASA Grant NAG-1-1580

INTRODUCTION

The general topic of atmospheric turbulence effects on sonic boom propagation is addressed with especial emphasis on taking proper and efficient account of the contributions of the portion of the turbulence that is associated with extremely high wavenumber components. The recent work reported by Bart Lipkens in his doctoral thesis is reexamined to determine whether the good agreement between his measured rise times with the 1971 theory of the author is fortuitous. It is argued that Lipken's estimate of the distance to the first caustic was a gross overestimate because of the use of a sound speed correlation function shaped like a gaussian curve. In particular, it is argued that the expected distance to the first caustic varies with the kinematic viscosity ν and the energy ϵ dissipated per unit mass per unit time, and the sound speed c as

$$d_{\text{first caustic}} = \frac{\nu^{7/12} c^{2/3}}{\epsilon^{5/12}} \left(\frac{\nu \epsilon}{c^4} \right)^a$$

where the exponent a is greater than $-7/12$ and can be argued to be either 0 or $1/24$. In any event, the surprising aspect of the relationship is that it actually goes to zero as the viscosity goes to zero with ϵ held constant. It is argued that the apparent overabundance of caustics can be grossly reduced by a general computational and analytical perspective that partitions the turbulence into two parts, divided by a wavenumber k_c. Wavenumbers higher than k_c correspond to small-scale turbulence, and the associated turbulence can be taken into account by a renormalization of the ambient sound speed so that the result has a small frequency dependence that results from a spatial averaging over of the smaller-scale turbulent fluctuations. Selection of k_c can be made so large that only a very small number of caustics are encountered if one adopts the premise that the frequency dispersion of pulses is caused by that part of the turbulence spectrum which lies in the inertial range originally predicted by Kolmogoroff. The acoustic propagating wave's dispersion relation has the acoustic wavenumber being of the form $k = (\omega/c) + F(\omega)$, where c is a spatially averaged sound speed and where, for mechanical turbulence, the extra term $F(\omega)$ must depend on only the angular frequency ω, the sound speed c, and the turbulent energy dissipation ϵ per unit fluid mass and per unit time. If the turbulence is weak, then the quantity $F(\omega)$ has to be of second order in the portions of the turbulent fluid velocity in the inertial range, so, following Kolmogoroff's reasoning, it must vary with ϵ as $\epsilon^{2/3}$. Simple dimensional analysis then reveals that $F(\omega)$ is $K\epsilon^{2/3}c^{-7/3}\omega^{1/3}$, K being a universal dimensionless complex constant.

Different Scales of Atmospheric Turbulence affect Different Parts of Sonic Boom Waveforms

1. Smallest scales affect the rise times.
2. Larger scales cause spiking and rounding near the positions of the two shocks
3. Larger (yet) scales cause uniform magnification and demagnification of the waveform as a whole.
4. Larger (yet) scales cause perceptible shifts in the direction of propagation by the time the boom reaches the ground.

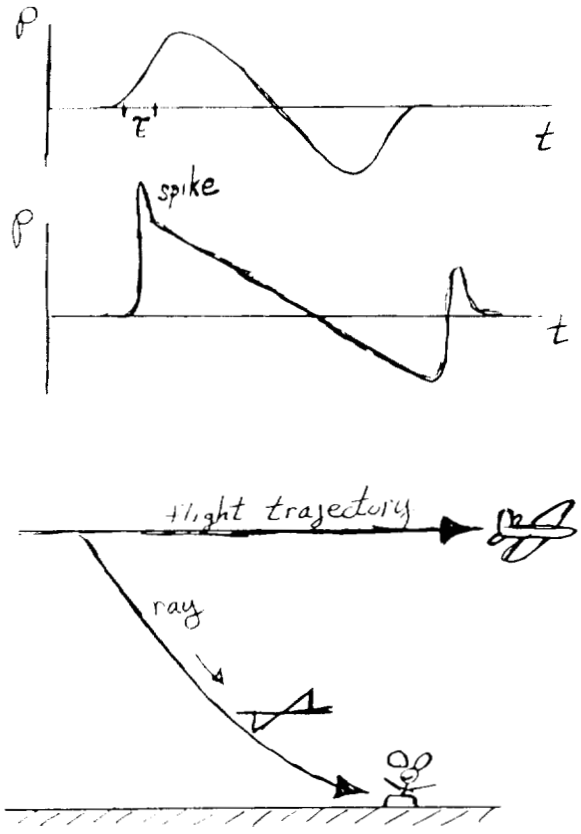

Experiment Reported by Lipkens

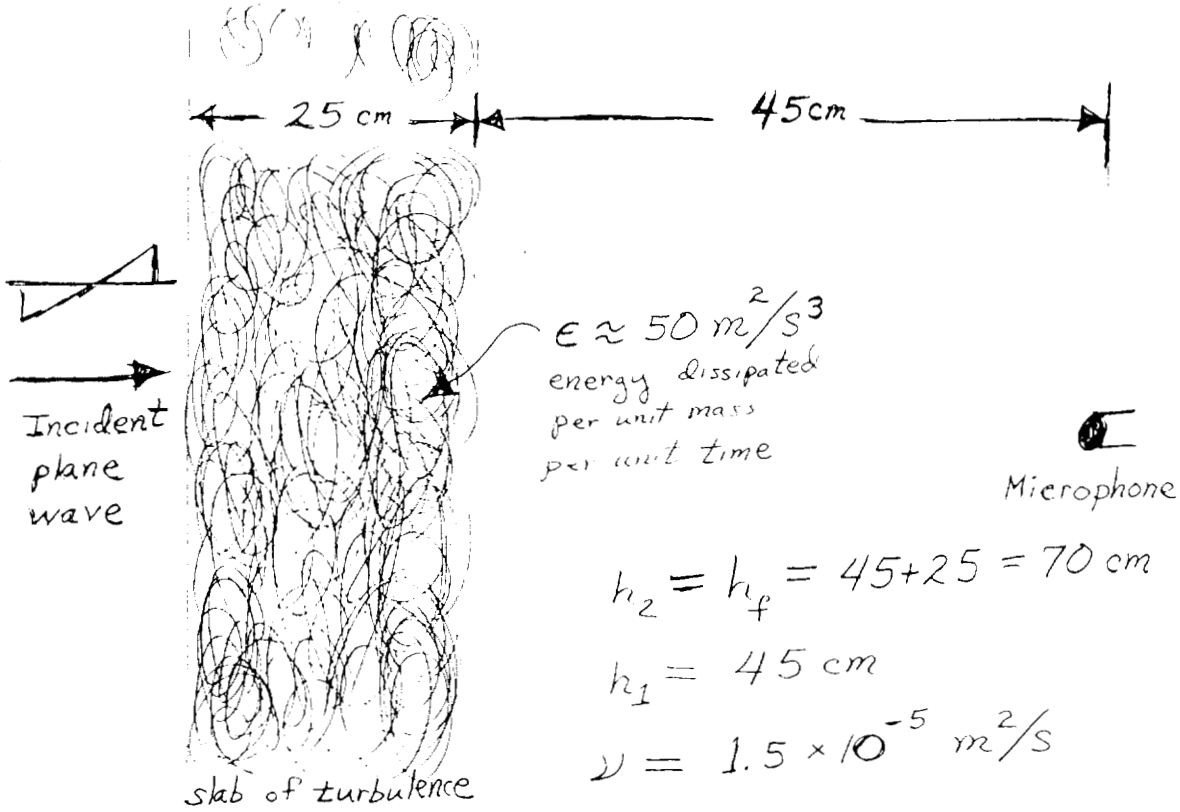

$h_2 = h_f = 45+25 = 70\ cm$

$h_1 = 45\ cm$

$\nu = 1.5 \times 10^{-5}\ m^2/s$

Rise Time Results Reported by Lipkens

First column: conditions of experiment

Second column: calculated value of Crow's characteristic time t_c, proportional to "measured" value of $\epsilon^{4/7}$

Third column: calculated value of rise time according to theory published in JASA in 1971, nearly equal to $2.40t_c$.

Fourth column: measured value of rise time

jet nozzle velocity (m/s)	charact. time (μs)	τ_{Pierce} (μs)	$\tau_{meas.}$ (μs)
12.4	0.23	0.554	0.685
18.3	0.32	0.769	0.745
22.7	0.37	0.889	0.922
26.6	0.41	0.984	1.061
31.3	0.46	1.091	1.308

Lipkens is Surprised

"For the highest jet velocity, the distance where most likely a caustic occurs is 0.556 m"

"The fairly accurate values for the rise time calculated according to Pierce's theory seem a bit surprising since it is based on the passing of the wavefront through multiple caustics."

"In order to calculate σ we assume that the correlation function of the plane jet turbulence is approximated by a Gaussian function as

$$R_{11}(r,0,0) = v^2 \exp\left(\frac{-r^2}{L^2}\right)$$

[L is approximately 3cm, of the order of the width of the slit through which the jet passes.]

White's formula [1964]

$$d_{\text{first caustic}} \approx \left[\frac{2}{c^2}\int_0^\infty \left(\frac{1}{r}\frac{d}{dr}\right)^2 R(r)dr\right]^{-1/3}$$

is extremely sensitive to second derivative at $r = 0$.

Estimate of Distance to First Caustic Based on Patched Structure Function Kolmogoroff + Viscous Subrange

$$d_{\text{first caustic}} \approx \frac{\nu^{7/12}\epsilon^{2/3}}{\epsilon^{5/12}}$$

$$d_{\text{first caustic}} \approx \frac{(1.54 \times 10^{-5})^{7/12}(340)^{2/3}}{(50)^{5/12}}\ \text{m}$$

$$d_{\text{first caustic}} \approx 1.5\,\text{cm}$$

Expected Number of Ray Arrivals at Microphone Location

$$\langle N \rangle = (3)^{1/2} K_c$$

$$K_c = [6.6 \times 10^{-3}] \frac{\epsilon^{5/4}}{\nu^{7/4} c^2} \left[h_2^3 - h_1^3 \right]$$

The important dependence is on the dynamic viscosity $\nu = 1.54 \times 10^{-5}$ m/s^2.

$$K_c \approx 500$$

$$\langle N \rangle \approx 870$$

Current Crisis for Sonic Boom Simulation and for Computational Aeroacoustics

1. Sonic boom shocks can be nearly abrupt, thicknesses of order of 1 m.
2. Propagation through turbulence is 3-D.
3. Turbulence scales of relevance presumably extend down to 10 cm.
4. Propagation is over distances of order of 3000 m.
5. Turbulence is a random process, so simulation must be repeated many times to get a representative ensemble.

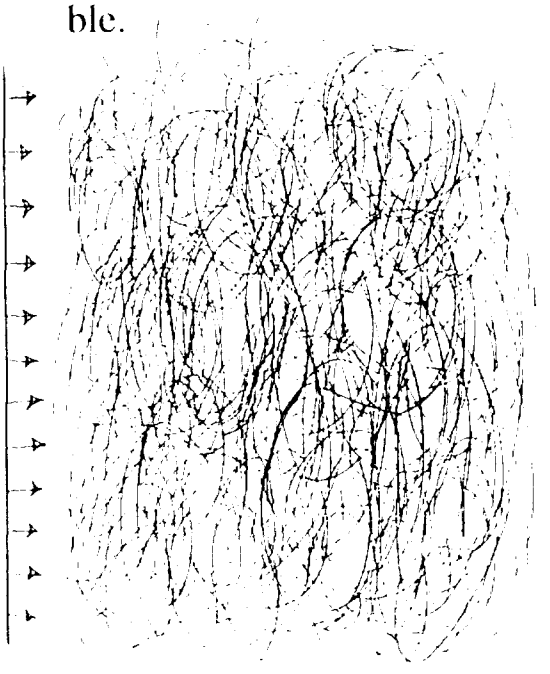

Box of Turbulence

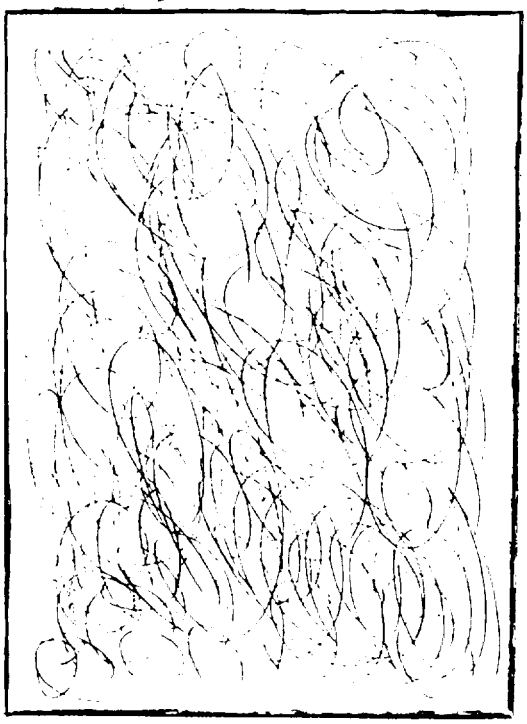

Fluid velocity associated with the turbulence:

$$\vec{\mathbf{v}} = \sum_n \vec{\mathbf{v}}_n e^{i\vec{\kappa}_n \cdot \vec{\mathbf{x}}}$$

Kinetic energy per unit mass averaged over volume:

$$\frac{1}{V}\int_V \tfrac{1}{2}v^2 dV = \left\langle \tfrac{1}{2}v^2 \right\rangle$$

$$= \frac{1}{2}\left(\sum_n \vec{\mathbf{v}}_n \cdot \vec{\mathbf{v}}_n^*\right)$$

$E(\kappa) =$ kinetic energy per unit mass per unit wavenumber,

$$\left\langle \tfrac{1}{2}v^2 \right\rangle = \int_0^\infty E(\kappa)d\kappa$$

Turbulence is Comprised of a Wide Range of Scales

Kolmogoroff microscale:

$\eta \approx 1$ mm

If $\kappa > 1/\eta$,

then viscosity plays a dominant role

Outer scale:

$L_0 \approx$ height above the ground.

We expect the turbulence that primarily affects sonic boom shapes and rise times to be for those wavenumbers where

$$0.1\,\text{m} < \frac{1}{\kappa} < 100\,m$$

$E(\kappa)$ = kinetic energy per unit mass per unit wavenumber,

$$\left\langle \tfrac{1}{2} v^2 \right\rangle = \int_0^\infty E(\kappa) d\kappa$$

Crow's Hypothesis:

All recognizable sonic boom distortion by atmospheric turbulence is associated with the Kolmogoroff inertial range.

$$E(\kappa) \approx C_K \epsilon^{2/3} \kappa^{-5/3}$$

$$C_K \approx 1.6$$

ϵ has units of length^2/time^3 and equals the energy dissipated by viscosity per unit mass per unit time in a turbulent flow, typical magnitude is 0.05 m^2/s^3.

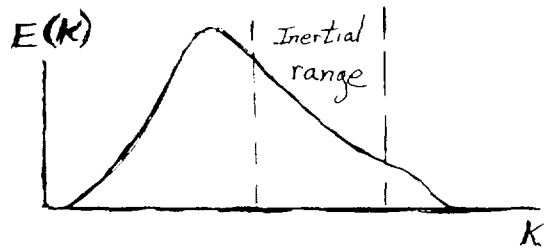

Heuristic Derivation of NPE or KZK Equations begins with Dispersion Relation

$$\omega = c_{00}k; \qquad -i\omega + ic_{00}k = 0$$

dispersion relation => wave equation

$$-i\omega \rightarrow \frac{\partial}{\partial t}; \qquad ik \rightarrow \frac{\partial}{\partial x}$$

Revising sound speed:

(Whitham's rule?)

$$c_{00} \rightarrow c_{00} + c_{\text{turb}} + v_{x,\text{turb}} + \frac{\beta p}{\rho_{00} c_{00}}$$

$$\frac{\partial p}{\partial t} + [VT] + [VRT] + [DT] + \left[c_{00} + c_{\text{turb}} + v_{x,\text{turb}} + \frac{\beta p}{\rho_{00} c_{00}} \right] \frac{\partial p}{\partial x} = 0$$

Burgers's equation (Bateman-Cole)
parabolic equation
KZK equation
NPE
PSUPE

$[VT]$ = viscous dissipation term

$[VRT]$ = vibrational relaxation terms

$[DT]$ = diffraction term

Suggested Method of Simplifying Simulation

Instead of beginning with the simple dispersion relation

$$k = \frac{\omega}{c_{(0)}}$$

in the "heuristic" derivation

begin instead with

$$k = \frac{\omega}{c_{(0)}} + F(\omega)$$

for some approxiate choice of $F(\omega)$ and leave out the small scale turbulence in the term

$$\left[c_{(0)} + c_{\text{turb}} + v_{x,\text{turb}} + \frac{\beta p}{\rho_{(0)} c_{(0)}} \right] p$$

Supposition: $F(\omega)$ depends only on deterministic averages of small scale turbulence.

A stochastic-deterministic problem!

BURPE = BU renormalized propagation equation

Fluid Dynamic Equations

Euler:

$$\frac{D\vec{\mathbf{v}}}{Dt} + \frac{1}{\rho}\vec{\nabla} p = 0$$

Mass:

$$\frac{D\rho}{Dt} + \rho\vec{\nabla}\cdot\vec{\mathbf{v}} = 0$$

No heat transfer:

$$\frac{Ds}{Dt} = 0$$

$$s = s(\rho, p)$$

$$\frac{\partial s}{\partial \rho}\frac{D\rho}{Dt} + \frac{\partial s}{\partial p}\frac{Dp}{Dt} = 0$$

$$c^2 = -\frac{\partial s/\partial \rho}{\partial s/\partial p}$$

Perturbation Formulation

$$p = p_{00} + \Delta p_0 + p'$$

$$\rho = \rho_{00} + \Delta\rho_0 + \rho'$$

$$\vec{\mathbf{v}} = \vec{\mathbf{v}}_0 + \vec{\mathbf{v}}'$$

Keep only first order in acoustic quantities $p', \rho', \vec{\mathbf{v}}'$

Keep up to only second order in turbulent field quantities $\Delta p_0, \Delta\rho_0, \vec{\mathbf{v}}_0$.

Acoustic Wave Equation to Second Order in Turbulent Field

$$\nabla^2 p' + \frac{\omega^2}{c_{00}^2} p' + \mathcal{L}_1(\mathbf{x}, \nabla) p' + \mathcal{L}_2(\mathbf{x}, \nabla) p' = 0$$

where $\mathcal{L}_1(\mathbf{x}, \nabla)$ and $\mathcal{L}_2(\mathbf{x}, \nabla)$ are linear operators involving a sum over spatial derivatives of various orders, with coefficients that are of first and second order, respectively, in the turbulent field quantities.

Example: turbulent flow velocity contribution to the first order perturbation operator

$$\mathcal{L}_1(\mathbf{x}, \nabla) p' = +i \frac{\mathbf{v}_0}{c_{00}} \frac{\omega}{c_{00}} \cdot \nabla p' - \frac{2i}{\omega} \sum_{\sigma,\tau} \frac{\partial v_{0,\sigma}}{\partial x_\tau} \frac{\partial^2 p'}{\partial x_\sigma \partial x_\tau} - \frac{i}{\omega} (\mathbf{v}_0 \cdot \nabla) \nabla^2 p'$$

Obukhov, Kraichnan, Batchelor

Note: $\vec{\nabla} \cdot \vec{\mathbf{v}}$ is regarded as second order because turbulence is a nearly incompressible flow.

Perturbation Solution to Second Order in Turbulent Field

$$p' = Pe^{ikx}\left[1 + \Psi_1 + \Psi_2 + \cdots\right]$$

with the wavenumber k taken of the form

$$k = \frac{\omega}{c_{00}} + k_1 + k_2 + \cdots$$

P is the constant nominal amplitude of the pressure wave.

k is independent of position

Auxiliary condition needed to determine both k and Ψ simultaneously:

spatial average

$$\left\langle \Psi_1(\mathbf{x}) \right\rangle = \lim_{\Delta V \to \infty} \left\{ \frac{1}{\Delta V} \int_{\mathbf{x} \in \Delta V} \Psi_1(\mathbf{x}) dV \right\} = 0$$

and similarly for Ψ_2.

Causality and/or radiation condition: ω has arbitrarily small imaginary positive part so that

$$e^{ikx} \to 0 \quad \text{as} \quad x \to \infty$$

Formal Results for Perturbation Solution to Second Order in Turbulent Field

$$k_2 = \frac{1}{2}\frac{c_{00}}{\omega}\left\langle \mathcal{L}_1\left(\mathbf{x}, i\mathbf{e}_x[\omega/c_{00}] + \nabla\right)\Psi_1 \right\rangle + \frac{1}{2}\frac{c_{00}}{\omega}\left\langle \mathcal{L}_2\left(\mathbf{x}, i\mathbf{e}_x\omega/c_{00}\right)\right\rangle$$

$$k_1 = 0$$

$$\Psi_1 = -\mathcal{H}^{-1}\mathcal{L}_1\left(\mathbf{x}, i\mathbf{e}_x\omega/c_{00}\right)$$

$$\mathcal{H} = \nabla^2 + 2i\frac{\omega}{c_{00}}\frac{\partial}{\partial x}$$

Example: turbulent flow velocity contribution to the first order perturbation operator

$$\mathcal{L}_1(\mathbf{x}, \nabla)p' = +i\frac{\mathbf{v}_0}{c_{00}}\frac{\omega}{c_{00}}\cdot\nabla p' - \frac{2i}{\omega}\sum_{\sigma,\tau}\frac{\partial v_{0,\sigma}}{\partial x_\tau}\frac{\partial^2 p'}{\partial x_\sigma \partial x_\tau} - \frac{i}{\omega}(\mathbf{v}_0\cdot\nabla)\nabla^2 p'$$

Perturbation to Wavenumber for Isotropic Turbulence

$$\Delta k = \frac{\omega}{c_{00}^3} \int_0^\infty \int_0^\pi \frac{\left(\kappa \cos\theta_\kappa + [\omega/c_{00}]\right)^2 E(\kappa)}{\left(\kappa + 2[\omega/c_{00}]\cos\theta_\kappa\right)\kappa} \sin^3\theta_\kappa \, d\theta_\kappa \, d\kappa$$

Correction to wavenumber has form:

$$k_2 = \frac{1}{c_{00}^3} A\omega + \Delta k$$

where Δk is the dispersive term

We are not interested in the numerical value of A, as the first term only renormalizes the sound speed

Factor of $\sin^2\theta_\kappa$ associated with $\nabla \cdot \mathbf{v} \approx 0$

Denominator in integral can be zero. Patch up by replacing

$$\omega \to \omega + i\epsilon, \qquad \epsilon \to 0^+$$

Circumstances when the denominator vanishes

$$\kappa + 2[\omega/c_{00}]\cos\theta_\kappa = 0$$

is Bragg reflection condition.

Recall:

$$\frac{1}{2}\langle v^2 \rangle = \int_0^\infty E(\kappa) d\kappa$$

The Challenge

Given, the "dispersive correction" to the wave number:

$\Delta k =$ weighted integral over $E(\kappa)$

Can you rewrite expression in "elegant manner" so that

$$\Delta k = PFEBR + PFIR$$

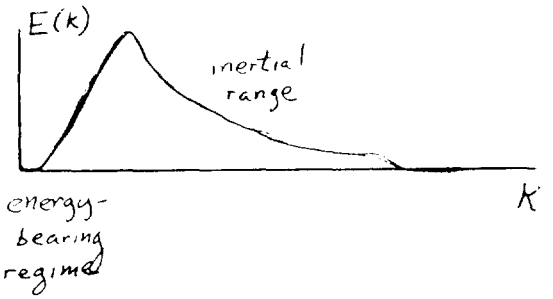

PFEBR = part that depends on $E(\kappa)$ entirely from the energy-bearing regime, the part that is sensitive to the outer scale, or equivalently the part that is dominated by the very small wavenumbers.

PFIR = part that depends on $E(\kappa)$ almost entirely from the higher wavenumber regime, or the inertial range. This is the part where (Kolmogoroff)

$$E(\kappa) \approx C_\kappa \epsilon^{2/3} \kappa^{-5/3}$$

Subtleties:

$$\int_0^\infty G(\kappa)E(\kappa)d\kappa \approx \int_0^\infty G(\kappa)C_\kappa \epsilon^{2/3}\kappa^{-5/3}d\kappa$$

if $G(\kappa) \to 0$ faster than $\kappa^{2/3}$ as $\kappa \to 0$

and if $G(\kappa) \to \infty$ slower than $\kappa^{2/3}$ as $\kappa \to \infty$.

One also uses notion that

$$\int_0^\infty E(\kappa)\frac{1}{\kappa}d\kappa$$

depends primarily on small wavenumbers; it is insensitive to the inertial range.

WAVEFORM FREEZING OF SONIC BOOMS REVISITED[1]

Robin O. Cleveland[2] and David T. Blackstock
Applied Research Laboratories,
The University of Texas at Austin,
P.O. Box 8029,
Austin, TX 78713-8029

SUMMARY

Nonlinear distortion of sonic booms propagating in the atmosphere is strongly affected by stratification and geometrical spreading. For a downward propagating sonic boom in a standard atmosphere, stratification and spreading cause a slowing down of nonlinear distortion. In certain cases a stage is reached where no further distortion takes place. When this happens, the waveform is said to be frozen. In previous work the authors argued that for most HSCT designs and flight conditions being considered, the sonic boom is not frozen when it reaches the ground (*J. Acoust. Soc. Am.* **92**, 2331 (A) (1992)). The criterion used was the value of the distortion distance $\tilde{x}$, which is a measure of the nonlinear distortion suffered by the wave (and is closely related to Hayes's age variable). The aircraft must be at an altitude greater than 27 km (80,000 ft) for $\tilde{x}$ at the ground to be within 95% of its asymptotic value. However, work reported here demonstrates that the ground waveform is much closer to the frozen state than indicated by the previous analysis. In the new analysis, duration of the sonic boom is used as the criterion for judging closeness of approach to the frozen state. In order for the duration of the sonic boom at the ground to be within 95% of its frozen value, the flight altitude of the aircraft needs to be only 15 km (45,000 ft).

[1]Work supported by NASA

[2]Present address: Applied Physics Laboratory, Univ. of Wash. at Seattle, 1013 NE 40th St., Seattle, WA 98105.

INTRODUCTION

Stratification, normally regarded as a deterministic inhomogeneity of the atmosphere, causes large scale refraction or bending of the sound rays. Refraction determines the shape of the primary sonic boom carpet on the ground, produces the secondary carpet, and can cause focusing.[1] Stratification also modifies the effect of nonlinear distortion on the propagating boom. Indeed so-called "freezing" of the sonic boom signature[2, 3, 4] can occur. A frozen waveform is one that is subject to no further nonlinear distortion. The purpose of this paper is to investigate waveform freezing and its relevance to sonic booms.

When this work was initiated about four years ago, it was commonly believed that waveform freezing does occur for sonic booms in the atmosphere.[3] Indeed some HSCT (high speed civil transport) designs took advantage of the benefits of waveform freezing. However, results from the computer code ZEPHYRUS (1991) cast doubt on the belief that freezing is complete by the time the sonic boom reaches the ground.[5] We then performed an analysis of freezing. It was found that while distortion of sonic booms has slowed down by the time the boom reaches the ground, the waveform there does not appear to be frozen.[6, 7] Plotkin coined the term "waveform chilling" as a more accurate description of the distortion slow-down process.[8] In more recent work, however, we have found that the perception of freezing depends on the criterion chosen to assess it.[9, 10]

In this paper the role of spreading and stratification in slowing down distortion is described. First we review the earlier analysis,[6, 7] in which the distortion distance $\tilde{x}$ was used as the criterion by which to measure waveform freezing. Then we show how the conclusions are altered when duration of the sonic boom is used as the criterion. A "lossless" Burgers equation for a stratified medium, combined with weak shock theory and ray theory, is our mathematical model because it provides analytical expressions for the propagation. The analytical expressions are easily analyzed for two illustrative cases: cylindrical waves in a homogeneous atmosphere and cylindrical waves in an isothermal atmosphere.

MATHEMATICAL MODEL

The standard model for the propagation of sonic booms through the atmosphere is a very general form of the Burgers equation.[9] This equation accounts for nonlinear distortion, geometrical spreading, impedance variation, and absorption and dispersion. It is assumed that diffraction and self-refraction are negligible, and that linear ray theory can be used to predict sonic boom ray paths. For a quiet atmosphere the equation is

$$\frac{\partial p'}{\partial s} + \frac{\frac{\partial}{\partial s}S}{2S}p' - \frac{\frac{\partial}{\partial s}(\rho_0 c_0)}{2\rho_0 c_0}p' - \frac{\beta}{2\rho_0 c_0^3}\frac{\partial p'^2}{\partial t'} = l(t')p' \,. \tag{1}$$

Here p' is acoustic pressure, s distance along the ray tube, S ray tube area, $t' = t - \int \frac{\mathrm{d}s}{c_0}$ retarded time, c_0 small-signal sound speed, ρ_0 ambient density, β the coefficient of nonlinearity, and $l(t)$ an operator describing the absorption and dispersion. The effect of a motion of the medium has been considered elsewhere.[3, 5]

In this work weak shock theory[11] is used to account for losses at shocks and to keep the waveform singlevalued. Because ordinary losses are ignored, the right-hand side of Eq. 1 may be dropped. The resulting "lossless" Burgers equation,

$$\frac{\partial p'}{\partial s} + \frac{\frac{\partial}{\partial s}S}{2S}p' - \frac{\frac{\partial}{\partial s}(\rho_0 c_0)}{2\rho_0 c_0}p' = \frac{\beta}{2\rho_0 c_0^3}\frac{\partial p'^2}{\partial t'} \,, \tag{2}$$

has an analytical solution (Eq. 1 does not), use of which greatly simplifies the ensuing analysis.

POISSON SOLUTION

The use of weak shock theory to account for shock losses in an otherwise lossless fluid is described in this section. For plane waves in a homogeneous medium Eq. 2 becomes

$$\frac{\partial p'}{\partial x} = \frac{\beta}{2\rho_0 c_0^3} \frac{\partial p'^2}{\partial t'} , \tag{3}$$

where x is the propagation distance. An implicit solution of this equation is a variant of the Poisson solution; see, e.g., [12]. If the source excitation is $p'(0,t) = f(t)$, the solution of Eq. 3, is

$$p'(x,t') = f\left(t' + \frac{\beta x p'}{\rho_0 c_0^3}\right) . \tag{4}$$

The argument $t' + \beta x p'/\rho_0 c_0^3$ may be thought of as the phase of the wave. The first term moves the reference frame along at the small-signal sound speed (the small-signal solution is $p'(x,t') = f(t')$). The second, or distortion, term describes the nonlinear distortion the wave suffers as it propagates. The distortion term may be rewritten as $\beta x u/c_0^2$, where u is the particle velocity. The factor $\beta x/c_0$ has dimensions of time and is a simple form of what Hayes calls the age variable.[3]

Because losses are not included in Eq. 4, multivalued waveforms are usually predicted. Figure 1 shows this effect for an N wave (a reasonable model of a sonic boom). The left-hand sketch shows the source waveform. The right-hand sketch shows, for various model solutions, the waveform away from the source. The dotted line is the linear-theory prediction. The dashed lined shows the waveform based on Eq. 4 (the Poisson solution). The solid line shows the physically meaningful waveform recovered by using *weak shock theory* (see, e.g., [11, 13]) to remove multivaluedness. Shocks (discontinuities) are located at points determined by the Rankine-Hugoniot relations.

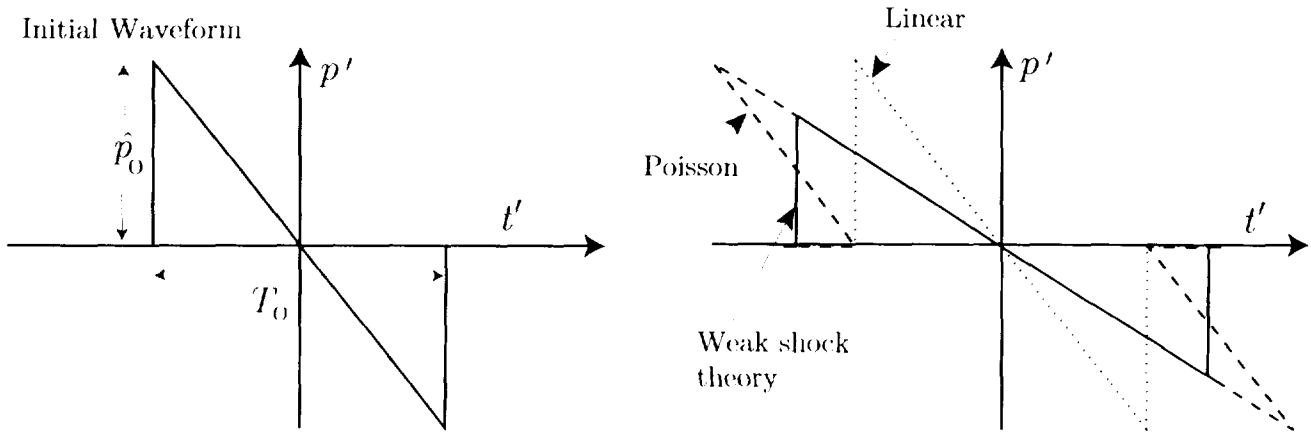

Figure 1: Finite-amplitude distortion of an N wave.

GENERAL SOLUTION

The general solution of Eq. 2 may be obtained by transforming the equation into one which has the same form as the plane wave equation, Eq. 3. Two transformations are required. First, a new dependent variable q (a scaled pressure) is defined,

$$q = \sqrt{\frac{\overline{\rho_0}\,\overline{c_0}\,\overline{S}}{\rho_0\, c_0\, S}}\, p' \,, \tag{5}$$

where an overbar is used to denote a value at the source.[3] This transformation may be deduced from the fact that in a ray tube the energy flow, which is proportional to $Sp'^2/\rho_0 c_0$, is constant. The transformation thus compensates for any amplification or diminution to which a small-signal, lossless wave would be subject. Equation 2 becomes

$$\frac{\partial q}{\partial x} = \frac{\beta}{2\overline{\rho_0}\,\overline{c_0}^3}\sqrt{\frac{\overline{S}\,\overline{\rho_0}\,\overline{c_0}^5}{S\,\rho_0\, c_0^5}}\,\frac{\partial q^2}{\partial t'} \,, \tag{6}$$

which has a form similar to that of Eq. 3 except that the coefficient of the right hand side is not constant. The second transformation removes the spatial dependence of the coefficient. If a new independent variable $\tilde{x}$ (a scaled distance) is introduced,

$$\tilde{x} = \int_0^s \sqrt{\frac{\overline{S}\,\overline{\rho_0}\,\overline{c_0}^5}{S\,\rho_0\, c_0^5}}\,\mathrm{d}s' \,, \tag{7}$$

Eq. 6 becomes

$$\frac{\partial q}{\partial \tilde{x}} = \frac{\beta}{2\overline{\rho_0}\,\overline{c_0}^3}\,\frac{\partial q^2}{\partial t'} \,, \tag{8}$$

which has the same form as Eq. 3. In terms of the new variables, the Poisson solution of Eq. 8 is

$$q(s, t') = f(t' + \frac{\beta\,\tilde{x}\,q}{\overline{\rho_0}\,\overline{c_0}^3}) \,. \tag{9}$$

This solution is similar to Eq. 4 except that the actual distance x in the distortion component of the phase term is replaced by the scaled distance $\tilde{x}$. The scaled distance is hereinafter called the *distortion distance* because $\tilde{x}$ plays the same role in determining the amount of distortion in the general case as the true distance x does for plane waves. The distortion distance is equivalent to Hayes's age variable.

[3]Other authors may use the ground as a reference point.

CYLINDRICAL SPREADING

Here we present the first of two examples to illustrate the slowing of nonlinear distortion. In one case waveform freezing does not occur; in the other case it does. The examples have direct relevance to sonic boom propagation. In the absence of refraction the spreading of a sonic boom is cylindrical. Therefore first consider a cylindrically spreading wave in a homogeneous medium.

In this case ρ_0 and c_0 are constant (overbars for these quantities are therefore omitted), the rays are straight lines, and the ray tube area is proportional to r (distance s along the ray tube is the radial distance $r - r_0$, where r_0 is the source radius). See Fig. 2. Equations 5 and 7 become

$$q = \sqrt{\frac{r}{r_0}}p' , \tag{10}$$

$$\tilde{x} = 2\sqrt{r_0}(\sqrt{r} - \sqrt{r_0}) , \tag{11}$$

respectively. The first relation shows that q is the acoustic pressure, scaled to compensate for cylindrical spreading. When the second relation is combined with Eq. 9, the result is

$$q(r, t') = f\left(t' + \frac{\beta 2\sqrt{r_0}(\sqrt{r} - \sqrt{r_0})q}{\rho_0 c_0^3}\right) . \tag{12}$$

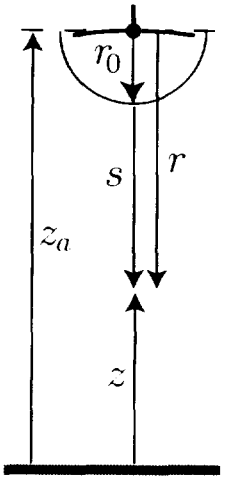

Figure 2: Cylindrical coordinate system.

The distortion grows as $2\sqrt{r_0}(\sqrt{r} - \sqrt{r_0})$ (in place of the factor x that appears in Eq. 4). Thus cylindrical waves distort more gradually than do plane waves. Note, however, that although the distortion grows ever more slowly as distance increases, the growth never ceases altogether. For this case, therefore, waveform freezing does not occur.

ISOTHERMAL ATMOSPHERE

Now let the cylindrical wave propagate in an isothermal atmosphere. Since in such an atmosphere the sound speed does not change with altitude, no overbar on c_0 is needed. The static condition for the atmosphere is $\frac{dp_0}{dz} = -\rho_0 g$, where z is altitude (positive upward); see Fig. 2. We solve this equation for an ideal gas, $p_0 = \rho_0 R T_0$, noting that T_0 is constant for an isothermal atmosphere. The density is found to be $\rho_0(z) = \rho_g e^{-z/H}$, where ρ_g is the density at the ground and $H = RT_0/g$ is the *scale height* of the atmosphere. The universal gas constant is $R = 287\ \mathrm{J/(kg \cdot K)}$ for air and gravitational acceleration is taken to be $g = 9.81\ \mathrm{ms}^{-2}$. For $T_0 = 240$ K (average ambient temperature in the lower 17 km of the atmosphere), the scale height is $H = 7.0$ km.

Consider a cylindrical wave propagating straight downward through an isothermal atmosphere. For this case the distance traveled is $r = z_a - z$ (positive downward) where z_a is the altitude of the aircraft (see Fig. 2). If the source radius is r_0 the density increases with propagation distance as $\rho_0 = \overline{\rho_0} e^{(r-r_0)/H}$. The expressions for q and $\tilde{x}$ are found to be

$$q = \sqrt{\frac{r}{r_0}} e^{(r-r_0)/2H}\, p' , \tag{13}$$

$$\tilde{x} = \sqrt{2\pi H r_0}\, e^{r_0/2H} (\mathrm{erf}\sqrt{r/2H} - \mathrm{erf}\sqrt{r_0/2H}) . \tag{14}$$

Notice that the distortion distance $\tilde{x}$ does *not* increase indefinitely with propagation distance r ($\lim_{r\to\infty} \mathrm{erf}(\sqrt{r/2H}) = 1$) but instead only approaches the asymptotic value

$$\tilde{x}_{\max} = \sqrt{2\pi H r_0}\, e^{r_0/2H} (1 - \mathrm{erf}\sqrt{r_0/2H}) . \tag{15}$$

Equation 9, with s replaced by $r - r_0$ and $\tilde{x}$ given by Eq. 14, now applies. It is seen that in this case the distortion has an upper bound. In the limit as $r \to \infty$, the solution is

$$\lim_{r\to\infty} q(r, t') = f\left(t' + \frac{\beta\, \tilde{x}_{\max}\, q}{\overline{\rho_0} c_0^3}\right) . \tag{16}$$

Because $\tilde{x}_{\max}$ is a constant, the phase term has no explicit dependence on r. The propagation is like that for a small-signal wave. Distortion, although present (as indicated by the dependence of the phase on q), no longer changes with distance: the waveform is frozen.

COMPARISON OF DISTORTION DISTANCES

The two example solutions are now used to investigate the phenomenon of waveform freezing. The role of propagation distance on the distortion is seen by examining the distortion distance for each case. In Fig. 3 the distortion distance is plotted against the actual path length (1) for plane waves in a homogeneous medium, (2) for cylindrical waves in a homogeneous medium, and (3) for cylindrical waves in an isothermal atmosphere. To mimic downward travel of sonic booms through the atmosphere, we have expressed propagation distance downward along the vertical axis.

For case 1, we see that 4 km of propagation yields 4 km worth of distortion. For case 2, 24 km of propagation is required to yield the same amount of distortion. For case 3 the wave can never distort as much as a plane wave does at 4 km. In fact the maximum distortion is only equal to that of a plane wave that has traveled 2.6 km. Waveform freezing therefore occurs for case 3. Nevertheless, a propagation distance of at least 25 km is required for the distortion distance in case 3 to approach its asymptote. This is the first indication that for an aircraft at an altitude of 17 km the sonic boom on the ground is only chilled, not frozen.

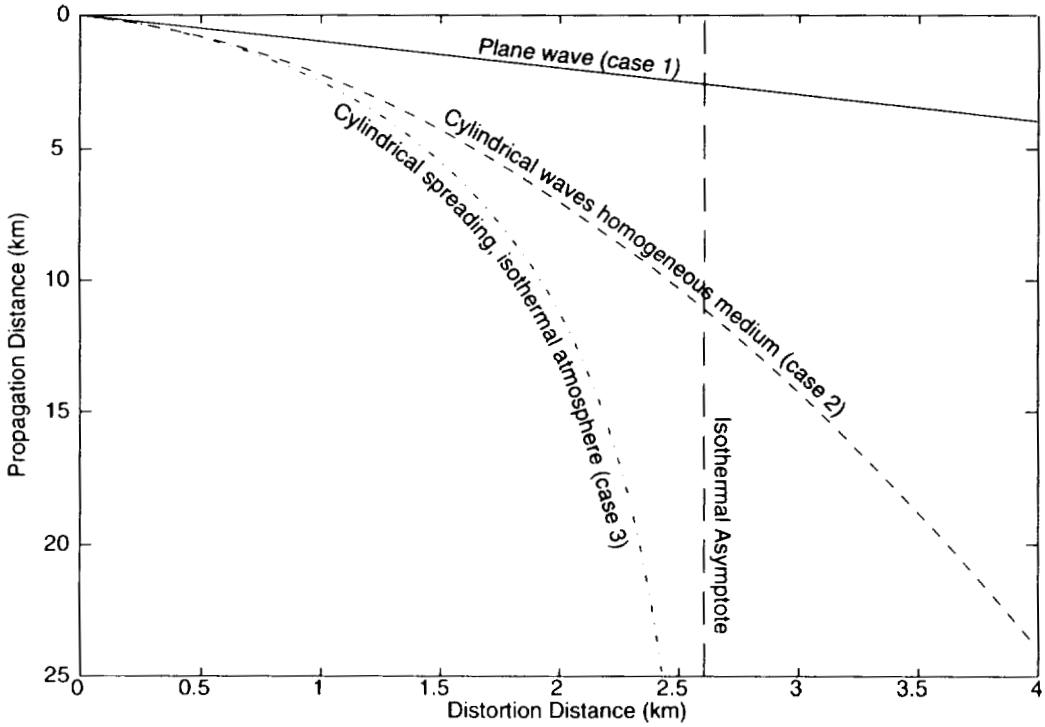

Figure 3: Comparison of distortion distances for plane waves, cylindrical waves, and cylindrical waves in an isothermal atmosphere.

EFFECTIVE COEFFICIENT OF NONLINEARITY

A physical explanation for the slowing of nonlinear distortion is that the wave appears to propagate in a medium with a decreasing coefficient of nonlinearity. To see this, inspect the nonlinear term in the scaled wave equation, Eq. 6. For plane waves in a homogeneous medium, Eq. 6 reduces to Eq. 3:

$$\frac{\partial p'}{\partial x} = \frac{\beta}{2\rho_0 c_0^3} \frac{\partial p'^2}{\partial t'} ,$$

For cylindrical waves in a homogeneous medium the equation is

$$\frac{\partial q}{\partial r} = \frac{\beta\sqrt{\frac{r_0}{r}}}{2\rho_0 c_0^3} \frac{\partial q^2}{\partial t'} , \tag{17}$$

and for cylindrical waves in an isothermal atmosphere

$$\frac{\partial q}{\partial r} = \frac{\beta\sqrt{\frac{r_0}{r}} e^{-(r-r_0)/2H}}{2\overline{\rho_0} c_0^3} \frac{\partial q^2}{\partial t'} . \tag{18}$$

We now define an effective coefficient of nonlinearity β_{eff} as β times the function of r in the numerator of the right-hand side of Eqs. 3, 17, and 18. All three equations then have the same form:

$$\frac{\partial q}{\partial x} - \frac{\beta_{\text{eff}}}{2\overline{\rho_0}\,\overline{c_0}^3} \frac{\partial q^2}{\partial t'} = 0 , \tag{19}$$

For plane waves β_{eff} is a constant ($= \beta$). The expression for cylindrical waves, $\beta_{\text{eff}} = \beta\sqrt{r_0/r}$, suggests a medium in which the coefficient of nonlinearity decreases as $1/\sqrt{r}$. Similarly, the expression for cylindrical waves in an isothermal atmosphere, $\beta_{\text{eff}} = \beta\sqrt{r_0/r}e^{-(r-r_0)/2H}$ suggests a medium in which the nonlinearity coefficient decreases as $e^{-r/2H}/\sqrt{r}$. These interpretations provide a new perspective on the slowing down of distortion: The tendency of a wave to distort, as measured by β_{eff}, changes with distance. In particular, if $\beta_{\text{eff}} \to 0$, waveform freezing occurs.[4]

[4]Stratification does not always cause distortion to slow down. For an upward propagating wave distortion accelerates, i.e., β_{eff} increases with propagation distance.

WAVEFORM FREEZING: CRITERION 1

The concept of an effective coefficient of nonlinearity is easily extended to include all changes in cross sectional area and properties of the medium. Equation 6 shows that the general definition of β_{eff} should be

$$\beta_{\text{eff}} = \beta \sqrt{\frac{\overline{S}\,\overline{\rho_0}\,\overline{c_0}^5}{S\,\rho_0\,c_0^5}}\,. \tag{20}$$

Recall that Eq. 6 was solved by introducing the distortion distance transformation to replace the varying coefficient of nonlinearity with a constant β, the actual coefficient of nonlinearity. The relationship between $\tilde{x}$ and β_{eff} is

$$\int_0^s \beta_{\text{eff}}\,\mathrm{d}s = \beta\,\tilde{x} \tag{21}$$

Note that β_{eff} is independent of the source waveform or amplitude. Whether the waveform freezes then depends on whether the infinite integral of β_{eff} (or equivalently the distortion distance) is bounded. The integral is proportional to the age variable introduced by Hayes *et al.*[3] In the case of cylindrical waves, the integral is proportional to $\sqrt{r}$, a result implying that distortion, while slowing down as propagation distance increases, never comes to a full stop. For cylindrical waves traveling downward in an isothermal atmosphere, however, the integral approaches a finite value as $r \to \infty$. In this case the waveform freezes.

It should be noted that, as appropriate for the lower atmosphere, β has been treated as a constant in this analysis. For a medium in which β varies, such as the ocean, the variation may be accounted for by replacing β in Eq. 20 by $\overline{\beta}(\beta/\overline{\beta})$,[14] where the overbar denotes a reference value, usually the value at the source.

Strictly a waveform freezes only when $s = \infty$. What we seek is a criterion for the distance beyond which further distortion is small. Our first criterion is based on the distortion distance itself. A waveform is considered to be frozen when $\tilde{x}$ reaches a value such that

$$\tilde{x}/\tilde{x}_{\text{max}} > 0.95\,. \tag{22}$$

The appeal of this criterion is that it is independent of the waveform. Freezing is determined solely by spreading and the stratification of the medium.

APPLICATION TO THE ATMOSPHERE

The foregoing analysis is now applied to the atmosphere. For simplicity a quiet medium is assumed. Attention is restricted to the atmosphere below the expected cruise altitude of the HSCT aircraft, about 17 km (roughly 55,000 ft). Figure 4 shows the sound speed and density profiles (solid lines) for the U. S. Standard Atmosphere.[15] Although an analysis of waveform freezing could have been done for this model of the atmosphere, much of the calculation would have had to be done numerically. We chose instead to assume an isothermal atmosphere because for it the distortion distance may be expressed analytically. The sound speed and density profiles for the isothermal atmosphere are shown as dashed lines in Fig. 4. The sound speed corresponding to the average temperature ($T_0 = 240$ K) is $c_0 = 311$ m/s. The isothermal model is seen to be a reasonable approximation of the U. S. Standard Atmosphere. A more realistic atmosphere, one with a bilinear temperature profile, is treated in Refs. 6 and 9; the conclusions about waveform freezing are not materially different from those reached here.

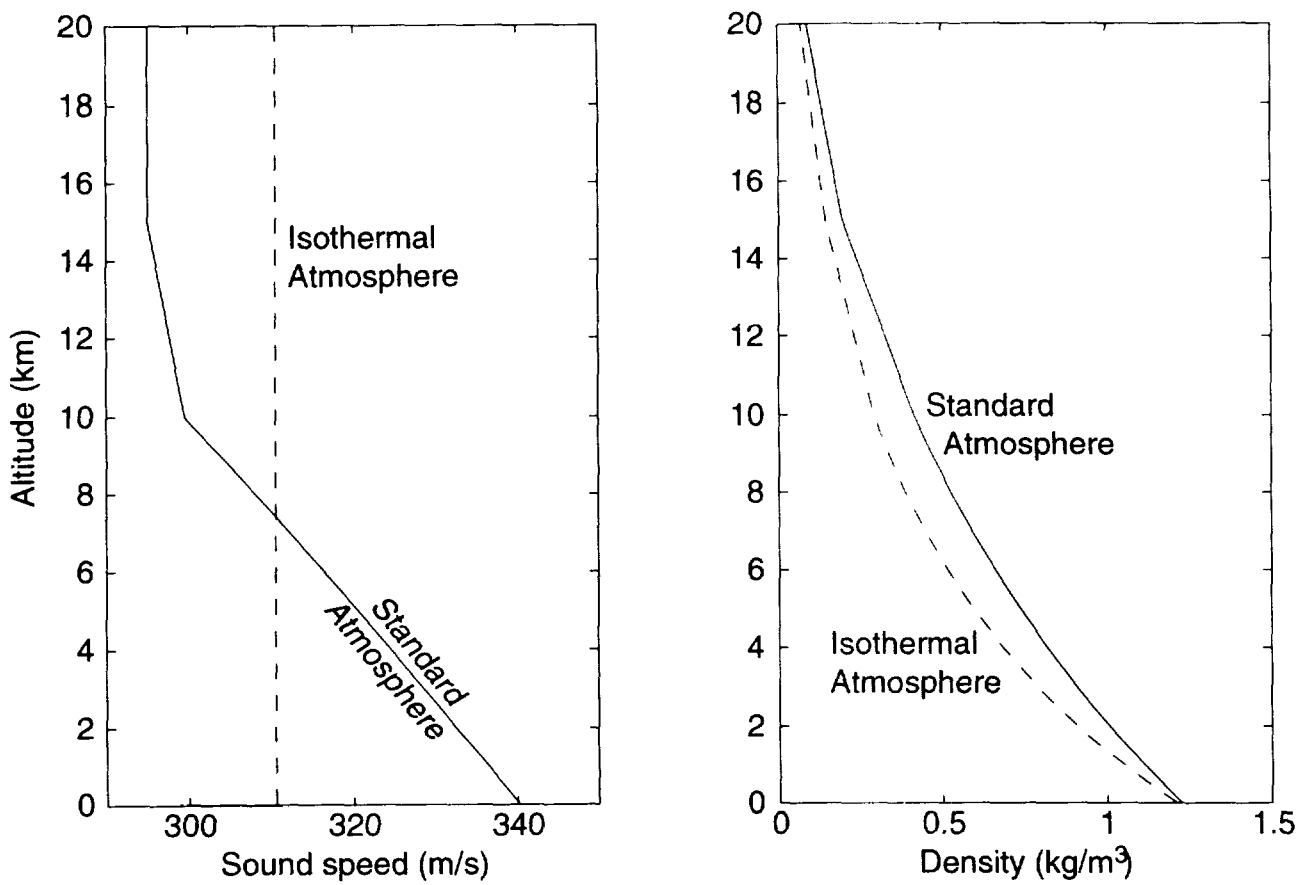

Figure 4: The profiles for the standard atmosphere and the isothermal atmosphere used in this paper.

To make the analysis more general, we drop the restriction to straight downward propagation and consider other ray paths. Rays can be by uniquely determined by the Mach cone and an azimuthal angle ϕ. The configuration for a ray coming off a Mach cone is shown in Fig. 5. The grazing angle θ_0 is given by $\cos\theta_0 = \cos\psi \cdot \cos\phi$, where ψ is the angle of the Mach cone. For downward propagation we define θ_0 to be negative. If the propagation distance along a ray is s (from the source), the change in altitude is $\Delta z = s \sin\theta_0$. The ray tube area for cylindrical spreading is given by

$$\frac{S}{\overline{S}} = \frac{s + s_0}{s_0},$$

where s_0 is a reference path length, e.g., source radius. "Source" sonic boom signatures are given at a distance ζ, a few body lengths beneath the aircraft (ζ is negative), and $s_0 = \zeta / \sin\theta_0$.

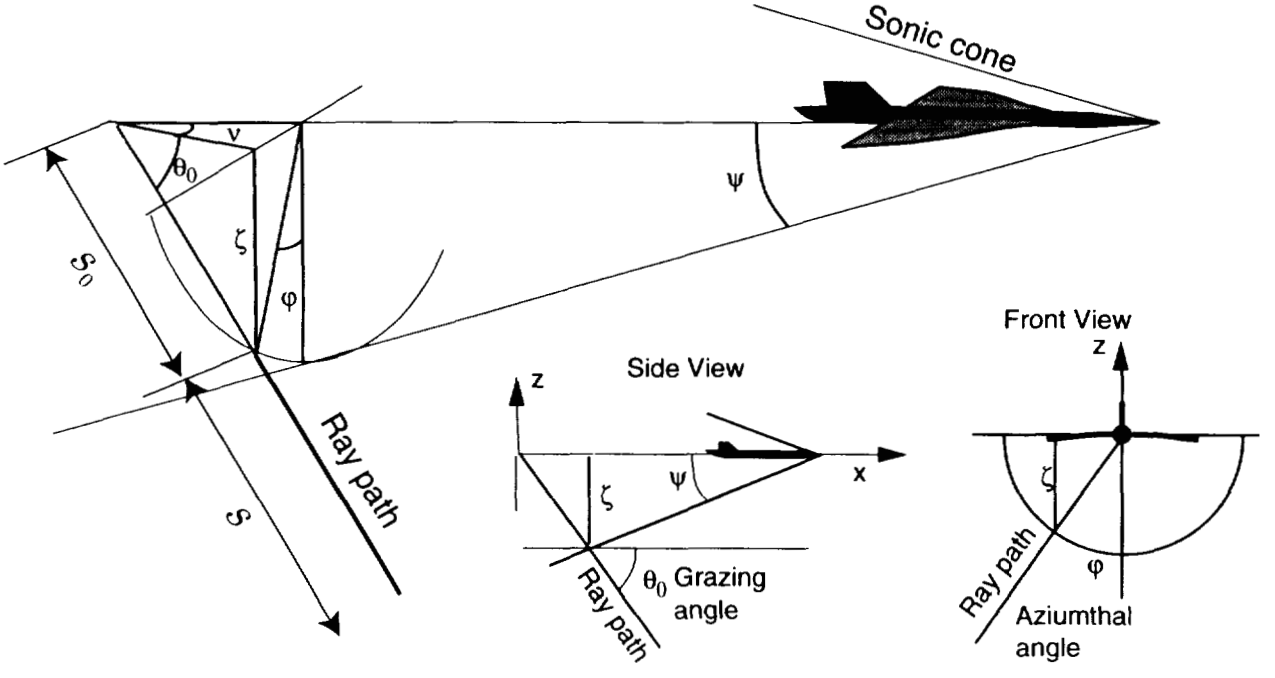

Figure 5: Ray angles from a sonic cone.

For a sonic boom in an isothermal atmosphere the expressions for q and $\tilde{x}$ are

$$q = \sqrt{\frac{s+s_0}{s_0}} e^{-s\sin\theta_0/2H}\, p' , \tag{23}$$

$$\tilde{x} = \sqrt{\frac{2\pi H s_0}{\sin(-\theta_0)}} e^{s_0\sin(-\theta_0)/2H} \left(\operatorname{erf}\sqrt{\frac{(s+s_0)\sin(-\theta_0)}{2H}} - \operatorname{erf}\sqrt{\frac{s_0\sin(-\theta_0)}{2H}} \right) , \tag{24}$$

respectively. Since θ_0 is negative for downward propagating rays, the minus sign inside the square root is acceptable. For straight downward ($\theta_0 = -\pi/2$) cylindrical propagation, where r is the radial distance and r_0 is the source radius, Eqs. 23 and 24 reduce to Eqs. 13 and 14.

Examination of Eq. 24 shows that the asymptotic value of the distortion distance is

$$\tilde{x}_{\max} = \sqrt{\frac{2\pi H s_0}{\sin(-\theta_0)}} e^{s_0\sin(-\theta_0)/2H} \left(1 - \operatorname{erf}\sqrt{\frac{s_0\sin(-\theta_0)}{2H}} \right) .$$

If the distortion distance is normalized by $\tilde{x}_{\max}$, we can see how the distortion along each ray approaches its asymptotic value. In subsequent plots $\tilde{x}_{\max}$ is used to normalize the distortion distance. Recall that freezing is deemed to have occurred once the distortion distance has reached 95% of its maximum value.

The normalized distortion curves for straight downward propagation ($\phi = 0$) from an aircraft flying at Mach 2 are shown in Fig. 6. It is apparent that for aircraft at the HSCT altitude waveform the sonic boom is not frozen when it reaches the ground (as shown below, this conclusion is almost independent of Mach number and azimuthal angle). For an aircraft at 17 km the distortion distance at the ground is about 87% of the maximum value. If a greater percentage is to be achieved, the aircraft has to fly higher. The 95% figure requires a flight altitude of 27 km.

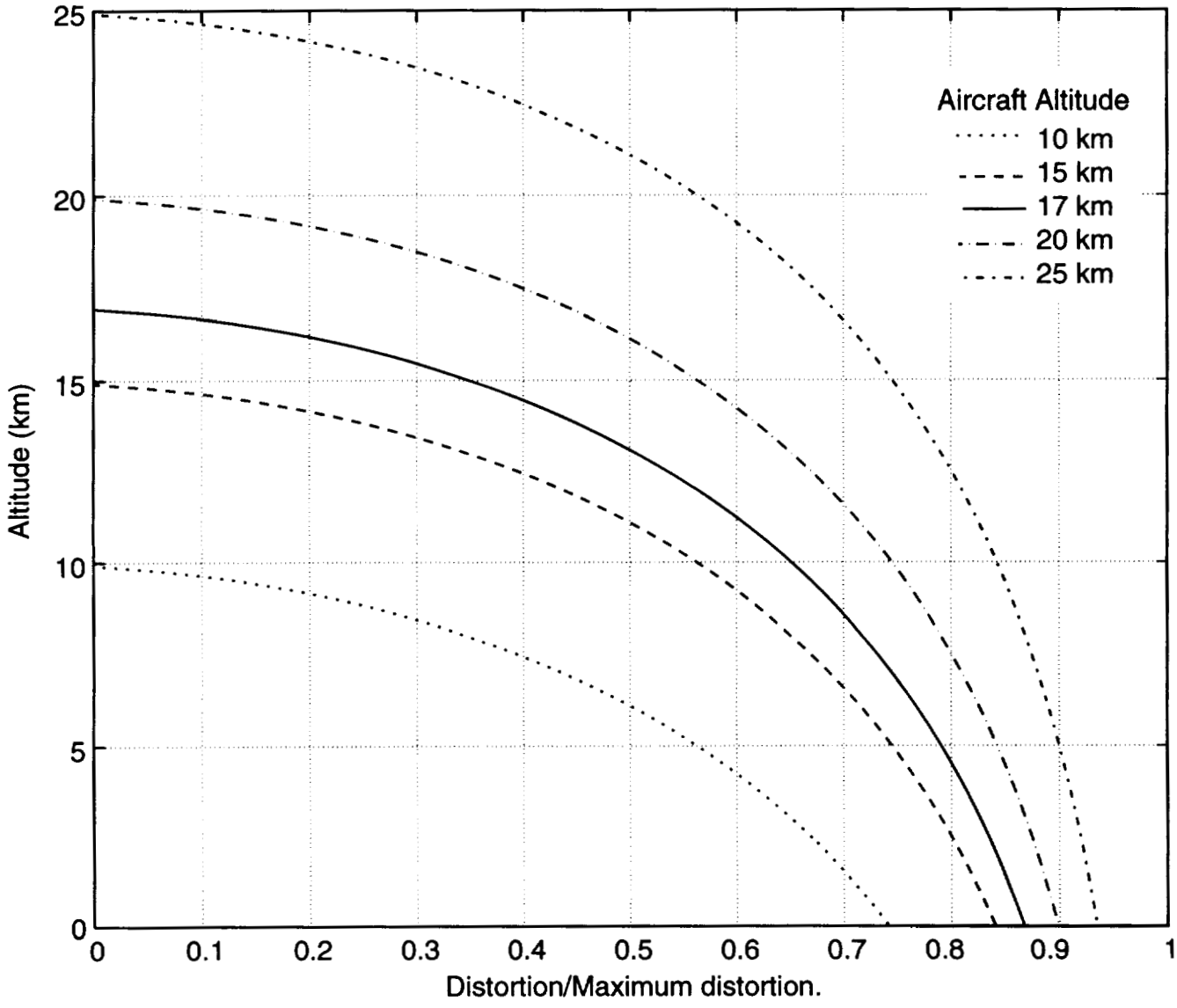

Figure 6: Normalized distortion distance for aircraft at various altitudes.

EFFECT OF MACH NUMBER AND AZIMUTHAL ANGLES ON FREEZING

Figure 7 shows the freezing fraction at the ground as a function of Mach number, for various azimuthal angles. As Mach number is reduced (or ϕ is increased), more spreading occurs because increases the ray path to the ground is longer. Nevertheless, varying the Mach number has virtually no effect on freezing except at very low Mach numbers. The variation with ϕ is also small. It appears then that spreading has very little effect on the onset of freezing. The major parameter controlling the occurrence of freezing is the density variation between the source and the ground. Therefore if a boom is to be closer to freezing at the ground, the aircraft must fly higher.

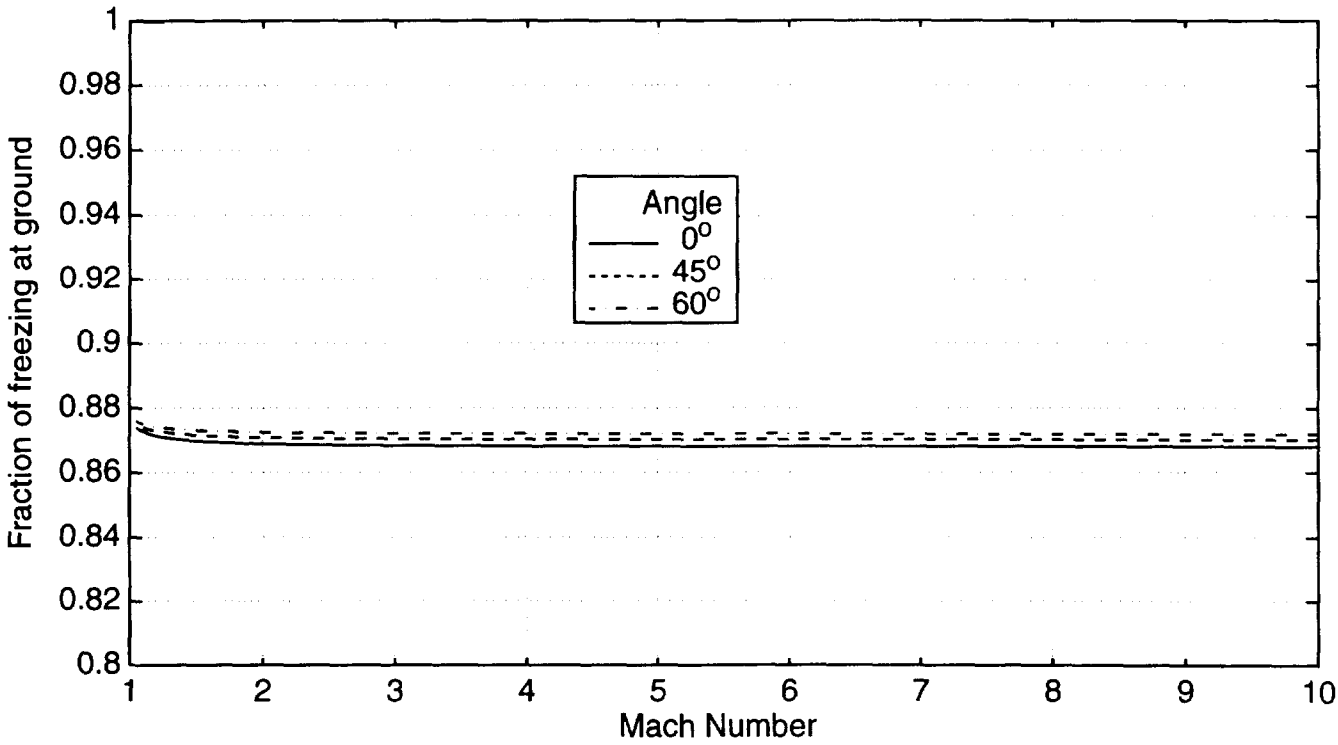

Figure 7: Closeness to waveform freezing at the ground using criterion 1, as a function of Mach number and azimuthal angle.

Having analyzed waveform freezing by using distortion distance as the criterion for determining whether freezing actually occurs, we now test the results qualitatively. Figure 8 shows the source, ground, and frozen waveforms for an N wave in an isothermal atmosphere. The source is a Mach 2 aircraft at 17 km, and values $\phi = 0$, $\zeta = 100$ m, peak amplitude $\hat{p}_0 = 300$ Pa, and duration $T_0 = 100$ ms have been used. Although the distortion distance at the ground is only 87% of $\tilde{x}_{\max}$, the ground waveform itself nevertheless closely resembles the frozen waveform. In fact the duration T at the ground is 95% of that for the frozen waveform. This leads us to consider using a different criterion for judging the extent of freezing, namely, some important characteristic of the waveform itself. For sonic booms an obvious choice is the duration of the boom. In the last part of this paper the use of duration as an alternative criterion is explored.

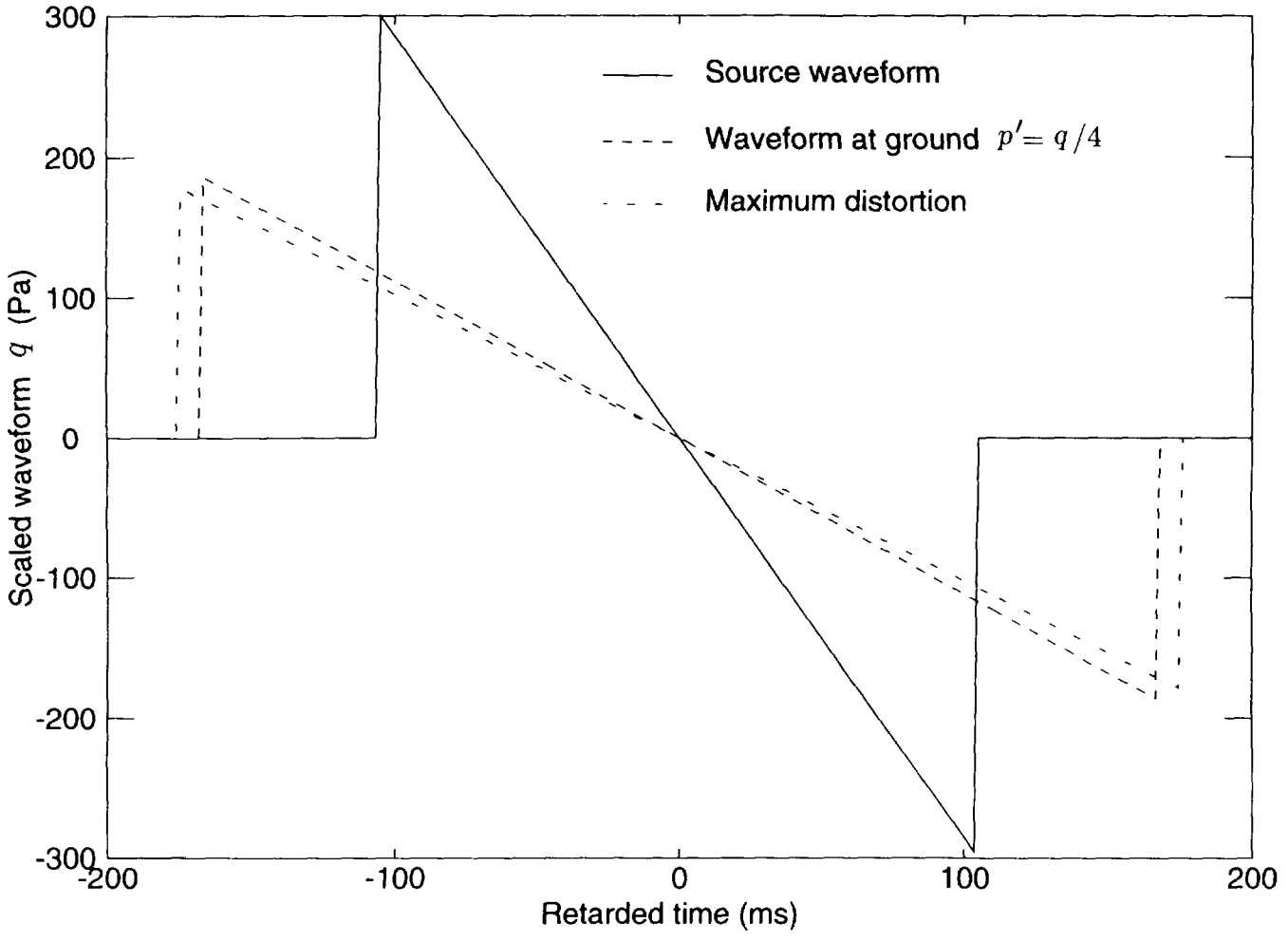

Figure 8: The distortion of a model sonic boom in the isothermal atmosphere.

SONIC BOOM DURATION: FREEZING CRITERION 2

We now show why using sonic boom duration as the criterion changes the conclusion about freezing at the ground. The sonic boom is modeled as an N wave. The duration T of a plane N wave varies with propagation distance as follows:[12]

$$T = T_0\sqrt{1 + ax}\ .$$

Here T_0 is the duration of the N wave at the source, a is the constant $2\beta\hat{p}_0/\rho_0 c_0^3 T_0$, and $\hat{p}_0$ is the peak pressure at the source.[5] For a nonplanar N wave in an inhomogenous medium the result generalizes to

$$T = T_0\sqrt{1 + \bar{a}\tilde{x}}\ ,$$

where $\tilde{x}$ is the distortion distance and $\bar{a} = 2\beta\hat{p}_0/\overline{\rho_0}\,\overline{c_0}^3 T_0$ is based on conditions at the source. When the waveform freezes, the duration has its maximum value,

$$T_{\max} = T_0\sqrt{1 + \bar{a}\tilde{x}_{\max}}\ .$$

We base our second criterion for waveform freezing on the normalized duration $T/T_{\max}$,

$$\left(\frac{T}{T_{\max}}\right) = \sqrt{\frac{1 + \bar{a}\tilde{x}}{1 + \bar{a}\tilde{x}_{\max}}}\ .$$

In particular, the second criterion is taken to be

$$T/T_{\max} > 0.95\,. \tag{25}$$

The distortion distance at which this criterion is met is

$$\frac{\tilde{x}}{\tilde{x}_{\max}} = 0.9025 - \frac{0.0975}{\bar{a}\tilde{x}_{\max}}\ .$$

That is, using the duration criterion, waveform freezing occurs when the distortion distance is only at 90% of its maximum value. For cases in which $\bar{a}\tilde{x}_{\max}$ is small, freezing (as determined by N wave duration) occurs even sooner.

[5]Note: $a = 1/\pi\bar{x}$, where $\bar{x}$ is the shock formation distance for a sinusoidal wave of peak pressure $\hat{p}_0$ and period T_0.

FREEZING BASED ON CRITERION 2

Figure 9 is a repeat of Fig. 6, but this time the horizontal axis is normalized duration instead of normalized distortion distance. For this plot the source N wave properties are $\hat{p_0} = 300$ Pa, $T_0 = 200$ ms. Other conditions are the same as for Fig. 6. The table below lists both $\tilde{x}/\tilde{x}_{\max}$ and $T/T_{\max}$ for various altitudes. If criterion 1 is used, the aircraft has to be at an altitude of 27 km for freezing to occur. If criterion 2 is used, the altitude can be as low as 10 km.

Altitude	$\tilde{x}/\tilde{x}_{\max}$	$T/T_{\max}$
10 km	0.729	0.947
17 km	0.869	0.957
25 km	0.939	0.974

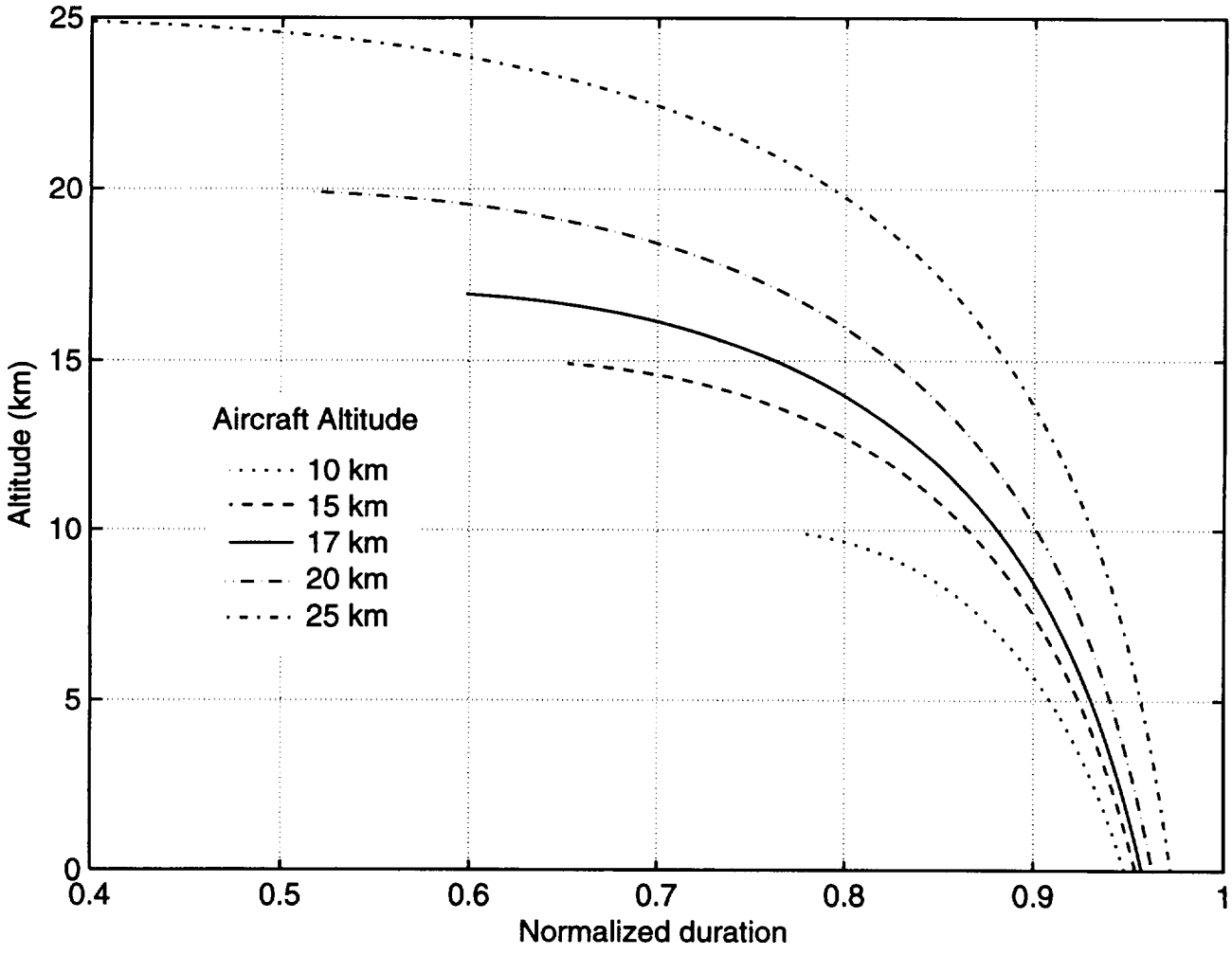

Figure 9: Normalized distortion using criterion 2 for aircraft at various altitudes.

The drawback to the use of duration as the criterion for waveform freezing is that the results vary with source conditions, i.e., the results are waveform dependent. For N waves the important source characteristic is the ratio of duration to peak pressure. Figure 10 shows the minimum altitude at which the ground waveform is frozen as a function of $T_0/\hat{p}_0$. Mach number is a parameter. Note that the source conditions are those measured 100 m below the aircraft. For aircraft flying at an altitude above a given curve, the ground waveform can be considered frozen. For example, if the Mach number is 2.0 or greater and the altitude is 15 km or more, the ground waveform is frozen for sonic booms having a large range of values of $T_0/\hat{p}_0$.

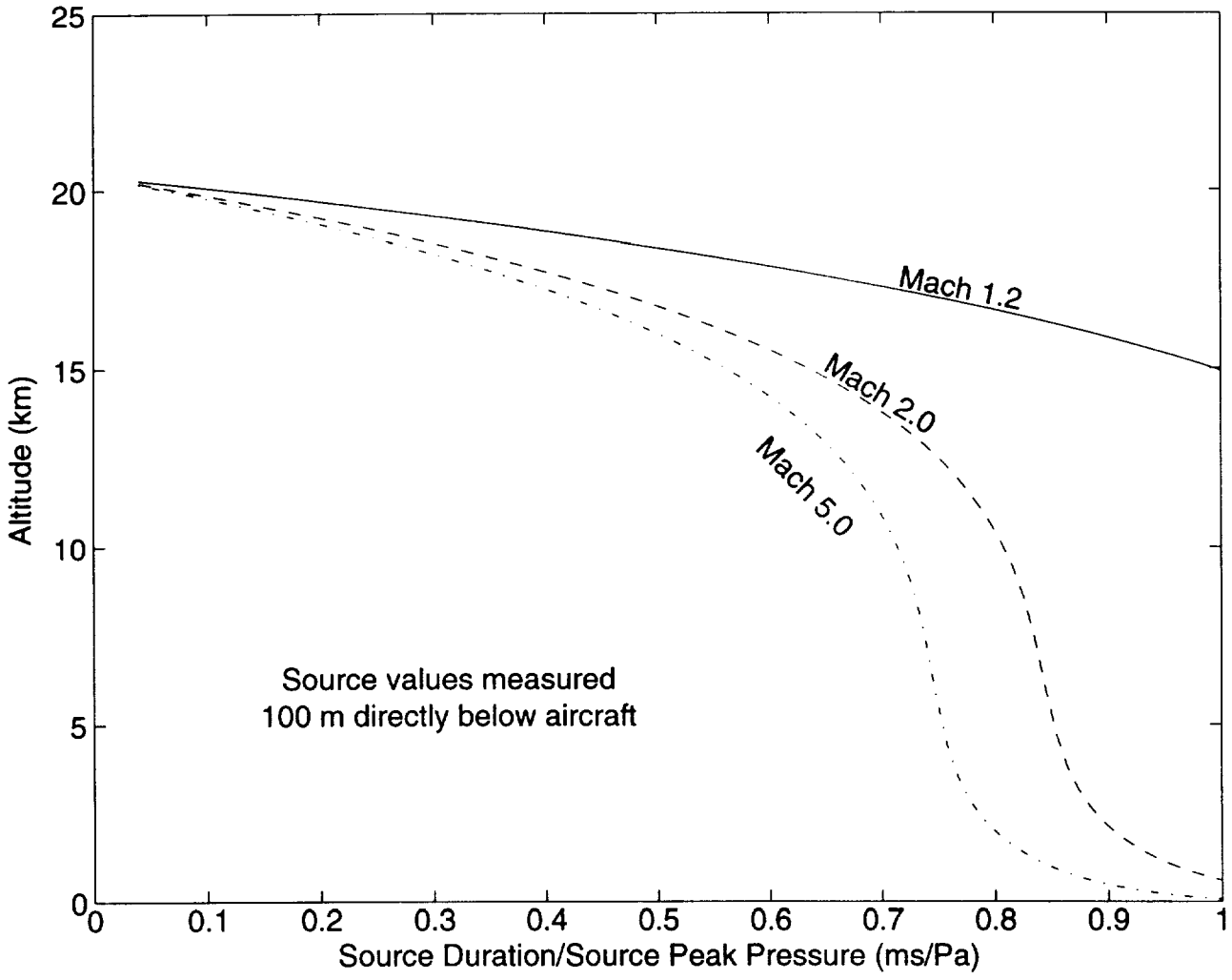

Figure 10: The minimum altitude an aircraft should fly for its sonic boom to be frozen at the ground.

CONCLUSIONS

A study has been made of nonlinear distortion of spreading waves of finite amplitude that propagate downward in a stratified atmosphere. The application is to sonic booms. Distortion, here quantified by the distortion distance (related to Hayes's age variable), can be slowed by both spreading and stratification. We have presented a new interpretation of the slowing of distortion: the fluid appears to have an effective coefficient of nonlinearity β_{eff} that decreases with range. In cases for which $\int \beta_{\text{eff}}\, ds$ is bounded over the travel path, the amount of distortion suffered by the wave is finite. When the distortion reaches its limit, the waveform is said to be frozen.

We have analyzed the question of whether sonic booms in an isothermal atmosphere are frozen at the ground. Two different criteria are used to judge whether the waveform at the ground is frozen. The first criterion is based on the distortion distance $\tilde{x}$: is $\tilde{x}$ within 95% of its asymptotic value when the wave reaches the ground? The answer is "No" for aircraft flying at an altitude of 27 km or lower. Varying the aircraft Mach number and azimuthal angle has little effect on this conclusion. Moreover, it is shown that stratification, in particular the density variation, is the important factor in controlling waveform freezing. Spreading has only a weak effect.

A different answer is however given by the second criterion, which is based on sonic boom duration T: is T within 95% of its asymptotic value when the ground is reached? The answer is "Yes" even for aircraft flying as low as 10 km. A comparison of the two criteria shows that the 95% figure applied to boom duration corresponds to a figure of approximately 90% applied to distortion distance. The use of $\tilde{x}$ as the criterion therefore leads to predictions that may be too conservative. On the other hand predictions based on $\tilde{x}$ are independent of waveform.

REFERENCES

[1] C. M. Darden, C. A. Powell, W. D. Hayes, A. R. George, and A. D. Pierce, "Status of Sonic Boom Methodology and Understanding," NASA CP 3027 (1989).

[2] W. D. Hayes, "Brief review of basic theory," in *Sonic Boom Research*, A. R. Seebass, ed., NASA SP-147 (1967), pp. 3 7.

[3] W. D. Hayes, R. C. Haefeli, and H. E. Kulsrud, "Sonic Boom Propagation in a Stratified Atmosphere, with Computer Program," NASA-CR1299, Aeronautical Research Associates of Princeton, Inc., April 1969.

[4] W. D. Hayes and H. L. Runyan, Jr., "Sonic-boom propagation through a stratified atmosphere," *J. Acoust. Soc. Am.* **51**, 695-701 (1971)

[5] L. D. Robinson "Sonic boom propagation through an inhomogeneous windy atmosphere," Ph.D. dissertation, Department of Physics, The University of Texas at Austin, (1991).

[6] R. O. Cleveland and D. T. Blackstock, "Waveform freezing of sonic booms in the atmosphere," *J. Acoust. Soc. Am.* **92** (4), 2331(A) (1992).

[7] R. O. Cleveland, M. F. Hamilton, and D. T. Blackstock, "Effect of stratification of the atmosphere on sonic boom propagation," in *Proceedings of the Sixth International Conference on Long Range Sound Propagation,* Ottawa, Canada, D. I. Havelock and M. R. Stinson, eds., pp. 59–76 (1994).

[8] K. J. Plotkin, "On the aging of sonic booms," *J. Acoust. Soc. Am.* **93**, 2407(A) (1993).

[9] R. O. Cleveland, "Propagation of sonic booms through a real, stratified atmosphere," Ph.D. dissertation, Department of Mechanical Engineering, The University of Texas at Austin, (1995).

[10] R. O. Cleveland, "Effects of atmospheric stratification on sonic boom propagation," *J. Acoust. Soc. Am.* **97**, 3257(A) (1995).

[11] D. T. Blackstock, "Connection between the Fay and Fubini solutions for plane sound waves of finite amplitude," *J. Acoust. Soc. Am.* **39**, 1019–1026 (1966).

[12] D. T. Blackstock, "Nonlinear Acoustics (Theoretical)," in *American Institute of Physics Handbook*, D. E. Gray, ed. (McGraw-Hill, New York, 1972), Chap. 3n, pp. 3-183 to 3-205.

[13] A. D. Pierce, *Acoustics: An Introduction to Its Physical Principles and Applications* (McGraw-Hill, New York, 1981).

[14] C. L. Morfey, "Nonlinear Propagation in a Depth-Dependent Ocean," Tech. Rep. ARL-TR-84-11, Applied Research Laboratories, The University of Texas at Austin (1 May 1984) (AD A145079).

[15] U.S. Committee on Extension to the Standard Atmosphere *U.S. Standard Atmosphere,* 1962 Government Printing Office, Washington D.C., (1962).

WAVEFORM PERTURBATIONS OF SPHERICAL TRANSIENT WAVES PROPAGATING IN A RANDOM MEDIUM[1]

Alan R. Wenzel
Virginia Consortium of Engineering and Science Universities
303 Butler Farm Road, Suite 101
Hampton, VA 23666

INTRODUCTION

Of those aspects of sonic-boom propagation that are not yet fully understood, one of the more important is that which relates to the perturbations of the waveform. This phenomenon, which arises also in connection with the propagation of other types of transient waves in real media, generally takes the form, in the case of sonic-boom N-waves, of a random high-frequency structure (sometimes called finestructure) that is most prominent in the regions immediately behind each of the shocks. The perturbations in those regions can be large, occasionally attaining magnitudes comparable to that of the incident wave itself. Such magnitudes, in combination with the high-frequency character of the perturbations, can lead to a considerable increase in the perceived noisiness of the sonic boom. Waveform perturbations are consequently an important factor as regards the question of sonic-boom acceptability.

On the basis of observations, and some early theoretical studies (refs. 1 and 2), it is now generally accepted that perturbations of sonic-boom waveforms are a manifestation of the effect on the propagating wave of relatively small-scale variations in the acoustic properties of the atmosphere — variations that are usually associated with turbulence.

Although the mechanism underlying perturbations of sonic-boom waveforms seems thus to be well understood, no fully-satisfactory theory of such perturbations has emerged. Indeed, even for the relatively simple case of an incident step-function pulse, no theory of waveform perturbations, formulated in a realistic three-dimensional context, has been advanced that is valid in the region of strongest perturbations; viz., the region immediately behind, and including, the wave front. The work reported herein represents an attempt to develop such a theory.

[1] Research supported by NASA Langley Research Center

FORMULATION

The mathematical model on which the present investigation is based is fully three-dimensional, in that the medium is assumed to be three-dimensional and to have properties that vary in all three spatial directions. (These properties are, however, independent of time.) The medium is, moreover, assumed to be unbounded and quiescent. Thus, only thermal scattering is considered. (Mechanical turbulence, which gives rise to inertial scattering, is ignored.) Dissipation is not considered, and non-linear effects are disregarded.

The starting point of the analysis is the scalar wave equation, as shown in Figure 1. Here w is the wave function, and f is the source term. Both w and f are assumed to be functions of $\bar{r}$, the spatial coordinate, and of t, the time. (Note that letter superscripts denote derivatives.)

The sound speed c_* is assumed to be a random function of $\bar{r}$; c is a constant reference sound speed, and μ is a statistically homogeneous function of $\bar{r}$ having zero mean and unit variance. (The angle brackets denote an ensemble average.) The parameter ε is the standard deviation of the index of refraction of the medium, and is assumed to be small.

In the atmosphere, the standard deviation of the acoustic index of refraction is typically about one part in one thousand; hence the assumption of a weakly-inhomogenous medium is appropriate for the study of sonic-boom propagation.

The disturbance that generates the wave begins at $t = 0$, prior to which the medium is at rest.

$$c_*^{-2} w'' - \nabla^2 w = f \; ; \quad t > 0$$

$$\nabla^2 = \partial_x^2 + \partial_y^2 + \partial_z^2 \; ; \quad \bar{r} = (x, y, z)$$

$$c_*(\bar{r}) = \frac{c}{1 - \varepsilon\mu(\bar{r})} \; ; \quad < \mu > = 0 \; ; \quad < \mu^2 > = 1$$

Figure 1. The mathematical model

PERTURBATION ANALYSIS

The assumption of a weakly inhomogeneous medium allows the problem to be solved by a perturbation method. To begin, one assumes that the wave function w has an expansion in powers of ε, as shown below in Figure 2. By substituting this expansion back into the wave equation, equations for the coefficients w_0, w_1, w_2, etc., are obtained. The first two such equations, for w_0 and w_1, are shown. This procedure is carried out here only as far as the first-order term. The wave function w is then approximated by the sum of the first two terms of the expansion.

The function w_1 thus represents (apart from the factor ε) the departure of the observed wave from the incident wave, and hence characterizes the waveform perturbations.

Instead of specifying the source term f, it is more convenient to specify the general form of the zeroth-order wave function; i.e., the w_0 term, which corresponds to the incident wave. This form is shown on the next-to-last line below. The function h is required to be piecewise twice differentiable, with at most a finite number of jump discontinuities, and to vanish for negative values of its argument, but is otherwise unrestricted.

Expressing the incident wave in this form is equivalent to specifying a source function that is concentrated at the point $\bar{p}_-$, having a time dependence determined by the function h.

Once the incident wave has been specified, the right-hand side of the equation for w_1 is determined, provided that μ is regarded as a known function. That equation can then be solved with the aid of the free-space Green's function for the scalar wave equation. The procedure is well understood and so will not be described here. Instead, only the final result will be shown. The expression appears on Figure 3.

$$w(\bar{r},t;\varepsilon) = w_0(\bar{r},t) + \varepsilon w_1(\bar{r},t) + \varepsilon^2 w_2(\bar{r},t) + \cdots$$

$$c^{-2}w_0'' - \nabla^2 w_0 = f$$

$$c^{-2}w_1'' - \nabla^2 w_1 = 2c^{-2}\mu w_0''$$

$$w_0(\bar{r},t) = |\bar{r} - \bar{p}_-|^{-1} h\left(t - c^{-1}|\bar{r} - \bar{p}_-|\right)$$

$$\bar{p}_- = (0,0,-a)$$

Figure 2. Perturbation analysis of the wave equation.

FIRST-ORDER SCATTERED WAVE

The first line of Figure 3 shows the expression obtained for the first-order scattered wave. The x, y, z coordinate system is oriented so that the source and receiver both lie on the z axis, with the origin midway between them. The source point $\bar{p}_-$ is at $z = -a$; the receiver is at $\bar{p}_+$; i.e., at $z = +a$, where a is one-half the source-receiver distance. (The rationale for orienting the coordinate system in this way will become clear shortly.) The quantities r_+ and r_- are, respectively, the distances from the field point $\bar{r}$ to the source and to the receiver. The primes on the function h denote derivatives.

This expression is valid provided that $ct > 2a$; i.e., provided that the incident wave, travelling at the speed c, has had time to reach the receiver. If this condition is not met then the wave field at the receiver is zero.

The integration in Figure 3 extends over all of x, y, z space; however, because the function h vanishes when its argument is negative, the integrand is non-zero only in a bounded region of space. The boundary of this region is the ellipsoid determined by the condition $r_+ + r_- = ct$. This observation suggests the possibility of simplifying the integral by transforming to ellipsoidal coordinates. The procedure by which this transformation is accomplished is outlined in the next figure.

$$w_1(\bar{p}_+,t) = \frac{1}{2\pi c^2}\int \mu(\bar{r}) r_+^{-1} r_-^{-1} h''\left[t - c^{-1}(r_+ + r_-)\right] d\bar{r} \;\; ; \;\; t > 2a/c$$

$$r_+ = |\bar{r} - \bar{p}_-| \;\; ; \;\; r_- = |\bar{r} - \bar{p}_+|$$

$$\bar{p}_- = (0,0,-a) \;\; ; \;\; \bar{p}_+ = (0,0,+a)$$

Figure 3. The expression for the first-order scattered wave in cartesian coordinates.

ELLIPSOIDAL COORDINATES

The first three equations in Figure 4 define the transformation from cartesian coordinates x, y, and z to ellipsodial (actually prolate-spheroidal) coordinates ξ, $\emptyset$, and θ. In this coordinate system, every point in space is determined as the intersection of an ellipsoid, a hyperboloid, and a half plane, which are in turn specified by the coordinates ξ, $\emptyset$, and θ, respectively. The ellipsoids are all centered with respect to the origin, with their major axes aligned along the z axis. All of the ellipsoids and hyperboloids have their foci at the source and receiver points.

The symmetric relation that exists between the cartesian and the ellipsoidal coordinate system defined above, which simplifies somewhat the analysis that follows, is a consequence of the way in which the cartesian system is oriented with respect to the source and receiver points.

The expression for the first-order scattered wave, after transformation to the ellipsoidal coordinate system, is shown in Figure 4. The quantity ν is just the function μ written in terms of the ellipsoidal coordinates; the dimensionless parameter ρ is the elapsed time since the arrival of the wave at the receiver, normalized by the source-receiver travel time t_0. The integration in this expression is over a solid rectangular region in ellipsoidal coordinates, which corresponds to an ellipsoidal region in cartesian coordinates; namely, the ellipsoid that is determined by the parameter β.

The integral in this expression simplifies when the function h, which determines the waveform of the incident wave, is a step function. The resulting expression for the first-order scattered wave is shown in Figure 5.

$$x = a\sinh\xi\sin\emptyset\cos\theta\ ;\quad y = a\sinh\xi\sin\emptyset\sin\theta$$

$$z = a\cosh\xi\cos\emptyset$$

$$0 \le \xi < +\infty\ ;\quad 0 \le \emptyset \le \pi\ ;\quad 0 \le \theta < 2\pi$$

$$w_1(\bar{p}_+, t) = \frac{a}{2\pi c^2}\int_0^{\beta}\int_0^{\pi}\int_0^{2\pi} \nu(\xi,\emptyset,\theta)h''(t - t_0\cosh\xi)\sinh\xi\sin\emptyset\,d\theta\,d\emptyset\,d\xi$$

$$\nu(\xi,\emptyset,\theta) = \mu(x,y,z)\ ;\quad \beta = \cosh^{-1}(1+\rho)$$

$$\rho = \frac{t - t_0}{t_0}\ \ (t \ge t_0)\ ;\quad t_0 = 2a/c$$

Figure 4. The expression for the first-order scattered wave in ellipsoidal coordinates.

STEP-FUNCTION INCIDENT WAVE

Shown on the first line of Figure 5 is the expression for the first-order scattered wave for the case in which the function h is equal to the Heaviside unit step function multiplied by a positive amplitude factor P. The superscript on the function ν denotes a derivative. The derivation of this formula makes use of some results from the theory of generalized functions.

Note that the expression for w_1 now involves an integration over a plane rectangular region, rather than a solid rectangular region, in ellipsoidal - coordinate space. This is equivalent to an integration over the surface of the ellipsoidal region of cartesian - coordinate space mentioned previously, rather than over the interior of the region.

An approximate form of this expression can be obtained by expanding the right-hand side in powers of the parameter ρ. Since ρ is a measure of the time elapsed since the arrival of the wave at the observation point, this procedure is equivalent to a wave-front expansion of w_1. Term-by-term partial integration of that expression (of which only the first two terms are treated explicitly) leads to the result shown in Figure 6.

$$w_1(\vec{p}_+,t)=\frac{P}{8\pi a}\left[(1+\rho)^2-1\right]^{-1/2}\int_0^{\pi}\int_0^{2\pi} v^5\left[\cosh^{-1}(1+\rho),\emptyset,\theta\right]\sin\emptyset\, d\theta\, d\emptyset$$

$$h(s)=P\begin{cases}1 \text{ if } s>0;\\ 0 \text{ if } s<0\end{cases}$$

Figure 5. The expression for the first-order scattered wave for the case in which the incident wave is a step function.

WAVEFRONT EXPANSION

On the first line of Figure 6 is shown the approximate expression for the first-order scattered wave at the observation point, obtained by means of a wavefront expansion as described above. In the derivation of this result, terms of order ρ^2 have been discarded.

Note that this result is expressed in terms of the original cartesian coordinates, as are all results presented hereinafter.

It should be pointed out that the terms I_0 and I_1, which appear as the zeroth-order and first-order coefficients, respectively, in the expansion of w_1 in powers of ρ, are themselves approximations. Each is, in fact, the leading term in the expansion of the respective full coefficient in powers of the parameter l/a, where l is a characteristic length scale associated with the inhomogeneities of the medium. As a consequence, in order that the approximate expression for w_1 shown here be valid, the condition $a >> l$, as well as the condition $\rho << 1$, must be satisfied. The expression for w_1 is thus valid only near the wave front, as defined by the latter condition, and only for large propagation distance, as defined by the former.

It should be noted also that a phase-shift term, similar to the term discussed by Crow (Ref. 2), has been dropped from the expression for w_1. As Crow pointed out, a term of this type does not represent a physical quantity that would be measured by an observer who is not concerned with small travel-time discrepancies between the observed and incident waves. In any event, such terms disappear when a travel-time-corrected averaging procedure (see, e.g., Ref. 3) is performed in order to calculate wave statistics.

The operator Δ is the transverse Laplacian. It operates only on functions of three spatial variables, and, when so doing, it is the Laplacian with respect to the first two of those variables. Thus, since it operates here (i.e., in Figure 6) on a function of x, y, and z, it is the Laplacian with respect to x and y.

The form of the expression for the coefficients I_0 and I_1 shows that, at least within the context of the present theory, only those index-of-refraction variations in the immediate vicinity of the straight-line path from source to receiver affect the waveform perturbations close to the wave front.

The appearance of the term $\Delta\mu$ in the expression for I_0, which determines the waveform perturbations at the wave front, indicates that those perturbations arise primarily as a result of focusing and de-focusing of rays along the propagation path. Note in this connection that, because of the weighting function $1 - z^2/a^2$ appearing in the integrand of that expression, those inhomogeneities located midway between the source and receiver have the most influence on the perturbations at the wave front, whereas those located at either end of the propagation path have the least influence.

$$w_1(\bar{p}_+,t) = (P/8)\left[I_0(a) + I_1(a)\rho\right]$$

$$I_0(a) = \int_{-a}^{+a}\left(1 - z^2/a^2\right)\Delta\mu(0,0,z)dz$$

$$I_1(a) = \frac{1}{4}a^2\int_{-a}^{+a}\left(1 - z^2/a^2\right)^2\Delta^2\mu(0,0,z)dz$$

$$\Delta = \partial_x^2 + \partial_y^2 \quad ; \quad \rho << 1 \quad ; \quad a >> l$$

Figure 6. An approximate expression for the first-order scattered wave obtained using a wavefront expansion.

VARIANCE OF THE PERTURBATIONS

Squaring and averaging the expression for w_1 given in Figure 6 yields, after terms of order ρ^2 are discarded, the formula for $< w_1^2 >$ that appears on the first line of Figure 7. The various terms appearing in that formula are defined below. The function Γ is the correlation function of the medium, which is assumed statistically homogeneous.

The integrals appearing in the expression for $< w_1^2 >$ have been partially evaluated by means of a transformation to sum and difference coordinates. In addition, each integral has been approximated by expanding it in a series of powers of the parameter l/a and discarding all but the lowest-order term. The results, which are thus valid provided that $a >> l$, are shown. The formula for I^{-3} gives a precise definition of the length scale l.

Upon multiplying through by ε^2 in the expression for $< w_1^2 >$ and dividing by $(P/2a)^2$ (the square of the amplitude of the incident wave at the observation point) one obtains an expression for σ^2, the normalized variance of the waveform perturbations. With the aid of the approximations for the integral terms, that expression can be put into the form shown on the last line of Figure 7.

The expression for σ^2 given in Figure 7 is the main result of this investigation. It is valid at, and immediately behind, the wave front, as defined by the condition $0 \leq \rho << 1$. It is, moreover, valid only for large propagation distance, as defined by the condition $a >> l$.

No systematic attempt has been made as yet to use the expression for σ^2 derived here to study the waveform perturbation in the region <u>behind</u> the wave front. Instead, only calculations of σ^2 <u>at</u> the wave front have been made. (Those results are shown in the next figure.) It should be mentioned, however, that, in the special case in which the medium is isotropic with an exponential correlation function, the integral appearing in that expression has been shown to be negative. In that case, then, σ^2 decreases with increasing ρ; that is, the magnitude of the waveform perturbations decreases with time, relative to the arrival time of the wave at the receiver. This result agrees with observations of sonic-boom and other types of transient waves propagating in real media

$$\left\langle w_1^2(\vec{p}_+,t)\right\rangle = (P/8)^2\left(\left\langle I_0^2\right\rangle + 2\left\langle I_0 I_1\right\rangle\rho\right)$$

$$\left\langle I_0^2\right\rangle = \int_{-a}^{+a}\int_{-a}^{+a}\left(1-z_1^2/a^2\right)\left(1-z_2^2/a^2\right)\Delta^2\Gamma(0,0,z_2-z_1)dz_1dz_2$$

$$\left\langle I_0 I_1\right\rangle = \frac{1}{4}a^2\int_{-a}^{+a}\int_{-a}^{+a}\left(1-z_1^2/a^2\right)\left(1-z_2^2/a^2\right)^2\Delta^3\Gamma(0,0,z_2-z_1)dz_1dz_2$$

$$\Gamma(\xi,\eta,\varsigma) = \left\langle \mu(x,y,z)\mu(x+\xi,y+\eta,z+\varsigma)\right\rangle$$

$$\left\langle I_0^2\right\rangle \simeq \frac{32a}{15l^3} \;\; ; \;\; \left\langle I_0 I_1\right\rangle \simeq \frac{16a^3}{35}\int_0^\infty \Delta^3\Gamma(0,0,\varsigma)d\varsigma \;\; ; \;\; a >> l$$

$$l^{-3} = \int_0^\infty \Delta^2\Gamma(0,0,\varsigma)d\varsigma$$

$$\sigma^2 = \frac{2\varepsilon^2 a^3}{5}\left[\frac{1}{3l^3} + \frac{a^2\rho}{7}\int_0^\infty \Delta^3\Gamma(0,0,\varsigma)d\varsigma\right]$$

Figure 7. The expression for the variance of the waveform perturbations.

PERTURBATIONS AT THE WAVE FRONT

Setting ρ equal to zero in the expression for σ^2 given in Figure 7 yields an expression for the normalized variance of the waveform perturbations at the wave front, which is denoted here by σ_0^2. Taking the square root of both sides of that relation yields an expression for σ_0, the normalized standard deviation of the waveform perturbations at the wave front. That result is shown in Figure 8. Note that σ_0 is written here in terms of R, the propagation path length, instead of a. The condition for the validity of this result is that $R >> l$.

Perhaps the most striking feature of this result is the predicted unbounded growth of σ_0 with R. Such unbounded growth would not, of course, actually be observed; indeed, one can expect the theory to break down at propagation ranges for which the formula yields a value of σ_0 of order one or greater. Nevertheless, the growth of σ_0 with R shown by this result indicates that waveform perturbations of transient waves propagating in real media can be large, especially under conditions of long-range propagation, even when the variations in the index of refraction of the medium are small. As was pointed out in the introduction, such behavior is, in fact, observed in the case of sonic-boom waves, in which context waveform perturbations can be, in magnitude, comparable to the amplitude of the incident wave itself.

Theoretical studies based on one-dimensional models have revealed that, in one dimension, waveform perturbations are practically independent of propagation range and remain small (with normalized standard deviation of order ε) at all ranges. (see, e.g., Ref. 4) The results obtained here show that the behavior of waveform perturbations in three dimensions is very different from the behavior in one dimension.

$$\sigma_0 \simeq \frac{\varepsilon}{2\sqrt{15}}\left(\frac{R}{l}\right)^{3/2}$$

$$R = 2a \;\; ; \;\; R >> l$$

Figure 8. The expression for the normalized standard deviation of the waveform perturbations at the wave front.

CONCLUDING REMARKS

The most important findings to emerge from this investigation are the following (all results cited are for the case of a step-function wave, and refer to waveform perturbations in the region immediately behind – and including – the wave front):

(1) Only those medium inhomogeneities in the immediate vicinity of the straight-line propagation path from source to receiver affect the perturbations;

(2) those inhomogeneities located midway between the source and receiver have the most influence on the perturbations, whereas those located at either end of the propagation path have the least influence;

(3) the perturbations are primarily a consequence of focusing and de-focusing of rays along the propagation path;

(4) the magnitude of the perturbations decreases with time, relative to the arrival time of the wave at the receiver (this has been established only for the case of an isotropic medium with an exponential correlation function);

(5) the perturbations can be large – in magnitude, comparable to the amplitude of the incident wave – at sufficiently long ranges, even when the variations in the index of refraction of the medium are small.

(This last result is indicated, although not firmly established, by the theory.)

The results numbered 4 and 5 of those listed above are, as has already been pointed out, consistent with observations of sonic-boom waves. Result number 3 accounts for the differences mentioned herein as regards the behavior of waveform perturbations in one and three dimensions.

Despite the qualitative agreement of the present theory with observations of sonic-boom waves, as noted above, quantitative comparison of the theory with sonic-boom measurements does not seem warranted. Of the idealizations inherent in the theory that make such a comparison inappropriate (such as the neglect of inertial scattering, the assumption of a spherical, rather than a conical, wave, etc.), the most important is perhaps the assumption of a statistically-homogeneous medium. In most cases of sonic-boom propagation, the medium is, in fact, far from homogeneous. Inasmuch as the atmospheric boundary layer extends to an altitude of only 3000 ft. or so, a typical sonic-boom wave undergoes appreciable scattering over no more than a fraction of its propagation path – a fraction that may be as small as 1/20. Relaxation of the assumption of a statistically-homogeneous medium would therefore seem to be the next logical step in the development of a theory, along the lines described herein, of transient-wave propagation in a random medium that would be applicable in a quantitative sense to the problem of sonic-boom propagation in the atmosphere.

REFERENCES

1. Pierce, A. D. Spikes on sonic boom pressure waveforms. J. Acoust. Soc. Am. 44 (1968) 1052-1061.

2. Crow, S. C. Distortion of sonic bangs by atmospheric turbulence. J. Fluid Mech. 37 (1969) 529-563.

3. Wenzel, A. R. Asynchronous ensemble averaging: a travel-time-corrected averaging method for transient waves in random media. Proceedings of the Sixth International Symposium on Long-Range Sound Propagation, Ottawa, Canada, June 1994.

4. Wenzel, A. R. Finestructure of transient waves in a random medium: the correlation and spectral density functions. NASA Conference Publication 3279, October 1994.

54-71

THEORETICAL BASIS FOR FINITE DIFFERENCE EXTRAPOLATION OF SONIC BOOM SIGNATURES

14P.
036740

Kenneth J. Plotkin
Wyle Laboratories
Arlington, VA

1.0 INTRODUCTION

Calculation of sonic boom signatures for aircraft has traditionally followed the methods of Whitham[1] and Walkden.[2] The wave disturbance generated by the vehicle is obtained by area rule linearized supersonic flow methods,[3,4] which yield a locally axisymmetric asymptotic solution. This solution is acoustic in nature, i.e., first order in disturbance quantities, and corresponds to ray acoustics. Cumulative nonlinear distortion of the signature is incorporated by using this solution to adjust propagation speed to first order, thus yielding a solution second order in disturbance quantities.[1] The effects of atmospheric gradients are treated by Blokhintzev's method of geometrical acoustics.[5] Both nonlinear signature evolution and ray tracing are applied as if the pressure field very close to the vehicle were actually that given by the source term (the "F-function") of the asymptotic linearized flow solution.

The viewpoint is thus that the flow solution exists at a small radius near the vehicle, and may be treated as an input to an extrapolation procedure consisting of ray tracing and nonlinear aging. The F-function is often regarded as a representation of a near-field pressure signature, and it is common for computational implementations to treat it interchangeably with the pressure signature. There is a "matching radius" between the source function and the subsequent propagation extrapolation. This viewpoint has been supported by wind tunnel tests of simple models, and very typically yields correct results for actual flight vehicles.

The assumption that the F-function and near-field signature are interchangeable is generally not correct. The flowfield of a vehicle which is not axisymmetric contains crossflow components which are very significant at small radii and less so at larger distances. From an acoustical viewpoint, the crossflow is equivalent to source diffraction portions of the wave field. Use of the F-function as a near-field signature effectively assumes that the diminution of the crossflow/diffraction component may be applied all at once at the matching radius noted above. This approximation, though not rigorously validated, is responsible for the usual correct far-field results. On the other hand, if an actual near-field signature (either from wind tunnel or CFD data) is used at a starting point rather than one based on the effective source distribution, the predicted far-field signature is generally wrong.

The crossflow issue was recognized by Ferri *et al.*[6] and Darden[7] who developed the "modified method of characteristics" for use in extrapolating near-field wind tunnel measurements of low-boom aircraft models. This method accounts for crossflow effects in a plane of symmetry (nominally under the flight path for a symmetric aircraft) and is based on a taking the second-order terms (first non-zero terms for the plane of symmetry) of a lateral expansion.

Current HSCT designs are developed using CFD methods. This is partly because it is the current design tool, and partly because there are elements of the flow involving strong local shocks or other details not properly handled by linear theory. It is obvious that these solutions should be used as the source for the sonic boom part of the analysis. Due to a combination of computational costs and numerical algorithms losing resolution after many steps, CFD cannot be brought all the way to the ground or even very many body lengths away from the aircraft. It is necessary to conduct the analysis in at least two zones, with CFD being the inner and a standard propagation scheme being the outer. CFD calculations are typically limited to distances of one or two body lengths, which is not far enough for simple pressure matching between the two zones. There are special annular grid schemes which allow practical CFD out to 5 or 10 lengths,[8] but even that is not adequate in the presence of features such as outboard nacelles and wing cranks which cause significant crossflow/diffraction at large radii. Because analysis is required across the full width of the boom footprint, a method is needed which is not limited to planes of symmetry.

One two-zone method, that of Page and Plotkin,[9] has demonstrated some success. That method used a Fourier decomposition in the crossflow direction and a multipole source formulation[10] to account for the cumulative diffraction associated with each component. This restored the net far-field quantity omitted by simple pressure-matching methods, but with the same approximation inherent in the classical linear approach: applying it all at the matching radius, rather than being distributed from there to the far field.

Cheung *et al.*[11] have suggested that this be treated as a three-zone problem. The middle zone (beyond full CFD practicality, but before ray tracing validity) must be handled by a quasi-acoustic code. A linear acoustic code will properly handle the crossflow/diffraction effects, and numerical methods are available which are economical and which retain resolution over long propagation distances.[12,13] An algorithm has also been developed which shows similar capability for integrating the two-dimensional inviscid Burgers equation over long distances.[14] These codes, if extended to three dimensions and applied to a nonuniform atmosphere, would form the middle zone of a three-zone scheme.

The governing equations for sonic boom propagation are the Euler equations to second order: the same quasi-linear order as the Burgers equation. These equations have been written, in a sonic boom propagation context, as a systematic expansion of the full Euler equations.[15] The current study reviews these equations and the simpler equations which have been numerically solved by Davis.[12,14] The steps necessary to apply Davis's numeric algorithms to the full quasi-linear equations are presented.

Section 2 of this report presents a review of traditional area rule analysis and the multipole matching method of Page and Plotkin. This establishes the baseline for sonic boom configuration analysis, and allows specific identification of the phenomena which are accounted for (or not) at each level of refinement. Section 3 presents the governing equations and their reduction to the appropriate form for numeric solution of the middle zone.

2.0 LINEARIZED METHODS AND FAR-FIELD MATCHING

2.1 Elements of Sonic Boom Generation and Propagation

There are generally four elements which must be considered when predicting sonic boom at the ground:

- Local flow around the vehicle
- Three-dimensional crossflow effects from the near field to the far field
- Nonlinear distortion/evolution of the signature
- Refraction by atmospheric gradients

These are listed in order of the size of the regions over which the details of each plays a significant role. The regions for all elements overlap considerably, although local flow and 3-D crossflow evolution are thought of as generation issues while nonlinear distortion and atmospheric refraction are thought of as propagation issues.

Section 2.1.1 contains a review of local flow and crossflow effects. Section 2.1.2 contains a summary of evolution and refraction.

2.1.1 The F-Function as an Acoustic Source

The source term for sonic boom generation is generally given by the following relation:

$$\delta p = p_0 \frac{\gamma M^2 \, F(x-\beta r;\theta)}{(2\beta r)^{1/2}} \tag{1}$$

where δp = disturbance pressure
p_0 = undisturbed ambient pressure
x = axial coordinate (body fixed)
r = radius
γ = ratio of specific heats
M = Mach number
θ = Azimuthal angle about axial centerline
$\beta = \sqrt{M^2 - 1}$ = Prandtl-Glauert factor

and

$$F(\tau;\theta) = \frac{1}{2\pi}\int_0^{\xi} \frac{A''(\xi;\theta)}{(\tau-\xi)^{1/2}}\,\delta\xi \tag{2}$$

where $A(\xi;\theta)$ is the equivalent cross-sectional area of the vehicle, $\tau = x-\beta r$, and ξ is an axial dummy variable. From the Lomax/Walkden theory, A is an equivalent area based on the actual cross-sectional area distribution plus a quantity derived from the distribution of lift on the wings. In the sense of locally axisymmetry, A (and consequently F) is a function of azimuthal angle θ.

In Equations (1) and (2), τ (which identifies which characteristic is being followed) is of interest for values up to a vehicle length or two. Equations (1) and (2) are asymptotic results which are correct when

$$x \gg x - \beta r \tag{3}$$

Equation (3) should be taken as a general statement. The specific condition depends on whether the coordinate viewpoint is axial or radial (interchangeable along small values of $x - \beta r$) and whether the vehicle has wings (reference length is related to span and Mach angle, rather than vehicle length). The key element is that Equation (1) is a far-field result. Note that it has a very simple dependence on r, simply cylindrical spreading $1/\sqrt{r}$.

The dependence of the acoustic signature on distance is generally more complex than cylindrical spreading. It may be schematically written as

$$\delta p(r,\theta) = [\text{Equation (1)}] + [\text{Crossflow}] \tag{4}$$

where [Crossflow] denotes all that is not included in Equation (1). Since Equation (1) applies to locally axisymmetric regimes (i.e., the wave at one θ is independent from that at other θ), it is appropriate to refer to this missing part as crossflow. From an acoustics viewpoint, it can also be viewed as diffraction. The key point is that the dependence on r is complicated, and is interrelated with θ.

The crossf'ow terms can be extracted in a form closely related to Equation (2) by Fourier decomposition:

$$F(\tau,\theta,r) = \Sigma \cos(n\theta)\, F_n(\tau,r) \tag{5}$$

where r is included as a parameter because F is now considered to be the combination of both terms in Equation (4). This is a decomposition into multipoles, where n=0 is monopole, n=1 is dipole, n=2 is quadrupole, etc. George[10] formulated linearized flow in terms of the velocity potential, and showed that the strength of a multipole of order n is given by

$$g_n = \frac{-1}{2\pi}\,\frac{\cosh\left[n\cdot\cosh^{-1}(x/\beta r)\right]}{\sqrt{x^2-\beta^2 r^2}} \tag{6}$$

At large distance, g_n asymptotes the $1/(r-\xi)^{1/2}$ form of the kernel of Equation (2). Page and Plotkin[9] called this form g_∞, and wrote

$$g_n(\tau,r) = g_\infty(\tau,r)\cdot G_n(\tau,r) \tag{7}$$

so that

$$F_n(\tau,r) = \int_0^\tau \frac{A_n''(\xi)}{\sqrt{\tau-\xi}}\, G_n(\tau-\xi, r)d\xi \tag{8}$$

where A_n'' represents axial distributions of multipole source strengths. Figure 1 shows G_n for n up to 6. All orders of G approach 1 at large r, so that the Fourier sum of A_n reduces to equivalent area distribution A. Note that G_0 and G_1, associated with the traditional monopole (volume) and dipole (lift) components of boom are close to unity at small r, so the neglect of crossflow for simple vehicles is reasonable.

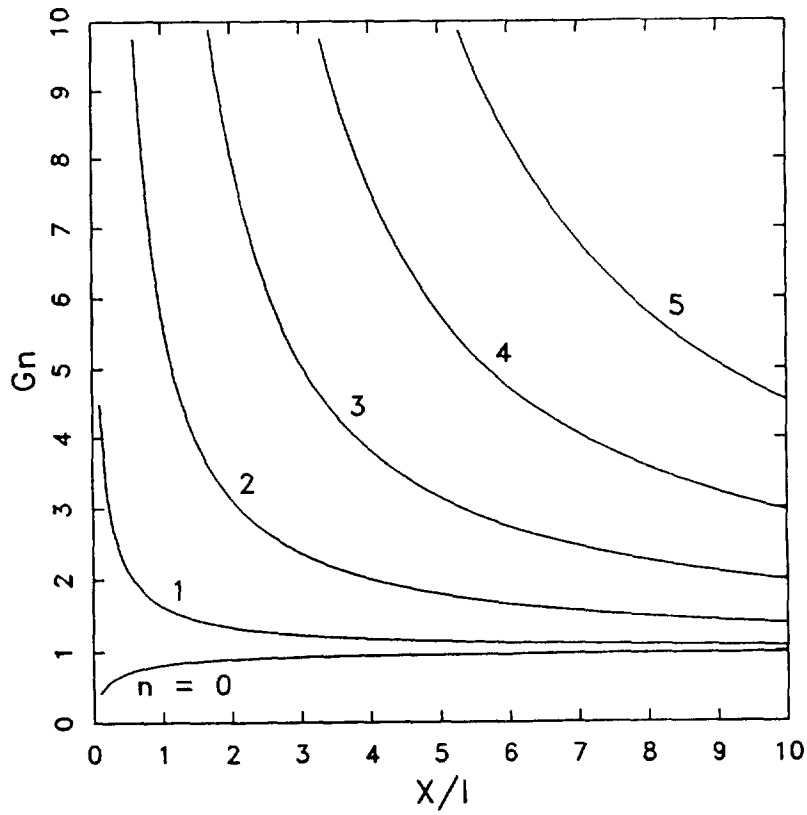

Figure 1. Variation $G_n(\tau, \beta r)$ As a Function of Body Lengths Behind Vehicle.

The Page/Plotkin scheme used a CFD solution which provided a pressure solution on a cylinder of radius comparable to aircraft length or wingspan. The coefficients (actually, axial functions) A_n were then obtained by matching Equation (8) on the cylinder, accounting for the actual values of G_n at that radius. The effective far-field source distribution was then obtained by re-composing A from A_n, replacing G_n with unity. This effective F-function was then used in Equation (1) as an initial condition for ray tracing and aging. The method thus had full CFD detail near the vehicle, and handled the crossflow in effectively the same way as traditional methods, lumping it near the aircraft.

This summation shows what the crossflow terms are, and that their integrated effect on the far field is accounted for in traditional linear theory. Replacing the area rule source with a CFD calculation requires inclusion of this effect, and potentially improvement of the lumping approximation.

2.1.2 Signature Evolution: Refraction and Aging

The amplitude of sonic booms is such that nonlinear effects cause a cumulative distortion, or aging, of signatures. The physical process was pointed out by Landau[16] and experimentally validated by DuMond *et al.*[17] Whitham[1] showed that this second-order effect could be treated as a consistent first-order solution. By this method, the solution given by Equations (1) and (2) is correct to first order but its detailed location, as given by the argument $x - \beta r$ of F, is correct to the zero'th order. This is adjusted to first order by replacing the ambient sound speed with a propagation speed corrected to first order:

$$a_0 \rightarrow a_0 + \delta a + \delta u \tag{9}$$

where δa and δu are the incremental sound speed and convection speed, respectively, associated with the first-order pressure disturbance δp. This speed adjustment is applied to the linear solution cumulatively from near the vehicle to the far field.

Atmospheric gradients are handled by the ray tracing method of geometrical acoustics.[5] In this method, acoustic energy propagates along rays and is contained within ray tubes. Within a ray tube, waves exhibit locally plane behavior and their amplitude is given by the wave energy, the ray tube area, and the acoustic impedance. The $1/\sqrt{r}$ relation in Equation (1) represents the amplitude relation for a plane wave in a uniform medium. Whitham[18] developed results for plane, cylindrical, and spherical waves in a uniform medium, and pointed out that a geometrical acoustics amplitude factor could also be substituted. All current sonic boom codes (beginning with the ARAP code,[19] which was the first to have all details correct) apply Bokhintzev's ray tracing and amplitude relations to Equation (1) or equivalent. This carries the assumption that the acoustic solution may be fairly represented by locally plane waves, which is equivalent to the locally axisymmetric assumption of Equation (1). This assumption is also implicit in the application of Whitham's rule for aging, which is implemented in the various codes.

2.2 Approaches to Matching

Four schemes present themselves for sonic boom prediction.

- Traditional linear analysis.
- CFD flowfield, match pressure at CFD cylinder radius [per Equation (1)], then propagate to the ground.
- CFD flowfield, multipole matching at the cylinder radius, then propagation of effective source function to the ground.
- CFD flowfield to inner radius r_{inner}, then 3-D quasi-acoustic numeric analysis to an outer radius r_{outer} where G_n approach 1, then propagation from r_{outer} to the ground.

Table 1 summarizes the features of each of these analyses in terms of their attention to the four components cited in Section 2.1.

Table 1

Summary of Quality of Schemes

Method	Source Details	Crossflow	Aging	Refraction
Traditional	X	▯	■	■
Press. match	■	X	■	■
Multipole	■	▯	■	■
Three Zone	■	■	■	■

X Not accounted for
▯ Lumped inclusion of total far field
■ Full detail

Aging and refraction always include full detail in that they properly account for these effects as they are accumulated from near the aircraft to the ground. The traditional approach models the aircraft only by area rule, while the other three schemes use CFD for full detail up to r_{inner}. The traditional method accounts for crossflow effects by its implicit generation of an effective far-field source, but does this as a lumped quantity at near the aircraft. If the pressure of a CFD solution is simply used as a starting point for propagation ("pressure match"), then the lumped crossflow effect is lost. The multipole matching method restores this accounting of crossflow. It is lumped, but the approximation is the same as in the traditional method, so there is a net gain of the improved near-field flow. The three-zone method offers the promise of accounting for crossflow detail, having it evolve with distance just as the refraction and aging elements do.

3.0 GOVERNING EQUATIONS FOR SONIC BOOM ANALYSIS

3.1 Euler Equations in a Nonuniform Atmosphere

The governing equations are mass:

$$\frac{D\rho}{Dt} + \rho\vec{\nabla} \bullet \vec{u} = 0 \tag{10}$$

momentum:

$$\rho\frac{D\vec{u}}{Dt} + \vec{\nabla}p + \rho\vec{\nabla}\Omega = 0 \tag{11}$$

energy (isentropic form):

$$\frac{D\rho}{Dt} - a^2\frac{Dp}{Dt} = 0 \tag{12}$$

and gas law (perfect gas):

$$\gamma p = a^2 \tag{13}$$

where a = sound speed
p = pressure
t = time
$\vec{u}$ = velocity
γ = ratio of specific heats
ρ = density
Ω = gravitational potential

$$\frac{D}{Dt} = \frac{\partial}{\partial t} + \vec{u} \bullet \vec{\nabla} \qquad \text{(substantial derivative)}$$

These equations (or slight variations) are numerically implemented in the CFD codes which would be used for the near-field solution. Equation (12) is used here for simplicity because solutions through second order will be sought and entropy changes occur at third order.

Viscosity is not included (i.e., the Euler equations are used rather than Navier Stokes) because sonic boom propagation is generally treated as inviscid. Viscous losses occur in the shocks, but these are treated as weak shocks with jump conditions based on the conservation laws embodied in the Euler equations. Details of losses in the shocks can be accounted for, and affect the high-frequency content of the boom, but do not affect the basic shape (i.e., shock strengths and locations) of the boom signature.[20]

3.2 Quasi-Linearization of Euler Equations

The acoustic equations are linearized forms of Equations (10) to (13). Those are the first terms of a series expansion in wave amplitude, while the quasi-linear equations needed here are second order. A solution is sought in the form

$$\begin{aligned} p &= p_0 + \delta p_1 + \delta^2 p_2 + \ldots \\ \vec{u} &= \delta \vec{u}_1 + \delta^2 \vec{u}_2 + \ldots \\ \rho &= \rho_0 + \delta \rho_1 + \delta^2 \rho_2 + \ldots \end{aligned} \tag{14}$$

The ambient is assumed to be windless ($\vec{u}_0 = 0$) and quiescent ($\frac{\partial ()_0}{\partial \tau} = 0$).

Equations (14) are substituted into Equations (10) to (13), and terms of various powers of δ separated. Equations formed from δ^0 are hydrostatic, those from δ^1 are acoustic, and those from δ^2 are quasi-linear. Prior to the substitution, Equation (13) can be used in Equation (12) to eliminate a^2 as a variable, and leaving three equations: mass, momentum and energy.

The hydrostatic (δ^0) equations are obvious or trivial. The acoustic (δ^1) forms of the mass, momentum, and energy equations are:

$$\frac{\partial \rho_1}{\partial \tau} + \vec{u}_1 \bullet \vec{\nabla}\rho_0 + \rho_0 \vec{\nabla} \bullet \vec{u}_1 = 0 \tag{15}$$

$$\rho_0 \frac{\partial \vec{u}_1}{\partial t} + \vec{\nabla} p_1 + \rho_1 \vec{\nabla}\Omega = 0 \tag{16}$$

$$\rho_0 \frac{\partial p_1}{\partial t} + \rho_0 \vec{u}_1 \bullet \vec{\nabla} p_0 - \gamma p_0 \frac{\partial \rho_1}{\partial t} - \gamma p_0 \vec{u}_1 \bullet \vec{\nabla}\rho_0 = 0 \tag{17}$$

Equation (15) may be rearranged as

$$\frac{\partial \rho_1}{\partial t} + \vec{\nabla} \bullet \rho_0 \vec{u}_1 = 0 \tag{15a}$$

The quasi-linear (δ^2) mass, momentum, and energy equations are

$$\frac{\partial \rho_2}{\partial t} + \vec{u}_2 \bullet \vec{\nabla}\rho_0 + \rho_0 \vec{\nabla} \bullet \vec{u}_2 + u_1 \bullet \vec{\nabla}\rho_1 + \rho_1 \vec{\nabla} \bullet \vec{u}_1 = 0 \tag{18}$$

$$\rho_0 \frac{\partial \vec{u}_2}{\partial t} + \vec{\nabla} p_2 + \rho_2 \vec{\nabla}\Omega + \rho_1 \frac{\partial \vec{u}_1}{\partial t} + \rho_0 \vec{u}_1 \bullet \vec{\nabla}\vec{u}_1 = 0 \tag{19}$$

$$\begin{aligned} &\rho_0 \frac{\partial p_2}{\partial t} + \rho_0 \vec{u}_2 \bullet \vec{\nabla} p_0 - \gamma p_0 \frac{\partial \rho_2}{\partial t} - \gamma p_0 \vec{u}_2 \bullet \vec{\nabla}\rho_0 \\ &+\rho_1 \frac{\partial p_1}{\partial t} + \rho_0 \vec{u}_1 \bullet \vec{\nabla} p_1 + \rho_1 \vec{u}_1 \bullet \vec{\nabla} p_0 - \gamma p_1 \frac{\partial \rho_1}{\partial t} - \gamma p_0 \vec{u}_1 \bullet \vec{\nabla}\rho_1 - \gamma p_1 \vec{u}_1 \bullet \vec{\nabla}\rho_0 = 0 \end{aligned} \tag{20}$$

Equation (18) can be regrouped in a manner similar to Equation (15).

Note that Equations (15), (16), and (17) have the form of linear operators on $(\ )_1$ quantities. Equations (18), (19), and (20) begin with these same operators, but acting on $(\ )_2$ quantities, and also have terms involving products of pairs of $(\ )_1$ quantities. Because of the similar first-order operator, Equations (18) through (20) can be combined with (15) through (17) for a single set of second-order equations in quantities $(\ )_1 + \delta(\ )_2$, as well as kept in the separate orders as written above.

3.3 Computational Equations and Algorithms

As noted earlier, two codes have been developed at NASA–Ames Research Center which solve simplified forms of the acoustic and quasi-linear equations. One solves the two-dimensional linear acoustic equations in a uniform atmosphere.[12,13] The other solves the two-dimensional quasi-linear equations in a uniform atmosphere.[14] Both use algorithms for which solutions remain coherent for long propagation distances. The equations solved are presented below.

3.3.1 Acoustic Equations

Davis[12] introduced an algorithm which was applied to solving the two-dimensional acoustic equations:

$$\frac{\partial p}{\partial t} + a^2 \rho \frac{\partial u}{\partial x} + \rho \frac{\partial v}{\partial y} = 0 \tag{21}$$

$$\frac{\partial u}{\partial t} + \frac{1}{\rho} \frac{\partial p}{\partial x} = 0 \tag{22}$$

$$\frac{\partial v}{\partial t} + \frac{1}{\rho} \frac{\partial p}{\partial y} = 0 \tag{23}$$

where ρ and a are constant ambient quantities. In vector form, these are

$$\frac{\partial p}{\partial t} + \rho a^2 \vec{\nabla} \cdot \vec{u} = 0 \tag{24}$$

$$\frac{\partial \vec{u}}{\partial t} + \frac{1}{\rho} \vec{\nabla} p = 0 \tag{25}$$

The vector form could equally well represent three-dimensional forms. Equations (24) and (25) correspond to Equations (15) and (16), except that here ρ_0 and a_0 are constant. At this level, the energy equation reduces to simple terms such that γp and $a^2\rho$ are interchangeable.

The numeric solution method was based on tracking a local phase variable. This provides phase and amplitude fidelity suitable for propagation over long distances. Example one- and two-dimensional problems are solved, demonstrating this low dispersion capability. An example of a two-dimensional wave interacting with a flat plate was included, demonstrating the capability to handle diffraction effects.

The obvious difference between Equations (24) and (25), as compared to (15) and (16), is that in Equations (15) and (16) ρ_0 is a function of space, and there is a gravitational potential term in Equation (16). The variability of ρ_0 can be treated by noting that in Equation (15) it can be merged with $\vec{u}_1$, while in Equation (16) (where it is not involved in any derivatives) it may be treated as a local quantity, with variations over scales much longer than wavelengths. For short wavelengths, it can be shown[15,21] that the potential term (which represents buoyancy) is negligible. Thus, Equations (15) and (16) can be brought to a form very close to that of (24) and (25), such that an algebraic equivalence can be established. Ambient gradients thus do not appear to pose a problem. A key requirement is the continued development of the numeric algorithm from two dimensions to three. The approximate two-dimensional aspects of sonic boom (near axisymmetric geometry) should be beneficial in this regard.

3.3.2 Burgers Equation

The equations discussed in Section 3.3.1 are linear acoustic. They will account for the diffraction effects of interest here and also for normal atmospheric gradients. They do not include the nonlinear steepening central to sonic boom aging. That level of nonlinearity is equivalent to the inviscid Burgers equation. Davis has extended the low dispersion algorithms to the following set of equations:[14]

$$u \frac{\partial R}{\partial x} + v \frac{\partial R}{\partial y} + \frac{\partial u}{\partial x} \frac{\partial v}{\partial y} = 0 \tag{26}$$

$$a^2 \frac{\partial R}{\partial x} + u \frac{\partial u}{\partial x} + v \frac{\partial u}{\partial y} = 0 \tag{27}$$

$$a^2 \frac{\partial R}{\partial y} + u \frac{\partial v}{\partial x} + v \frac{\partial v}{\partial y} = 0 \tag{28}$$

where $R = \log(\rho)$. While written as steady-state two-dimensional, these equations are equivalent to one-dimensional unsteady, analogous to the three-dimensional unsteady Equations (18) through (20). The following form is developed in Reference 14:

$$\frac{\partial v}{\partial \eta} - \frac{M^3(\gamma-1)}{2\beta^2} v \frac{\partial v}{\partial \xi} = 0 \tag{29}$$

Coordinate η, ξ may be interpreted as two spatial coordinates [as in Equations (26) through (28)] or as time and one spatial coordinate. When η is interpreted as time, Equation (29) is directly analogous to the inviscid Burgers equation implicit to Whitham's method of steepening of locally plane propagating waves. Davis presents various numeric solutions, using the same algorithms as applied to the acoustic equations discussed in Section 3.3.1.

While the algorithm has shown itself to be effective for this nonlinear problem, Equations (26) through (28) are somewhat further removed from Equations (18) through (20) than Equations (24) and (25) are from (15) and (16). Approaches toward bridging this gap are discussed in the next section.

3.4 Application to Full Quasi-Linear Equations

As seen in Section 3.3, the numeric methods developed at NASA–Ames have been applied to equations analogous to the governing equations presented in Section 3.2. The linear acoustic equations are close, requiring only adaptation to three dimensions and smooth atmospheric gradients. The nonlinear case is somewhat further from the governing equations, having been used only for two-dimensional steady (equivalent to one-dimensional unsteady) examples. The success of the same basic algorithm for both types of problem, however, suggests that these are the appropriate algorithms. There are three paths which can be taken:

1. Extend the acoustic formulation to three dimensions and nonuniform atmosphere [Equations (15) through (17)], as outlined in Section 3.3.1. This will permit calculation of diffraction effects in the middle zone. Nonlinear steepening may then be applied on top of this solution, using traditional sonic boom propagation methods. This represents an improvement over current lumped procedures, but will still lack full synchronization of crossflow and steepening in the middle zone.

2. Perform the same steps as above, but then also apply the numeric algorithms to Equations (18) through (20). This is a sequential approach, which would first yield $(\ )_1$ linear terms then $(\ )_2$ nonlinear steepening. Because of the analogy noted between the nonlinear and linear equations, the equations for $(\ )_2$ are inhomogeneous versions of those for $(\ )_1$, with the inhomogeneous terms being based on the known $(\ )_1$ solution. While this sequence solution is normally used for problems like scattering, and not "bootstrapping" a nonlinear solution, it has been shown[15] that such a sequenced analysis can exactly yield the inviscid Burgers equation.

3. Continue development of the application of the numeric algorithm to the nonlinear equations, working toward the equivalent of the combined second-order equations discussed in Section 3.2. The most important step will be extension to two and three dimensions.

These three paths are not separate, but effectively represent three stages of a holistic approach to this problem. Practicality of each will be established as they are implemented in the two codes.

4.0 SUMMARY AND RECOMMENDATIONS

The requirements for consistent treatment of nonlinear and crossflow effects in the middle zone of a three-zone sonic boom calculation scheme have been presented. A multipole matching scheme, which incorporates crossflow effects in a lumped fashion similar to traditional area rule methods, illustrates the magnitude of the issue and provides an objective method to establish the size of the middle zone. The governing equations for the middle zone have been derived from the Euler equations. Two numeric schemes, developed by NASA–Ames and successfully applied to subsets of these equations, have been reviewed. Analogies have been drawn between the simple cases solved thus far and the full equations. A sequenced approach has been presented, directed toward applying these numeric schemes to the three-dimensional non-uniform atmosphere case required for the middle zone.

REFERENCES

1. Whitham, G.B., "The Flow Pattern of a Supersonic Projectile", *Communications on Pure and Applied Mathematics, 5,* 301-348, 1952.

2. Walkden, F., "The Shock Pattern of a Wing-Body Combination, Far From the Flight Path", *Aeronautical Quarterly, IX* (2), 164-194, 1958.

3. Whitcomb, R.T., "A Study of the Zero-Lift Drag-Rise Characteristics of Wing-Body Combinations Near the Speed of Sound", NACA RM L52H08, 1952.

4. Lomax, H., "The Wave Drag of Arbitrary Configurations in Linearized Flow as Determined by Areas and Forces in Oblique Planes", NASA RM A55A18, 1955.

5. Blokhintzev, D.I., "The Propagation of Sound in an Inhomogeneous and Moving Medium I", *J. Acoust. Soc. Am., 18,* 322-328, 1946.

6. Ferri, A., Ting, L., and Lo, R.W., "Nonlinear Sonic-Boom Propagation Including the Asymmetric Effects", *AIAA Journal, 15* (5), 653-658, 1977.

7. Darden, C.M., "An Analysis of Shock Coalescence Including Three-Dimensional Effects With Application to Sonic Boom Extrapolation", NASA Technical Paper 2214, 1984.

8. Siclari, M.J., "Ground Signature Extrapolations of Three-Dimensional Near-Field CFD Predictions for Several HSCT Configurations", in *High Speed Research: Sonic Boom,* NASA Conference Publication 3173, compiled by Darden, C.M., October 1992.

9. Page, J.A., and Plotkin, K.J., "An Efficient Method for Incorporating Computational Fluid Dynamics into Sonic Boom Prediction", AIAA Paper 91-3275, 1991.

REFERENCES (Continued)

10. George, A.R., "Reduction of Sonic Boom by Azimuthal Redistribution of Overpressure", AIAA Paper 68-159, 1968.

11. Cheung, S.H., Edwards, T.A., and Lawrence, S.L., "Application of Computational Fluid Dynamics to Sonic Boom Near- and Mid-Field Prediction", *J. Aircraft, 29* (5), 920-926, 1992.

12. Davis, S., "Matrix-Based Finite Difference Algorithms for Computational Acoustics", AIAA Paper 90-3942, 1990.

13. Davis, S., "An Algorithm for Solving the Perturbed Gas Dynamic Equations", AIAA Paper 93-0664, 1993.

14. Davis, S., "Aeroacoustic Model for Weak Shock Waves Based on Burgers Equation", *AIAA Journal, 33* (1), 27-32, January 1995.

15. Plotkin, K.J., "The Effect of Atmospheric Inhomogeneities on the Sonic Boom", Ph.D. Thesis, Cornell University, 1971.

16. Landau, L.D., "On Shock Waves at Large Distances From the Place of Their Origin", *J. Phys. USSR, 9,* 496, 1945.

17. DuMond, J.W.M., Cohen, E.R., Panofsky, W.K.H., and Deeds, E., "A Determination of the Wave Forms and Laws of Propagation and Dissipation of Ballistic Shock Waves", *JASA, 18* (1), 97-118, 1946.

18. Whitham, G.B., "On the Propagation of Weak Shock Waves", *J. Fluid Mech., 1,* 290-318, 1956.

19. Hayes, W.D., Haefeli, R.C., and Kulsrud, H.E., "Sonic Boom Propagation in a Stratified Atmosphere, With Computer Program", NASA CR-1299, April 1969.

20. Chambers, J.P., Bass, H.E., Raspet, R., Cleveland, R.O., Hamilton, M.F., and Blackstock, D.T., "Comparison of Computer Codes for Propagation of Sonic Booms Through the Atmosphere", Paper 1pPA13, 129th Meeting of the Acoustical Society of America, Washington, DC, 30 May–3 June 1995.

21. Officer, C.B., *Introduction to the Theory of Sound Transmission, With Application to the Ocean,* McGraw-Hill, New York, 1958.

Active Sonic Boom Control

by Steven C. Crow and Gene G. Bergmeier

Aerospace and Mechanical Engineering Department
The University of Arizona
Tucson, Arizona

Summary

A theory and simulation code are developed to study nonsteady sources as means to control sonic booms of supersonic aircraft. A key result is that the source of sonic boom pressure is not confined to the length of the aircraft but occupies an extensive segment of flight path. An aircraft in nonsteady flight functions as a synthetic aperture antenna, generating complex acoustic waves with no simple relation to instantaneous volume or lift distributions.

The theory applies linear acoustics to slender nonsteady sources but requires no far field approximation. The solution for pressure contains a term not seen in Whitham's theory for sonic booms of distant supersonic aircraft. The term describes a pressure field that decays algebraically behind the Mach cone and, in the case of steady flight, integrates to a ground load equal to the weight of the aircraft. The algebraic term is separate from those that describe the sonic boom.

Two nonsteady source phenomena are evaluated: periodic velocity changes (surge), and periodic longitudinal lift redistribution (slosh). Surge can attenuate a sonic boom and convert it into prolonged weak reverberation, but accelerations needed to produce the phenomenon seem too large for practical use. Slosh may be practical and can alter sonic booms but does not, on the average, result in boom attenuation. The conclusion is that active sonic boom abatement is possible in theory but maybe not practical.

Table of Contents

1. Introduction

This is a study of sonic booms produced by aircraft in nonsteady flight. Our goal was to find whether nonsteady source phenomena can scramble or attenuate sonic booms heard by listeners on the ground. Such source phenomena would constitute active sonic boom control, similar to the active methods recently developed to control sound in enclosures.

A freely propagating sonic boom is very different than sound in an enclosure. Active sound control methods work best on sound fields in small enclosures or on sources near resonance, but neither condition applies to sonic booms. Active sonic boom control must somehow prevent the pressure waves generated by a supersonic aircraft from coalescing into compact and coherent wave at large distances. The control method must work for listeners located anywhere on the ground. A method that reduces sound at specific locations but increases it elsewhere could not be considered successful.

Pioneers of sonic boom theory were Landau (1945), Hayes (1954), and Whitham (1956). They developed a model of sonic booms that has guided thinking for forty years and has produced many accurate predictions. Figure 1.1 illustrates a few aspects of that model. An aircraft flying at a steady supersonic speed produces local flow perturbations, which can be treated by linear compressible flow theory if the perturbations are not too large. The perturbations evolve outward from the flight path on Mach cones, the characteristic surfaces of the underlying compressible flow equations. Linear theory implies that the Mach cones all incline at the same angle, but weak nonlinearities cause the cones to coalesce where pressure increases with distance back along the flight path. The coalesced cones form shock waves, and the shocks absorb more Mach cones until only a simple N-shaped pressure wave remains far from the flight path.

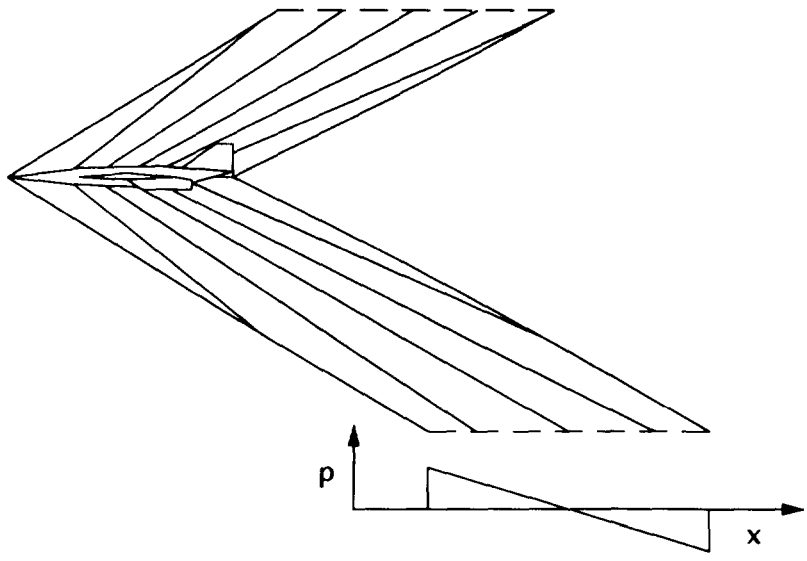

Figure 1.1. Sonic boom below an aircraft in steady supersonic flight. The Mach cones signify mathematical but not physical causality.

The model of Landau, Hayes, and Whitham has guided thinking about sonic booms for the past forty years. The model implies that sonic booms are likely to be robust, and indeed they are. The processes depicted in figure 1.1 seem inexorable. Each Mach cone seems able to convey information about the local shape of the aircraft outward and downward to the hapless listeners on the ground.

Yet there is a subtle loophole in the classic model of sonic booms. Landau developed the original theory of weakly converging characteristics in the context of signaling problems, where the characteristics really are trajectories of information flow. An example might be an oscillating point source, radiating spherical sound waves. Characteristics can be plotted as lines in coordinates of radius and time, and each characteristic can convey a message about the source until both characteristic and message are absorbed in a shock.

The characteristic cones of figure 1.1 are not characteristic surfaces of the compressible flow equations in three dimensions plus time and are not paths of information flow. They are mathematical conveniences resulting from the assumption that the aircraft is flying steadily. The aircraft in figure 1.1 could have ceased to exist, and the N-wave would arrive at the indicated location as though nothing had changed (sounds of disintegration would come later). The sonic boom was created somewhere back along the flight path and reflects flight conditions during some epoch before the instant depicted in the figure.

So where and when was the sonic boom created? A plausible answer involves ray paths, as seen in figure 1.2. Ray paths are orthogonal to Mach cones and are lines along which acoustic energy propagates. Perhaps the boom heard at a point on the ground propagated down a ray path that originated on the flight path of the aircraft. The source of the boom was the aircraft at an earlier time, an acoustic image shown as a dashed outline in the figure.

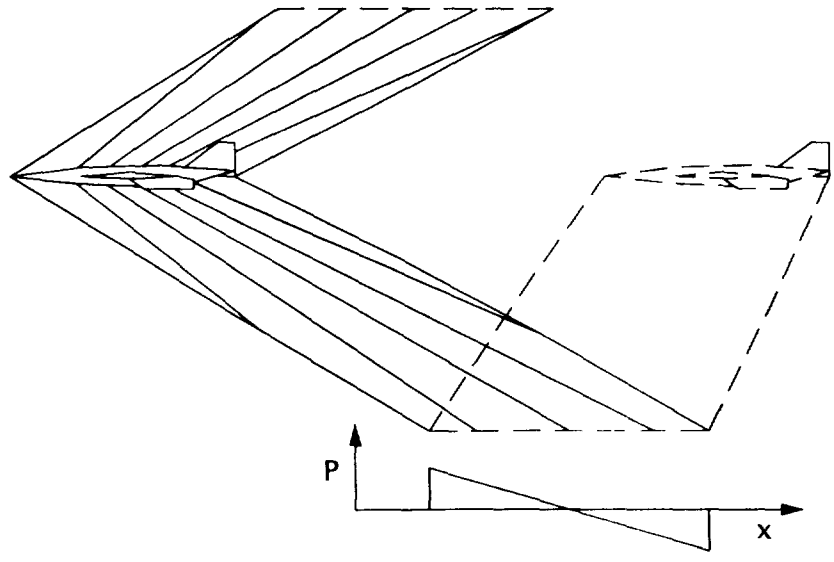

Figure 1.2. Ray model of a sonic boom source. Ray theory handles boom propagation phenomena well, but the phantom aircraft is not a valid source concept.

Ray theory, or geometrical acoustics, has played an important role in the study of sonic boom propagation. Most sonic boom prediction codes have combined Whitham's theory of weakly nonlinear wave propagation with ray tracing to account for maneuvers and atmospheric refraction (Hayes, Haefeli, and Kulsrud 1968). Despite its success with propagation phenomena, however, ray theory cannot provide a satisfactory account of the origin of sonic booms. Ray theory is based on a short-wave approximation that fails wherever the acoustic wave length is comparable to the scale for changes of pressure amplitude. Precisely such conditions prevail close to an aircraft, so the rays cannot be used to follow a sonic boom to its source.

The phantom aircraft of figure 1.2 is not the source of the sonic boom. The real source is more like a motion picture segment of the phantom aircraft and occupies a region extended in space and time, usually much longer than the aircraft itself. The extended source can be made to function as a synthetic aperture wave generator, which is why active sonic boom control is worth considering.

An aircraft can be an active acoustic source in two ways: by maneuvering or by changing shape. Elegant theories have been developed for the effects of large scale maneuvers, with emphases on the formation of "super booms" where shock waves fold into caustics (Seebass 1970). Those theories involve four modeling stages: linear steady compressible aerodynamics near the source, weakly nonlinear wave propagation, ray theory to locate caustics, and nonlinear transonic flow theory to handle the caustics themselves. Those theories may have some bearing on active control by maneuvers, but effective active control maneuvers take place at frequencies to high for steady aerodynamics and ray tracing to apply.

Garrick and Maglieri (1968) conducted flight tests that bear on the possibility of active sonic boom control. Figure 1.3 is reproduced from their report to illustrate the test conditions. The aircraft was an F106 flying at Mach 1.5 and an altitude of 35,000 ft. The pilot subjected the aircraft to a sinusoidal porpoising maneuver at a frequency of 1 Hz, with vertical accelerations of ± 0.5 g. Aerodynamic lift must have varied from 0.5 to 1.5 times the weight of the aircraft, so the source strength for the component of sonic boom due to lift varied by a factor of 3.0. Garrick and Maglieri expected the sinusoidal source variation to "print through" to the ground, producing a sinusoidal boom strength variation with a wave length around 1,500 ft. Notice that the figure shows both characteristics and rays, presumably path options along which the source variations might propagate to the ground.

When the records from the ground-based microphones were processed, they revealed no periodicity whatever near a wave length of 1,500 ft. Instead the wave forms seemed to vary at random as though subject to atmospheric turbulence (Crow 1969). Yet the tests had been conducted during early morning hours when the atmosphere was stable.

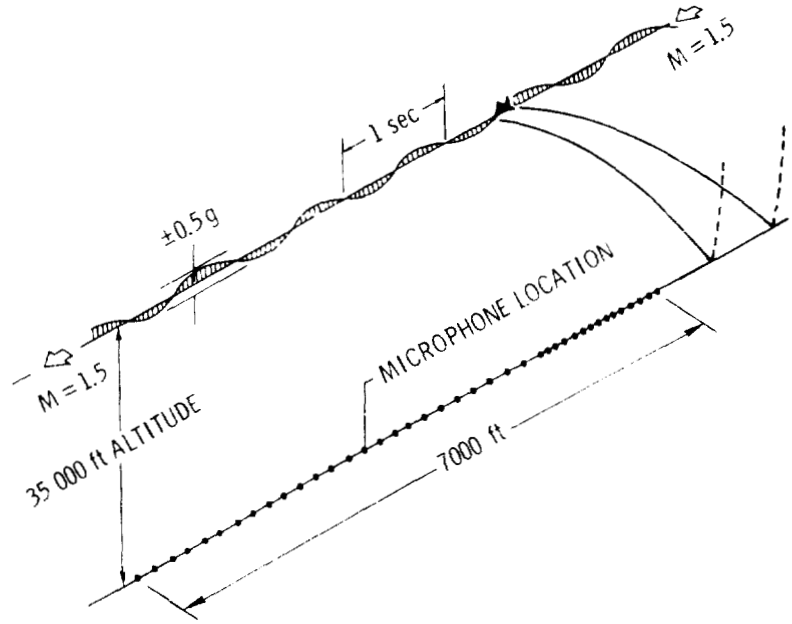

Figure 1.3. Schematic of test arrangements for evaluating the effects of aircraft motion on sonic boom pressure signatures on the ground (from Garrick and Maglieri 1968).

The results of the flight tests seemed anomalous and negative at the time, but they are consistent with the theory developed in this paper. Garrick and Maglieri's tests showed that the notion of boom source "print through" is wrong at frequencies as high as 1 Hz. The relation between an actively controlled source and a sonic boom on the ground is much more complicated. Even the simplest case of a point source moving steadily and oscillating sinusoidally produces a complex wave form with a spectrum of Doppler-shifted frequencies (Goldstein 1976). The acoustic signature of an aircraft with active sonic boom control will be even more complex.

2. Formulation

Our study of active sonic boom control is based on slender body theory and linear acoustics. Nonlinear shock formation and propagation may be important, but linear acoustics should provide a useful first look at prospects for active control.

The coordinates for the theory are time t and the three dimensions of space,

$$\mathbf{x} = (x, y, z), \tag{2.1}$$

fixed with respect to the atmosphere far from the aircraft. The aircraft flies along the x axis in the direction of decreasing x. The z axis points upward, and the y axis points along the starboard wing. The origin of time is chosen so that the aircraft nose intercepts the origin of coordinates at time zero.

Pressure is the sum of ambient pressure p_0 and a perturbation p,

$$p_0 + p(\mathbf{x}, t), \tag{2.2}$$

and density is expressed in similar form:

$$\rho_0 + \rho(\mathbf{x}, t). \tag{2.3}$$

The ambient pressure p_0 and density ρ_0 are defined at the altitude of the flight path, while p and ρ are perturbation pressure and density in our notation. The flow velocity $\mathbf{u}(\mathbf{x}, t)$ is measured relative to the atmosphere far from the aircraft.

Three equations set forth the principles of linear acoustics. They are conservation of mass,

$$\frac{\partial \rho}{\partial t} + \rho_0 \nabla \cdot \mathbf{u} = \rho_0 q, \tag{2.4}$$

conservation of momentum,

$$\rho_0 \frac{\partial \mathbf{u}}{\partial t} + \nabla p = \mathbf{f}, \tag{2.5}$$

and the equation of state for isentropic compression,

$$p = c_0^2 \rho. \tag{2.6}$$

The scalar source on the right of (2.4) represents a distributed volume flow of fluid of ambient density, while the vector source on the right of (2.5) is a distributed body force imposed on unit volumes of fluid. The quantity c_0 in (2.6) is the ambient speed of sound. The distributed sources are used to represent the passage of the aircraft.

The three equations can be combined into an equation for a single scalar variable, either the pressure perturbation or a velocity potential. To obtain an equation for the pressure perturbation, we differentiate (2.4) with respect to time, take the divergence of (2.5), and use (2.6) to eliminate density in favor of pressure. The result is a wave equation for pressure with source terms on the right:

$$\nabla^2 p - \frac{1}{c_0^2}\frac{\partial^2 p}{\partial t^2} = \nabla \cdot \mathbf{f} - \rho_0 \frac{\partial q}{\partial t} \tag{2.7}$$

That equation, with the addition of a nonlinear quadrupole source term, is the basis for the famous theory of aerodynamic sound (Lighthill 1953).

A second and complementary wave equation can be derived by introducing the concept of a distributed body *impulse* $\mathbf{i}$, defined by the ordinary differential equation

$$\mathbf{f} = \partial \mathbf{i} / \partial t . \tag{2.8}$$

A velocity potential ϕ is defined so that

$$\mathbf{u} = \frac{\mathbf{i}}{\rho_0} + \nabla \phi . \tag{2.9}$$

Impulse is not used much in acoustics but does play a role in classical hydrodynamics (Lamb 1933). In the context of linear acoustics, impulse is simply the integral of body force over all past times. Notice from (2.9) that the velocity field is not entirely potential, but includes a rotational component equal to the ratio of body impulse over density. The rotational component would include trailing vortices laid down by a traveling impulse.

An equation for velocity potential follows a derivation similar to that for pressure. We combine (2.5) and (2.9) to show that

$$\nabla\left(\rho_0 \frac{\partial \phi}{\partial t} + p\right) = 0 , \tag{2.10}$$

and the term in brackets is zero if the pressure perturbation and velocity potential decay to zero at infinity. We combine that result with (2.4), (2.6), and (2.8) to obtain a wave equation for velocity potential:

$$\nabla^2\phi - \frac{1}{c_0^2}\frac{\partial^2\phi}{\partial t^2} = q - \frac{1}{\rho_0}\nabla\cdot\mathbf{i}. \tag{2.11}$$

Equation (2.11) is useful for calculations of velocity components and wave drag.

The balance of the study is based on solutions of wave equations (2.7) and (2.11). The initial conditions are that the flow was zero in the distant past, and the boundary conditions are that the flow remains zero far from the origin. The source field q and force field $\mathbf{f}$ then determine the flow uniquely.

To define the source and force fields, we assume the aircraft is a slender body such that q and $\mathbf{f}$ are concentrated along the x axis. Slender body approximations do involve some loss of generality but are consistent with the nature of our study as a first look at active sonic boom control.

The essence of slender body theory is that the source and force fields are delta functions of y and z times functions of x and t. If the lift per unit length along the aircraft is $\mathcal{L}(x,t)$ reckoned positive upward, then the force field imposed on the air must have the form

$$\mathbf{f} = -\delta(y)\delta(z)\mathcal{L}(x,t)\mathbf{e}_z, \tag{2.11}$$

with an integral over y and z equal and opposite the longitudinal lift distribution. The impulse distribution satisfies a similar formula,

$$\mathbf{i} = -\delta(y)\delta(z)\mathcal{I}(x,t)\mathbf{e}_z, \tag{2.12}$$

with

$$\mathcal{L} = \partial\mathcal{I}/\partial t. \tag{2.13}$$

The formula for the source field has the form

$$q = \delta(y)\delta(z)\frac{\partial\mathcal{S}}{\partial t}(x,t), \tag{2.14}$$

where $\mathcal{S}(x,t)$ is the area of the fuselage cross section. Equation (2.14) implies that source strength is proportional to the local pulsation rate of the fuselage, an intuitively appealing result, but one that requires some care to prove (Cole 1953).

The formulation of the nonsteady sonic boom theory is complete. Equations (2.7) and (2.11) are to be solved subject to zero initial and boundary conditions at infinity and to the body force and source fields of (2.11) and (2.12). Aircraft speed and Mach number play no roles in the formulation but appear in specific selections of $S(x,t)$ and $\mathcal{L}(x,t)$. Fundamentally, the theory is indifferent to whether the aircraft is flying at subsonic or supersonic speed.

3. Pressure and Velocity

Equations (2.7) and (2.11) are linear nondispersive wave equations with inhomogeneous terms on the right. The simplest version is (2.11) with no body impulse, a wave equation for velocity potential driven by a scalar source field. The solution is a volume integral over all the sources,

$$\phi(\mathbf{x},t) = -\int_{\infty} q(\mathbf{x}',t')\frac{dV'}{4\pi R}, \tag{3.1}$$

where R is the distance between a source location $\mathbf{x}'$ and the point $\mathbf{x}$ where ϕ is evaluated,

$$R = |\mathbf{x} - \mathbf{x}'|, \tag{3.2}$$

and t' is a retarded time,

$$t' = t - R/c_0 . \tag{3.3}$$

Solution of wave equation (2.7) for pressure follows by differentiating and superposing terms of the form (3.1):

$$p(\mathbf{x},t) = \rho_0 \int_{\infty} \frac{\partial q}{\partial t'}(\mathbf{x}',t')\frac{dV'}{4\pi R} - \nabla \cdot \int_{\infty} \mathbf{f}(\mathbf{x}',t')\frac{dV'}{4\pi R}. \tag{3.4}$$

The integrals are performed over the three dimensions of space, but they simplify greatly when the slender body approximations for q and $\mathbf{f}$ are used. From (2.11) and (2.12),

$$p(\mathbf{x},t) = \rho_0 \int_{-\infty}^{\infty} \frac{\partial^2 S}{\partial t'^2}(x',t')\frac{dx'}{4\pi R} + \frac{\partial}{\partial z}\int_{-\infty}^{\infty} \mathcal{L}(x',t')\frac{dx'}{4\pi R}. \tag{3.5}$$

The divergence of the second term on the right simplifies to a derivative on z, because the body force $\mathbf{f}$ has a z component only.

The final step in the solution for pressure is to bring the derivative $\partial/\partial z$ into the second volume integral. The variable z occurs in R and also in the retarded time t', which depends on R through (3.3). Thus

$$p = \rho_0 \int_{-\infty}^{\infty} \frac{\partial^2 \mathcal{S}}{\partial t'^2} \frac{dx'}{4\pi R} - z \int_{-\infty}^{\infty} \left[\frac{\mathcal{L}}{R^2} + \frac{\partial \mathcal{L}/\partial t'}{c_0 R} \right] \frac{dx'}{4\pi R}. \tag{3.6}$$

The pressure wave forms presented in this paper are based on (3.6). We could compute pressure at any point and time $(\mathbf{x},t)$ but have generally assumed that the listener is located a distance h below the flight path, directly under the origin of coordinates. Thus

$$x=0, \quad y=0, \quad z=-h, \tag{3.7}$$

and

$$R=\left(x'^2+h^2\right)^{1/2}, \tag{3.8}$$

where h is altitude of the flight path above the listener. At location (3.7), pressure is a function of time:

$$p(0,0,-h,t)=p(t). \tag{3.9}$$

The fuselage area $\mathcal{S}$ and longitudinal lift distribution $\mathcal{L}$ remain as functions of (x',t') in the integrands of (3.6).

When the altitude h is more than a few thousand feet, the ambient density ρ_0 increases substantially from the flight path at $z=0$ to the ground at $z=-h$. The energy flux of a propagating wave tends to be conserved and is proportional to p^2/ρ_0, so the pressure amplitude increases as the square-root of ambient density as the wave propagates to the ground. A second phenomenon that alters a pressure wave is ground reflection, which doubles the amplitude when the ground is firm and smooth. The amplification factor

$$2\left[\rho_0(0)/\rho_0(-h)\right]^{1/2} \tag{3.10}$$

allows for both phenomena and has been included in all the pressure signatures presented here. If pressures computed by (3.6) were not multiplied by (3.10), they would appear small to those familiar with measurements of sonic booms on the ground.

Solution of wave equation (2.11) for velocity potential follows much the same line as the solution of (2.7) for pressure perturbation. The fundamental solution (3.1) and some differentiation and superposition produce the formula

$$\phi = -\int_{-\infty}^{\infty} \frac{\partial S}{\partial t'} \frac{dx'}{4\pi R} + \frac{z}{\rho_0} \int_{-\infty}^{\infty} \left[\frac{\mathcal{I}}{R^2} + \frac{\mathcal{L}'}{c_0 R} \right] \frac{dx'}{4\pi R} \tag{3.11}$$

analogous to (3.6) for pressure. The potential ϕ is a function of $(\mathbf{x},t)$, while the source terms $\mathcal{S}$, $\mathcal{L}$, and $\mathcal{I}$ in the integrals are functions of (x',t').

Velocity is the gradient of (3.11) plus an impulse vector, as seen in (2.9). We have used velocity only to compare formulas for velocity components and wave drag with classical formulas of steady flight. Two velocity components are important for the comparisons: the axial component u along the x-axis, and a radial component v normal to the x-axis. To facilitate calculation of the radial component, a change of coordinates from rectangular (x,y,z) to cylindrical (x,r,θ) is appropriate, with the substitutions

$$y = r\cos\theta\,, \quad z = r\sin\theta\,, \tag{3.12}$$

on the right of (3.11). The distance between the source and listener takes the form

$$R = \left[(x-x')^2 + r^2\right]^{1/2}, \tag{3.13}$$

and the desired velocity components follow from (2.9):

$$u = \frac{\partial\phi}{\partial x}\,, \quad v = -\frac{\sin\theta}{\rho_0}\frac{\delta(r)}{2\pi r}\mathcal{I}(x,t) + \frac{\partial\phi}{\partial r}\,. \tag{3.14}$$

The derivatives in (3.14) can be evaluated in a straightforward way from (3.11), and the orders of differentiation and integration exchanged to produce computable formulas for velocity components in nonsteady flight. The results, however, are hard to compare with established formulas for the velocity components around a supersonic aircraft (Whitham 1974, page 225). The reasons are not fundamental, but have to do with the fact that "judicious integration by parts is used to avoid divergent integrals" in the steady theory (*ibid.*, page 221). Parallel judicious integrations are needed to match the outcomes of (3.14) with Whitham's steady state theory.

To evaluate the first of equations (3.14), we recognize that the integrands of (3.11) have the form

$$\mathcal{J}(x',x-x',r,t), \tag{3.15}$$

where x' appears explicitly and also in the combination $(x-x')$ through (3.13). Thus

$$\frac{\partial\mathcal{J}}{\partial x} = \frac{\partial\mathcal{J}}{\partial x'} - \frac{d\mathcal{J}}{dx'}\,, \tag{3.16}$$

where $\partial\mathcal{J}/\partial x$ is the partial derivative that needs to be evaluated for the axial component of velocity u, and $d\mathcal{J}/dx'$ is a total derivative that allows for all dependencies on x'

with x, r, and t held fixed. An integration by parts can be performed on the term involving $d\mathcal{J}/dx'$, with the result that

$$u = -\int_{-\infty}^{\infty} \frac{\partial^2 \mathcal{S}}{\partial x' \partial t'} \frac{dx'}{4\pi R} + \frac{z}{\rho_0} \int_{-\infty}^{\infty} \left[\frac{\partial \mathcal{I}/\partial x'}{R^2} + \frac{\partial \mathcal{L}/\partial x'}{c_0 R} \right] \frac{dx'}{4\pi R}. \tag{3.17}$$

Evaluation of the radial component of velocity requires several tricks similar in flavor to (3.16), with the result that

$$\begin{aligned} v = {} & \frac{1}{4\pi r} \int_{-\infty}^{\infty} \left[\frac{1}{c_0} \frac{\partial^2 \mathcal{S}}{\partial t'^2} + \frac{(x-x')}{R} \frac{\partial^2 \mathcal{S}}{\partial x' \partial t'} \right] dx' - \frac{\sin\theta}{\rho_0} \frac{\delta(r)}{2\pi r} \mathcal{I}(x,t) \\ & - \frac{\sin\theta}{4\pi\rho_0} \int_{-\infty}^{\infty} \left\{ \frac{\mathcal{I}}{R^3} + \frac{(x-x')}{R} \left[\frac{\partial \mathcal{I}/\partial x'}{R^2} + \frac{\partial \mathcal{L}/\partial x'}{c_0 R} \right] + \frac{1}{c_0} \left[\frac{\mathcal{L}}{R^2} + \frac{\partial \mathcal{L}/\partial t'}{c_0 R} \right] \right\} dx' \end{aligned} \tag{3.18}$$

Equations (3.17) and (3.18) are easy to integrate numerically and easy to compare with Whitham's theory of steady supersonic flow about slender axisymmetric bodies.

4. Domain of Dependence

The integrals in solution (3.6) for pressure and the corresponding solutions (3.17) and (3.18) for velocity range over all values of x' from negative to positive infinity. To compute the integrals numerically, we need to put limits on the domain of integration. Selecting those limits takes us back to the question posed in the introduction: where and when was the sonic boom created?

In the usual acoustics terminology, the sources depend on the *dummy* variable of integration x' and the *retarded* time t'. We prefer more dignified names from relativity theory, where x' is the *proper* location of a source, and t' is *proper* time. From the vantage of the source, x' and t' are the variables that really matter. The fact that a source at proper location and time $(x',0,0,t')$ happens to be heard at $(0,0,-h,t)$ is no concern of the source!

Figure 4.1 shows an aircraft cutting a swath through the plane of proper coordinates (x',t'). The aircraft speed is assumed constant, so its nose traces a straight line through the origin, and its tail traces a parallel line shifted an aircraft length in the x' direction. The aircraft can generate sound only from a *zone of sources* between the two lines.

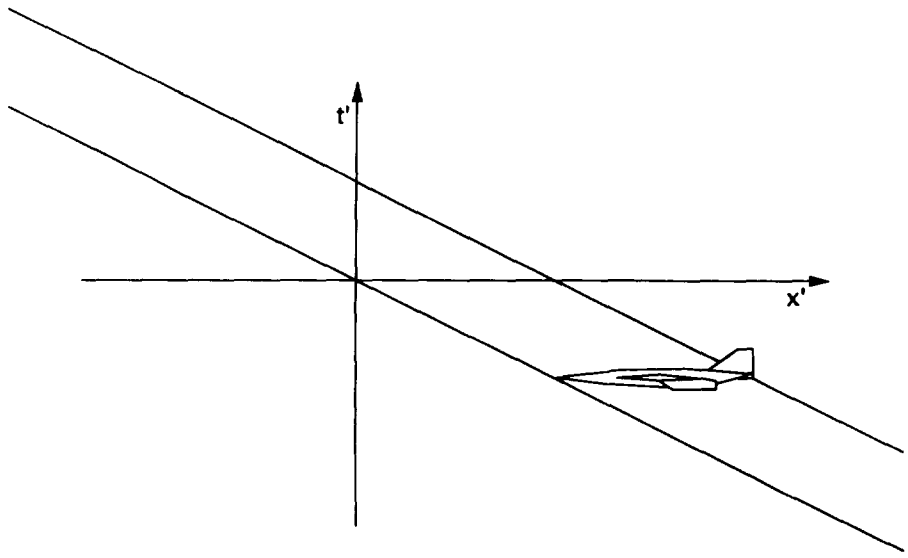

Figure 4.1. Zone of sources in proper coordinates (x',t'). The aircraft creates flow perturbations only within the zone of sources.

Not all of the zone of sources can contribute to the sound at a specific location and time below the flight path. Equation (3.3) imposes a functional relation between the proper location x' and time t' of the source. The shape of the function $t'(x')$ happens to be a hyperbola, which we call the *hyperbola of dependence.*

Figure 4.2 illustrates the zone of sources and hyperbola of dependence under conditions when the two overlap. Only sources along the segment of the hyperbola within the zone of sources can contribute to sound heard under those conditions. That segment of the hyperbola of dependence answers the question of where and when the sonic boom arose.

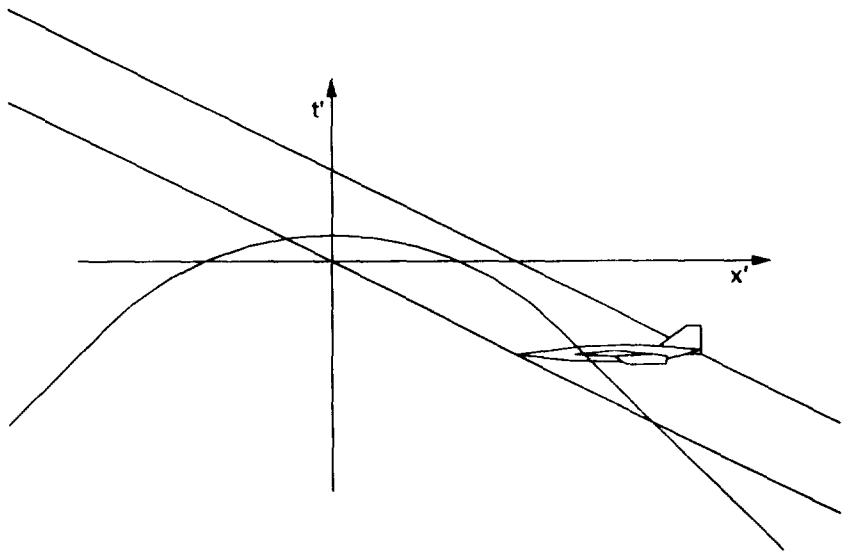

Figure 4.2. Hyperbola of dependence in proper coordinates (x',t'). Only sources along the segment of the hyperbola within the zone of sources contribute to sound at the listener position and time $(0,0,-h,t)$.

The nature of the overlap between the hyperbola of dependence and zone of sources depends on aircraft altitude and Mach number and on listener time t. The slope of the lines bounding the zone of sources is $-1/U$, where U is the speed of the aircraft. The asymptotes of the hyperbola of dependence have slopes $\pm 1/c_0$, where c_0 is the speed of sound. The ratio of the two slopes is the Mach number,

$$M = U/c_0 . \tag{4.1}$$

When $M < 1$, the zone of sources has a steeper slope than the asymptotes of the hyperbola of dependence. The two always overlap, and they overlap in one segment only. The physical consequence is that the listener always hears a subsonic aircraft, and the acoustic image of the aircraft occupies a single segment of sky. The acoustic image does not coincide with the current location of the aircraft and may be highly elongated.

When $M > 1$, the case shown in the figure, the hyperbola of dependence may overlap the zone of sources not at all, once, or twice, depending on aircraft altitude h and listener time t. Equation (3.3) implies that the hyperbola $t'(x')$ rises along the t' axis with advancing t, as shown in figure 4.3. No overlap occurs at early times, a single segment of overlap occurs at intermediate times, and two segments of overlap occur later. The physical consequences for the supersonic case are that the listener hears nothing for

awhile, then hears sources from an elongated but continuous segment of sky, and finally hears sources from *two* elongated segments of sky, which separate with time.

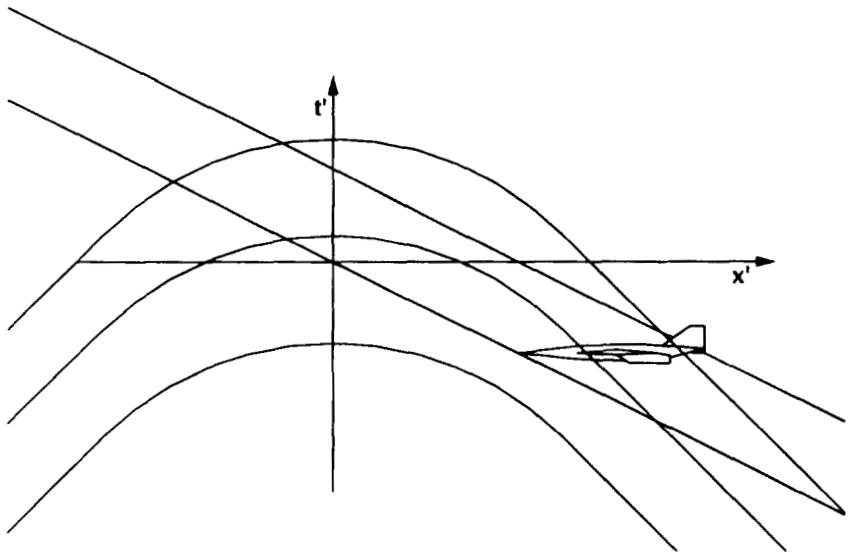

Figure 4.3. Upward migration of the hyperbola of dependence with increasing time t.

The path of the aircraft nose in the $(x't')$ plot satisfies the equation

$$t' = -x'/U, \tag{4.2}$$

while (3.3) provides the path of the hyperbola of dependence:

$$t' = t - \left(x'^2 + h^2\right)^{1/2} / c_0 . \tag{4.3}$$

The two equations are satisfied simultaneously where the hyperbola of dependence intersects the path of the nose, which is the lower boundary of the zone of sources. Equations (4.2) and (4.3) can be combined into a quadratic equation for x', which has one real solution for $M < 0$. For $M > 0$, the quadratic has no real solutions when t is less than the time

$$t_{nose} = \left(M^2 - 1\right)^{1/2} h / U \tag{4.4}$$

when sound first reaches the listener from the nose of the aircraft. When $t > t_{nose}$, the quadratic has two solutions

$$x'_{1,4} = \frac{Ut \mp MU\left(t^2 - t_{nose}^2\right)^{1/2}}{M^2 - 1}, \tag{4.5}$$

and those are the outer limits of the integrals that need to be performed to compute pressure and velocity from (3.6), (3.17), and (3.18).

Further contraction of the limits of integration can be achieved when the listener time t is greater than

$$t_{tail} = t_{nose} + L/U\,, \tag{4.6}$$

where L is the length of the aircraft. Equation (4.6) gives the time when sound from the tail of the aircraft first reaches the listener. The equation for the path of the aircraft tail in the (x', t') plot is

$$t' = (L - x')/U\,, \tag{4.7}$$

which replaces (4.2) in the simultaneous solution with (4.3). Two real solutions are found when $t > t_{tail}$, namely

$$x'_{2,3} = \frac{(Ut - L) \mp MU\left[(t - L/U)^2 - t_{nose}^2\right]^{1/2}}{M^2 - 1}, \tag{4.8}$$

which mark the intersections of the hyperbola of dependence with the upper boundary of the zone of sources.

The prescription for evaluating the solution integrals for supersonic flight is as follows. When $t < t_{nose}$, no sound has reached the listener. When $t_{nose} < t < t_{tail}$, the integrations are performed over the interval

$$x'_1 \le x' \le x'_4\,. \tag{4.9}$$

Finally, when $t > t_{tail}$, the integrations are performed over two intervals,

$$x'_1 \le x' \le x'_2\,, \quad x'_3 \le x' \le x'_4\,. \tag{4.10}$$

The limits of integration depend on sound speed, aircraft speed, aircraft length, aircraft altitude, and listener time. Figure 4.4 is a plot of the limits as functions of listener time for

$$\begin{aligned} c_0 &= 1{,}000 \text{ ft / sec}\,, \\ U &= 2{,}000 \text{ ft / sec}\,, \\ h &= 50{,}000 \text{ ft}\,, \\ L &= 400 \text{ ft}\,. \end{aligned} \tag{4.11}$$

The two curves in the plot are $x'_{1,4}$ and $x'_{2,3}$, double-valued functions of the listener time t. The region between the two curves is the comprehensive domain of dependence for the sonic boom heard by the listener.

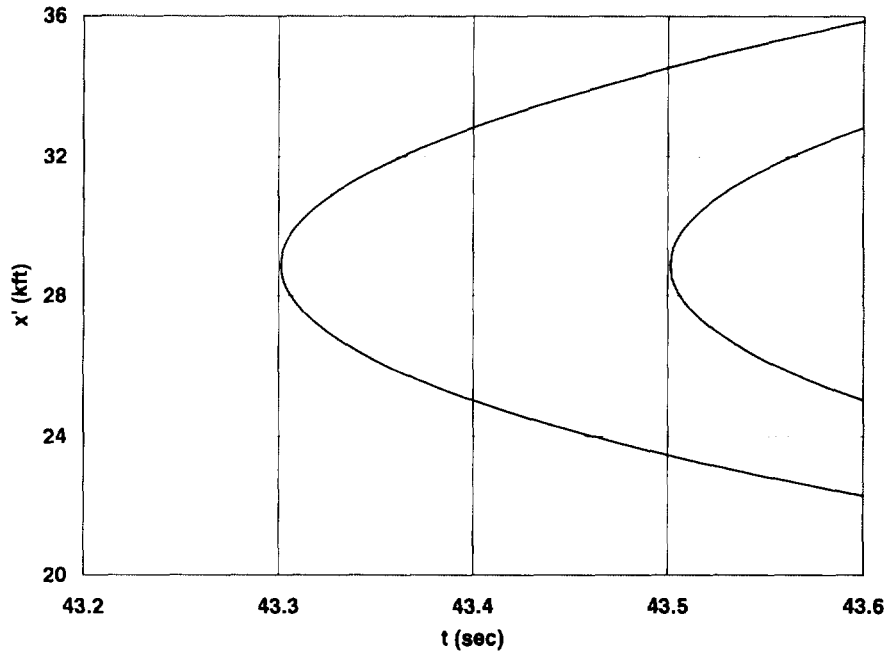

Figure 4.4. Domain of dependence for a sonic boom under conditions (4.11). Events between the two curves can influence the sonic boom heard by a listener on the ground.

The main lesson of figure 4.4 is that the domain of dependence extends over proper distances much larger than the aircraft. At $t = 43.4$ sec, for example, the sonic boom amplitude encompasses events that occurred over 8,000 ft of sky. At $t = 43.6$ sec, the listener hears sound from two segments of sky, each about 3,000 ft long, separated a distance of about 8,000 ft. Typical dimensions of the domain of dependence greatly exceed the length of the aircraft.

5. Lift and Drag

An enduring problem of sonic boom theory has been to explain how pressure transfers the weight of a supersonic aircraft to the ground. Equation (2.5) can be cast into integral momentum form, leaving no doubt that the integral of pressure over a rigid ground plane must equal the weight of the aircraft in steady flight regardless of Mach number. In a memorable section of their monograph on applied aerodynamics, Prandtl and Tietjens (1934) derived the asymptotic form of ground pressure below a low speed aircraft and showed that the pressure integrates to the weight of the aircraft. Yet an N-wave has equal positive and negative pressure lobes, so how can it support the weight of an aircraft? The answer can be found in nonsteady pressure solution (3.6).

The integral of the pressure perturbation over any horizontal plane is a force

$$\mathsf{F}(z,t) = \int_{-\infty}^{\infty}\int_{-\infty}^{\infty} p(x,y,z,t)\,dx\,dy\,, \tag{5.1}$$

which becomes a triple integral when (3.6) is put in place of pressure. Since the integrals all extend from $-\infty$ to ∞, the order of integration does not matter, and we can replace the variables x and y with polar coordinates centered on x'. The angular integral can be performed at once, leaving integrals over x' and the polar radius

$$a = \left[(x-x')^2 + y^2\right]^{1/2}. \tag{5.2}$$

Thus

$$\mathsf{F}(z,t) = \int_0^{\infty} 2\pi a \left\{ \int_{-\infty}^{\infty} \left[\rho_0 \frac{\partial^2 \mathcal{S}}{\partial t'^2} - \frac{z\mathcal{L}}{R^2} - \frac{z\,\partial\mathcal{L}/\partial t'}{c_0 R} \right] \frac{dx'}{4\pi R} \right\} da\,, \tag{5.3}$$

where

$$R = \left(a^2 + z^2\right)^{1/2}, \tag{5.4}$$

and

$$t' = t - R/c_0\,. \tag{5.5}$$

The sources $\mathcal{S}$ and $\mathcal{L}$ still depend on (x',t'), but R and t' no longer depend on x'. The integrals over x' can be performed independently of the integral over a. Define the total aircraft volume at time t',

$$\mathsf{V}(t') = \int_{-\infty}^{\infty} \mathcal{S}(x',t')dx', \tag{5.6}$$

and the total lift

$$\mathsf{L}(t') = \int_{-\infty}^{\infty} \mathcal{L}(x',t')dx'. \tag{5.7}$$

Force on the horizontal plane assumes a simpler form

$$\mathsf{F}(z,t) = \int_{0}^{\infty} \left[\rho_0 \frac{d^2\mathsf{V}}{dt'^2} - \frac{z\mathsf{L}}{R^2} - \frac{z\, d\mathsf{L}/dt'}{c_0 R} \right] \frac{a\, da}{2R}, \tag{5.8}$$

with only a single integral remaining. The first and third terms are zero in steady flight, and the second can be integrated explicitly:

$$\mathsf{F}(z) = -sgn(z)\mathsf{L}/2 \tag{5.9}$$

Equation (5.9) implies that pressure force on a plane below the aircraft ($sgn(z)$ negative) is half the total lift, and that is fine. The other half is suction above the aircraft. If there is a ground plane at some z below the aircraft, then the pressure doubles there. The ground bears the full lift, and a reflected pressure field cancels the suction above.

The term responsible for steady lift in (5.8) derives from the term involving $\mathcal{L}/R^2$ in the integrands of the pressure solution (3.6). That term differs structurally from the other two, which fall away with distance as $1/R$. Those two terms represent acoustic waves and are fully responsible for the N-wave. The term involving $\mathcal{L}/R^2$ is weaker but more extensive at large distances, extensive enough to account for the weight of the aircraft.

Wave drag presents some interesting conceptual issues for nonsteady flight. Should virtual mass effects be included in drag calculations, for example? Certainly virtual mass phenomena contribute forces in nonsteady flight but should average to zero when the nonsteady control measures are periodic. How about acoustic power radiation from a nonsteady *subsonic* aircraft? We may not think of such radiation as wave drag, but the power must some from somewhere and detract from power available to propel the aircraft.

A clean way to resolve such issues is to is to define a power equivalent wave drag on the basis of the acoustic energy equation. To derive an energy equation from (2.4)-(2.6), we form the scalar product of (2.4) and $\mathbf{u}$, multiply (2.5) by p/ρ_0, eliminate ρ through (2.6), and sum the results:

$$\frac{\partial}{\partial t}\left(\frac{\rho_0|\mathbf{u}|^2}{2}+\frac{p^2}{2\rho_0 c_0^2}\right)+\nabla\cdot(p\mathbf{u})=\mathbf{u}\cdot\mathbf{f}+pq \tag{5.10}$$

The right side of (5.10) is power input per unit volume, and the left is the sum of the rate of change of energy per unit volume plus the divergence of power flux. Power delivered to the flow is a volume integral of the right side,

$$P=\int_{\infty}(\mathbf{u}\cdot\mathbf{f}+pq)dV, \tag{5.11}$$

and a power equivalent wave drag D can be defined as P/U. By averaging the drag over a control cycle, we can show from (5.10) that

$$D=\frac{1}{U}\oiint pv\,dS \tag{5.12}$$

where the surface integral extends over an infinite cylinder whose axis is the flight path, and v is the radial component of velocity given by (3.18). Use of a cylinder surrounding the flight path as a surface of integration avoids the power imparted to trailing vortices, which is infinite in slender body theory!

6. Steady Source Examples

Once the limits of integration are understood, the pressure perturbation (3.6) is easy to evaluate by numerical integration. We have developed several codes to explore features of the pressure perturbation, all using Simpson's rule to integrate between the limits (4.9) and (4.10). The formulation is nonsteady, but the codes apply just as well to steady flight. This section provides two examples.

Figure 6.1 illustrates the first example, an aircraft with a parabolic fuselage and delta wing. The fuselage and wing are assumed for simplicity to have the same length. The wing is assumed to be flat, so the lift distribution has the triangular form shown in the lower part of the figure. The triangular lift distribution derives from slender body theory.

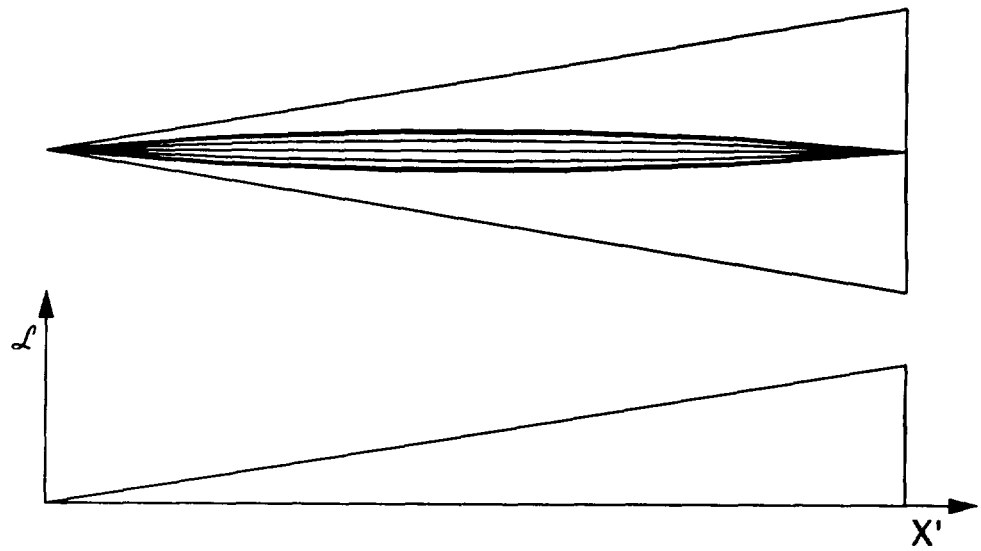

Figure 6.1. Aircraft with a parabolic fuselage and a delta wing.

A steady source or lift distribution depends on the proper variables x' and t' only in the combination

$$X' = x' + Ut' . \tag{6.1}$$

We introduce a boxcar function

$$B(X') = \begin{cases} 1, & 0 \le X' \le L \\ 0, & \text{otherwise} \end{cases} \tag{6.2}$$

to account for the fact that the source and lift distributions are nonzero only over the length of the aircraft. The formula for the area distribution of a parabolic fuselage is

$$\mathcal{S}(X') = \pi B(X')\left\{4R_{max}\frac{X'(L-X')}{L^2}\right\}^2, \tag{6.3}$$

where R_{max} is the maximum fuselage radius. The lift distribution of a delta has the form

$$\mathcal{L}(X') = B(X')\frac{2WX'}{L^2}, \tag{6.4}$$

where W is the weight of the aircraft. The pressure solution (3.6) involves $\mathcal{L}$ and its first time derivative, as well as the second time derivative of $\mathcal{S}$. Because of the cusped shape of the area distribution, the derivatives of the boxcar function contribute nothing to the second derivative of (6.3), but the first derivative of (6.4) produces a delta-function singularity at $X' = L$, which needs special treatment during numerical integration.

Figure 6.2 shows sonic boom wave forms computed from (3.6) times the amplification factor (3.10) to correct for density altitude and ground reflection. Flight conditions include equations (4.11) plus a radius and weight appropriate for a supersonic transport:

$$\begin{aligned} R_{max} &= 10 \text{ ft}, \\ W &= 600{,}000 \text{ lbs}. \end{aligned} \tag{6.5}$$

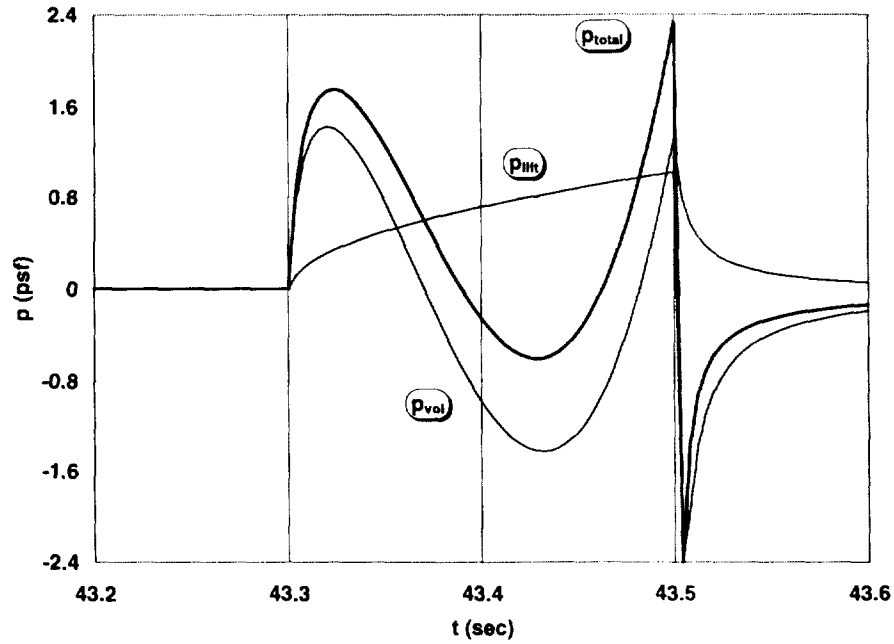

Figure 6.2. Sonic boom wave forms for a supersonic transport with a parabolic fuselage and delta wing. Volume and lift contributions are shown separately, along with their sum.

The thin curves in figure 6.2 depict pressure wave forms due to volume and lift, while the thicker curve is the total pressure perturbation. The maximum overpressure, about 2 psf, is typical for sonic booms from large aircraft. The theory does not account for nonlinear propagation phenomena, so the sonic boom has only a vague resemblance to an N-wave.

Wave forms similar to those of figure 6.2 can be found in past work on steady supersonic flows. A plot of the pressure wave from a parabolic fuselage, for example, appears on page 92 of a monograph on aerodynamic theory by Lighthill (1960). The agreement of figure 6.2 with steady state analyses helps validate our computational methods.

Our second steady example has a fuselage shaped as a half sine wave and a quarter wave wing. When the wing is flat, slender body theory implies that the lift distribution is a half sine wave, as seen in figure 6.3. The fuselage area and lift distributions have the forms

$$\mathcal{S}(X') = \pi B(X')\left\{ R_{max}\, sin\left(\frac{\pi X'}{L}\right)\right\}^2, \tag{6.6}$$

$$\mathcal{L}(X') = B(X')\frac{\pi W}{2L} sin\left(\frac{\pi X'}{L}\right). \tag{6.7}$$

Lift is symmetric around the midpoint of the wing and tapers to zero at both the apex and trailing edge. The time derivative of (6.7) produces no delta function, and no allowance must be made for a singularity at the trailing edge when performing the integrals of (3.6).

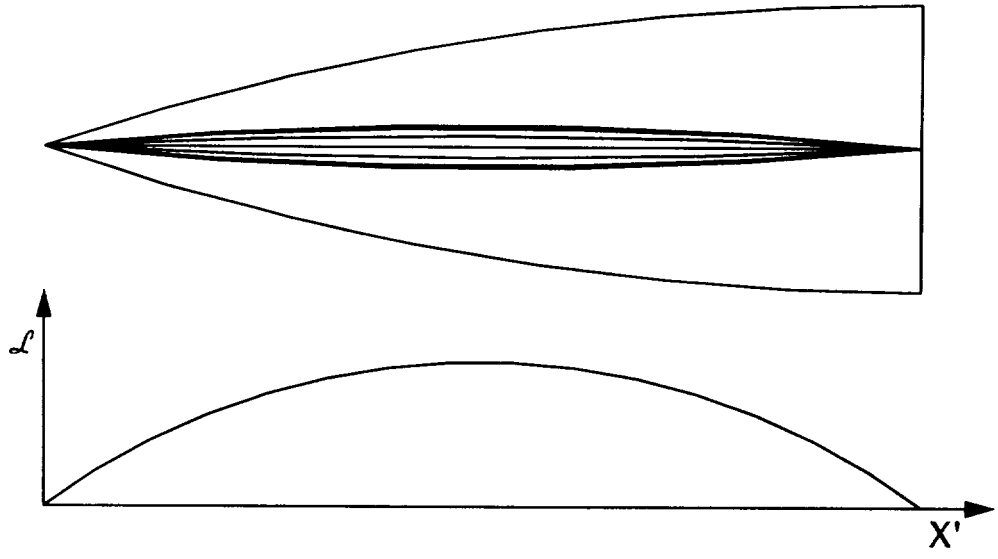

Figure 6.3. Aircraft with a half sine fuselage and a quarter sine wing.

Figures 6.4 and 6.5 show pressure waves and their sources for the second steady example. Flight conditions are those of (4.11) and (6.4). The pressure wave due to volume is about the same as seen in figure 6.2, as is maximum overpressure. The wave form due to lift is

smoother around the time waves first arrive from the trailing edge of the wing because of the absence of a lift discontinuity.

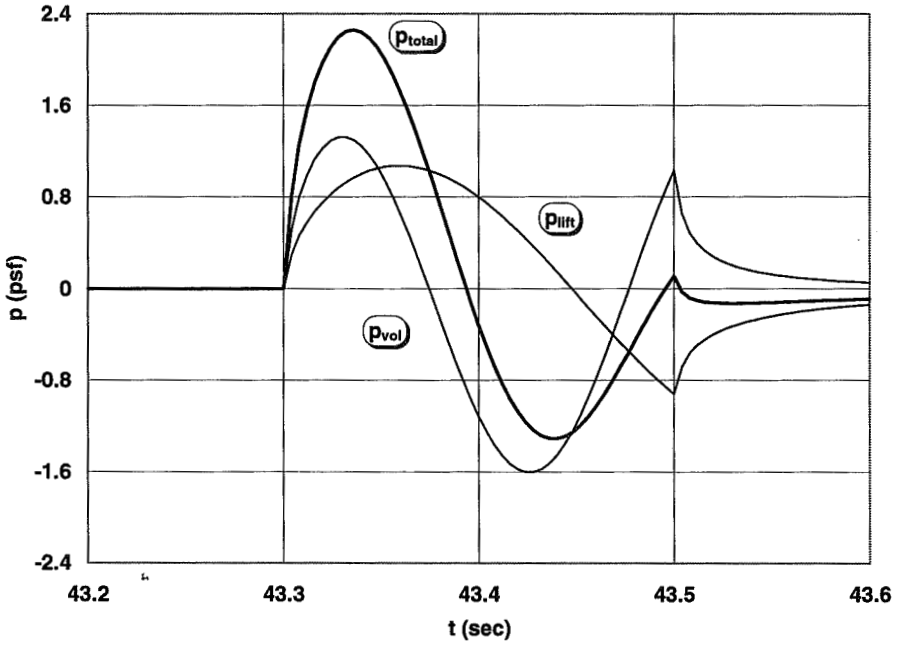

Figure 6.4. Sonic boom of a supersonic transport with a half sine fuselage and a quarter sine wing.

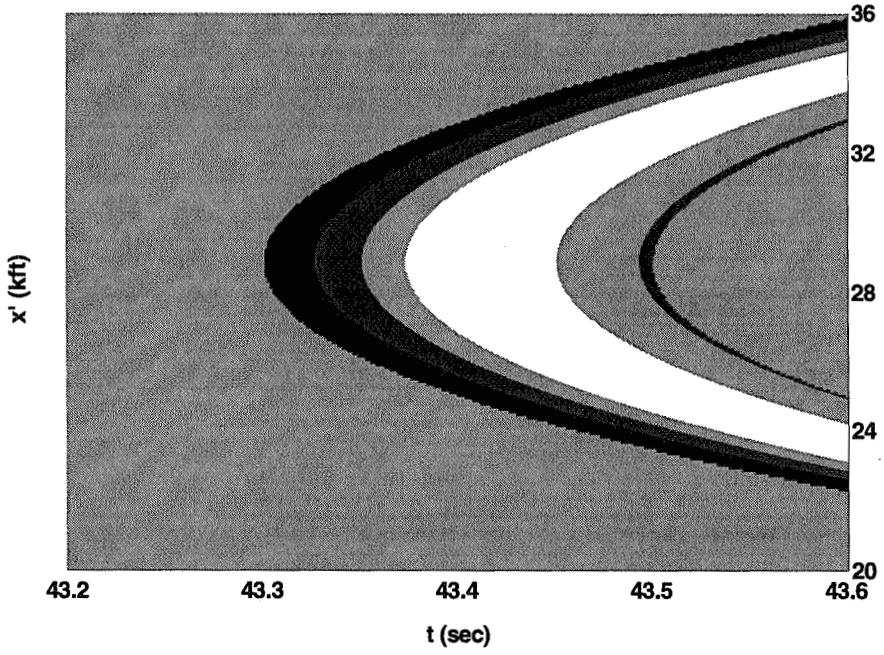

Figure 6.5. Source distribution for the sonic boom of figure 6.4. The domain of dependence is the same as seen in figure 4.4.

Figures 6.4 and 6.5 are a complete picture of the amplitude and origin of a sonic boom. The two figures have the same horizontal axis, listener time t. At any t, the sonic boom amplitude of figure 6.4 is an integral of sources along the x' axis of figure 6.5. The gray levels of figure 6.5 indicate the sum of the three integrands in the pressure solution (3.6). The region with the largest positive sources is black, intermediate positive sources are dark gray, sources near zero are light gray, and negative sources are white. Because the sources are so extensive, their actual values are small. The largest source in the domain of dependence is 0.00034 psf/ft, and the most negative is -0.00022 psf/ft. When integrated over proper distances of 8,000 ft, those sources are fully capable of producing the sonic boom amplitudes shown in figure 6.4.

7. Steady Pressure Solution

The examples of the foregoing section are steady but were computed from the nonsteady pressure solution (3.6). This section shows how to transform (3.6) into an explicitly steady solution for comparison with past theory. The transformed steady solution is almost the same as past results but contains an additional term due to lift, the term that accounts for transfer of aircraft weight to the ground.

A source moving steadily along the x' axis is a function of the composite variable X' defined by (6.1). Pressure around a steady source is likewise a function of a composite variable

$$X = x + Ut, \tag{7.1}$$

together with the coordinates y,z transverse to the direction of travel. When the variables X and X' are included in (3.6), the pressure solution takes the form

$$p(X,y,z) = \rho_0 U^2 \int_{-\infty}^{\infty} \mathcal{S}''(X')\frac{dx'}{4\pi R} - \int_{-\infty}^{\infty}\left[\frac{\mathcal{L}'(X')}{R^2} + \frac{M\mathcal{L}''(X')}{R}\right]\frac{dx'}{4\pi R}, \tag{7.2}$$

where

$$R = \left[(x-x')^2 + r^2\right]^{1/2} \quad \text{and} \quad r = \left(y^2 + z^2\right)^{1/2}. \tag{7.3}$$

Primes on the area and lift distributions indicate differentiations with respect to their argument. The right side of (7.2) may seem to retain a separate dependence on x, but that is not so. Only the difference $(x-x')$ appears in the integrand, and the difference could be used as a dummy variable of integration.

To recover past results for steady sonic booms, we have only to substitute X' in place of x' as the variable of integration on the right of (7.2). The two variables are related by definition (3.3) of proper time, which may be written in the forms

$$\begin{aligned} X - X' &= x - x' + U(t - t') \\ &= x - x' + MR. \end{aligned} \tag{7.3}$$

The latter can be solved for $(x-x')$ as a function of $(X - X')$ to substitute one variable for the other.

Figure 7.1 illustrates the relation between X' and x' for the case of supersonic flight. X' has a maximum,

$$X' \leq X - Br, \tag{7.4}$$

where

$$B = \left(M^2 - 1\right)^{1/2} \tag{7.5}$$

The maximum is negative where X lies ahead of the Mach cone whose apex is the nose of the aircraft. There the area and lift distributions are zero for all x', and the pressure perturbation is zero. Otherwise a each value of X' corresponds to two values of x', and contributions from both must be included in the transformed integral.

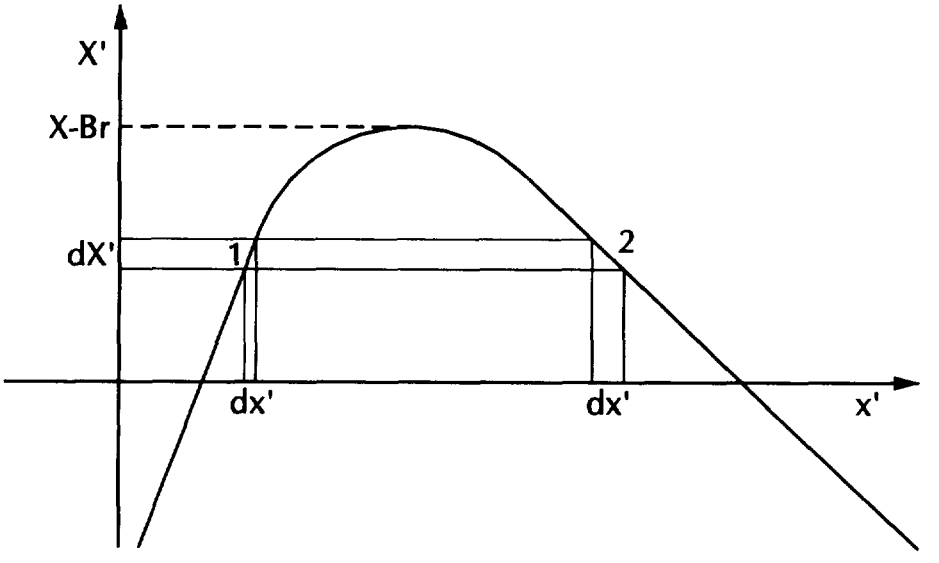

Figure 7.1. Relationship of the alternative integration variables X' and x'.

The Jacobian of the transformation proves to be

$$\left|\frac{dx'}{dX'}\right| = \frac{R}{\lambda}, \tag{7.6}$$

where

$$\lambda = \left[(X - X')^2 - B^2 r^2\right]^{1/2} \tag{7.7}$$

The Jacobian (7.6) applies to each of the two values of x' at a single X', so a term of the integral over x' produces two terms in the integral over X'. The integral simplifies fairly well after a good deal of algebra, with the result that

$$p = \rho_0 U^2 \int_0^{X-Br} \mathcal{S}''(X') \frac{dX'}{2\pi\lambda}$$
$$- z \int_0^{X-Br} \left\{ \frac{M^2 (X-X') \mathcal{L}'(X')}{(X-X')^2 + r^2} + \frac{\left[\left(M^2+1\right)(X-X')^2 - B^2 r^2 \right] \mathcal{L}(X')}{\left[(X-X')^2 + r^2 \right]^2} \right\} \frac{dX'}{2\pi\lambda} \tag{7.8}$$

Equation (7.8) is the solution for the pressure perturbation around a slender body with lift in steady supersonic flight. The solution is based on linear flow equations, but no assumptions have been made about distance from the slender body, and (7.8) should be valid everywhere.

The first integral of (7.8) represents the pressure perturbation caused by the fuselage. The integral can be found in various references (*e.g.* Whitham 1974) but is most commonly seen in an asymptotic form valid far from the flight path. The second integral represents the pressure perturbation due to lift. It has two terms. The first dominates close to the Mach cone and contributes to the N-wave, while the second is more extensive and accounts for transfer of weight to the ground. The asymptotic form of the first term agrees with published work (*e. g.* Hayes 1971), but we have not found the general form in the literature. We found no references to the second term due to lift but presume it was published in early papers on sonic booms, perhaps in the 1950's.

The steady solution (7.8) is more complicated than the nonsteady solution (3.6). Both involve single integrals over finite domains of integration, and the nonsteady solution is faster to compute than the steady solution, even for steady sources. Nonsteady sonic boom theory has received little attention in the past, but maybe it could become a basis for efficient computations in the future.

8. Steady Lift and Drag

The second term of the lift integral of (7.8) has an asymptotic limit quite different than those that make up the sonic boom. To evaluate the integral far from the flight path, note that $\mathcal{L}'(X')$ is nonzero only from 0 to L, regardless of the upper limit $X - Br$. As r becomes large, X' becomes negligible in the factors multiplying $\mathcal{L}'(X')$ everywhere that $\mathcal{L}'(X')$ is nonzero. The second term due to lift can be integrated to yield an asymptotic pressure formula proportional to total lift L,

$$p_{\mathcal{L}'} \to \frac{h\left[\left(M^2+1\right)X^2 - B^2r^2\right]\mathsf{L}}{2\pi\left(X^2+r^2\right)^2\left(X^2-B^2r^2\right)^{1/2}}, \tag{8.1}$$

valid behind the Mach cone where $X > Br$. Equation (8.1) is singular at $X = Br$, but the singularity is integrable. The integral over a horizontal plane below the aircraft is $\mathsf{L}/2$, and ground reflection doubles the integral to the full lift of the aircraft. Equation (8.1) is the analogue of the famous asymptotic formula for the ground pressure of a low speed aircraft (Prandtl and Tietjens 1934, pages 186-188).

Equation (8.1) is hard to plot because of the singularity at the Mach cone, but figure 8.1 shows exact values of the same pressure term for our aircraft with sinusoidal fuselage radius and lift distributions flying at Mach 2 and an altitude of 10,000 ft. The figure shows ground pressures at several lateral locations to indicate the extent of the pressure footprint. Not shown are the much larger sonic boom pressures near the Mach cone.

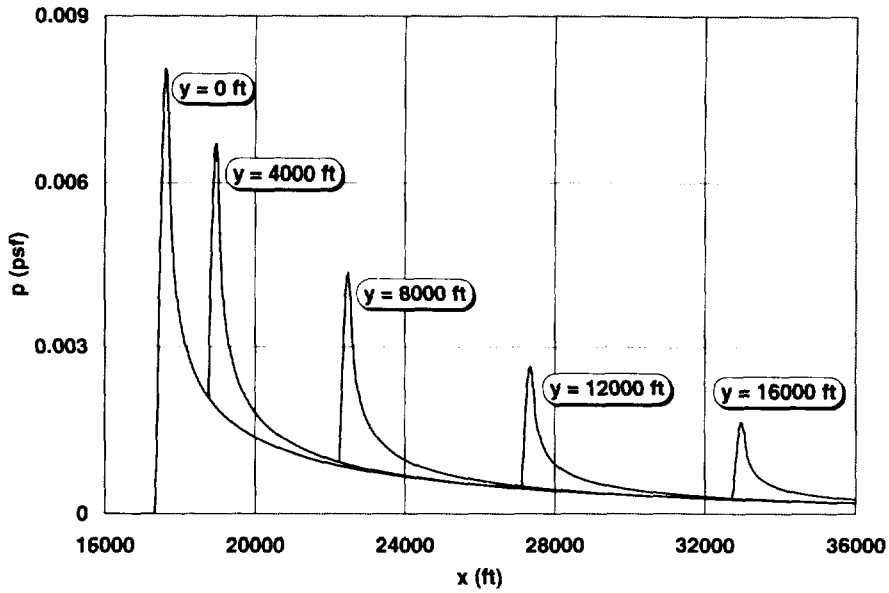

Figure 8.1. Ground pressure behind the Mach cone at various lateral distances from the flight path.

Our concept of power equivalent wave drag may seem exotic, but it reduces to the classical definition of wave drag when the flow is steady. With the substitution (7.1), the x component of the acoustic momentum equation (2.5) takes the form

$$\partial(\rho_0 Uu + p)/\partial X = 0, \tag{8.2}$$

when no body force is directed along the x axis. We conclude that the term in brackets is zero, and the drag formula (5.12) becomes a surface integral of momentum flux:

$$D = -\rho_0 \oiint uv dS. \tag{8.3}$$

Equation (8.3), together with asymptotic formulas for the longitudinal and radial velocity components, reproduces classical results for wave drag of slender bodies in supersonic flight (von Karman and Moore 1932).

9. Periodic Sources

The balance of this paper concerns periodic moving sources of the sort that might be used to control sonic booms. Of course any nonsteady sources aboard supersonic transports would face formidable constraints. We cannot seriously contemplate nonsteady fuselage shape changes, but perhaps leading edges with smart skins could periodically alter the longitudinal lift distribution. The total lift and center of lift could remain constant, but the lift distribution could "slosh" in and out from the middle of the aircraft to the nose and tail. Periodic maneuvers without shape changes are unattractive but theoretically possible. Without altering its flight path, an aircraft could "surge" periodically in speed. Both "slosh" and "surge" are examples of periodic moving sources.

Important information about active sonic boom control can be obtained from a general definition of periodic moving sources, without recourse to specific examples. The definition proves to be curiously subtle. In the context of slender body theory, any source is a function of the proper variables x', t'. A less obvious variable is the phase τ of the clock that times the periodic control measures aboard the aircraft. Any conclusions about active sonic boom control should be independent of the phase of the aircraft clock. Put another way, the conclusions should not depend on the location x of a listener under the flight path.

We thus assume that a periodic moving source is a function q of three variables (x', t', τ) including the phase of the control clock. "Moving" means that x' and t' combine into a single variable so that

$$q(x', t', \tau) = f(x' + Ut', t' - \tau). \tag{9.1}$$

"Periodic" means that q does not change when the phase increases by a time equal to the period T of the control system:

$$q(x', t', \tau + T) = q(x', t', \tau) \tag{9.2}$$

Equations (9.1) and (9.2) fully define a periodic moving source.

The source has a phase average

$$Q(x', t', \tau) = \frac{1}{T} \int_{\tau}^{\tau+T} q(x', t', \tau') d\tau'. \tag{9.3}$$

The phase average appears to be a function of the three variables (x', t', τ), but we can easily show from (9.1)-(9.3) that

$$\frac{\partial Q}{\partial \tau} = 0\,, \quad \frac{\partial Q}{\partial t'} - U\frac{\partial Q}{\partial x'} = 0\,. \tag{9.4}$$

Thus the phase average is a function of one variable only,

$$Q(x', t', \tau) = Q(x' + Ut')\,, \tag{9.6}$$

and has the same form as a steady moving source. Phase averaging smears the source distribution along a direction parallel to the boundaries of the zone of sources.

Phase averaging commutes with the spatial integrals of solution (3.6) for the pressure perturbation. Thus the phase-averaged pressure perturbation is the same as a pressure perturbation from the phase-averaged source, and the phase-averaged source is the same as a steady moving source. *The phase-averaged sonic boom is the same as the sonic boom of a steady aircraft whose source distributions are phase averages of sources under active control.*

Can active control have any effect on the average sonic boom? The answer may be no for control methods like slosh but clearly is yes for maneuvers like surge. Figure 9.1 shows how surge alters the extent of the zone of sources, stretching the zone from the aircraft length L to a greater length Λ, the sum of aircraft length plus twice the amplitude of surge. The phase-average theorem (9.6) still applies, but the phase-averaged source is an aircraft of length Λ rather than L.

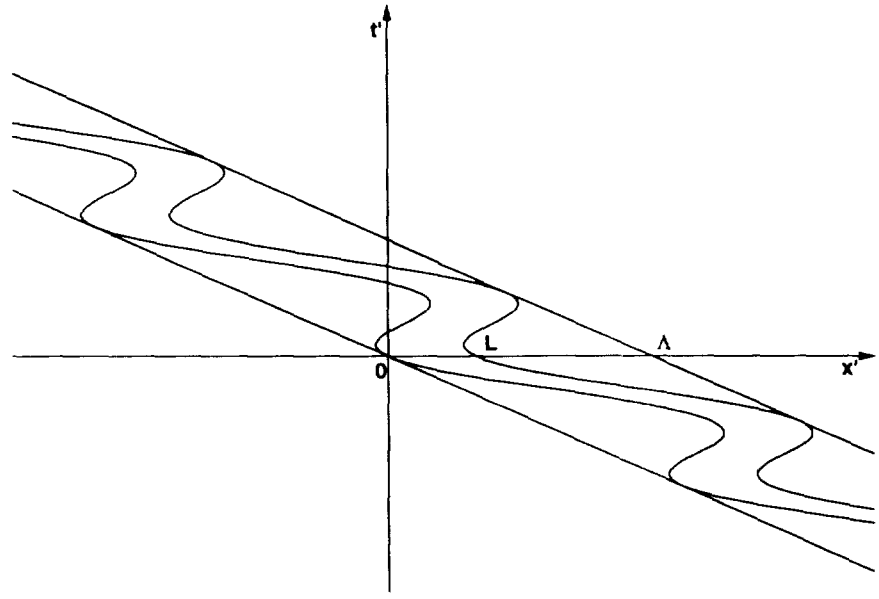

Figure 9.1. Zone of sources with periodic surge. Surge stretches the zone from the aircraft length L to some larger dimension Λ.

10. Periodic Slosh

Our first example of a periodic source is "slosh", a longitudinal flow of lift back and forth from the middle of the aircraft to the nose and tail. An aircraft with three lifting surfaces could implement slosh by oscillating control surfaces at the three trailing edges, with the canard and tail synchronized and the wing 180 deg out of phase. Alternatively, an elongated delta or quarter sine wing could have piezoelectric leading edges capable of bending into S shapes, thereby altering the longitudinal distribution of angle of attack.

We retain the sinusoidal fuselage radius of (6.6) but add a three-halves sine wave to the lift distribution (6.7):

$$\mathcal{L}(x',t') = B(X')\frac{\pi W}{2L}\left[(1-\beta)\sin\left(\frac{\pi X'}{L}\right)+3\beta\sin\left(\frac{3\pi X'}{L}\right)\right] \tag{10.1}$$

The lift distribution (10.1) is always symmetrical around the middle of the aircraft, so the center of lift never changes. The factors $(1-\beta)$ and 3β are selected so the total lift is constant as well. β determines whether the lift distribution is peaked in the middle or peaked toward the nose and tail. The formula

$$\beta = \beta_0 + \beta_1 \sin(2\pi f t' + \phi) \tag{10.2}$$

specifies a mean allocation of lift to the three-halves sine term as well as a periodic allocation of frequency f and phase ϕ in radians. The mean allocation is proportional to β_0 and the periodic allocation to β_1.

Figure 10.1 displays lift distributions for

$$\beta_0 = 0, \quad \beta_1 = 0.25. \tag{10.2}$$

The aircraft parameters are those of (4.11) and (6.5), while the proper time t' is zero in all cases. Lift plots for eight evenly spaced phases are shown: ϕ = 0, 90, 180, ... deg. Three of the plots overlap others. The amount of slosh is seen to be extreme. The lift at the middle of the aircraft periodically falls to zero and becomes double the mean value. We should not expect to attain greater lift variability in practice.

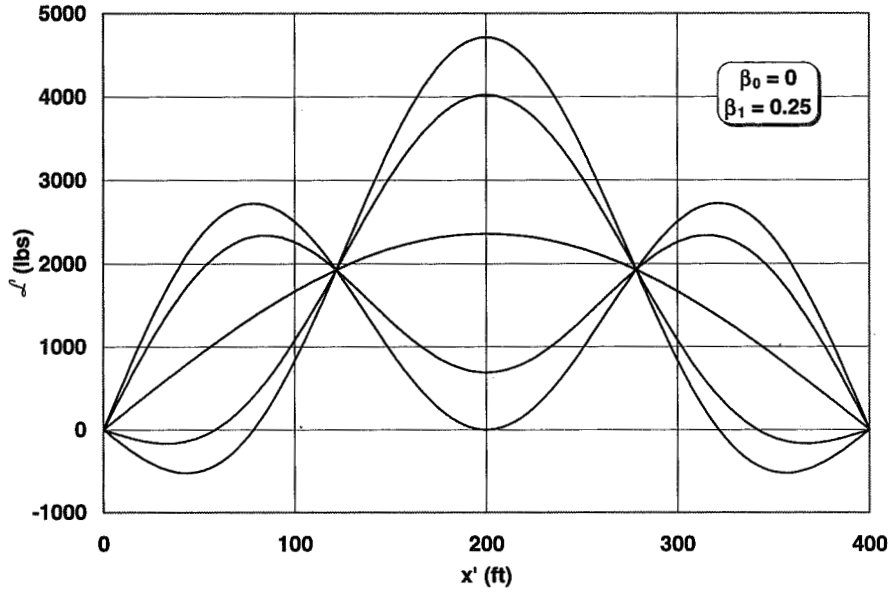

Figure 10.1. Longitudinal lift distribution under extreme slosh.

Figure 10.2 shows the source distribution that results when the slosh is imposed at a frequency f of 0.5 Hz, with a phase ϕ of zero. Extreme slosh has dramatic effects on the source distribution, as may be seen by comparing gray levels of figures 10.2 and 6.5. Convoluted source regions have replaced the clean arcs of the steady source example.

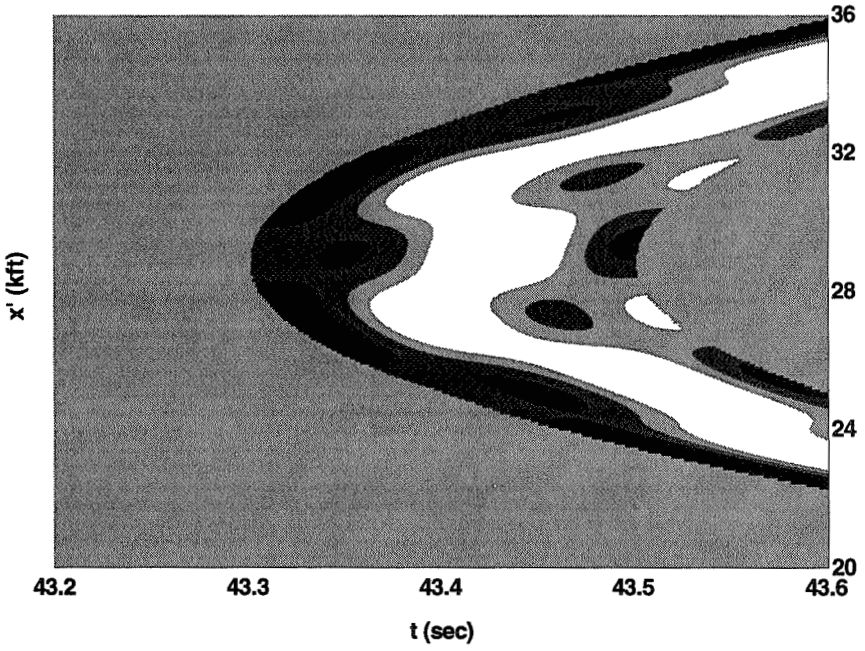

Figure 10.2. Source distribution under extreme slosh at a frequency of 0.5 Hz.

Figures 10.3 and 10.4 display sonic booms arising from periodic slosh. The darker curve in figure 10.3 is the boom at zero phase, while the lighter curve is the boom of the steady

source example, reproduced from figure 6.4. The lighter curves of figure 10.4 are booms at four phases of the slosh cycle: ϕ = 0, 90, 180, and 270 deg. The darker curve is the average of the four and is the same as the boom from the steady source, in conformity with the phase-average theorem of Section 9. We conclude from the plots that slosh alters the boom profoundly but does not reduce its pressure level.

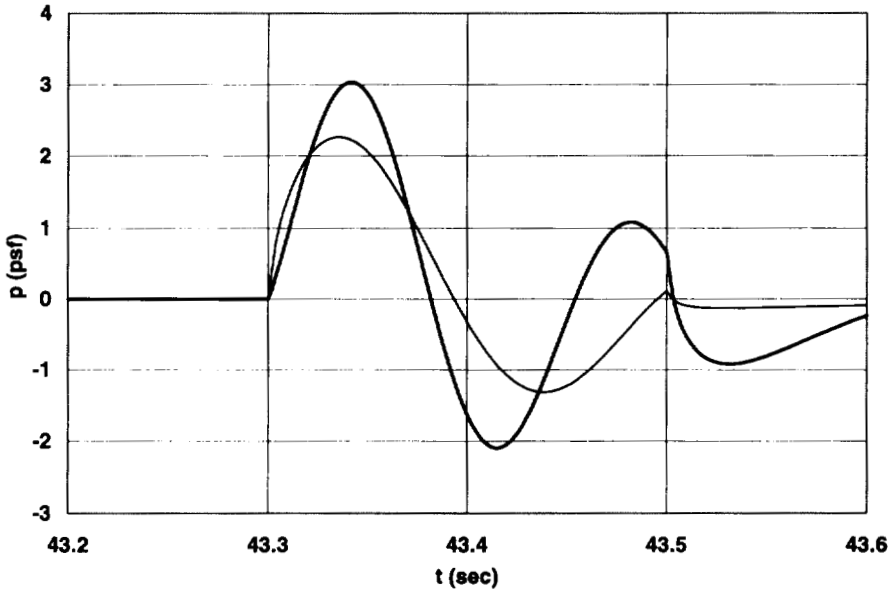

Figure 10.3. Sonic boom from a sloshed lift distribution. The light line depicts the sonic boom for steady lift.

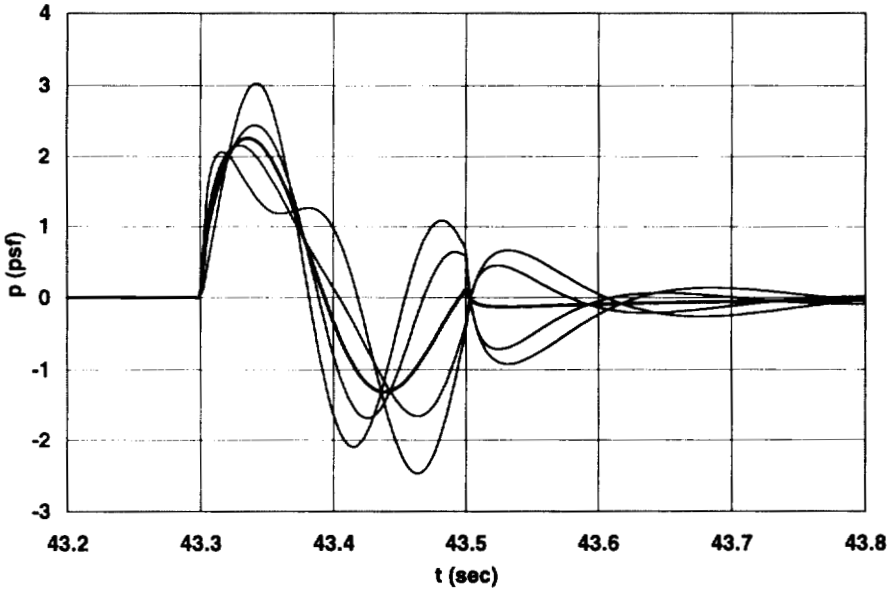

Figure 10.4. Sonic booms from four phases of the slosh cycle, together with their average shown as a darker curve. The average is the same as the boom from the steady source of figure 10.3.

11. Periodic Surge

Our second example of a periodic source is "surge", a periodic acceleration of the aircraft along its flight path. In principle, engine thrust variations could implement surge. A deliberately excited phugoid oscillation could do so also, with the complication of small periodic changes of altitude. We recommend neither mode of implementation for commercial supersonic transports!

The half sine fuselage and quarter sine wing of (6.6) and (6.7) suffice without change to demonstrate surge phenomenology. What must change is the definition of the composite proper coordinate X'. In place of (6.1), we require that

$$X' = x' + Ut' - \frac{(\Lambda - L)}{2}\left[1 - cos(2\pi f t' + \phi)\right], \tag{11.1}$$

where f is surge frequency and ϕ is an arbitrary phase. Surge is a sinusoidal motion superposed on the mean translatory motion of the aircraft. The amplitude of sinusoidal motion is $(\Lambda - L)/2$, where Λ is the length of the zone of sources shown in figure 9.1.

Figure 11.1 shows the source distribution derived from (6.6), (6.7), and (11.1) for a frequency of 0.5 Hz and zero phase. The aircraft parameters and flight conditions are from (4.11) and (6.5) as usual, while the amplitude of the surge is assumed to be 400 ft, the same as the length of the aircraft. The length of the zone of sources is 1,200 ft, three times longer than the aircraft.

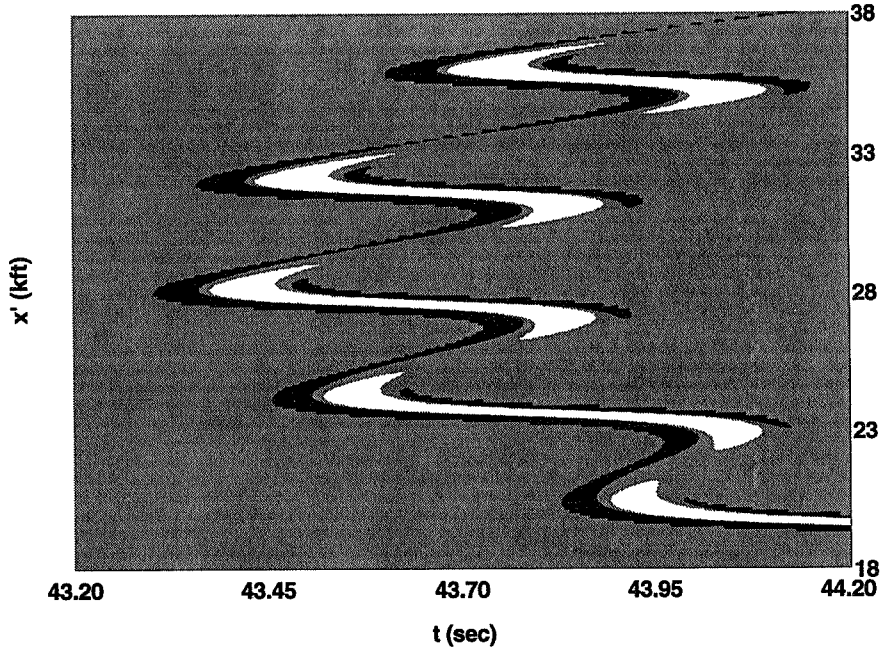

Figure 11.1. Source distribution for surge at a frequency of 0.5 Hz.

The sources in figure 11.1 are no longer compact within the nominal zone of sources. They snake back and forth between the boundaries of the zone, creating a stretched and attenuated virtual source of sound. Sonic booms from the surging aircraft are similarly stretched and attenuated, as shown in figures 11.2 and 11.3. The sonic boom of figure 6.4 has collapsed into waves of low amplitude resembling broad band noise. The waves seem oddly complicated in view of their origin from a simple aircraft undergoing a simple sinusoidal surge.

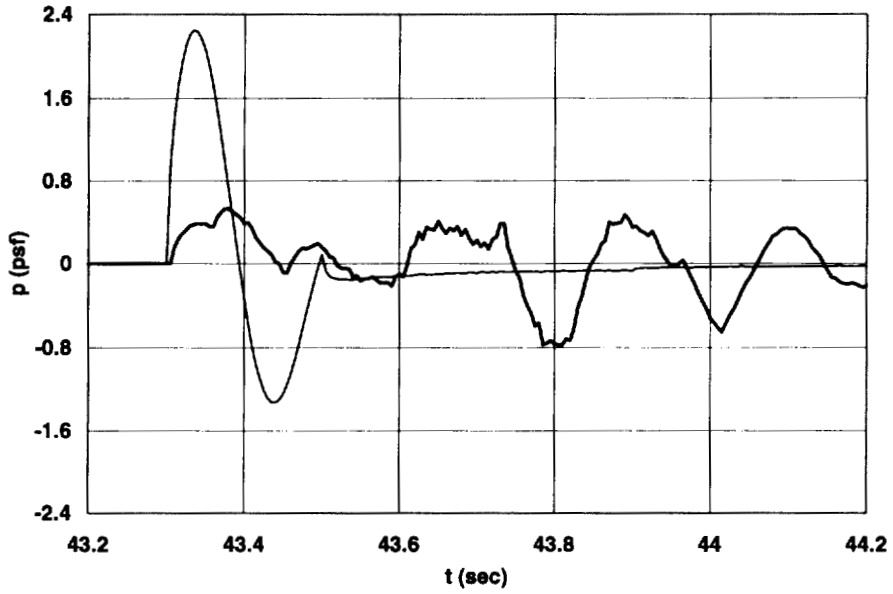

Figure 11.2. Sonic boom from an aircraft subject to extreme periodic surge. The lighter curve depicts the boom without surge.

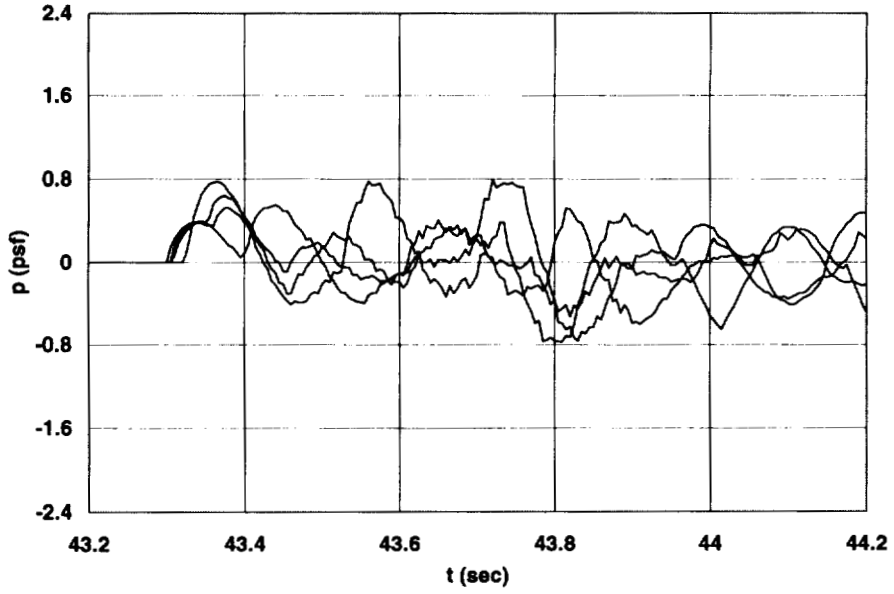

Figure 11.3. Sonic booms from four phases of the surge cycle.

Unfortunately the assumed surge amplitude is anything but practical. Position oscillates with an amplitude of 400 ft and frequency of 0.5 Hz. The amplitude of speed oscillations is 1,257 ft/sec, so the speed varies from 743 ft/sec to 3,257 ft/sec in the course of a cycle. Acceleration oscillations have an amplitude of 3,948 ft/sec^2, about 123 times the acceleration of gravity!

The speed and acceleration amplitudes diminish as the frequency falls, but so does the efficacy of surge as a means of reducing sonic boom intensity. At a frequency of 0.1 Hz, the amplitude of acceleration is "only" 4.9 times gravity, but the sonic boom is hardly changed from the case of steady flight. Surge with more moderate accelerations shifts the boom back and forth without chopping it to pieces, like the fragmented booms of figures 11.2 and 11.3. The phase-averaged boom is still weak, but the weakness reflects only boom displacements, not intensity reductions that a listener would notice.

12. Conclusion

Nonsteady acoustics and slender body theory serve well as bases for a linear theory of sonic booms. The nonsteady solution for sonic boom pressure is easy to understand and compute, a little easier than the equivalent steady solution, even when the sources are steady. Lift evolves naturally in the nonsteady formulation and gives rise to a term, apparently missing from previous steady theories, that accounts for the transfer of aircraft weight to the ground. The other terms are responsible for the N-wave but impose no net ground load.

A major conclusion of nonsteady theory is that the source of a sonic boom is much larger than the aircraft. For an aircraft flying at an altitude of 50,000 ft, the source region at any instant is typically 8,000 ft long. The sonic boom emanates from an extensive region of sky, a kind of synthetic aperture acoustic antenna. By exploiting the dimension of time, an aircraft can alter the source distribution along the synthetic aperture antenna and subject the sonic boom to active control.

A theorem limits the options for effective active control, at least within the realm of linear theory. The theorem states that the phase-averaged sonic boom is the same as the sonic boom of a steady aircraft whose source distributions are phase averages of sources under active control. The only way the aircraft can reduce the phase average sonic boom is by maneuvering to enlarge the source region beyond the bounds defined by flight at constant velocity.

We assume that fuselage shape must be constant and consider two means of active sonic boom control called "slosh" and "surge". Slosh is periodic contraction and expansion of the longitudinal lift distribution, with total lift and center of lift held constant. Surge is a periodic aircraft maneuver, not a change of shape. The aircraft speed surges faster and slower along an unchanged flight path.

Slosh of sufficient magnitude has a dramatic effect on sonic booms, but the phase average theorem precludes any average change of boom strength. If boom amplitude decreases at one point below the flight path, it must increase at another. Surge, by contrast, can reduce sonic boom amplitudes everywhere below the flight path and transform the boom into seemingly random noise. The accelerations needed to produce that happy outcome seem much too large to be practical, but the fact that surge can reduce sonic booms to rumbles is surprising and intriguing.

We conclude that active sonic boom abatement is possible but not necessarily practical. There could be some means beyond slosh and surge that can reduce sonic booms actively without imposing impractical burdens on the aircraft. Nonlinear propagation could also bear on the ultimate utility of active sonic boom control. A boom heard on the ground comes from a wide swath of sky. Some points of origin are strong with active control,

and others are weak. The fact that the boom coalesces from strong and weak sources may influence the formation and propagation of shock waves.

Another nonlinearity may be important, one involving sources rather than propagation. An aircraft vortex wake is a nonlinear source of pressure perturbations superposed on the pressure perturbations from the fuselage and wing. Vortex boom phenomena would be easy to include in nonsteady sonic boom theory and could have some bearing on steady booms as well.

References

Cole, J. D. 1953 Note on non-stationary slender body theory. *J. Aero. Sci.* **20**, 798-799.

Crow, S. C. 1969 Distortion of sonic bangs by atmospheric turbulence. *J. Fluid Mech.* **37**, 529-563.

Garrick, I. E. and Maglieri, D. J. 1968 A summary of results on sonic-boom pressure-signature variations associated with atmospheric conditions. NASA TN D-4588.

Goldstein, M. E. 1976 *Aeroacoustics*. New York: McGraw-Hill, 45-53.

Hayes, W. D. 1954 Pseudotransonic similitude and first-order wave structure. *J. Aero. Sci.* **21**, 721-730.

Hayes, W. D. 1971 Sonic boom. *Ann. Rev. Fluid Mech.* **3**, 269-290.

Hayes, W. D., Haefeli, R. C., and Kulstrud, H. E. 1969 Sonic boom propagation in a stratified atmosphere with computer program. NASA Contractor Report CR-1299.

Lamb, H. 1933 *Hydrodynamics, 6th Edition*. Cambridge University Press.

Landau, L. 1945 On shock waves at large distances from the place of their origin. *J. Phys. USSR* **9**, 496.

Lighthill, M. J. 1952 On sound generated aerodynamically, I. General theory. *Proc. Roy. Soc. A,* **211**, 564-587.

Lighthill, M. J. 1960 *Higher Approximations in Aerodynamic Theory*. Princeton University Press.

Prandtl, L. and Tietjens, O. G. 1934 *Applied Hydro- and Aeromechanics*. New York: Dover.

Seebass, R. 1970 Nonlinear acoustic behavior at a caustic. *Third Conference on Sonic Boom Research*, NASA SP-255, 87-120.

von Karman, T. and Moore, N. B. 1932 Resistance of slender bodies moving with supersonic velocities with special reference to projectiles. *Trans. Am. Soc. Mech. Engrs.* **54**, 303-310.

Whitham, G. B. 1956 On the propagation of weak shock waves. *J. Fluid Mech.* **1**, 290.

Whitham, G. B. 1974 *Linear and Nonlinear Waves*. New York: John Wiley.

Theoretical and Computational Studies on Sonic Boom Propagation and Its Submarine Impact

H.K. Cheng, C.J. Lee
Dept. Aerospace Eng., University of Southern California
Los Angeles, CA. 90089-1191 (213) 740-5365 Fax: (213) 740-7774
and
M.M. Hafez, W.H. Guo
Dept. Mechanical and Aerospace Engineering, University Calif., Davis
Davis, CA. 95616 (916) 752-0212 Fax: (916) 752-4158

1. Introduction

Sonic boom impact on the environment of populated area and habitat has been a major concern for the design, operation, and program planning of super/hypersonic vehicles as well as space launch.[1-6] Recent development in sonic boom studies reviewed in Refs. [1–6] has made evident the need for amending the near-field analysis with nonlinear calculations, but an unambiguous matching procedure to assure waveform-prediction improvement is still lacking. Another problem receiving much attention recently is the renewed issue with "transition focus booms"[2,3], particularly the "superboom"[7-9] which occurs during a speed change through a *threshold* Mach number and gives rise to strong wave-focussing effects; however, its intensity and the extent of the impact area can not be established from existing methods. A third aspect of a more recent concern is the potential sonic boom impact on pelagic and coastal environment, of which the methodology for defining the impact has yet to be adequately developed. The study addresses these three aspects in the frame work of a wave-field analysis for a *stratified* atmosphere, employing coordinates fixed to the vehicle in *steady* horizontal motion.

Whereas the analyses of the midfield (a region of the nonlinear wave field sufficiently far from the vehicle) based on the ray acoustics in Refs [3,10,11] and the corresponding analysis in this paper may be considered being equivalent, the present approach makes the treatment of the aforementioned problems, including several of its unsteady extensions, more straight forward and explicit. The resulting mid-field analysis furnishes a procedure for F-function determination, which is capable of retaining the accuracy gained from the near-field nonlinear calculation. In the superboom problem the development identifies 3-D wave refraction as an indispensable feature in matching the mid-field structure. For studies of sonic-boom penetration and propagation in water, the approach reduces the submarine problem to one analogous to that in the aerodynamic theory of planar wing in subsonic, transonic or supersonic flows, depending on the vehicle speed range. This paper will examine our recent theoretical and computational studies[12,13] in these areas, and discuss the more recent development. In response to interest in its potential application to waveform control, the procedures of near-field matching and shock-fitting, and the capability to treat shock coalescence are discussed along with comparison with results from modified method of characteristics (MMOC)

of Darden's [14] and other suitable examples. Studies of additional examples assessing merits of the methods will be presented at the conference.

2. Sonic Boom Propagation in Stratified Atmosphere

The problem is formulated in an aircraft-fixed coordinate system; the solution procedure for the mid field will employ the Mach conoid as a coordinate reference.

2.1 Near field behavior at large lateral distance

The small-disturbance version of the inviscid (Euler) equations admits a development in which the leading term has a form consistent with the supersonic equivalence rule of the linear theory[15–17]. In the cylindrical polar coordinates r, ω and the (out-going) characteristic variable $\xi = x - B_o r$. The streamwise perturbation velocity u' at large r has an expansion

$$\frac{u'}{\tau U} \sim \frac{F(\xi,\omega;\tau)}{\sqrt{B_o r}} - \frac{\frac{1}{4}G + G_{\omega\omega}}{2(B_o r)^{3/2}} - \tau\left[(F^2)_\xi - \frac{M_o(FG)_\xi}{B_o r}\right] + O(r^{-5/2}, \tau r^{-2}) \qquad (1)$$

where $G \equiv \int_{-\infty} F d\xi$, $\Gamma \equiv \frac{\gamma+1}{2} M_o^4/B_o^2$, for an arbitrary Whitham F-function; normalization of x and r by the body-length scale L, $B_o \equiv \sqrt{M_o^2 - 1}$, and the convention of aligning the x-axis with the relative free stream, are understood. Here, the subscript "o" refers to the condition at the *cruise* altitude corresponding to $z = 0$ (cf. Figs. 1,2). The parameter τ controls the near-field disturbance

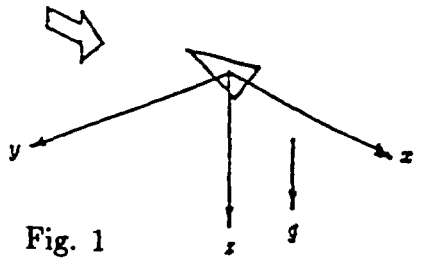

Fig. 1

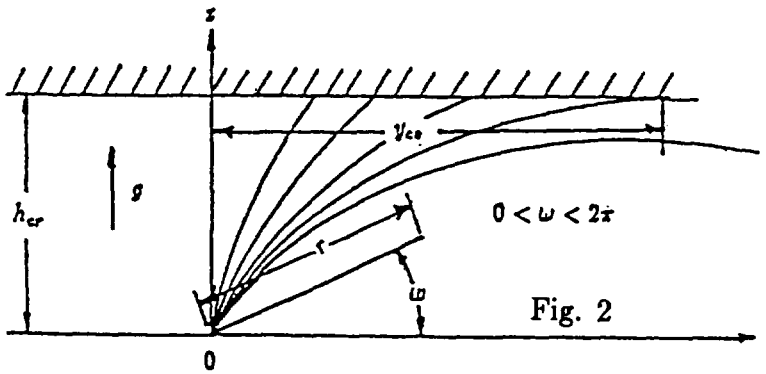

Fig. 2

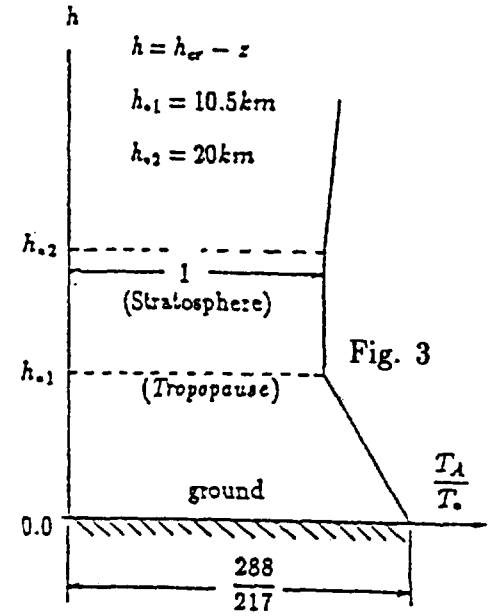

Fig. 3

level and is comparable to the thickness ratio of a wing of unit or higher aspect ratio; for a slender body of revolution, τ must be taken as the square of the thickness ratio. The form of dependence of F on τ may be assumed to be expressible as

$$F(\xi,\omega;\tau) = F^{(0)}(\xi,\omega) + \tau F^{(1)}(\xi,\omega) \tag{2}$$

where $\tau F^{(1)}$ represents a nonlinear improvement of the F-function in a linear theory.[17]

For the equivalence rule to be useful, r must be large, but not so large that $F/\sqrt{B_o r}$ in Eq. (1) reduces to a magnitude comparable to $\tau(F^2)_\xi\Gamma$, i.e., r must satisfy adequately

$$1 << B_o r << \tau^{-2}\left(\frac{2}{\gamma+1}\right)\frac{B_o^4}{M_o^8} \tag{3}$$

Thus, a *nonlinear* mid-field region can be identified with $\tau^2 B_o^{-3} M_o^8 r = O(1)$. It is clear that the matching of the mid- and near-field solutions must be made in the range of Eq. (3), otherwise sizable errors will result from the mismatch.

2.2 Mid-field theory

Although not apparent from the nonlinear geometric acoustics,[3,10,11,18] the mid-field solution requires a departure from the irrotational assumption to account for a mechanism of *baroclinic-vorticity generation* mentioned. Denoting the mid-field disturbance level by τ' (to be identified later with τ^2), and assuming an atmospheric scale height large compared to the vehicle length L, Helmholtz's equations yield a vorticity field due to a disturbance in an atmosphere with entropy nonuniformity, which leads to a velocity disturbance (vector) with a vorticity correction[12,13]

$$\frac{\vec{u}'}{U} = \tau'\nabla\varphi - \frac{\tau' L}{\gamma H_s}\varphi\vec{k} \tag{4}$$

where $H_s \equiv (\nabla s/C_v)^{-1}$ is a scale height based on entropy. The potential φ satisfies the partial differential equation

$$-B^2\varphi_{xx} + \varphi_{rr} + \frac{1}{r}\varphi_r + \frac{1}{r^2}\varphi_{\omega\omega} = \tau' M_A^2\frac{\partial}{\partial x}\left[\left(1+\frac{\gamma-1}{2}M_A^2\right)\varphi_x^2 + \varphi_r^2 + \frac{1}{r^2}\varphi_\omega^2\right]$$
$$-\frac{L}{H_\rho}\left(\sin\omega\varphi_r + \frac{\cos\omega}{r}\varphi_\omega\right) \tag{5}$$

where $B^2 \equiv M_A^2 - 1$, $M_A \equiv U/a_A$, with the subscript "A" referring to the *ambient* condition at z. The remainders omitted are of the order $(\tau')^2$ and higher.

2.3 Mach envelope as reference surface

Let the outgoing Mach envelope based on the *linear theory* be $x = x^{1c}(r,\omega)$, which satisfies

$$(x_r^{1c})^2 + \left(\frac{1}{r}x_\omega^{1c}\right)^2 = B^2(\bar{z}) \tag{6}$$

where $\bar{z} \equiv z/\Delta$ and Δ is a reference scale height. Its solution can be obtained by integrating the ordinary differential equation (ODE) system along its own characteristics.[12,13,21] The surface $x = x^{1c}(r,\omega)$ represents a distorted Mach cone, referred to hereafter as the *Mach Conoid*, and will be used as a *reference* surface for the mid-field variables (ξ,η,ω)

$$\xi \equiv x - x^{1c}(r,\omega), \quad \eta = r/\Delta, \quad \omega' = \omega \tag{7}$$

For convenience, we normalize x^{1c} and introduce two functions of η and ω, σ^{1c} and $\tilde{\Gamma}$, as

$$\tilde{x}^{1c} \equiv x^{1c}/B_o\Delta, \quad \sigma^{1c} \equiv \tilde{x}^{1c}_\omega/\eta\tilde{x}^{1c}_\eta, \quad \tilde{\Gamma} \equiv \left(\tau'\frac{\Delta}{L}\right)\frac{\gamma+1}{2}M_A^4/B_o\tilde{x}^{1c}_\eta, \tag{8}$$

where B_o is used as a reference value for B. In the mid-field analysis, the product $(\tau'\Delta/L)$ will be treated as a unit-order quantity. This will be seen to be equivalent to $(\tau^2\Delta/L) = O(1)$.

2.4 The reduced PDE and solution by characteristics

In the unit-order ranges of ξ, η, and ω, corresponding to the vicinity along the Mach conoid of interest, PDE (5) can be reduced to a quasilinear first-order PDE for $\tilde{u} \equiv \varphi_\xi$, subject to an error of order τ',

$$\tilde{\Gamma}\tilde{u}\frac{\partial\tilde{u}}{\partial\xi} + \frac{\partial\tilde{u}}{\partial\eta} + \frac{\sigma^{1c}}{\eta}\frac{\partial\tilde{u}}{\partial\omega} = -\frac{1}{2}\left(\frac{1}{\eta} + \Theta + \kappa\right)\cdot\tilde{u} \tag{9}$$

$$\text{where} \quad \Theta \equiv \frac{\Delta}{H_\rho}(\sin\omega + \sigma^{1c}\cos\omega), \quad \frac{1}{\eta} + \kappa = (\nabla_\perp^2\tilde{x}^{1c})/\tilde{x}^{1c}_\eta.$$

The $\nabla_\perp^2\tilde{x}^{1c}$ corresponds to a ray-tube divergence in the geometric acoustics. This quasilinear PDE of the first order can be solved again as an ODE system as for Eq. (6). Using η to denote successive locations along a *characteristics curve* originally passing through $\xi = \xi^*$ and $\omega = \omega^*$, the coordinates of ξ and ω, and the solution $\tilde{u}$, can be expressed as a function of ξ^*, η^* and η [12,13]

$$\xi = \xi^* + \int_o \tilde{\Gamma}\tilde{u}^c d\eta, \quad \omega = \omega^* + \int_o \frac{\sigma^{1c}}{\eta}d\eta, \quad \tilde{u} = \tilde{U}(\xi^*,\omega^*)\left(\frac{\rho_0}{\eta\rho_A}\right)^{1/2}\exp\left[-\frac{1}{2}\int_0\kappa d\eta\right] \tag{10a,b,c}$$

where the superscript 'c' (not to be confused with '1c' used earlier) signifies a *line* integration along the characteristics curve $d\xi^* = d\omega^* = 0$; $\tilde{U}$ is an arbitrary function to be determined by the initial data from the matching, and ρ_0 is the atmospheric density at the cruise altitude.

2.5 Matching the near and mid field

As η vanishes, Eq. (10a) become $\xi^* \sim \xi - 2\tilde{\Gamma}\tilde{U}\sqrt{\eta}$; thus, in the inner limit $\eta \to 0$, Eq. (10c) can be expressed as

$$\frac{u'}{\sqrt{\tau' U}} \sim \frac{\sqrt{\tau'\Delta}\tilde{U}}{\sqrt{\tau}} - \sqrt{\tau'}\tilde{\Gamma}(\tilde{U}^2)_\xi \tag{11}$$

with remainders of order $(\tau')^{3/2}\tau^{1/2}$ Matching this with the near-field behavior Eq. (1) in the overlapping range $\tau' \ll \tau'\tau \ll 1$ identifies of τ' and $\tilde{U}$ as

$$\tau' = \tau^2, \quad \tilde{U} = F(\xi,\omega)/\sqrt{B_o\tau'\Delta} \tag{12a,b}$$

Since the error in the mid-field solution Eqs. (10a,b,c) is of the order τ', identified now with τ^4, the improved mid-field accuracy resulted from an increased accuracy in the F-function from the near field to an order τ, as in Eq. (2), may indeed be maintained by the theory. Note that the projection of the characteristics curve $d\xi^* = d\omega^* = 0$ on the cross-flow (y-z) plane is the *same* as that in the linear acoustics, subject to errors of the order τ^2. While the explicit form of Eq. (10c) together with the identifications made in Eqs. (12a,b) support Whitham's idea [20] used in Ref. [17], how F or U can be determined to the accuracy level of interest remains a key issue of the investigation.

2.6 Characteristic surface, waveform and shock discontinuity

The shock discontinuity surface $\xi = \xi^D(\eta, \omega)$ admissible to the *weak* solution of PDE (9) is governed by a (linear) first-order PDE controlled by the *arithmetical* mean of $\tilde{u}$ across the discontinuity, $\langle\tilde{u}\rangle$, from which it follows that $d\xi^D : d\eta : \eta d\omega^D = \tilde{\Gamma}\langle u\rangle : 1 : \sigma^{1c}$,[12,13] leading to

$$\frac{d\xi^D}{d\eta} = \tilde{\Gamma}\langle\tilde{u}\rangle = \langle\frac{d\xi^c}{d\eta}\rangle, \qquad \frac{d\omega^D}{d\eta} = \frac{\sigma^{1c}}{\eta} = \frac{d\omega^c}{d\eta} \tag{13a, b}$$

Thus, the shock is displaced at a rate which is the arithmetical mean of the displacement rate of the characteristics, while the projection of this wave family of ω^* in the cross-flow plane is unchanged. In passing, we point out that, as long as the vehicle-acceleration time scale does not far exceed a/Δ, the steady-state Mach conoid, Eq. (6), may still be used as a coordinate reference for a time-dependent version of the mid-field PDE (9).

2.7 Wave refraction pattern: examples

The projected wave refraction patterns in the cross-flow plane, unaffected by the nonlinearity, can be determined from the ODE (11) or $dz^c/dy = (z^c + y\sigma^{1c})/(y - z^c\sigma^{1c})$, for each ω^*. Figure 4 presents the projected pattern of constant ω^* contours in the y-z plane for a supersonic, stratospheric cruise at altitude $h_{cr} = 1.5h_{*1}$ in the standard atmosphere (cf. Fig. 3), at Mach number $M_\infty = 2$. The location of the upper and lower stratospheric boundaries are shown in long dashes. The limiting characteristics which reaches the ground level at a glancing incidence occurs for a particular value of ω^*, the *cut-off* value, $\omega^* = 35.1°$. This defines the lateral cut-off boundary for the sonic-boom impact area; in its vicinity, the mid-field description must be amended for the ground influence, as being treated by Pierce.[19]

2.8 Numerical implementation: matching, multiple shocks coalescence

Most current mid-field propagation methods with exception of Refs. [14,36] have been based on ray acoustics approach. In order to establish the usefulness and merit of the present body-fixed procedure, comparison with existing studies where *suitable* solution details are available is essential. Remarks on aspects of related analyses, which either provide a departure point, or serve to highlight an issue in the methods of attack, will first be made. Implementation of the mid-field calculation procedure and comparison of solution examples by other methods are next examined for their adequacy in treating multiple shocks and their coalescence. The procedure and the issues on the F-function determination will then be discussed.

Remarks on related analyses

Although recent results of extrapolating the nonlinear near-field calculation or wind-tunnel measurement data to the mid/far field appear encouraging, the study by Siclari & Darden[5] on the low-boom design shown sensitivity of the ground signatures to the location r/L where initial mid-field data are obtained. One obstacle in exploiting Euler or full-potential codes for sonic-boom prediction lies in the fact that in order to provide a meaningful initial data to the mid-field calculation, one must provide data at r/L far beyond 3 or 4, which most existing codes cannot perform well; on the other hand, at a low enough r/L, say $r/L = 1/2$, where the nonlinear near-field calculation may furnish accurate solutions, the mid-field theory or its ray acoustics equivalence ceases to hold*. Results of Ref. [5] show also clearly that for aircrafts typified by certain low-boom designs, multiple shocks remains in the ground signature, indicating therefore the importance of treating shock coalescence in the mid field. Another unique feature of the ground signature brought out in Ref. [5] is the occurrence of over-pressure maxima at some distances away from the flight track, which is thought to be peculiar to the type of low-boom designs considered. Applying the mid-field code based on Secs. 2.4 and 2.6, however, we found over pressure maxima to occur away from the flight track at some M_∞ slightly above the threshold value, even for an N-waveform uniformly distributed in ω. Thus a comparison study to assess critically the validity and adequacy of our mid-field program is important. Since results presented in Ref. [5] are not sufficiently detail

*The "L" in "r/L" appears hereafter may be omitted, if the definition of r in Sec. 2.1 is to follow.

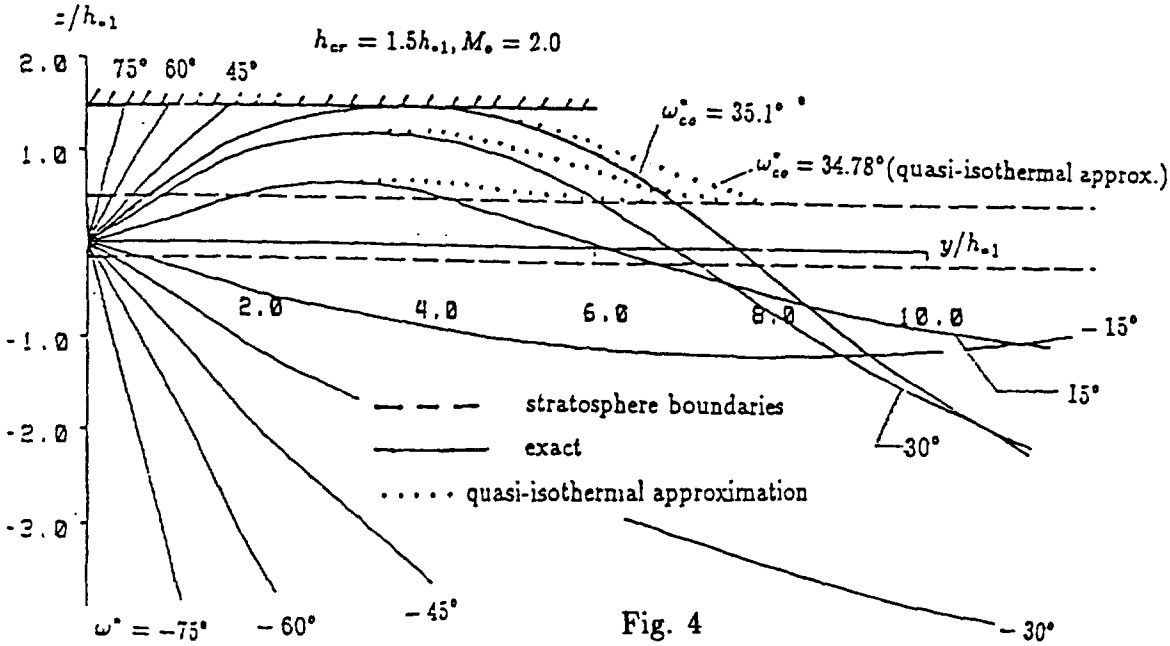

Fig. 4

to allow adequate assessment of our procedures and solutions, most of the comparison studies were made with data from the earlier works by Darden[14] and Carlson.[17]

Carlson's data were obtained from wind-tunnel experiment at $M = 2.01$, deduced from pressure measurement at different radial distances from the model, and have been a basis for establishing the sufficiency of an efficient prediction method by Page and Plotkin.[36] Instead of following the rather tedious Mach-plane cutting procedure[16,24,36] to find the cross-section area of the equivalent body (for each azimuthal angle), the procedure in Ref. [36] determines the F-function by summing the contributions from an multi-pole expansion of the linear near-field solution (furnished by CFD calculation). The cross-field azimuthal and nonlinear corrections at large r/L corresponding to the second and third terms of Eq. (1) were not considered. Comparison with Carlson's results was nevertheless very encouraging; the method is believed to work well as an alternative to that in the classical linear theory.[16,17,24]

The problem to retain accuracy gained from nonlinear calculation in the near field calls for a CFD effort to adequately *extend* the near-field nonlinear calculations out to r/L of 10 or higher. This effort is currently undertaken by M.M. Hafez and W.H. Guo using a second-order small-disturbance code. Having a successful nonlinear near-field computation with this capability, a direct matching with the mid-field calculation should cause little loss in accuracy. Results from studies in this direction will be reported at the conference.

Mid-field calculation and comparison

The mid-field solution according to Sec. 2.4 can be determined with initial date by stepwise integration of two ODE systems of the characteristics for PDE's (6) and (9), considering $\tilde{u}, \xi$ and ω, as well as $\tilde{x}^{1c}(\eta, \omega)$ as functions of η along the characteristics. Shock jump and its location are determined at the junction of two intersection outgoing mid-field characteristics according to the arithmetical-mean rule, Eqs. (13a,b), which relates the shock slope $d\xi^D/d\eta$ and the characteristic slop $d\xi^c/d\eta$ across the discontinuity. This is implemented at each η level with extrapolations of

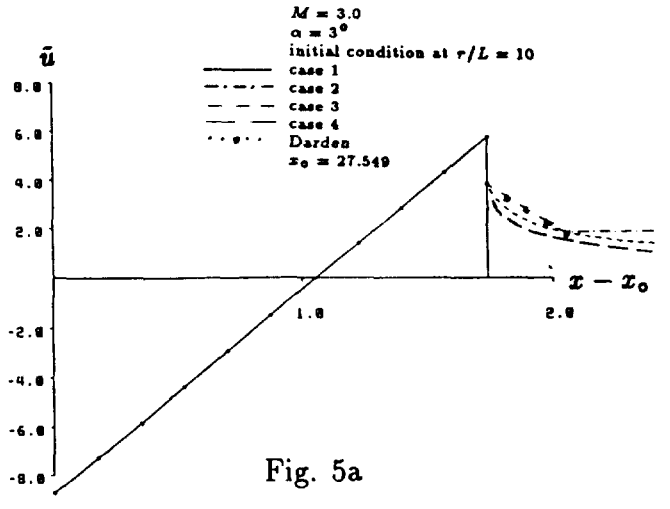

Fig. 5a

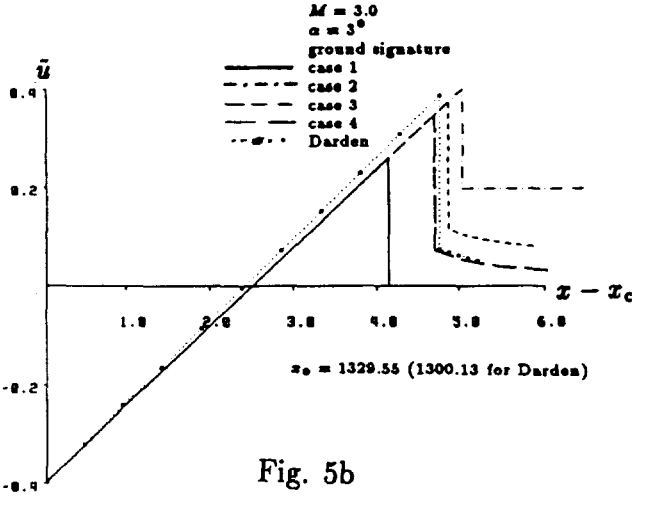

Fig. 5b

$\tilde{u}$ values on the characteristics from both sides, so that the $< d\xi^c/d\eta >$ will determine the shock location at the next η-step. Some programming effort on indexing is needed at each η level, since characteristic members are continuously consumed by the shock.

Slender body: testing for $r/L \geq 10$

The 3-D slender-body problem analyzed by Darden [14] in the symmetry plane employs the "Modified Method of Characteristics" (MMOC) based on a eight-term (truncated) azimuthal expansion of the *Euler* solution. It has demonstrated capability for fitting (sharp) shocks and treating their coalescence, and therefore provides an ideal basis to ascertain our mid-field method's adequacy. Among the several examples analyzed in Ref. [14], two are considered suitable for comparison with our mid-field analysis, they are the flows at Mach 3.0 about a body of revolutions (cf. sketch in Fig. 5a) at two attack angles $\alpha = 3°, 7°$. The shock coalescing features in these examples occur in regions *rather close* to the body $r/L = 1 - 2.5$, which add complications to the planned matching analysis, but comparison study for the mid field at $r/L \geq 10$ where wave form data at several r-stations are available for comparison, while the cross-field azimuthal influence and its nonlinear dependence, corresponding to the second and the last terms of Eq. (1), can be omitted with little error†. Now, with these corrections omitted, as in Eq. (11), it follows that the the over pressure, or the $\tilde{u}$, from the near field can be used directly as initial data at $r/L = 10$.

Figures 5a shows the waveform data for $\tilde{u}$ taken from Darden's results at $r/L = 10$ in the symmetry plane ($\omega = \pi/2$), to be used as initial data for our mid-field calculation, which are plotted as a function of $x - x_o(\eta)$, where x_o given the front shock location at $r/L = 10$. A portion of this waveform between $x - x_o = 2$ and 4.6 aft of the real shock was not provided in Ref. [14]; therefore the tail shock development at the high r/L levels can not be uniquely predicted. Several models for the tail-end profile have been tried in order to study the extent to which the missing information may impact the predication. Four alternative tail shapes are shown next to the original MMOC data curve in Fig. 5a. The ground signatures from these five initial wave forms are presents in Fig. 5b, assuming a ground reflection factor of 1.8 as in Ref. [14] and an altitude of 50,000 ft. in the standard atmosphere. Except for the strength and location of the real shock, the agreement

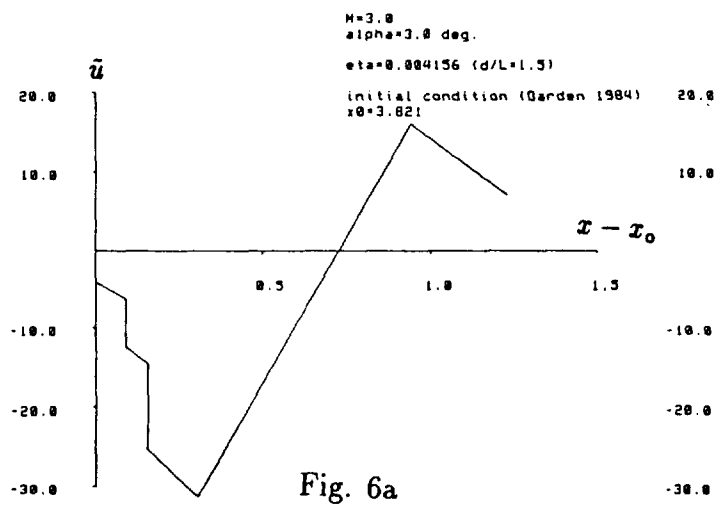

Fig. 6a

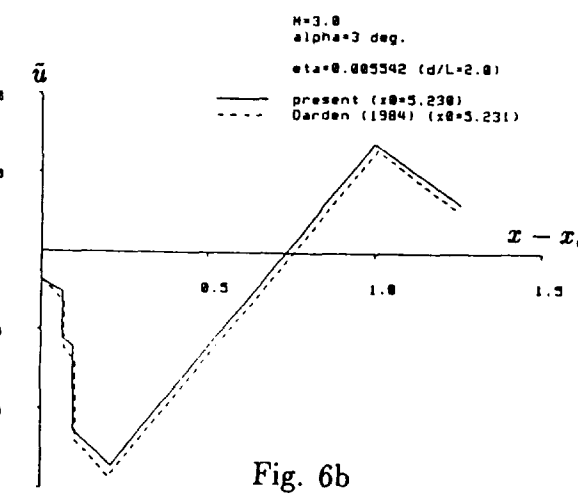

Fig. 6b

with Darden's more exact calculation is encouraging, especially for the first half of the signature, including the front shock. The strong dependence of the tail end of the input signature is made very evident here. The particular waveform on the ground with its real shock in agreeing closely with the ground signature of Ref. [14] is the one with an added tail that fits best with Darden's data at the far end around $x - x_o = 5$ at $r/L = 10$.

Slender body: shock coalescence

Waveform with multiple shocks were shown in Ref. [14] for four radial distance in the symmetry plane $r/L = 1, 1.5, 2.0$ and 2.5, of which all are too low/small to be considered ideal for the matching study (cf. previous foot note on the matching range). We shall nevertheless apply our mid-field ODE systems to the range $r/L \geq 1.5$, which provide an opportunity to treat the program capability in treating shock coalescence, using the available MMOC waveform data at $r/L = 1.5$ as input. The latters are plotted in Fig. 6a for the case of 3° attack angle, showing three shocks. The signature developed subsequently at $r/L = 2.0$ and $r/L = 2.5$ (Figs. 6b,c) reprocedure well the MMOC's waveform evolution with minor differences, except near the downstream end after the peak at $r/L = 2.5$, where a drastic decrease in the slope from Darden's data is unexpected. While the capability of our mid-field program to treat shock coalescence has been demonstrated for this example, the mid-field description appears to work surprisingly well even in a lower r/L range down to as low as 1.5. Similar results and observation are found in comparing the mid-field analysis with Darden's symmetry plane solution for the same slender body for a higher attack angle $\alpha = 7°$. In fact, the calculation for both $\alpha = 3°$ and 7° using the mid-field program can be *continued* beyond $r/L = 2.5$ with minute differences from the MMOC results. Some reasons for the good agreement and the apparent independence of the locations of the initial-data boundary for the mid-field calculation in these two cases are offered in a later discussion.

†The nonlinear mid field may be estimated to occurs at $B_o r/L \sim 118$, cf. Eq. (3). If the domain around $B_o r/L \sim \sqrt{118}$ is taken to be the proper matching range, r/L must be about 4 in this case.

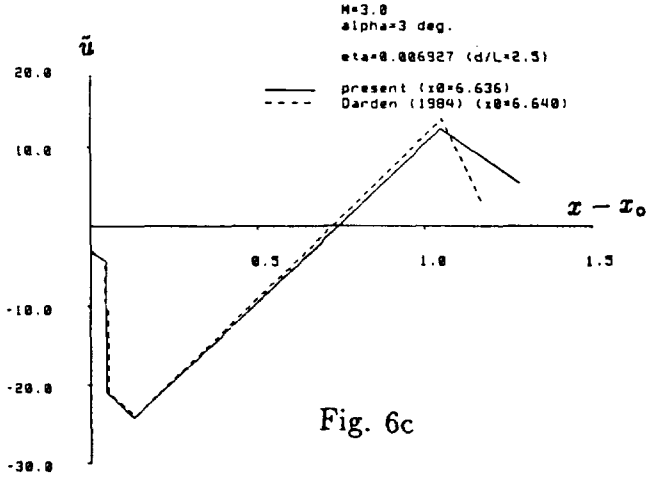

Fig. 6c

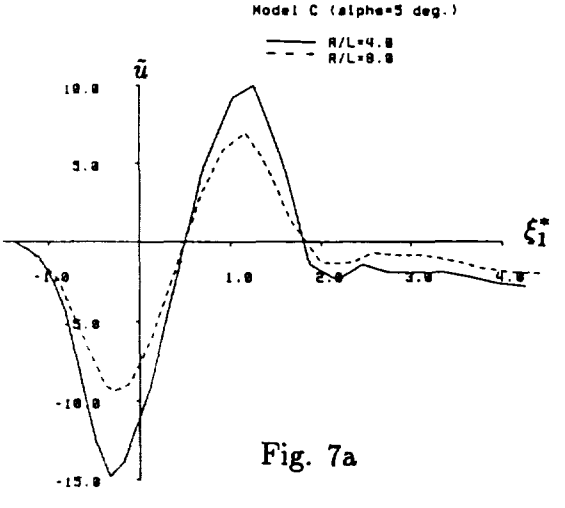

Fig. 7a

Correcting F-function deduced from the experiment/computation

The knowledge of the near-field behavior, Eq. (1) together with the matching principle will allows us to filter out the cross-field azimuthal and other higher-order effects from the experimental/computational waveform data in the task of determining the $F(\xi^*, \omega, \tau)$ or $\tilde{U}(\xi^*, \omega, \tau)$ [cf. Eqs. (10),(12b)]. The latter is all that matter in the mid-field theory. As observed earlier, at a far enough location in r/L or η, where all right-hand members in Eq. (1), except the first and the third terms, can be omitted, the result of matching stated by Eq. (11) signifies that the near- and mid-field solutions can be *directly* matched (equated directly there). This also signifies that the nonlinear correction in Eq. (1) can be eliminated by replacing ξ in $F(\xi, \omega, \tau)$ with the characteristic variable ξ^*, which is the Whitham's method. In the hope of reducing the near-field nonlinear calculation effort, we shall seek out and eliminate those terms from the right-hand members of Eq. (1), which are unwanted by the mid-field solution. Since functions like $(G/4 + G_{\omega\omega})$ and $(FG)_\xi$ can not be determined from the F-function alone, the basic idea of our matching/filtering procedure is simply to determine the three coefficients of $\tau^{-1/2}, \tau^{-3/2}$ and $\tau' r^{-1}$ as functions of ξ^* (i.e., for each ξ^*) at a fixed ω^* from *three* levels of r or η in the permissible matching range, Eq. (3). This is carried out by solving simply three simultaneous algebraic equations for each ξ^*. Note that waveform data at each level of r or η must first be transformed/shifted from a function in $\xi \approx x - B_o r$ to that in $\xi^* \approx \xi - 2\tilde{\Gamma}\tilde{U}\sqrt{\eta}$. In circumstances where the term proportional to $\tau' r^{-1}$, i.e., the fourth term in Eq. (1), is small compared to that proportional to $r^{3/2}$, one needs only data at two levels of r/L, and to solve two simultaneous algebraic equations, for each ξ^*.

As noted earlier, the waveform data available at $r/L = 1, 1.5, 2, 2.5$ and 10 from Darden's [14] MMOC calculation for a slender body may be considered exceptional, and not being suitable for application of the procedure outlined above. At r/L in the range of $1 - 2.5$, terms in Eq. (1) except the first prove to be not numerical small compared to $F/\sqrt{B_o r}$ for these examples. The values of the first, second and the fourth terms therein are typically in the proportion $6.3 : -6.7 : 7.9$. Interesting, contributions from the second and the fourth terms there combine to yield a much smaller correction, comparable to 1.2. This perhaps explain the little need of correcting the F-function for the examples in Ref. [14].

F-function determination from experiment

For the lack of detailed pressure-field data to test our procedure for current designs, we study its application and comparison to results for a delta wing which was one of the sting-mounted, half-inch models studied for sonic-boom propagation in a 4-foot test section of a Langley wind tunnel by H.W. Calson.[17] With the test section Mach number 2.01 and model Reynolds number close to 10^5, over pressure signature via the reflection-plate technique were measured at four locations corresponding to $r/L = 4, 8, 16$ and 32. For the Carlson's test model C, the mid field is estimated to occur typically at $B_o r/L = 36$, and the proper matching range may be taken to be $B_o r/L = \sqrt{36}$ or $r/L \approx 4$. We will utilize the experimental data at the first two levels $r/L = 4, 8$, for determining functions F as well as $(G/4 + G_{\omega\omega})$ and will make prediction by the mid-field calculation and comparison at the last two levels $r/L = 16, 32$. We recall that in Ref. [36], Page and Plotkin determine the F-function

in this case from the near-field solution *independently* from the experimental data.

Figure 7a gives the $\tilde{u}$ distributions as a function of ξ_1^* at the two levels $r/L = 4, 8$ in the symmetry plane, which were deduced and *read* from the over pressure data of Ref. [17] (Fig. 6 therein), using $u'/U_\infty \approx -p'/\gamma p_\infty M_\infty^2$. Here, ξ_1^* is a modified characteristic variable defined by the ξ value at the level $\eta = \eta_1$ where the initial value of $\tilde{u}$ is prescribed. It is related to ξ and η by

$$\begin{aligned} \xi_1^* &= \xi - \int_{\eta_1} \tilde{\Gamma}\tilde{u}^c d\eta \\ &\approx \xi - 2\tilde{\Gamma}\tilde{U}((\xi_1^*, \omega; \tau))\sqrt{\eta} \end{aligned} \tag{14}$$

Using the given $\tilde{u}$ values for each ξ_1^*, Eq. (1) applied at the two levels $r/L = 4, 8$ yeilds the results for $F(\xi_1^*, \omega; \tau)$ and the coefficient $(G/4 + G_{\omega\omega})$, presented in Figs. 7b,c. The ragged appearance of the plot in the Fig. 7c is a result of minute irregularity contained in, and read from, the original experiment data plots.[17] Its effect on the final result on the corrected F-function of interest is minor, being evident from the next figure. With the coefficient of $r^{-3/2}$ in Eq. (1) identified, the unwanted cross-field azimuthal term, which is unacceptable to the mid-field equation, can be eliminated/filtered out; a modified/new initial boundary value $\tilde{u}$ at $\eta = \eta_1$ is therefore

$$\tilde{u}_{mod} = \frac{F(\xi_1^*, \omega, \tau)}{\tau\sqrt{B_o \tau}} \tag{15}$$

The modified amd the original $\tilde{u}$ are represented in Fig. 8a; their difference indicates the "filtering" effects on F. The noticeable difference upstream of the first $\tilde{u}$ minimum, and immediately downstream of the first $\tilde{u}$ maximum, are not relevent for the present study since they are believed to have resulted from the shock-boundary layer interaction on the reflection plate. The difference behind the tail shock between $x/L = 9 - 11$ may have meaningful physical consequence. The result of the two mid-field calculations based on the modified and orignal $\tilde{u}$ used at $r/L = 4$ as initial data, are shown in Figs. 8b,c,d along with $\tilde{u}$ deduced from Carlson's original data for $r/L = 8, 16$ and 32, respectively. While the effect of employing the more appropriate initial waveform for the mid-field propagation is quite small for this example, noticeable changes in the shock locations and strength of the front and tail shocks as well as the tail end waveform can be seen from these results.

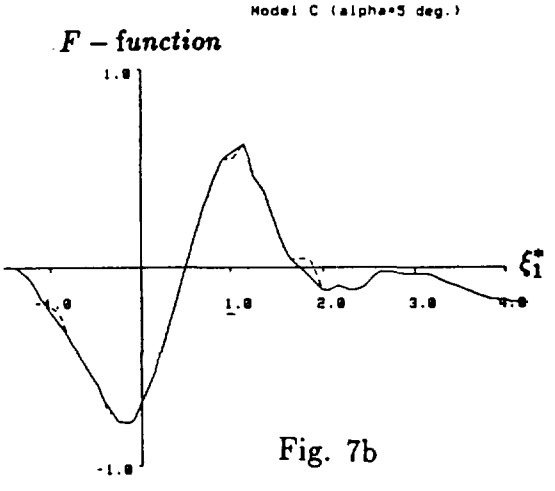

Fig. 7b

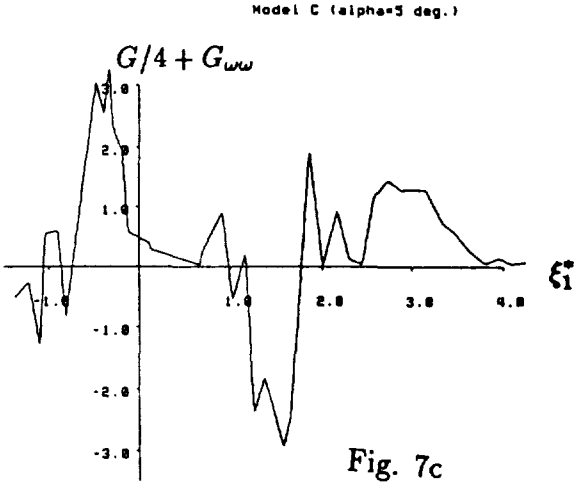

Fig. 7c

3. Superboom at Threshold Mach Number As a 3-D Problem

3.1 Importance of lateral wave refraction

At a position below the aircraft where the ambient sound speed $a(\bar{z})$ becomes close enough to the vehicle speed U_o, i.e., $U_o/a(\bar{z}) = 1$, the wave field looses its hyperbolic character and the mid-field description must be replaced by one of the mixed hyperbolic-elliptic type.[7–9] The phenomena, referred to often as the "superboom", may be regarded as a consequence of wave/ray focussing.[21] The flight Mach number $M_o \equiv U_o/a_o$ at which this occurs on the ground is called the threshold Mach number. However, a significant, attendant 3-D effect representing strong, *lateral* wave *refraction* has not been taken into consideration in existing two-dimensional (2-D) treatment following Hayes' study.[22,23] This overlooked aspect is made most evident by a display of the boundaries of the sonic-boom impact area for successively decreasing cruise Mach number. The results are shown in Fig. 9 for $M_o = 2.0, 1.6, 1.2, 1.175, 1.153$ at a cruise altitude $h_{cr} = 1.5h_{*1}$. As M_o approaches 1.153, which is the threshold Mach number $M_{thr} = a_{gr}/a_o$ of the standard atmosphere, the computed lateral boundaries according to the linear theory diminished to zero, signifying the need to account for the transverse field gradient omitted from the 2-D analysis.

3.2 The 3-D, nonlinear Tricomi equation

For this problem, Cartesian coordinates moving at the same speed as the air vehicle can be used, with the origin chosen to lie on the plane $z = z_{**}$ where B vanishes. The rescaled Cartesian variables and the perturbation velocity potential, resulting from a scale analysis to account for the transonic character of the zone and the scale of the neighboring mid field are

$$\hat{x} = \frac{(x - x_{**}^{lc})}{L}, \qquad \hat{y} = \left(\frac{L}{\Delta}\right)^{1/3} \frac{y}{L}, \qquad \hat{z} = \left(\frac{L}{\Delta}\right)^{1/3} \frac{z - z_{**}}{L}; \tag{16a, b, c}$$

$$\hat{\phi} = \left(\frac{\Delta}{L}\right)^{2/3} (\gamma + 1) \frac{\varphi}{UL} \tag{16d}$$

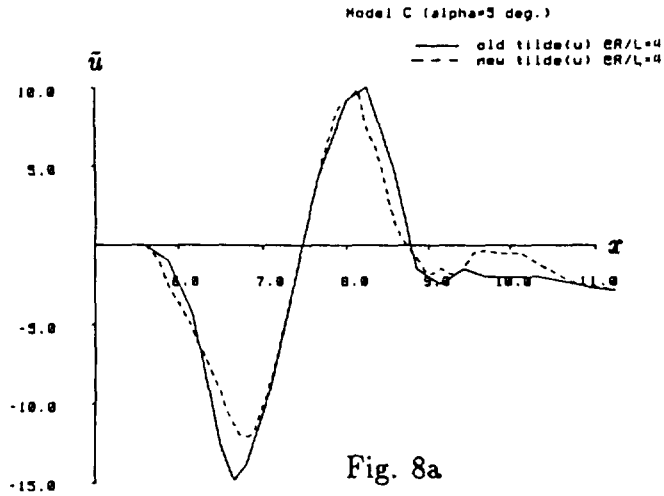

Fig. 8a

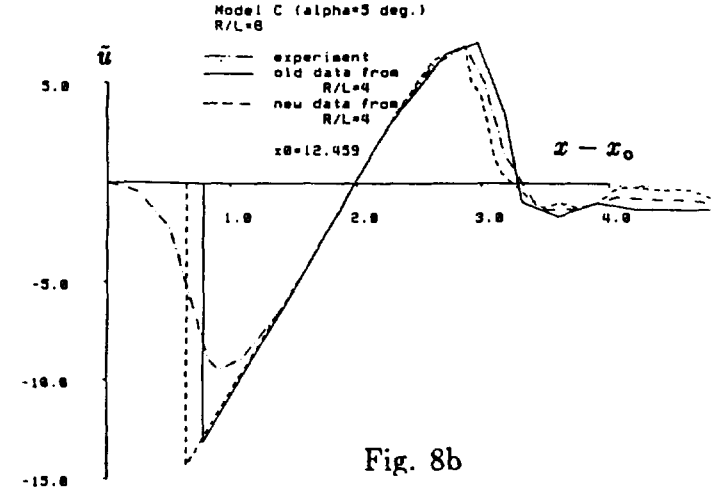

Fig. 8b

where L and Δ are a reference length comparable to the vehicle length and a reference (typical) atmospheric scale height, respectively; φ is the perturbation velocity potential. The reduced PDE governing $\hat{\phi}$ in the domain of interest takes the nonlinear mixed, hyperbolic-elliptic form familiar in transonic aerodynamics, subject to errors of order $(L/\Delta)^2$,[24,25]

$$\frac{\partial}{\partial \hat{x}}\left(\frac{1}{2}\hat{\phi}_{\hat{x}}^2 + \hat{K}\hat{\phi}_{\hat{x}}\right) - \left(\frac{\partial^2}{\partial \hat{y}^2} + \frac{\partial^2}{\partial \hat{z}^2}\right)\hat{\phi} = 0; \quad \hat{K} = \left[\frac{d}{d\bar{z}}B^2(\bar{z})\right]_{**} \cdot \hat{z}, \tag{17}$$

where $\hat{K} \equiv (M_A^2 - 1)(\Delta/L)^{2/3}$ corresponds to the classical transonic similarity parameter, and $(\hat{\phi}_{\hat{x}} + \hat{K}) = 0$ defines a *transition* boundary corrected for the nonlinearity. Its linearized, 2-D version is recognized as the Tricomi equation[26] and has been a model equation for treating "transition focus boom".[21–23,27] In the present work, however, the 3-D effect is recognized to be of the *first-order* importance. As an asymptotic theory, the present formulation is satisfactory in that the transverse scales of this domain is found to be comparable to $\tau^{-2/3}L$, and the wave amplitude is found to be $\tau^{-2/3}$ fold stronger than in the mid field, befitting therefore the term "superboom" used in the earlier studies.[7–9] The shock jump relations admissible to the system follow readily from Eq. (17) together with the condition of continuity in $\hat{\phi}$.

A distinct difference between the 2-D and 3-D versions of Eq. (17) is seen from their solution behavior near the transition boundary, which corresponds to a caustic in a ray-acoustics analysis. It suffices to illustrate this difference by examining the linear version of the 3-D characteristic curves $\hat{x} = \hat{x}^{1c}(\hat{y}, \hat{z}; \omega_*)$ continuing down from an upper level of $|\hat{z}|$, where the input data are furnished by matching with the mid-field solution. Figure 10 shows an example of $\hat{x}^{1c}$ and $\hat{y}$ as functions of $\hat{z}$; the 3-D characteristic curve emanating from an azimuthal angle away from the symmetry plane is shown as a solid curve. Shown in dashes is the exceptional characteristic curve which continues down directly in the symmetry plane. Here, only the exceptional characteristics curve can remain in the symmetry (vertical) plane ($\hat{y} = 0$) and reach the transition boundary plane with a *cuspidated* singularity. The characteristic solution of Eq. (17) can be shown to match that of the mid field.[12,13]

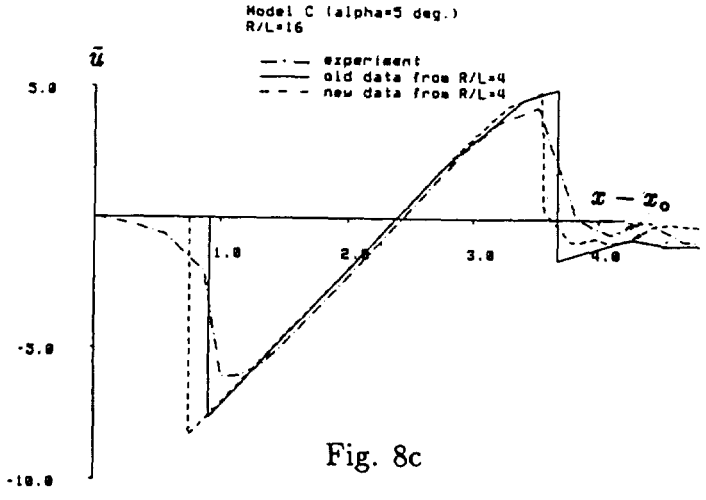

Fig. 8c

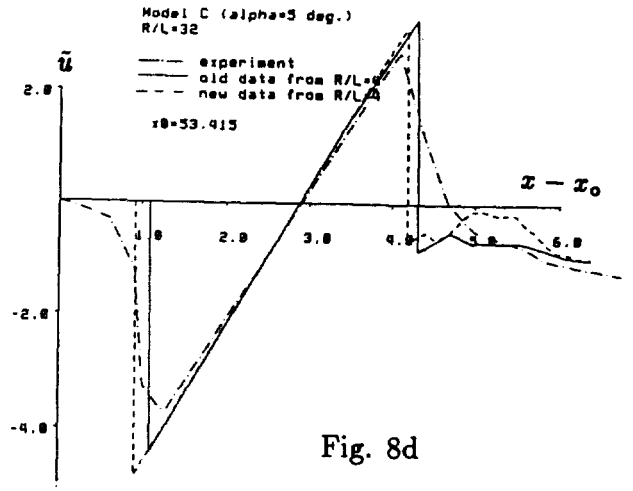

Fig. 8d

3.3 The Boundary Value Problem and Computational Study

The far boundary on the hyperbolic part of the domain is chosen to be a horizontal plane, say $\hat{z} = \hat{z}_*$,sufficiently far from the transition boundary $\hat{z} = 0$. The locations of the upstream and downstream boundaries are chosen by guidance from a knowledge of the characteristic curves of the linear Tricomi equation.[12,13]

Across the transition boundary, $\hat{K} + \hat{\phi}_{\hat{x}} = 0$, continuity of $\hat{\phi}$ and its derivatives are assumed. In the elliptic domain, $\hat{\phi}$ is required to vanish at large distances and to satisfy the impermeability surface condition on a ground plane with $\hat{\phi}_{\hat{z}} = 0$.

Except for the slightly different boundary conditions at $\hat{z} = \hat{z}_*$, application of shock-capturing and/or shock-fitting algorithm [28] presents no basic difficulty to the reduced 3-D nonlinear Tricomi equation. We will describe several features of the solution examples for the 2-D and 3-D problems. Although the 3-D aspect is more relevant to the superboom problem considered, more detailed discussions will be given below on 2-D examples which serve to test the calculation procedure and the boundary-value problem posted.

3.4 2-D example as test of CFD procedure

Seebass[22] made analytical study of the Tricomi equation in the hodograph plane for a square-hat incident wave form, and Seebass et al.[27] obtained numerical solution to the nonlinear Tricomi equation in the physical plane for a step-function incident waveform. In the 2-D examples illustrated below, we consider an incident N-wave, allowing an impermeable *ground* plane. The latter yields additional features helpful to the understanding of *bow-wave* and *ground* interaction.

The far boundary on the hyperbolic side is set at $\hat{z}_* = -3$ in this example, and will be called the "upper boundary" for convenience. The radiation condition on the downstream portion of the upper boundary was not considered for this calculation, since its influence is not expected to be significant for these examples. Three levels for the ground plane at $\hat{z} = \hat{z}_{gr}$ have been studied, corresponding to $U_\infty > a_{gr}$, $U_\infty = a_{gr}$ and $U_\infty < a_{gr}$. Only results of the second case corresponding to flight at the threshold Mach number will be shown to illustrate several features and issues of the nonlinear problem and the computation method.

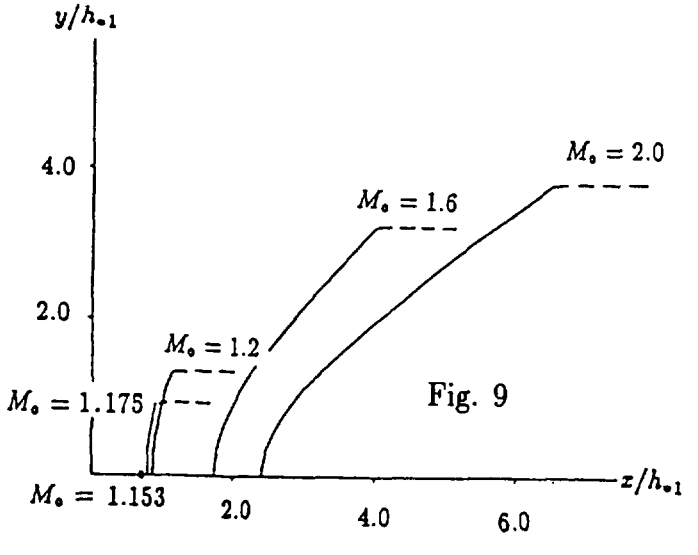

Fig. 9

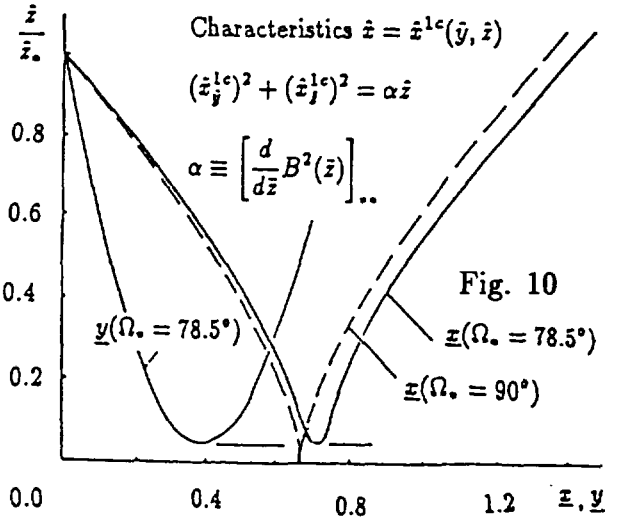

Fig. 10

were made with $\phi_{\hat{x}} = 0$ everywhere on the upper boundary $\hat{z} = \hat{z}_*$ except on the rectangular area where the N-wave form is prescribed. Three test cases were considered, corresponding to M_o above, equal, and below the threshold value. Results for $M_o = M_{thr}$ using a $550 \times 20 \times 320$ grid are shown in Figs. 12a,b, for the symmetry plane ($\hat{y} = 0$) and in Fig.s 12c,d for the mid span ($\hat{y} = 0.5$). Whereas noticeable differences between results at the mid span and at the symmetry plane are not immediately apparent, significant 3-D effects can be found by a comparison of the 2-D and 3-D results in the symmetry plane (cf. Figs. 7a,b and Figs. 8a,b).

Most 2-D and 3-D examples of our computational study exhibit waveform behavior on the ground at the real of the N wave, corresponding to a *pressure overshot*, which appears to be consistent with the U-shape waveform observed during overflights near the threshold condition reported by Haglund et al.[29]

4. Submarine Sonic Boom Impact

4.1 Model of a flat ocean

The problem of sonic-boom penetration into water is complicated by interaction of the sonic boom with the surface and internal waves. The analysis can be simplified nevertheless by considering surface waves of small slope. Thus the assumption of a *flat* ocean surface made by Sawyers[30] and other subsequent studies[31,32] may be justified at least for those long ocean waves. The model appears to have received support from an early experiment.[33] The flat-ocean model is to be applied only to the submarine acoustic field of interest, which may then be superimposed on to existing water waves. A thorough, theoretical argument leading to the flat-ocean model can not be found in the literature, and is elucidated below.

Basic to an inviscid analysis of air-water interaction are the two conditions expressing the continuity of the pressure and of the normal-velocity component across the interface (in the absence of surface tension). Since the pressure disturbance is determined by the change in dynamic pressure, the pressure continuity requires an exceeding small change in the velocity field of the water, as

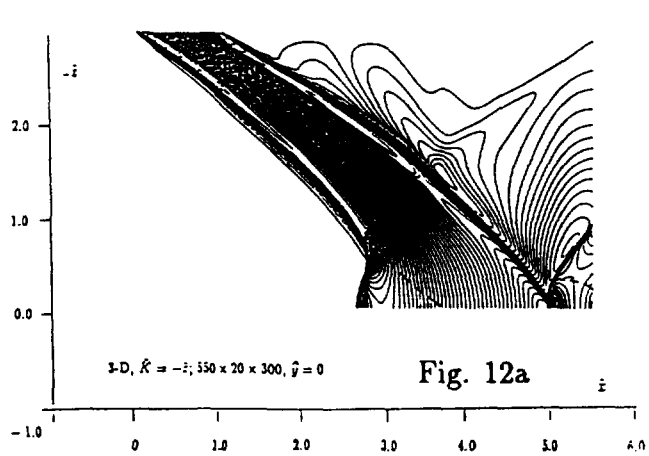

Fig. 12a

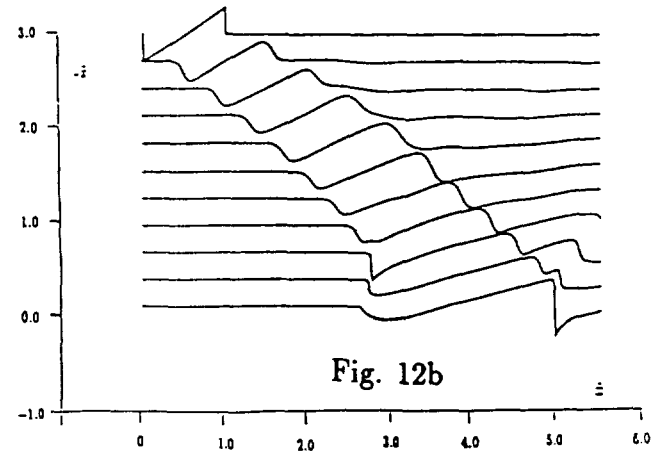

Fig. 12b

Solutions in our preliminary study were obtained by the finite-difference procedure similar to the type-sensitive schemes of Murman's.[24] The field of perturbation velocity generated from a 275×150 mesh is shown as contour-plot for $\hat{u}$ in Fig. 11a, and as waveform (signatures) at different heights in Fig. 11b. Also shown in dashes in Fig. 11a is the displaced sonic boundary ($\hat{u} + \hat{K} = 0$). Unlike the Mach-wave pattern from the linear Tricomi equation, the contour of constant $\hat{u}$ from the nonlinear calculation shows a wave-front displacement far removed from the linear prediction.

The sonic boundary shown is generally similar to those obtained in Refs.[22,27], including certain wave-reflection details near the sonic boundary's upper corner. The shocks are well captured in the waveform description (Fig. 11b) for the lower levels $0.5 < |\hat{z}| < 1$, where the shock is nearly *normal* and shows a much sharper transitions than at the higher levels ($|\hat{z}| > 1$). On the other hand, this examination confirms the need for an improvement in Murman's scheme which cannot provide the correct switching from an up-wind to shock-point operators for the *oblique* part of the shock. Interestingly, the computed waveform at $\hat{z} = 0$ in Fig. 11b indicates that the shock strength of the *bow* wave vanishes at $\hat{z} = 0$, and this is a correct confirmation of a general property of PDE (17), because the flow upstream is sonic at $B = 0$. To be sure, at precisely the threshold Mach number ($M_\infty = M_{th}$), the superboom can *not*-produce a *front shock* on the ground.

Unlike examples in Refs [22,27] which did not consider a ground plane, we found supercritical regions to exist on the ground plane in all cases; their existence renders possible a *regular reflection* for the real shock of an N wave, with its strength nearly doubled on the ground. The need for an improvement via shock-fitting or other means, to reduce unwanted spreading of the artificial shock structure elsewhere on the oblique part of the shock, is obvious.

3.5 3-D example

To test the adequacy of the boundary-value problem so formulated in the 3-D case, we prescribed an N-wave signature *uniformly* distributed (spanwise) over a *rectangular* segment of the far boundary, $\hat{z} = \hat{z}_*$; this simplification is suggested by the limiting form of the impact boundaries as $M_\infty \to M_{thr}$ (cf. Fig. 9). Consistent with the transonic scaling law, the aspect ratio of the rectangular segment of this model is chosen to be *two* in the reduced coordinates. 3-D calculations

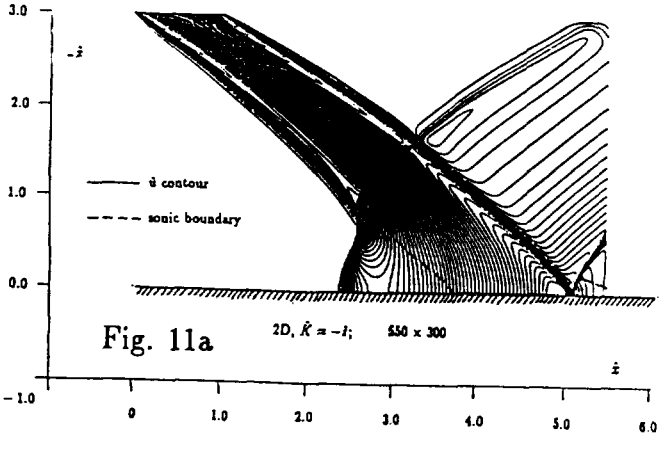

Fig. 11a

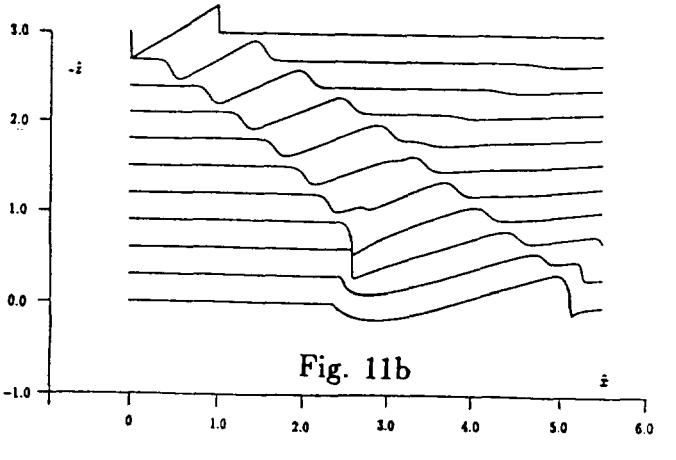

Fig. 11b

compared to those in the (sonic-boom) wave field in the air. Similar requirement and consequence are found also in the change of the wave elevation $z = Z_w(x, y, t)$. Parametrically, the fractional change due to the sonic-boom impact on Z_w can be established from a detailed formulation as

$$\left|\frac{Z_w - Z_w^\circ}{Z_w}\right| = O\left(\epsilon\frac{\rho_A}{\rho_B}\right) << 1 \tag{18}$$

where the superscript "o" on Z_w° refers to condition in the absence of the sonic-boom disturbance, the quotient ρ_A/ρ_B is the air-to-water density ratio, and ϵ is a typical fractional change in pressure or velocity in the mid-field of the air wave. Therefore an excellent (first) approximation which greatly simplifies the "interaction" analysis is to neglect the fractional change in Z_w due to air-water interaction. Formally, $\epsilon\rho_A/\rho_B$ can be regarded as being of the *second* or *higher order* in smallness.

Critical to the problem formulation is then the question: whether the part of over pressure at the interface due to the reflected waves (in the air) can be adequately determined as reflected waves from a *flat*, impermeable surface. This issue can be studied by examining the impermeability condition on a wavy surface, $z = Z_w(x, y, t)$, written for the time being in a reference frame fixed to the ocean/lake bottom (cf. the sketch in Fig. 13). Let u, v, and w be the fluid velocity components parallel to axes of x, y and z (not necessarily small compared to the sound/vehicle speed), and u_o, v_o and w_o denote the corresponding components in the air in the *absence* of the sonic-boom disturbance. The impermeability condition in question gives, at either side of $z = Z_w(x, y, t)$,

$$w = \left(\frac{\partial}{\partial t} + u\frac{\partial}{\partial x}\right) Z_w + v\frac{\partial}{\partial y} Z_w, \tag{19}$$

where $-(\partial Z_w/\partial t)/(\partial Z_w/\partial x)$ can be considered as the (instantaneous, local) surface-wave propagation velocity. The sonic-boom contributions to the flow velocity components, $u' \equiv u - u_o, v' \equiv v - v_o$ and $w' \equiv w - w_o$ must then satisfy the impermeability condition at $z = Z_w$, as

$$w' = u'\frac{\partial}{\partial x} Z_w + v'\frac{\partial}{\partial y} Z_w + \frac{\partial}{\partial t}(Z_w - Z_w^\circ) \tag{20}$$

where, by virtue of the inequality (18), the right-hand members are small like *second-order* quantities if the slopes are also small. Thus, with the assumption of small surface slopes the surface boundary

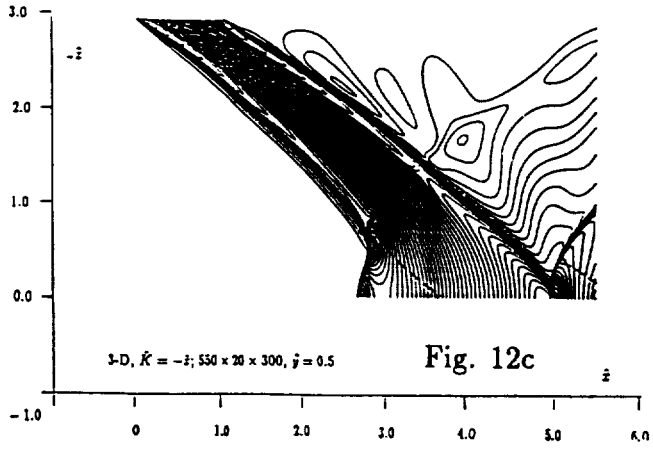

Fig. 12c

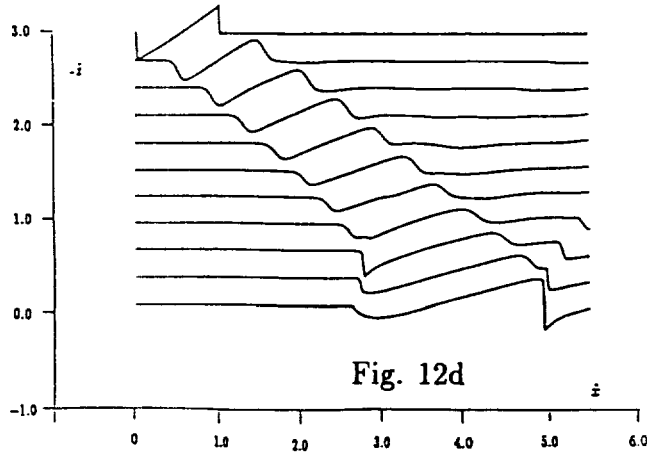

Fig. 12d

condition for the acoustic field (above and below the water) can be represented by the that of a *flat* surface

$$w' = 0 \quad \text{at } z = h, constant \tag{21}$$

subject to relative errors comparable to the surface slopes (and also the air-to-water density ratio). The same condition is reached if the reference frame were fixed to the traveling acoustic source or to the surface wave.

4.2 Traveling acoustic-wave patterns in water

In a reference frame fixed to the air vehicle, the submarine acoustics under the flat ocean may be classified according to the Mach number based on the sound speed in *water*, as being *subsonic, transonic* and *supersonic*. Since sound speed in water is 4.35 times higher than that in air at standard conditions, supersonic stratospheric flights at Mach number below 4.35×1.153, or 5.02, are expected to produce only the subsonic-type pressure field under water. Existing studies on the sonic-boom penetration[31,32] based on Sawyer's 2-D flat-ocean model has revealed several important features and scaling laws. It is recognized, however, that these results and the analytic solution obtained via the transfer-function procedure therein can be recovered completely from the Prandtl-Glauert solution familiar in the steady-state, subsonic aerodynamics. Therefore, a 3-D extension can be readily carried out as one in steady-state aerodynamics. The knowledge of the 3-D wave field thus furnished may help the planning of field observation and measurement for sonic-boom impact studies under water, and will serve a departure point for improving the flat-ocean model as well as for delineating the influence of sea state on the sonic-boom generated submarine acoustics. A 3-D example will be discussed in Sec. 4.3 to elucidate the type of problems encountered as well as certain unique features which may greatly simplify future analyses.

At higher flight speeds, such as during Space Shuttle's landing approach on a route over the ocean,[3,34] transonic and supersonic wave fields may be anticipated below the ocean surface. Although limited in its range, the transonic case (corresponding to a vehicle Mach number near 5.0 under standard conditions) offers a more novel scenario in that, apart from the nonlinearity and

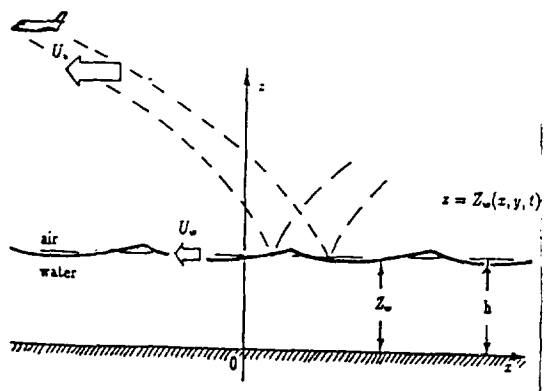

Fig. 13

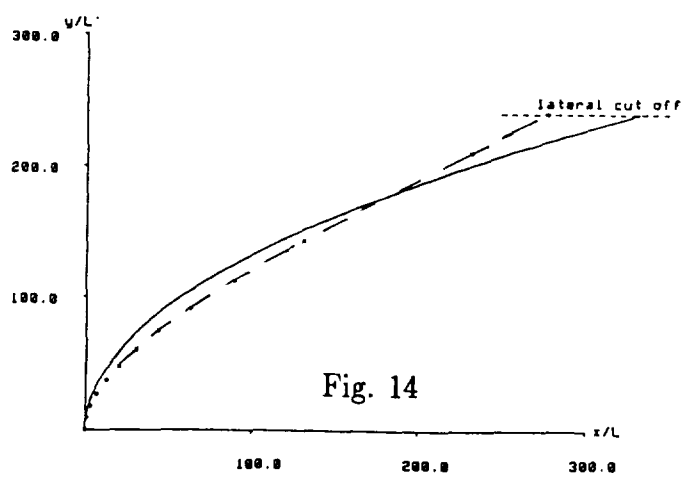

Fig. 14

mixed (elliptic-hyperbolic) wave character, receding *upstream-propagating* waves can move slowly enough to *interact* with some of the surface/internal water waves. In this instance, the wave field may *not* be reduced to a steady/quasi-steady one. This intriguing problem may still be studied by methods used in the analogous problems in unsteady transonic aerodynamics.[25,35]

4.3 3-D example

As noted before, the equivalent steady-state formulation of the flat-ocean model allows us to analyze it as one governed by the 3-D Prandtl-Glauert equation. Unlike the 2-D study, the Mach number in the submarine problem can not be scaled out completely in the 3-D case, because the boundaries delimiting the sonic-boom impact area on the water surface will depend on the cruise Mach number as well as the cruise altitude (cf. Fig. 9).

Impact zone of extremely high aspect ratio

For the purpose of examining the importance and nature of the 3-D influence, we assume the vehicle cruise Mach number to be $M_o = 2.1$, altitude $h_{cr} = 55,000$ft. in the standard atmosphere. The signal length scale on the ground is taken to be $L' = 580$ft (comparable to the Mach 2 low-boom design in Ref. [5]). The impact boundary on the water surface (observed from the aircraft) was computed from the Mach conoid and is shown in dashes, y/L' vs. x/L' in Fig. 14. This curve terminates at $|y/L'| = 243.13$ which is the lateral cut-off boundary. To ease computation work, the curve is replaces by a parabola $(y/L')^2 = 175(x/L')$, shown as solid curve, which is believed not

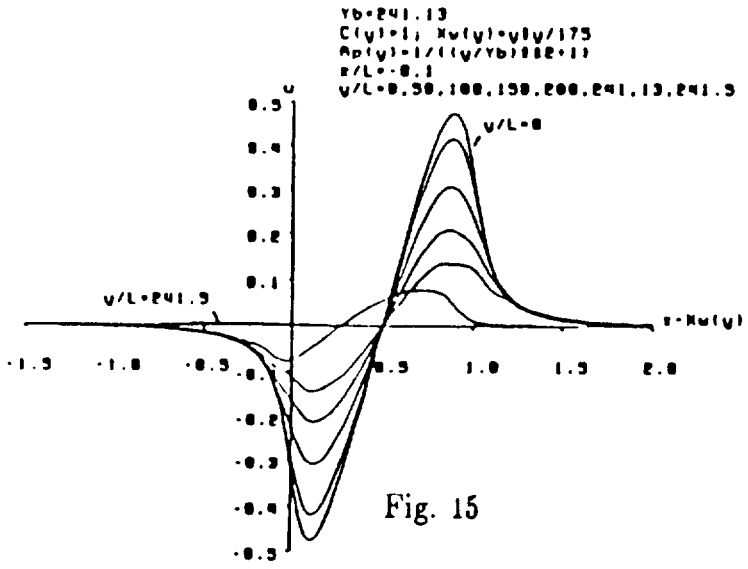

Fig. 15

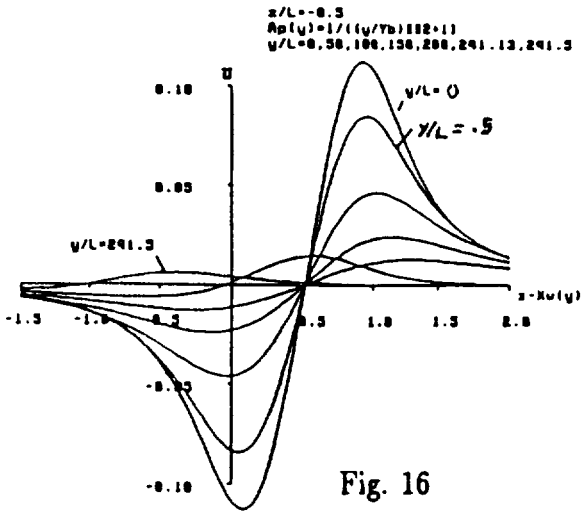

Fig. 16

to affect adversely the solution's major features. With the lateral cut off occuring at $y/L' = 341.13$ and the impact zone extending only a unit-order distance x/L' around the boundary, the region of interest is seen to be laterally wide (being 2 scale heights from the flight track or more) but extremely *narrow* in the wind-direction—the aspect ratio of this example is 2×241.13 or 482.26 ! A *lifting-line* concept should prove useful for this study, but not until a careful examination of the significant departure of the 3-D calculations form the 2-D solution to be brought out below.

In passing, we note that a 2-D solution at Mach 2.1 considered in Ref. [30] does not pertain to $M_o = 2.1$. Rather it corresponds to $M_o = 2.41$, since it was based on the sound speed on the ground, U_o/a_{gr}. The submarine Mach number in the present example is $M_{water} = 0.418$, whereas that for Mach 2.1 in Ref. [30] is $M_{water} = 0.483$; their difference in the Prandlt-Glauert factor $\beta_{water} \equiv (1 - M^2_{water})^{1/2}$, hence in the solution, is nevertheless not significant.

Submarine disturbance field calculation

The subsonic field under water is computed as an incompressible solution to the "inverse lifting planar wing problem" in which load distribution in an N-wave form is prescribed over each spanwise section of the planform, of which the leading edge x_{LE} and the side edge y_{SE} are given by boundaries for the impact area and the lateral cut off (in coordinates $\bar{x} \equiv x/L'$ and $\bar{y} \equiv \beta_{water} y/L'$). The trailing edge x_{TE} is located at a *unit* distance in x/L' from the leading edge where the sectional waveform is prescribed. This prescription is called for by the mid-field theory, in which the waveform evolves on the surface of a constant ω_* which intersect the ground along a line in the wind direction. As suggested by examples of mid-field calculations as well as ground observation,[2,3,6] we assume a nonuniform span load with amplitude reducing to a half of the symmetry-plane value at the tip

$$\frac{p'}{p'_{max}} = \frac{1}{1 + (\bar{y}/\bar{y}_{SE})^2} \tag{22}$$

With the assumptions on the local chord length and the span-wise load distribution as mentioned, the double integral in 3-D solution can be reduced to single line integral. Figure 15 presents results of the attenuated and dispersed wave form (u'/u'_{max}) vs. $(\bar{x} - \bar{x}_{LE})$ at seven span locations $(y/L' = 0, 50, 100, 150, 200, 241.13$ and $241.5)$ at a depth about 10% chord *below* the ocean surface $(z/L' = -0.1)$. The dispersed wave form at $y/L' = 241.13$ is that directly below the cut-off boundary. Whereas, 2-D result is recovered in the symmetry plane $(y/L' = 0)$, the large departure from the 2-D analysis is apparent from the results shown at other span stations. [A minor contribution to the departure is due to the span load nonuniformity assumed in Eq. (22); note that the quotient in Eq. (22) is nearly unity for the stations $y/L' = 50$ and 100 and is only 1/2 at the tip.] Similar and more pronounced departures from the 2-D wave form are predicted for a large depth corresponding to 50% chord below the ocean, as shown in Fig. 16 for $z/L' = -0.5$.

Reconciling with the lifting-line concept

The apparently large departure from the 2-D result revealed above is surprising, since an aspect ratio of nearly 500 considered here is expected to show little 3-D effects. Computations for a variety

of planforms with low to high aspect ratios, including rectangular and crescent-moon shapes with uniform span load, were performed to ascertain the program accuracy and the roles of aspect ratio and of center-line sweep and curvature. While these results confirm the insignificance of the aspect ratio as a parameter in explaining the discrepancy, it is realized that the pronounced difference is a consequence of the manner in which the results are presented and compared for the span sections of constant y/L' parallel to the relative wind. This is not strictly in accord with the lifting-line concept when applied to a swept and curved center line, for which the dominating field gradients occur in directions *normal* to the lifting/center line. That is, the "wing section" in the *normal* direction is responsible to the disturbance determination, while the local chord for this wing section C' is now *reduced* from the chord of constant y/L' by the factor $cos\Lambda$, with Λ being the local sweep angle. Therefore the dispersed waveforms below different span stations shown in the above figures correspond actually to the waveform at successively increasing depth ratio z/C'. This explains the noticeable amplitude reduction at successive span station in Figs. 14, 15. Hence, a prediction procedure for the submarine wave field based on the lifting-line concept can be used and will allow fruitful applications of the 2-D results[30–32] to a class of genuine 3-D sonic-boom impact problems.

References

1 Darden, C.M. (ed.), "Status of Sonic Boom Methodology and Understanding," *NASA Conf. Pub. 3027*, 1988.

2 Maglieri, D.J., Sothcott, V.E. and Bobbit, P.J., "Sonic Booms Associated with X-30 Flight Operations (U)," *Proc. 10th Nat. Aero-Space Plane Tech. Symp*, paper 129 (1991); also see Maglieri, D.J., Sothcott, V.E. and Hicks, J. "Influence of Vehicle Configuration and Flight Profile on X-30 Sonic Booms," *AIAA paper 90-5224*, 1990.

3 Plotkin, K.J., Downing, M. and Page, J.A., "USAF Single-Event Sonic Boom Prediction Model: PC Boom 3," *High-Speed Research NASA Sonic Boom Workshop, NASA Conf. Pub. 3279*, pp. 171–184; also see Plotkin, K.J. (1989) "Potential Sonic Boom Focal Zone from Space Shuttle Reentries," *WR 89-11*, Wylie Lab., 1994.

4 Darden, C.M., "Study of the Limitations of Linear Theory Methods as Applied to Sonic Boom Calculations," *AIAA paper 90-0368*, 1990.

5 Siclari, M. and Darden, C. M., "CFD Predictions of the Near-Field Sonic Boom Environment for Two Low-Boom HSCT Configurations," *AIAA paper 91-1631*, 1991.

6 Holloway, P.E., Wilhold, G.A., Jones, J.H., Garcia, F. and Hicks, R.M., "Shuttle Sonic Boom—Technology and Predictions," *AIAA paper 73-1039*, 1973.

7 Coakley, T.J., "Preliminary Numerical Investigation of Sonic Boom at threshold Mach Number," Proc. 3rd Conf. Sonic Boom Research, Oct. 29–30, 1970 (ed. I.B. Schwartz), *NASA SP-255*, pp. 181–191, 1970.

8 Maglieri, D.J., Hilton, D.A., Huckel, V. and Henderson, H., "Measurements of Sonic Boom signatures from Flights at Cutoff Mach Number," Proc. 3rd. Conf. Sonic Boom Research, Oct. 29–30, 1970 (ed. I.B. Schwartz), *NASA SP-255*, pp. 181–191, 1970.

9 Davis, S.S., "A preliminary Investigation of Sonic Boom Waveform Near Focusing Ray System," Proc. 3rd. Conf. Sonic Boom Research, Oct. 29–30, 1970 (ed. I.B. Schwartz), *NASA SP-255*, pp. 133–146, 1970.

10 Hayes, W. D., Haefeli, R. C., and Kulsrud, H. E., "Sonic Boom Propagation in a Stratified Atmosphere with Computer Program," *NASA CR–1299* (1969); also see Hayes, W. D. "Geometric Acoustics and Wave Theory," *Proc. 2nd Conf. on Sonic Boom Research* (ed. I. R. Schwartz) *NASA SP–180*, pp. 158-, 1968.

11 Thomas, C. L., "Extrapolation of Sonic Boom Pressure Signatures by the Waveform Parameter Method," *NASA TND-6832*, 1972.

12 Cheng, H.K., "On Sonic Boom Propagation in a Stratified Atmosphere," *Proc. Internat. Conf. Fundamental Research in Aerospace Science,* TsAGI, Zhukousky, Russia, Sept. 22–24, 1994.

13 Cheng, H.K., Lee, C.J., Hafez, M.M. and Guo, W.H., "The CFD Problem of Sonic-Boom Propagation in a Stratified Atmosphere," *First Asian CFD Conference*, Hong Kong Univ. of Science and Technology, Hong Kong, Jan. 16–19, 1995.

14 Darden, C.M., "An Analysis of shock Coalescence Including Three-Dimensional Effects with Application to Sonic Boom Extrapolation," *NASA TP2214*, 1984.

15 Hayes, W. D., "Linearized Supersonic Flow," Calif. Inst. Tech. Thesis, reproduced as North American Aviation Report *AL–222*, 1947.

16 Lomax, H., "Wave Drag of Arbitrary Configurations in Linearized Flow as Determined by Area and Forces in Oblique Plane," *NASA RM A55A18*, 1955.

17 Carlson, H.W., "Correlation of Sonic Boom Theory with Wind-Tunnel and Flight Measurements," *NASA TR–213*, 1964.

18 Seebass, R., "Sonic Boom Theory," *J. Aircraft*, vol. 6, no. 3, pp. 177–184, 1969.

19 Pierce, A.D., "Atmospheric Propagation at Larger Lateral Distances from the Flight Track," *High-Speed Research: 1994 Sonic Boom Workshop, NASA Conf. pub. 3279*, pp. 99–122, 1994.

20 Whitham, G. B., "The Flow Pattern of a Supersonic Projectile," *Comm. Pure Appl. Math*, vol. 5, pp. 301–348, 1952.

21 Hayes, W.D., "Similarity Rules for Nonlinear Acoustic Propagation Through a Caustic," 2nd Conf. sonic Boom Research, *NASA SP-180*, pp. 165–171, 1969.

22 Seebass, R., "Nonlinear Acoustic Behavior at a Caustic," *Proc. 3rd. Conf. Sonic Boom Research, NASA SP-255*, pp. 87–120, 1970.

23 Plotkin, K.J. and Cantril, J.M., "Prediction of Sonic Boom at a Focus," *AIAA paper 76–2*, 1976.

24 Ashley, H. and Landahl, M., *Aerodynamics of Wings and Bodies,* Addison-Wesley Pub. Co., pp. 81–148; also see Sears, W.R. 91954) "Small Perturbation Theory," Sec. C, *General Theory of High-Speed Aerodynamics* (ed. W.R. Sears), Prinston Univ. Press, pp. 61–116, 1965.

25 Cole, J.D. and Cook, L.P., *Transonic Aerodynamics*, pp. 173–181, 1986.

26 Ferrari, C. and Tricomi, F.G., *Transonic Aerodynamics*, transl. R.H. Cramer, Acad. Press, 1968.

27 Seebass, R., Murman, E.M. and Krupp, J.A., "Finite Difference Calculation of the Behavior of a Discontinuous Signal Near a Caustics," Proc. 3rd. Conf. Sonic Boom Research, Oct. pp. 29–30, 1970 (ed. I.B. Schwartz), *NASA SP-255*, pp. 361–371, 1970.

28 Hafez, M.M. and Cheng, H.K., "Shock-Fitting Applied to Relaxation Solutions of Transonic Small Disturbance Equations," *AIAA J.*, vol. 15, no. 6, pp. 786–793, 1977.

29 Haglund, G.T. and Kane, E.J., "Analysis of Sonic Boom Measurements Near Shock Wave Extremities for Flight Near Mach 1.0 and for Airplane Acceleration," *NASA CR-2417*, 1974.

30 Sawyers, K.H., "Under Water Sound Pressure from Sonic Boom," *J. Acoust. Soc. Amer.*, vol. 44, no. 2, pp. 523-524, 1968.

31 Cook, R.K., "Penetration of Sonic Boom into Water," *J. Acoust. Soc. Amer.*, vol. 47, no. 5, pp. 1430–1436, 1970.

32 Sparrow, V.W., "The Effect of Aircraft Speed on the Penetration of Sonic Boom Noise into a Flat Ocean," *Proc. High-Speed Research: 1994 Sonic Boom Workshop, NASA Conf. Pub. 3279,* pp. 137-156, 1994.

33 Water, J., "Penetration of Sonic Boom Energy into the Ocean: An Experimental Simulation," *Noise & Vibration Control Engineering* (ed. M. Croker), *Proc. Noise Control Conf.,* Purdue Univ., July 11–16, 1971,pp. 554–557, 1971.

34 Stansbery, E.G. and Stanley, J.F., "Descent Sonic Boom Measurements of STS-26, Including a $M = 23$ Measurements," *NASA JSC-23579*, 1989.

35 Balhaus, W.F. and Gorjian, P.M., "Implicit Finite-Difference Computation of Unsteady Transonic Flow About Airfoils," *AIAA J.*, vol. 15, pp. 1728–1735, 1970.

36 Page, J.A. and Plotkin, K.J., "An Efficient Method for Incorporating CFD Into Sonic Boom prediction," *AIAA paper 91-3275*, 1991.

Fig. 1 Body-fixed, Cartesian coordinates

Fig. 2 Anticipated cross-field wave pattern in cylindrical coordinates. The hashed line represents the ground.

Fig. 3 Standard atmosphere model

Fig. 4 Example of cross-field pattern of characteristics emitted at various azimuthal angles for cruise Mach number 2.0 and cruise altitude 1.5 h, or in standard atmosphere. Solid curves are exact solutions of $x^{lc}(\eta, \omega)$.

Fig. 5 Comparison of mid-field waveforms with Darden's MMOC results for a slender body at attack angle $\alpha = 3^0$, cruise Mach number M_0=3 with Darden's waveform prescribed at r/L=10 as initial data, showing sensitivity to assumed tail-end signature: (a) initial waveform (b) ground signature in standard atmosphere.

Fig. 6 Testing treatment of multiple shock coalescence against MMOC results: (a) Darden's waveform at r/L=1.5 as initial data, (b) waveforms at r/L=2, (c) waveforms at r/L=2.5

Fig. 7 Test of F-function determination procedure applied to wind tunnel data of model C at Mach 2.01 and 5^0 attack angle (Ref. [17]) at two levels r/L=4, 8 in symmetry plane. (a) $\tilde{u}$ waveforms from experiment expressed as functions of characteristic variable ξ_1^*, (b) F-function determined, (c) unwanted cross-field azimuthal contribution identified.

Fig. 8 Waveform comparison of mid-field solutions based on modified and original/unmodified u as initial data at r/L=4: (a) $\tilde{u}$ at r/L=4 with the unmodified distribution deduced from Ref.[17], (b) Waveform at r/L=8, (c) Waveform at r/L=16, (d) Waveform at r/L=32.

Fig. 9 Sonic boom impact boundaries for cruise altitude h_{cr}=1.5h_{*1}, in standard atmosphere for flight Mach number M_0=2.0, 1.6, 1.2, 1.175 and 1.153, illustrating shrinkage of the lateral extent as M_0 tends to threshold value.

Fig. 10 Illustration of characteristic behavior of the linear 3-D Tricomi equation showing smooth *refraction* in both longitudinal and transverse directions. Characteristic curves reflected/refracted from the transition boundary in a cupidated manner may be considered exceptional.

Fig. 11 Solution to 2-D nonlinear Tricomi equation in normalized form computed for N-wave signature from the mid-field at threshold Mach number: (a) at constant $\tilde{u}$,(b) Waveforms at different elevations including the ground plane.

Fig. 12 CFD analysis of superboom at threshold Mach number based on nonlinear 3-D Tricomi equation, assuming N-wave uniformly distributed over a rectangular slot $0<\hat{x}<1$, $-1<\hat{y}<2$: (a) $\hat{u}$ contours and sonic boundary in symmetry plane (y=0), (b) waveforms at different elevations in symmetry plane, (c) $\hat{u}$ contours and sonic boundary in plane $\hat{y}$=1/2, (d) waveforms at different elevations in plane $\hat{y}$=1/2.

Fig. 13 Sketch for submarine sonic-boom impact analysis in a body-fixed frame.

Fig. 14 Leading and side edges of sonic boom impact boundaries on flat-ocean model surface and a simplified analytical description for cruise at Mach = 2.01 and altitude 55,000 ft. For a uniform chord length in x of L=580 ft on the surface, the trailing and leading edge of the impact zone are almost indistinguishable in this sketch.

Fig. 15 Spanwise distribution of sonic-boom generated disturbance (normalized) under water at depth of 10% chord. Conditions same as in previous figure.

Fig. 16 Spanwise distribution of sonic-boom generated disturbance (normalized) under water at depth of 50% chord. Conditions same as in previous figure.

The work is presented at the High Speed Research Program Sonic Boom Workshop at NASA Langley Research Center, Sept. 12-13, 1995.

IMPACT OF WEATHER AND FLIGHT CONDITION ON SECONDARY BOOMS*

57-71

Hugh W. Poling
Boeing Commercial Aircraft Group
P.O. Box 3707
Seattle, Washington 98124

15P.

D36748

INTRODUCTION

Upward propagating sonic booms may be refracted down to the ground with the proper combination of temperature and wind profiles above the aircraft following paths as shown in figure 1. Long propagation distances and passage through at least one caustic at ray reversal serve to disperse shocks from the original signature, resulting in low frequency "rumbles" at the ground. Public reaction to these "secondary booms" from the Concorde initiated field studies with measurements up to 60 dBA (ref. 1 and ref. 2). Building vibration from the infrasonic portion of the secondary boom signature is also a contributor to annoyance (ref. 3). Adverse public reaction to secondary booms may be circumvented by assessing the impact of weather and flight condition on occurrence, location and signature strength and adjusting flight operations to compensate, if required.

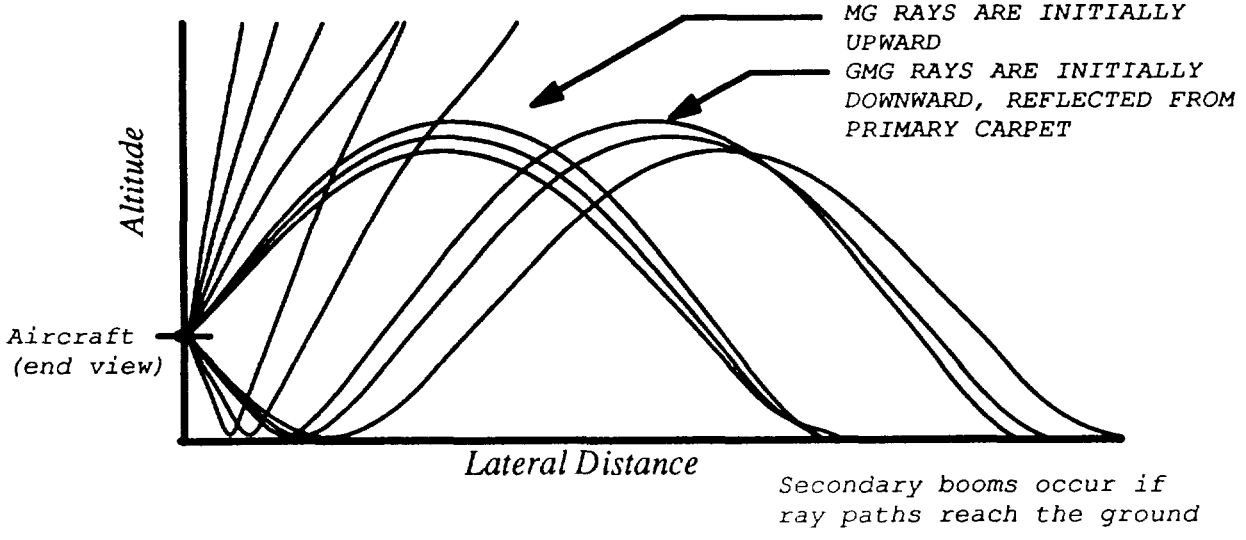

Figure 1. Schematic of sonic boom ray paths leading to secondary booms

*This work was done under NASA Contract NAS1–20220, Task 12

OBJECTIVE

The objective of this study is to determine the occurrence and acoustic characteristics of secondary booms from HSCT aircraft for varying weather and flight conditions. Temperature and wind conditions allowing secondary booms will be determined. The ground location and acoustic impact of secondary booms for an HSCT aircraft will be estimated.

STATUS OF TECHNOLOGY

COMPARISON OF PROPAGATION CODES

Two computer programs were available for secondary booms propagation, TRAPS and ZEPHYRUS. TRAPS was written by A. Taylor in 1980 (ref. 4), to add the capability of ray path reversal and secondary booms to its predecessor program, ARAP (ref. 5). ZEPHYRUS was written within the last several years by L. Robinson as a tool to include air absorption effects in sonic boom propagation. Features of the two programs are compared in table I. Both codes were checked against results of prior studies.

TRAPS' ray tracing essentially duplicates the location of secondary boom focus lines for the sample Concorde descent described in ref. 1.

As a check of TRAPS' pressure propagation, levels were calculated for a baseline HSCT. The TRAPS overpressure levels were found to be too high by a factor of about 1.5 compared to the Hayes method (described in ref. 5), which uses F–functions like TRAPS. TRAPS overprediction was up to 1.8 times the results of the Carlson Simplified Method (ref. 6) applied to F–111 and SR–71 aircraft. The Carlson Simplified Method uses generalized airplane shape factors based on geometric data rather than F–functions. This result, plus the neglect of air absorption (by design) led to the preference of using ZEPHYRUS for signature calculation.

ZEPHYRUS uses the conceptually straightforward, but computing intensive, technique of applying propagation effects in the time domain and absorption and dispersion effects in the frequency domain. Cases take several hours to run, which inhibits investigation of a large number of scenarios as might be done with TRAPS. Propagation of signatures within the primary carpet and not including air absorption was found to match results using the Hayes method, which gives some confidence in the cases run with air absorption.

FEATURE	TRAPS	ZEPHYRUS
Aircraft flight track	arbitrary maneuvers	straight and level only
Stratified atmosphere and winds	Yes	Yes
Geometric acoustics	Yes	Yes
Ray specification	User–input and edge rays	User–input angles only
Caustics along ray path	Allowed	Allowed
Signature Aging	linear theory – equal area rule	?
Non–linear distortion of high–intensity sound	?	Yes
Attenuation effects	No	Yes
Dispersion effects	?	Yes
Ground surface	Flat and level	Flat and level
Ground reflection	Multiplier to simulate ground reflection	Total reflection or ground impedance

Table I. Comparison of Features in Propagation Codes, TRAPS and ZEPHYRUS

TECHNICAL APPROACH

SECONDARY BOOM OCCURRENCE

In the presence of temperature and wind gradients, pressure signatures emitted from the aircraft follow ray paths which curve toward regions where the temperature (and thus, sound speed) is lower and where the wind component in the ray direction is greater. For each upward propagating ray there is a critical combination of temperature and wind velocity gradients that will cause the ray's vertical motion to slow, stop, and reverse. Secondary booms are the result of such rays reaching the ground. Secondary boom occurrence is essentially determined by conditions in the band of altitude above the aircraft up to the temperature peak in the middle of the mesosphere (around 160,000 ft). The decreasing temperature above the mid–atmosphere temperature peak is unfavorable to secondary booms and so sets a practical upper bound for altitudes of interest. Rays beneath the aircraft which reverse before striking the ground will never go below their reversal altitude because of the horizontally stratified atmosphere assumption in the ray trace code. Specific aircraft altitude was determined to have little impact on secondary boom occurrence and was set at 50,000 feet for all cases.

Secondary booms will occur under no–wind conditions when the ground temperature is lower than the mid–altitude temperature peak shown in the standard atmosphere (figure 2) which

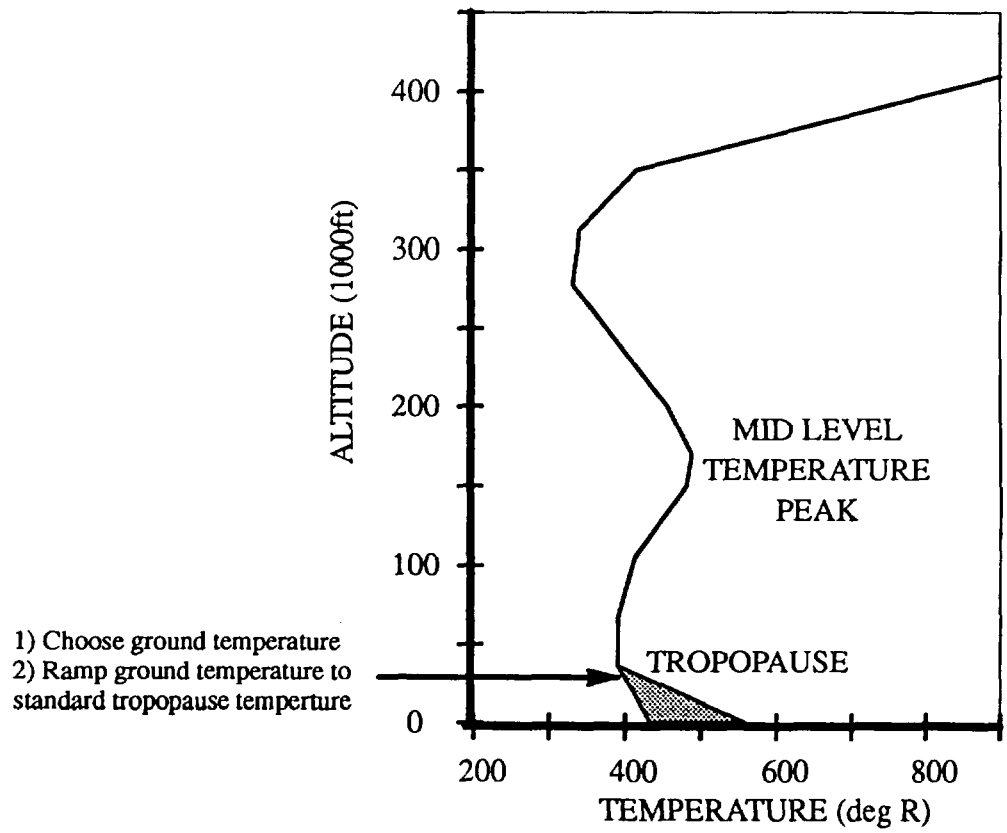

Figure 2. Model temperature profile used to determine occurrence of secondary booms.

is approximately 22° F (481° R). Since meteorological events are most variable near the ground and damp out with altitude, temperature profiles were constructed with a variable ground temperature linearly ramped to the standard tropopause temperature and the standard atmosphere above the tropopause.

The two wind profiles modeling wind gradient extremes are shown in figure 3. The first is a large gradient "spike" where the wind velocity is zero except for a 10,000 ft band of altitude. The spike wind profile has the effect of deflecting the ray path since the non–zero wind speed is concentrated in a small increment of altitude.

The second model wind profile has the lowest gradient to a given maximum wind speed by starting with zero speed at the aircraft altitude of 50,000 ft and having a linear increase in speed

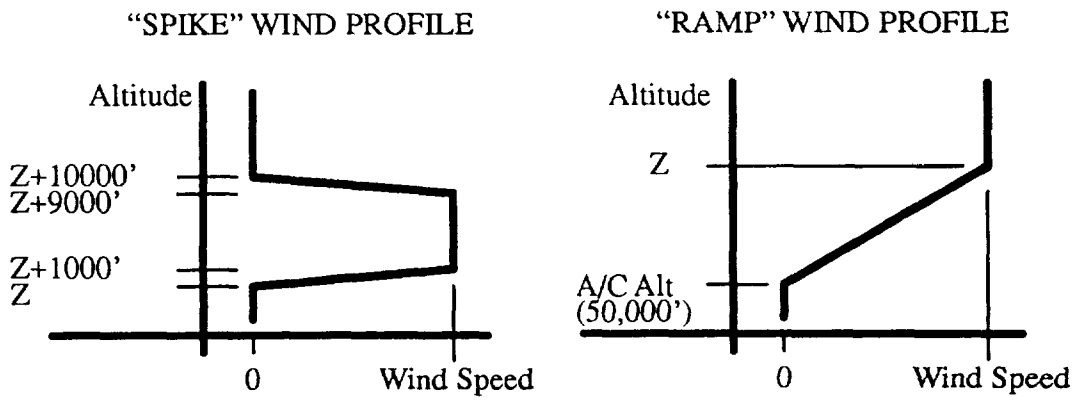

NOTE: "Z" is altitude for a given profile
"W" is maximum wind speed for a given profile

Figure 3. Model wind profiles used to determine occurrence of secondary booms.

to the specified altitude and magnitude. The large range of non–zero wind speed for the ramp profiles encourages secondary booms since the wind effect is applied to most of the ray path length above the aircraft.

Maximum windspeed values of 25, 50 and 100 knots were used in this study. Results at 50 knots are shown in the following sections to illustrate trends. Changing the wind speed shifts the results without changing the form. The impact of wind speed is included in the overall summary charts.

Wind direction including tailwind, headwind, and sidewind were accounted for. Upwind and downwind were considered separately for the sidewind case. Although none of these wind directions were exactly aligned with the initial ray direction for maximum effect, they are consistent relative to the aircraft flight direction over changes in aircraft Mach number.

TAILWIND

Tailwind conditions favor ray reversal and the wind profile (altitude) has a marked influence on the temperature limit for secondary boom occurrence. The spike wind at altitudes just above the aircraft only causes secondary booms near the no–wind temperature limit but the spike wind at higher altitudes allows secondary booms at higher ground temperatures, converging to the ramp wind limit at the temperature peak in the mesosphere ($\approx$ 160,000 ft). These results are shown in figure 4 for 50 knot wind speed and several Mach numbers.

Since the ramp wind can influence the ray path over a wide range of altitude and path length, the ramp tailwind promotes secondary boom with ground temperatures above the no–wind boundary temperature. Wind altitude does not affect the boundary temperature so that a given aircraft Mach number and maximum wind speed simply maps to a maximum ground temperature for secondary boom occurrence. Increasing Mach number raises the boundary temperature as the wind component in the ray path direction becomes smaller.

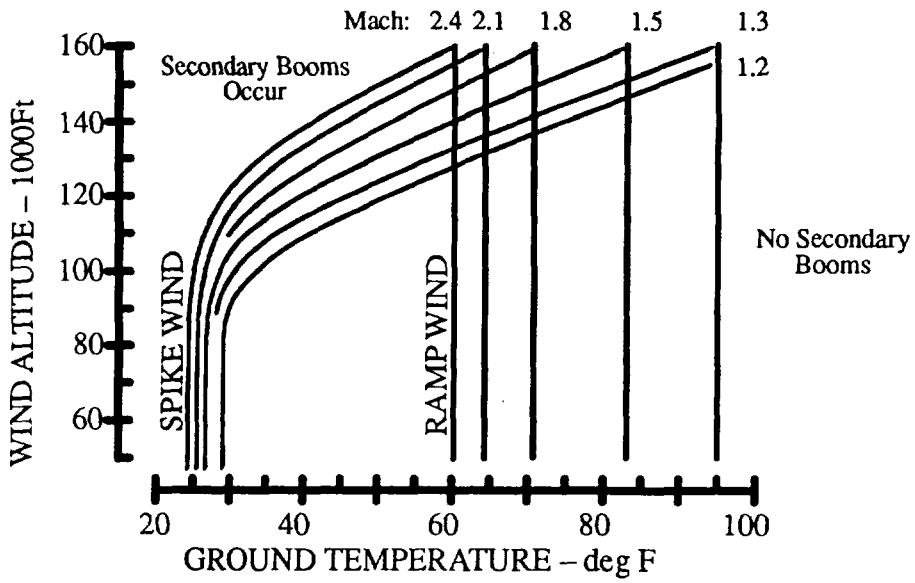

Figure 4. Occurrence of secondary booms with tailwind at 50 knots maximum.

HEADWIND

Headwinds discourage ray reversal and also eliminate the impact of wind altitude by raising it above the mesosphere limit. The important weather parameters become simply the ground temperature and wind magnitude. The spike wind boundary temperature remains near the no–wind boundary temperature but the ramp wind lowers the boundary temperature significantly, as shown in figure 5.

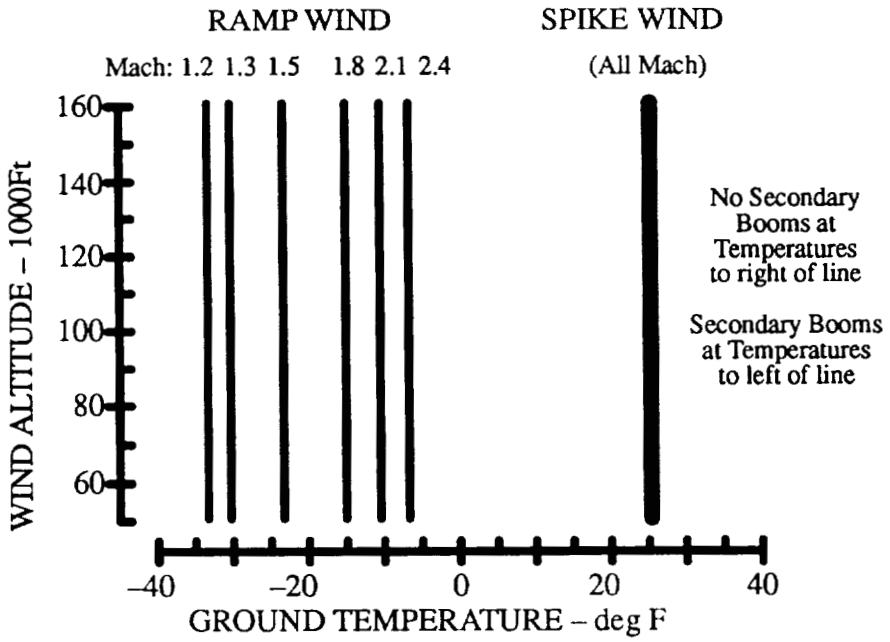

Figure 5. Occurrence of secondary booms with headwind at 50 knots maximum.

SIDEWIND

The upwind and downwind sides for a 90° sidewind were treated separately. The downwind side is a situation similar to tailwinds except the wind component is on the opposite side of the ray path vector. This reverses the impact of Mach number compared to the tail wind case since the ray path vector and the wind vector become more closely aligned.

The reverse effect is seen on the upwind side of the sidewind case. The boundary temperature is always close to the no–wind value.

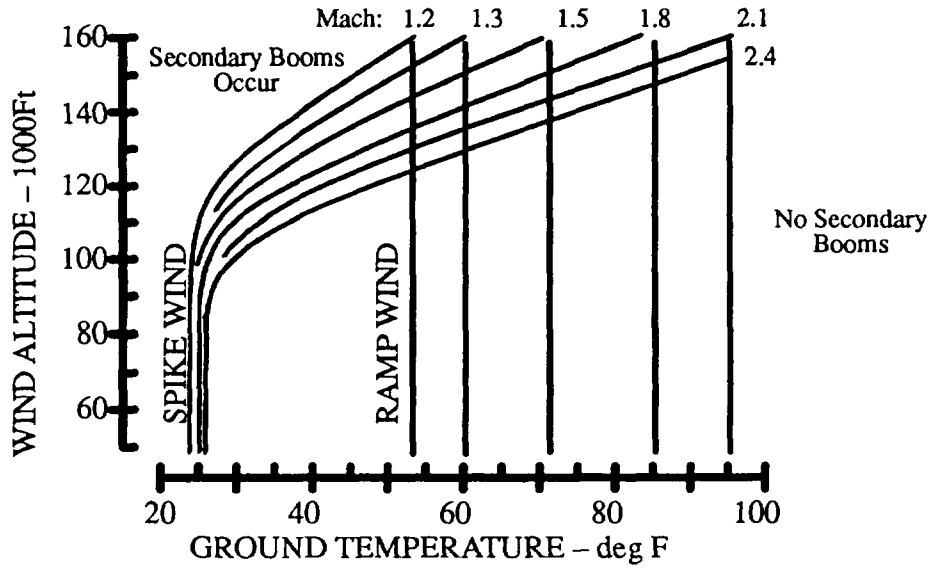

Figure 6. Occurrence of secondary booms with (downwind) sidewind at 50 knots maximum.

SUMMARY OF SECONDARY BOOM OCCURRENCE

Considering that a spike wind just above the aircraft is the least effective in deflecting ray paths and a ramp wind at any altitude above the aircraft is the most effective in deflecting ray paths, these two extremes define the borders of secondary boom occurrence described previously. The ground temperature of these borders is dependent on aircraft Mach number so figures 7 to 12 are presented to cover the range 1.2 to 2.4.

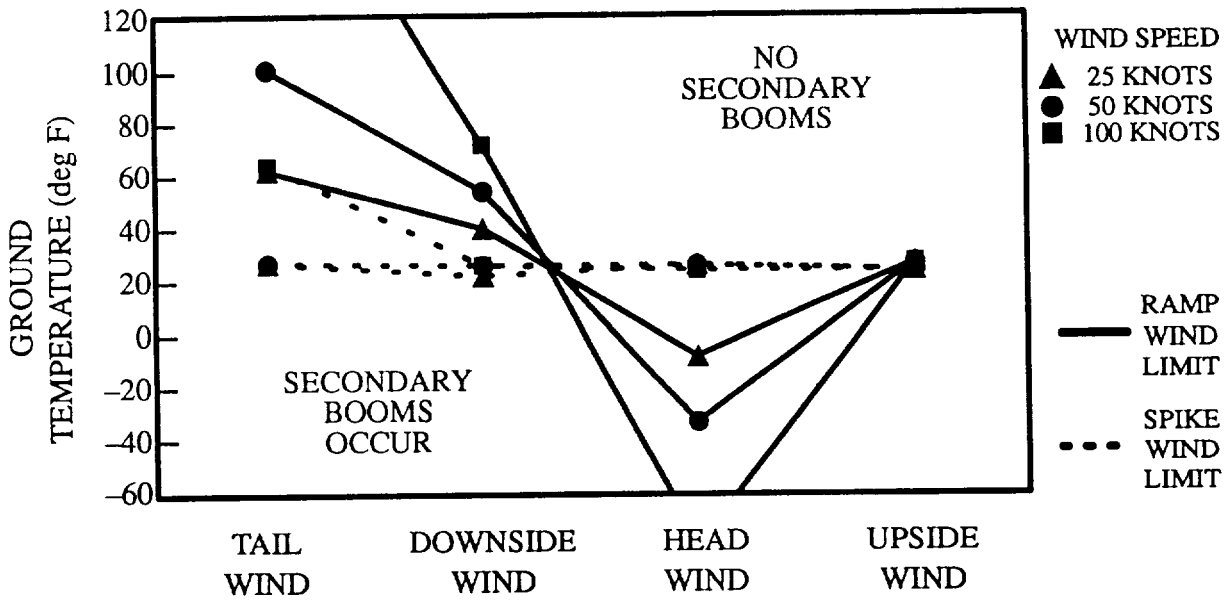

Figure 7. Generalized occurrence of secondary booms with aircraft Mach = 1.2.

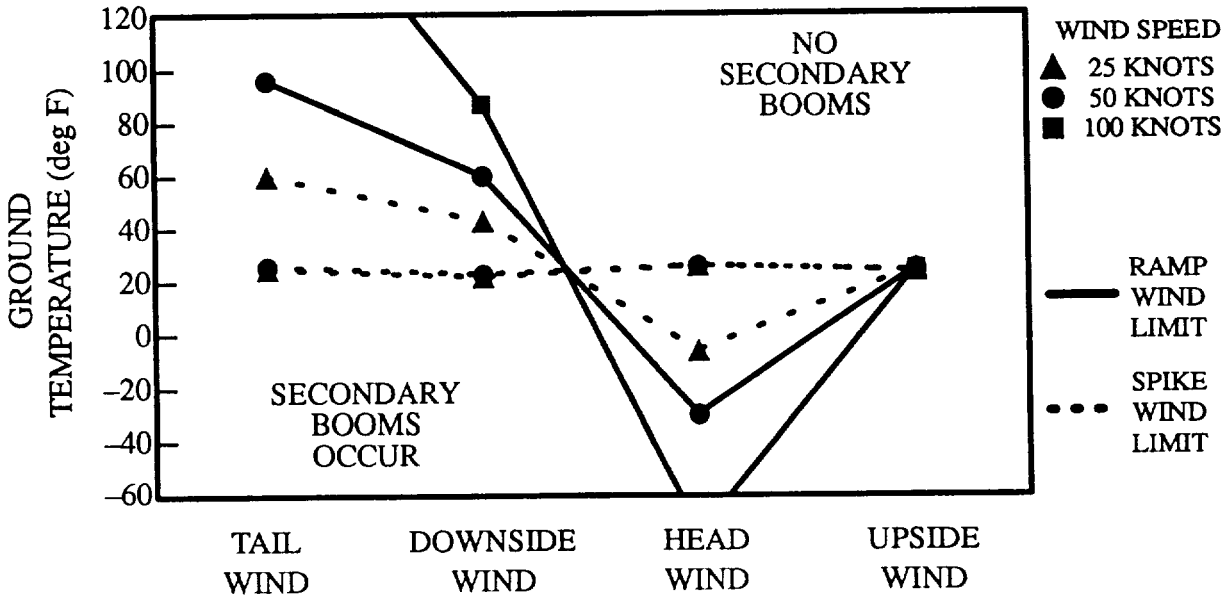

Figure 8. Generalized occurrence of secondary booms with aircraft Mach = 1.3.

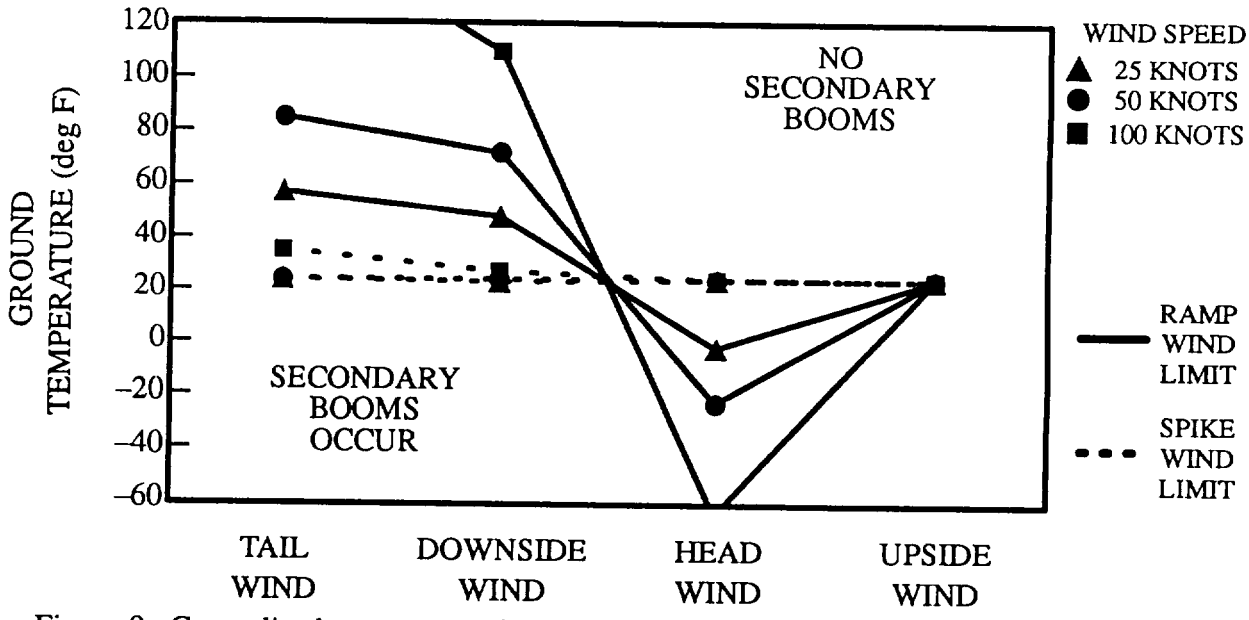

Figure 9. Generalized occurrence of secondary booms with aircraft Mach = 1.5.

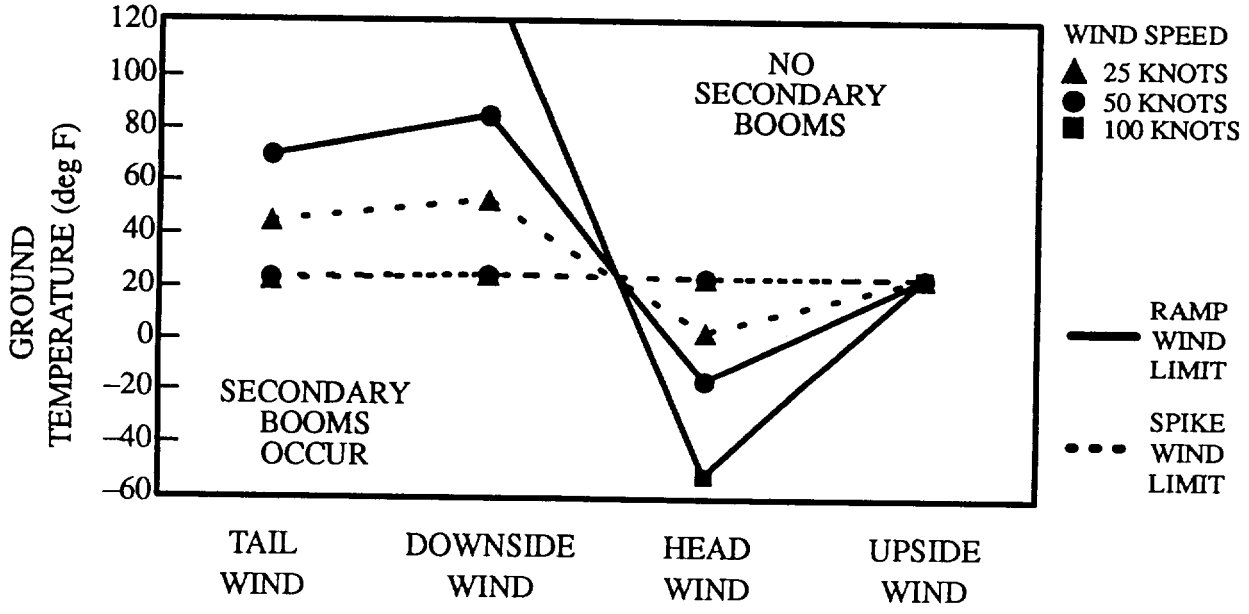

Figure 10. Generalized occurrence of secondary booms with aircraft Mach = 1.8.

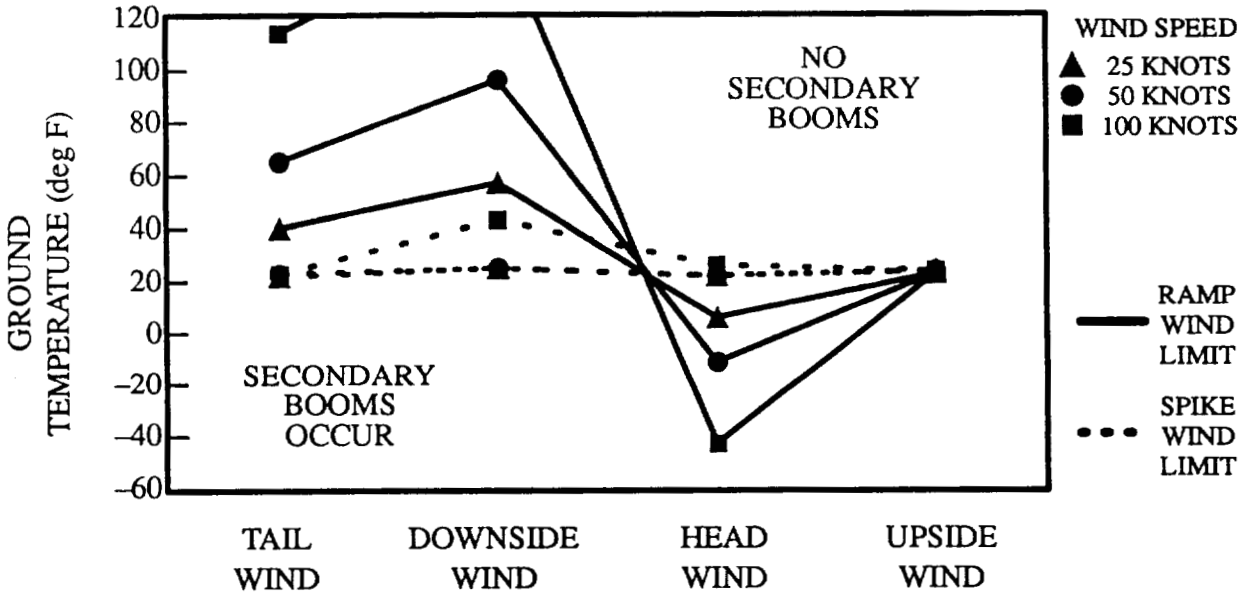

Figure 11. Generalized occurrence of secondary booms with aircraft Mach = 2.1.

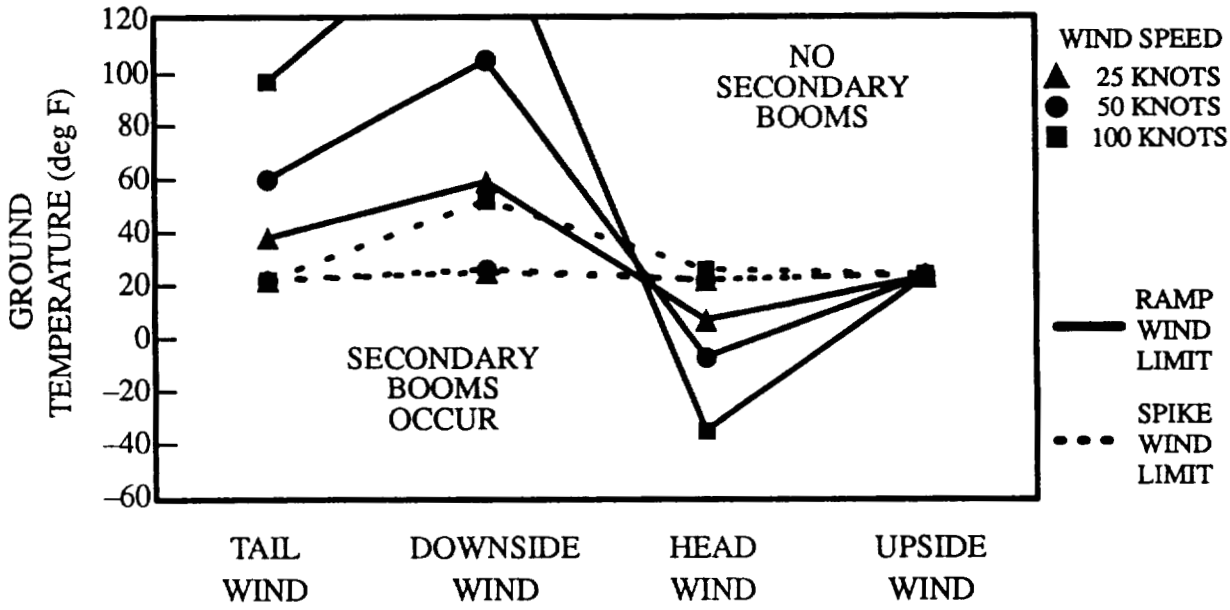

Figure 12. Generalized occurrence of secondary booms with aircraft Mach = 2.4.

SECONDARY BOOM GROUND LOCATION

Since secondary booms propagate ahead and to the side of the aircraft, the ground location of secondary booms is primarily a consideration for HSCT approach to land and possibly for routes threading between islands. To estimate the distances involved, ray traces were done with the arctic standard temperature profile (figure 13) and an "average" ramp wind profile with an altitude of 100,000 ft. The arctic temperature profile was chosen since it is a known standard that favors secondary booms under no–wind conditions. It is defined up to 100,000 and is ramped into the standard temperature profile above that. The aircraft was at 50,000 ft with Mach numbers ranging from 1.2 to 2.4.

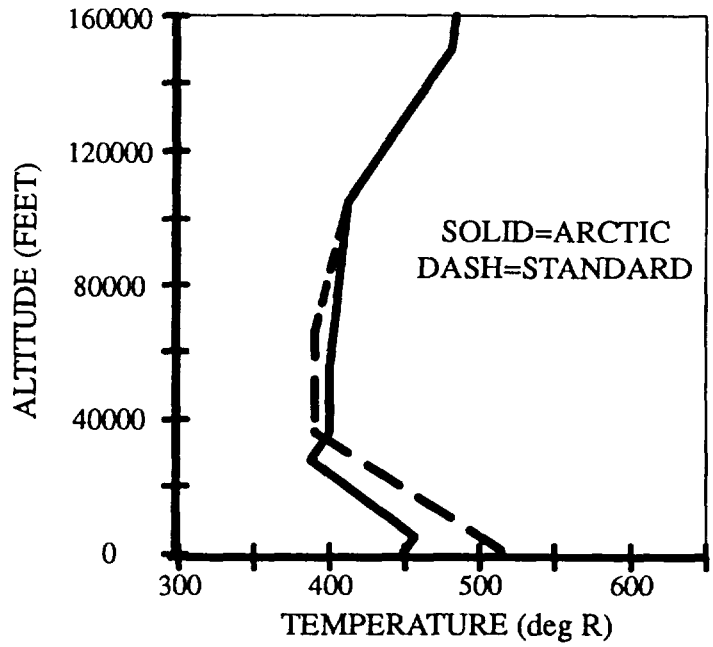

Figure 13. Arctic temperature profile used to determine ground location of secondary booms.

Both initially upward and initially downward ray intercept the ground slightly forward of the boundary marked by the initial ray cone half–angle (also known as the co–Mach angle), measured from the direction of flight and defined by:

$$co - Mach\ Angle = \arccos\left(\frac{1}{Mach}\right) \tag{1}$$

The zero wind condition sets the maximum reach that ray extends from the aircraft. This is shown in figure 14, where the ground location is only a function of Mach number since aircraft altitude has been held constant. The effect of wind is not so much to change the distance to the furthest ground intercept as it is to bring the closest intercept (not shown in the figure) closer to the aircraft. Tailwinds move the closest ray closer to the flight track as well as closer to the airplane. Downwind of the 90° sidewind the closest ray is brought directly closer along the ray cone angle to the airplane without as much lateral spreading as the tailwind case. Headwind may expand the boundary shown in figure 14, but for conditions in this study, only the 10 knot head wind had a few rays return to the ground at about 10 n.m. beyond the boundaries shown.

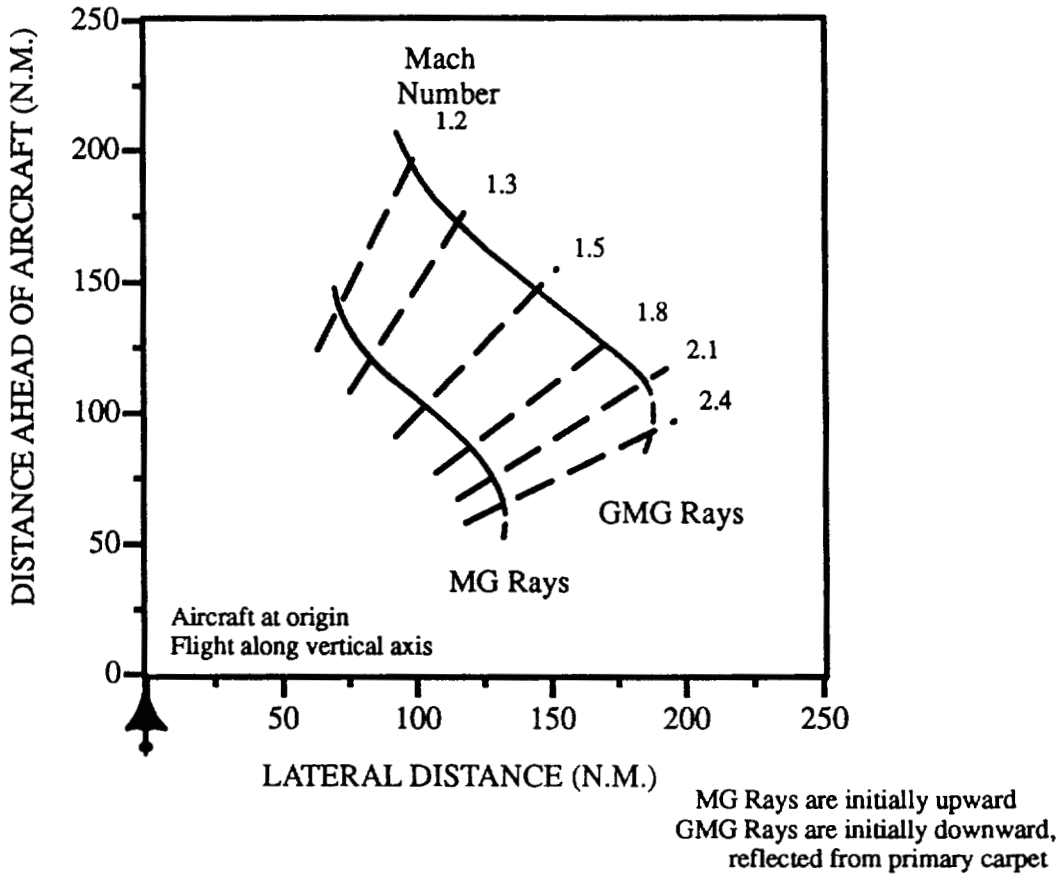

Figure 14. Maximum extent of secondary boom ground interception

PRESSURE SIGNATURES

(Not Completed)

CONCLUSIONS

Ground temperatures higher than a certain threshold value are sufficient to prevent secondary booms irrespective of wind profile details. Similarly, ground temperature lower than a certain threshold value (different than the first) are sufficient to allow secondary booms irrespective of wind profile details. The two threshold values depend on wind direction, maximum wind speed and aircraft Mach number as shown in figures 7 to 12.

When secondary booms occur, they will touch the ground in front of the aircraft at a location that is primarily dependent on the aircraft flight condition. Winds will increase the width of the affected region due to ray spreading, but the maximum extent of the ground intercept is practically constant with values shown in figure 14. Higher aircraft Mach numbers increase the maximum extent laterally and decreasing Mach numbers increase the extent in front of the aircraft. Either case may be expected to reach distances 200 n.m. from the aircraft.

FUTURE DIRECTIONS

The following list contains items that the results of this study suggest would improve understanding and prediction accuracy of secondary booms:

Complete signature propagation with ZEPHYRUS to estimate ground noise levels.

Include effect of atmospheric turbulence.

Investigate impact of real weather, including statistical variation. This effort could be combined with a survey of significant HSCT airports and descent restrictions to avoid secondary booms overland.

Consider wind direction effects relative to initial ray angles. The coordinate system would change with Mach number.

Assess secondary boom annoyance response, particularly with respect to infrasound–induced building vibrations.

Combine strengths of programs into one package (Ray tracing from TRAPS, signature propagation from ZEPHYRUS).

Compare ZEPHYRUS to other codes that account for absorption only in the time domain (Rudenko, Cleveland). These should run much faster.

REFERENCES

1. Rickley E.J.; and Pierce A.D.: *Detection and Assessment of Secondary Sonic Booms in New England.* U.S. Department of Transportation, Cambridge, MA, May 1980.

2. Gardener J.H.; and Rogers P.H.: *Thermospheric Propagation of Sonic Booms from the Concorde Supersonic Transport.* Naval Research Laboratory Memorandum Report 3904, February 14, 1979.

3. Maglieri D.J.; Carlson H.W.; and Hubbard H.H.: Status of Knowledge of Sonic Booms. *Noise Control Engineering*, vol. 15, number 2, September–October 1980, pp 57–64.

4. Taylor A.D.: *The TRAPS Sonic Boom Program.* NASA Technical Memorandum ERL ARL–87, July 1980.

5. Hayes, W.D.; *et al*: *Sonic Boom Propagation in a Stratified Atmosphere with Computer Program.* NASA CR–1299, 1969.

6. Carlson H.W.: *Simplified Sonic–Boom Prediction*, NASA TP–1122, 1978.

A COMPARISON OF COMPUTER CODES FOR THE PROPAGATION OF SONIC BOOMS THROUGH REALISTIC ATMOSPHERES UTILIZING ACTUAL ACOUSTIC SIGNATURES[a,b]

James P. Chambers,
National Center for Physical Acoustics, University of Mississippi, University, MS 38677

Robin O. Cleveland[c]
Applied Research Laboratories and Mechanical Engineering Department, The University of Texas at Austin, P.O. Box 8029, Austin, TX 78713-8029

Henry E. Bass, Richard Raspet
Dept. of Physics and Astronomy, University of Mississippi, University, MS 38677

David T. Blackstock and Mark F. Hamilton
Mechanical Engineering Department and Applied Research Laboratories, The University of Texas at Austin, P.O. Box 1063, Austin, TX 78713-8029

[a] A similar paper has been submitted to The Journal of the Acoustical Society of America, July 1995.

[b] This work was performed under NASA Grant # NAG-1-1460

[c]Current Address: Applied Physics Labs., University of Washington at Seattle, Seattle, WA 98105.

INTRODUCTION

A numerical exercise to compare computer codes for the propagation of sonic booms through the atmosphere is reported. For the initial portion of the comparison, artificial, yet realistic, waveforms were numerically propagated through identical atmospheres. In addition to this comparison, one of these codes has been used to make preliminary predictions of the boom generated from a recent SR71 flight. For the initial comparison, ground waveforms are calculated using four different codes or algorithms: 1) weak shock theory, an analytical prediction, 2) SHOCKN, a mixed time and frequency domain code developed at the University of Mississippi, 3) ZEPHYRUS, another mixed time and frequency code developed at the University of Texas, and 4) THOR, a pure time domain code recently developed at the University of Texas. The codes are described and their differences noted. They are then used to predict the booms

produced by two different source waveforms through a uniform and an isothermal atmosphere, with and without the presence of molecular relaxation. In all cases, the results of THOR, SHOCKN, and ZEPHYRUS are in excellent agreement. Because the weak shock theory algorithm does not include the effect of ordinary absorption, its predictions contain amplitudes that exceed those of the other codes, particularly for an atmosphere that includes relaxation effects. For the prediction of the SR71 flight, only SHOCKN was used. Initial results are encouraging with good agreement in the overall waveform shape and amplitude. The rise time of the actual signature is longer than that predicted by SHOCKN but the effects of atmospheric turbulence have been neglected in this preliminary test. Including turbulence effects will increase the predicted rise time of the boom.

The recent upsurge of research on the propagation of sonic booms in the atmosphere is part of a NASA effort to determine the feasibility of a High Speed Civil Transport (HSCT). The prediction of sonic boom waveforms on the ground is important for determining the annoyance, and hence acceptability, of a given aircraft design, and for locating possible corridors for supersonic flight. Atmospheric propagation of pressure disturbances due to sonic booms was previously carried out by codes such as the Thomas code and the ARAP code, which do not take into account atmospheric effects due to absorption and relaxation. For simple N-wave signatures on the ground, such codes gave a good approximation in both amplitude of the shocks and the duration of the signature on the ground. However, for the purposes of accurately reproducing the exact atmospheric effects on the shock system of any and all signatures which are to be propagated through a defined atmosphere, these codes are inadequate. For this reason, attempts were made to incorporate the missing effects due to the atmosphere. New codes which do incorporate the missing atmospheric effects were written by two different universities. However, before these codes can be substituted as the new industry standard propagation code, they must be evaluated and compared against the current standard. A study was undertaken which would effectively accomplish this task and hopefully provide useful information which can be used to reduce the effects of sonic booms from supersonic aircraft.

In order to further evaluate all of the codes, it was necessary to acquire actual flight data. This data package would ideally include: a near-field signature taken several body lengths directly below the aircraft by a stationary probe, several mid-field signatures at various distances directly below the aircraft, and a ground pressure signature also taken directly below the flight path of the same aircraft pass. Additional information must include weather data at or very near the measurement sight, and humidity data.

The goal of this paper is to compare numerically some of the codes that are in the literature as well as to predict the actual sonic booms at the ground given the initial signature near a plane as well as the

atmospheric conditions. In order to compare the various codes, an exercise was initiated by the NASA Langley Research Center following the NASA Sonic Boom Workshop in 1994.[1] Although several groups initially indicated an interest in the exercise, in the end only two participated, The National Center for Physical Acoustics at the University of Mississippi and The Nonlinear Acoustics Division of Applied Research Laboratories at the University of Texas at Austin. The scope of the tests reported here is quite small. We are primarily concerned with the shock profiles, which are determined by the competing forces of nonlinear distortion and absorption and dispersion. Although the codes are capable of handling rather general atmospheric conditions, only uniform and isothermal, still, non-turbulent atmospheres are considered for the initial comparison. For the SR71 predictions, the atmospheric information at the time of the flight was used.

In the first section of this paper the equations used to model the propagation of sonic booms through a quiet but stratified atmosphere are presented. The second section contains a description of the codes used to solve the equations. Results from the numerical computations are presented and compared in the third section. Preliminary results from the SR71 flight are discussed in the fourth section and in the final section the overall results are discussed.

I. MODEL

The propagation of sonic booms through a quiet atmosphere can be modeled by a very general form of the Burgers equation (see, e.g., Ref. 2). It is assumed that small-signal ray theory can be used to describe sonic boom wavefronts, i.e., that diffraction and self-refraction (bending of rays due to finite-amplitude effects) can be neglected. The Burgers equation, which is essentially the transport equation for the signal in the ray tubes, accounts for nonlinear distortion, thermoviscous absorption (called classical-rotational absorption in the ANSI standard[3] for atmospheric absorption), absorption and dispersion due to molecular relaxation, geometrical spreading, and stratification of all the ambient properties. In operator notation the "extended" Burgers equation may be written

$$\frac{\partial p}{\partial s} = \frac{\beta}{2\rho_0 c_0^3}\frac{\partial p^2}{\partial t'} + l(t')p - \frac{1}{2S}\frac{\partial S}{\partial s}p + \frac{1}{2\rho_0 c_0}\frac{\partial(\rho_0 c_0)}{\partial s}p. \qquad (1)$$

Here $p=p(s,t')$ is the acoustic pressure, s is the distance along the ray tube, S is the ray tube area, $t' = t - \int(1/c_0)ds$ is the retarded time, c_0 is the small-signal sound speed, ρ_0 is the ambient density, and β is the coefficient of nonlinearity. The linear operator $l(t')$ is the small-signal absorption law. All atmospheric properties, including $l(t')$, are evaluated at the local position.

The absorption of sound in air depends on thermoviscous absorption and on the relaxation processes of oxygen and nitrogen.[3] For a thermoviscous fluid

$$l(t') = \frac{\delta}{2c_0^3}\frac{\partial^2}{\partial t'^2} \tag{2}$$

where $\delta = \frac{\mu}{\rho_0}\left[\frac{\lambda + 2\mu}{\mu} + \frac{\gamma - 1}{\mathrm{Pr}}\right]$ is the diffusivity of sound, μ is the shear viscosity coefficient, λ is the dilatational viscosity coefficient, γ is the ratio of specific heats, and Pr is the Prandtl number. In the frequency domain, the thermoviscous operator (acting on $e^{j2\pi ft'}$) is $L(f) = -\delta(2\pi f)^2 / 2c_0^3$, where f is the frequency. The frequency domain operator for a single relaxation process is (see, e.g., Ref. 4)

$$L(f) = -\pi\frac{m}{c_0}\frac{f^2}{f^2 + f_r^2}(f_r - jf) \ . \tag{3}$$

Here j is the unit imaginary number, $m = c_\infty^2 / c_0^2 - 1$ is the dispersion, c_∞ is the frozen (high frequency) small-signal sound speed, c_0 is the equilibrium (low frequency) small-signal sound speed, and f_r is the relaxation frequency. For air the absorption is modeled as the sum of components due to thermoviscous absorption, oxygen relaxation, and nitrogen relaxation. The formulae for the coefficients can be found in the ISO 9613-1 standard[5] and the proposed new ANSI standard.[6] Note that although Eq. 1 is written in terms of a retarded time frame based on c_0, to within the accuracy of the equation, it could be rewritten using c_∞ instead.

An important special case arises when one assumes that weak shock theory alone is sufficient to account for absorption, i.e., that dissipation is limited to that occurring at the shocks in the waveform. In this case the explicit absorption term $l(t')p$ in Eq. 1 is dropped. The resulting lossless equation can be solved by converting it to plane wave form, which has a known solution. Two transformations are introduced (see, e.g., Ref. 2), a scaled pressure

$$q = p\sqrt{\frac{\overline{\rho_0 c_0} S}{\rho_0 c_0 \bar{S}}}, \tag{4}$$

where an overbar indicates a reference value (value at the source), and a *distortion distance*,

$$\tilde{x} = \int_0^s \sqrt{\frac{\overline{\rho_0 c_0}^5 \overline{S}}{\rho_0 c_0^5 S}}\, ds. \tag{5}$$

Other authors use an *age variable*[7] in place of a distortion distance. In terms of q and $\tilde{x}$, the lossless equation can be written

$$\frac{\partial q}{\partial \tilde{x}} = \frac{\beta}{2\overline{\rho_0 c_0}^3} \frac{\partial q^2}{\partial t'}, \tag{6}$$

which has the same form as the equation for plane progressive waves. The equation is therefore solved analytically by distorting the source waveform according to the Earnshaw solution (see, e.g., Ref. 8). One uses Eqs. 4 and 5 to obtain the final waveform. Because of the distortion a multivalued waveform is usually predicted. Weak shock theory (see, e.g., Refs. 9 or 10) may be used to replace multivalued sections of the waveform with appropriately placed shocks. Although a physically meaningful waveform is realized, the shocks are actual discontinuities, that is, they have zero rise time.

When the loss term $l(t')p$ is retained, Eq. 1 must be solved numerically. It is common to use a marching scheme as the basis for the algorithm. As the code marches along, at each step it takes separate account of nonlinear distortion, absorption and dispersion, and any other effects. The marching steps must be small to justify calculating the effects separately. The separate calculations are made by breaking down the extended Burgers equation into its component effects. Equation 1 is replaced by four separate equations, which are to be solved at each step:

Nonlinear distortion:
$$\frac{\partial p}{\partial s} = \frac{\beta}{2\rho_0 c_0^3} \frac{\partial p^2}{\partial t'} \tag{7}$$

Absorption, either in the time domain:
$$\frac{\partial p}{\partial s} = l(t')p \tag{8a}$$

or in the frequency domain:
$$\frac{\partial P(f)}{\partial s} = L(f)P(f) \tag{8b}$$

Geometrical spreading:
$$\frac{\partial p}{\partial s} = -\frac{1}{2S}\frac{\partial S}{\partial s} p \tag{9}$$

Effect of stratification:

$$\frac{\partial p}{\partial s} = \frac{1}{2\rho_0 c_0}\frac{\partial(\rho_0 c_0)}{\partial s}p \tag{10}$$

In Eq. 8b $P(f)$ and $L(f)$ are the Fourier transforms of $p(t')$ and $l(t')$, respectively.

Given a pressure time waveform at distance s, the task is to individually solve Eqs. 7-10, one after the other, over a small distance step Δs, to obtain the waveform at $s + \Delta s$. The process is repeated for additional steps until the propagation is complete. The solution of Eq. 7 is the Earnshaw or the Poisson solution (see, e.g., Ref. 10, Chap. 11). The solution is implemented computationally by shifting the time coordinate of each point on the waveform as follows:

$$t'_{s+\Delta s} = t'_s - \frac{\beta p(t'_s)\Delta s}{\rho_0 c_0^3}, \tag{11}$$

where t'_s is the retarded time for the point at the beginning of the step and $t'_{s+\Delta s}$ is the retarded time at the end of the step. Thus each point on the waveform advances or retreats from its previous place in the waveform according to the value of the pressure (magnitude and sign) at the point. In general, the cumulative distortion produced by a succession of marching steps causes the waveform to steepen and eventually become multivalued. Multivaluedness may be avoided (1) by invoking weak shock theory, (2) by relying on absorption (and dispersion) to counter steepening so that a true shock never forms, or (3) by combining Methods (1) and (2). All three methods simply provide a way of getting dissipation, which opposes steepening and ultimately prevents multivaluedness, into the algorithm. If Method (2) alone is used, the step size must be small enough that the waveform is still single-valued when absorption and dispersion are applied. Methods (2) and (3) require that Eq. 8 be solved. The main difference in SHOCKN, THOR, and ZEPHYRUS is how they cope with Eq. 8 (absorption and dispersion); each uses a different technique. Finally, Eqs. 9 and 10 are accounted for by a simple scaling operation. The scaling ensures that, if absorption were absent, the acoustic power in a given ray tube, $p^2 S / (\rho_0 c_0)$ (the simplest form of the Blokhintzev invariant[11]), would stay constant.

II. DISCUSSION OF CODES

A. Introduction

Early sonic boom codes, such as those of Hayes *et al.*[7] and Thomas,[12] make use of weak shock theory. No account is taken of ordinary atmospheric absorption and dispersion. A ground waveform is

calculated by distorting the source waveform, as described above, and using Method (1) (weak shock theory alone) to remove any multivaluedness. The equal area rule[13] is used to place a shock at its proper place in the waveform. Since no other absorption calculation is made, no marching scheme is required, and the code runs quickly. The penalty paid is the lack of information about the shock structure, in particular, shock rise time, on which annoyance is dependent. To overcome this difficulty, users commonly append an empirical formula to the results in order to estimate rise time.[14] The weak shock theory predictions reported in this paper were obtained by a mainly analytical method.[2] Although an oversimplification, the method is referred to here as a code because it mimics the behavior of the Hayes and Thomas codes. In addition to stratification, the Hayes and Thomas codes include the effects of wind. Since the test reported here is for a quiet atmosphere, our weak shock theory code does not include wind.

SHOCKN, ZEPHYRUS, and THOR all include ordinary absorption and dispersion in the propagation model. This means that the fine structure of the waveform, in particular the profile and rise time of each shock, can be predicted.[15,16,17] The computational price paid to obtain this information is high. First, since all three codes use a marching scheme, small steps must be used to march the signal from the aircraft all the way to the ground (however, efficiency is improved by using adaptive step sizing). Second, a very high sampling rate is required to properly represent the shocks: the sampling rate should be less than a tenth of the shock rise time.[2] Unfortunately, because SHOCKN, ZEPHYRUS, and THOR all require a uniformly sampled waveform, the entire waveform must be sampled at a very high rate even though only a very small fraction of the waveform needs it.

The sampling rate and total number of samples required vary a great deal over the propagation path. A typical shock thickness for a sonic boom at the ground is of order 0.5 ms, and a duration of 250 ms or more. Because a 0.5 ms shock should be sampled with a period no greater than 50 μs, at least 5,000 points are required to describe the waveform. In the upper atmosphere, however, where the shocks are much stronger, shock thickness can be less than 1 μs. This means that sampling rates of the order 10 MHz are required, i.e., in excess of 2,000,000 samples are needed to represent the entire wave. Full calculation of the sonic boom waveform near the aircraft is therefore computationally prohibitive. Computational adjustments to deal with stronger shocks near the aircraft are described below.

Both SHOCKN and ZEPHYRUS have their roots in the work of Pestorius,[18] whose algorithm is a marching scheme developed to calculate the propagation of finite-amplitude noise in a tube. For this case (plane waves in a homogeneous medium) Eqs. 9 and 10 are superfluous; only nonlinear distortion and absorption and dispersion are accounted for. In the Pestorius code distortion, including weak shock theory, is calculated in the time domain, absorption and dispersion in the frequency domain. Transfers back and forth between the two domains is done by FFT and FFT^{-1} operations. Since these operations

are time consuming and also introduce error, they are in practice kept to a minimum by correcting for absorption and dispersion only after several distance steps, not at every step. In addition for non-periodic waveforms, e.g., sonic booms, the time waveform needs to be zero padded before the FFT operation to avoid aliasing effects. Guidelines were given for optimizing the number of steps between corrections. The absorption and dispersion was due to tube wall boundary layers (a special version of Eq. 8b). The reason weak shock theory had to be included is that boundary absorption is not strong enough by itself to prevent the formation of multivalued waveforms. The Pestorius code is thus an example of the use of Method (3) to ensure single-valuedness.

A variation on the Pestorius code was devised by Anderson,[19] who was concerned with propagation of short-duration spherical N waves in air. The air was modeled as a thermoviscous fluid. Anderson simplified Pestorius's code by dropping weak shock theory, that is, he used Method (2) to prevent multivaluedness. Thermoviscous absorption is sufficient to keep the waveform single-valued, provided the step size is small enough. Spherical spreading made Method (2) attractive, since as the wave loses amplitude, it can propagate progressively further without forming a shock. Anderson took advantage of this effect by using an adaptive step size. In order to be able to handle an initial wave that already contains shocks, such as an ideal N wave, Anderson reversed the order of the calculations in each step, i.e., his code subjects the wave to absorption first, then distortion. In the Anderson code, unlike the Pestorius code, absorption is applied at every distance step.

B. SHOCKN

SHOCKN is the extension of the Anderson code to include relaxation effects and the effects of atmospheric stratification.[20,21,22] Both effects are applied in the frequency domain. Spreading and impedance variation associated with stratification are dealt with by keeping the Blokhintzev invariant constant.

The version of SHOCKN used in the exercise reported here contains a special feature added by Raspet to deal with the high sampling rate problem associated with stronger shocks and longer duration waveforms in the HSCT program. For sufficiently strong shocks, the absorption calculation switches from ordinary atmospheric absorption and dispersion to an amplitude-dependent artificial attenuation that mimics the effects of weak shock theory.[23] The artificial viscosity is scaled so that 10 points are always used to describe the shock. Although this procedure preserves the overall waveform, it can give the shock an unrealistic profile. When the amplitude becomes small enough, the program reverts to standard atmospheric absorption, which has the effect of repairing or "healing" any unrealism in the shock profile.

C. ZEPHYRUS

ZEPHYRUS[24] uses an algorithm that reduces some of the computational problems associated with stronger shocks that occur in the early stages of propagation. The high sampling rate that would ordinarily be required for stronger shocks is avoided by using Method (3), in this case a mix of weak shock theory and ordinary atmospheric absorption and dispersion. Instead of calculating the profile of stronger sonic boom shocks exactly, ZEPHYRUS uses a low sampling rate and relies on weak shock theory to model the shocks. Shocks that cannot be profiled accurately by the sparse sample points are treated as discontinuities. Because ZEPHYRUS does not try to model stronger shocks exactly, it does not have to make the absorption-dispersion calculation at every step. Like the Pestorius code, it skips several steps before applying absorption. Both computational cost and numerical error are reduced because of the much lower number of FFT operations. While in the frequency domain, ZEPHYRUS applies all components of atmospheric attenuation and dispersion, including thermoviscous effects. Since weak shock theory indirectly accounts for dissipation, ZEPHYRUS is open to the criticism of double dipping in that absorption is applied twice. Because of the way weak shock theory works, however, it is probably only the thermoviscous component that is counted twice.

D. THOR

THOR[2] runs entirely in the time domain and therefore avoids time consuming excursions to the frequency domain. It also does not require zero padding of the time waveform. Otherwise, the marching scheme is similar to that of SHOCKN. Thermoviscous absorption and each relaxation process are treated independently. The algorithm that applies thermoviscous absorption in the time domain is the same one that was employed by Lee and Hamilton,[25,26] i.e., Eq. 8a, with the operator defined in Eq. 2, is solved using a standard Crank-Nicolson finite difference scheme.[27] Lee and Hamilton[26] also proposed a method for including the effects of multiple relaxation phenomena in the time domain, which was implemented recently by Cleveland *et al.* Each relaxation operator has the form

$$l_{\text{relax}}(t') = \frac{m}{2c_0}\left(2\pi f_r + \frac{\partial}{\partial t'}\right)^{-1}\frac{\partial^2}{\partial t'^2}, \tag{12}$$

which again is solved by means of a Crank-Nicolson finite difference approximation.

THOR too has a modification to cope with the very thin shocks that occur high up in the atmosphere. It uses a similar scheme to that developed by Raspet for SHOCKN. Whenever a shock is sampled by less than 10 points, THOR automatically spreads the shock over 10 points by artificially

increasing the thermoviscous absorption. Because THOR calculates absorption in the time domain it needs to increase absorption only at places in the waveform where the steep shocks occur. Absorption and dispersion for the rest of the waveform are calculated normally.

E. Step Size

All three codes select the step size adaptively. Step size is taken to be a given fraction of the local shock formation distance. Let $p_i(t')$ represent the time waveform of the pressure at the beginning of step i. The local shock formation distance is the propagation distance at which the steepest part of the waveform would, in the absence of dissipation, develop a vertical tangent. This distance is, in terms of the distortion distance $\tilde{x}$,

$$\tilde{x}_{\text{shock}} = \frac{\rho_0 c_0^3}{\beta} \frac{1}{(\partial p_i / \partial t)_{\max}}. \tag{13}$$

In practice, the plane wave shock formation distance x_{shock} is used as a more conservative measure, since unless the wave is growing, $x_{\text{shock}} < \tilde{x}_{\text{shock}}$. The maximum step size is thus taken to be

$$\Delta s_{\max} = \frac{\rho_0 c_0^3}{\beta} \frac{1}{(\partial p / \partial t)_{\max}}. \tag{14}$$

As long as the step is less than $\Delta s_{\max}$ the waveform will not become multivalued. For the results presented here, SHOCKN and THOR use a step size that is 20% of the local shock formation distance. When steep shocks are present very small steps are taken. When the shocks are more diffuse larger steps can be taken. ZEPHYRUS on the other hand has two step size parameters, the nonlinearity step and the absorption step. The nonlinear step is 10% of the local shock formation distance and weak shock theory is applied if necessary. Absorption is applied no more often than every two shock formation distances (20 nonlinearity steps). ZEPHYRUS actually monitors the amount of absorption along the propagation path and in cases of weak absorption transforms to the frequency domain even less often.

F. Code Summary

1) Weak shock theory runs in the time domain and includes losses only due to shock dissipation, not ordinary absorption and dispersion. Because the latter is neglected, the program runs quickly. However, since the shocks are modeled as true discontinuities, no information is provided about shock profile or rise time.

2) SHOCKN includes ordinary absorption and dispersion. It calculates nonlinear distortion in the time domain and all other effects in the frequency domain. The fast Fourier transform is used to transfer between the time and frequency domains. In the event of stronger shocks, the shocks are artificially thickened by replacing atmospheric attenuation with an exaggerated viscous attenuation that is amplitude dependent. When the shock strength becomes small enough, the calculation reverts to standard atmospheric attenuation.

3) ZEPHYRUS is similar to SHOCKN but combines weak shock theory, which is done in the time domain, with ordinary absorption and dispersion, which is done in the frequency domain. Transfers to the frequency domain occur approximately every 20 steps. In between absorption calculations weak shock theory is used to avoid multivaluedness.

4) THOR calculates all effects, including absorption and dispersion, in the time domain. In the event of stronger shocks, the sound diffusivity is artificially increased in the neighborhood of the shock. Standard absorption and dispersion are applied to the rest of the waveform.

III. NUMERICAL CALCULATIONS

Two idealized atmospheres were chosen for the numerical experiment. The first is a uniform atmosphere, which has no variation in pressure, density, or temperature with altitude. The second, an isothermal atmosphere, is more realistic and is commonly used for analytical calculations. Temperature is constant but because of gravity, density and pressure decay exponentially with altitude. We considered both atmospheres with and without the presence of molecular relaxation. For the relaxing atmosphere the absorption of sound was calculated by using the formulas given in the ISO standard.[5] These formulas are slightly different from the old ANSI[3] standard but the same as those in the new proposed ANSI standard.[6] It should be noted that in the absence of dispersion, the frozen sound speed c_∞ is used to propagate the booms. When dispersion is added, it acts to slow the low frequency components of the sonic boom.

Three test waveforms, referred to here by the names "flat top", "ramp", and "N wave", were provided by K. E. Needleman and B. Sullivan of NASA Langley. The three waveforms are not associated with any aircraft design that NASA is considering. Although they bear some resemblance to a waveform near an aircraft in supersonic flight, they are not representative of a real nearfield waveform. The flight altitude is specified to be 14,630 m (48,000 ft) and the Mach number 1.8. The test waveforms

are given at a distance of 183 m (600 ft) below the aircraft. In the two atmospheres considered the small-signal sound speed is not a function of altitude. Acoustic rays therefore travel in straight lines, and the geometrical spreading is simply cylindrical. Figure 1 shows the flat top and ramp test waveforms. The insert gives the spectrum of the flat top signal. These two waveforms were used to obtain the results presented in this paper. Because results using the N wave[2] are quite similar, they are not reported here. All predicted ground waveforms are aligned using the zero crossing in the middle of each waveform as a reference point. This zero crossing is the most stable, readily identified point in the waveform.

A. Uniform Atmosphere without Relaxation

The uniform, nonrelaxing atmosphere has the following properties: ambient temperature T_0=273.15 K, ambient pressure P_0=101.3 kPa, universal gas constant R=287 J/(kg K), ratio of specific heats γ=1.4, and coefficient of nonlinearity $\beta = (\gamma + 1)/2 = 1.2$. This first test was undertaken to ensure that nonlinearity is properly handled. The thermoviscous attenuation is arbitrarily chosen to be $\alpha_{tv}=2\times10^{-9}$ f^2 Np/m (0.174 dB/km at 100 Hz), or approximately 100 times larger than the value given in the standards. If the nominal value for thermoviscous absorption ($\alpha_{tv}=1.78\times10^{-11}$ f^2 Np/m) had been used, accurate representation of the shocks would have required a prohibitively high sampling rate. The chosen value is small enough that weak shock theory should still be a good propagation model.[10]

Figure 2 compares the predicted ground waveforms of weak shock theory, SHOCKN, and THOR for the uniform atmosphere. Both SHOCKN and THOR used a sampling rate of 27.6 kHz, SHOCKN used a time window 16,384 samples long, and THOR a time window 9,500 samples long (THOR requires minimal zero padding). ZEPHYRUS was not run for this case because it was not easy to modify to handle a purely thermoviscous atmosphere. Agreement between SHOCKN and THOR is excellent. By neglecting the rounding due to absorption weak shock theory slightly overestimates the shock amplitudes. This in turn, by virtue of the corresponding inaccuracy in shock speed, leads to a slight discrepancy in the location of the shocks. Both SHOCKN and THOR give rise time (defined as the time it takes the pressure to increase from 10% to 90% of the peak shock amplitude) for the head shock of 0.87 ms for the flat top and 1.22 ms for the ramp waveform. Notice the effect of nonlinear propagation distortion in steepening the shocks and stretching the waveform between the head and tail shocks.

B. Uniform Atmosphere with Relaxation

We now add relaxation due to oxygen and nitrogen to the previous atmosphere and reduce thermoviscous absorption to its nominal value. Since low humidity provides strong absorption and dispersion, we chose a relative humidity of 20%. The other properties are the same as those for the first

atmosphere. The absorption is calculated according to the ISO standard[5] (see also the new ANSI standard[6]). The absorption and dispersion depend on temperature, pressure, and relative humidity. For the conditions of this atmosphere the nitrogen relaxation frequency is 41.0 Hz and the oxygen relaxation frequency is 1.362 kHz. For reference, the sound absorption at 100 Hz is 0.449 dB/km, about 2.5 times that for the first atmosphere

The predicted ground waveforms of SHOCKN, THOR, weak shock theory, and ZEPHYRUS for the uniform relaxing atmosphere are shown in Fig. 3. SHOCKN, THOR, and ZEPHYRUS used a sampling rate of 27.6 kHz. SHOCKN and ZEPHYRUS used a time window 16,384 samples long, THOR a window 9,500 samples long. Agreement between the four codes is outstanding. Even weak shock theory gives a good account of the overall waveform. Its failure to predict the rounding of corners, particularly very sharp corners, is more serious than in the previous case and leads to noticeable errors in shock amplitudes.

The rise time of the front shock is 1.56 ms for the flat top, 2.20 ms for the ramp. Notice that these figures are about 80% higher than those for the previous atmosphere. The results provide an example of the dominance of molecular relaxation in determining shock rise time in a quiet atmosphere. Figure 4 shows a close up of the front and rear shocks for the ramp waveform. The shock profiles calculated by SHOCKN, THOR, and ZEPHYRUS are almost identical. Notice the asymmetry of the profiles (for example, rounding is more pronounced at the top of the shock than at the bottom), which is due to the dispersion introduced by the relaxation processes. It is also interesting to note that while weak shock theory obviously cannot model the shock profile, it does locate the shocks pretty well.

C. Isothermal Atmosphere with Relaxation

The isothermal atmosphere has the same ambient temperature as the uniform atmosphere, T_0=273.15 K. The ambient pressure at the ground is 101.3 kPa and decreases exponentially with altitude as $P_0(z) = P_0(0)e^{-z/H}$, where z is altitude above the ground, $H=g/RT_0$ is the scale height of the atmosphere, and g is the acceleration due to gravity, 9.81 m/s^2. The scale height of the isothermal atmosphere is H=7991 m.

The initial waveforms for the isothermal atmosphere have the same pressure amplitude as in the previous cases. Since the ambient pressure at flight altitude is much lower for the isothermal atmosphere, the effective strength of the shocks is much higher. The shock rise times are therefore much smaller, of order 1 μs near the aircraft. In this case it was necessary for SHOCKN and THOR to be run with the artificial attenuation previously mentioned. For SHOCKN the artificial attenuation was switched off after

2 km for the ramp waveform, after 5 km for the flat top. THOR used artificial attenuation for approximately the first 1.6 km of propagation. ZEPHYRUS automatically includes weak shock theory in the event of stronger shocks. The same sampling rate, 27.6 kHz, was used. SHOCKN and ZEPHYRUS used a time window of 16,384 samples, and THOR used a time window of 9,500 samples.

Figure 5 shows the predicted ground waveforms for the isothermal atmosphere. Once again agreement between the predictions of the three main codes is good. The overprediction of shock amplitude by weak shock theory is again apparent. The rise times are 0.99 ms for the flat top and 1.17 ms for the ramp. The small distortion of the waveform predicted by SHOCKN is probably due to errors associated with FFT use. Since the shocks are stronger, the step sizes are smaller and more FFT routines are required.

Although a test was run for the isothermal atmosphere without relaxation,[2] the results yield no new insights about the codes and therefore are not presented

IV. PRELIMINARY SR71 RESULTS

Figure 6 shows the waveforms from an SR71 flight both near the aircraft (31,000 ft above sea level) as well as at the ground (2,000 ft above sea level). These shocks are quite a bit stronger than those presented earlier. One can see the overall decrease in amplitude of the boom at the ground as well as the elongation caused by the wave steepening effects. Figure 7 shows the actual waveform at the ground as well as the waveform predicted by SHOCKN. There is good agreement in the overall shapes and amplitudes of the two waveforms. However, SHOCKN underpredicts the overall duration of the waveform. It is quite possible that this effect can be corrected for by including wind effects which have been neglected in the preliminary analysis. For the measured wind speeds, the elongation could change by approximately 5%. Furthermore, SHOCKN under predicts the rise time of the boom as seen in Figure 8 which is a close up of the front shock. The rise time of the actual boom is approximately 2 ms while that predicted by SHOCKN is only approximately 0.1 ms. It should be pointed out, however, that the effects of turbulence have not been included in the model yet. It has been shown that including turbulence effects yields rise times of approximately to 2 ms for T38 flybys[28]. Incorporating wind and turbulence effects will be the next major phase of the research.

V. DISCUSSION AND CONCLUSIONS

The results in this paper show excellent agreement between weak shock theory, SHOCKN, THOR, and ZEPHYRUS. It has been demonstrated that weak shock theory, by neglecting absorption, overestimates the amplitude of shocks at the ground. The overestimation was greatest in the atmospheres which included relaxation. One expects that predictions based on weak shock theory will overestimate loudness. Of the codes that include full atmospheric absorption, agreement on shock profiles was excellent. Initial calculations using SHOCKN indicate good agreement between the prediction routines and actual field data. It is assumed that THOR and ZEPHYRUS will work equally well based on the preceding agreement between the codes. Current predictions have underestimated the duration and rise time of an actual sonic boom. It is expected that including the effcets of wind and turbulence will account for the current discrepancies.

ACKNOWLEDGMENTS

The authors acknowledge financial support from NASA. In addition, the authors would like to individually thank the following personnel who work for and with NASA: Jack Ehrenberger, Christine Darden, Ed Haering, Dominic Maglieri, Kathy Needleman ,Kevin Shepherd, and Brenda Sullivan. We also thank Leick Robinson for providing us with a copy of ZEPHYRUS. Computer resources at The University of Texas at Austin were provided by the Department of Mechanical Engineering. Cleveland also acknowledges support of the Applied Research Laboratories IR&D program.

REFERENCES

[1] McCurdy, D. A.: High-Speed Research: 1994 Sonic Boom Workshop. NASA CP 3279 (1994).

[2] Cleveland, R. O.: Propagation of Sonic Booms Through a Real, Stratified Atmosphere. Ph.D. dissertation, Department of Mechanical Engineering, University of Texas at Austin (1995).

[3] ANSI S1.26-1978: American National Standards Method for the Calculation of the Absorption of Sound by the Atmosphere. American National Standards Institute, New York, 1978.

[4] Blackstock, D. T.: Generalized Burgers Equation For Plane Waves, *J. Acoust. Soc. Am.* vol. 53, pp. 2050-2053 (1985).

[5] ISO9613-1: Acoustics - Attenuation of Sound During Propagation Outdoors - Part 1: Calculation of The Absorption of Sound by the Atmosphere. International Organization for Standardization, Geneva, Switzerland, 1993.

[6] Bass, H. E.; Sutherland, L. C.; Zuckerwar, A. J.; Blackstock, D. T.; and Hester, D. M.: Atmospheric Absorption of Sound: Further Developments. *J. Acoust. Soc. Am.* vol. 97, pp. 680-683 (1995).

[7] Hayes, W. D.; Haefeli, R. C.; and Kulsrud, H. E.: Sonic Boom Propagation in a Stratified Atmosphere, with Computer Program. Aeronautical Research Associates of Princeton, Inc., NASA-CR1299, April 1969.

[8] Blackstock, D. T.: Nonlinear Acoustics (Theoretical). *American Institute of Physics Handbook*, Chap. 3n, pp. 3-183 to 3-205, Gray, D. E. ed. McGraw-Hill, New York, 1972.

[9] Blackstock, D. T.: Connection Between the Fay and Fubini Solutions for Plane Sound Waves of Finite Amplitude. *J. Acoust. Soc. Am.* vol. 39, pp. 1019--1026 (1966).

[10] Pierce, A. D.: *Acoustics: An Introduction to Its Physical Principles and Applications* . McGraw-Hill, New York, 1981.

[11] Blokhintzev, D.: The Propagation of Sound in an Inhomogeneous and Moving Medium Parts I and II. *J. Acoust Soc. Am.* vol. 18, pp. 322-334 (1946).

[12] Thomas, C. L.: Extrapolation of Sonic Boom Pressure Signatures by the Waveform Parameter Method. NASA TN D-6832, June 1972.

[13] Landau, L. D.; and Lifshitz, E. M.: *Fluid Mechanics* . Art. 95. Addison-Wesley, Reading, MA, 1959

[14] Plotkin, K. J.: Review of Sonic Boom Theory. AIAA Paper 89-1105, 1989.

[15] Pierce, A. D.; and Kang, J.: Molecular Relaxation Effects on Sonic Boom Waveforms. *Frontiers of Nonlinear Acoustics: Proceedings of the 12th ISNA*, Hamilton, M. F. ; and Blackstock, D. T. eds., pp. 165-170. Elsevier Applied Science, London, 1990.

[16] Raspet, R.; Bass, H.; Yao, L.; and Wu, W.: Steady State Risetimes of Shock Waves in the Atmosphere. NASA CP 3172: High-Speed Research: Sonic Boom, NASA Langley Research Center, Hampton, Virginia. Darden, C. M. ed., Vol. I, pp. 109--116 (1992).

[17] Cleveland, R. O.; Hamilton, M. F.; and Blackstock, D. T.: Effect of Stratification and Geometrical Spreading on Sonic Boom Rise Time. NASA CP 3279: High Speed Research: 1994 Sonic Boom Workshop, NASA Langley Research Center, Hampton, Virginia. McCurdy, D. A. ed., pp. 19-38 (1994).

[18] Pestorius, F. M.: Propagation of Plane Acoustic Noise of Finite Amplitude. Technical Report ARL-TR-73-23, Applied Research Laboratories, The University of Texas at Austin (August 1973) (AD 778 868).

[19] Anderson, M. O.: The Propagation of a Spherical N Wave in an Absorbing Medium and its Diffraction by a Circular Aperture. Tech. Rep. ARL-TR-74-25, Applied Research Laboratories, The University of Texas at Austin (August 1974) (AD 787878).

[20] Bass, H. E.; and Raspet, R.: Vibrational Relaxation Effects on the Atmospheric Attenuation and Rise Times of Explosion Waves. *J. Acoust. Soc. Am.* vol. 64, pp. 1208--1210 (1978).

[21] Bass, H. E.; Ezell, J.; and Raspet, R.: Effect of Vibrational Relaxation on Rise Times of Shock Waves in the Atmosphere. *J. Acoust. Soc. Am.* vol. 74, pp. 1514--1517 (1983).

[22] Bass, H. E.; Layton, B. A.; Bolen L. N.; and Raspet, R.: Propagation of Medium Strength Shock Waves Through the Atmosphere. *J. Acoust. Soc. Am.* vol. 82, pp. 306--310 (1987).

[23] Von Neumann, J.; and Richtmyer, R. D.: A Method for the Numerical Calculation of Hydrodynamic Shocks. *John Von Neumann Collected Works,* Vol. IV pp. 380-385. Pergammon Press, New York, 1963.

[24] Robinson, L. D.: Sonic Boom Propagation Through an Inhomogeneous Windy Atmosphere. Ph.D. Dissertation, Department of Physics, The University of Texas at Austin (1991).

[25] Lee, Y.-S.; and Hamilton, M. F.: Nonlinear effects in pulsed sound Beams. *Ultrasonics International 91 Conference Proceedings*, Gray, D. E. ed. (Butterworth-Heinemann, Oxford, 1991), pp. 177-180.

[26] Lee, Y.-S.; and Hamilton, M. F.: Time-Domain Modeling of Pulsed Finite-Amplitude Sound Beams. *J. Acoust. Soc. Am.* vol. 97, pp. 906--917 (1995).

[27] Ames, W. F.: *Numerical Methods for Partial Differential Equations* Second Edition. Academic Press, New York, 1977.

[28] Wilshire, W. L. Jr.; Garber, D.P.; and deVilbiss, D.W.: The effect of Turbulence on the propagation of Sonic Booms. Proceedings of the Fifth International Symposium on Long Range Sound Propagation, The Open University, Milton Keynes, England, May 1992.

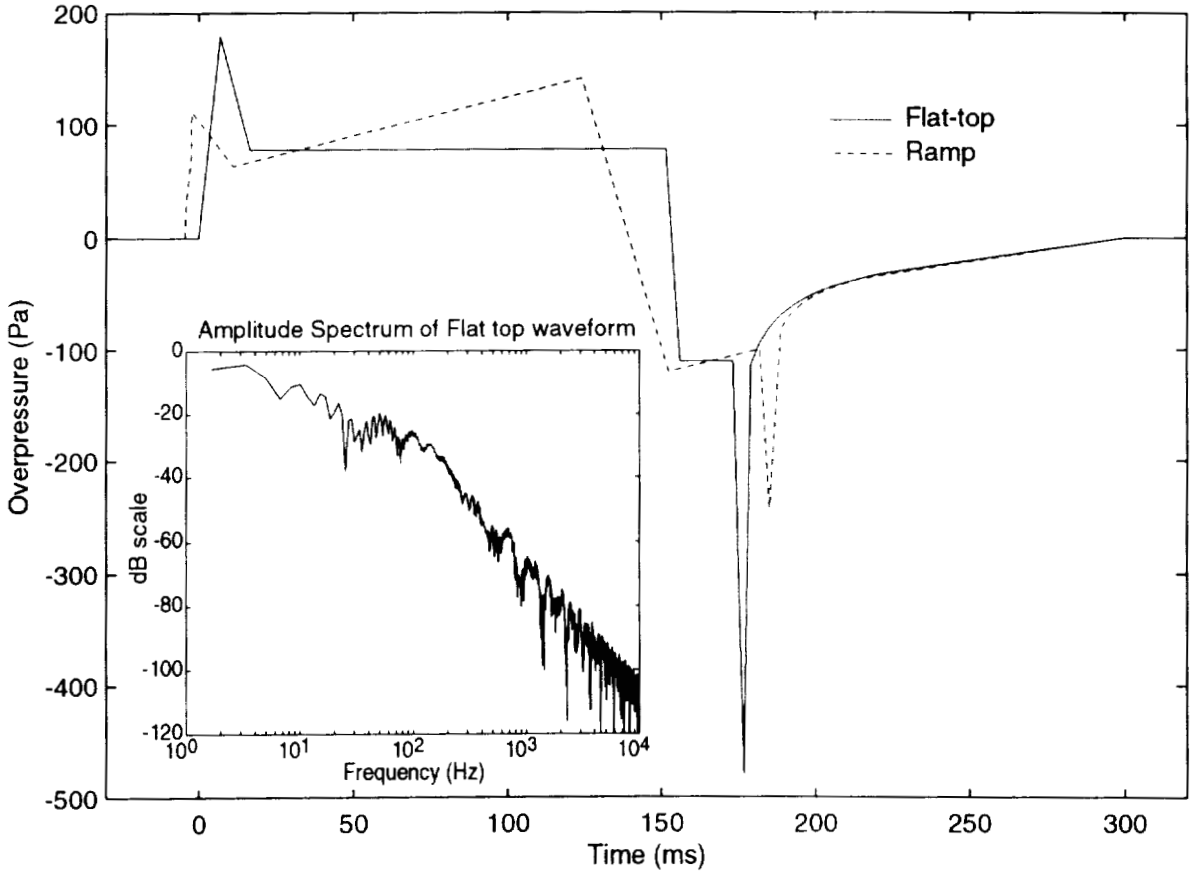

Fig 1. The two initial source waveforms, the flat top and ramp, used in this article. The insert gives the spectrum of the flat top waveform. The waveforms were provided by NASA.

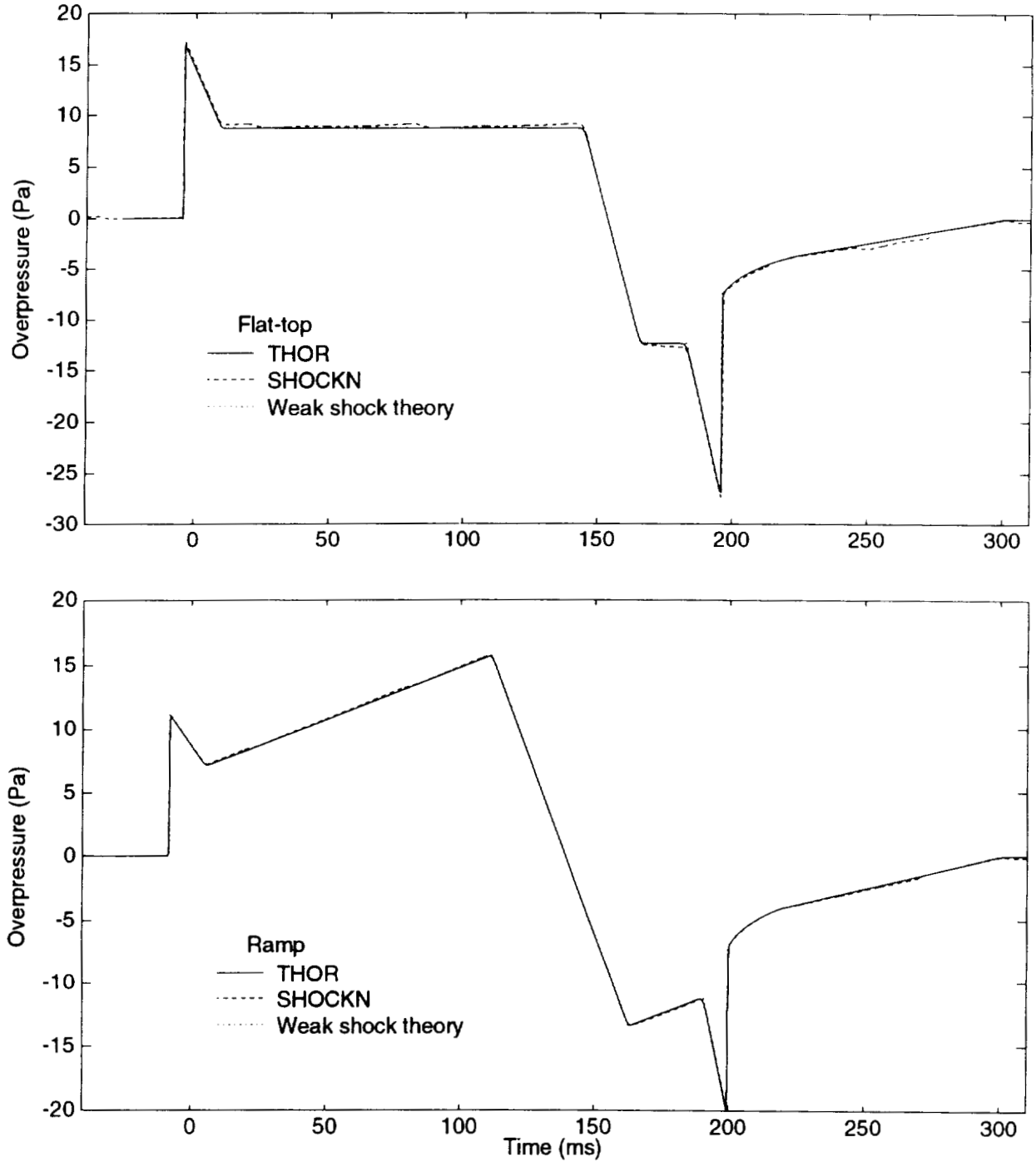

Fig 2. Predicted ground waveforms in the uniform atmosphere with thermoviscous absorption only. We compare SHOCKN, THOR, weak shock theory, for the flat top (upper) and the ramp (lower).

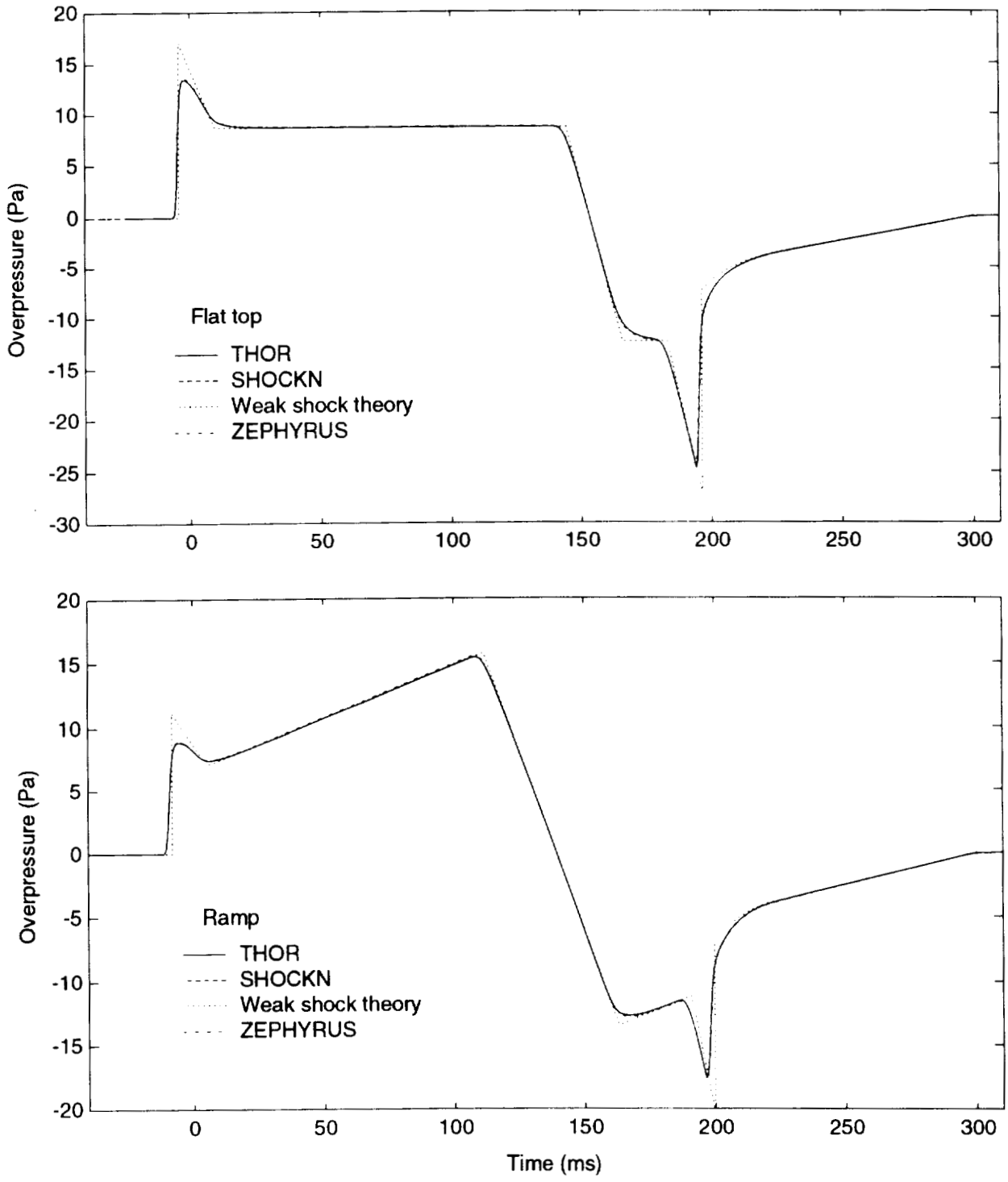

Fig 3. Predicted ground waveforms in the uniform atmosphere with full atmospheric absorption and dispersion (relative humidity 20%). We compare SHOCKN, THOR, weak shock theory, and ZEPHYRUS, for the flat top (upper) and the ramp (lower).

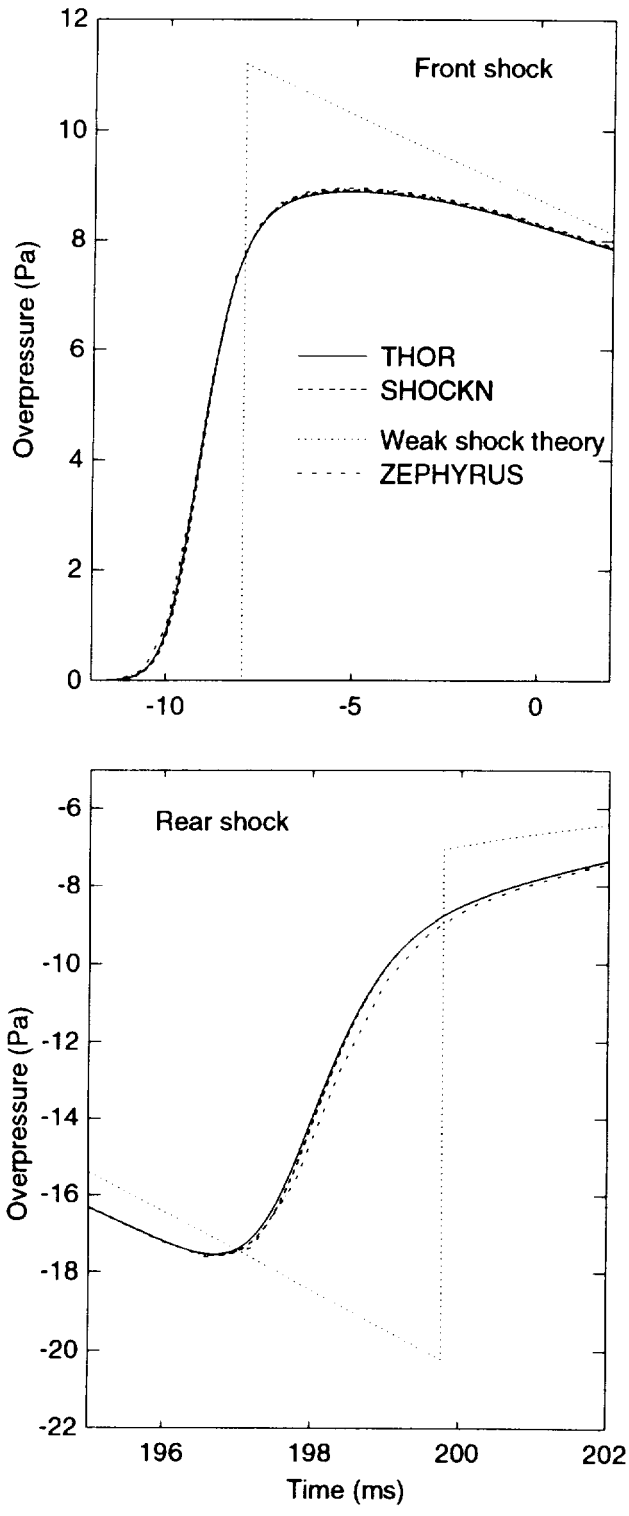

Fig 4. Close up of the front and rear shocks predicted at the ground for the ramp waveform in the uniform atmosphere with full absorption.

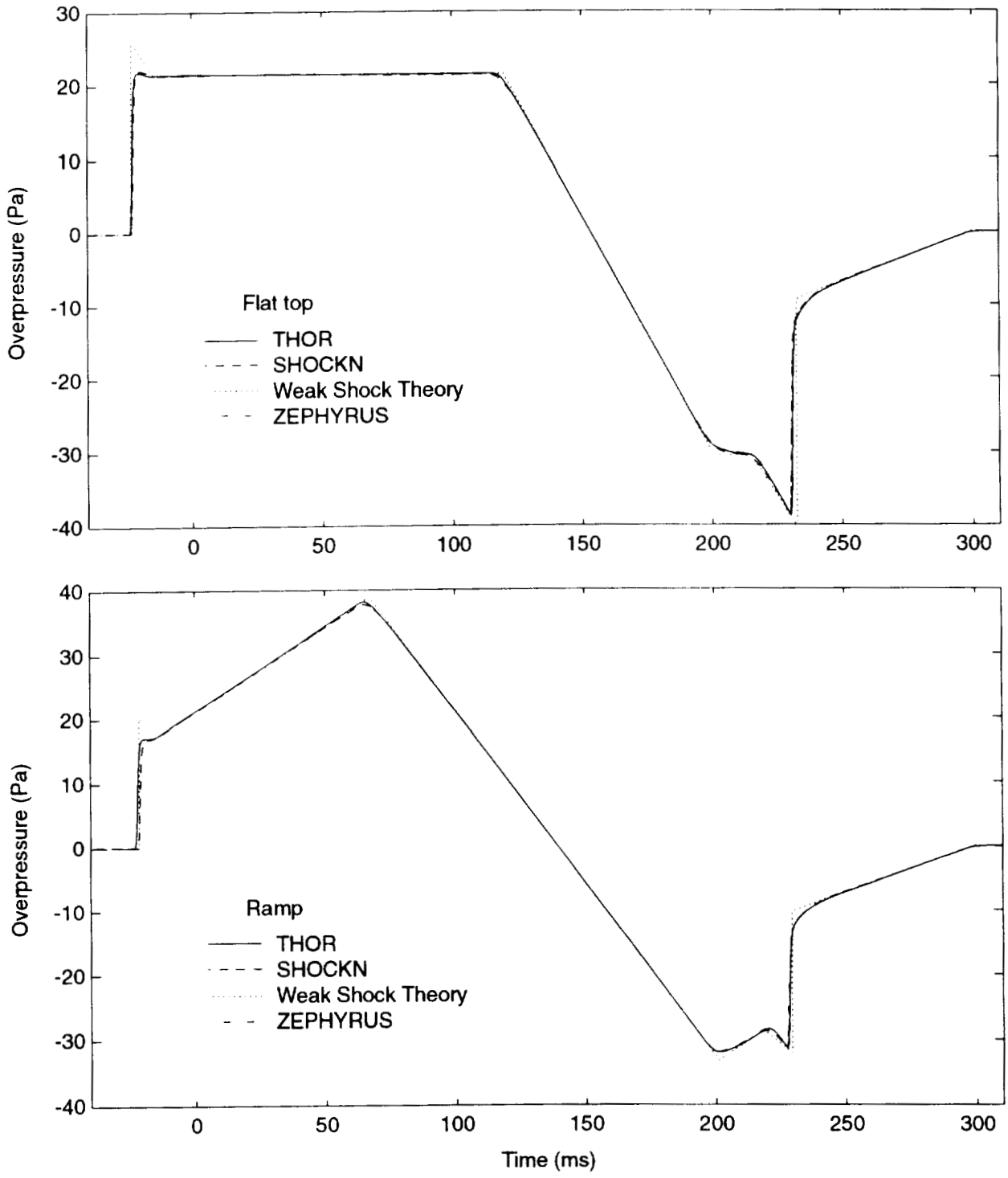

Fig 5. Predicted ground waveforms in the isothermal atmosphere with full atmospheric absorption and dispersion (relative humidity 20%). We compare SHOCKN, THOR, weak shock theory, and ZEPHYRUS, for the flat top (upper) and the ramp (lower).

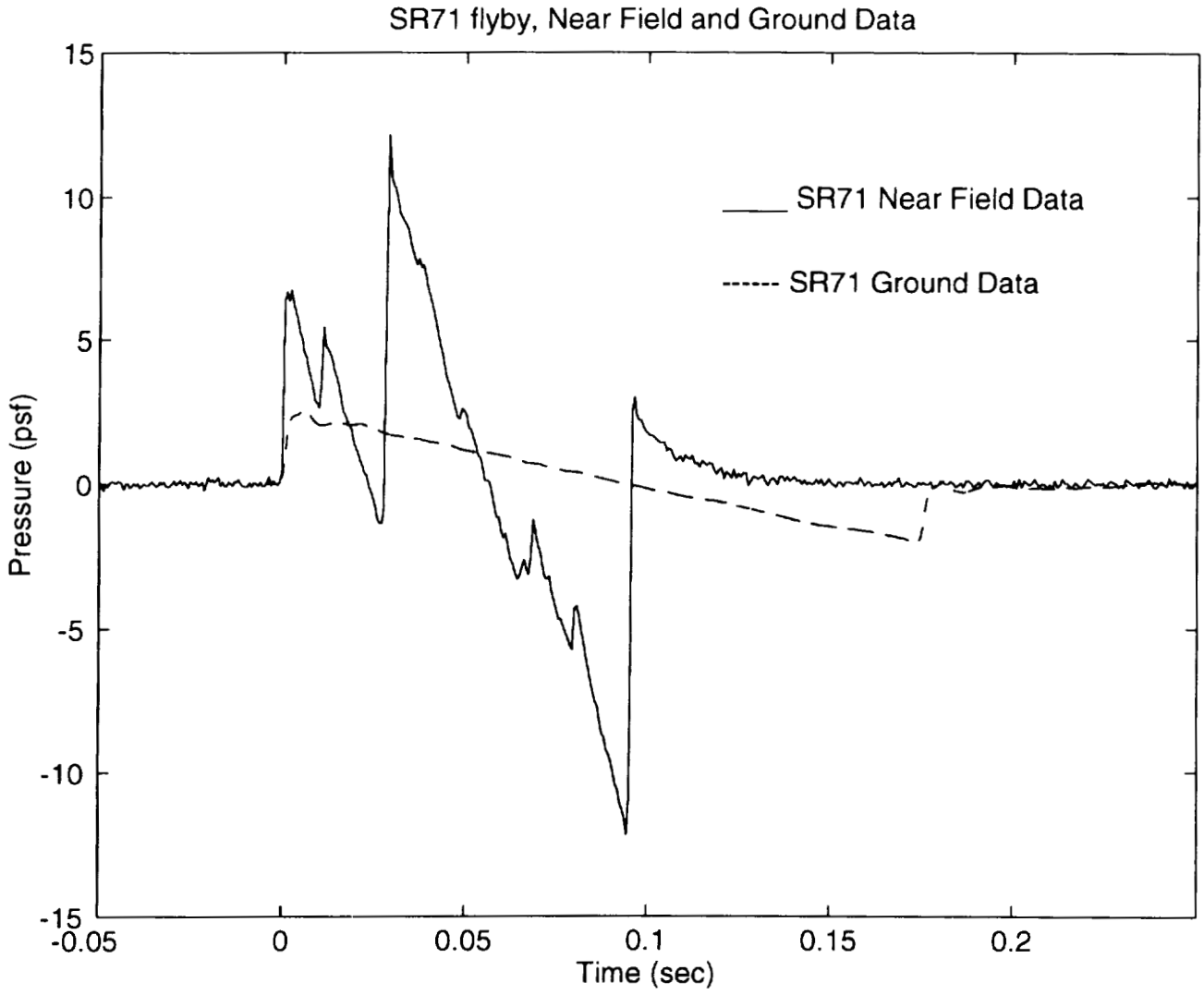

Fig 6. The initial source waveform and the captured signal at the ground for the SR71 flyby The waveforms were provided by NASA.

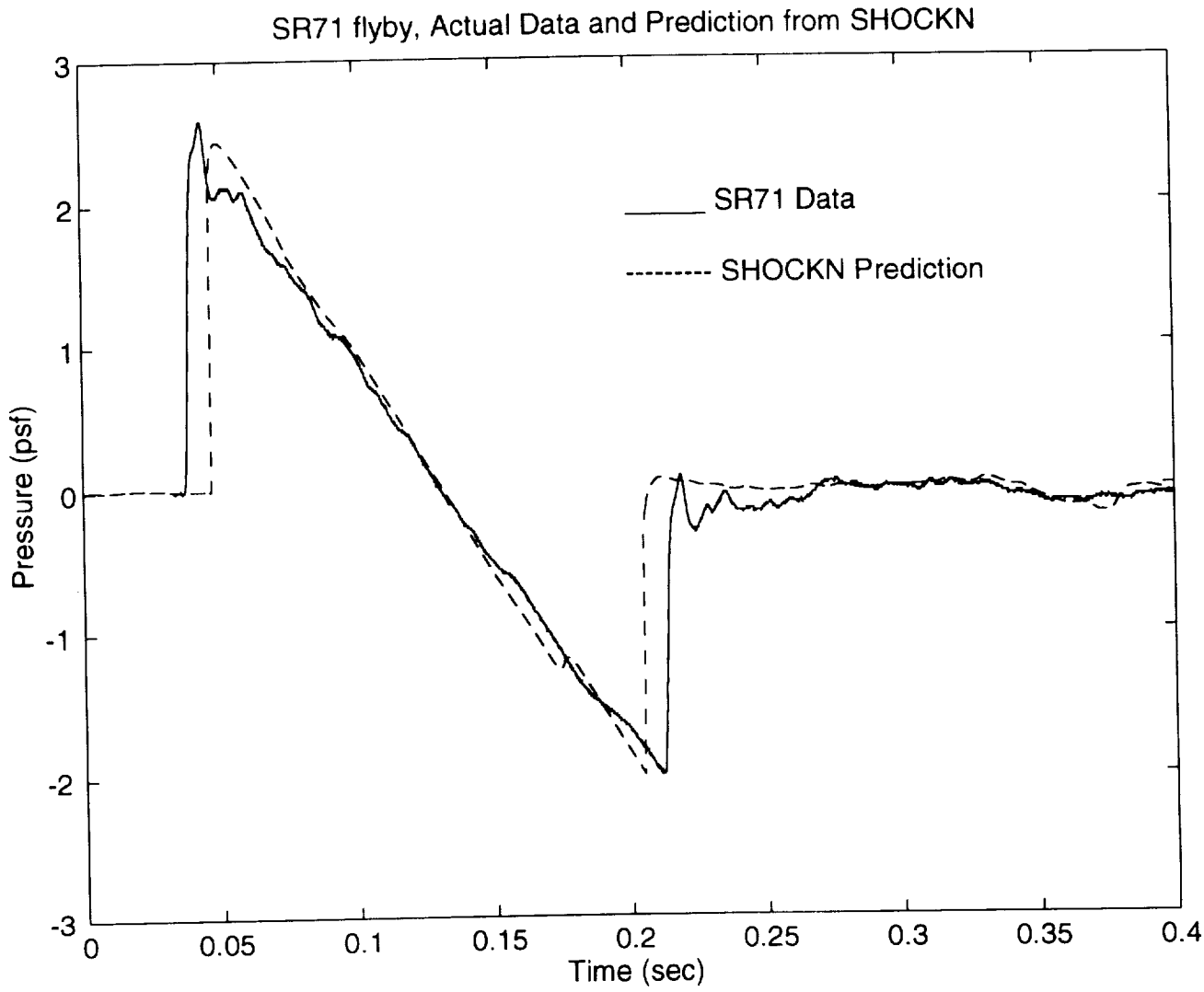

Fig 7. Actual and predicted waveforms at the ground. The predictions were done with the SHOCKN program.

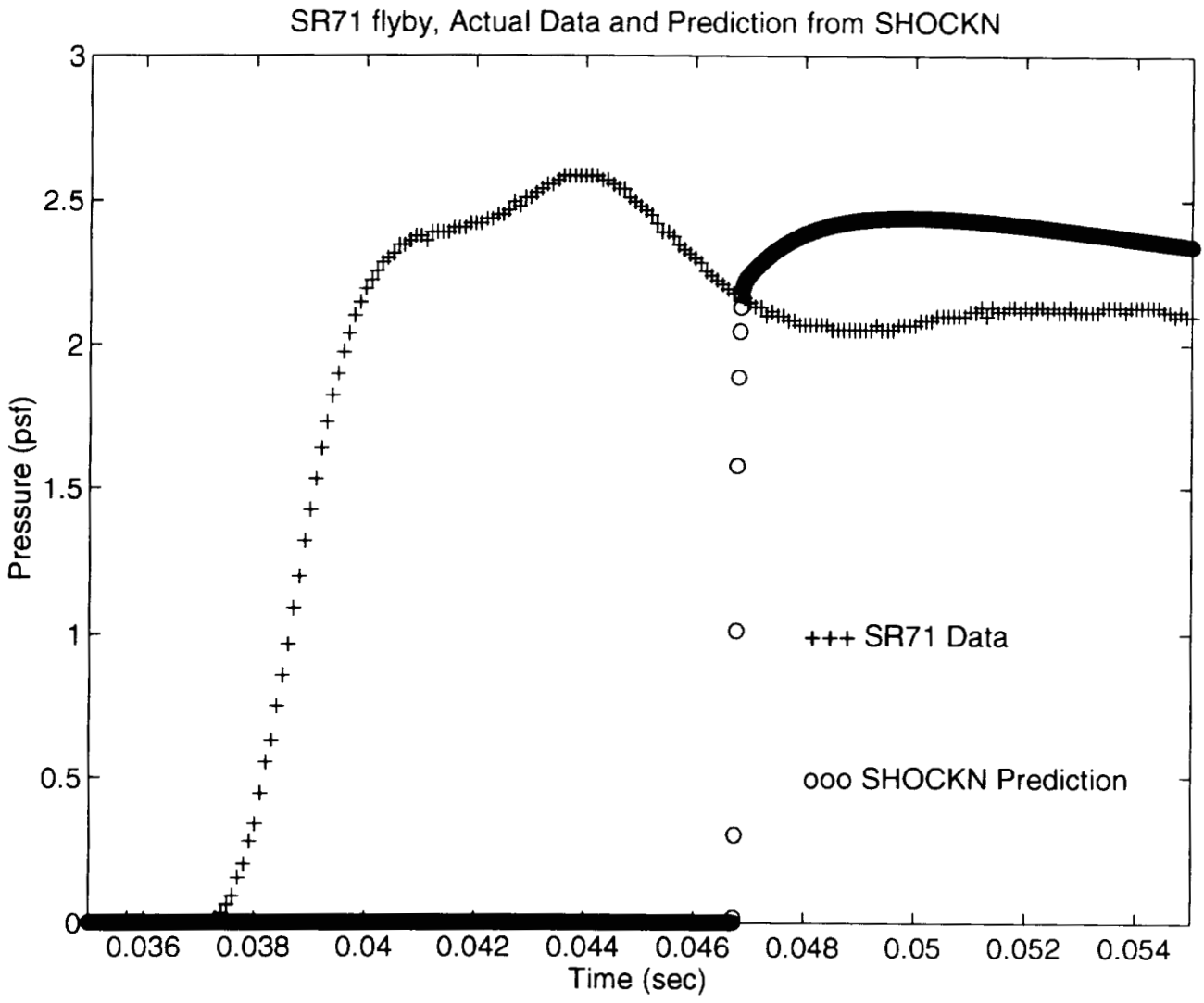

Fig 8. Close up of the front shock for the SR71 flyby and prediction.

SR-71
85886

PRELIMINARY AIRBORNE MEASUREMENTS FOR THE SR-71 SONIC BOOM PROPAGATION EXPERIMENT

23 p.

Edward A. Haering, Jr., L. J. Ehernberger, Stephen A. Whitmore A-36751
NASA Dryden Flight Research Center
Edwards, California

ABSTRACT

SR-71 sonic boom signatures were measured to validate sonic boom propagation prediction codes. An SR-71 aircraft generated sonic booms from Mach 1.25 to Mach 1.6, at altitudes of 31,000 to 48,000 ft, and at various gross weights. An F-16XL aircraft measured the SR-71 near-field shock waves from close to the aircraft to more than 8,000 ft below, gathering 105 signatures. A YO-3A aircraft measured the SR-71 sonic booms from 21,000 to 38,000 ft below, recording 17 passes. The sonic booms at ground level and atmospheric data were recorded for each flight. Data analysis is underway. Preliminary results show that shock wave patterns and coalescence vary with SR-71 gross weight, Mach number, and altitude. For example, noncoalesced shock wave signatures were measured by the YO-3A at 21,000 ft below the SR-71 aircraft while at a low gross weight, Mach 1.25, and 31,000-ft altitude. This paper describes the design and execution of the flight research experiment. Instrumentation and flight maneuvers of the SR-71, F-16XL, and YO-3A aircraft and sample sonic boom signatures are included.

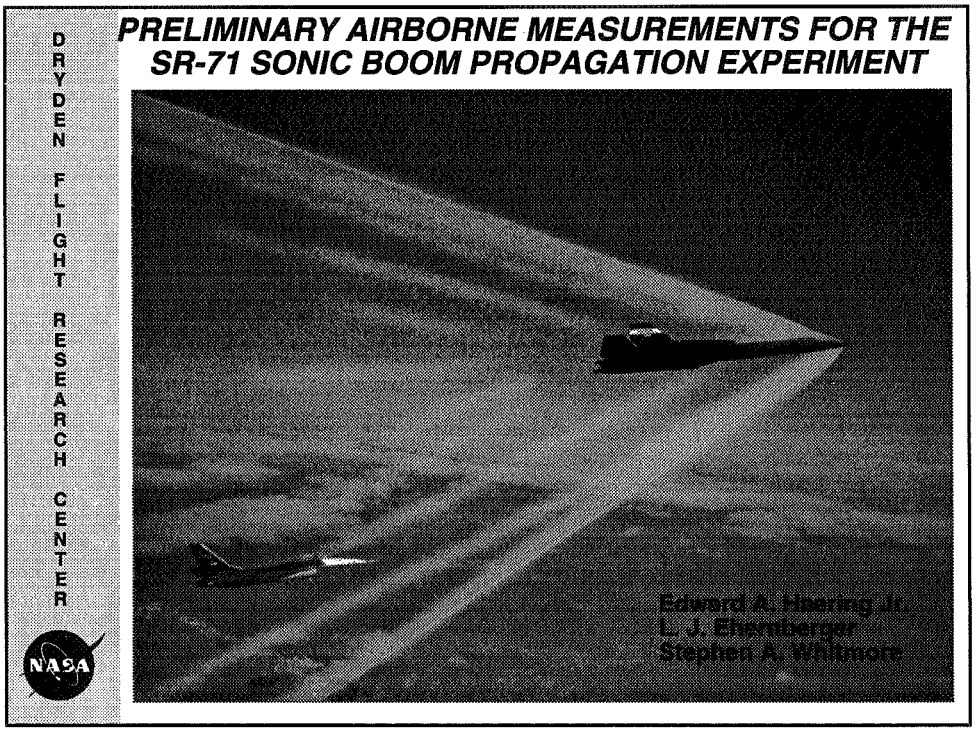

Figure 1

Propagation of sonic booms through the atmosphere has been studied for decades. Many of these studies involved measuring of the sonic booms at ground level; however, limited flight data has been gathered in the region where the shock waves begin to coalesce and before they attain the N-wave shape (Mullens, 1956, Smith, 1960, and Maglieri, 1963). The Sonic Boom Integrated Technology Development Team of the High Speed Research Program required a detailed database of sonic boom propagation flight data, concentrating on the non-N-wave region, to validate and refine sonic boom propagation prediction codes. These sonic boom propagation prediction codes would then be used to design and assess the environmental impact of the High Speed Civil Transport. Figure 2 lists objectives of the SR-71 Sonic Boom Propagation Experiment. The SR-71 was manufactured by Lockheed Aircraft, Burbank, California. The development of this flight test technique was used in the planning for the Tu-144LL (Tupolev Design Bureau, Moscow, Russia) Sonic Boom Signature Experiment.

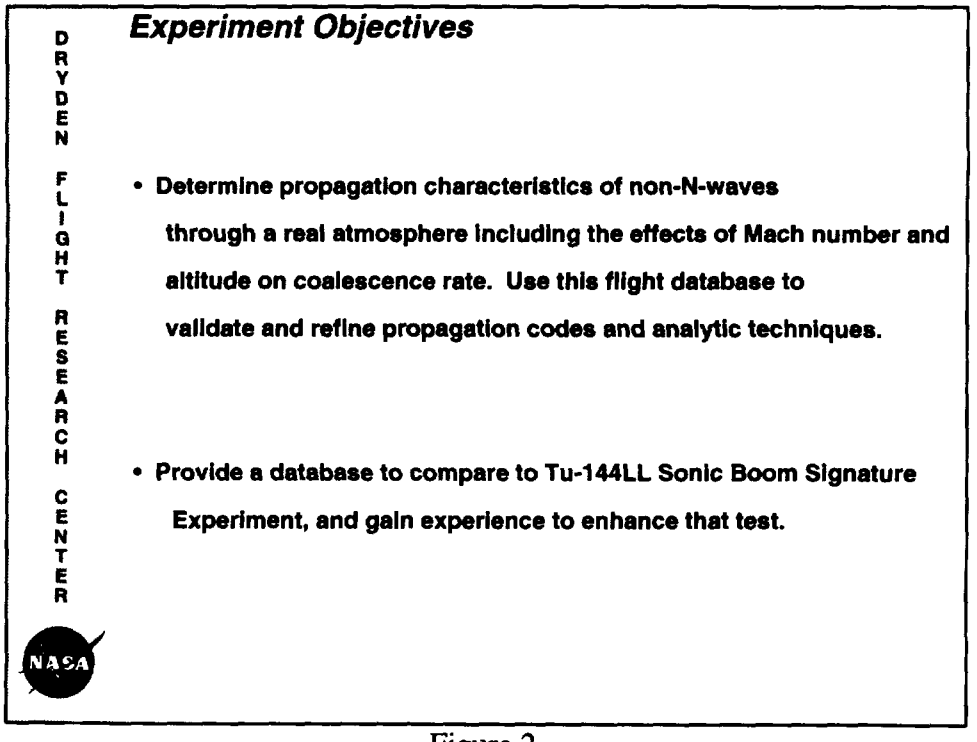

Figure 2

The near field of a supersonic aircraft can be very complex because of the three-dimensional nature of the flow around the vehicle. Sonic boom signatures measured beneath and to the sides of the aircraft show the shocks and expansions generated by the various components and varying lift distribution of the aircraft. It would be convenient if these near-field pressure signatures could be extrapolated through the atmosphere all the way to the ground and provide predictions of sonic boom noise levels. Because current extrapolation methods are based on two-dimensional, cylindrical propagation models, they are best applied beginning at a minimum separation distance where the complex, three-dimensional flow disturbances around the aircraft have become cylindrical or quasi-cylindrical waves. At present, no generally agreed upon method for defining this minimum separation distance exists. Preliminary analysis suggests that distances of 7 to 10 span lengths or 5 body lengths may be sufficient. The SR-71 aircraft is 104 ft long, not including the noseboom, and has a wingspan of 56 ft; therefore, this paper reports signatures measured at distances greater than 520 ft, which is 5 body lengths or nearly 10 span lengths.

This paper presents the design and execution of the SR-71 Sonic Boom Propagation Experiment conducted at the National Aeronautics and Space Administration, Dryden Flight Research Center, Edwards, California. Flight maneuvers and instrumentation of the SR-71, F-16XL (General Dynamics, Ft. Worth, Texas), and YO-3A (Lockheed Corporation, Burbank, California) aircraft are included. Several auxilliary ground and flight tests are also discussed to validate the quality of the airborne instrumentation used. A sampling of the airborne data recorded from 540 to 21,000 ft below the SR-71 aircraft is presented. Descriptions of the ground-level sensors and measurements have been reported (Norris, 1995).

Use of tradenames or names of manufacturers in the document does not constitute an official endorsement of such products or manufacturers, either express or implied, by the National Aeronautics and Space Administration.

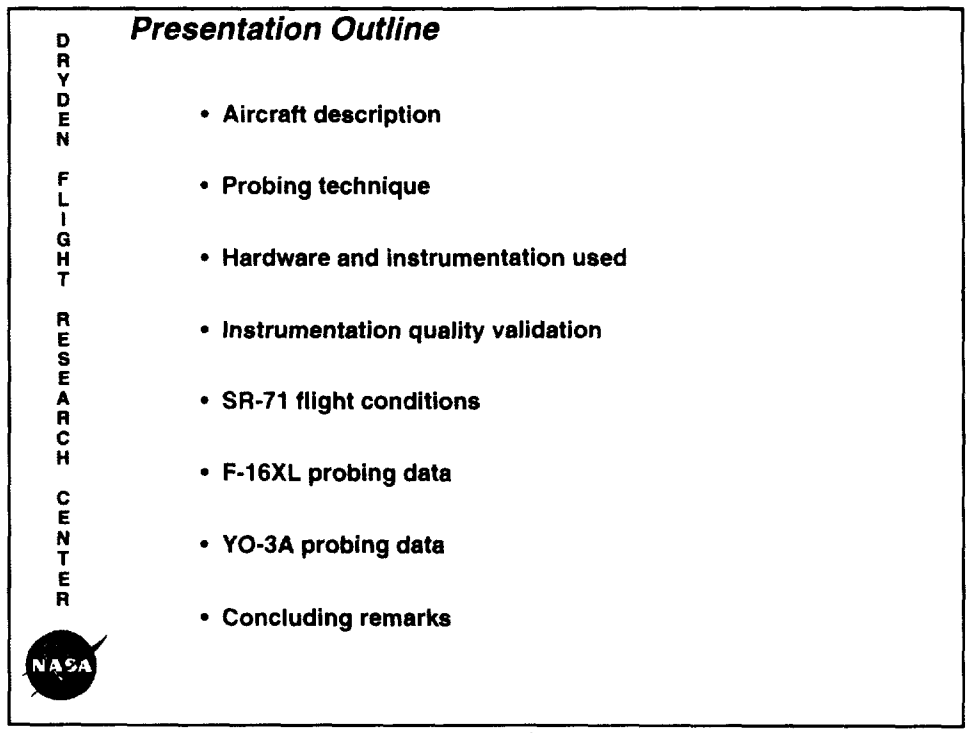

Figure 3

Figure 4 shows the three research aircraft used for this experiment: an SR-71, an F-16XL, and a YO-3A. A large sonic boom generating aircraft is desirable because it better approximates a High Speed Civil Transport, and it allows a more detailed spatial resolution of its shock waves. The SR-71 aircraft was selected as the sonic-boom-generating aircraft because of its large size and supersonic endurance. The SR-71 aircraft was flown from Mach 1.25 to Mach 1.6, altitudes from 31,000 to 48,000 ft, and gross weights from 73,000 to 118,000 lbf in steady, level flight.

Using a probing aircraft that could match the speed of the SR-71 aircraft was important for two reasons. First, having a small difference in speed maximizes the data collected during each probing and increases spatial resolution of the shock waves. Second, an increased number of probings can be taken if the probing aircraft has the ability to maintain a close proximity to the SR-71 aircraft. The F-16XL aircraft was used as the near-field probing aircraft because of its ability to keep in formation with the SR-71 up to Mach 1.5. In addition, the cranked delta wing design allowed for greater supersonic endurance than the majority of supersonic fighter type aircraft. The SR-71 aircraft has greater supersonic endurance than the F-16XL aircraft, so aerial refueling of the F-16XL aircraft was performed to maximize data collection on a single flight. The F-16XL was equipped with special pressure instrumentation in and behind its flight test noseboom.

Sonic boom predictions had shown that some of the SR-71 flight conditions planned could result in noncoalesced sonic boom signatures on the ground. These predictions assumed a quiescent atmosphere. A turbulent atmospheric layer near the ground might severely distort these signatures. Because this turbulent atmospheric layer may extend several thousand feet above ground level, it was important to record the sonic boom signatures above this layer to provide undistorted data of the noncoalesced sonic boom signatures. The slow-speed YO-3A aircraft was flown at an altitude of 10,000 ft to record the sonic booms above the turbulent atmospheric layer. The F-16XL aircraft could not probe to such a low altitude at supersonic speeds because of aircraft and airspace limitations. The YO-3A aircraft is typically used at the NASA Ames Research Center, Mountain View, California, to measure the acoustics of helicopters in flight (Cross, 1984), but its quiet and slow flight characteristics made it an excellent airborne platform for sonic boom recordings.

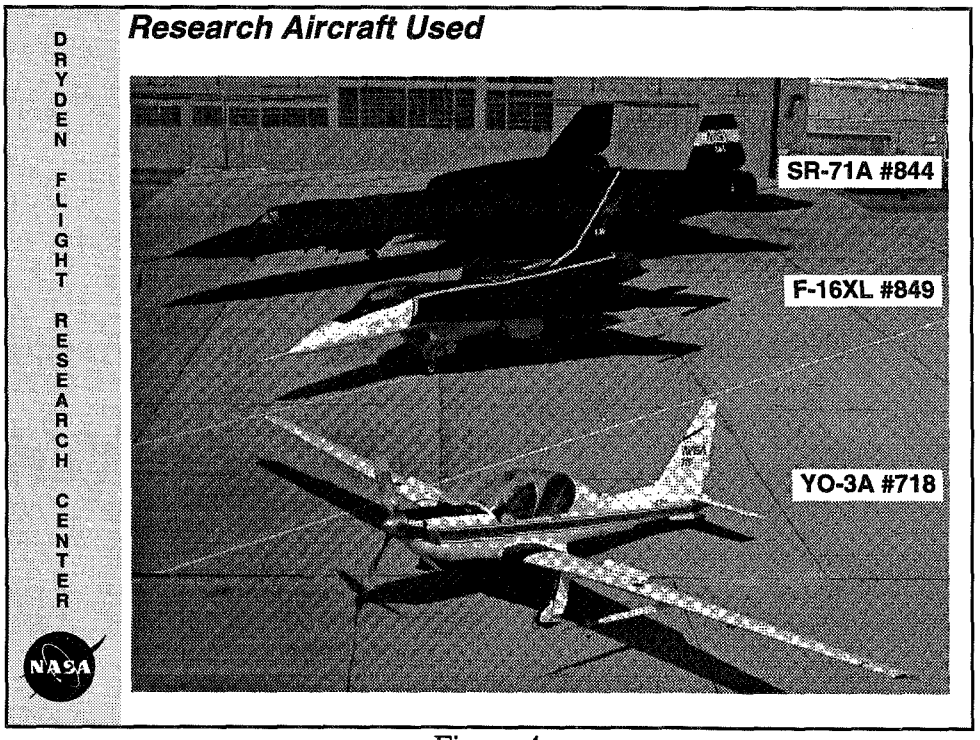

Figure 4

Figure 5 shows the path of the F-16XL aircraft during one probing of the SR-71 shock waves. The F-16XL aircraft would start behind the SR-71 tail shock and move forward, ahead of the bow shock. Then, the F-16XL aircraft would slow down to repeat the probing backward from the bow shock past the tail shock. Because the shock waves sweep behind the SR-71, longitudinal separation occurred between the tail of the SR-71 aircraft and the nose of the F-16XL aircraft during the probings. These probings were attempted to hold in level flight with no lateral offset from the SR-71 aircraft. While some of the probings gathered are quite level with very little lateral offset, most signatures have some variability in altitude and lateral offset.

When the F-16XL aircraft probed within 1000 ft of the SR-71 aircraft, its pilot had several indications of crossing the shock waves. These indications include feeling the pressure changes within the cockpit, being slightly jostled by the shock waves, and hearing the SR-71 engines when aft of the tail shock. When probings were conducted at vertical separations greater than about 1000 ft, the pilot was unaware when the shock waves were penetrated. Pressure and temperature data from the SR-71 and F-16XL aircraft were recorded on the vehicles and transmitted to the control room in real time. The pressure data from the F-16XL aircraft was displayed real time in the control room on stripcharts and computer plots. The pilot was then advised when he was ahead or behind the shock system of the SR-71 aircraft.

The YO-3A aircraft flew along the predetermined SR-71 flight track at an altitude of 10,000 ft and about 65 kn airspeed uptrack of the ground array of sonic boom recorders (Norris, 1995). The sonic boom signatures were recorded by the YO-3A aircraft as the SR-71 aircraft passed overhead.

In the cylindrical wave region, the F-16XL aircraft measured the SR-71 near-field shock to more than 8000 ft below the SR-71 aircraft and gathered 105 signatures during 7 flights. The YO-3A aircraft measured the SR-71 sonic booms from 21,000 to 38,000 ft below the SR-71 aircraft and recorded 17 passes. An array of several types of ground-based sonic boom recorders was used to complete the data set of sonic boom propagations, and 172 signatures were recorded (Norris, 1995). Atmospheric data were gathered for flight data analysis and for sonic boom propagation prediction codes (Ehernberger, 1992).

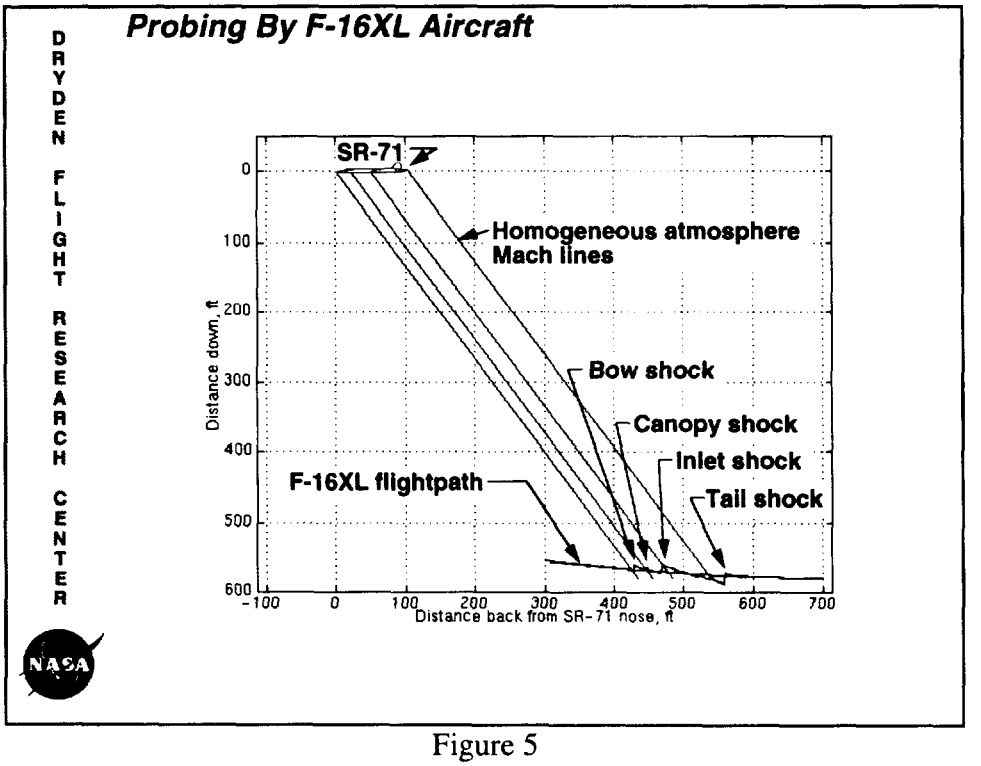

Figure 5

This SR-71 aircraft was equipped with research instrumentation (fig. 6). These instruments are used to measure the raw parameters needed for the flight conditions of the SR-71. A flight research quality airdata calibration will be determined during the final data analysis. Additionally, all SR-71 aircraft have a mission recording system, MRS. The MRS records many aircraft parameters once every 3 sec for use by the maintainence crew and aircrew after a flight. Even though MRS data are of a slow rate and low resolution, they are of great value because of the wide range of parameters recorded, especially parameters for the engines. The total fuel weight from the MRS will be used to give an improved measurement of angle of attack and lift coefficient.

The primary positioning and velocity data for this experiment were measured with the differentially corrected carrier phase Global Positioning System, GPS. Because the GPS data were not available during the flights, ground-based radar data (Haering, 1995) were used in real-time control room displays and as a backup for the GPS data. A radar beacon is installed in the SR-71 aircraft to enhance the quality of the radar data.

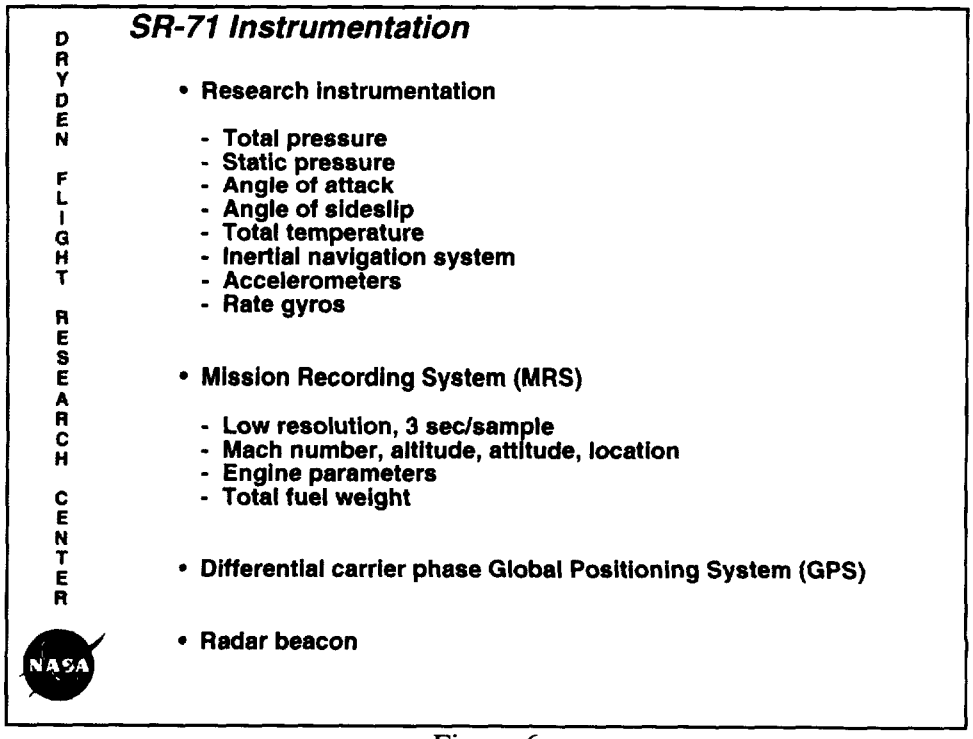

Figure 6

The primary instrumentation for this experiment was the pressure instrumentation installed in the F-16XL aircraft (fig. 7). The overpressures of the SR-71 shock waves were measured using four independent systems.

The first system measured the pressure difference between P1 and P2, which is called dp2 (fig. 7). The flush ports at location P1 were two holes ±37.5° from the top of the noseboom manifolded together. The ports at P2 have the same orientation as those at P1. This orientation was used to minimize variations in pressure because of angle-of-attack changes (Ritchie, 1959). The P1 ports were connected to the front side of the transducer using the shortest tubing possible. The back, or reference, side of the transducer was plumbed to the flush ports at P2, but with a reference tank, T, in between. This arrangement made this system essentially a very sensitive rate of descent sensor.

The second system measured the pressure difference between P3 and P2, which is called dp1. The flush ports located at P3 were two holes ±90° from the top of the noseboom manifolded together and were intended to minimize noseboom reflection factor effects.

The transducers used to measure dp1 and dp2 were identical highly accurate ±1 psi transducers sampled at 200 samples/sec. The reference tank was sized to give maximum lag without overranging the transducers during aircraft climbs and descents. The pressure of the tank, PR, and tank temperature was measured. Heater blankets were installed around these transducers to minimize calibration shifts because of temperature changes in the radome.

The third system used an absolute digital pressure transducer to record the indicated static pressure, Psi. This transducer was plumbed into the aircraft static pressure line close to the noseboom. The fourth and last system measured indicated total pressure, Pti, using an absolute digital pressure transducer plumbed into the aircraft total pressure line close to the noseboom. The transducers used to measure Psi and Pti were identical zero to 19 psi 16-bit digital pressure transducers. These transducers did not need heater blankets because they had internal temperature calibration compensation. The effects of aircraft speed and altitude changes on Psi and Pti will be removed using trajectory reconstruction to give shock wave overpressures.

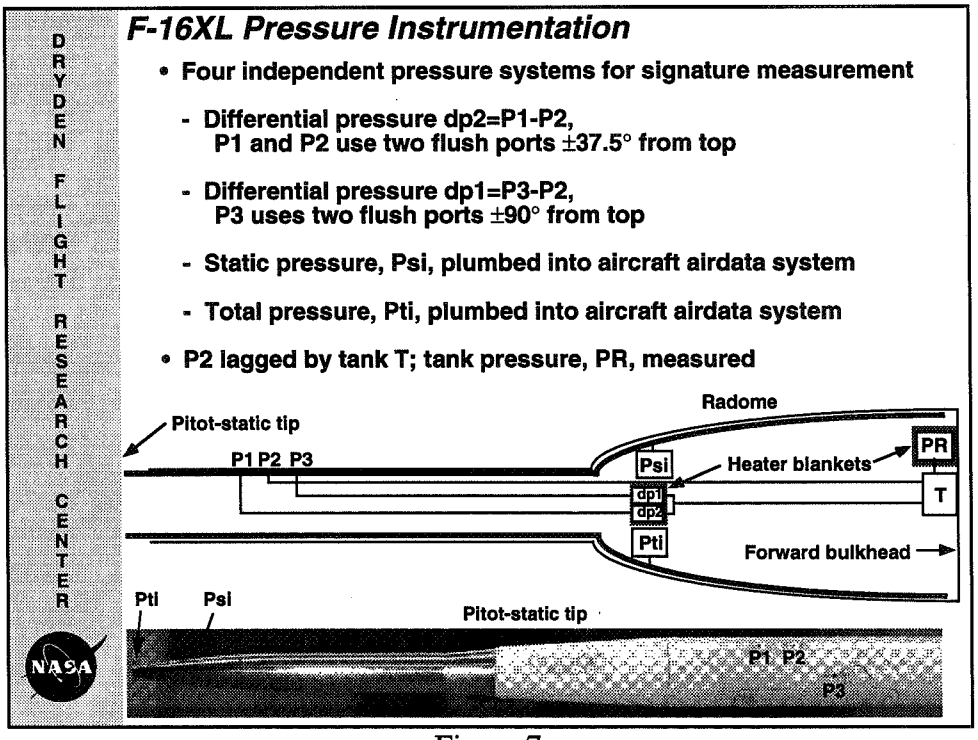

Figure 7

To ensure the quality of the pressure instrumentation aboard the F-16XL aircraft, special tests beyond normal calibrations were conducted on the ground and in flight. These tests were inspired by some of the challenges described in a B-58 (General Dynamics, Fort Worth, TX) experiment (Maglieri, 1963). Because the noseboom probe used in the B-58 experiment was quite long and thin, noseboom vibration affected the pressure data gathered. A noseboom ground vibration test was performed on the F-16XL aircraft to determine the natural vibration frequencies. Analysis of this vibration test is pending, but the pressure data measured in flight does not seem to show effects from noseboom vibration.

Another ground-based test involved applying step pressure inputs into each of the pressure port arrays. The front side of the differential pressure transducers showed no perceptible lag during these tests. Because the total and static pressure lines ran to the cockpit instrumentation and the airdata computer, large lag and attenuation were present. Pressure deconvolution techniques will be used with the pressure step responses to remove the lag and attenuation effects from the total and static pressures. The reference tank also had large lag by design.

There was some concern that the orientation of the flush ports to the incident shock wave would affect the overpressure values. Probing data below the SR-71 aircraft showed that the ±37.5° ports gave the same overpressures as the ±90° ports when the F-16XL aircraft was steady in pitch and yaw. The two sets of ports also gave the same overpressures when probing data were gathered to the side of the SR-71 aircraft. As a result for steady flight, the orientation of the ports to the incident shock wave had no effect on the data.

These ports were affected by changes in the pitch and yaw dynamics of the F-16XL aircraft. While the F-16XL aircraft was supersonic but not probing the SR-71, pitch and yaw sweeps were performed. The ±90° ports gave pressure variations with pitch changes. Because slight pitch changes occur in the F-16XL aircraft when probing below the SR-71 aircraft, the overpressure data using the ±90° ports are slightly affected. The ±37.5° port pressures were steady during pitch changes, but these pressures were affected by yaw changes. Because yaw remains steady while probing below the SR-71 aircraft, the ±37.5° ports give better pressure data than the ±90° ports.

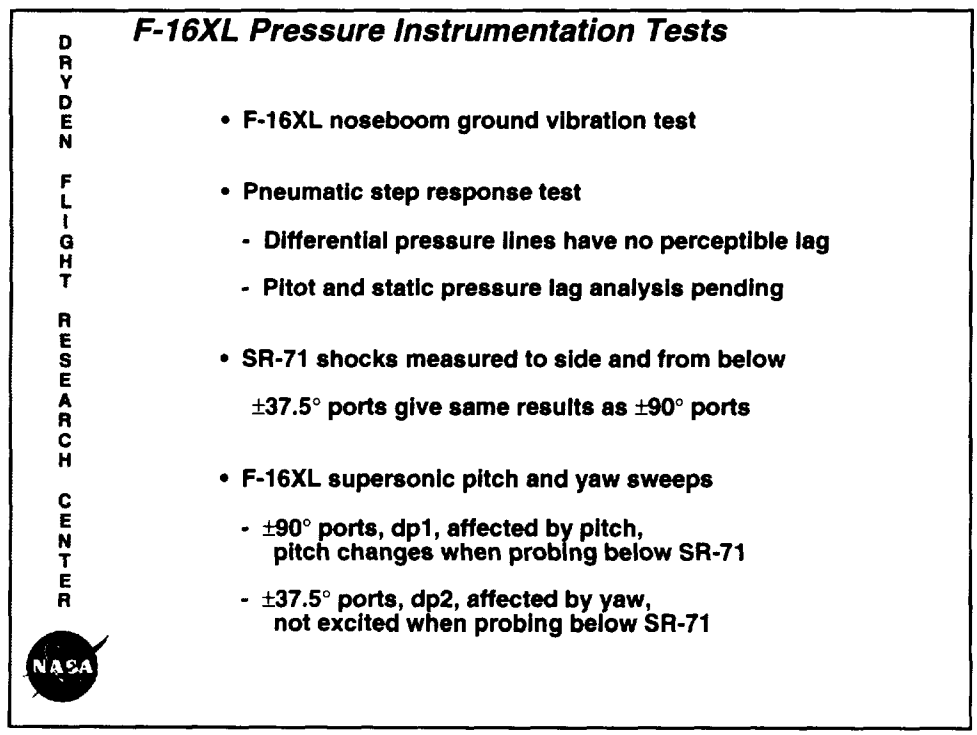

Figure 8

Shock wave pressures can be amplified by the shape of the sonic boom probe used. The ratio of the measured overpressure to the actual overpressure is called the reflection factor. On the B-58 experiment (Maglieri, 1963), one sensor on the noseboom probe had reflection factors of 1.07 to 1.23. These reflection factors were determined using wind tunnel tests. The reflection factors for the F-16XL aircraft will be determined later by comparing the pressures from the four independent measurement systems. This comparison will rely on the success of the total and static pressure deconvolution analysis. If this analysis is unsuccessful, a wind tunnel test of the F-16XL noseboom configuration may be needed to determine the reflection factors.

Another test to address F-16XL reflection factors was conducted using the sonic boom from an F-18 aircraft. The F-16XL aircraft was stationary on the ground with its instrumentation system operational. Several Portable Automatic Triggering System, PATS, sonic boom recorders (Norris, 1995) were placed with their pressure sensors at the same height and a few feet to the side of the F-16XL noseboom. An F-18 aircraft (McDonnell Douglas, St. Louis, MO) was flown at Mach 1.20 and an altitude of 30,000 ft. The F-16XL aircraft and the PATS recorders measured the sonic boom (fig. 9). The pressure data from both differential pressure transducers on the F-16XL aircraft compare favorably to the PATS units, so from this test the F-16XL reflection factor is 1.0. Whether the reflection factor for the F-16XL is significantly different while at supersonic speeds is unknown.

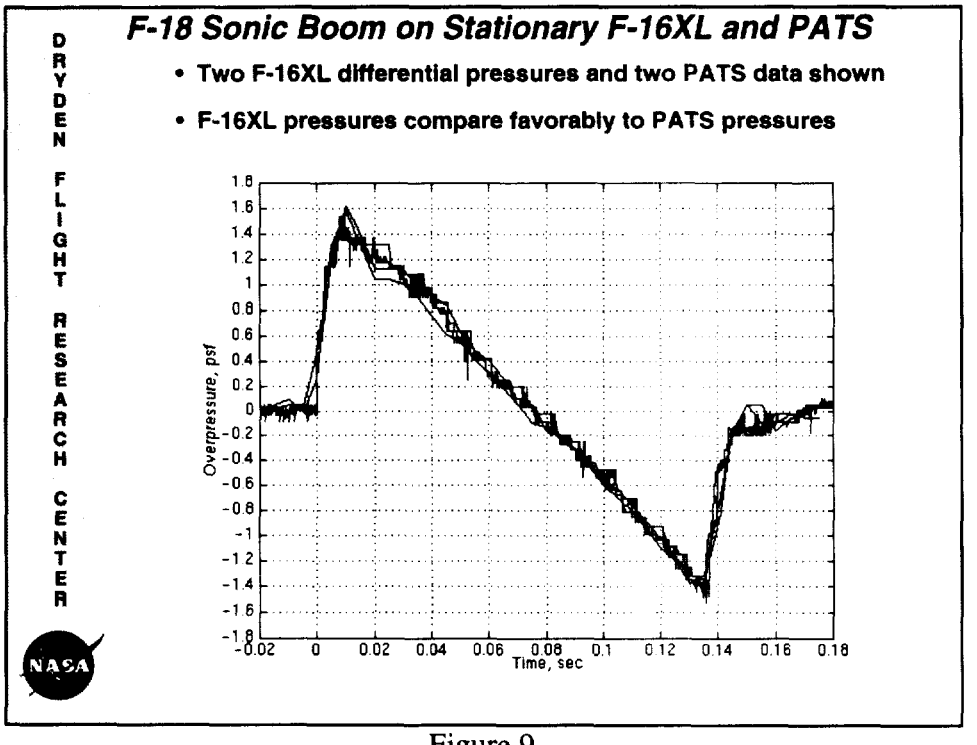

Figure 9

The primary instrumentation of the YO-3A aircraft consists of three microphones mounted on each wingtip and the top of the vertical tail (fig. 10). Each microphone element was protected within a cone-shaped housing that minimized noise caused by the forward motion of the aircraft. The aircraft was designed to be extremely quiet in flight, in part, because of a long muffler that runs the length of the fuselage and a specially designed low-speed propeller.

In addition to the three microphones, airspeed, altitude, ambient temperature, angle of attack, angle of sideslip, voice, and time were recorded in analog on a FM tape recorder (Cross, 1984). The airspeeds of the YO-3A and SR-71 aircraft will be used to transform the time-based sonic boom signatures into overpressures in terms of length. Before this test and each flight, a calibration signal of 123.8 dB and 251.8 Hz was applied to each of the microphones. This calibration signal allows conversion of the recorded microphone voltage into overpressure.

A handheld coarse acquisition, C/A, code GPS receiver was used to establish the position of the YO-3A aircraft when a sonic boom was detected. The sonic booms were not heard aboard the YO-3A aircraft, but an oscilloscope monitoring the microphone signals and the pilot's vertical speed indicator indicated sonic boom passage.

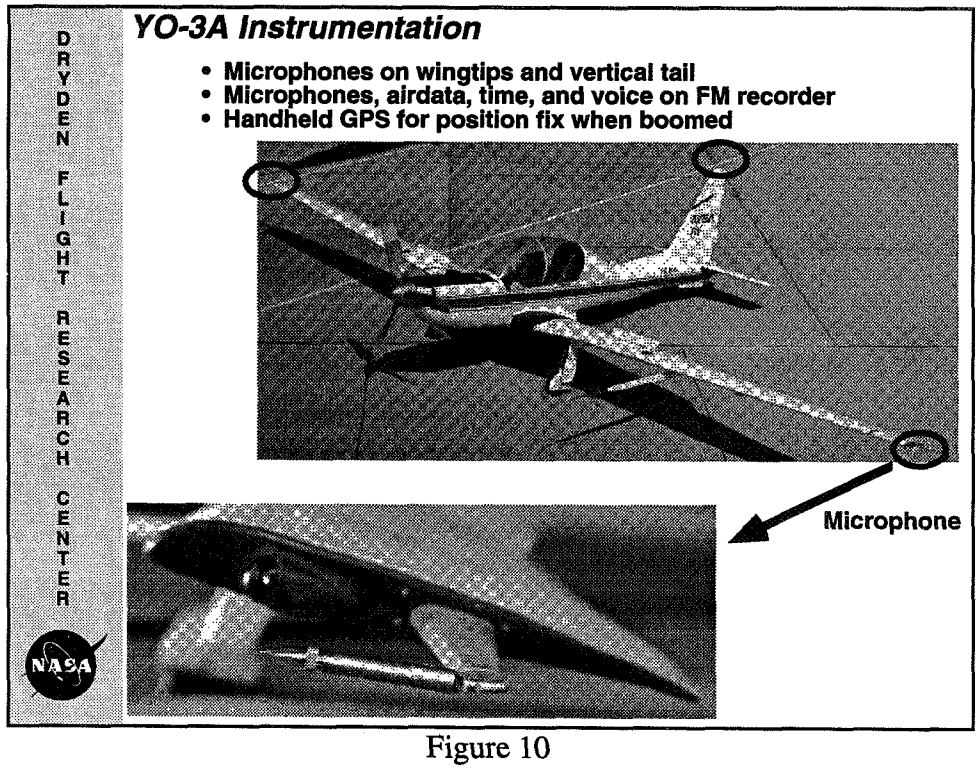

Figure 10

A reflection factor test for the YO-3A aircraft was conducted in the same manner as for the F-16XL aircraft. A sonic boom from an F-18 aircraft was recorded by the stationary YO-3A aircraft, a PATS, and a Small Airborne Sonic Boom Recorder, SABER, located near the microphones (Norris, 1995). These data have not been digitized for analysis, but stripchart playback of the analog microphone signals shows these data to have been high passed filtered. This filtering gives the bowed shape to the ordinarily straight diagonal pressure drop of an N-wave (fig. 11). The YO-3A microphones have demonstated flat response to as low as 2 Hz, but these microphones are filtered at some lower frequency. In spite of this, the separation distance between shocks, the pressure rises of each shock, and their rise times were adequately recorded.

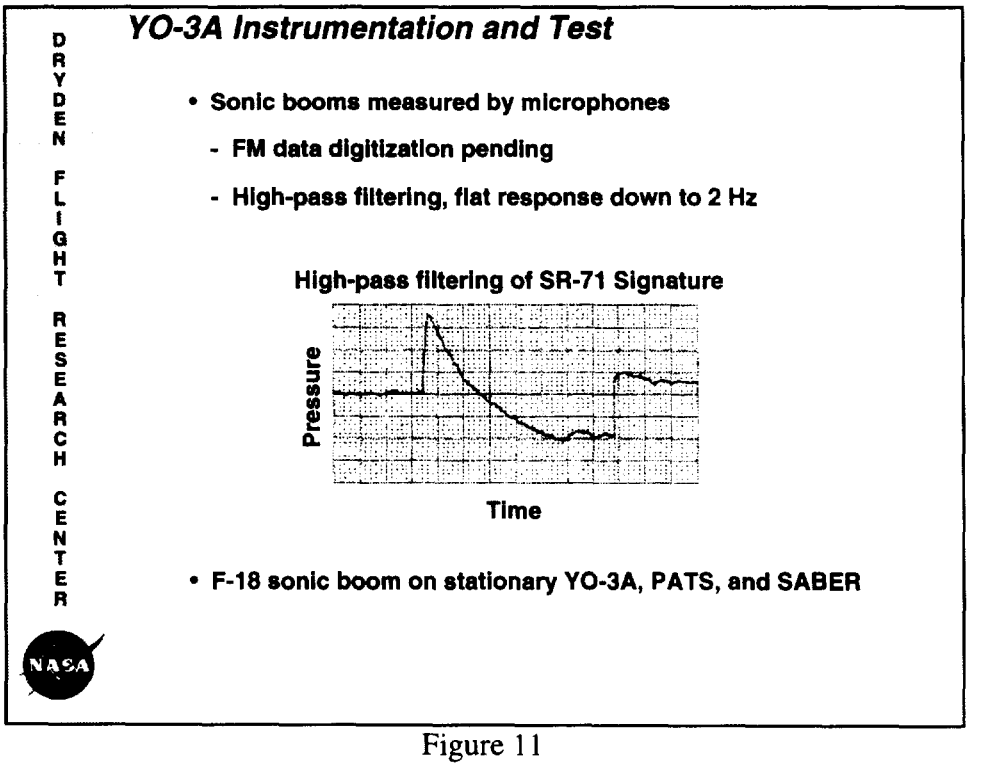

Figure 11

Pressure data gives one part of the propagation information (fig. 7). The remaining parts needed are the location where those pressures were recorded relative to the SR-71 aircraft, and the relative speed of the SR-71 aircraft to the F-16XL aircraft. Also, the position of the SR-71 relative to the ground-level sonic boom recorders is needed. Differentially corrected carrier phase GPS data were selected to determine these positions and speeds because its accuracy is superior to ground-based radar and cine-theodolite data, especially over the vast distances required to conduct high-speed flight research. The Z-12 GPS receivers (Ashtech, Sunnyvale, CA) were located in the SR-71, the F-16XL, and at a ground station to provide differential corrections. The Z-12 units were also used to survey the locations of the ground-level sonic boom recorders (Norris, 1995). Each airborne unit recorded its own data, and these data were downloaded after each flight. The sample rate of the GPS receivers was set to 1 sample/sec to allow about 4.5 hr of recording time. Data from each airborne unit were then processed with the ground station data to give the differentially corrected data.

Several tests were conducted to assess both the absolute position accuracy and the accuracy of the separation between the two airborne GPS units. On one flight, the SR-71 and F-16XL aircraft were flown side by side at subsonic speeds while being videotaped from an F-18 aircraft which was flying below these aircraft. Using the span and length of both vehicles to judge scale, the relative separation was determined from the videotape. The separation distance data from the video images and the GPS agree to within ±10 ft. A portion of this difference may result from parallax and optical distortion of the F-18 canopy.

On another flight, the SR-71 aircraft was tracked by cine-theodolite during two approaches to the runway. The absolute position data from the cine-theodolite and GPS agree to within ±2 ft. The velocities agree to within ±1 fps, which is the accuracy of the cine-theodolite.

For the last test, two GPS units were placed in an automobile, with the unit antennas mounted on a board 7 ft, 8 in. apart and then driven up to 80 mph. The GPS data showed that the relative separation of the antennas was correct to within ±0.5 ft, and the velocities of the two receivers agreed to ±1.0 fps. This agreement indicates that GPS data are an excellent source for aircraft relative separation measurements.

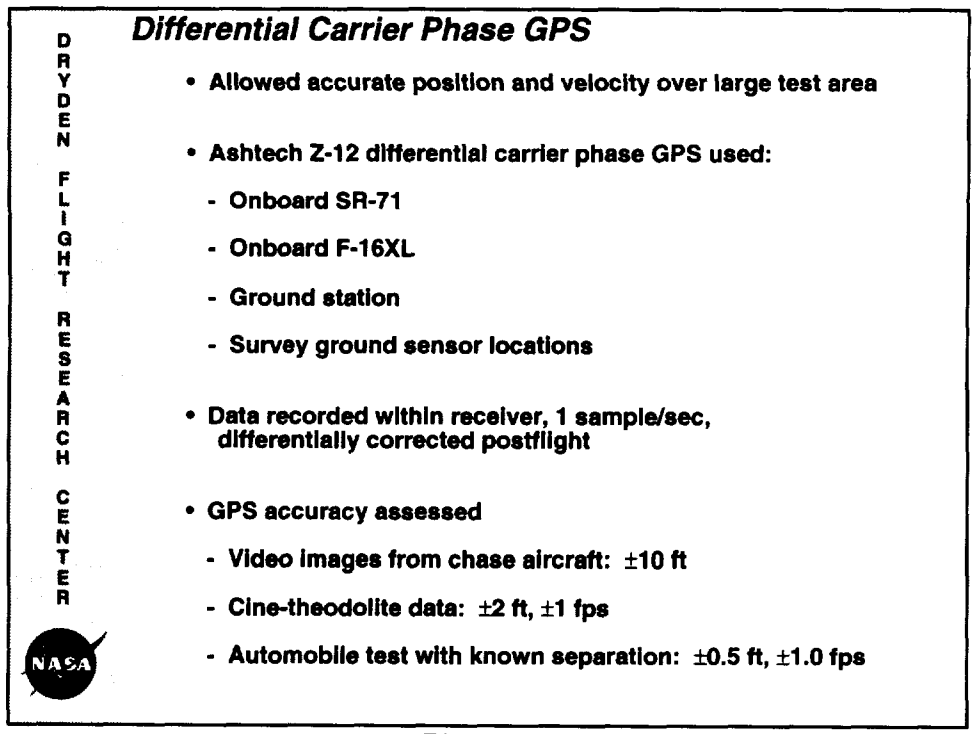

Figure 12

For this experiment, the SR-71 aircraft flew in level, stabilized flight. Figure 13 shows the flight conditions. The test points at Mach 1.25, an altitude of 31,000 ft, and low gross weight were intended to allow noncoalesced signatures to propagate down to the ground. Flying at the same Mach number but at 44,000 ft allowed altitude effects on the propagation to be seen. A third group of test points were flown at Mach 1.48 and an altitude of 48,000 ft to show Mach number effects on propagation. A few additional test points were gathered at other conditions. Data gathering was attemped at Mach 1.6, but the F-16XL aircraft could achieve that Mach number only very slowly. Only one data point was collected. Other probings occurred while the SR-71 aircraft was accelerating to one of the three main flight conditions. The YO-3A aircraft also gathered data at the same flight conditions as the SR-71 aircraft.

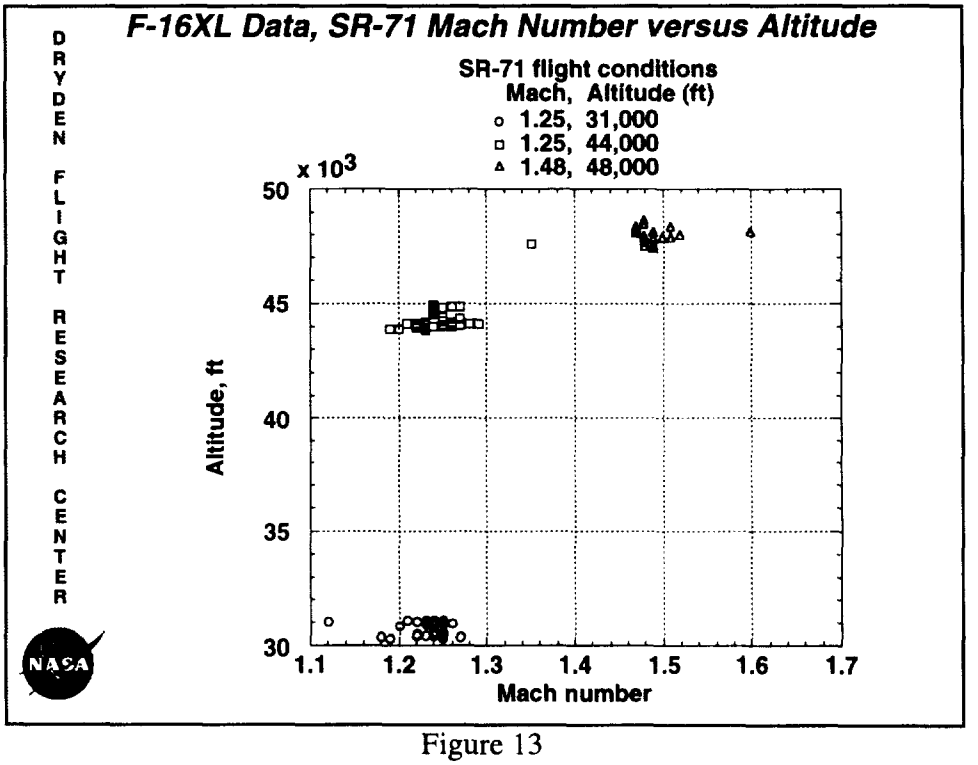

Figure 13

Figure 14 shows the F-16XL aircraft probed the SR-71 shock waves at several vertical separations, and signatures are available at these conditions. The F-16XL aircraft probed more than 8,000 ft below while the SR-71 aircraft was at Mach 1.25 and 31,000-ft altitude; more than 6,000 ft below while the SR-71 was at Mach 1.25 and 44,000-ft altitude; and more than 4,000 ft below while the SR-71 was at Mach 1.48 and 48,000 ft altitude. In addition, because the YO-3A aircraft was recording at 10,000-ft altitude, vertical separations of 21,000, 34,000, and 38,000 ft were achieved for these three SR-71 flight conditions. The data that are shown closer than 540 ft vertical separation had an additional lateral offset component. Because of normal fuel usage on the SR-71 aircraft, these data cover a range of gross weights and, therefore, lift coefficients.

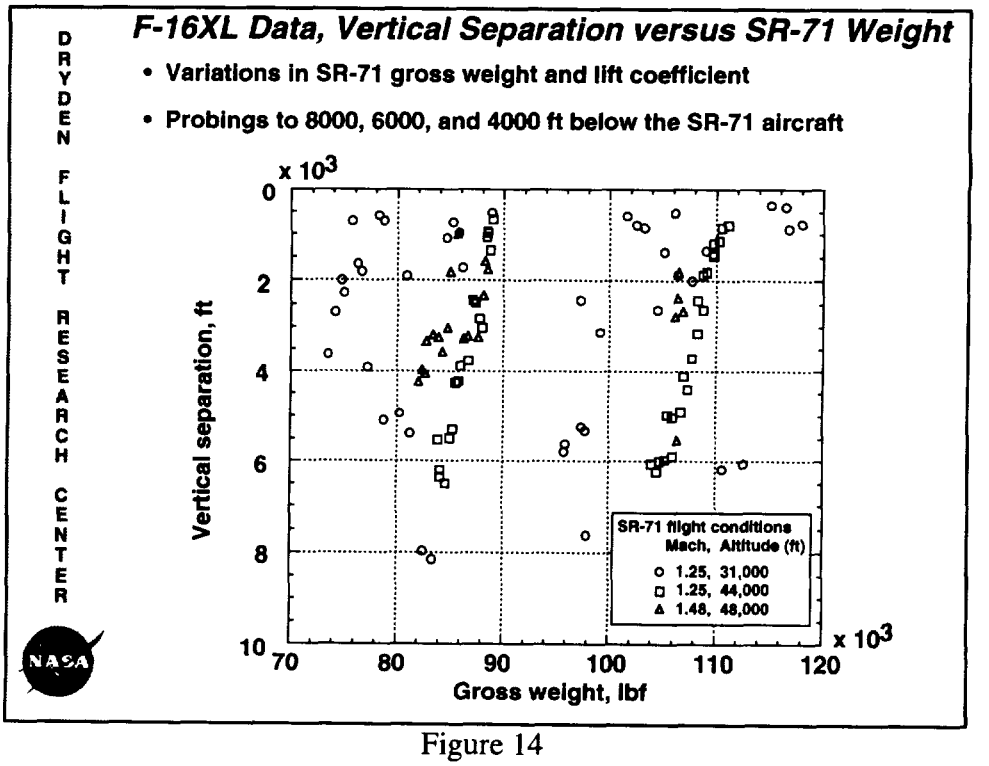

Figure 14

Figure 15 shows vertical separation as a function of maximum overpressure for the 105 probings. These data are preliminary because a reflection factor is not yet known, and other data corrections are still needed. The expected trend of decreasing maximum overpressure with increasing vertical separation is seen. Theory, wind tunnel, and other flight data show that overpressure should be a function of separation to the -3/4 power (Carlson, 1962), and these data confirm this relationship. Also, the lower altitude SR-71 data have the higher maximum overpressures. Some of the scatter in these data may be attributed to varying lateral offsets and SR-71 gross weight changes between data points.

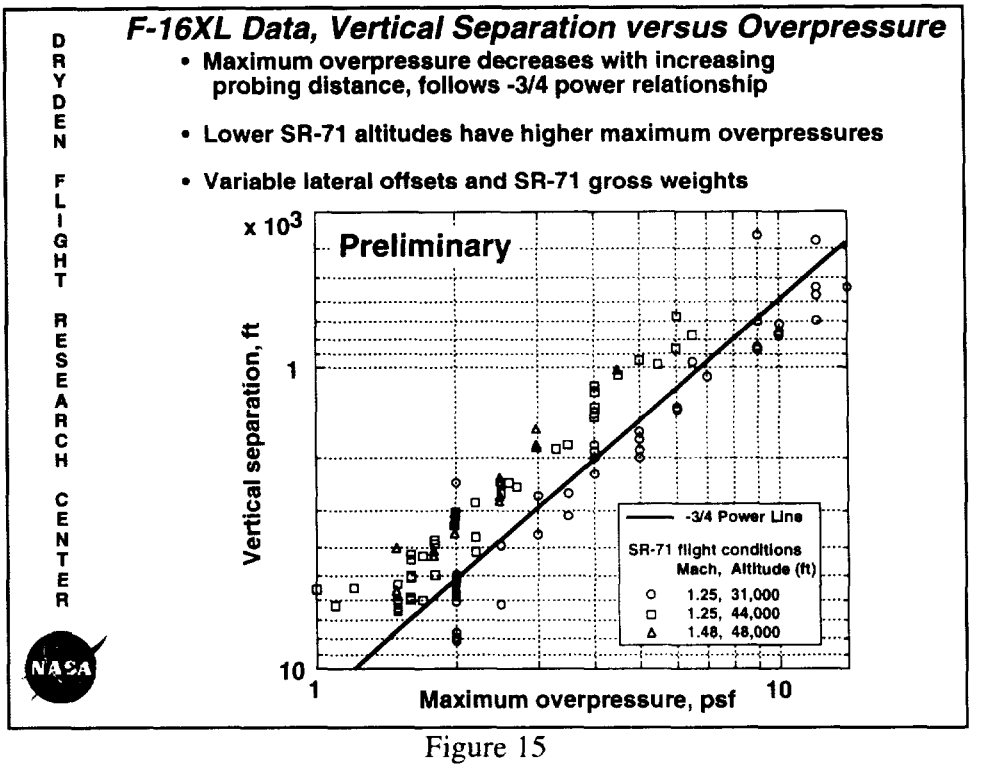

Figure 15

Figure 16 shows sonic boom signatures from the SR-71 aircraft at Mach 1.25 and an altitude of 31,000 ft with 540- to 7,980-ft vertical separation. These data are also preliminary because of the unknown reflection factor, and an estimate was used for the mean pressure line. Because the differential pressure systems act as rate of descent sensors, future analysis will be needed to calculate rate of descent from GPS and weather data to give a more nearly accurate mean pressure line.

As expected, several trends can be noted in figure 16. As vertical separation increases, the overall signature length increases, the overpressures decrease, and the inlet and canopy shocks move toward the bow shock. One interesting and unexpected trend concerns the plume pressures aft of the tail shock. All of the plumes from each signature collapse to one curve.

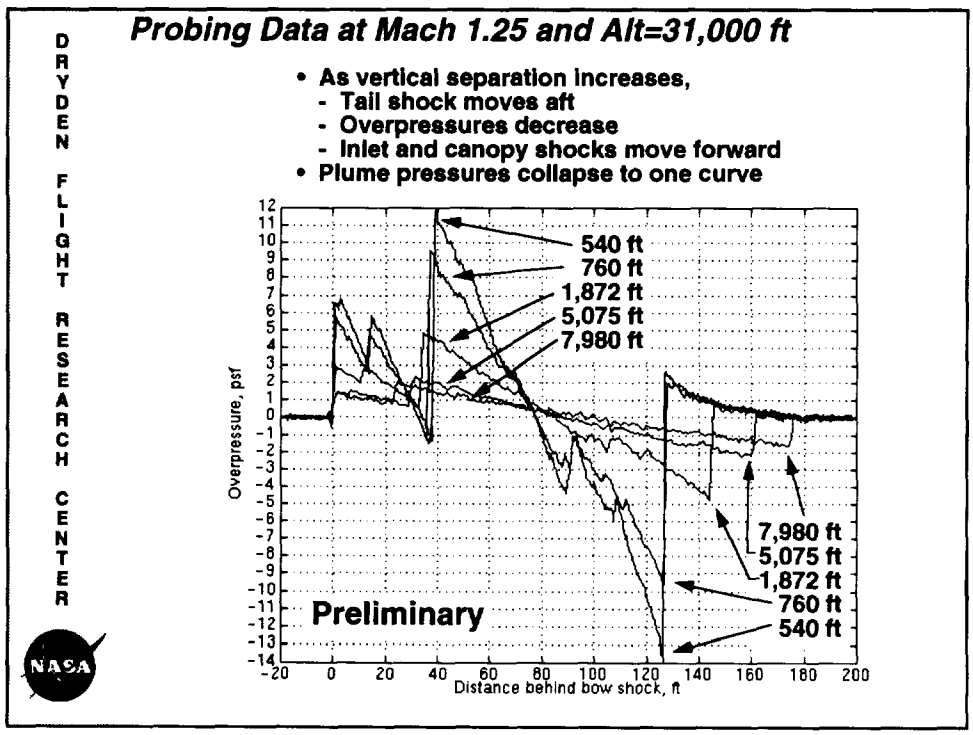

Figure 16

Figure 17 shows sample probing data for SR-71 flight conditions of Mach 1.25 at an altitude of 44,000 ft with 680- to 6,000-ft vertical separation. Again, the data follow the same trends as seen at Mach 1.25 and an altitude of 31,000 ft.

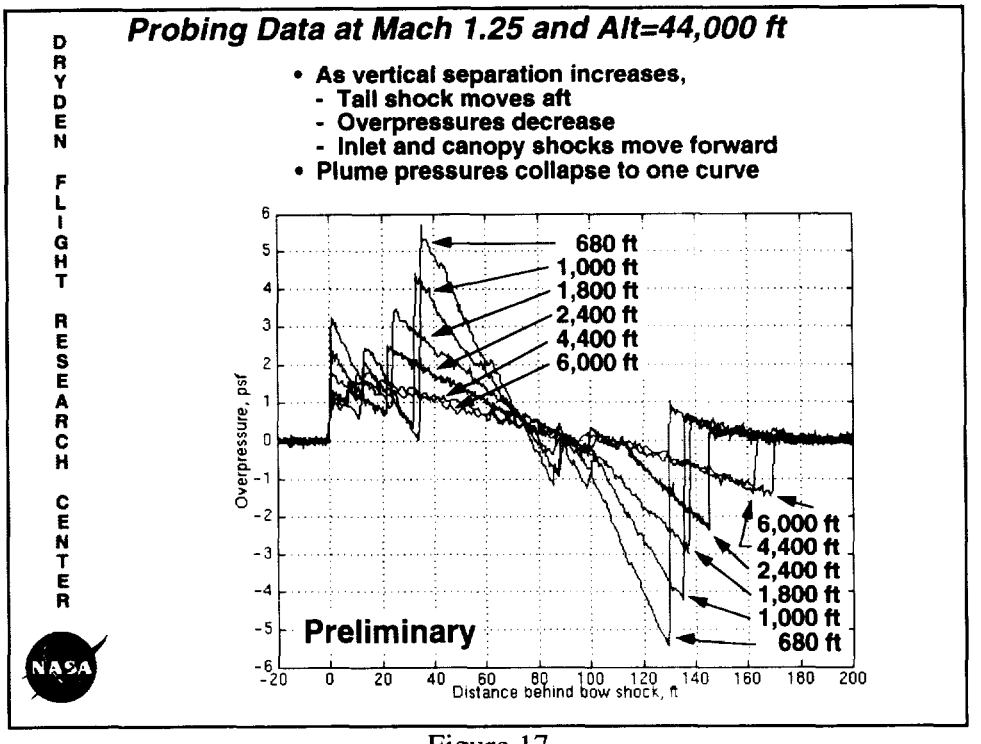

Figure 17

Sonic boom signatures from the SR-71 at a Mach 1.48 and at an altitude of 48,000 ft with 1,000- to 3,370-ft vertical separation follow the same trends as the two data sets shown in figures 16 and 17 (fig. 18).

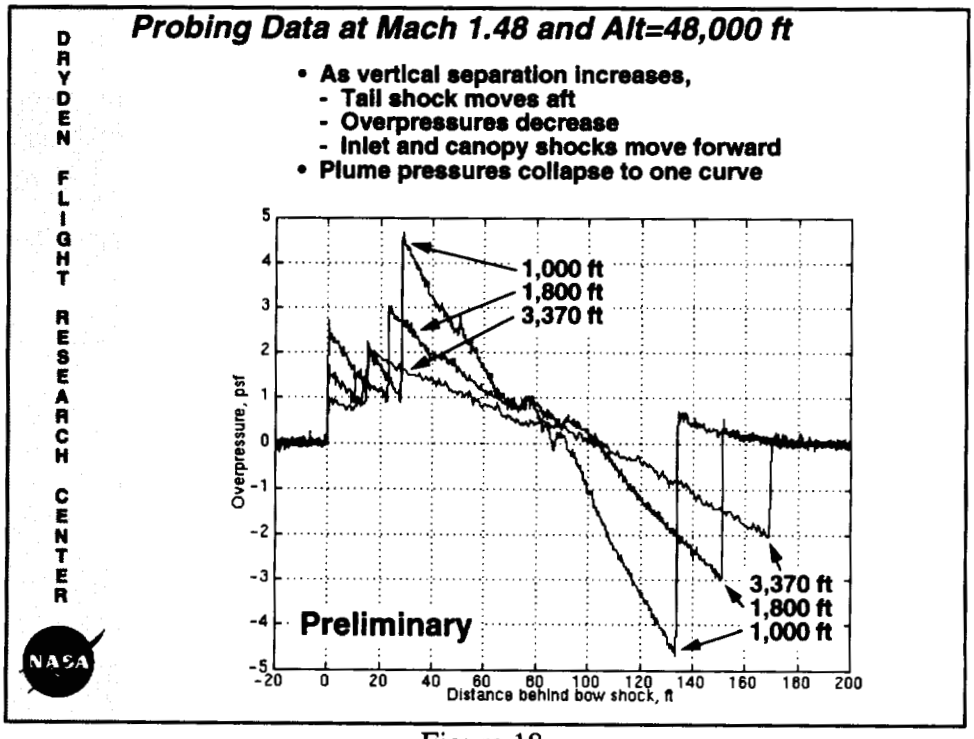

Figure 18

Figure 19 shows the distance of each major shock wave as a function of vertical separation for the three flight conditions. Four trends can be seen in these data. First, the tail shock is farther aft at Mach 1.48, the highest Mach number flown, than at Mach 1.25. Second, the canopy and inlet shocks travel forward slowest for an SR-71 altitude of 31,000 ft, the lowest altitude flown. Third, the canopy and inlet shocks coalesce for Mach 1.48. Fourth, the bow and canopy shocks coalesce for Mach 1.25.

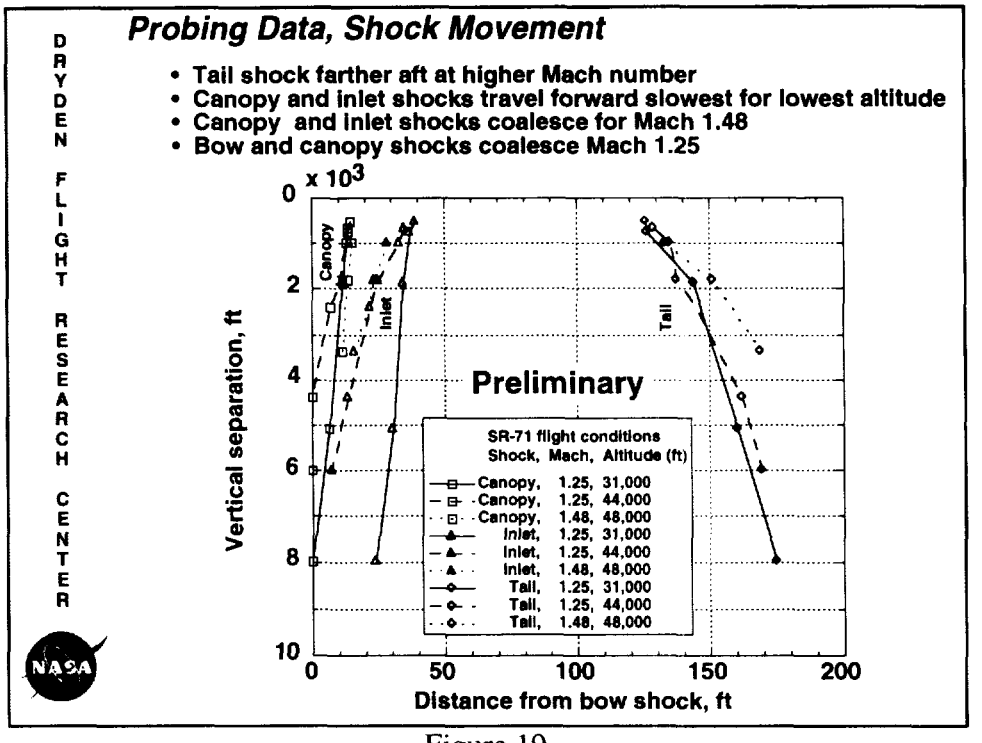

Figure 19

Figure 20 shows the overpressures of each major shock wave as a function of vertical separation for the three flight conditions. Here tail overpressure is expressed as a positive number. These overpressures are the peak value of each shock from the zero pressure line of the entire signature, not the pressure rise within the shock. Again, the attenuation rate follows the -3/4 power relationship. These pressure data fall into three groupings. In the first group, the tail and inlet shock waves from an SR-71 altitude of 31,000 ft, the lowest SR-71 altitude flown, have the highest overpressure. A second grouping occurs with the bow and canopy shocks when the SR-71 flys at altitudes from 44,000 to 48,000 ft. These shocks have the lowest overpressures. The remaining shock waves are in an intermediate overpressure group.

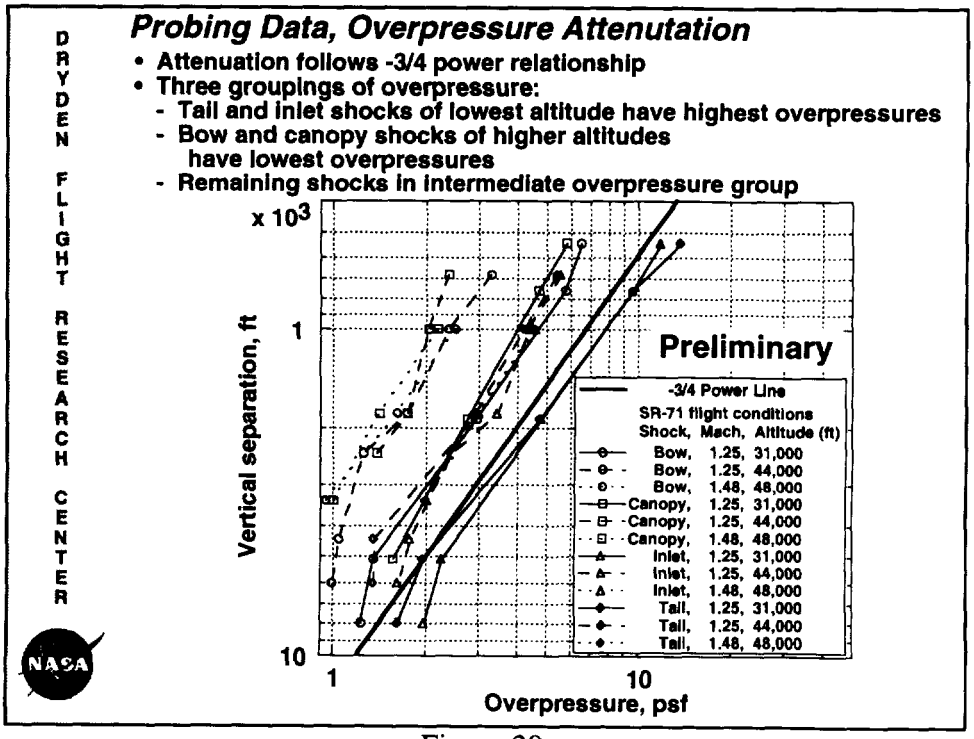

Figure 20

Figure 21 shows sample SR-71 sonic boom signatures recorded by the YO-3A. These data were gathered with the SR-71 aircraft flying at Mach 1.25 and an altitude of 31,000 ft during three passes on one flight, and the gross weight of the SR-71 decreased with each pass. The YO-3A was flown at an altitude of 10,000 ft for all the flights. The bowed expansion in each signature shows the high-pass filtering of the data. As expected, the maximum overpressure decreases as the gross weight of the SR-71 aircraft decreases. The heaviest weight pass shows a coalesced bow and inlet shock. The medium and lightest weight passes show separation between the bow and inlet shocks, with the separation increasing with decreasing SR-71 gross weight. The corresponding ground signatures from this flight were all coalesced N-waves (Norris, 1995).

In addition, the YO-3A aircraft measured the signatures from the supersonic F-16XL aircraft. Some of the recorded sonic booms from the SR-71 and F-16XL aircraft had reflected off the ground and propagated up to the YO-3A. The reflected shocks would have traveled twice through the lower level of the atmosphere. These data are being reduced.

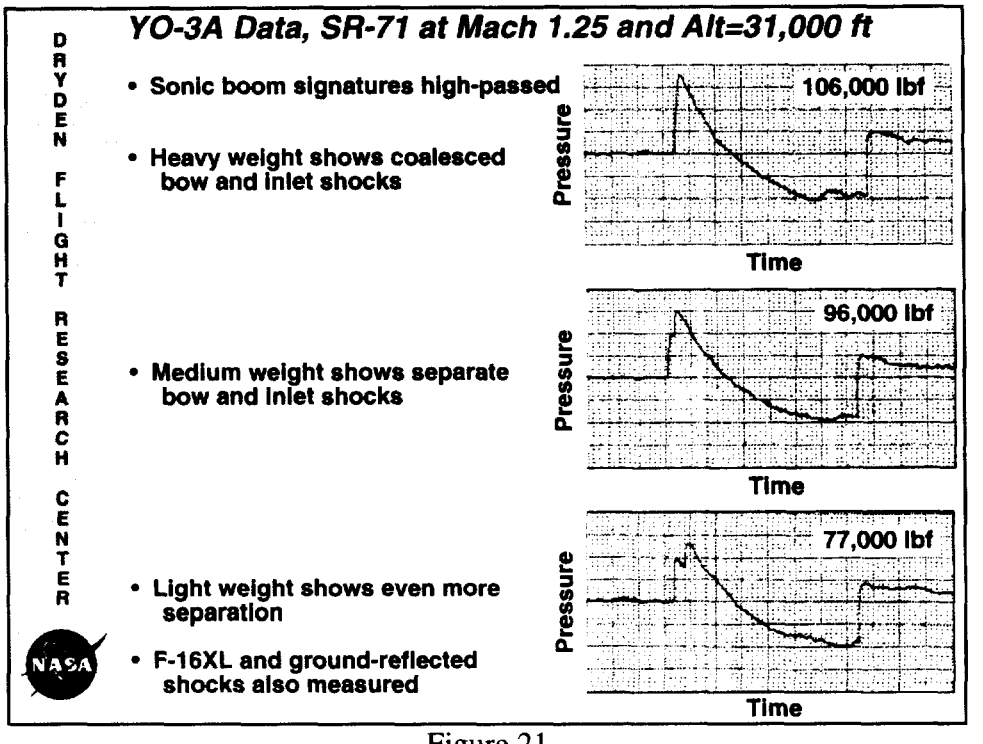

Figure 21

Three aircraft were used for the SR-71 Sonic Boom Experiment: the SR-71 as the sonic boom generator; the F-16XL as the supersonic probing aircraft; and the YO-3A as the far-field, slow speed microphone platform. These aircraft used flight research quality instrumentation systems, including specialized pressure sensors on the F-16XL and differential carrier phase GPS on the SR-71 and F-16XL. These instruments underwent several ground and airborne calibration tests to assess their accuracies.

The SR-71 was flown at three flight conditions to assess the effects of Mach number and altitude on sonic boom propagation. The F-16XL probed the sonic boom signatures at nearly the same speed as the SR-71, while the YO-3A was overflown by the SR-71. Seven flights gathered 105 F-16XL probings, 17 passes of the YO-3A sensors, and 172 ground-recorded signatures (Norris, 1995). These data are spatially dense signatures of high fidelity and will give the sonic boom community an opportunity to fully validate sonic boom propagation codes for the flight conditions flown.

Preliminary data from this experiment was shown in figures 13 through 21. Shock location and overpressures are affected by Mach number, altitude, and aircraft gross weight. The analysis of these data is ongoing. Plans include releasing the full database with all corrections to the sonic boom community.

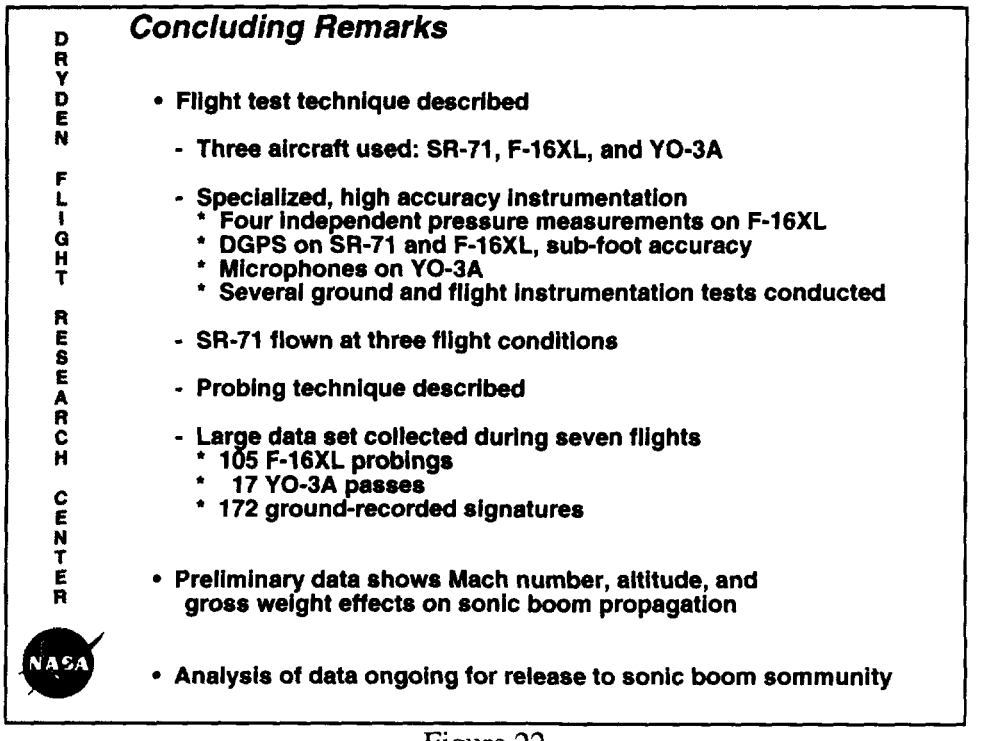

Figure 22

REFERENCES

Carlson, Harry W.: *The Lower Bound of Attainable Sonic Boom Overpressure and Design Methods of Approaching This Limit*, NASA TN D-1494, 1962.

Cross, J.L.: *YO-3A Acoustics Research Aircraft Systems Manual*, NASA TM-85968, Jul. 1984.

Ehernberger, L.J.; Haering, Edward A., Jr.; Lockhart, Mary G.; and Teets, Edward H.: *Atmospheric Analysis for Airdata Calibration on Research Aircraft*, AIAA-92-0293, 1992.

Haering, Edward A., Jr.; and Whitmore, Stephen A.: *FORTRAN Program for Analyzing Ground-Based Radar Data: Usage and Derivations, Version 6.2*, NASA TP-3430, 1995.

Maglieri, Domenic J.; Ritchie, Virgil S.; and Bryant, John F., Jr.: *In-Flight Shock-Wave Pressure Measurements Above and Below a Bomber Airplane at Mach Numbers from 1.42 to 1.69*, NASA TN D-1968, Oct. 1963.

Mullens, Marshall E.: *A Flight Test Investigation of the Sonic Boom*, AFFTC-TN-56-20, Air Research and Development Command, U.S. Air Force, May 1956.

Norris, Stephen R.; Haering, Edward A., Jr.; and Murray, James E.: *Ground-Based Sensors for the SR-71 Sonic Boom Propagation Experiment*, NASA TM-104310, 1995.

Ritchie, Virgil S.: *Several Methods for Aerodynamic Reduction of Static-Pressure Sensing Errors for Aircraft at Subsonic, Near-Sonic, and Low Supersonic Speeds*, NASA TR R-18, 1959.

Smith, Harriet J.: *Experimental and Calculated Flow Fields Produced by Airplanes Flying at Supersonic Speeds*, NASA TN D-621, 1960.

S10-71
85887
21P.

GROUND-BASED SENSORS FOR THE SR-71 SONIC BOOM PROPAGATION EXPERIMENT

Stephen R. Norris, Edward A. Haering, Jr., James E. Murray
NASA Dryden Flight Research Center, Edwards, California

A36752

ABSTRACT

This paper describes ground-level measurements of sonic boom signatures made as part of the SR-71 sonic boom propagation experiment recently completed at NASA Dryden Flight Research Center, Edwards, California. Ground-level measurements were the final stage of this experiment which also included airborne measurements at near and intermediate distances from an SR-71 research aircraft. Three types of sensors were deployed to three station locations near the aircraft ground track. Pressure data were collected for flight conditions from Mach 1.25 to Mach 1.60 at altitudes from 30,000 to 48,000 ft. Ground-level measurement techniques, comparisons of data sets from different ground sensors, and sensor system strengths and weaknesses are discussed. The well-known N-wave structure dominated the sonic boom signatures generated by the SR-71 aircraft at most of these conditions. Variations in boom shape caused by atmospheric turbulence, focusing effects, or both, were observed for several flights. Peak pressure and boom event duration showed some dependence on aircraft gross weight. The sonic boom signatures collected in this experiment are being compiled in a data base for distribution in support of the High Speed Research Program.

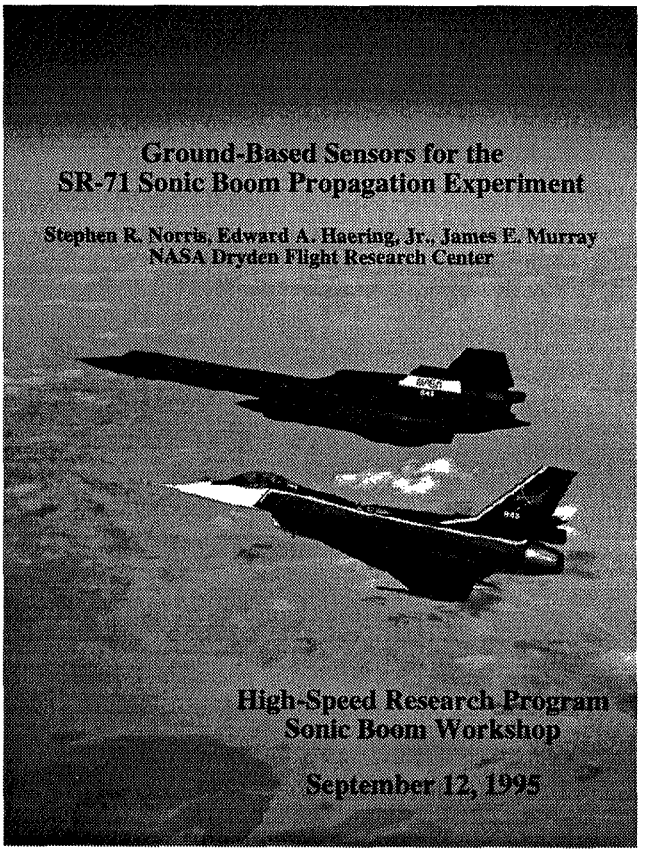

The behavior of shock wave systems propagating away from an aircraft is of interest to the High Speed Research program. A key objective is understanding the factors that determine the magnitude of the pressure rise across a shock, rate at which smaller shocks coalesce into larger shock fronts, pressure rise time, and overall boom shape. An experiment to investigate these characteristics was completed at NASA Dryden Flight Research Center, Edwards, California, in May 1995. The flight data will be made available to industry and academia for use in development and validation of sonic boom prediction methods.

In this study, an SR-71 research aircraft (Lockheed Corp., Burbank, California) was used to generate a shock wave system while flying at speeds from Mach 1.25 to Mach 1.60 and altitudes from 30,000 to 48,000 ft. The near-field shock system was probed by an F-16XL research aircraft (General Dynamics, Ft. Worth, Texas) at a vertical displacement from the SR-71 aircraft of distances up to 8000 ft. Low altitude measurements were taken by a Y0-3A aircraft (Lockheed Corp., Burbank, California) flying at approximately 10,000 ft and carrying microphones at its wingtips and tail (Haering, Ehernberger, and Whitmore, 1995). A third set of measurements was collected at ground level. Ground instrumentation consisted of Portable Automatic Triggering Systems (PATS), the prototype of a new sonic boom recorder called the Small Airborne Boom Event Recorder (SABER), and two digital MiniDisc recorders (Sony Corporation, Tokyo, Japan). See figure 1. This study extensively used the Global Positioning System (GPS) satellite navigation network to determine the relative positions of the shock-generating aircraft, probe aircraft, and ground-level recording equipment.

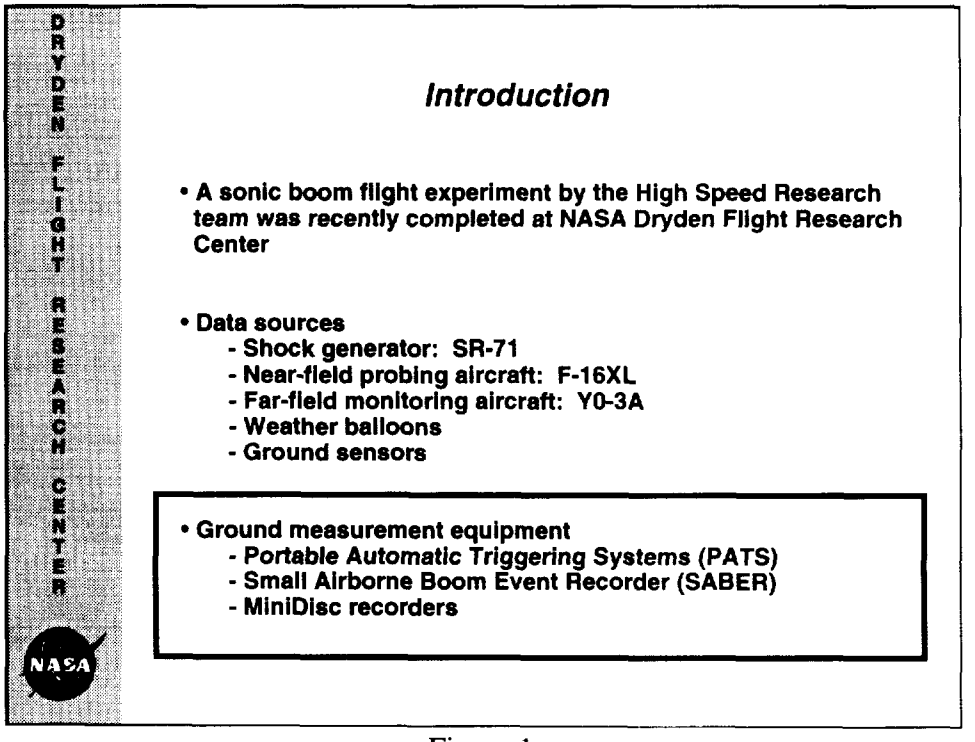

Figure 1

This presentation focuses on measurements made at ground level (fig. 2). Several sonic boom measurement systems, sensor layout, SR-71 flight conditions, and sample data sets will be discussed. These results are preliminary, but the full data sets will be published for future distribution.

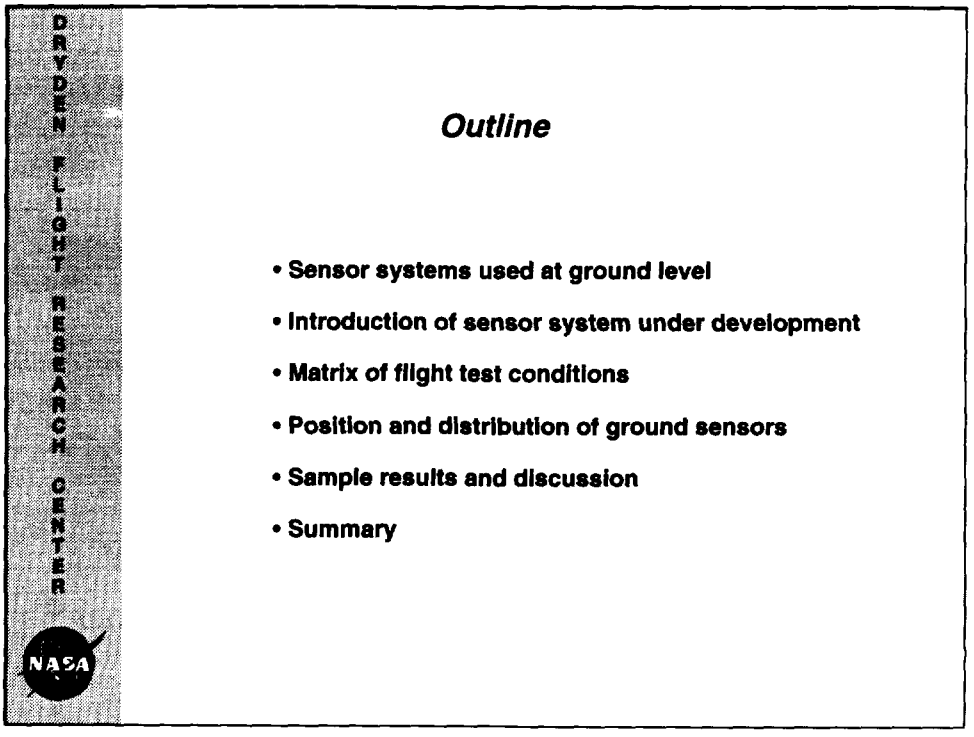

Figure 2

The PATS units were used as the primary instrumentation at the ground stations. Each PATS is the size of a large briefcase (fig. 3). The electronics are nested in a foam pad which is enclosed in a hard plastic case.

The transducer is at the end of a cable, so it can be moved several feet away from the main box. The reference side of this differential pressure transducer is evacuated to approximately one-half atmosphere and sealed. The transducer output is conditioned by a high-pass filter with a cutoff frequency of approximately 0.3 Hz.

Each PATS can record eight time histories of pressure data. At least one of these time histories must be a calibration signal from an acoustical calibrator, but typically more than one calibration signal was recorded on each unit.

The acoustical calibrator is a device that puts out a tone of known frequency and loudness (dB level). Postflight processing of calibration files is used to determine the relationship between digital counts recorded by the PATS and pressure levels from the recorded sonic boom data. This procedure is necessary because of changes in calibration parameters caused by shifts in ambient temperature and pressure.

Noise sources in the test environment, such as wind or the presence of other high speed aircraft, had the potential to cause false triggering of the units. Because of the small amount of memory in each PATS unit, it was necessary to monitor the PATS during testing to avoid using memory for extraneous data.

Two types of PATS were used. The 8-bit model had 8 bits of resolution, while the "16-bit" model had 15 bits of resolution. The additional resolution of the 16-bit units was not necessarily an advantage.

Transducer gain and trigger levels were adjusted to match the flight conditions. These adjustments were not perfected on the 16-bit units until after flight 23. Details about the PATS have been published previously (Stansbery and Stanley, 1989).

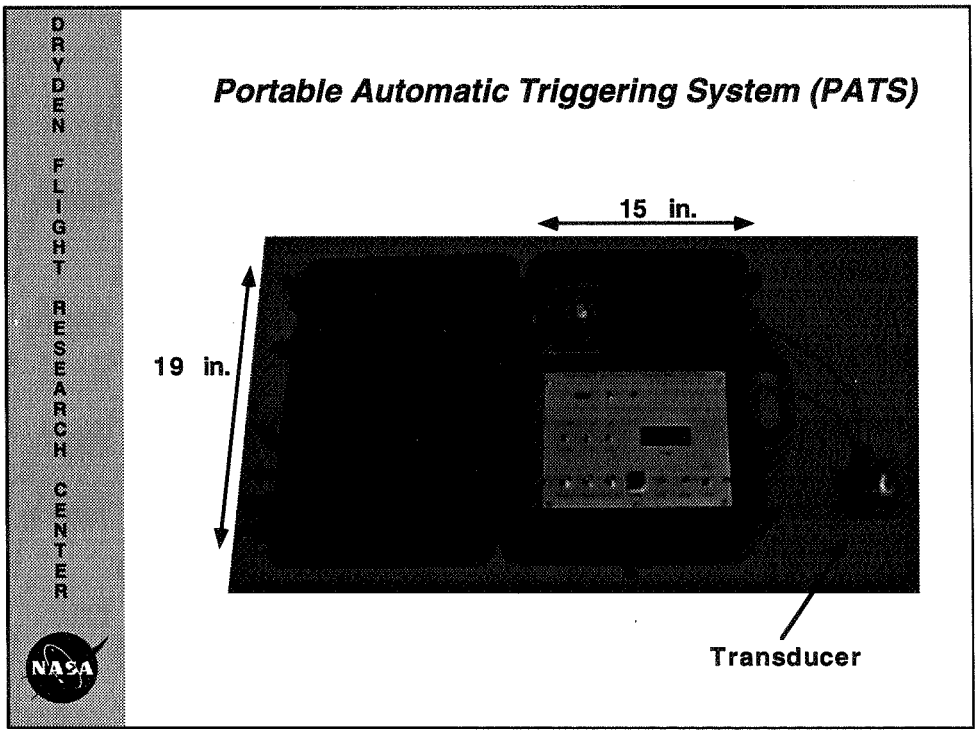

Figure 3

Figure 4 shows the schematic of a prototype device referred to as the SABER. Based on a commercially available single board computer, this device was used to record several ground signatures during the flight program. Such computers have been used in a variety of flight applications (Hamory and Murray, 1994). The SABER was designed as flight hardware, but successful in-flight use has not been demonstrated.

Operation of the SABER is the same as that of the PATS. The SABER "listens" for the rapid pressure rise associated with a sonic boom. It then records and holds that data until the user can download the buffer contents. Interface with the unit is accomplished with a laptop computer. Each signature is tagged with an appropriate time so that a data set can be correlated with the triggering event.

The SABER has a large amount of onboard random access memory (RAM), allowing approximately 50 separate pressure time histories of 2 sec length to be recorded at 10,000 samples/ sec. By comparison, the older PATS could hold 8 time histories of 2 sec length at 8000 samples/sec.

The SABER uses a differential pressure transducer as the sensing element. The sensor side of the transducer is vented directly to the atmosphere. The reference side of the transducer is plumbed to the atmosphere through a tank and line to form an overdamped low-pass filter with a time constant of several seconds. This blocks high-frequency pressure fluctuations (for example, sonic booms) from the transducer reference side while passing low frequency pressure fluctuations (for example, slow atmospheric variations). A low-pass antialiasing filter is also used, so the system acts as a band-pass filter.

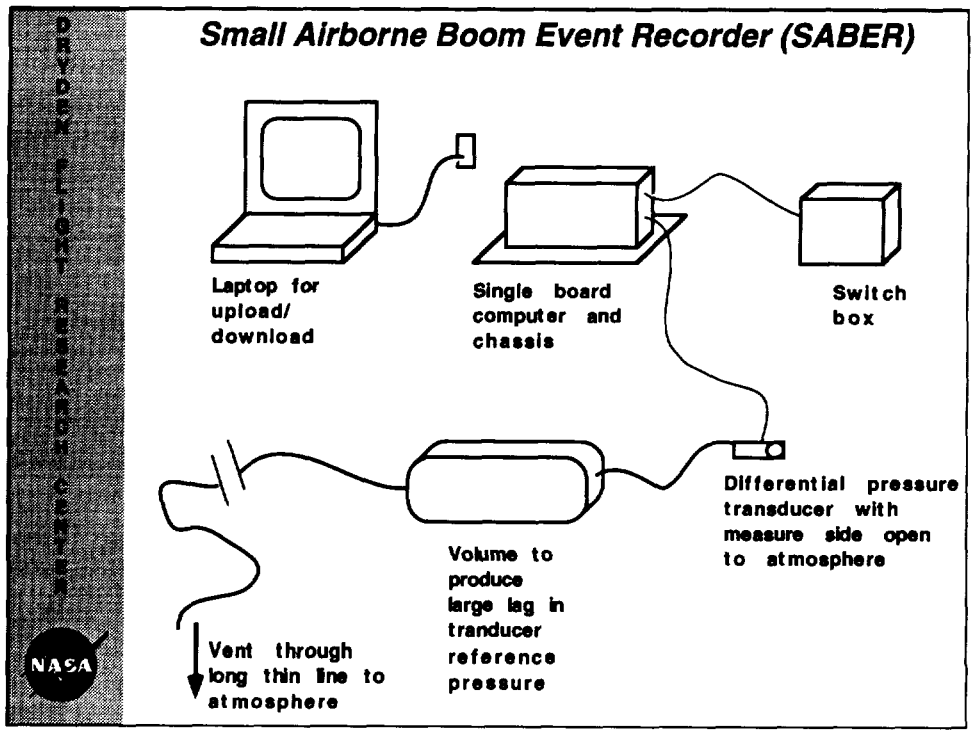

Figure 4

This configuration has two advantages over an absolute-pressure-based sensing system, such as the one used by the PATS. In a quiet atmosphere, the differential pressure is zero, allowing an extremely sensitive (± 21 psf) transducer to be used. Amplifier gain is reduced, thus signal-to-noise ratio is increased. Additionally, insensitivity of the system to slow atmospheric pressure changes allows it to be used on an aircraft at varying altitudes.

The SABER was designed to rely on an in-house calibration of its pressure transducer. While only one set of calibration parameters was used for these tests, the potential exists for the SABER to record transducer temperatures so that appropriate adjustments can be made to compensate for temperature fluctuations. This would be particularly important for large temperature ranges often encountered in flight.

The system allows quick adjustment of signal gain and antialias filter cutoff frequency through the use of its signal processing card. Trigger criteria may be changed at the software level.

Figure 5 shows a picture of the prototype SABER. Development of the package is still underway concerning choices of filter frequencies, optimum reference tank configuration, and triggering criteria.

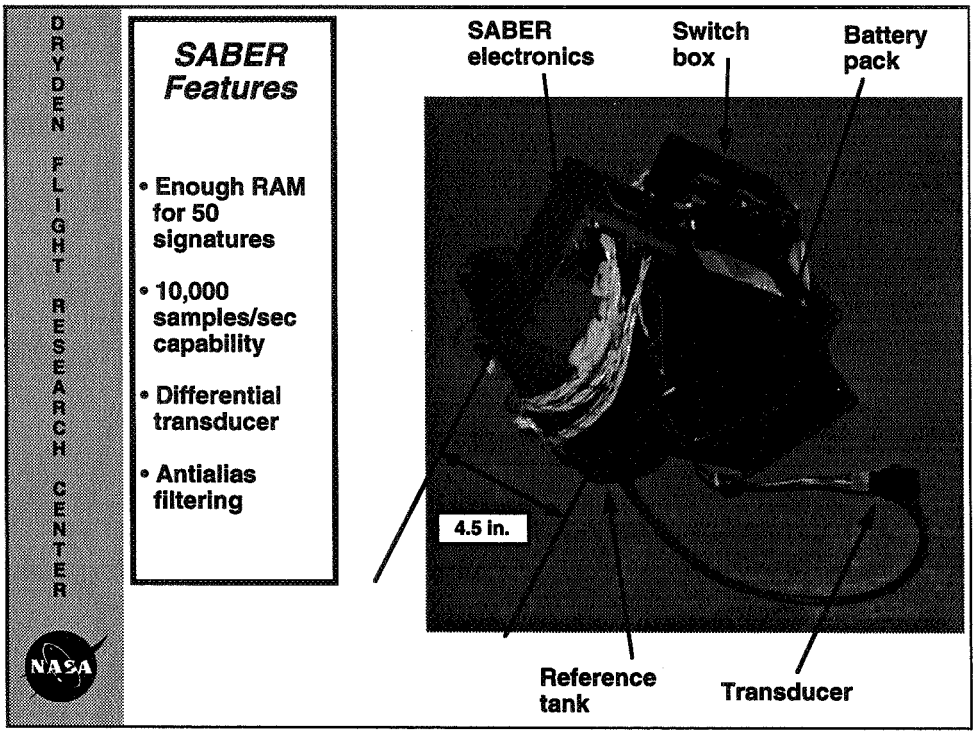

Figure 5

Audio recordings were obtained for most of the sonic boom flights using two MiniDisc recorders (fig. 6). A quarter is shown in the picture to demonstrate system size. The recorder writes to an optical magnetic disc that stores the information digitally. Each MiniDisc holds up to 74 min of audio recording on up to 255 tracks.

The recordings made later in the project are better than earlier efforts. Trial-and-error attempts showed the necessity of using manually controlled record levels set near the lowest level. Two instrumentation microphones were used with each of the two MiniDisc recorders. One was placed at ground level, and the other was elevated on a tripod.

A calibration signal was recorded for each microphone for every test flight to allow future conversion of the audio recordings to pressure levels. The microphones do not have the low-frequency capability of a pressure transducer, but the high-frequency data may be used to complement the transducer data. Listening to these recordings gives a qualitative measure of the loudness of a boom as well as some measure of ambient noise levels caused by wind and other aircraft.

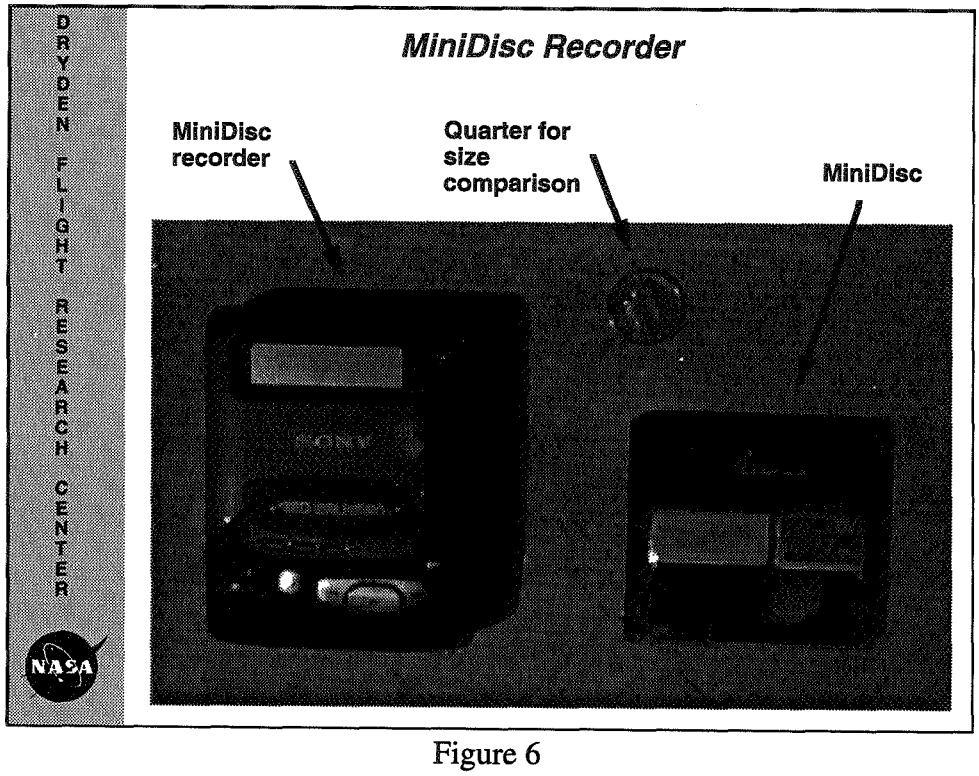

Figure 6

A time history of the pressure level during a sonic boom event contains very high and very low frequency components. Every sensor has its own frequency response. As a result, a recorded sonic boom signature consists of an actual physical boom event in combination with some distortion because of transducer or microphone dynamics. Figure 7 shows a comparison of the dynamic response of the different sonic boom sensors.

The PATS transducer has a sealed reference side. The transducer signal is conditioned by a high-pass filter with a cutoff frequency of approximately 0.3 Hz. The full-scale pressure range for each unit varies, with values of 11 to 16 psf for the 16-bit units. The 8-bit PATS have full-scale values of 6 to 15 psf. The 8-bit units have 2^8 levels of resolution, while the 16-bit units have 2^{15} levels of resolution.

The SABER uses a full-bridge differential pressure transducer with a full-scale range of 42 psf with 2^{12} levels of resolution. The transducer used in the prototype has a frequency response upper limit of approximately 2000 Hz, but the overall system response is forced lower by the antialiasing filter. The antialiasing cutoff frequency may be raised for future tests.

The MiniDisc recorders were connected to two capacitive microphones to record sound levels. The system is designed to capture frequencies of 20 to 20,000 Hz.

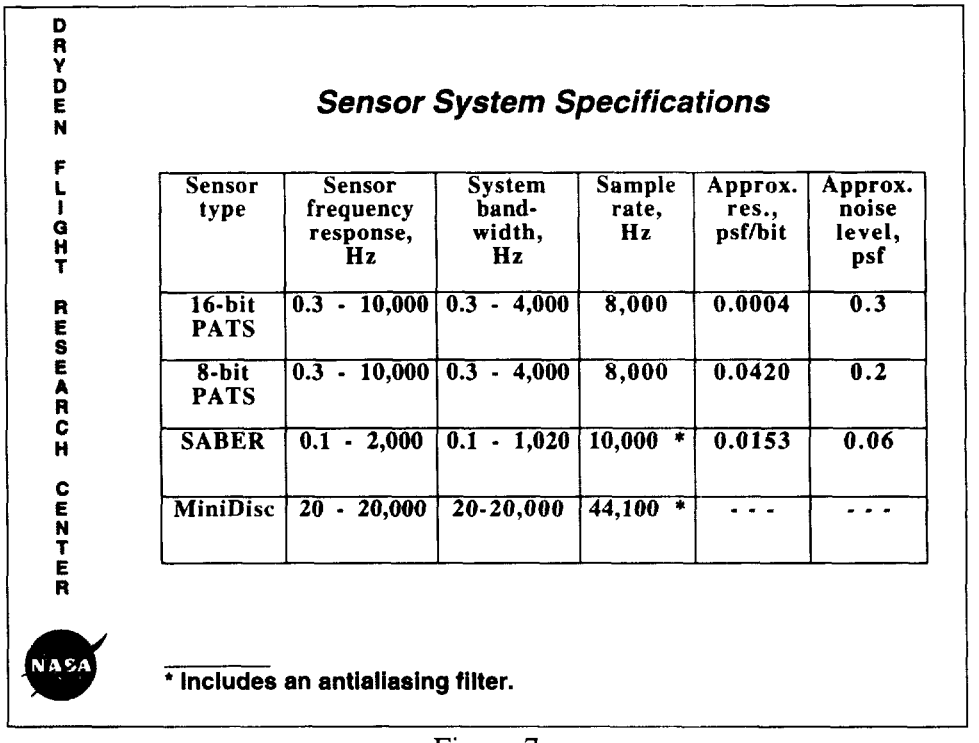

Figure 7

Eight research flights with 19 test points were conducted between February 15, 1995, and April 20, 1995. Figure 8 presents the nominal test conditions and number of ground signatures recorded for each test flight. The rows enclosed by the dark box correspond to flight conditions of high-altitude and low supersonic Mach number, resulting in ground signatures that were so weak that little or no data were captured. An asterisk (*) in the SABER column indicates that the SABER prototype was not deployed for the corresponding flight.

Actual flight conditions are not perfectly steady, so more precise determination of aircraft flight conditions may be obtained by iterative forward throw calculations. Forward throw is the distance from the point where a shock wave is generated (at the aircraft) to the spot where the propagating shock wave intercepts a point of interest (the ground station). Iterative calculations of forward throw for a selected segment of an SR-71 flight should reveal the actual flight conditions that correspond to a given boom event recorded on the ground. These step-wise calculations require weather data that will also be supplied in the data base.

DRYDEN FLIGHT RESEARCH CENTER

NASA

SR-71 Flight Test Matrix

Flight	Pass	Mach number	Altitude, ft	Gross weight, lb	8-bit PATS data sets	16-bit PATS data sets	SABER data set	MiniDisc data sets
23	1	1.25	30 K	110,000	2	3	No	2
	2	1.25	30 K	85,000	2	2	Yes	
24	1	1.25	30 K	110,000	4	6	Yes	2
	2	1.25	30 K	100,000	4	4	Yes	
	3	1.25	30 K	80,000	3	4	Yes	
25	1	1.25	30 K	120,000	3	7	No	5
	2	1.25	30 K	100,000	2	9	No	
	3	1.25	30 K	80,000	2	9	Yes	
26	1	1.50	48 K	95,000	4	8	No	3
	2	1.50	38 K	85,000	4	8	No	
27	1	1.50	48 K	110,000	4	6	No*	4
	2	1.50	48 K	90,000	4	6	No*	
28	1	1.50	48 K	110,000	4	3	Yes	4
	2	1.50	48 K	85,000	4	3	Yes	
29	1	1.25	44 K	110,000	0	0	No	4
	2	1.25	44 K	85,000	0	0	Yes	
30	1	1.25	44 K	110,000	0	0	No	3
	2	1.25	44 K	90,000	1	2	No	
	3	1.25	30 K	75,000	3	6	Yes	
Totals					50	86	9	27

Figure 8

Figure 9 shows a sample time history of altitude, Mach number, and gross weight for flight 28. This time history provides an example of altitude and Mach number variability during a research flight.

At supersonic speeds, the SR-71 aircraft generated numerous shock waves that emanated from major components, such as the bow, canopy, inlets, wings, and vertical tails. The F-16XL probe aircraft was flown behind and below the SR-71 at predetermined vertical separations of up to 8000 ft to measure the changes in pressure across the individual shocks. These measurements characterized the component shocks as well as the rate at which these shocks coalesced into two shock fronts.

The SR-71 and the F-16XL aircraft flew at nearly the same speed while the F-16XL aircraft probed in and out of the shock system. Both aircraft generated shock systems that usually propagated to ground level. The two shock systems rarely interfered with each other, so the ground-based sensors often recorded separate boom signatures from both aircraft.

The long supersonic endurance capability of the SR-71 aircraft required the F-16XL aircraft to refuel between test periods. Refueling took place while the SR-71 aircraft flew at subsonic speeds during the period noted in figure 9.

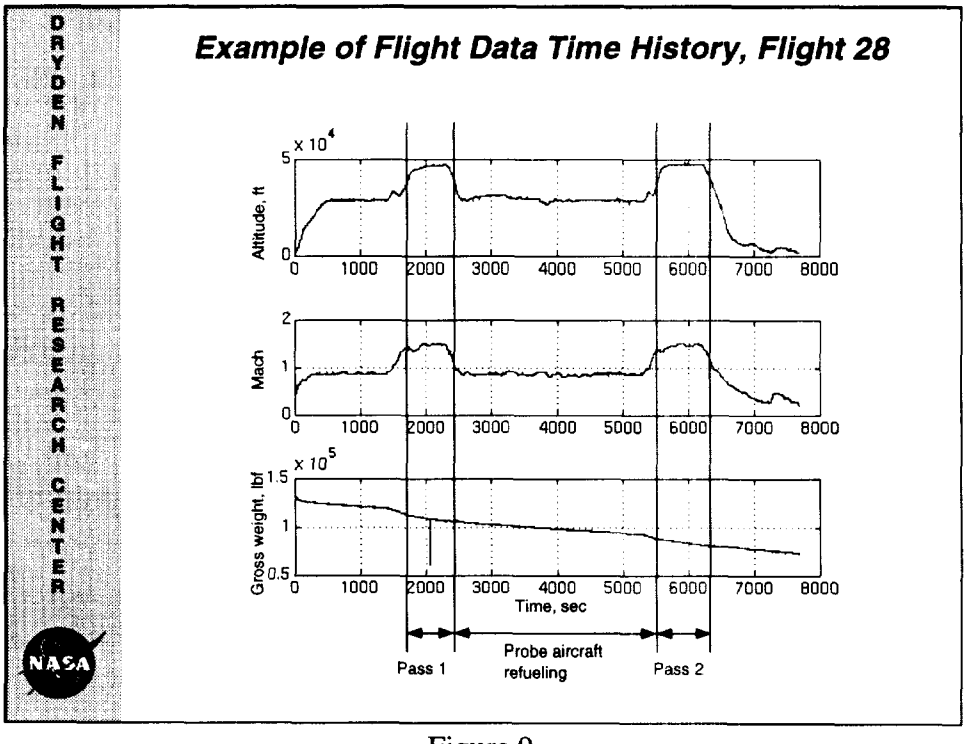

Figure 9

Ground recording equipment was separated into three stations. Station locations were determined with a differential GPS before the flight. The GPS data collected during test flights allow calculation of distances from the ground stations to the aircraft ground track. Figure 10 shows SR-71 GPS data from flight 28 converted to north and east displacement from the base ground station.

The base station was located as close to the predicted ground track of the SR-71 aircraft as possible. Two more stations were located approximately 2 miles north and south of the ground track, depending on site accessibility. This arrangement was chosen so that the SR-71 ground track would come very close to one of the stations even if there were a slight deviation from the predicted flightpath.

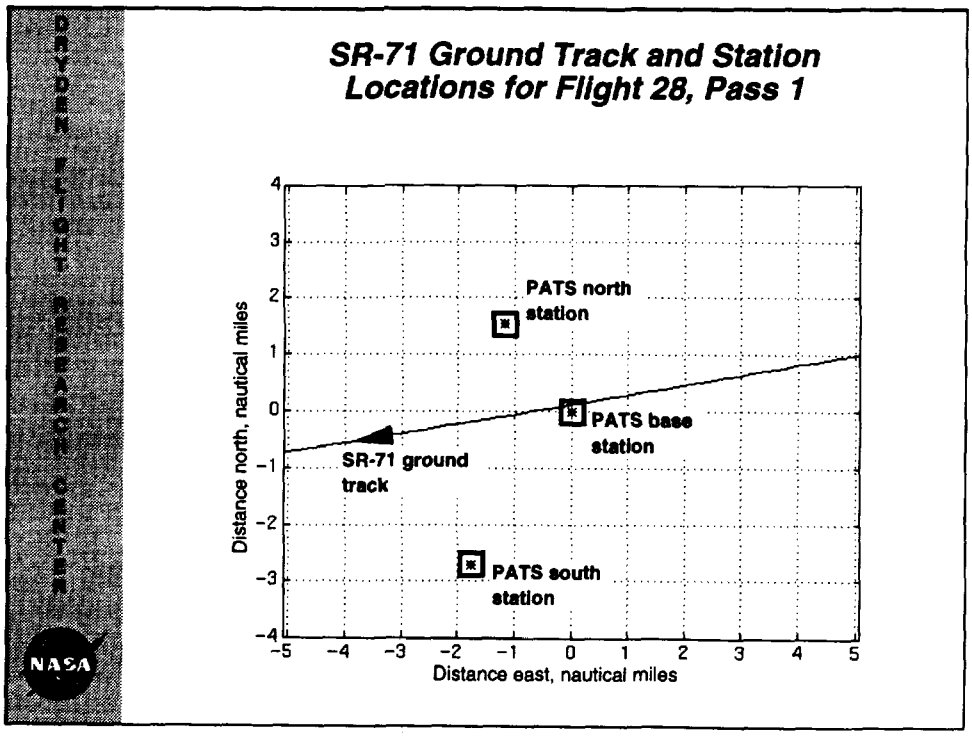

Figure 10

Figure 11 shows a typical distribution of the PATS units. Each ground station included an array of individual pressure sensors, with the PATS units placed approximately 100 ft from a central point. Four of the 8-bit units and 10 of the 16-bit units were used. At least one of the 8-bit PATS was placed at each of the stations. Typically six PATS were placed at the base station, and four were placed at the north and south stations.

Some sensors did not collect data from each pass because of operational problems, such as incorrect trigger levels, operator errors, or unit malfunctions. Documentation will be released with the data sets showing which units captured data successfully on any given flight.

MiniDisc recorders were also used at two of the ground stations to provide audio recordings of the boom events. The SABER prototype was located at the base station next to one of the PATS units.

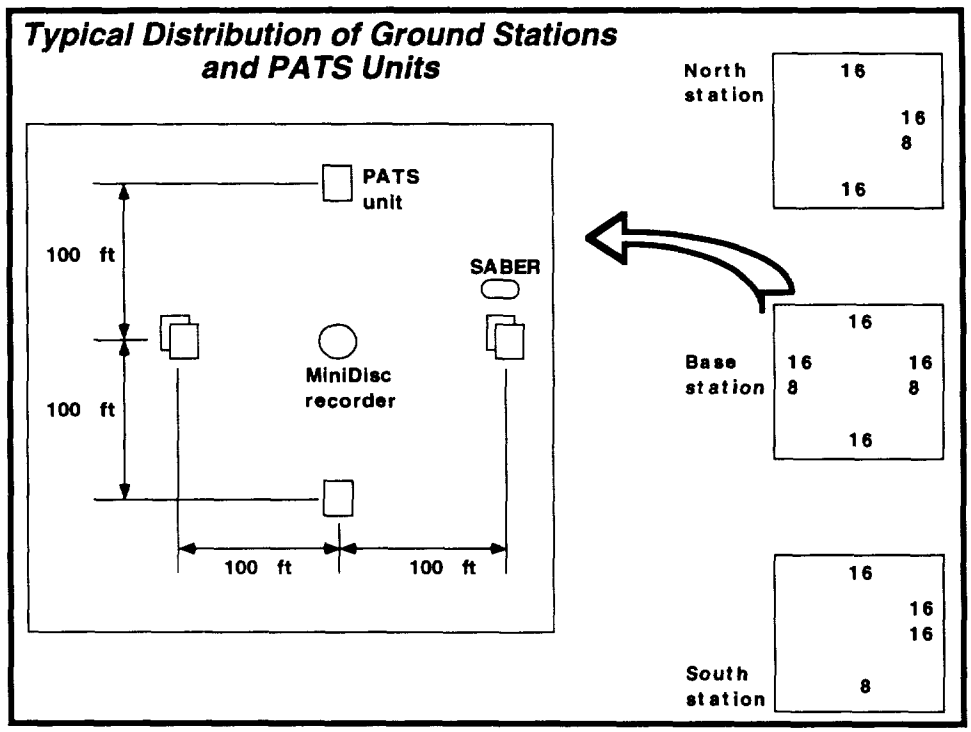

Figure 11

An N-wave boom shape forms when multiple shocks emanating from various parts of a supersonic aircraft coalesce into two large shock fronts. This process results from differences in the speed of sound between the various component shocks. Shocks in the middle of the signature catch up to and merge with the leading shock, resulting in two distinct shock fronts.

Near-field usually refers to regions close to the shock-generating aircraft where the individual component shocks have not yet coalesced. Far-field refers to regions at a great enough distance from the aircraft that the shock system has reached a coalesced condition.

The classic far-field, N-wave boom signature was recorded for many of the flight conditions in this study. Figure 12 shows an example of such a signature from flight 28. These data are from an 8-bit PATS unit with a fairly small noise level; however, the resolution is low, resulting in the stair-step appearance of the data.

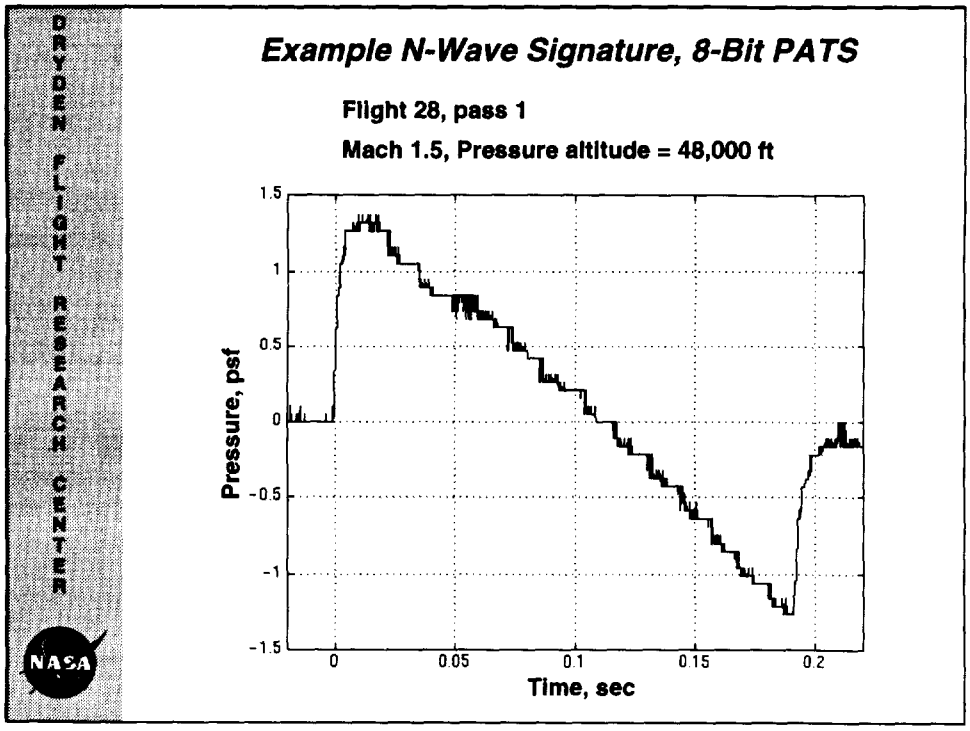

Figure 12

Figure 13 shows a boom signature captured from the same pass as figure 12. This signal came from a 16-bit unit located adjacent to the 8-bit unit that recorded the signature in figure 12.

The additional resolution of the 16-bit units over the older 8-bit units did not prove to be a large improvement because the new units had no corresponding reduction in signal noise levels. The high noise levels may have resulted from large gain values needed for the sealed pressure transducers used in the PATS.

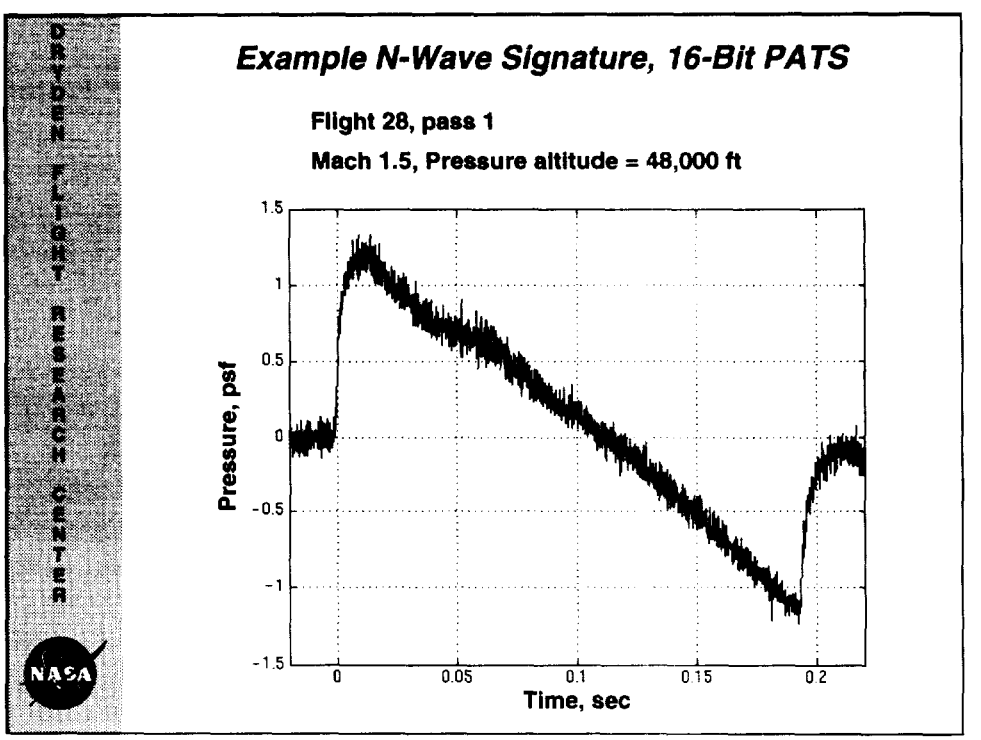

Figure 13

Figure 14 compares sonic boom signatures recorded at the north, base, and south stations for pass 2 of flight 28. These stations were each located close enough to the SR-71 ground track to record similar boom signatures. There is good agreement in the maximum overpressure, boom duration, and wave shape recorded by different PATS units. This agreement was aided by the calm weather conditions present for flight 28.

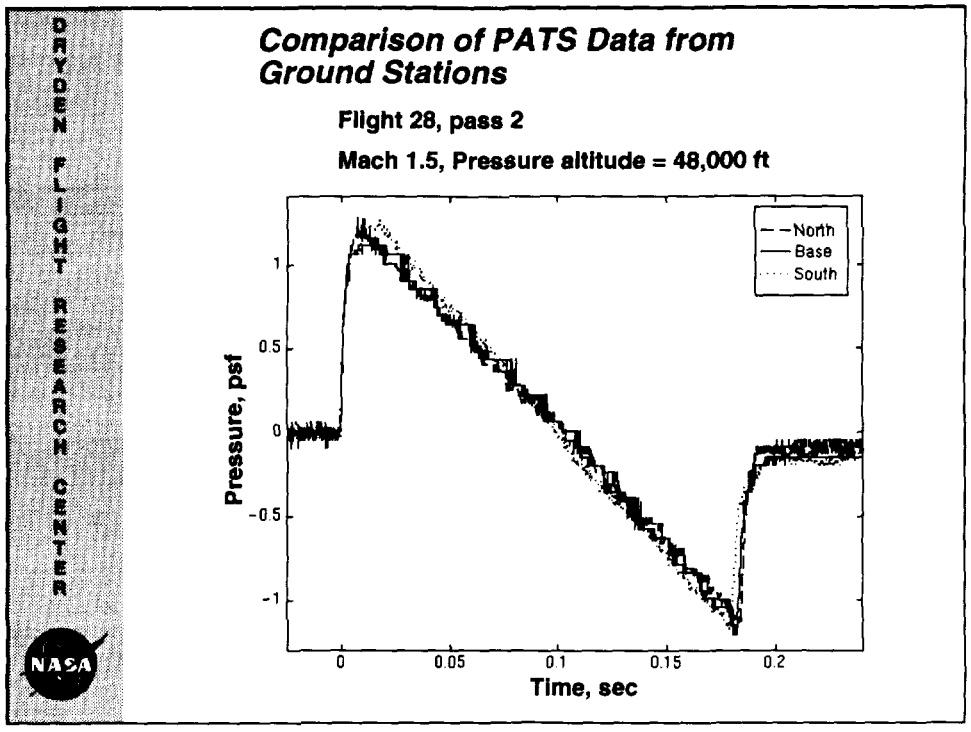

Figure 14

Figure 15 shows a comparison of data sets from the SABER and an 8-bit PATS unit. Excellent agreement is seen in the overpressure, rise time, and other features of the signature. Such comparisons have been used to verify correct operation of the new SABER prototype. The close agreement increased confidence in the results obtained with the PATS units.

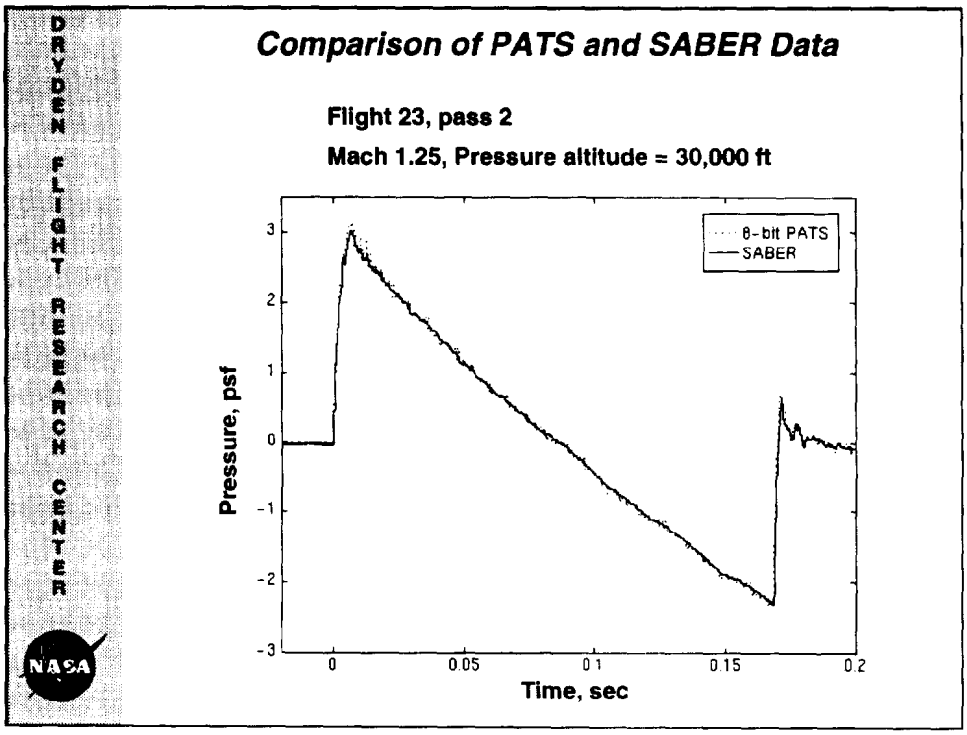

Figure 15

Figure 16 provides an example of the trend in boom signature shape with variations in SR-71 gross weight. These data sets show three passes at consecutively lower gross weights and, therefore, lower lift coefficients. A small peaking effect from the first pass may have somewhat exaggerated the change in maximum overpressure, but the general tendency was reduced maximum overpressure and boom length as the weight decreased with each successive overflight.

Other factors, such as atmospheric turbulence and Mach number, affect boom characteristics. For this reason, gross weight effects could not be isolated in this test. These gross weight effects would, however, be expected because lift magnitude is a significant factor in determining boom characteristics (Darden, et. al., 1989).

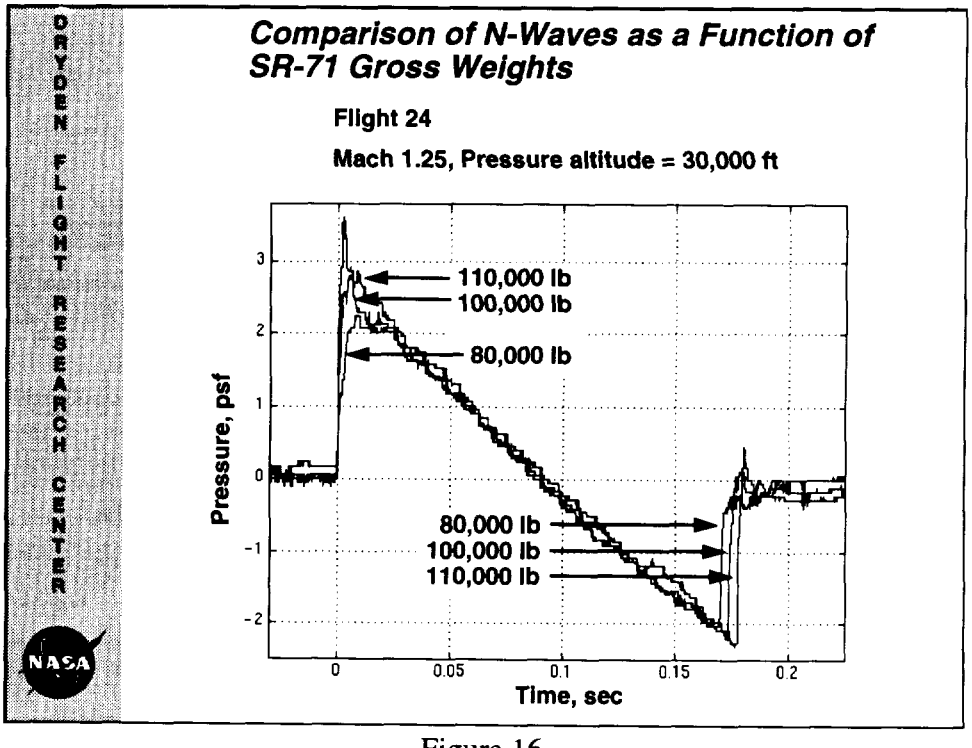

Figure 16

Various distortions caused by focusing effects and atmospheric turbulence are known to occur to propagating shock fronts (Lee and Downing, 1991). This focusing can result in a U-shaped boom with relatively high peak overpressures in areas where the foci exist. Several of these types of signatures were captured during flight testing (fig. 17).

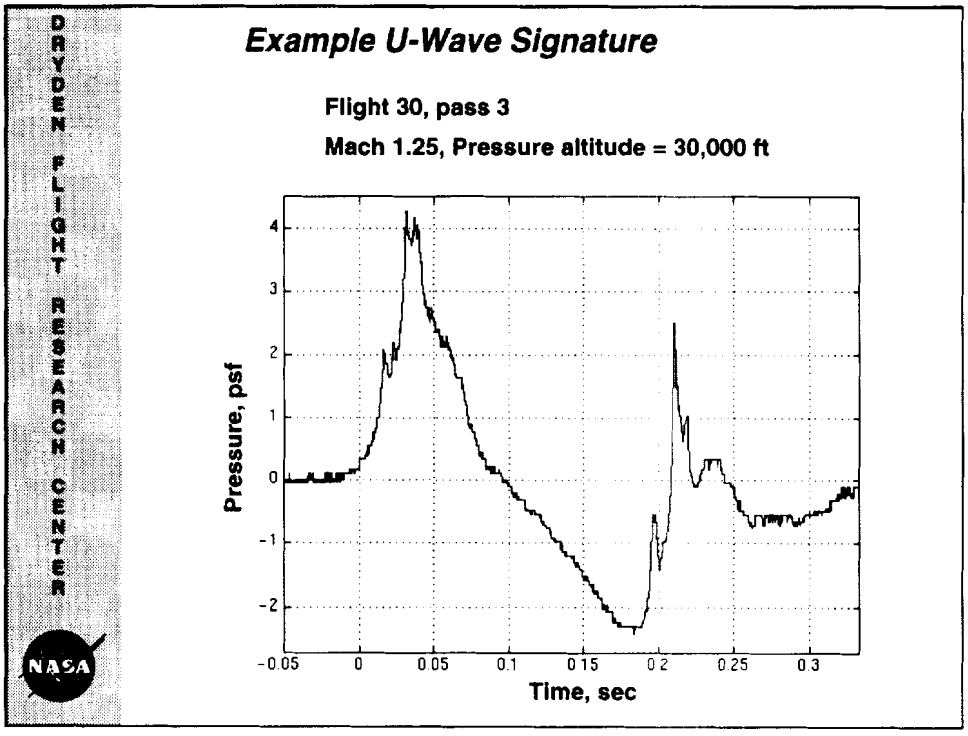

Figure 17

A total of 172 sonic boom ground signatures were captured during eight sonic boom research flights by an SR-71 aircraft and are being compiled into a data base (fig. 18). All three sensor types successfully captured sonic boom ground signatures. Similar results were obtained with both the 8- and 16-bit PATS units. The SABER is a promising device that shows potential as a new sonic boom recording system. Comparisons of pressure time histories recorded by the SABER and the PATS showed excellent agreement. Further development of the SABER is underway. MiniDisc recordings offer a qualitative analysis and expanded high-frequency content for most of the boom events.

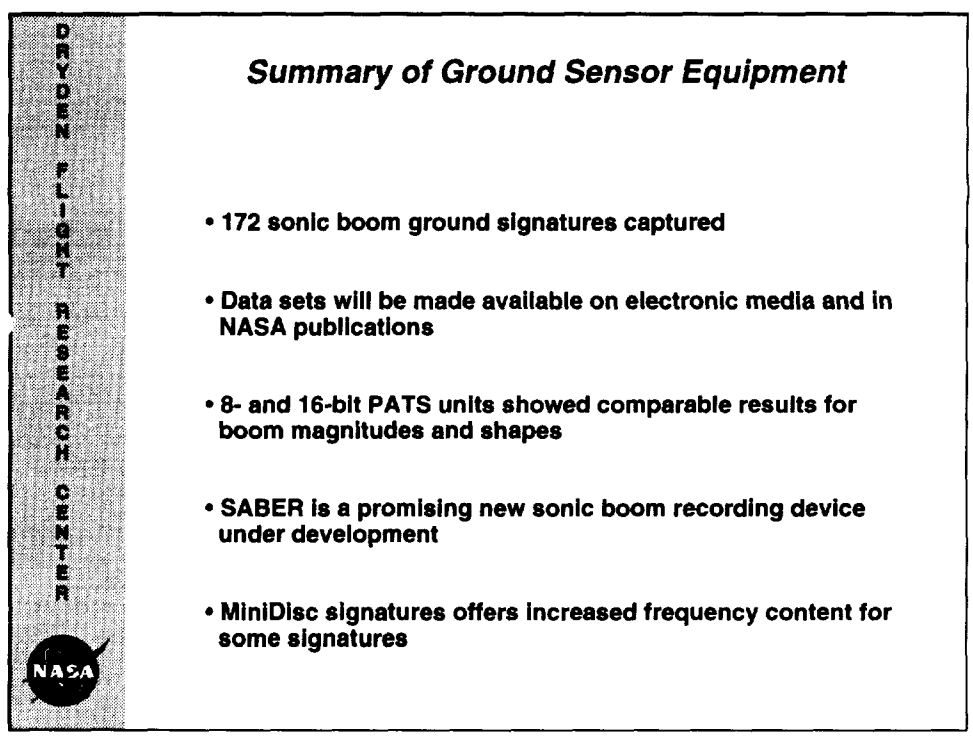

Figure 18

Ground signature trends are summarized in figure 19. The dominant feature of the boom signatures was the well-known N-wave shape which occurred in a number of variations. Results included cases of normal, peaked, and rounded N-waves similar to those described by Maglieri, et. al. (1972). These variations were most likely a result of atmospheric turbulence or wind shear creating distortions in the wave shape. Many deviations from an N-wave are associated with shock propagation through a turbulent atmosphere (Lipkens and Blanc-Benon, 1994). Ground measurements are particularly likely to include such distortions because of the turbulent nature of the lowest levels of the atmosphere.

Focusing conditions were reached at the ground stations for several flight conditions, resulting in U-shaped booms. The peak overpressures for some of these cases were relatively large in comparison to N-waves recorded from other flight conditions. A trend toward shorter boom event durations and lower peak overpressures was observed with decreasing gross weight.

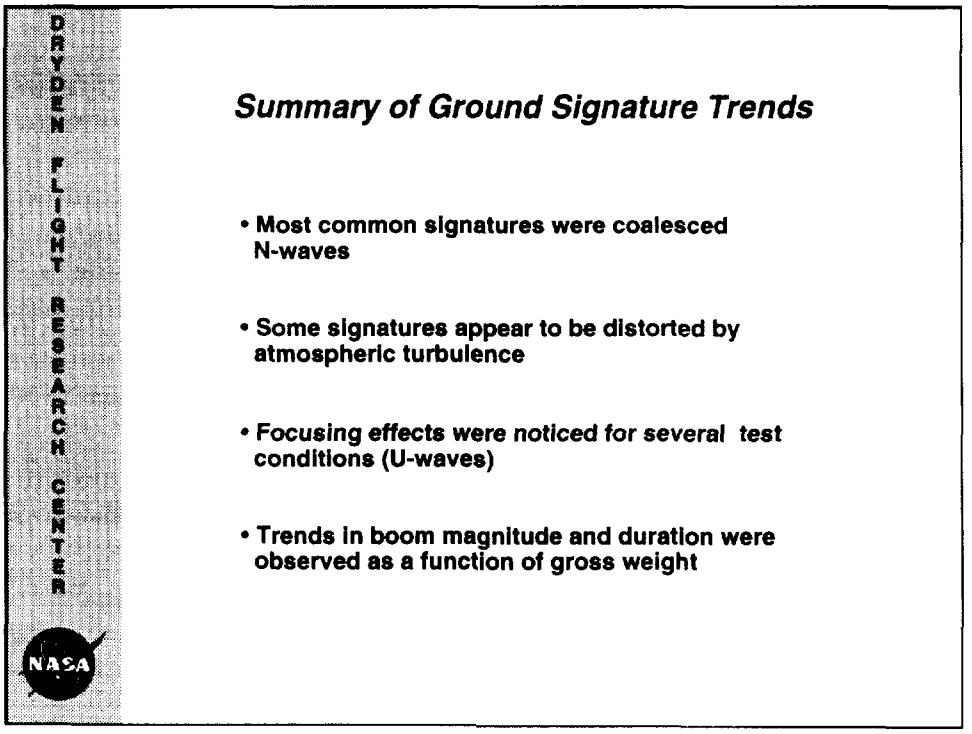

Figure 19

REFERENCES

Darden, C.M.; Clemans, A.P., Hayes, W.D.; George, A.R.; and Pierce, A.D.: *Status of Sonic Boom Methodology an Understanding*, NASA CP 3027, 1988.

Haering, Edward A., Jr.; Ehernberger, L. J.; and Whitmore, Stephen A.: *Preliminary Airborne Measurements for the SR-71 Sonic Boom Propagation Experiment*, NASA TM-104307, 1995.

Hamory, P.J.; and Murray, J.E.: "Flight Experience with Lightweight, Low-Power Miniaturized Instrumentation Systems," *J. of Aircraft*, vol. 31, no.5, Sept-Oct 1994, pp. 1016-1021.

Lee, R.A.; and Downing, J.M.: *Sonic Booms Produced by United States Air Force and United Sates Navy Aircraft: Measured Data*, USAF AL-TR-1991-0099, Jan 1991.

Lipkens, B.; and Blanc-Benon, P.: *Numerical Model for the Weakly Nonlinear Propagation of Sound Through Turbulence*, High-Speed Research: 1994 Sonic Boom Workshop — Atmospheric Propagation and Acceptability Studies, NASA CP 3279, Oct 1994, pp.61-80.

Maglieri, J.D.; Huckel, V.; and Henderson, H.R.: *Sonic Boom Measurements for SR-71 Aircraft Operating at Mach Numbers to 3.0 and Altitudes to 24384 Meters*, NASA TN D-6823, 1972.

Stansbery, E.G.; and Stanley, J.F.: *Descent Sonic Boom Measurements for STS-26, Including a Mach 23 Measurement*, JSC-23579, April 1989.

GROUND-RECORDED SONIC BOOM SIGNATURES OF F-18 AIRCRAFT IN FORMATION FLIGHT

Catherine M. Bahm and Edward A. Haering, Jr.
NASA Dryden Flight Research Center
Edwards, California

ABSTRACT

Two F-18 aircraft were flown, one above the other, in two formations, in order for the shock systems of the two aircraft to merge and propagate to the ground. The first formation had the canopy of the lower F-18 in the tail shock of the upper F-18 (called tail-canopy). The second formation had the canopy of the lower F-18 in the inlet shock of the upper F-18 (called inlet-canopy). The flight conditions were Mach 1.22 and an altitude of 23,500 ft . An array of five sonic boom recorders was used on the ground to record the sonic boom signatures. This paper describes the flight test technique and the ground level sonic boom signatures. The tail-canopy formation resulted in two, separated, N-wave signatures. Such signatures probably resulted from aircraft positioning error. The inlet-canopy formation yielded a single modified signature; two recorders measured an approximate flattop signature. Loudness calculations indicated that the single inlet-canopy signatures were quieter than the two, separated tail-canopy signatures. Signficant loudness occurs after a sonic boom signature. Such loudness probably comes from the aircraft engines.

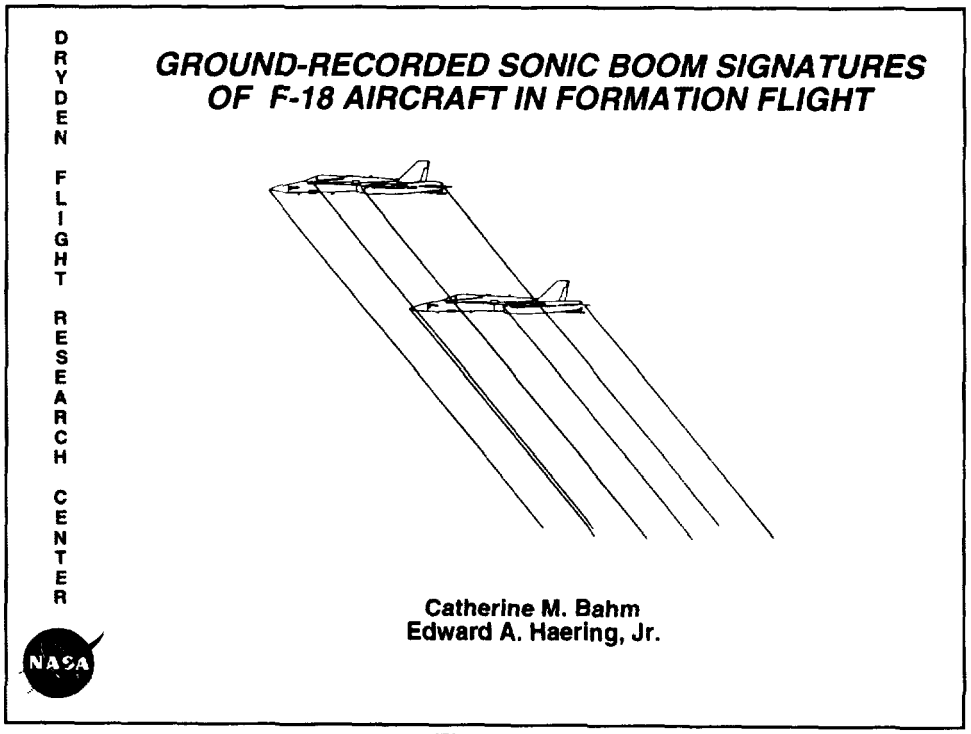

Figure 1

INTRODUCTION

When an aircraft travels supersonically through the air, shockwaves form at multiple components on the aircraft. As these shockwaves travel through the atmosphere, they typically coalesce to become an N-wave. An N-wave is characterized by a sharp rise to maximum overpressure (bow shock), a linear decrease to the maximum underpressure, and a sharp rise back to ambient pressure (tail shock). These sharp pressure rises are heard as sonic booms. The public generally responds negatively to sonic booms. This response is a concern in developing the High Speed Civil Transport, HSCT. Sheperd and Sullivan (1991) showed that minimizing the maximum overpressure and increasing the bow shock rise time produces less objectionable booms. Research is underway on techniques for modifying the sonic boom signatures to produce less objectionable booms (Mack and Darden, 1980).

The sonic boom signature of an aircraft can be modified through careful design of the distribution of volume along its length; however, modifying the signature near the aircraft does not ensure that the signature will remain modified to the ground. Whether or not a modified signature remains modified to the ground can only be verified through a flight test with propagation through a real atmosphere. An existing aircraft could have its volume distribution modified and then be flight tested but at a significant cost for the modification. A low-cost flight test approach was proposed which would use two SR-71 aircraft flying in formation, one above the other, to produce modified signatures through interaction of the two shock wave systems. The combined size of two SR-71 aircraft would approximate the size of an HSCT.

To assess the feasibility of such an experiment with two SR-71 aircraft, a precursor flight using two F-18 aircraft was flown on May 24, 1994, at the National Aeronautics and Space Administration, Dryden Flight Research Center, Edwards, California. This flight had two objectives. The first objective was to evaluate this formation aircraft flight test technique for two SR-71 aircraft. The second objective was to measure and evaluate the sonic boom signature characteristics from the merged shock waves.

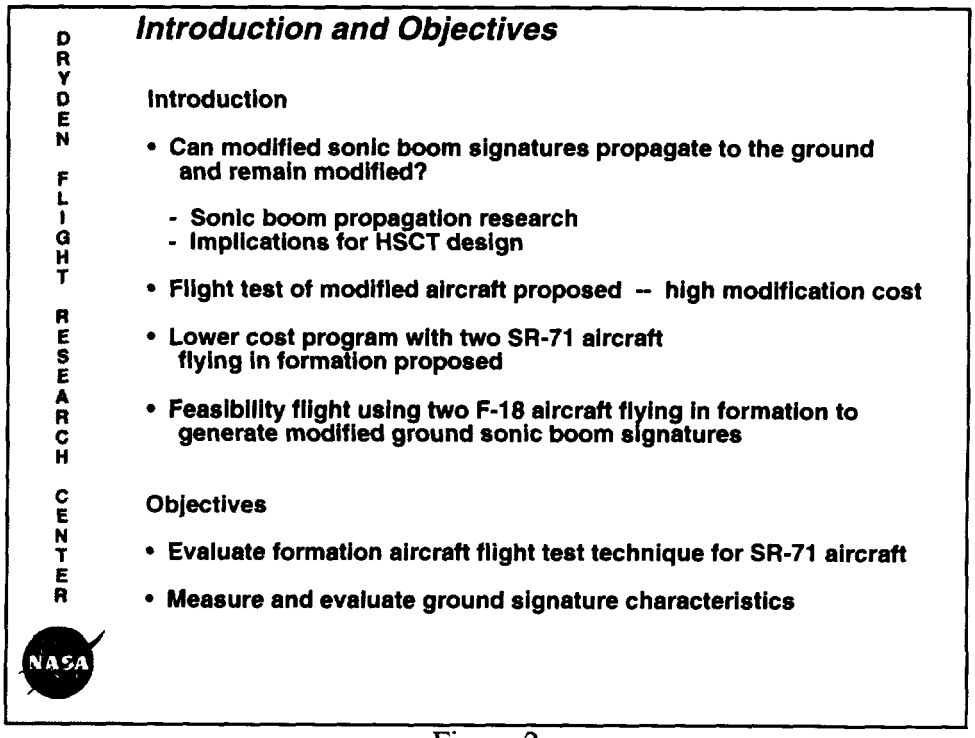

Figure 2

This presentation describes the flight test technique used and the recorded ground-level sonic boom signatures. Loudness of these sonic booms was calculated and is presented here.

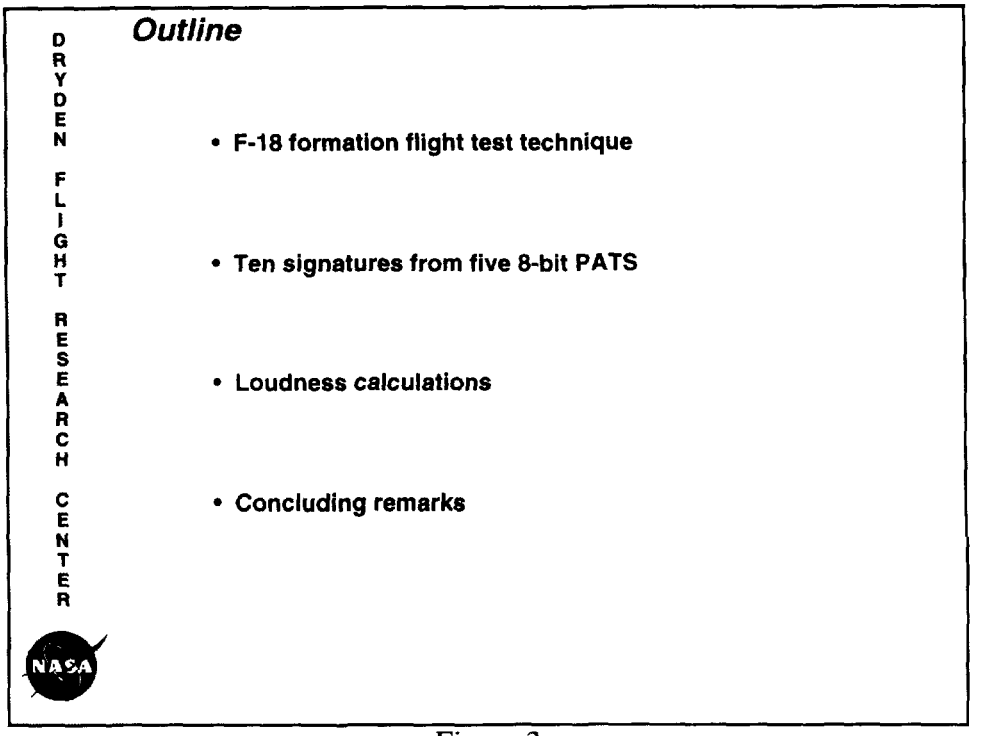

Figure 3

FLIGHT TEST TECHNIQUE

The following subsections describe the flight test technique. This description includes how the aircraft were positioned relative to each other, the sonic boom recorder array, and the aircraft flight conditions.

Aircraft Positioning

Two F-18 aircraft were flown in formation, one underneath the other, so their shock waves would interact. Two passes of the F-18 aircraft were flown over a ground array of sonic boom recorders. For the first pass, pilot A positioned the canopy of the lower F-18 aircraft in what was thought to be the tail shock of the upper F-18 (tail-canopy). Figure 4 shows this formation. Pilot A used the engine noise of the upper aircraft to position the lower aircraft. When the lower aircraft would creep forward of the desired location, the engine noise of the upper aircraft would abruptly stop. It was thought that this abrupt stop to the engine noise was caused by the tail shock, so pilot A remained at the division between hearing and not hearing the engine noise.

For the second pass, the lower F-18 aircraft was positioned so that its canopy was in the inlet shock of the upper F-18 (inlet-canopy) (fig. 4). Pilot A could see the inlet shock and used this view as a positioning cue.

Pilot A commented that the lower aircraft was positioned at approximately one body length (56 ft) and centered below the lead F-18 aircraft for both passes. This pilot also noted that use of such cues allowed the aircraft to remain within ±10 ft longitudinally of the desired location.

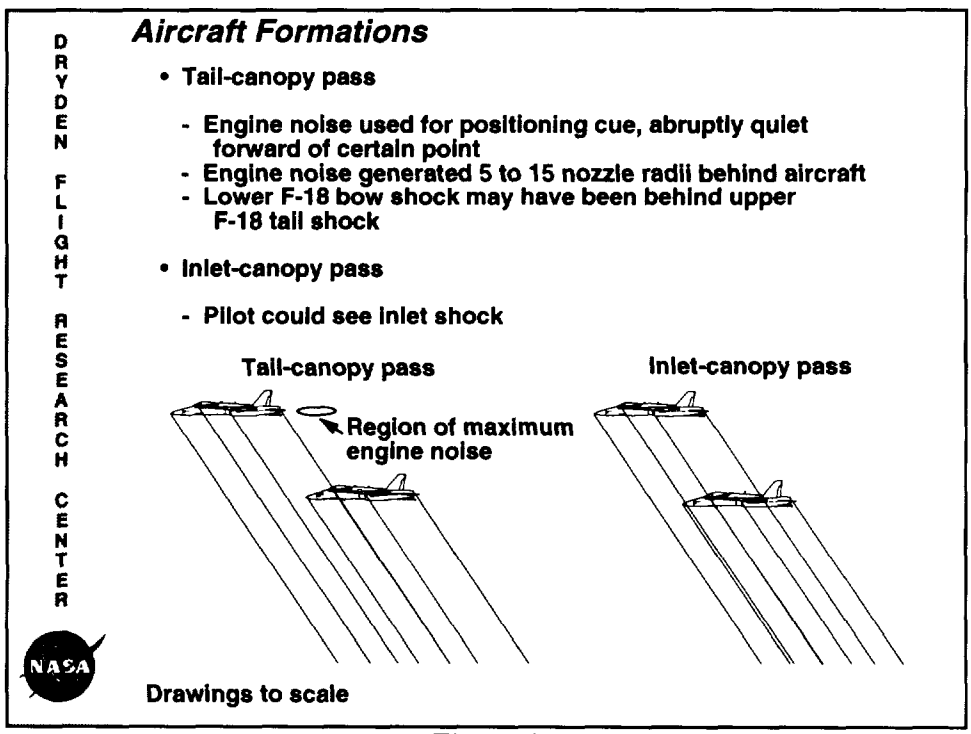

Figure 4

After the flight, it was realized that the region of maximum noise from a jet engine in afterburner is about 5 to 15 nozzle radii behind the engine, and the noise rapidly decreases forward of this point (fig. 4) (Tam, 1991). The engine noise cue may be inappropriate for locating the tail shock of an aircraft. As a result,the lower F-18 aircraft could have been positioned too far aft on the tail-canopy pass for the shock waves of the two aircraft to combine.

Both aircraft were tracked by separate AN/FPS-16 radars (Haering and Whitmore, 1995). The upper F-18 aircraft had a radar beacon which gives accurate ground-based radar tracking. The lower F-18 aircraft did not have a beacon. This aircraft was skin tracked, which provides greatly reduced accuracy. Although the flight conditions and location of the upper F-18 could be accurately determined, the radar data quality from the lower F-18 was insufficient to measure relative aircraft separation. As a result, only pilot observations were used to indicate relative separation. Differentially corrected carrier phase Global Positioning System, GPS, data could be used on a future test of this type to accurately determine the relative aircraft separation (Haering, Ehernberger, and Whitmore, 1995).

The pilot of the upper F-18 aircraft held airspeed and altitude as steady as possible and could not see the lower F-18 aircraft. The pilot of the lower aircraft looked up at the upper F-18 aircraft to maintain a safe separation. Similar to most fighter aircraft, an F-18 aircraft has a bubble canopy that gives excellent visibility in multiple directions. By comparison, the small windows to the front and sides of an SR-71 aircraft provide the pilot with no upward visibility. This aircraft is also large and relatively slow to respond, which makes the formation flying task difficult. After the flight of the two F-18 aircraft, pilot A stated that flying such a mission with two SR-71 aircraft would be extremely difficult because of its reduced visibility and maneuverability.

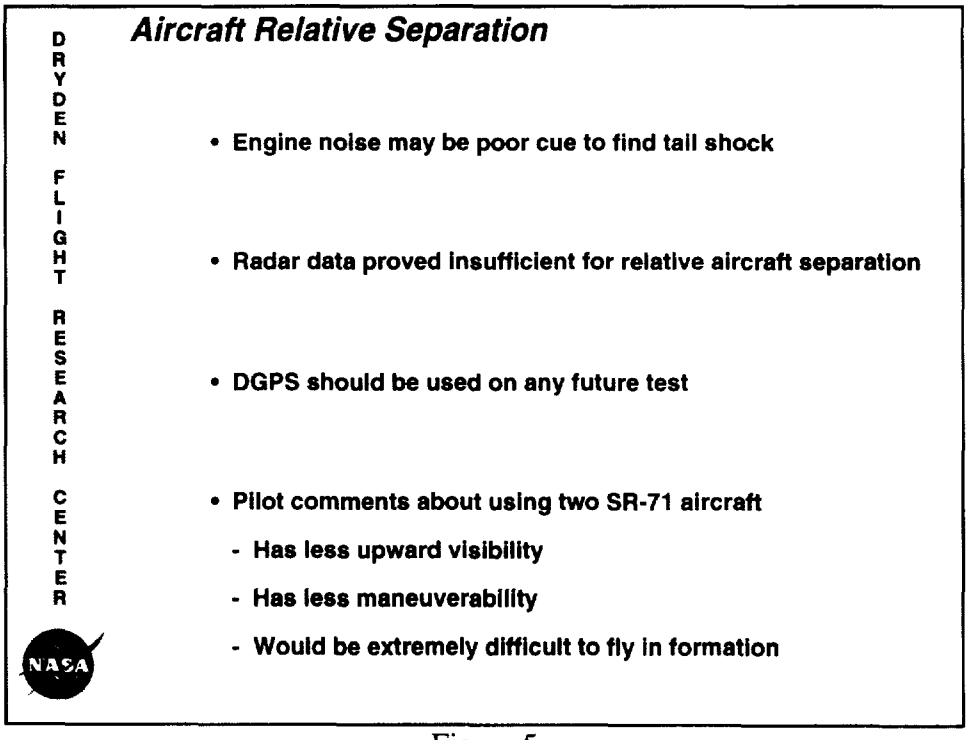

Figure 5

Sonic Boom Recorder Array

A ground array consisting of five sonic boom pressure recorders provided the signature data for this experiment. These recorders were placed along a 2-mile line with approximately one-half mile between each recorder. Traveling at Mach 1.22, the aircraft crossed the recorders at approximately 2-sec intervals.

The sonic boom signatures were recorded using the 8-bit PATS, Portable Automated Triggering System (Norris, 1995). These PATS were set to trigger on pressure fluctuations greater than approximately 0.3 psf, and their full-scale range varied from ±4 to ±13 psf. Because these recorders are 8-bit systems, their resolutions were from 0.03 to 0.10 psf. Each PATS recorded two sonic boom events and two calibration signals.

Aircraft Flight Conditions

A prediction method was used to calculate the sonic boom generation point for each sonic boom recorder (Carlson, 1978). Table 1 lists the results of this method. Figure 6 shows the flightpaths, the location of the five PATS recorders, and their corresponding generation points. The aircraft flew about 3 miles north of the recorders for the tail-canopy pass and almost directly over the recorders for the inlet-canopy pass.

The aircraft flight conditions at the generation points were determined using the ground-based radar data of the upper F-18 aircraft (Haering and Whitmore, 1995) and an atmospheric analysis (Ehernberger, et. al., 1992). The aircraft flight conditions during the tail-canopy pass were Mach 1.22 at an altitude of 23,600 ft, and the inlet-canopy pass flight conditions were Mach 1.22 and an altitude of 23,300 ft.

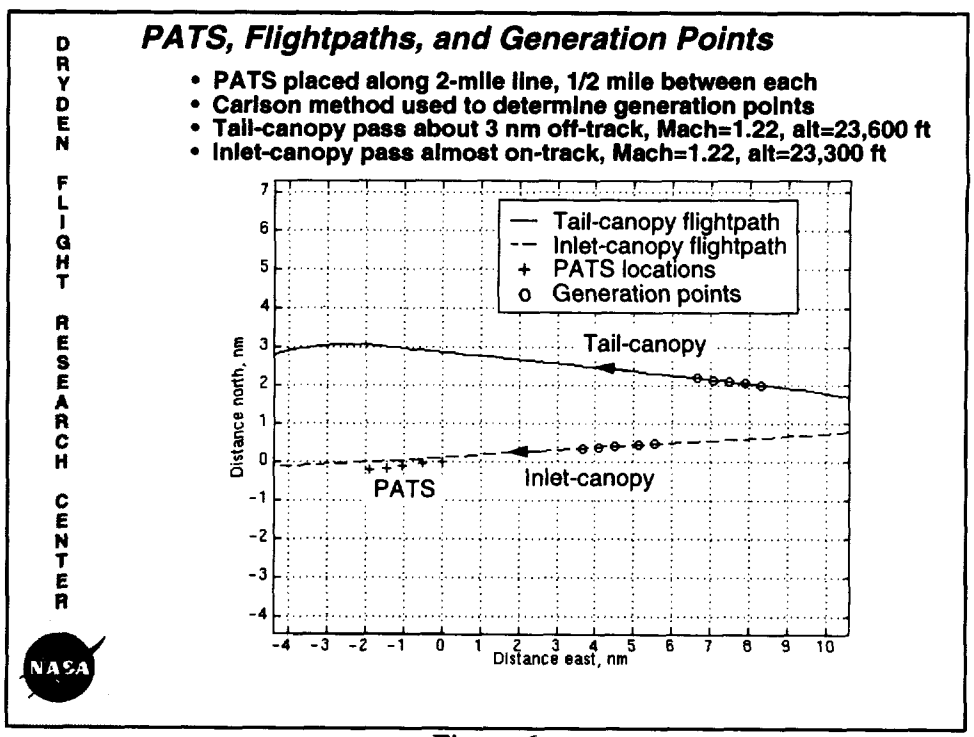

Figure 6

Results of Carlson generation point prediction.

	Tail-canopy pass		Inlet-canopy pass	
PATS number	Distance, ft	Delta time, sec	Distance, ft	Delta time, sec
5	50,400	53.2	33,597	38.5
8	51,391	54.9	33,554	39.4
3	51,758	53.5	33,661	37.8
6	52,879	56.6	34,531	39.7
9	53,162	56.6	33,716	38.9
mean	51,918	54.9	33,812	38.8

SONIC BOOM SIGNATURES

The recorded sonic boom signatures from the tail-canopy pass and the inlet-canopy pass are discussed next. Atmospheric effects are evident in the signatures. A single N-wave signature is compared to a modified signature. Lastly, the sonic boom trailer is described.

Tail-Canopy Pass

Figure 7a shows the sonic booms that were recorded in the tail-canopy pass. This plot shows the overpressure as a function of time for each of the sonic boom signatures and as a function of distance from the first PATS recorder. The signature at zero distance was the first signature recorded. The number by each signature denotes the PATS number. Figures 7b through 7f show individual plots of each of the tail-canopy signatures. Figure 7b shows the signature recorded by the first recorder, PATS 5, which has the lowest resolution, 0.10 psf/bit. Figures 7c, 7d, 7e, and 7f are the signatures recorded by PATS 8, 3, 6, and 9, respectively.

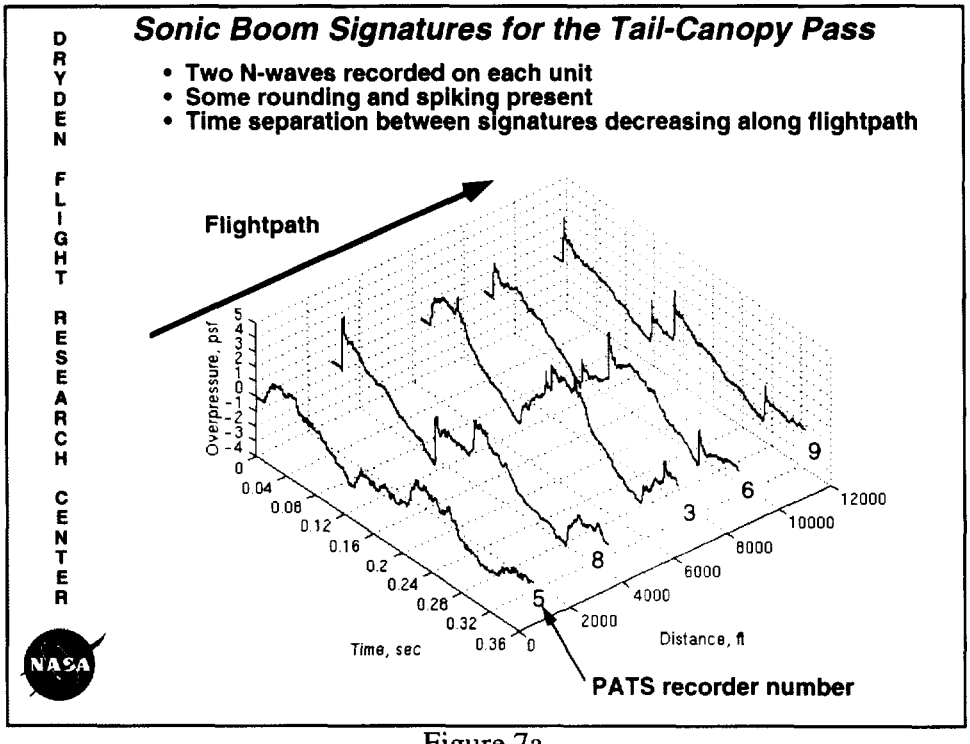

Figure 7a

It was hoped that a modified N-wave would be recorded on the ground; however, the signatures recorded for the tail-canopy pass contained two, separated N-waves. One reason these sonic boom signatures did not combine might be that the lower F-18 was too far aft because of the engine noise position mentioned earlier. In addition, because the lower F-18 aircraft was positioned underneath the upper F-18, the shock structure of the two aircraft would only be combined in a small corridor directly below the aircraft and possibly not 3 miles laterally off track where the recorders were located. Lastly, the time separation between the two signatures appears to decrease with each recording, possibly because the lower F-18 aircraft was creeping forward relative to the upper F-18 aircraft.

An anomaly was found while studying the recorded signatures in figure 7d. Normally spiking caused by turbulence occurs as the pressure rises to the maximum overpressure. In the case of the signature in figure 7d, spiking occurred about 0.03 sec after the initial rise to maximum overpressure, which is a rare occurrence. This rare, delayed spiking also occurred on a signature from an F-4 aircraft (Lee and Downing, 1991).

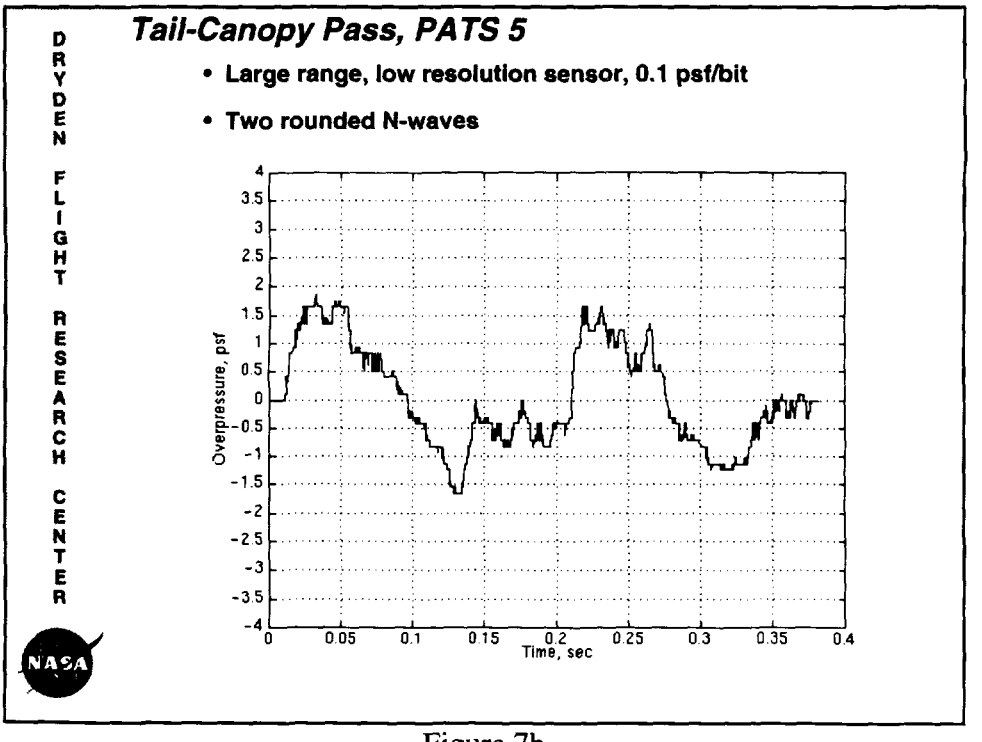

Figure 7b

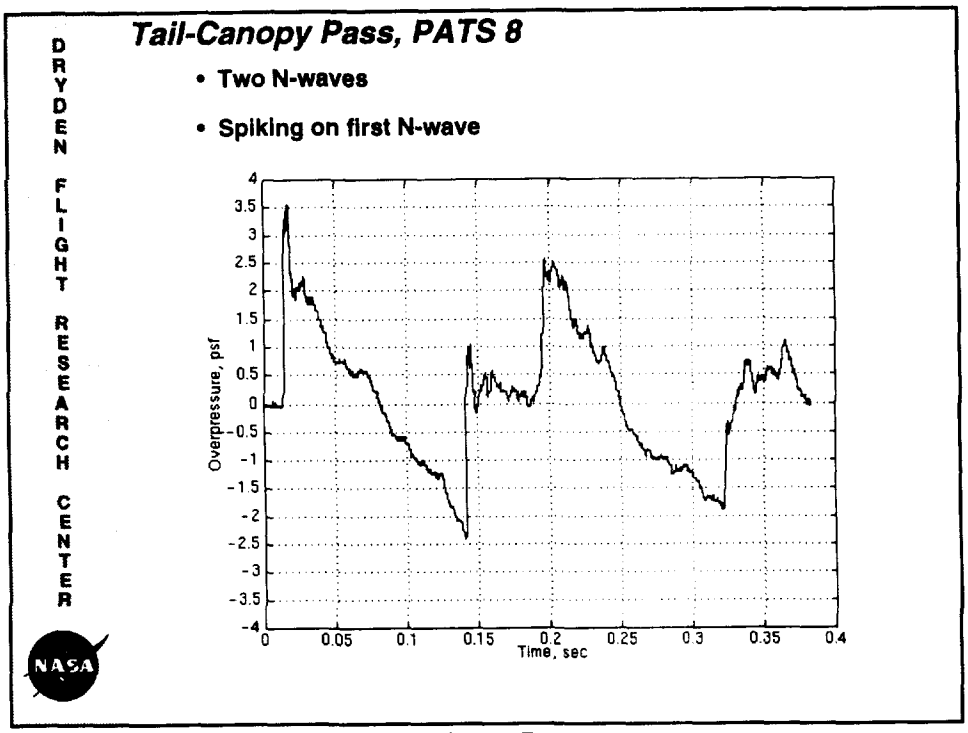

Figure 7c

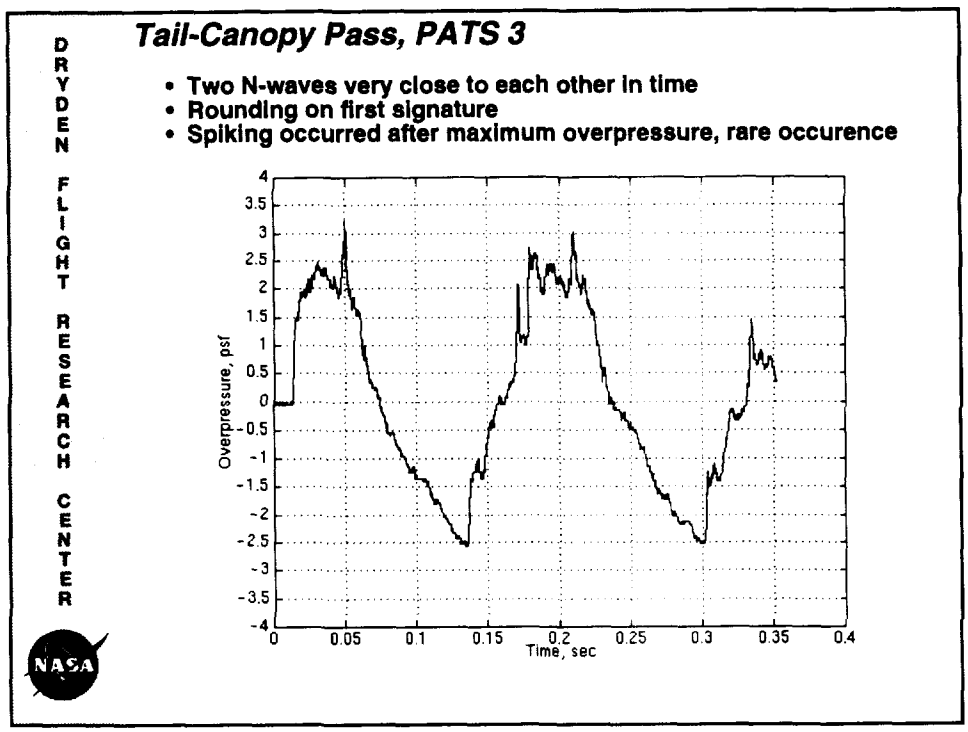

Figure 7d

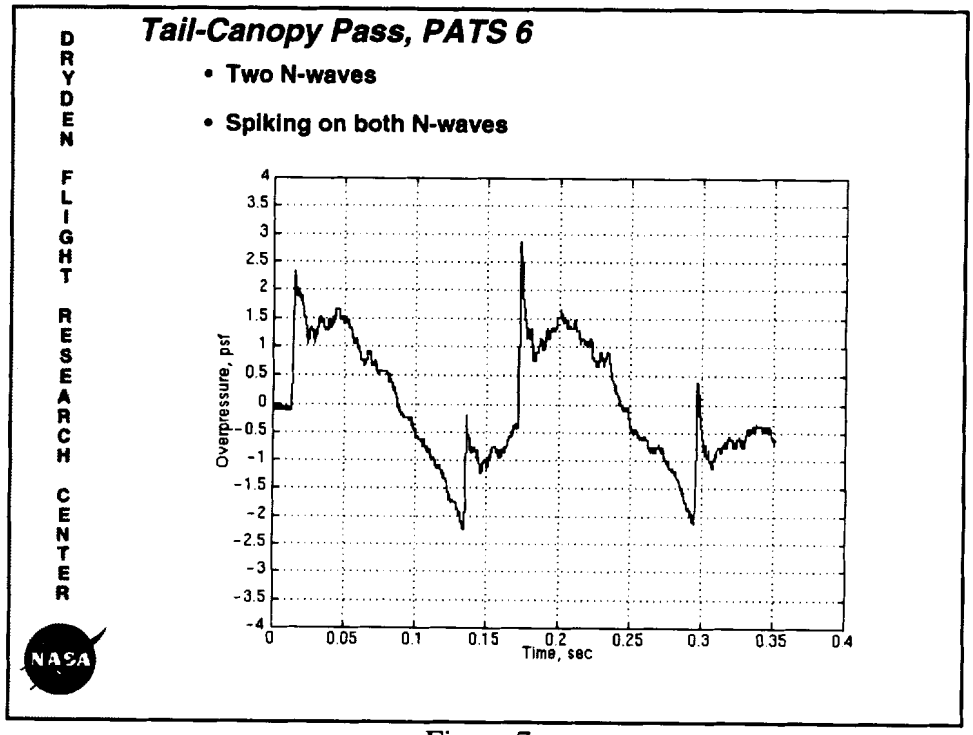

Figure 7e

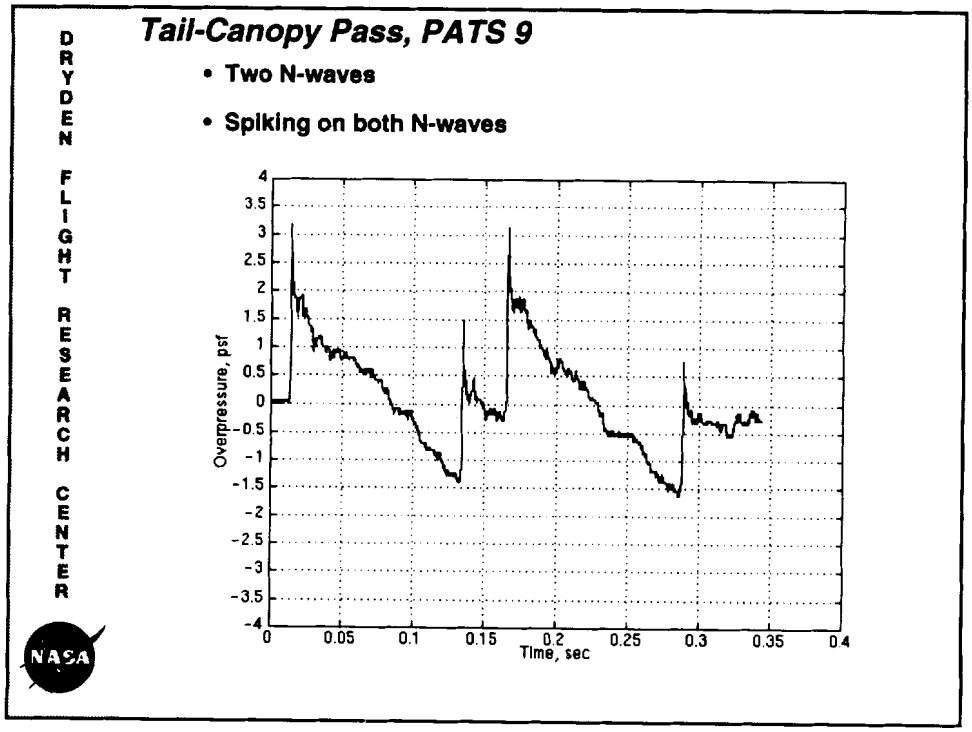

Figure 7f

Inlet-Canopy Pass

The sonic booms recorded during the inlet-canopy pass can be seen in figure 8a. Individual plots of each of the inlet-canopy signatures are shown in figures 8b through 8f. Figures 8a-8f show that the positioning of the F-18 aircraft allowed the shockwaves from the two aircraft to coalesce and generate a single sonic boom signature on the ground. Figures 8b and 8f show rounded signatures that approximate a flattop shape.

Atmospheric Effects

Figures 7a through 8f show that some of the signatures contain a peaked, or spiked, overpressure, while other signatures are rounded. The variation between the signatures in each of the passes probably results from the atmospheric conditions that the shockwaves passed through. Certain atmospheric conditions can cause spiking and rounding of the N-wave and can also increase the rise time to maximum overpressure (Likens and Blackstock, 1992; and Garrick and Maglieri, 1968).

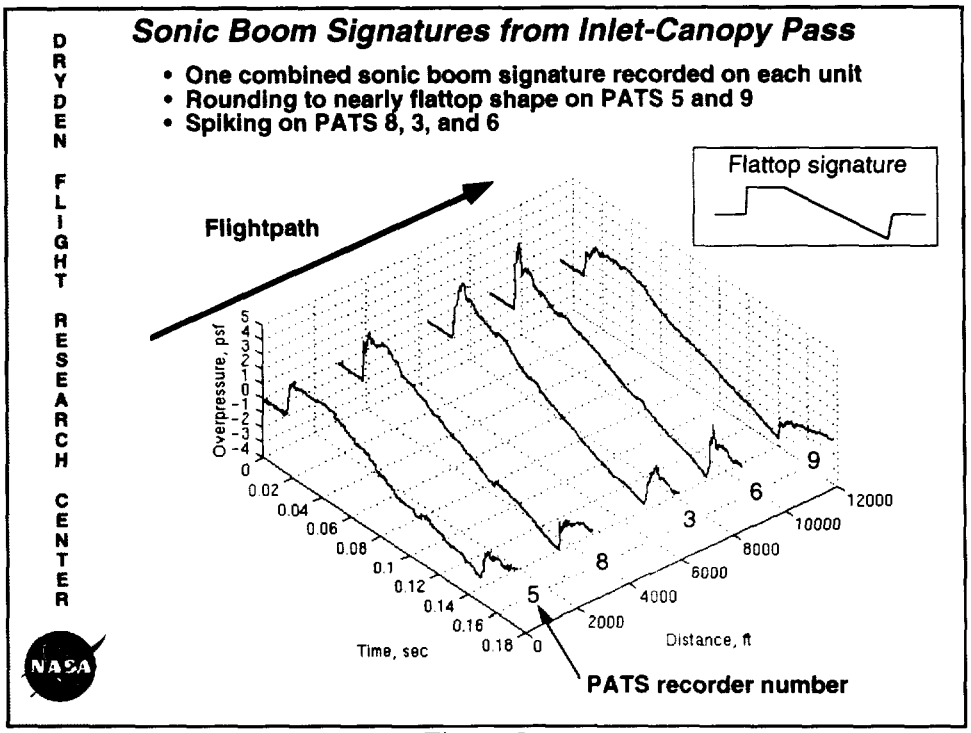

Figure 8a

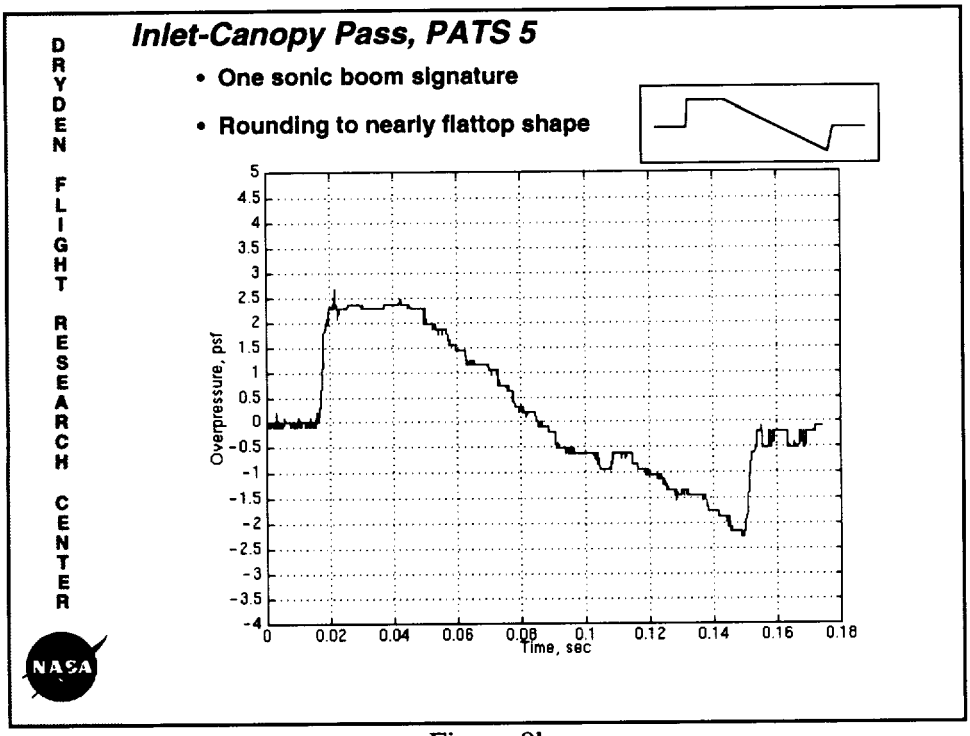

Figure 8b

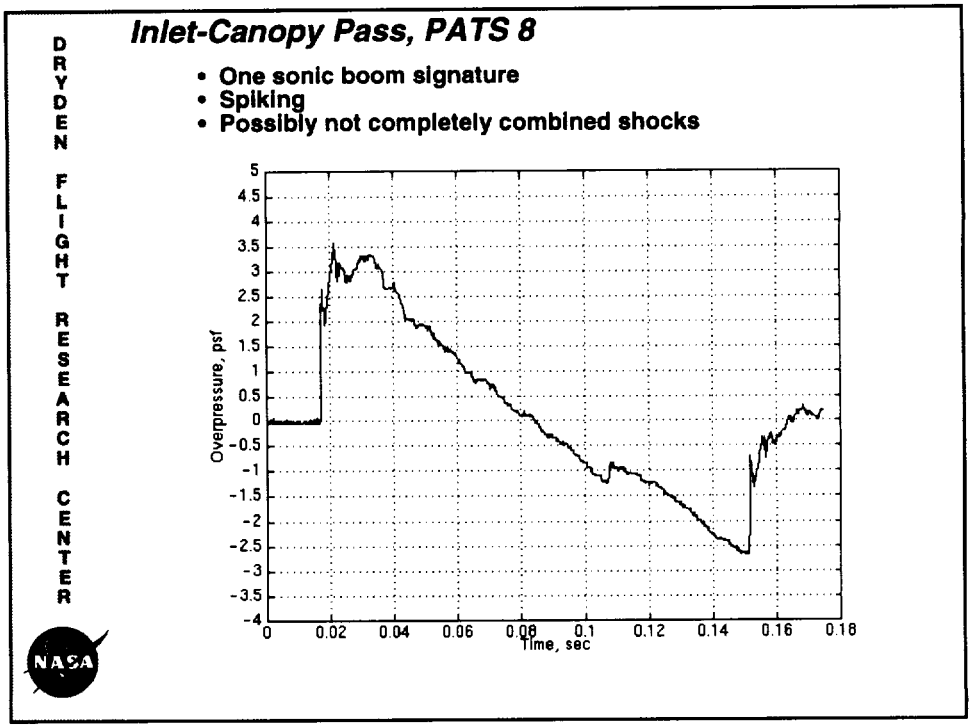

Figure 8c

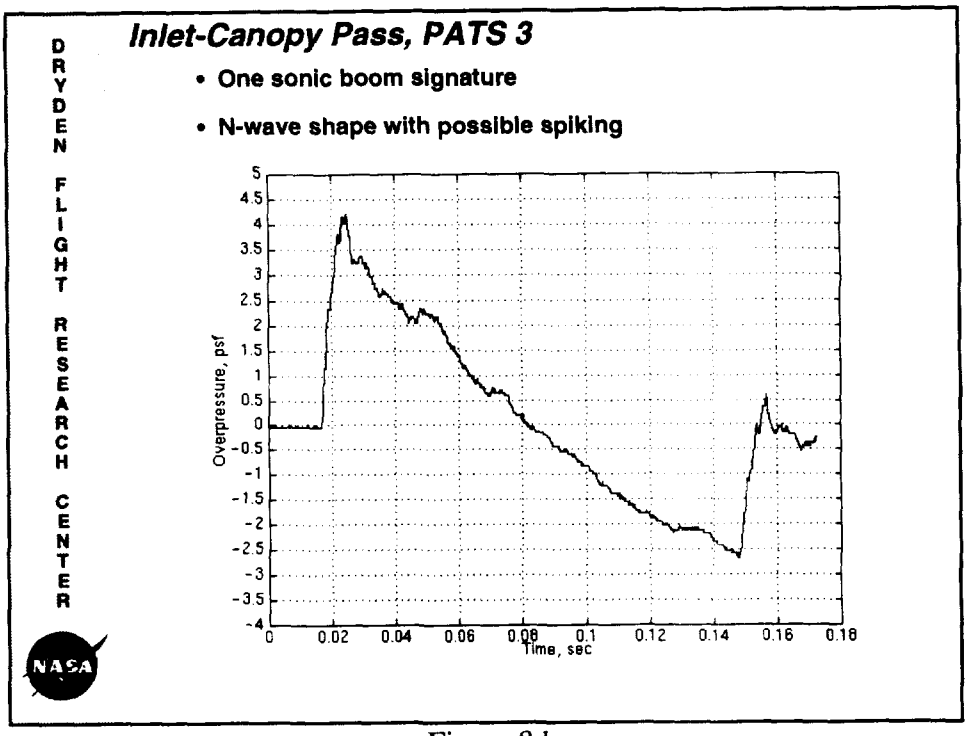

Figure 8d

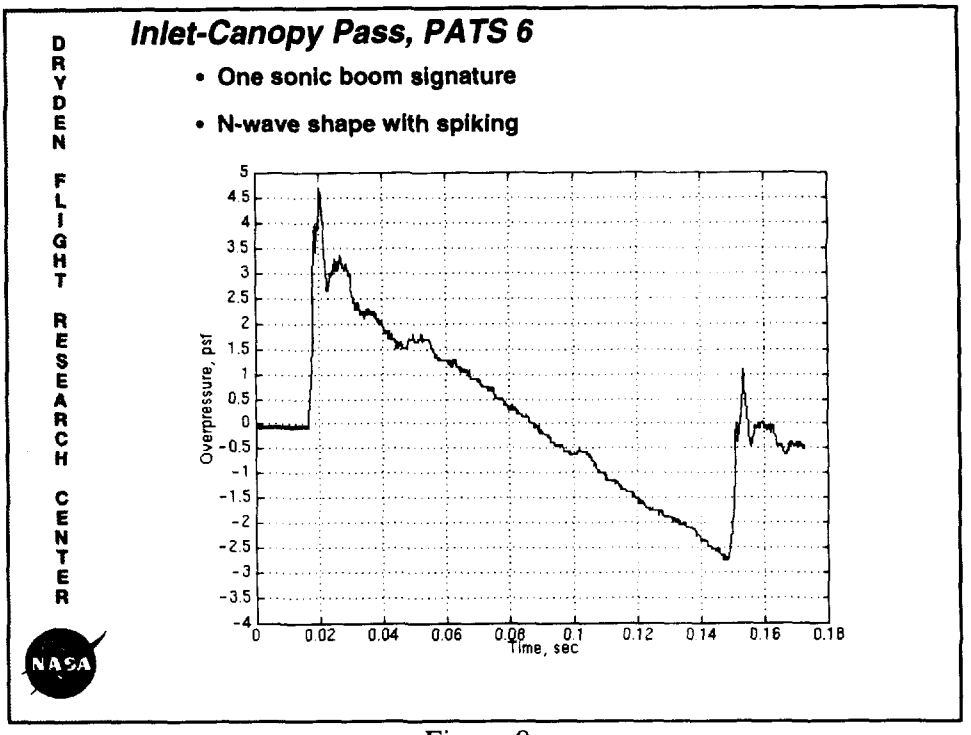

Figure 8e

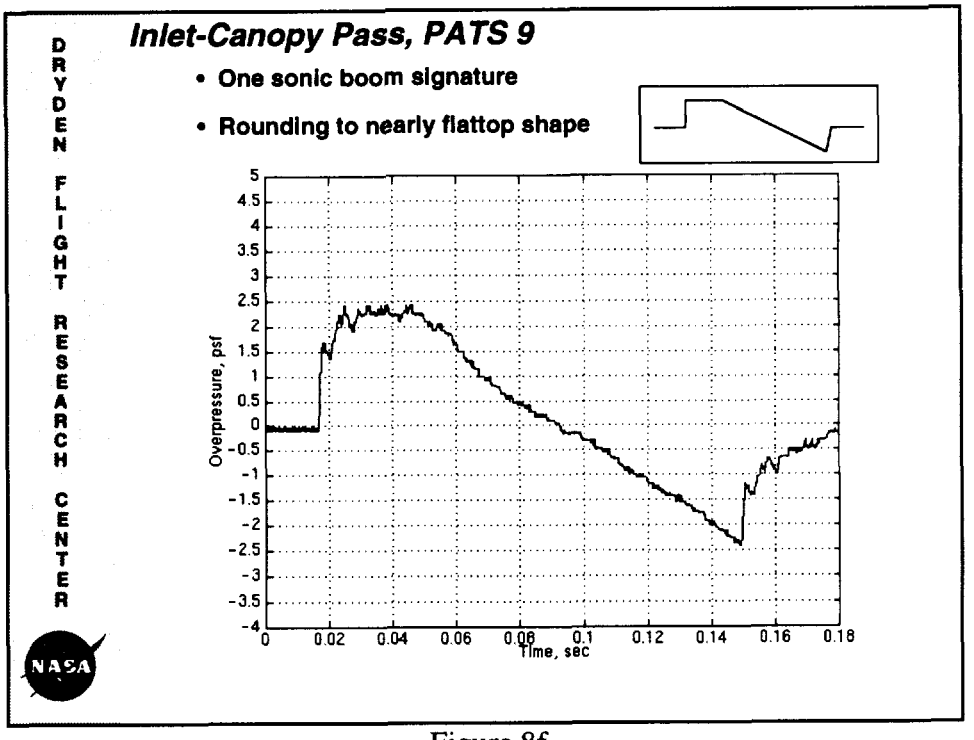

Figure 8f

Area intentionally left blank

Because two N-waves were recorded during the tail-canopy pass, it has been assumed that the longitudinal separation between the aircraft was great enough that no interaction between the shockwaves was measured at the sonic boom recorders. Under that assumption, a comparison was made between the first N-wave of the tail-canopy pass (one F-18 aircraft) and the single N-wave recorded during the inlet-canopy pass (two F-18 aircraft) of the same recorder (PATS 9 in figure 9). The maximum overpressure of the signature from the inlet-canopy pass is greater than that of the single F-18 signature if the spiking is ignored. There are two reasons for this occurrence. First, coalescing of the shocks from both aircraft reinforces the maximum overpressure. Second, the inlet-canopy pass occurred directly over the sonic boom recorders, while the tail-canopy pass occurred at a 3-mile lateral offset (fig. 6). Note also that the length of the inlet-canopy pass signature is longer than that of the single F-18 aircraft. This result was expected because the length of the signature depends on the length of the aircraft.

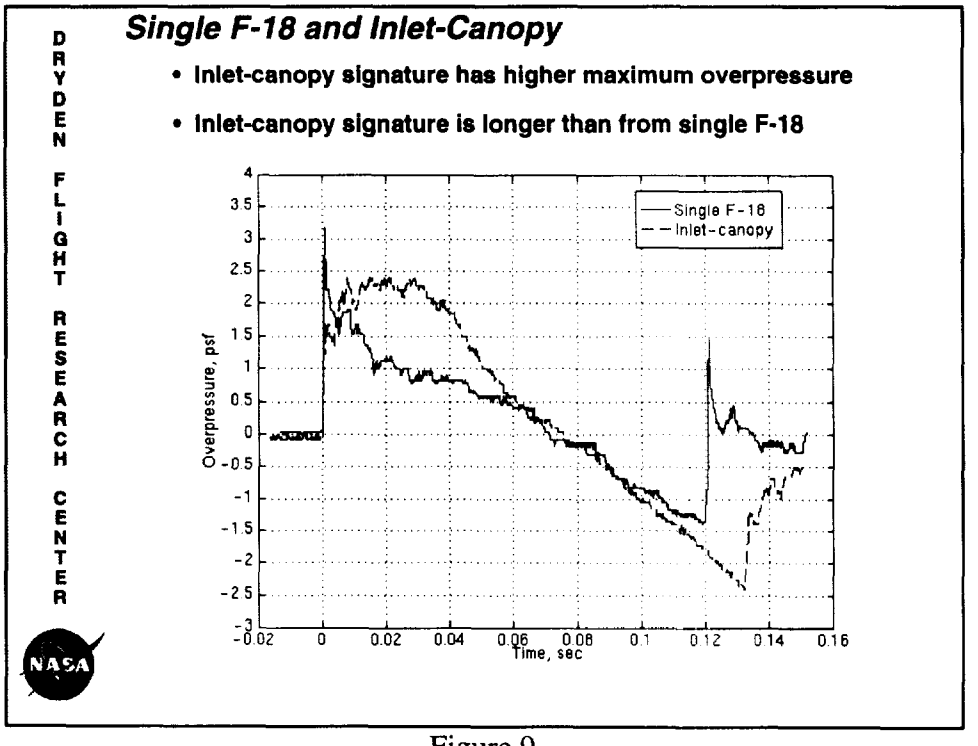

Figure 9

Because the PATS records 2 sec of data and a typical sonic boom signature is usually less than 0.2 sec long, there is additional data (or a trailer) after the signature. Figure 10 shows the signature and trailer recorded by PATS 8 during the inlet-canopy pass of the F-18 aircraft. After the sonic boom signature, the pressure normally returns to ambient.

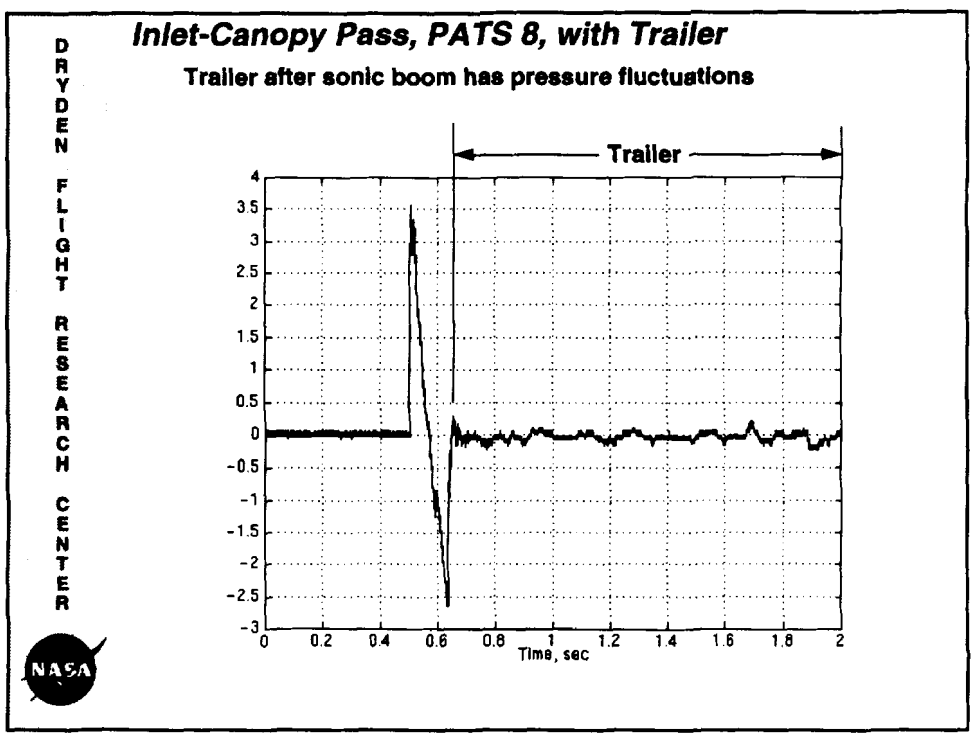

Figure 10

Figure 11 shows the entire 2 sec of data recorded by PATS 8 during the tail-canopy pass. This figure shows the two N-waves followed by high-amplitude rumble. This rumble was recorded on all recorders during the tail-canopy pass and was not recorded by any of the recorders during the inlet-canopy pass. The cause of this rumble is unknown. Maneuvering of aircraft may cause U-shaped waves after an N-wave, but these aircraft were just as steady on the tail-canopy pass as they were on the inlet-canopy pass. Additionally, a study has shown that "porpoising" an airplane with normal acceleration variations as great as ±0.5 times gravity will not affect ground signatures (Garrick and Maglieri, 1968). One cause of the rumble may be atmospheric effects that could have resulted in a reflected shock. This atmospheric effect is unlikely because the atmosphere differed over the 2-mile length of the ground array enough to affect each signature differently with rounding and spiking. Yet, all the PATS recorded the rumble on the tail-canopy pass.

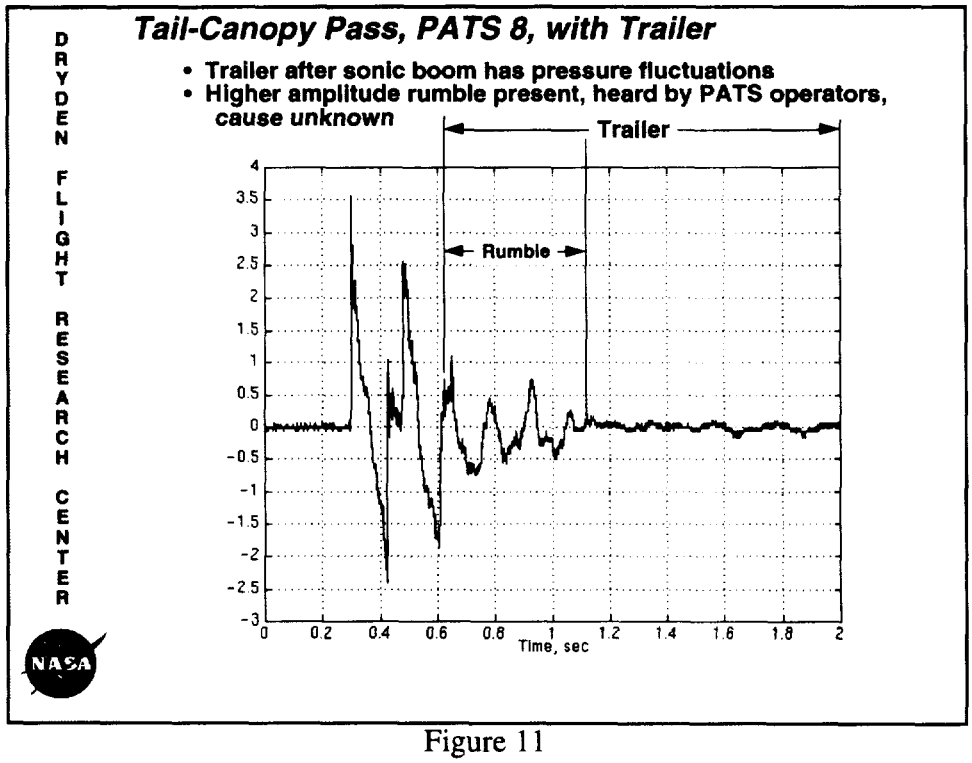

Figure 11

Calculation of Loudness

A computer program (Sheperd and Sullivan, 1991) was used to calculate the loudness of the recorded signatures. The program calculated A- and C-weighted loudness and perceived loudness for each signature. A-weighted loudness correlates well with human subjective response studies (McCurdy, 1994).

Figure 12 shows the A-weighted loudness for the first 1.2 sec for both passes, which includes both aircraft signatures from the tail-canopy pass. Equal time history segments of 1.2 sec were used for these loudness calculations, which eliminated most of the trailer. Note that the loudness program would not run using data from PATS 5, possibly because of the low resolution of this recorder.

The loudness for a given pass varied by several decibels among the recorders. The tail-canopy pass was as loud or louder than the inlet-canopy pass for all four recorders even though the inlet-canopy pass flight track was closer to the PATS array. The largest difference was seen on PATS 9 which has spiking on the tail-canopy pass and a nearly flattop signature on the inlet-canopy pass.

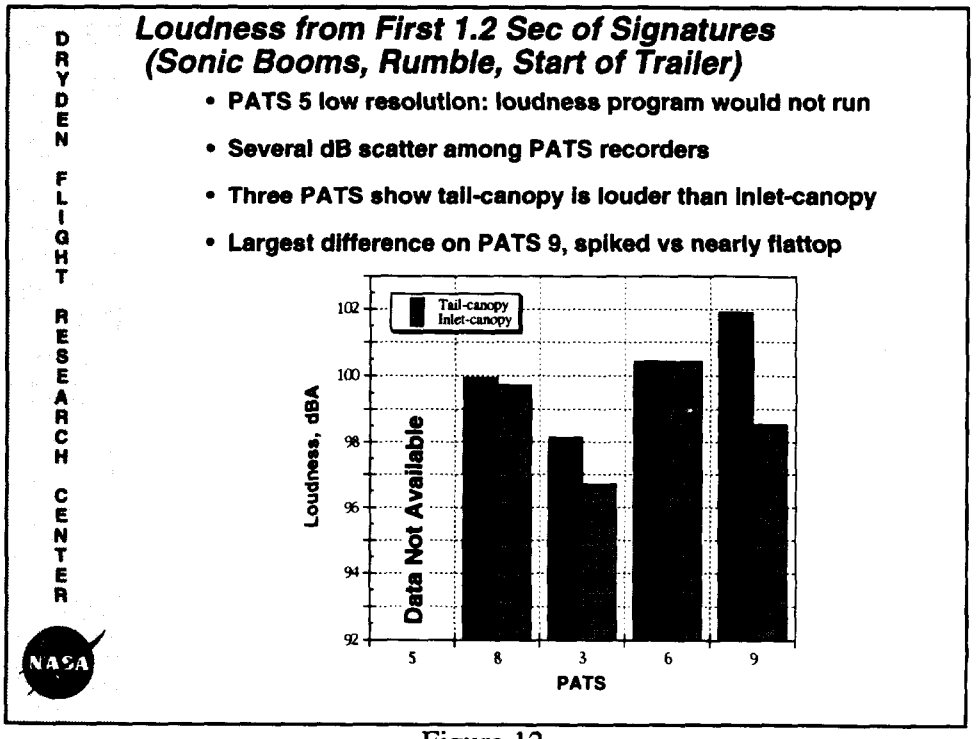

Figure 12

A plot of sound pressure level, SPL, as a function of frequency of the first 1.2 sec of PATS 9 data is shown in figure 13 for both passes. Significant spikes occur in both curves above 1500 Hz in the data, which contains the sonic boom signatures and the rumble for the tail-canopy pass. The PATS recorders do not have antialiasing filters (Norris, 1995), so the indicated frequencies of the spikes in figure 13 may actually be at higher frequencies.

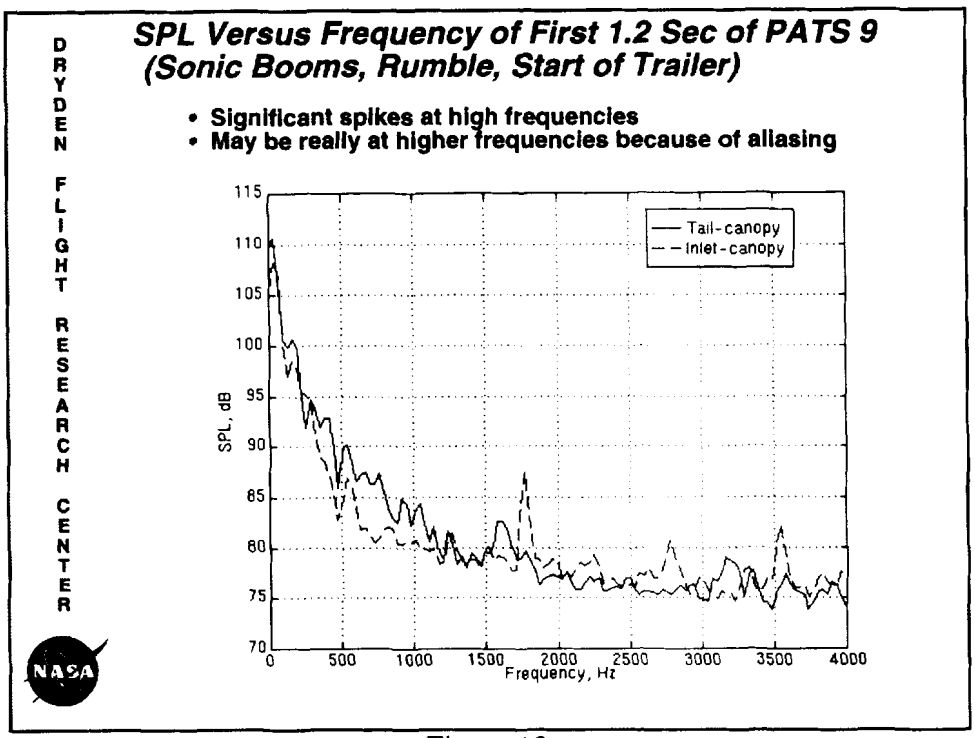

Figure 13

Figure 14 shows high-frequency spikes for the last 0.8 sec of PATS 9 data for both passes. These data contain neither the sonic boom signature nor the rumble from the tail-canopy pass, so high-frequency content was not expected; however, the PATS operators in the field noted that the aircraft engines were quite loud immediately after the sonic booms were heard. This engine noise may be the source for the high-frequency spikes in figure 14 and would be amplified by the A weighting.

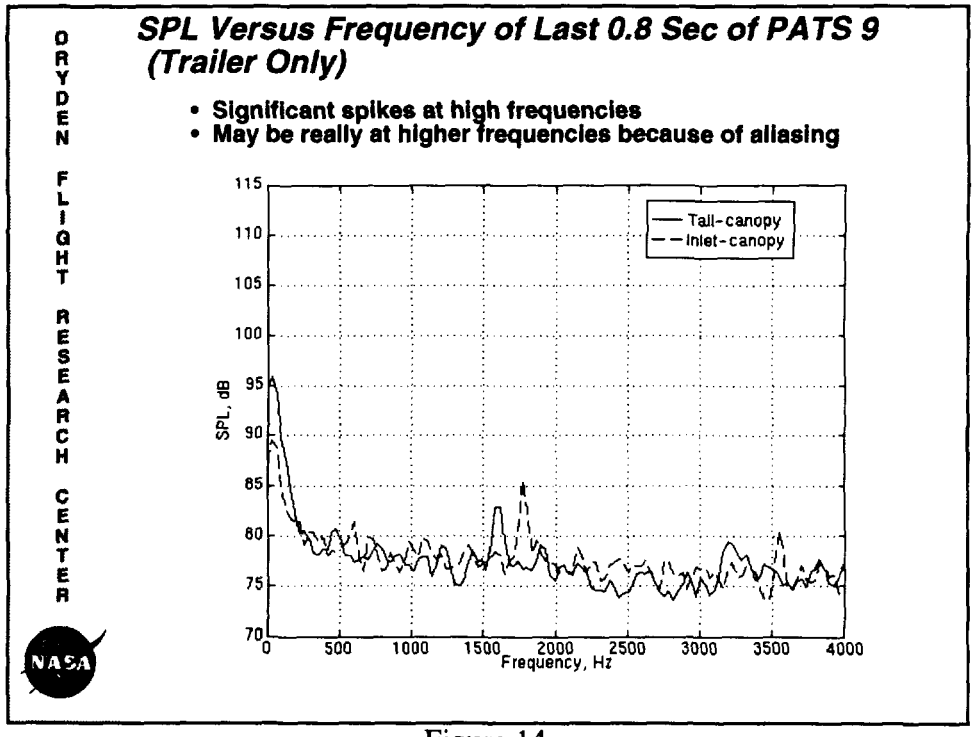

Figure 14

Figure 15 shows SPL as a function of frequency for a typical jet turbine engine (a Rolls-Royce engine). Spikes occur in the range from 1000 to 4800 Hz (Bushell, 1976)*. These high frequency spikes in figures 13, 14, and 15 suggests that high-frequency energy in the trailer of the sonic boom signature could be caused by the aircraft engine.

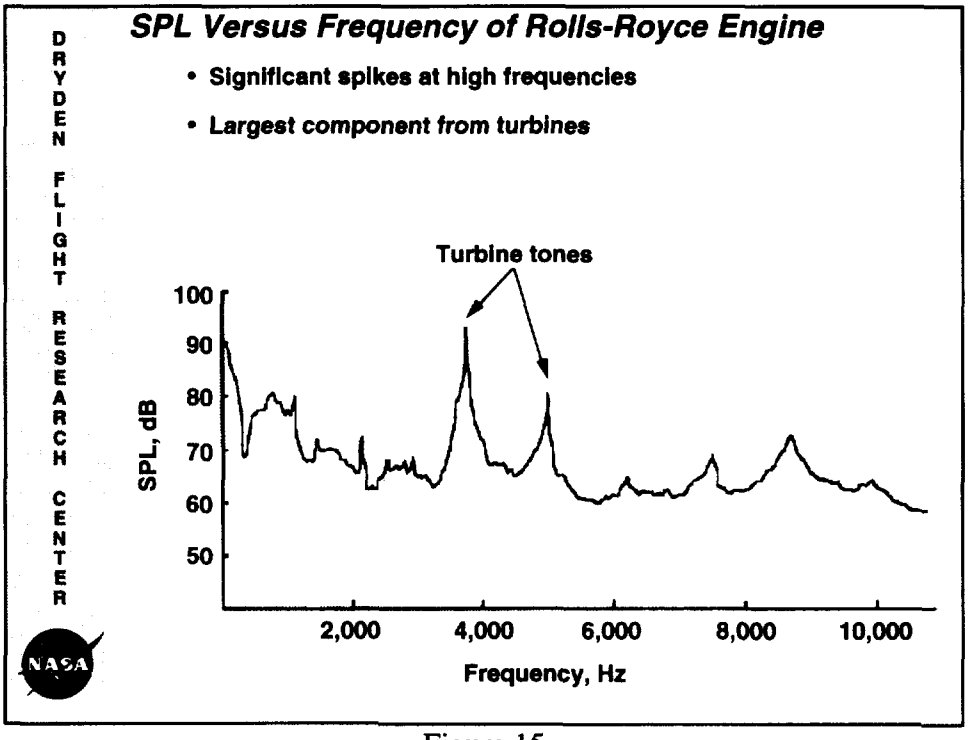

Figure 15

*The original version of this material was first published by the Advisory Group for Aerospace Research and Development, North Atlantic Treaty Organization (AGARD/NATO) in Lecture Series LS-80 "Aerodynamic Noise" in 1977. Used by permission.

Lastly, the loudness of the last 0.8 sec of data from each sonic boom recorder was calculated (fig. 16). Even though no sonic boom signature or rumble was part of the data analyzed, there was still 92 to 96 dBA of loudness, probably from the aircraft engines. Even though sonic booms may significantly startle people and animals, the trailer loudness apart from the sonic boom may be still quite annoying. In future flight experiments measuring sonic boom loudness, care should be taken to separate the loudness of the sonic boom from that of the trailer.

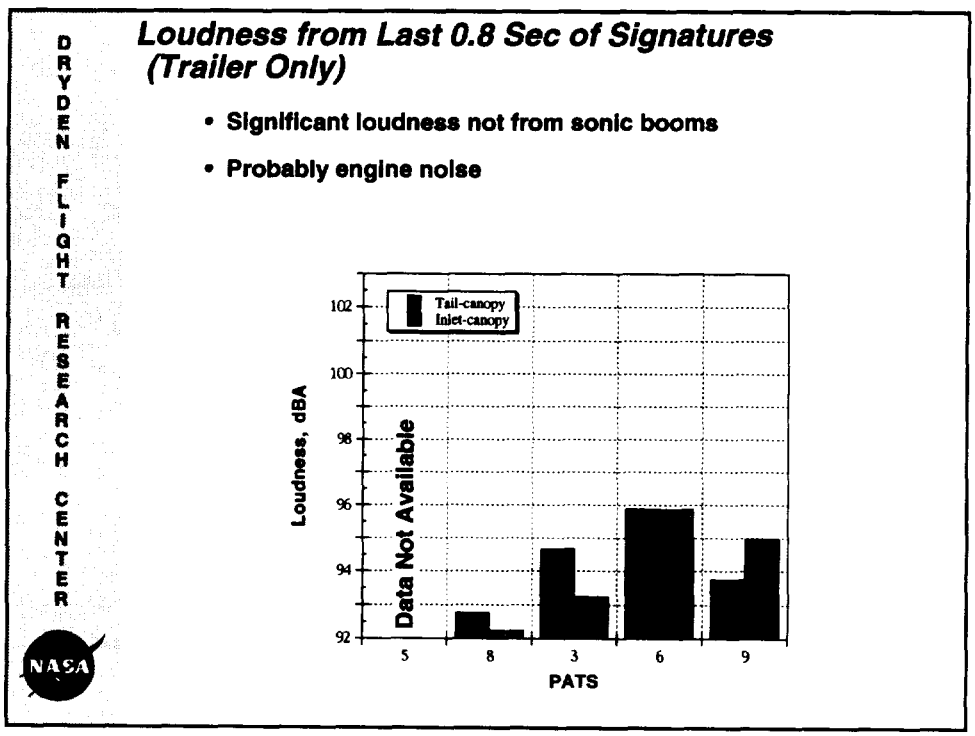

Figure 16

CONCLUDING REMARKS

A flight test technique that uses two F-18 aircraft flying in formation to generate modified ground sonic boom signatures was evalutated to determine the feasibility of the technique for possible SR-71 flight research. Results indicate that having the lower pilot see the shock of the upper aircraft for a positioning cue worked well. Using the engine noise cue for positioning may have resulted in the lower aircraft being too far aft for the shock waves to merge. Because of limited upward visibility and the relatively slow response of the SR-71 aircraft, use of two SR-71 aircraft flying in formation to generate modified ground signatures would be very difficult. Lastly, the relative separation of the two aircraft should be measured with a differentially corrected carrier phase global positioning system on any future test.

Although the flight was conducted primarily to evaluate a new flight test technique, data were recorded and analyzed that gave new insight into merged sonic booms from two aircraft. The inlet-canopy pass yielded modified signatures on the ground. Some approximated flattop signatures. These signatures had higher overpressure and longer length than signatures from a single F-18 aircraft. Modified signatures resulting from the combined signatures from two aircraft were quieter than signatures from two separated aircraft. The signatures recorded from the tail-canopy pass showed two separated signatures, which were followed by an unexplained rumble. All of the signatures showed some evidence of rounding or spiking. Lastly, aircraft engines may produce significant loudness in the trailers after the sonic booms.

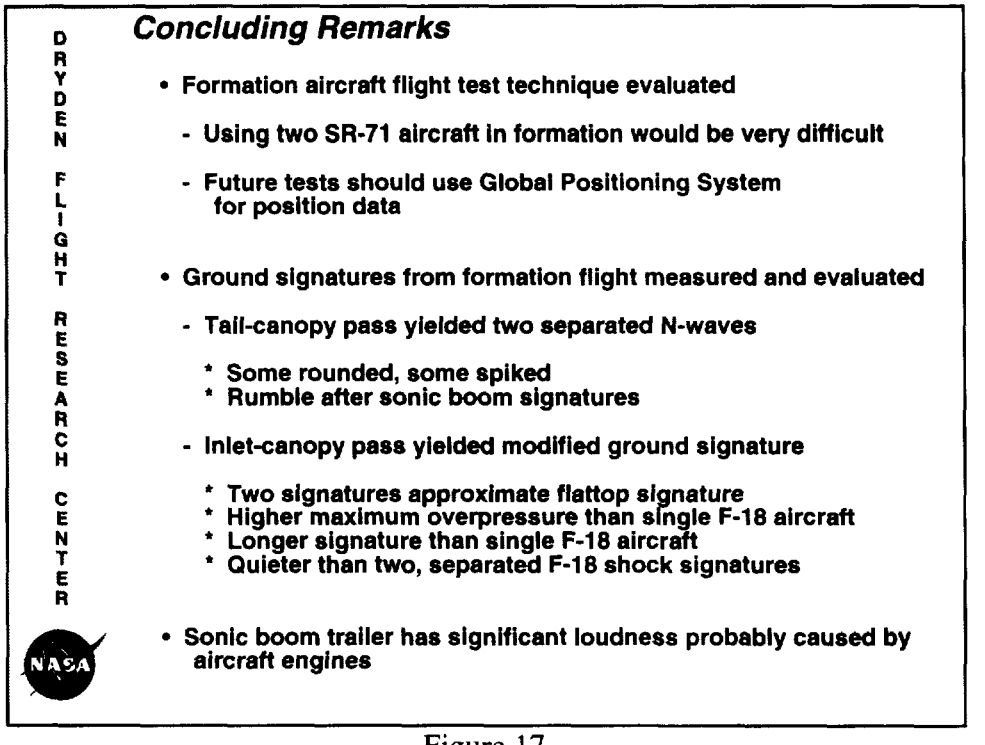

Figure 17

REFERENCES

Bushell, Kenneth W.: Gas Turbine Engine Exhaust Noise, *Aerodynamic Noise*, AGARD-LS-80, 1977, p.p. 4-25.

Carlson, Harry W.: *Simplified Sonic-Boom Prediction*, NASA TP-1122, 1978.

Ehernberger, L.J.; Haering, Edward A., Jr.; Lockhart, Mary G.; and Teets, Edward H.: *Atmospheric Analysis for Airdata Calibration on Research Aircraft*, AIAA-92-0293, 1992.

Garrick, I.E.; and Maglieri, D.J.: *A Summary of Results on Sonic-Boom Pressure-Signature Variations Associated with Atmospheric Conditions*, NASA TN D-4588, 1968.

Haering, Edward A., Jr.; Ehernberger, L. J.; and Whitmore, Stephen A.: *Preliminary Airborne Measurements for the SR-71 Sonic Boom Propagation Experiment*, NASA TM-104307, 1995.

Haering, Edward A., Jr.; and Whitmore, Stephen A.: *FORTRAN Program for Analyzing Ground-Based Radar Data: Usage and Derivations, Version 6.2*, NASA TP-3430, 1995.

Lee, R.A.; and Downing, J.M., *Sonic Booms Produced by United States Air Force and United States Navy Aircraft: Measured Data*, Air Force Systems Command, AL-TR-1991-0099, Jan. 1991.

Lipkens, Bart; and Blackstock, David T.: "Model Experiment to Study the Effect of Turbulence on Risetime and Waveform of N Waves," *High-Speed Research: Sonic Boom, Volume 1*, NASA CP-3172, 1992, pp. 97-107.

Mack, R.J.; and Darden, C.M.: Some Effects of Applying Sonic Boom Minimization to Supersonic Cruise Aircraft Design., *J. Aircr.*, vol. 17, no. 3, Mar. 1980, pp.182-186.

Mc Curdy, David A.: *Subjective Response to Sonic Booms Having Different Shapes, Rise Times, and Durations*, NASA TM-109090, 1994.

Norris, Stephen R.; Haering, Edward A., Jr.; Murray, James E.: *Ground-Based Sensors for the SR-71 Sonic Boom Propagation Experiment*, NASA TM-104310, 1995.

Shepherd, Kevin P.; and Sullivan, Brenda M.: *A Loudness Calculation Procedure Applied to Shaped Sonic Booms*, NASA TP-3134, 1991.

Tam, Christopher K.W.: "Jet Noise Generated by Large-Scale Coherent Motion," *Aeroacoustics of Flight Vehicles: Theory and Practice, Volume 1: Noise Sources*, NASA RP-1258, vol. 1, 1951.

AN ELECTRONIC SCHLIEREN CAMERA FOR AIRCRAFT SHOCK WAVE VISUALIZATION

Leonard M. Weinstein
NASA Langley Research Center
Hampton, VA

INTRODUCTION

Flow visualization has long played a crucial role in helping aerodynamicists understand complex fluid dynamic problems. High speed flows, which are currently becoming much more important, often have regions of large density variation. The location of the shock waves, the location of transition, the extent of separation, and the vortex details, are some of the flow details the aerodynamicist needs to know to help sort out the details of the physical processes occurring (ref. 1). In particular, the detailed properties of sonic booms have to be understood before commercial, next generation, supersonic and hypersonic aircraft can be properly developed.

While some of the experimental studies of these flows could be made in wind tunnels, where laboratory setups of light sources and optical devices allowed schlieren imaging of flow over models, there were real limitations on what could be measured. The need for full flight conditions simulation, the problem of tunnel wall interference, and the limited distance the shock waves could be examined from models, limit the usefulness of wind tunnel tests for these types of flows. The flight flow visualization techniques available up until recently were mainly limited to injected smoke visualization (ref. 2), and in vapor condensation visualization for rapidly expanded flows (ref. 1). Some naturally occurring shadowgraph images of strong shock waves have also been observed on aircraft, but this approach is neither sensitive enough nor repeatable enough to be of much use.

A new optical technique for examining compressible aircraft flow-field structures in flight, first described in reference 3, uses the sun as a light source, and obtains streak camera schlieren images. That version used film to record the image, and was used to study shock wave structures at different distances from aircraft. Several limitations were encountered with this design which were primarily due to the use of film as a recording medium.

A new version of the schlieren camera for aircraft shock wave visualization was developed to overcome the limitations of the previous version. The current paper describes the new improved camera, which uses an electronic recording camera. Test results are shown, comparing the film and electronic camera versions, and further suggestions for improvements are described.

BASIC SETUP FOR SCHLIEREN FOR AIRCRAFT IN FLIGHT

The basic optical system for the schlieren for aircraft in flight (SAF) is shown in figure 1. When the telescope is tracking the sun, the image is stationary at the primary focus. An opaque mask with a curved slit is used to block all but a thin sliver at the edge of the sun and a thin region of sky next to the sun. This results in a single source and cutoff line in a large field schlieren system (ref. 4). An aircraft, or the shock waves from an aircraft, is made to pass through the field of view, crossing this sliver of light, and the sharply focused image is recorded on to a moving image detector. This produces a streak camera schlieren image of the flow field examined. The recording medium can be film, or an electronic imager, as long as the detector area is able to track the image motion.

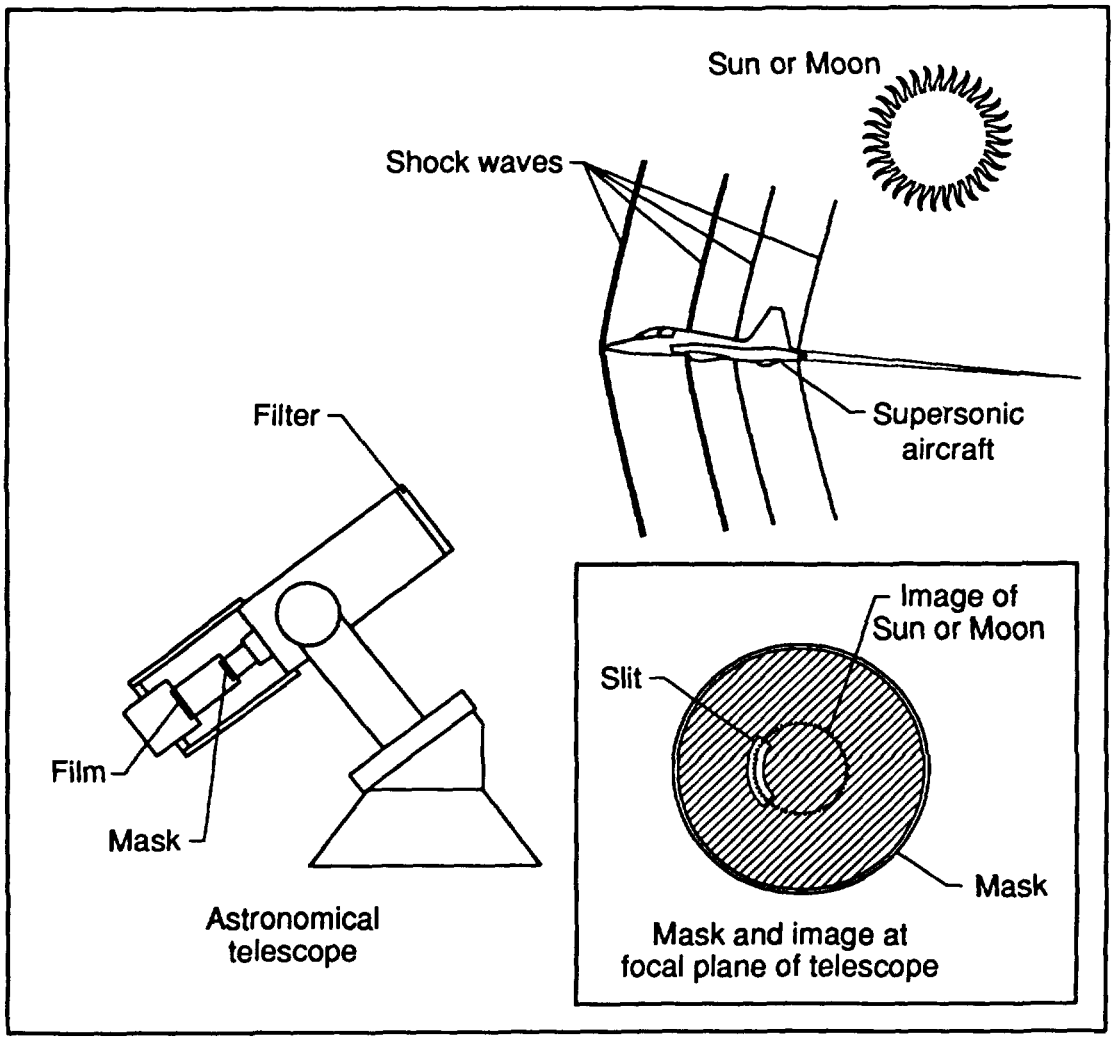

Figure 1. Setup for schlieren for aircraft in flight

IMAGE MOTION SMEARING

If the aircraft image were to horizontally cross the open area in the mask, and if the image speed exactly matched the detector motion, the image would be recorded as sharply as the optical system would allow. However, if the image motion were at an angle to the detector motion, or if the image speed did not match the detector motion, the final image would be smeared out and degrade the sharpness of the image. The amount of smear is shown in the equations at the bottom of the figure.

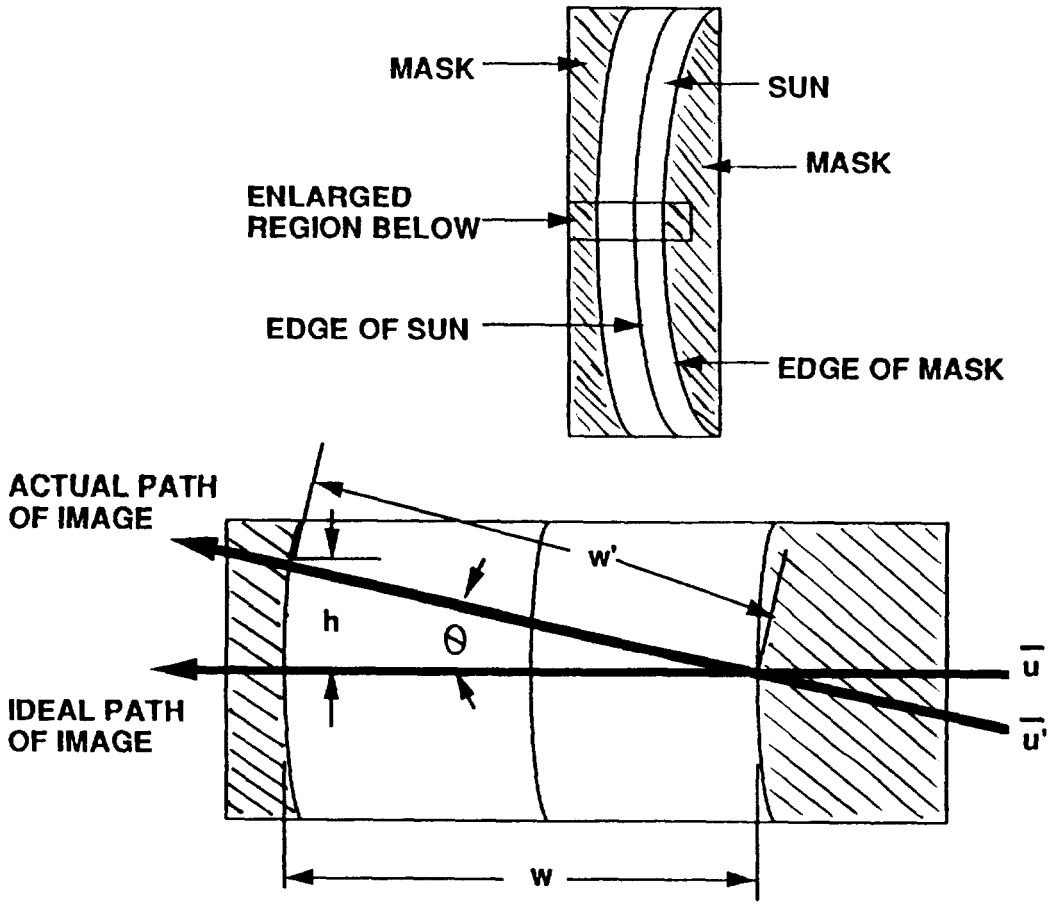

$$h/w = \tan\theta \quad \text{——————} \quad \text{Vertical smear}$$

$$(w' - w)/w = (1/\cos\theta - 1) \quad \text{—} \quad \text{Horizontal Smear Due To Angle}$$

$$(u' - u)/u = \text{Horizontal smear due to speed error}$$

Figure 2. Image motion smearing due to speed or alignment errors.

PROBLEMS WITH FIRST PROTOTYPE FILM BASED SAF

Several problems were encountered with the first film prototype SAF system that was built. Some of these were minor and easily correctable, such as choice of film. However, some required major design changes to correct. The major problems and the solutions selected are described in table 1.

Table 1. Main Problems With First Prototype Film Based SAF, and Solutions

PROBLEMS	SOLUTIONS
Film Banding	TDI Electronic Camera Imaging
Sun Tracking Errors	Auto Two-Axis Sun Tracker
Camera Rotation With Equatorial Tracker	Use of Altazimuth Mounting
Difficulty of Visual Focusing	Use of CCD Focusing Camera
Lack of Immediate Results From Film	TDI Camera Image Available

The solutions suggested in table 1 were used as a guide to make a second prototype SAF camera. The use of an electronic "Time Delay and Integration" (TDI) camera instead of film to record the image also required a image acquisition board and computer be used to take and record the image. The use of an auto sun tracker and altazimuth mounting allowed easier setup and operation, and the use of the focusing CCD camera allowed more accurate focusing of the telescope.

TDI CAMERA AND SENSOR DETAIL

A TDI camera moves the electronic charge obtained during exposure so that the detector acts just like a moving strip of film. The movement is computer controlled, so is very smooth and accurate. The TDI camera was about 3.5 inches long on each side, and had the sensor mounted a short distance inside the lens opening. The sensor was composed of silicon detectors 13 microns on a side arranged in an array of 96 X 512 elements. The tall dimension was perpendicular to the flight direction, with the mask area located as shown in figure 2 on the previous page. The camera appeared as shown in figure 3 below.

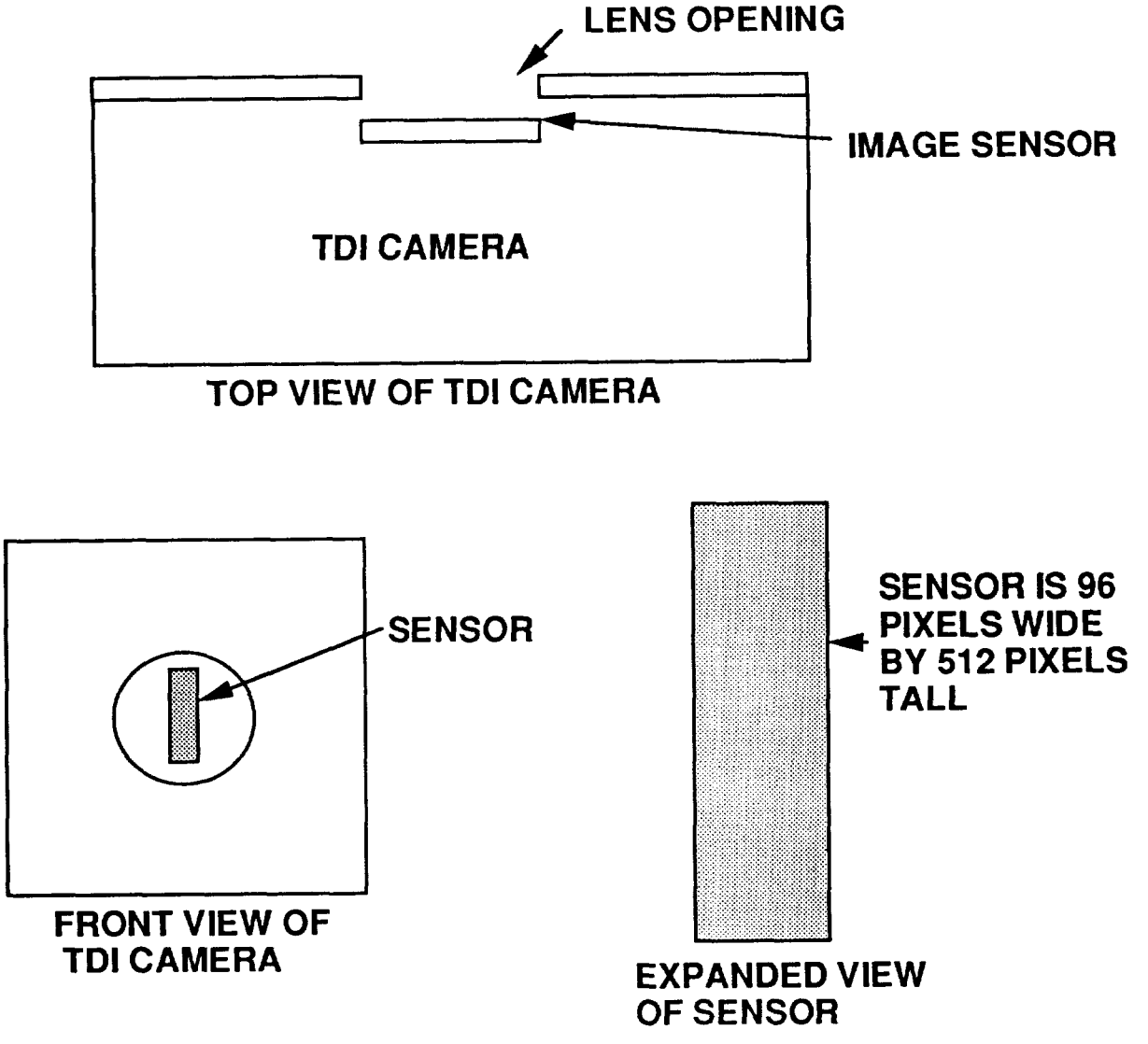

Figure 3. TDI camera and sensor detail

OPTICAL DESIGN OF ELECTRONIC TDI CAMERA ASSEMBLY

Figure 4 shows the optical design details. A 5 inch aperture telescope was used with a neutral filter across the full aperture to obtain a safe level of sunlight. The sun image was focused onto the mask, then reimaged to two new locations. At one location, a frosted screen was used along with a small CCD camera to refocus the telescope in the field. Fiber optic probes took the light from four locations on the sun to drive the auto tracker. The other image was sharply focused on the TDI detector. The assembly was pre adjusted in the lab so that when the sun image was centered behind the mask, and sharply focused in the CCD camera, the aircraft image would be sharp in the TDI camera.

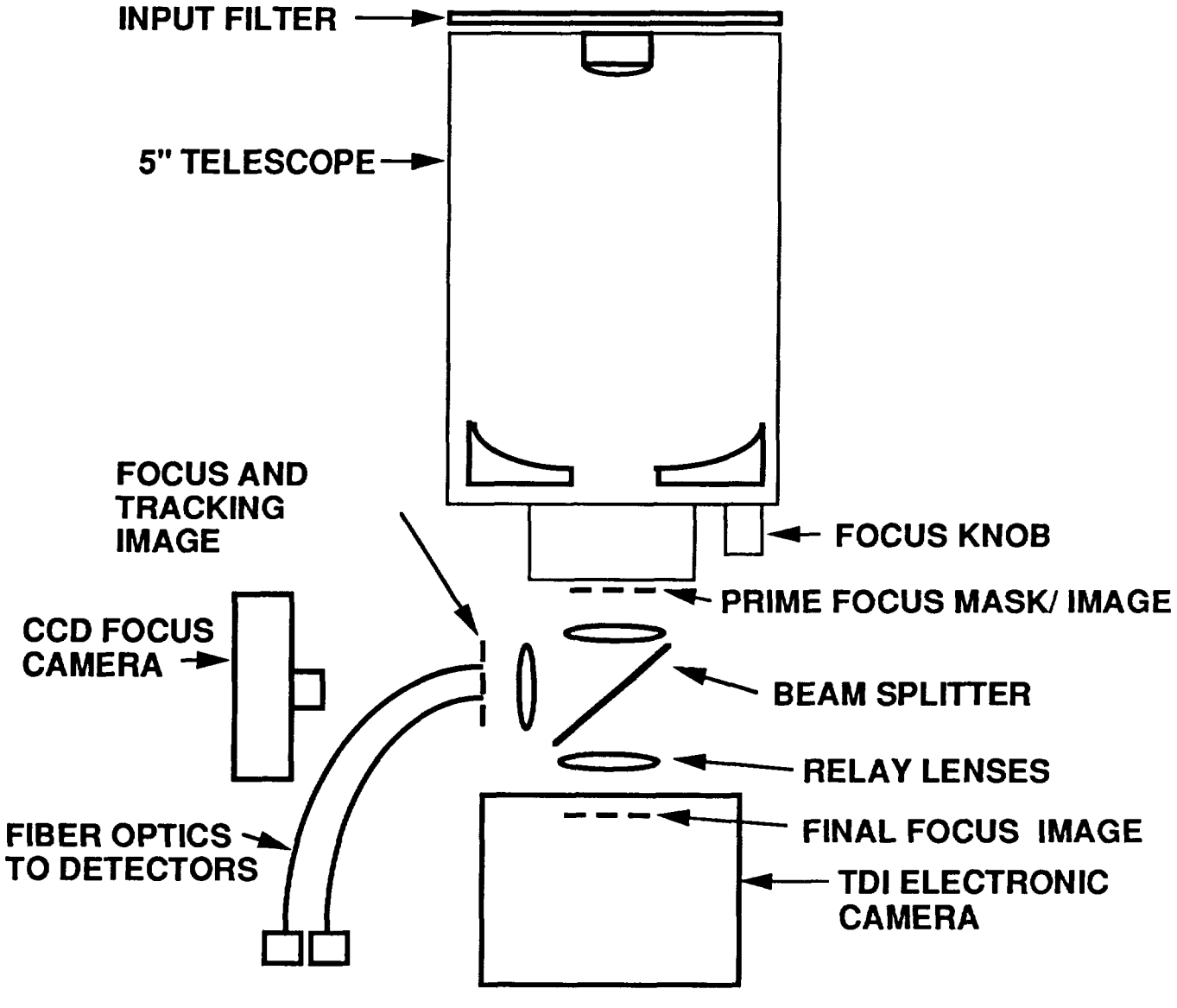

Figure 4. Optical design details of electronic TDI camera

INTERIOR VIEW OF TDI CAMERA ASSEMBLY

Figure 5 shows a photograph of the TDI camera and other optical components mounted in a box. A clamp on the left side was used to attach the box to the telescope. Since the suns apparent diameter changes slightly over the year, an adjustment was needed to change the suns image size. The entire box could be moved with a positioner (out of sight on the far side of the box) then refocused on the sun. This adjustment allowed us to accurately match the size of the sun to the mask.

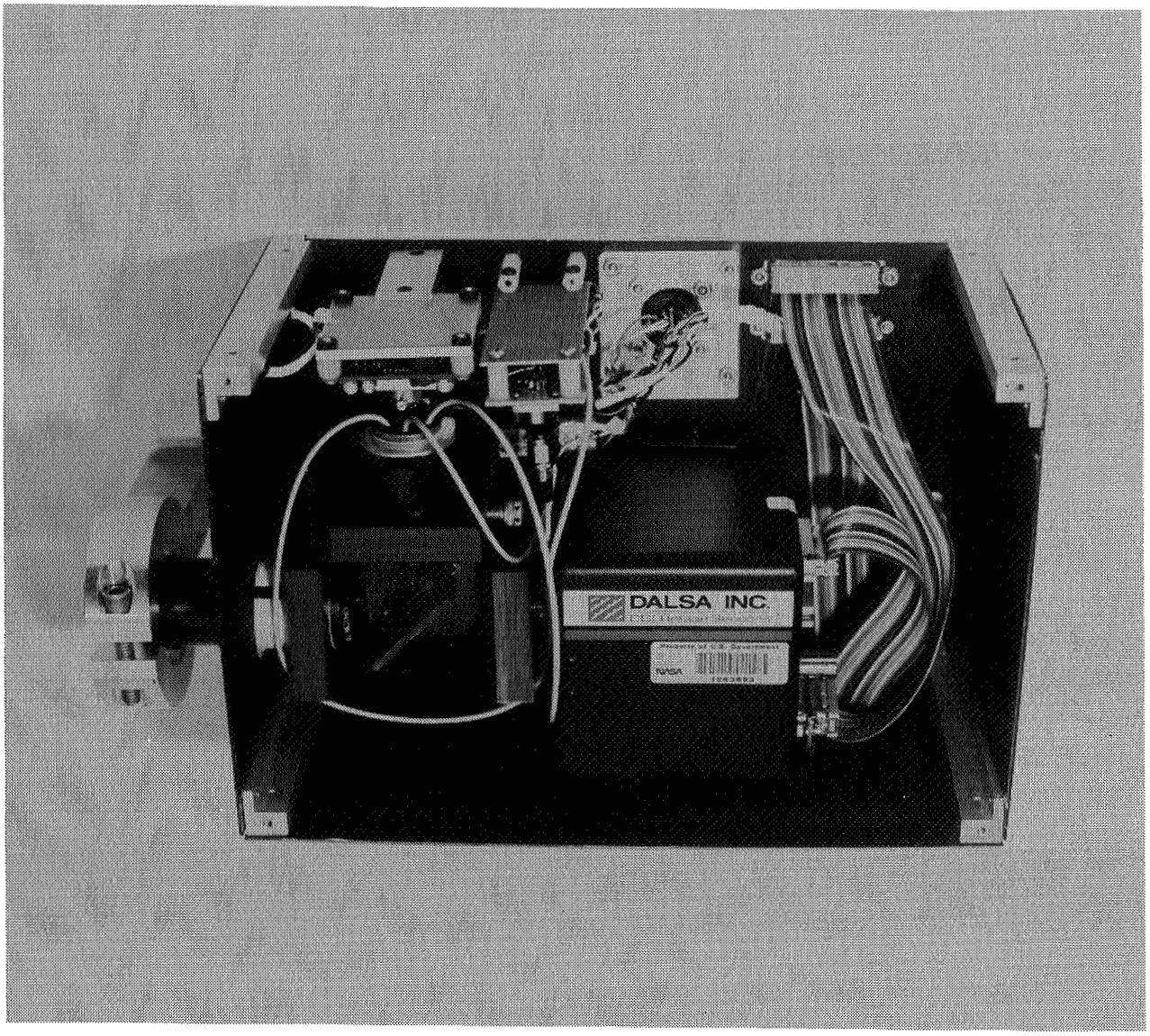

Figure 5. Interior view of TDI camera assembly

VERIFICATION TEST OF TDI CAMERA

The electronic TDI camera version of SAF was taken to NASA Dryden for verification of operation. Flight tests were conducted on June 21 and 22, 1995. Passes were made by an F-18 at a slant range of about 42,000 ft. and at M=1.2. The sun was only shortly past its zenith, and was at an altitude of nearly 70 deg., in a southerly to slightly westerly direction. The steep viewing angle resulted in a nearly plan view of the flow field

The TDI camera had been designed to automatically trigger the exposure when the plane passed, so the design had only included 0.8 seconds of exposure per picture. This would have been more than enough if the system worked properly. Unfortunately, the auto trigger was not working properly, and could not be used at this time. The camera had to be triggered manually for the present test. The correct trigger start time was difficult to estimate within the required fraction of a second (especially when the plane missed the sun and the swept back shock location had to be guessed at), so it was realized that the chance of getting a good exposure was limited.

In a total of nine passes, one set of F-18 shock waves was photographed, but this successfully demonstrated the TDI electronic camera system. Several areas for improvement were identified, and will be implemented before the next tests.

SETUP OF TDI CAMERA AT NASA DRYDEN

Figure 6 is a picture of the TDI camera set up at NASA Dryden. A counter weight extends in front of the telescope to balance the system. The high sun angle is seen in the camera tilt. This high angle caused an additional problem. As an altazimuth tracking system points near the vertical, rotation angles change rapidly. This would not be a problem if the aircraft flight path were exactly perpendicular to the line pointing to the sun, and if the altazimuth system were set up properly. Unfortunately, neither condition was satisfied. The telescope could not be tilted up high enough if the altazimuth axis were correct because of the overhang of the camera, so the system had to be tilted about 25 degrees off axis. In addition, the flight path was not exactly perpendicular to the sun line. These two problems, combined with an error in setup direction resulted in a large angle in flight path relative to the detector motion.

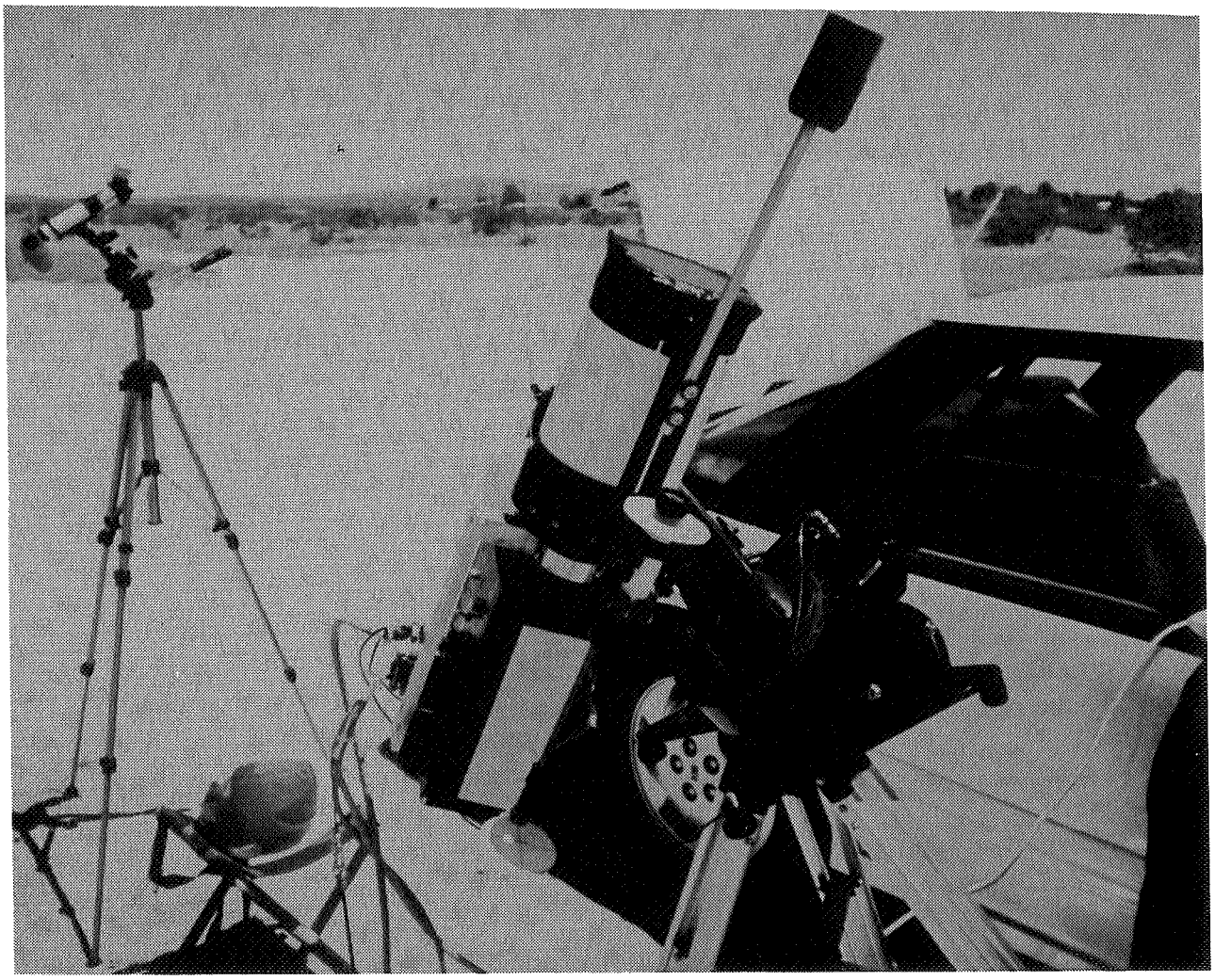

Figure 6. Setup of TDI camera at NASA Dryden on June 22, 1995

CONTRAIL OF F-18

At the large altitude used for the current test, the aircraft is difficult to see directly. Fortunately, the conditions were favorable for contrails to form. Figure 7 shows the contrail of the F-18 as it approaches the sun from the left. If the contrail had not been visible, the current test would have not been possible. This points out one of the major operational problems associated with SAF measurements (i.e., knowing where the aircraft is relative to the camera).

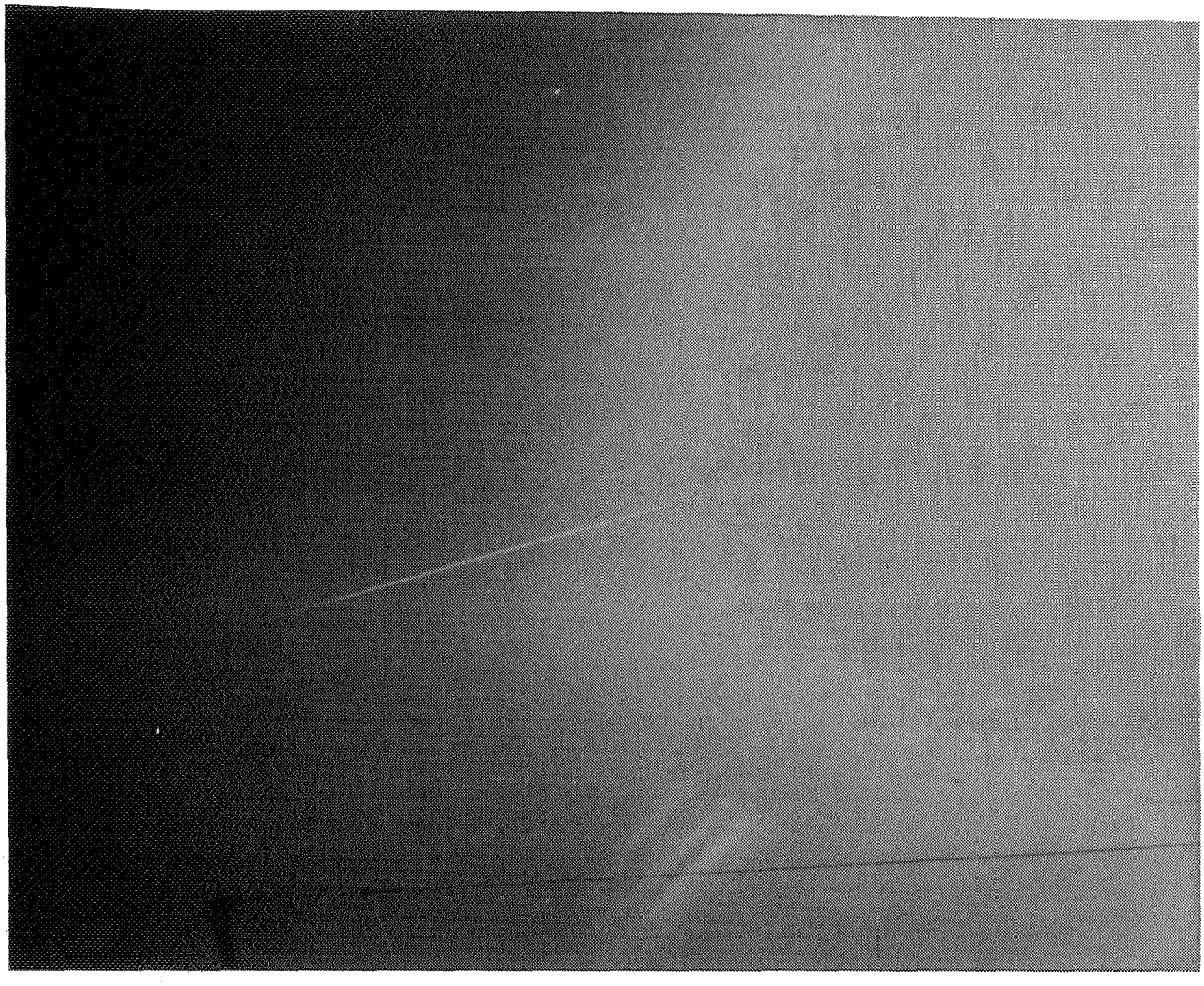

Figure 7. Contrail made by f-18 at M=1.2 and 41,000 ft altitude

TRIGGER PROBLEMS WITH TDI CAMERA AND TELEPHONE POLE SOLUTION

The short exposure available for the TDI camera for the present test made it necessary to manually trigger the start of exposure within a fraction of a second. A small finder telescope was first used to try to trigger the exposure start accurately. This could not be made to work with the setup used. The technique that was used consisted of standing near a telephone pole and blocking the sun with the pole. The author is shown in figure 8 standing behind a telephone pole. By observing the plane contrail, the plane could be tracked visually, and the exposure triggered. Even with this visual aid it was difficult to expose within the short time available. The shock waves from only one of the passes was recorded with the electronic camera. Fortunately, this was enough to verify its basic capability.

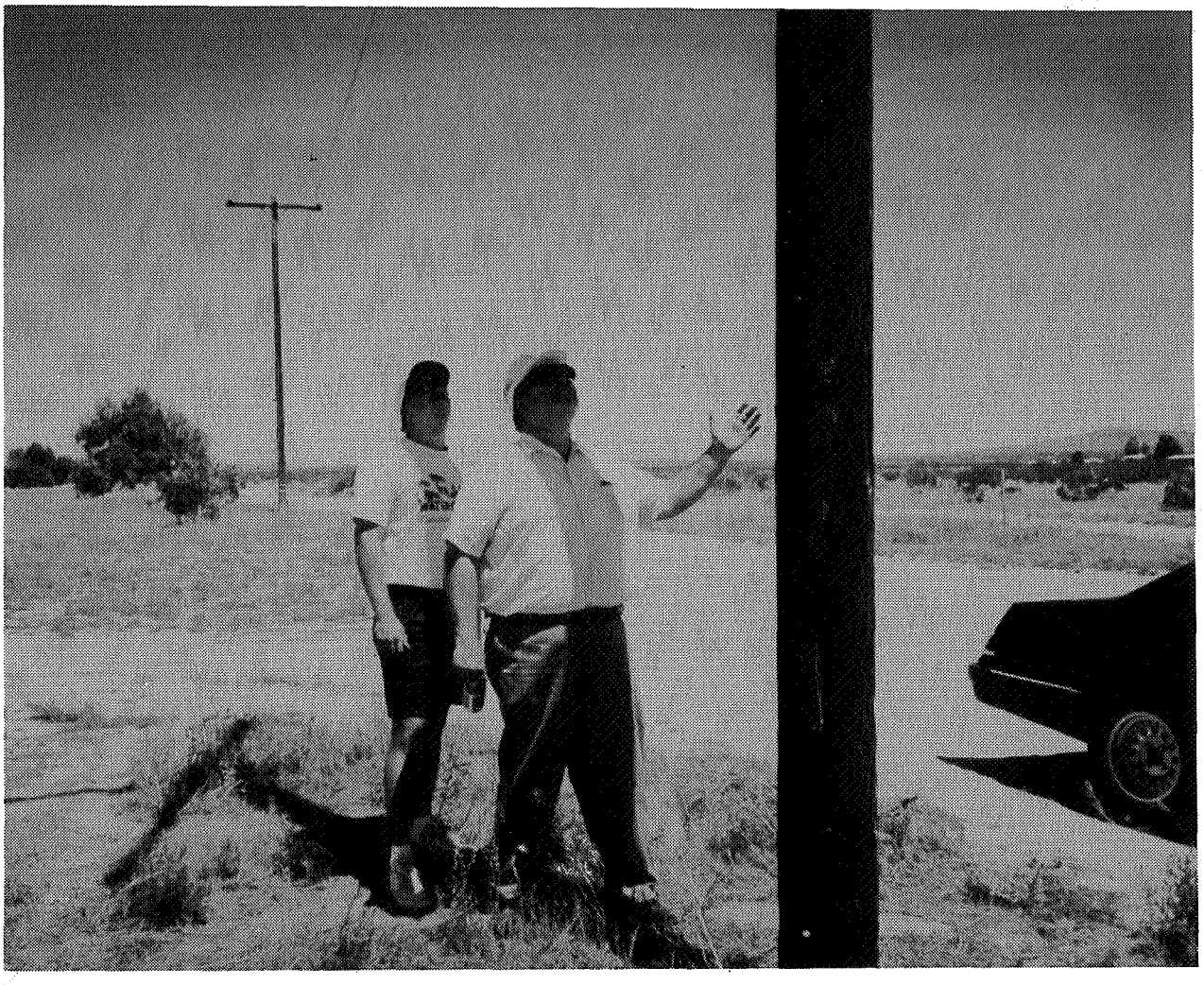

Figure 8. Use of telephone pole to block sun

ELECTRONIC TDI CAMERA IMAGE OF F-18 SHOCKS

Figure 9 shows the shock wave image taken with the TDI camera. The plane was below the field of view shown, at a lateral distance estimated to be about 2,000 ft. The shock system has merged to a clearly defined "N"wave. The shock angle corresponding to the M=1.2 speed would be about 56 degrees. The flight angle was tilted down about 33 degrees (from the recording detector motion) and thus shows the shocks nearly normal to the recording direction. The shock separation distance corrected to the flight direction was calculated to be about 118 ft. The curvature seen in the shocks was due to barrel distortion in the relay optics.

By showing the shocks nearly normal, the motion smear due to the angle is almost entirely in the direction along the shock, and this would not blur the shock thickness. Thus we were fortunate that the error was the optimum amount to minimize longitudinal smear.

The image banding typical of photographic images is totally absent, The curvature of the shocks due to relay optics distortion can be removed with better optics. The longitudinal streaks were due to small irregularities on the edge of the cut off mask, which can be avoided with a more carefully made mask.

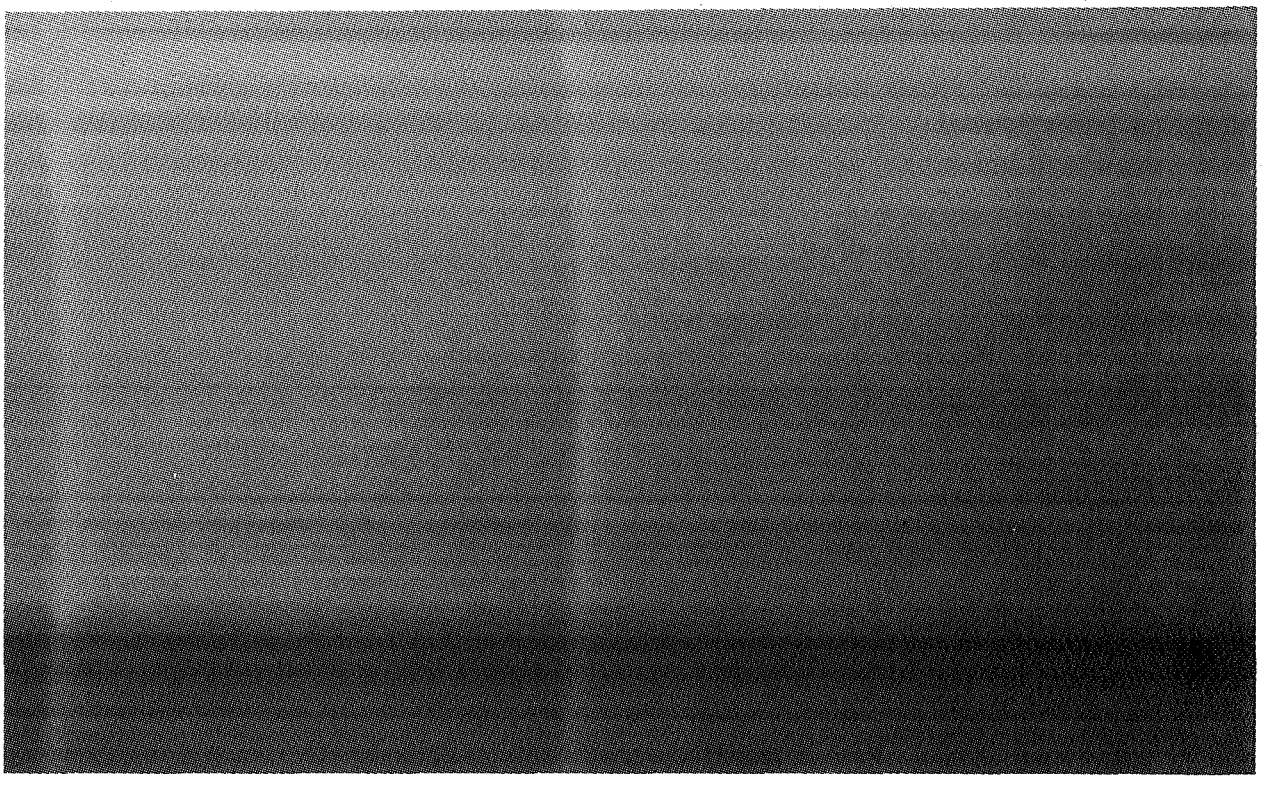

Figure 9. Electronic TDI camera image of F-18 at M=1.2 and 42,000 ft. slant range

FILM IMAGE OF F-18 SHOCKS CORRESPONDING TO TDI IMAGE

The film version of SAF was used in the current test for comparison with the electronic camera results. The film drive was started about 10 seconds before each plane pass, and continued several seconds after the pass to insure that flow field photographs were obtained.

The photographic image corresponding to the single successful electronic camera image is shown in figure 10. The shocks show up clearly, but film banding (strongly curved vertical lines) from non-uniform film motion, and also some longitudinal streaks from a bad scratch on the film and flaws on the mask cutoff also show up. This flight pass had all of the shocks merged into two strong shocks (N-wave). The shocks are inclined up at an angle of 66 deg. in the image, while the correct angle should be about 56 deg (from the M=1.2 condition). This indicates that the camera was inclined 10 deg. down relative to the image path. The shock separation in the aircraft flight direction was calculated to be 115 ft., which agrees with the TDI camera value within the sensor and film speed uncertainties.

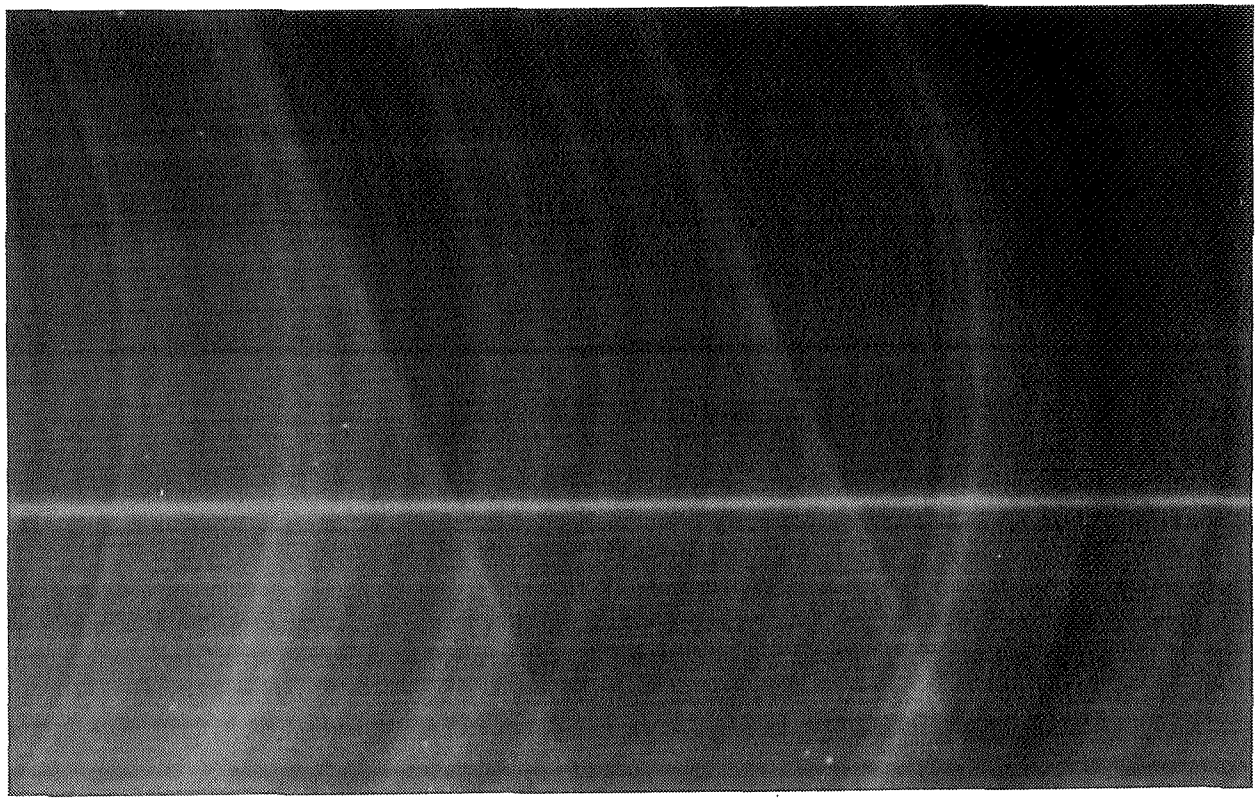

Figure 10. SAF film image of F-18 at M=1.2 and 42,000 ft. slant range

CONCLUSIONS

The electronic TDI camera was demonstrated to work properly at a flight test at NASA Dryden. The image from the TDI camera and a film image made with the film version of SAF were directly compared for the same flight, and showed the advantages of the TDI approach. However, some remaining difficulties resulted in less than optimum results, and must be overcome.

The main remaining problems with the cameras have to do with position alignment of the sensor axis with the flight direction, reliable operation of an automatic trigger to start the exposure, better relay optics, and a smoother mask edge. In addition, the plane location has to be known, even if contrails are not present, and the flight path has to be made to cross in the field of view. The flight path requirement will probable be taken care of with differential GPS.

REFERENCES

1. Campbell, James F.; and Chambers, Joseph R.: Patterns in the Sky. NASA SP-514, 1994.

2. Lamar, John E.; and Johnson, Jr., Thomas D.: Sensivity of F-106B Leading-Edge-Vortex Images to Flight and Vapor-Screen Parameters. NASA TP-2818, 1988.

3. Weinstein, L.M.: An Optical Technique for Examining Aircraft Shock Wave Structures in Flight. *High- Speed Research: 1994 Sonic Boom Workshop*. NASA CP-3279, 1994, pp.1-17.

4. Scharden, H.: Schlieren Methods and Their Application. *Ergenbnisse der Exakten Naturwissenchaften*, Vol. 20, pp.303-439, 1942 (English translation: NASA TT F-12,732)

USAF FLIGHT TEST INVESTIGATION OF FOCUSED SONIC BOOMS: PROJECT "HAVE BEARS"

Micah Downing
Armstrong Laboratory
Wright-Patterson AFB, OH, USA

Noel Zamot, Chris Moss, Daniel Morin, Ed Wolski, and Sukhwan Chung
USAF Test Pilot School
Edwards AFB, CA, USA

Kenneth Plotkin
Wyle Laboratories
Arlington, VA, USA

Domenic Maglieri
Eagle Engineering
Hampton, VA USA

INTRODUCTION

Supersonic operations from military aircraft generate sonic booms that can affect people, animals and structures. A substantial experimental data base exists on sonic booms for aircraft in steady flight and confidence in the predictive techniques has been established. All the focus sonic boom data that are in existence today were collected during the 60's and 70's as part of the information base to the US Supersonic Transport program[1-4] and the French Jericho studies for the Concorde[5]. These experiments formed the data base to develop sonic boom propagation and prediction theories for focusing. There is a renewed interest in high-speed transports for civilian application[6]. Moreover, today's fighter aircraft have better performance capabilities, and supersonic flights are more common during air combat maneuvers. Most of the existing data on focus booms are related to high-speed civil operations such as transitional linear accelerations and mild turns. However, military aircraft operating in training areas perform more drastic maneuvers such as dives and high-g turns. An update and confirmation of USAF prediction capabilities is required to demonstrate the ability to predict and control sonic boom impacts, especially those produced by air combat maneuvers.

In April 1994, the USAF Armstrong Laboratory in cooperation with USAF Test Pilot School conducted a measurement study of controlled focus boom generated by supersonic maneuvers. This study had three main objectives: to test the ability of pilots to control the placement of the focus region, to validate prediction methods, and to evaluate the effects of atmospheric turbulence on focusing[7]. The four air combat-type maneuvers used in the study were level linear acceleration, diving acceleration, constant g turn and a climbout/pushover. The test aircraft was the F-16B. Test were conducted within the Black Mountain Supersonic

Corridor at Edwards AFB which had a ground height of 2,900 feet Mean Sea Level (MSL). The maneuvers were flown at 10,000 feet MSL except for the dives which were started at 20,000 feet MSL. This altitude range is common for military operations and differs from previous focus sonic boom measurements[1,2,3,5]. These flights were flown under calm and turbulent atmospheric conditions since previous studies[3,5] have suggested that turbulent conditions may defocus and distort the booms within the focus region. A linear array of sonic boom monitors collected the sonic boom signatures along or parallel to the ground track. The Boom Event Analyzer Recorders, (BEAR)[8], were used to measure the sonic boom waveforms. The spacing of the BEARs ranged from 500 to 2,000 feet. The closer spacing was within the planned focus region with the wider spacing for the post focus and carpet region of the sonic boom footprint.

TEST PROCEDURES

To predict the flight profile, F-16B horizontal acceleration rates, sustained turn rates, and constant speed climb rates were determined using specific excess power curves from the F-16B flight manual[9]. Aircraft performance predictions for acceleration rates were made for standard day and standard day plus 10 degrees Celsius conditions. With this information, acceleration rates, climb rates, and sustained turn rates were calculated, and the sonic boom footprint from this profile was predicted using a ray tracing sonic boom model, PCBoom3[10]. With the boom prediction, the flight profile for each pass was aligned with the array for proper placement of the focus region. The alignment provided the distance-to-target for the maneuver point. The aircrews programmed these distances into the on-board guidance system along with the appropriate initial and steady point.

Rawinsonde balloon launches were scheduled within one hour of each test sortie launch time to gather atmospheric profile data. Data included temperature, pressure altitude, winds aloft, and relative humidity. As a backup to rawinsonde balloon data, the aircrew recorded inertial navigation system (INS) wind data from the Heads-Up Display (HUD) via the aircraft video tape recording (VTR) system. During the climbout, the pilot qualitatively assessed turbulence. Prior to each run, inertial winds at altitude were recorded by aircrew by hand and on the VTR tape. Surface weather data were measured at the test site.

The Black Mountain Supersonic Corridor was reserved from surface to 20,000 feet during all data runs to preclude noise interference from other aircraft activities. Ground personnel were stationed at specified locations throughout the array to provide real-time feedback to aid in determining the location of the sonic boom focus. Personnel uprange of the sonic boom focus should have heard no sonic boom. Personnel located in the vicinity of the focal region would hear a very loud "double boom" while those located downrange of the focus would hear a normal intensity "double boom" from the N-wave followed by a rumbling U-wave which indicated the trailing edge of the focal region. Feedback from these observers gave rapid qualitative feedback on the location of the focus. From this feedback, adjustments could be made to the timing of the profile flown to best place the location of the focal region on the array.

For all testing, aircraft tracking data were gathered via the Advanced Range Data System (ARDS). This information was used in flight along with normal air-traffic control radar

to provide course corrections to the aircrew for all runs except the autonomous level accelerations.

The level acceleration profile was the priority profile for data collection purposes. Prior to initiation of the maneuver, the test aircraft was stabilized at 0.9 Mach number and 10,000 feet pressure altitude. At initiation of the maneuver, the pilot selected full afterburner and accelerated on course to 1.2 Mach number. Course corrections were provided up to the maneuver point by controllers based on real-time display of ARDS data and were limited to five degrees of bank or less. The maneuver was terminated as the aircraft flew over the array, or reached 1.2 Mach number, whichever occurred first. To test the feasibility of pilots placing the focus region without external guidance several autonomous flights were performed with the linear acceleration. During the autonomous runs the pilots were given corrections to the maneuver point distance-to-target, if required, only between passes.

For the diving accelerations, the aircraft was stabilized at 0.9 Mach number and 20,000 feet pressure altitude. At the maneuver point, the pilot selected full afterburner, rolled inverted, and performed a 4g pulldown to a 30-degree nose low attitude on the flight path marker. No course corrections were provided after initiation of the maneuver. The maneuver was terminated as the aircraft reached 1.2 Mach number or descended below 13,000 feet pressure altitude.

For the constant-g turn, a load factor of 4g was chosen as a maximum sustainable load factor for the turn maneuver while trying to maintain 1.2 Mach number. Before the maneuver, the aircraft was stabilized at 1.2 Mach number and 10,000 feet pressure altitude. At the start of the turn, the pilot selected full afterburner and initiated a 4 g level turn. The maneuver was terminated after 50 degrees of turn.

For the climbout/pushover maneuver, the aircraft would start a ten degree climb at 1.2 Mach at 10,000 feet pressure altitude. At the pushover point, the pilot pushed the aircraft over with a load factor of 0.5 g to the level flight attitude while maintaining constant Mach number. The maneuver was terminated as the aircraft reached the level flight attitude.

RESULTS

For the overall study, 49 maneuvering passes were performed: 31 level accelerations (11 autonomous passes), nine diving accelerations, seven 4g turns, and two climbout/pushovers. The aircrews were successful in placing a focus boom within the array 37 times out of these 49 passes. Tables 1 - 5 list the summary information for the individual passes. Of the twelve 'misses', the focus was produced in front of the array five times and behind the array only once. For five passes, turbulence distorted the sonic boom within the array so that a focus region could not be clearly defined. The separation time of the leading shocks between the N and the U wave was used to estimate the location of the onset of the focus region. Note, for the table and the following boom signature plots, the zero point is the target point, positive distance is uptrack of the target, and negative is downtrack.

Level Acceleration

One objective of this test was to test the ability of pilots to control the placement of the focus region. In summarizing the statistics of the focus boom placement for the level acceleration profiles, the data is grouped into three different sets: total, calm atmospheric conditions, and autonomous run passes. The total group includes 25 passes and excludes two passes where turbulence defocused the boom and four passes where insufficient boom data were collected. For this group the focus boom had a mean placement of -1150 feet downtrack from the target point with a standard deviation of 3230 feet. The calm atmospheric conditions group that includes passes flown in the morning includes eight passes. The mean placement of the focus boom for this grouping was -60 feet from the target with a standard deviation of 2660 feet. The autonomous run group includes nine passes and excludes two passes in which turbulence severely distorted the focusing of the boom. For this group the focus placement had a mean of +1060 feet uptrack from the target point with a standard deviation of 980 feet. In comparing these different sets, the placement precision for the autonomous passes demonstrates the ability of the aircrews to control the placement of the focus region and of current USAF sonic boom prediction program to plan supersonic profiles. However, atmospheric turbulence greatly diminishes this ability, as seen with these summary statisitcs.

Three linear accelerations passes are considered in detail to show some the effects of atmospheric turbulence on sonic boom focusing. The first boom series was measured during calm atmospheric conditions, the second one during thermally turbulent conditions (low winds, high solar heating), the third series during mechanical turbulence (gusting winds, low heating). Figure 1 shows the Mach number versus time for each of these flights. This plots shows that the acceleration rates were fairly consistent between the flights. For flight during thermal turbulence, the acceleration was less than the other cases which would result in the focus region occurring slightly further downstream. Figure 2 shows the boom signatures recorded along the array under calm atmospheric conditions. The booms are aligned in relative time to the leading shock. The first boom recorded was 500 feet uptrack of the target point and had a peak overpressure of 10.8 psf. However, the maximum measured peak overpressure of 19 psf occurred at the target point. Figure 2 shows the increased separation between the N and U waves with distance from the focus region. The comparison between the amplitude of the N and U waves, Figure 3, shows the amplification of the peak overpressure within the focus region. For this case the measured amplification factor was 3. This plot also shows the decay of the post-focus U wave amplitude as it moves from the focus region[2-5].

Figure 4 shows the signature computed from PCBoom3[10], using the acceleration profile shown in Figure 1. Comparing this to Figure 2, it appears that the predicted focus is slightly too far uptrack and the N-U separations are larger than measured. However, the focal zone methodology in PCBoom3 applies a numeric focus solution by Gill and Seebass[11] to the linear ray acoustic caustic location. The Gill-Seebass solution shows non-linear distortion of the ray geometry, with the focus occurring slightly above the caustic. This displaces the focus downtrack. For the conditions of the Flight 46 focus, this displacement has been calculated to be 3,500 feet. Applying this offset, the measured and predicted N-U separation are in very good agreement. The offset predicted focus location is then about 1,500 feet downtrack of the measured focus, but this is associated with nonlinear displacement in the Gill-Seebass solution and is also a distance comparable to the focal zone dimension. The predicted overpressures also agree well with the measurements.

The second boom series, as shown in Figure 5, was measured during thermally turbulent conditions. This series demonstrates no clear focus region although the acceleration profile is similar to the previous case. The maximum peak overpressure was 10.0 psf and occurred 5,250 feet downtrack from the target point which can be expected from the reduced acceleration rate. The third boom series, shown in Figure 6, was measured during mechanically turbulent conditions. This series is drastically different since two focus regions occurred within the array. The first focus region was at 500 feet uptrack of the target point and had a peak overpressure of 20.9 psf. The second region was at 7,000 feet downtrack of the first and had a peak overpressure of 19.3 psf. The last measured signature shows two post-focus U wave trailing the N wave. These two boom series signatures suggest that turbulent conditions can minimize and distort the focus region and its amplified peak overpressures.

Dive

The boom series for the accelerating dive is shown in Figure 7. The maximum boom was 7.2 psf and measured 1,380 feet uptrack from the target point. This series shows that the post-focus region is narrower than the level acceleration maneuver since the post-focus U wave moves away from the N wave at a quicker rate. Figure 8 shows the peak overpressures of the N and U waves measured along the array. Within the focus region the peak overpressure was amplified by a factor of 2 for this flight.

Turn

The next boom series is for a 4g turn at a Mach number of 1.2. The profile was aligned with the array so that the array would capture the focal line from the steady part of the turn and not the superfocus region generated by the initiation of the turn. The measured booms are shown in Figure 9. At the first part of the array, the measured booms were from the steady portion prior to the maneuver point. Focusing was measured within a band of 2,500 feet about the target point with the maximum overpressure measured at -1,500 feet from the target. This shows that focal line is very narrow for this maneuver. The maximum overpressure was 8.7 psf. Post-focus signatures or disturbances appear in both directions similar to earlier measurements[5]. The measured focus boom from the turn amplified the boom by a factor of 4.

Pushover

The final maneuver performed during the study involved a climbout pushover type of profile. The ground track was set parallel to the measurement array by 1,370 feet. The booms measured from this flight are shown in Figure 10. The maximum peak overpressure was 11.6 psf and occurred 2,000 feet downtrack of the predicted focus point. This booms was amplified by a factor of 4. For this series only slight disturbances appear to trail behind the N wave in the post-focus region.

CONCLUSIONS

This paper summarizes the basic data collected for a controlled focus boom study completed in April 1994 at Edwards AFB CA, USA. The objectives of this study were to test the ability of aircrews to control the placement of focus booms with preplanned supersonic maneuvers, to validate prediction methods, and to measure the effect of turbulent conditions on

the focusing of the sonic booms produced by these maneuvers. Of the 49 flights 37 focus booms were placed within the array. Predictions of focal zone geometry (accounting for both linear ray geometry and nonlinear displacement from the caustic) agree well with measurements. Our results are consistent with previous focus sonic boom studies and show that the focus region produced by aircraft maneuvers have an width varying from 100 to 1,000 feet. This study demonstrates the ability of aircrews to control the focal region of the sonic boom footprints with preplanning of the flight profile. This finding could help in minimizing adverse impacts from planned supersonic training flights. Also, the results of this study confirm that turbulent conditions can defocus the focal regions as suggested by previous studies. Examples of this effect show that the focus regions can be distorted and/or diminished. One flight under mechanical turbulent conditions displayed two focus regions with reduced amplification of the peak levels, while one flight under thermal turbulent conditions showed that the focus region is almost completely diminished. These two examples demonstrate that turbulence can have a strong defocusing effect on sonic boom propagation.

REFERENCES

1. Maglieri, D.J., and Lansing, D.L., "Sonic Booms from Aircraft in Maneuvers," NASA TN D-2370, Washington D.C., July 1964.

2. Lansing, D.L., and Maglieri, D.J., "Comparison of Measured and Calculated Sonic-Boom Ground Patterns Due to Several Different Aircraft Maneuvers," NASA TN D-2730, Washington, D.C., April 1965.

3. Maglieri, D.J., and Hilton, D.A., "Experiments on the Effects of Atmospheric Refraction and Airplane Accelerations on Sonic-Boom Ground-Pressure Patterns," NASA TN D-3520, Washinton, D.C., July 1966.

4. Maglieri, D.J., "Sonic Boom Flight Research--Some Effects of Airplane Operations and the Atmosphere on Sonic Boom Signature," NASA SP 147, Washington, D.C., 1967, pp. 25 - 48.

5. Wanner, J-C.L., Vallee, J., Vivier, C., and Thery, C., "Theoretical and Experimental Studies of the Focus of Sonic Booms," *JASA*, Vol. 52, No. 1 (part 1), 1972, pp. 13-32.

6. Darden, C.M., Powell, C.A., Hayes, W.D., George, A.R., and Pierce, A.D., "Status of Sonic Boom Methodology and Understanding," NASA CP 3027, Proceedings of a workshop hed at NASA-Langley Research Center, January 19-20, 1988.

7. Zamot, N., *et al*, "Evaluation of Controlled Focus Sonic Booms Produced by Maneuvering Supersonic Aircraft," AFFTC-TLR-94-29, Edwards ARB, CA, May 1994.

8. Lee, R.A., and Downing, J.M., "Boom Event Analyzer Recorder (BEAR): The USAF Unmanned Sonic Boom Monitor," AIAA 93-4431, 15th AIAA Aeroacoustics Conference, Long Beach, CA, Oct. 1993.

9. *USAF Series F-16A/B Aircraft Flight Manual*, Technical Order 1F-16A-1, Lockheed Fort Worth Division, Forth Worth, Texas, Change 8, 7 June 1993.

10. Plotkin, K.J., Downing, J.M., and Page, J., "USAF Single Event Sonic Boom Prediction Model: PCBoom," *JASA*, 95 (5), Pt. 2, May 1994, 2839.

11. Gill, P.M., and Seebass, A.R., "Non-Linear Acoustic Behavior at a Caustic: An Approximate Solution," *AIAA Progress in Astronautics and Aeronautics*, H. Nagamatsu (Ed.), MIT Press 1975.

Table 1. Level Linear Accelerations (Guided) Focus Boom Placements

Pass No.	Date	Time (PDT)	Focus Location from target (feet)	Comments	Atmospheric Conditions
1	12 Apr 94	9:23:27	-2880		Sunny with high scattered clouds. 70-71° F at test site Winds at 1.0 knots gusting to 4 knots. 16% Rel. Hum.
2		9:29:01		Focus in array, no boom data	
3		9:32:12	960		
4		9:35:32	-5120		
5		9:39:06	3000	Focus up track of array	
6		9:43:55		Focus in array, no boom data	
7		12:10:20	-5690		Sunny with high scattered clouds. 68-70°F at site. Winds at 5 knots gusting to 8 knots. 7% Rel. Hum.
8		12:16:43		Focus in array, no boom data	
9		12:23:22	-1370		
10		12:27:36	-2580		
11		12:53:17		Focus in array, no boom data	
12		12:59:39	1900		
13		13:05:26	-3050		
23	13 Apr 94	12:34:47	0		Sunny with high scattered clouds. 63-65°F at site. Winds at 2.5 knots gusting to 5 knots. 9 % Rel. Hum.
24		12:40:23	-7000	Distorted focus region	
25		12:45:16	-3000		
26		12:49:48	~2000/ -8390	Multiple focus regions	
27		12:52:09	-1120		
28		13:00:43	-6940		
29		13:05:42	~-7500		

Table 2. Level Linear Accelerations (Autonomous) Focus Boom Placements

Pass No.	Date	Time (PDT)	Focus Location from target (feet)	Comments	Atmospheric Conditions
39	20 Apr 94	15:19:32	+1520/ -6870	Multiple focus regions	Sunny, clear skies. 95-97°F at site. Winds at 4 knots gusting to 8 knots. 8% Rel. Hum. Thermal turbulence
40		15:25:09	0/-7390	Distorted focus regions	
41		15:30:05		Defocused	
42		15:35:33		Defocused	
43	21 Apr 94	7:40:58	+1940		Sunny, clear. 61-63°F at site. Winds at 2.5 knots gusting to 5 knots. 50-46% Rel. Hum.
44		7:47:00	+80		
45		7:52:34	+1120		
46		7:58:06	+440		
47		16:51:50	+2860		Sunny clear, stiff winds at altitude. 81°F at site. Winds at 11 knots gusting to 20 knots. 15% Rel. Hum. Mech. Turb.
48		16:58:59	+1440	Distorted focus regions	
49		17:06:09	+140		

Table 3. 30° Diving Acceleration Focus Boom Placements

Pass No.	Date	Time (PDT)	Focus Location from target (feet)	Comments	Atmospheric Conditions
14	13 Apr 94	9:42:11		Missed array to west	Sunny, high scattered clouds. 55-58°F at site. Winds at 3 knots gusting to 7 knots. 19% Rel. Hum.
15		9:47:41	~-8000	Estimated from Observations	
16		9:52:53	-4450		
17		9:57:23	+2213	Focus up track of array	
18		10:10:00	+3950	Focus up track of array	
19		10:19:24	+2800	Focus up track of array	
20		10:25:56	+1450		
21		10:28:40	+2160		
22		10:35:50	+4930	Focus up track of array	

Table 4. Level 4g Turn Focus Boom Placement

Pass No.	Date	Time (PDT)	Focus Location from target (feet)	Comments	Atmospheric Conditions
30	15 Apr 94	12:18:28		Distorted	Sunny, clear. 65-66°F at site. Winds at 7 knots gusting to 14 knots. 8% Rel. Hum.
31		12:21:39		Distorted	
32		12:24:45	+1500/ -6390	Multiple focus regions	
33		12:28:45		Distorted	
34	18 Apr 94	12:05:23		Aborted Run	Sunny, high clouds. 91°F at site. Winds at3 knots gusting to 8 knots. 39% Rel. Hum.
35		12:11:15	-900		
36		12:17:05	-1920		

Table 5. Climbout/Pushover Focus Boom Placement

Pass No.	Date	Time (PDT)	Focus Location from target (feet)	Comments	Atmospheric Conditions
37	19 Apr 94	12:21:00	-170		Sunny, high scattered clouds. 90-91°F at site. Winds at 2 knots gusting to 7 knots. 21% Rel. Hum.
38		12:28:00	+2440		

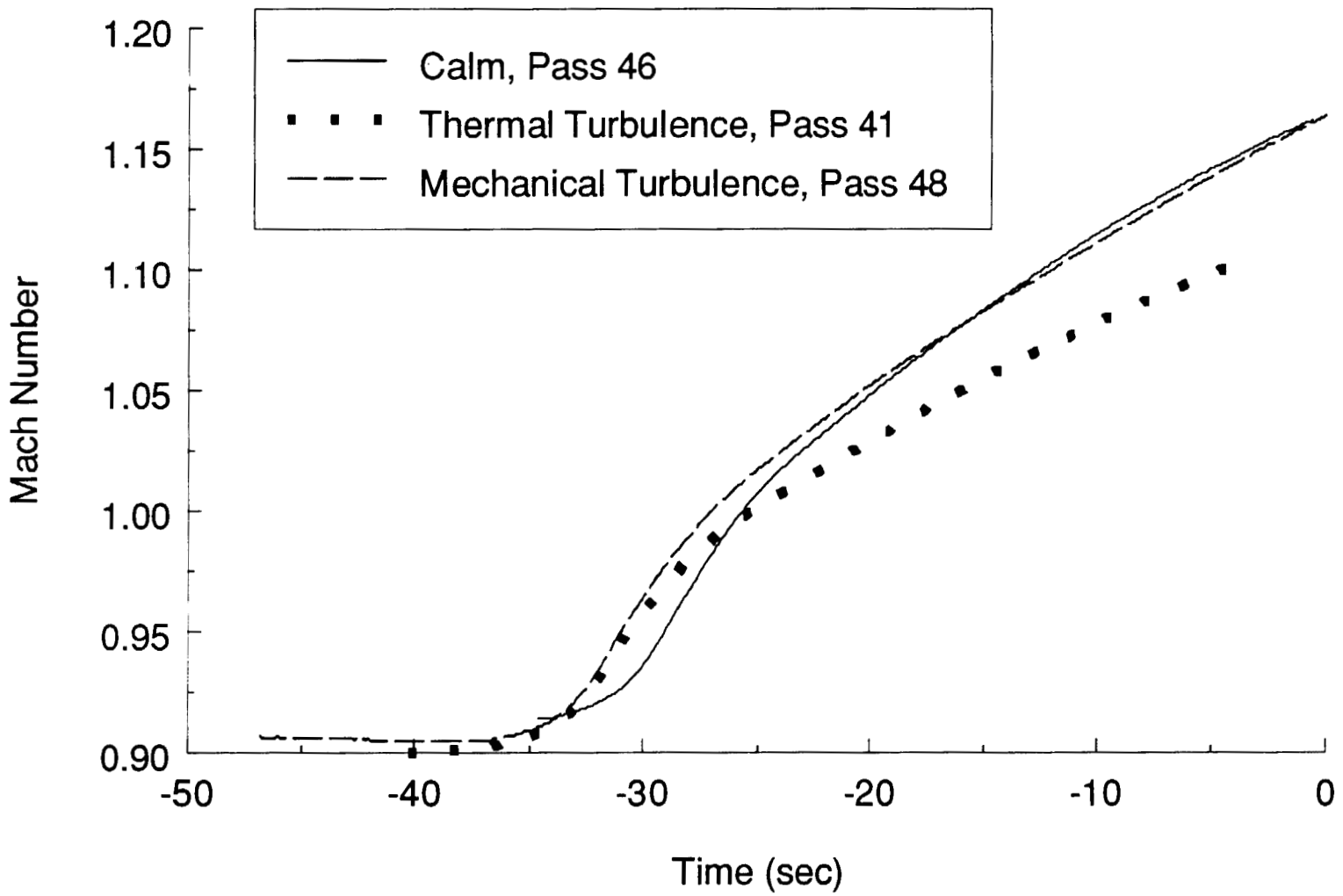

Figure 1.- Mach number versus time for the level linear accelerations during calm and turbulent atmospheric conditions. (Note time is relative to aircraft crossing target point.)

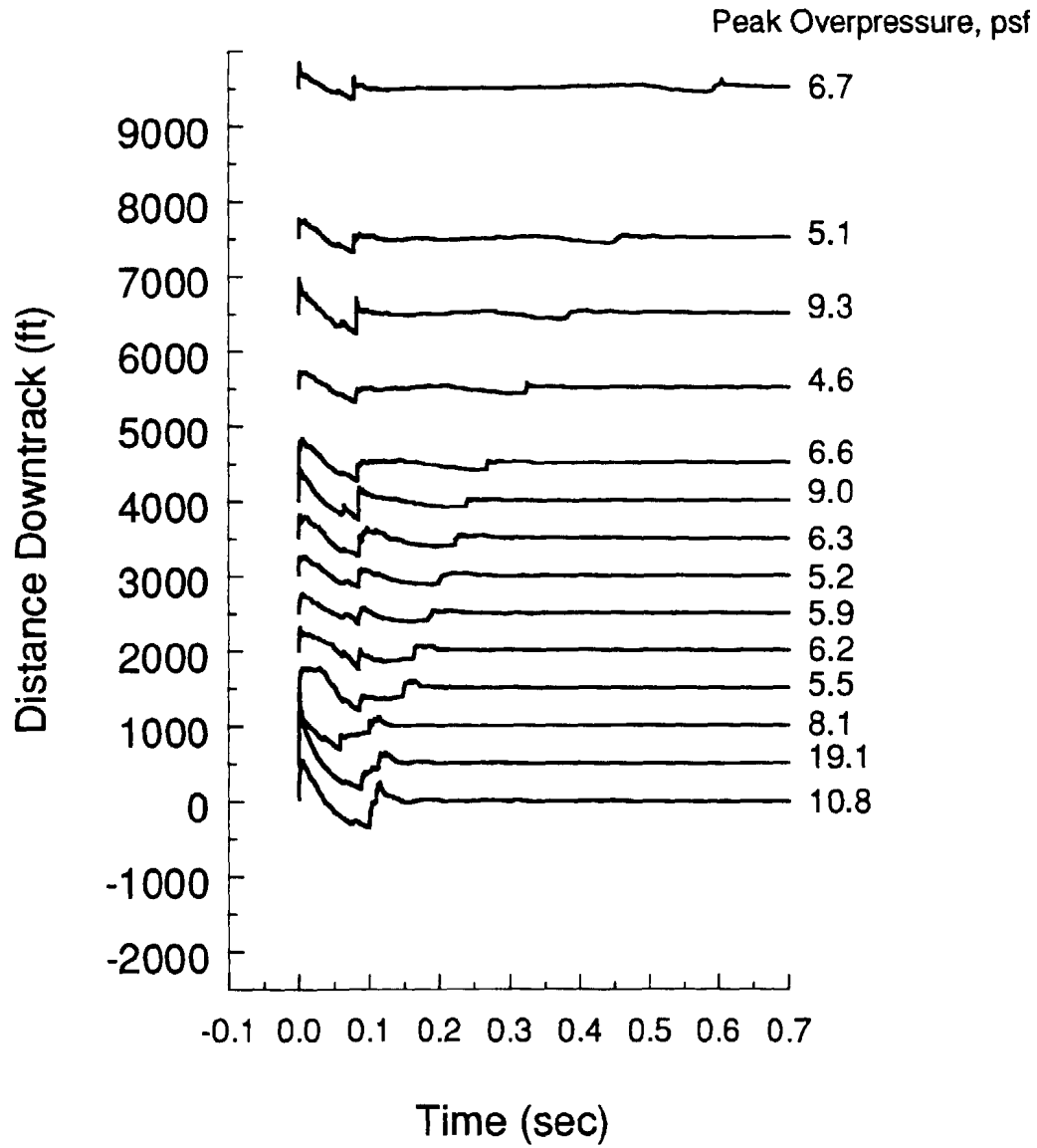

Figure 2.- Measured sonic boom waveforms produced by a level linear acceleration during calm atmospheric conditions. (Signatures are aligned in time relative to the leading shock.)

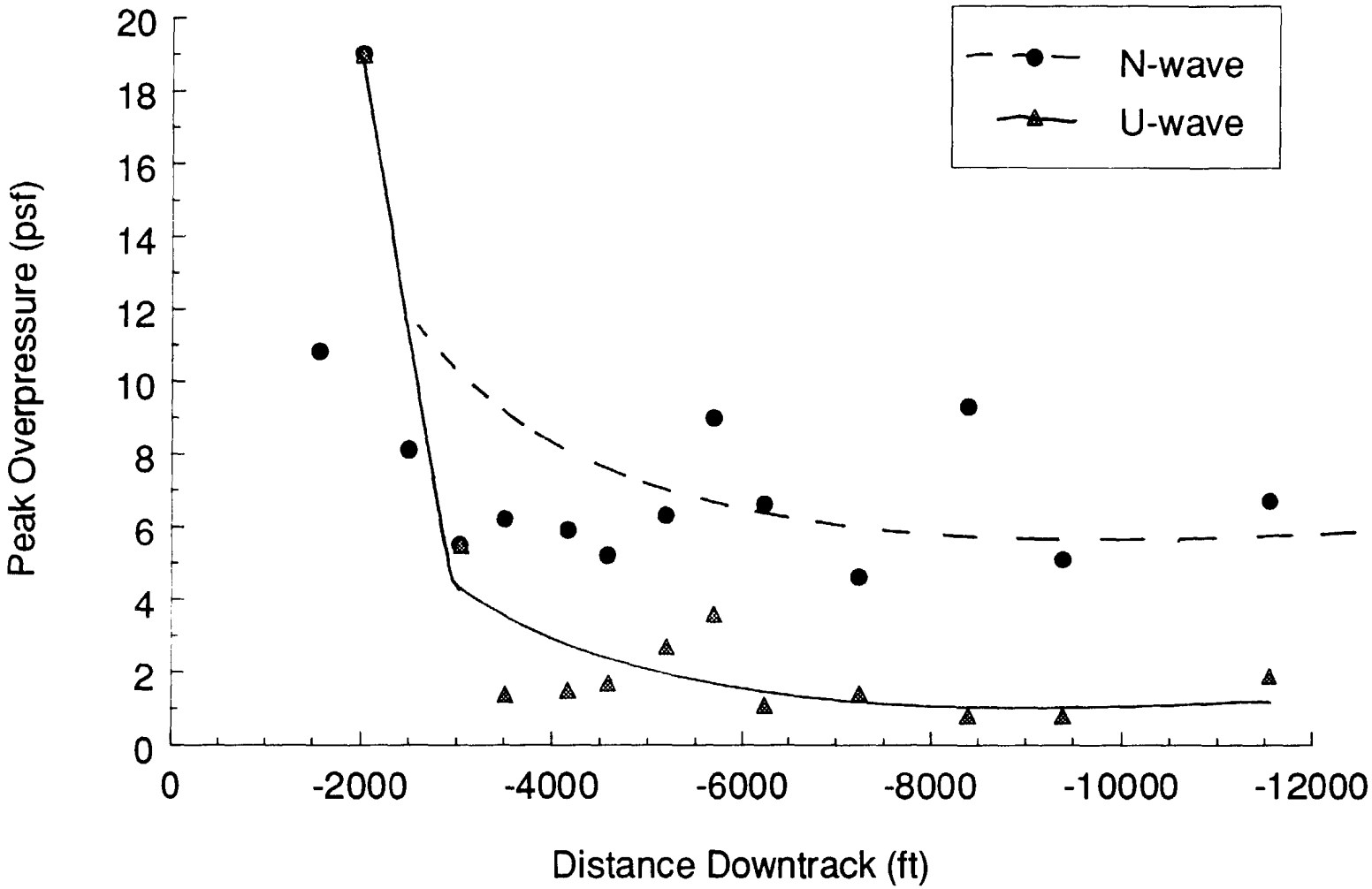

Figure 3.- N and U wave peak overpressures versus distance down track of focal zone for a level linear acceleration flight during calm atmospheric conditions.

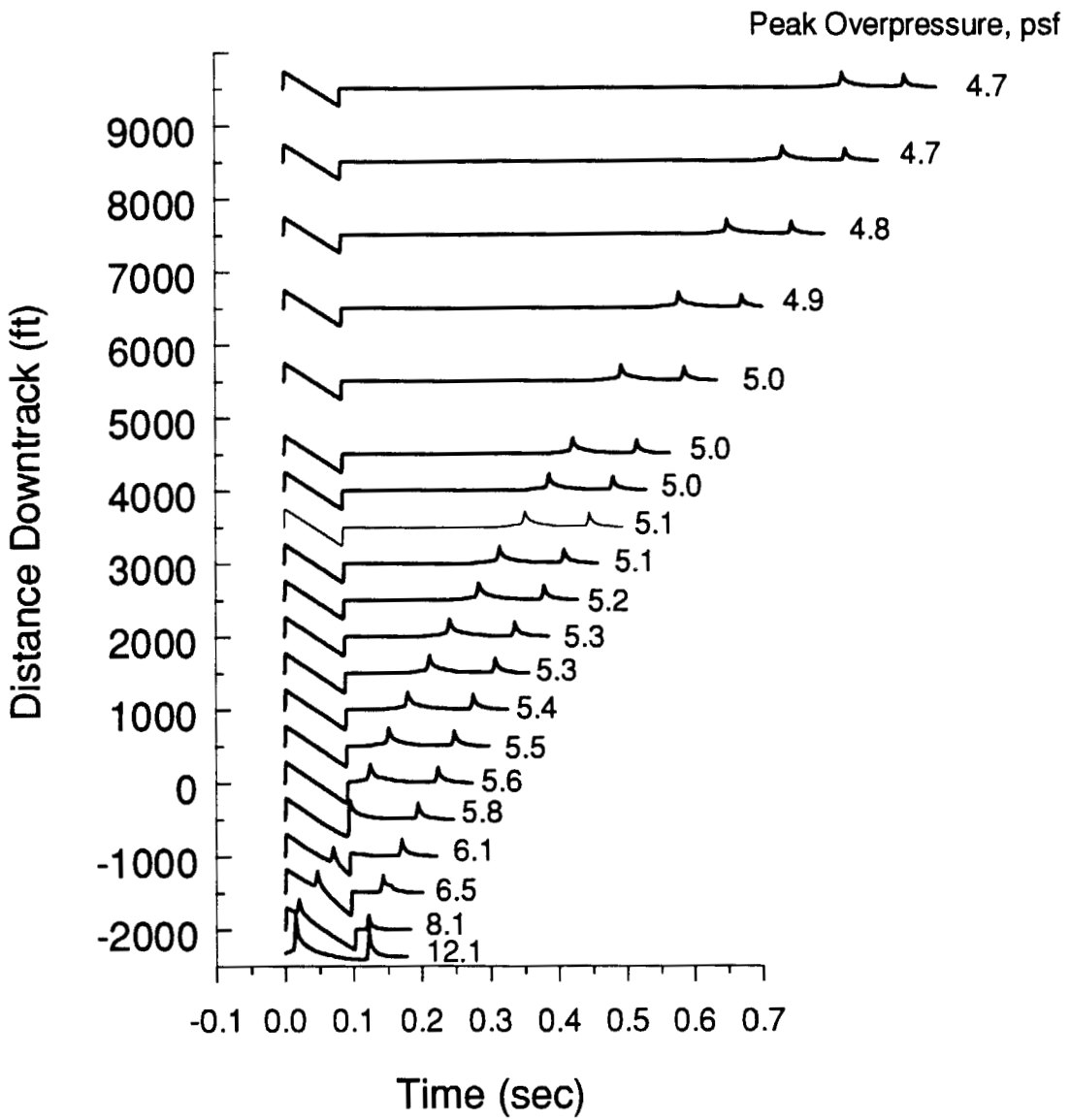

Figure 4.- Predicted sonic boom waveforms produced by a level linear acceleration during calm atmospheric conditions. (Signatures are aligned in time relative to the leading shock.)

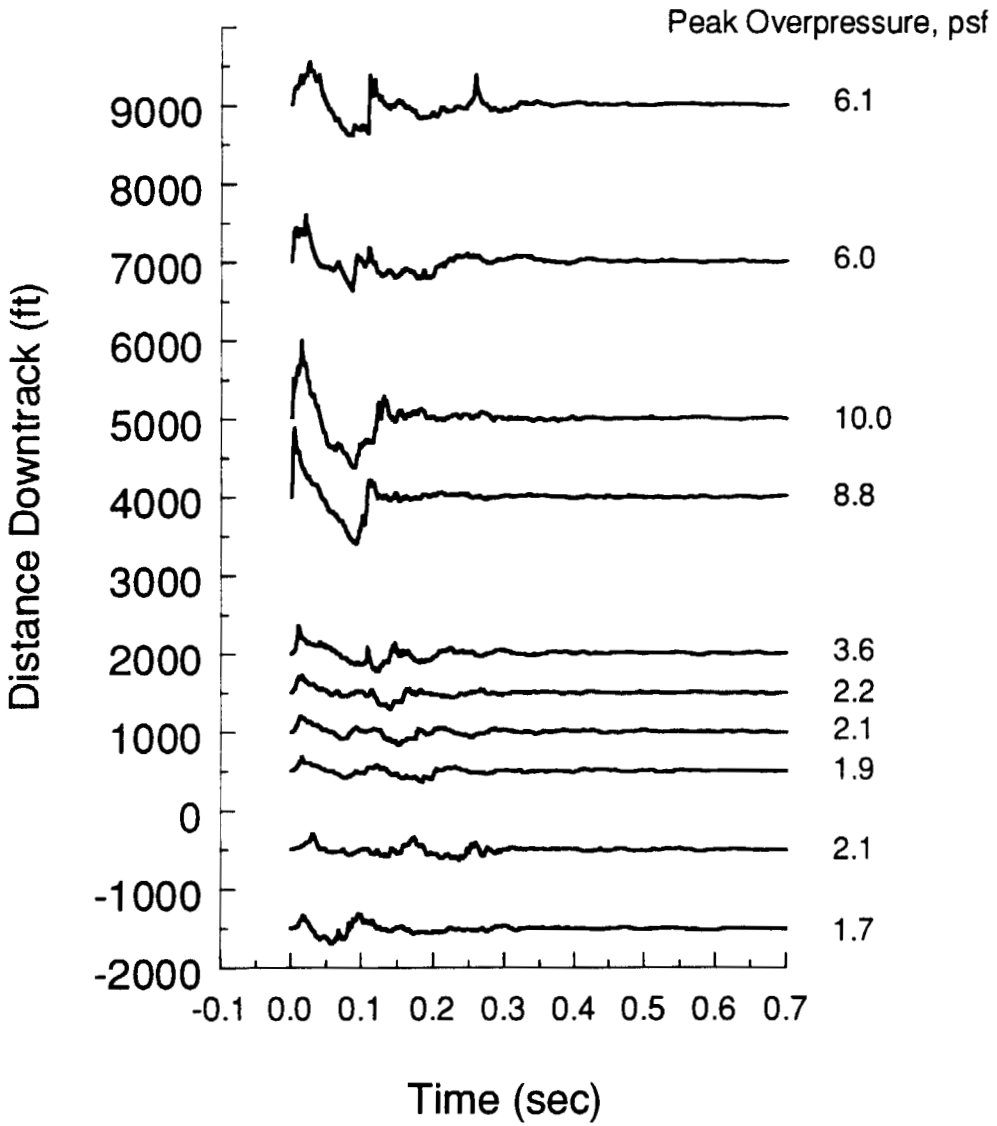

Figure 5.- Measured sonic boom waveforms produced by a level linear acceleration during thermally turbulent atmospheric conditions. (Signatures are aligned in time relative to the leading shock.)

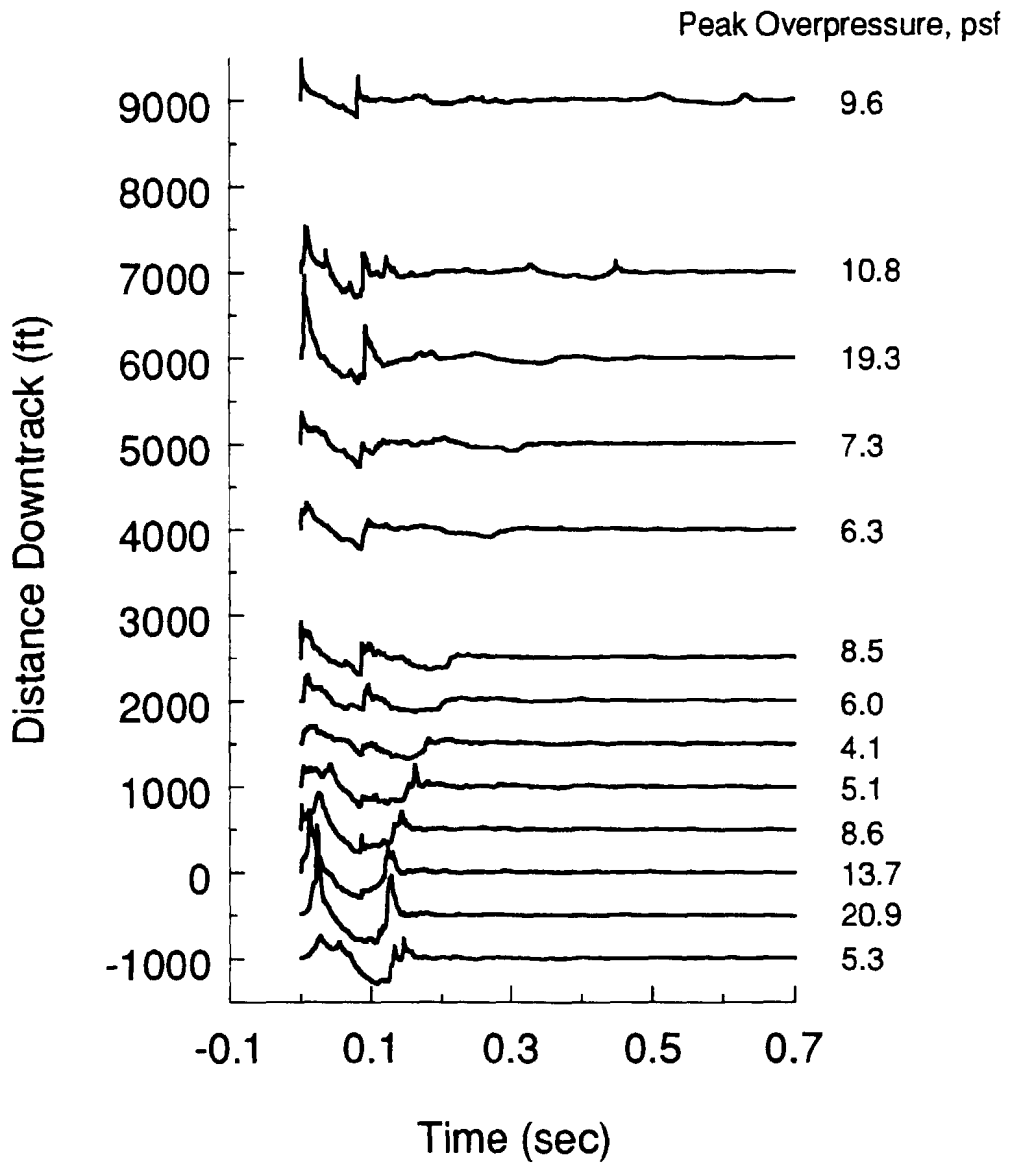

Figure 6.- Measured sonic boom waveforms produced by a level linear acceleration during mechanically turbulent atmospheric conditions. (Signatures are aligned in time relative to the leading shock.)

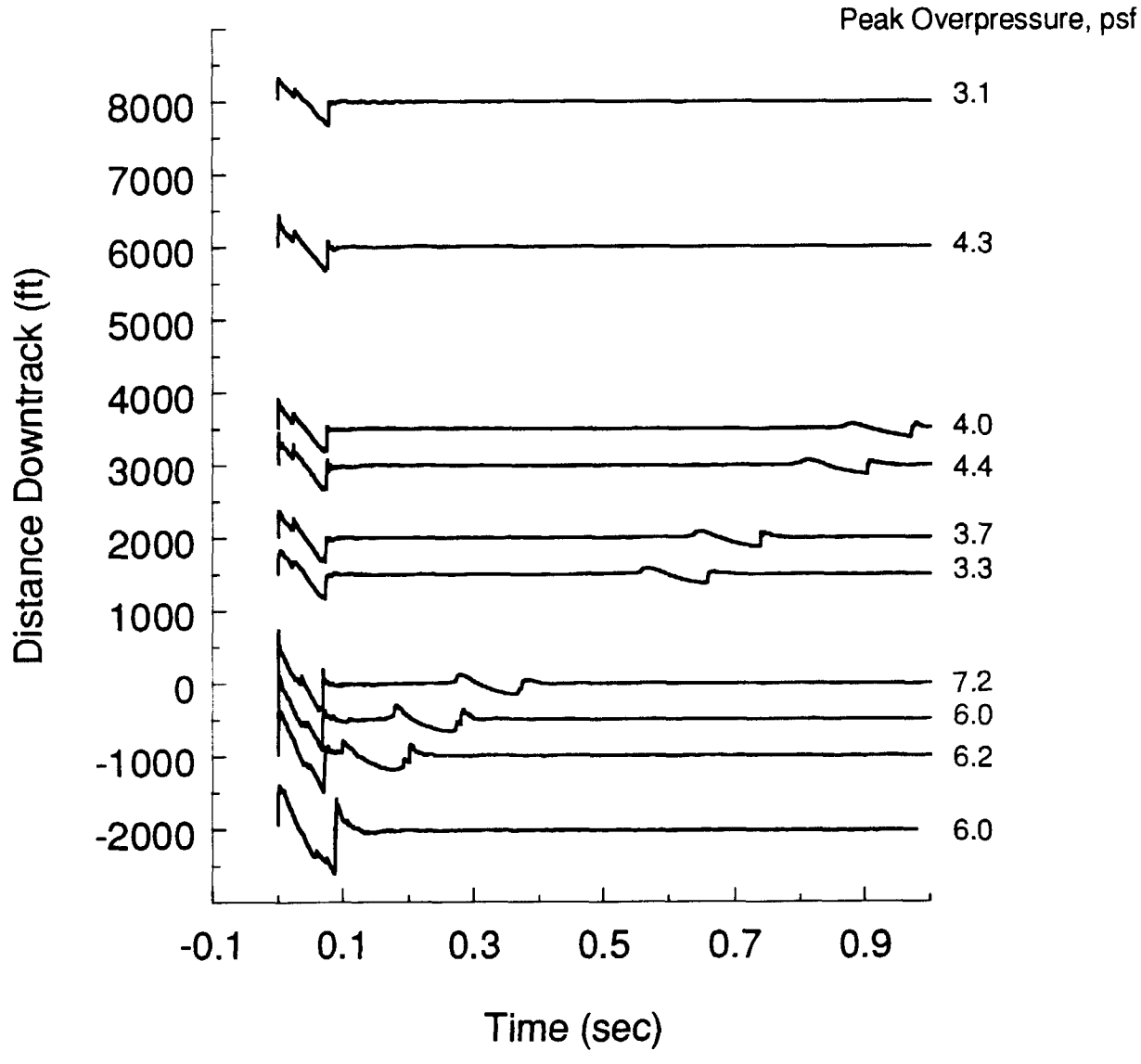

Figure 7.- Measured sonic boom waveforms produced by a 30° accelerating dive. (Signatures are aligned in time relative to the leading shock.)

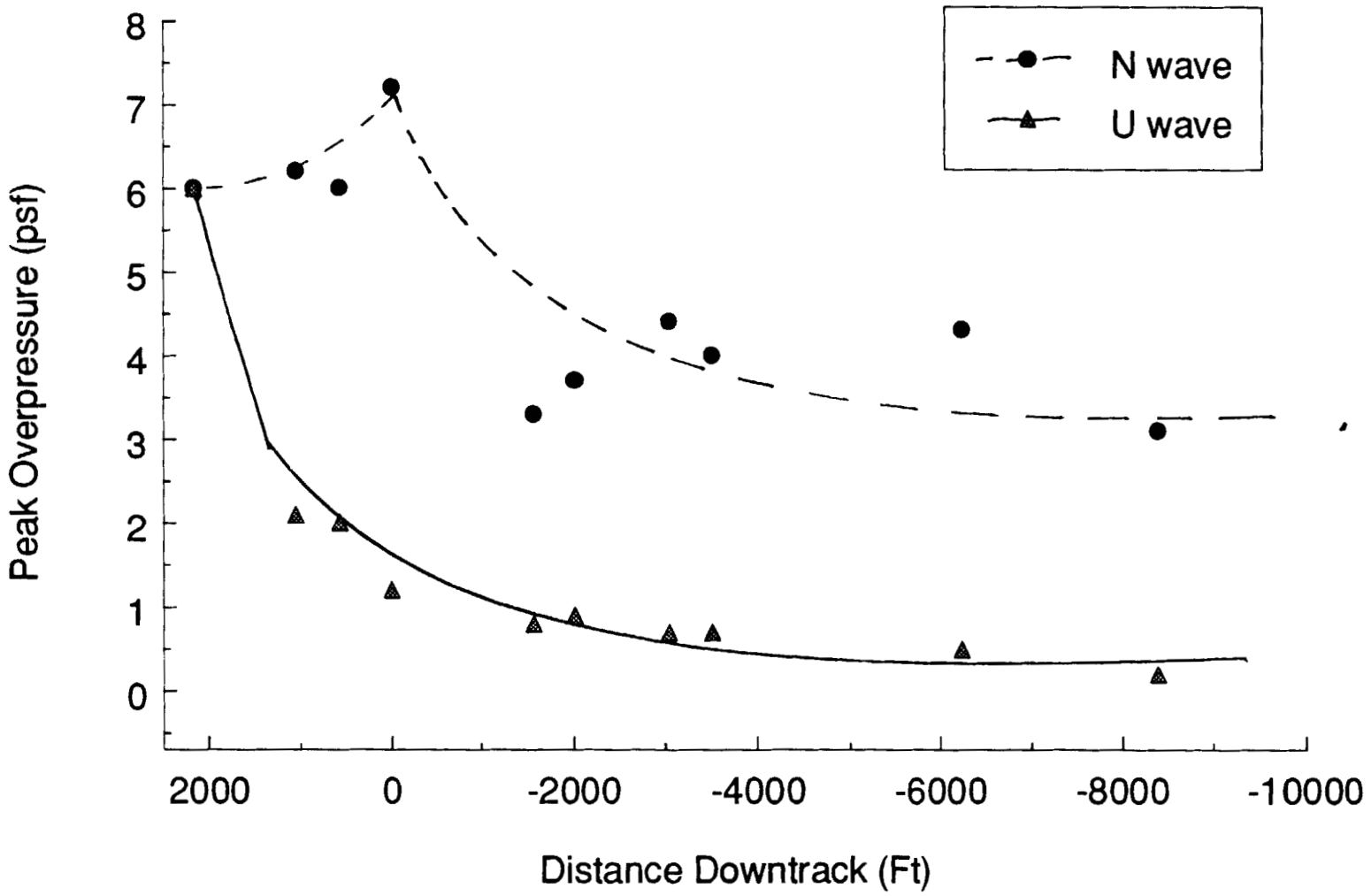

Figure 8.- N and U wave peak overpressures versus distance down track of focal zone for a 30° accelerating dive.

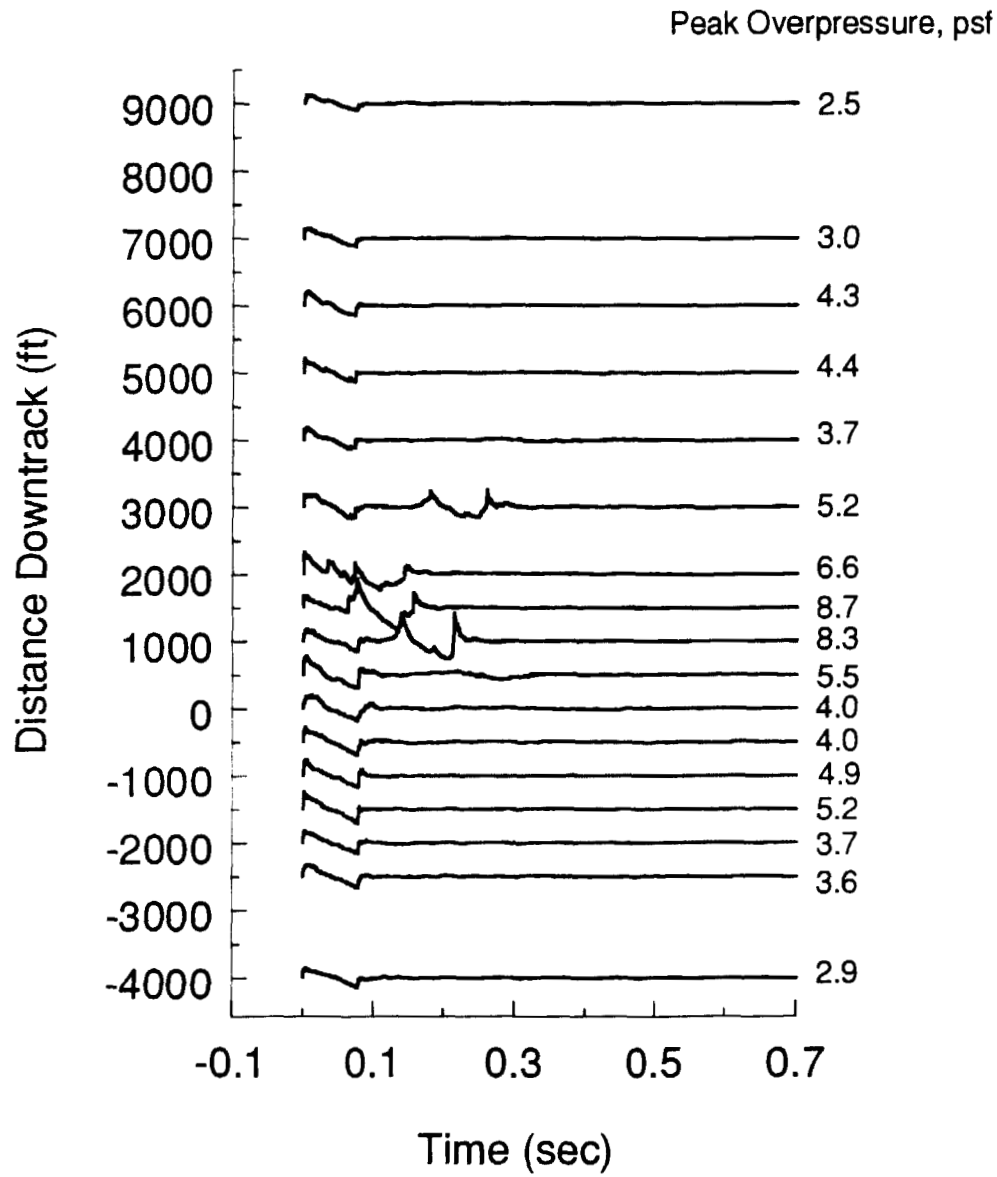

Figure 9.- Measured sonic boom waveforms produced by a 4g turn at 1.2 Mach. (Signatures are aligned in time relative to the leading shock.)

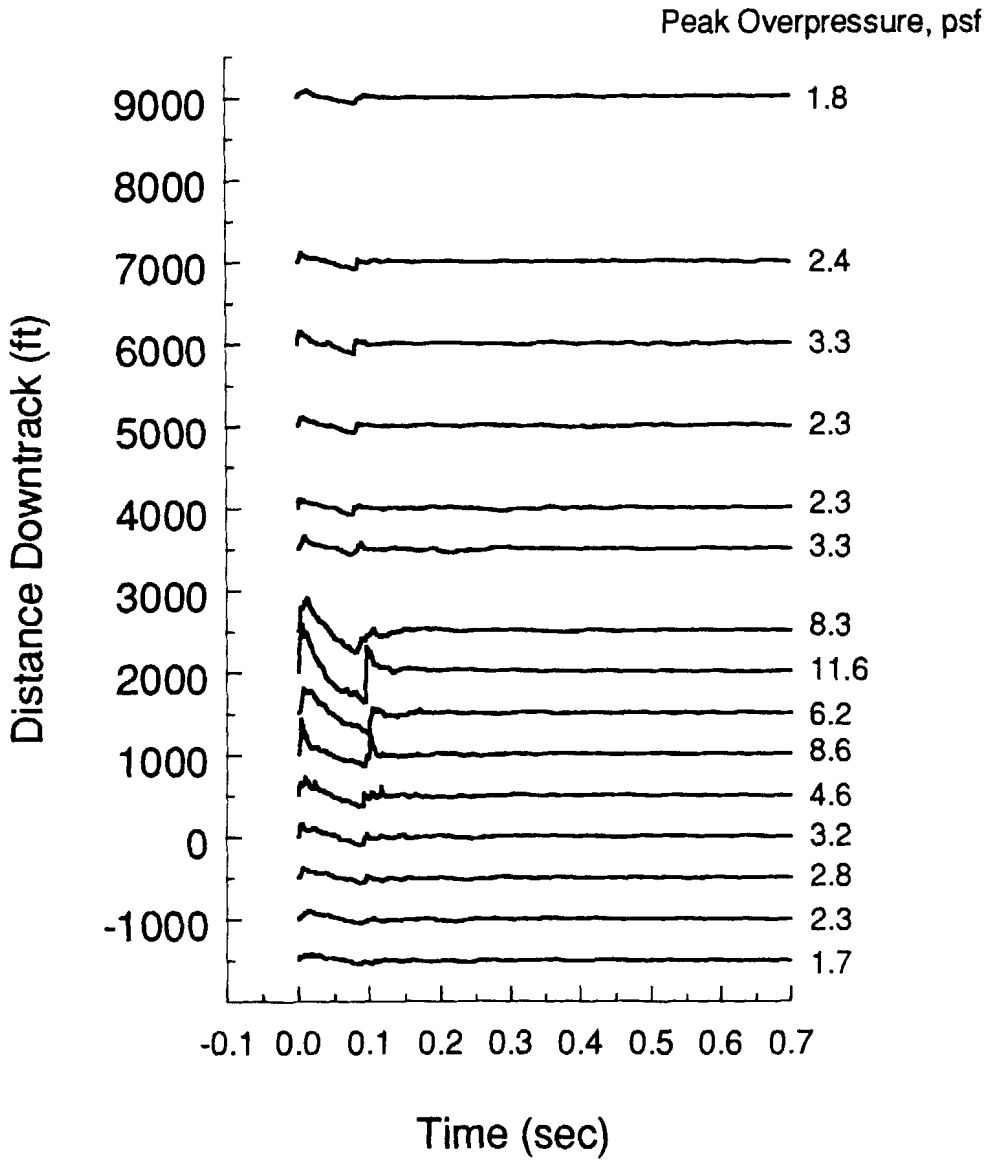

Figure 10.- Measured sonic boom waveforms produced by a 0.5g pushover maneuver. (Signatures are aligned in time relative to the leading shock.)

SUBJECTIVE RESPONSE TO SIMULATED SONIC BOOMS IN HOMES

David A. McCurdy[1] and Sherilyn A. Brown[2]
NASA Langley Research Center
Hampton, VA

INTRODUCTION

One of the environmental issues affecting the development of a second-generation supersonic commercial transport is the impact of sonic booms on people. Aircraft designers are attempting to design the transport to produce sonic boom signatures that will have minimum impact on the public. Current supersonic commercial aircraft produce an "N-wave" sonic boom pressure signature that is considered unacceptable by the public. This has resulted in first-generation supersonic transports being banned from flying supersonic over land in the United States, a severe economic constraint. By tailoring aircraft volume and lift distributions, designers hope to produce sonic boom signatures having specific shapes other than "N-wave" that may be more acceptable to the public. As part of the effort to develop a second-generation supersonic commercial transport, Langley Research Center is conducting research to study people's subjective response to sonic booms. As part of that research, a system was developed for performing studies of the subjective response of people to the occurrence of simulated sonic booms in their homes.

The In-Home Noise Generation/Response System (IHONORS) provides a degree of situational realism not available in the laboratory and a degree of control over the noise exposure not found in community surveys. The computer-controlled audio system generates the simulated sonic booms, measures the noise levels, and records the subjects' ratings and can be placed and operated in individuals' homes for extended periods of time. The system was used to conduct an in-home study of subjective response to simulated sonic booms. The primary objective of the study was to determine the effect on annoyance of the number of sonic boom occurrences in a realistic environment. The effects on annoyance of several other parameters were also examined.

Initially, data analyses were based on all the data collected (ref. 1-3). However, further analyses found that test subjects adapted to the sonic booms during the first few days of exposure. The first eight days of each testing period consisted of eight introductory exposures that were repeated on randomly selected days later in the testing period. Comparison of the introductory exposures with their repeats indicated that the test subjects adapted to the new sonic boom noise environment during the first days of the testing period. Because of the adaptation occurring, the introductory days were deleted from the data set and the analyses redone. This paper presents the updated analyses. Elimination of the introductory days did not significantly affect the results and conclusions of the initial analyses. This paper also presents analyses of the effects on annoyance of additional factors in the study not previously examined.

[1]Aerospace Engineer, NASA Langley Research Center, Mail Stop 463, Hampton, VA 23681-0001, Tel: (804)864-3596, Fax: (804)864-8823

[2]Aerospace Engineer, NASA Langley Research Center, Mail Stop 463, Hampton, VA 23681-0001, Tel: (804)864-3593, Fax: (804)864-8823

IN-HOME NOISE GENERATION/RESPONSE SYSTEM DIAGRAM

A diagram of the IHONORS system is shown in figure 1. The system consisted of a computer and compact disc player that played the simulated sonic booms at randomly-selected, pre-programmed times through a preamplifier and amplifier into three or four loudspeakers located in different rooms of the house. The two indoor microphones and sound level meters measured the levels of the booms as they occurred and also continuously measured the ambient noise levels in the home. The measurements were then transferred to the computer and stored on its hard disk. At the end of the day, the test subject used the trackball to answer a series of questions about his or her activities during the day and his or her subjective response to the sonic booms heard. Once a week the noise measurements and test subject responses were downloaded via a modem to a central computer. The data were then checked to ensure that the system was operating correctly.

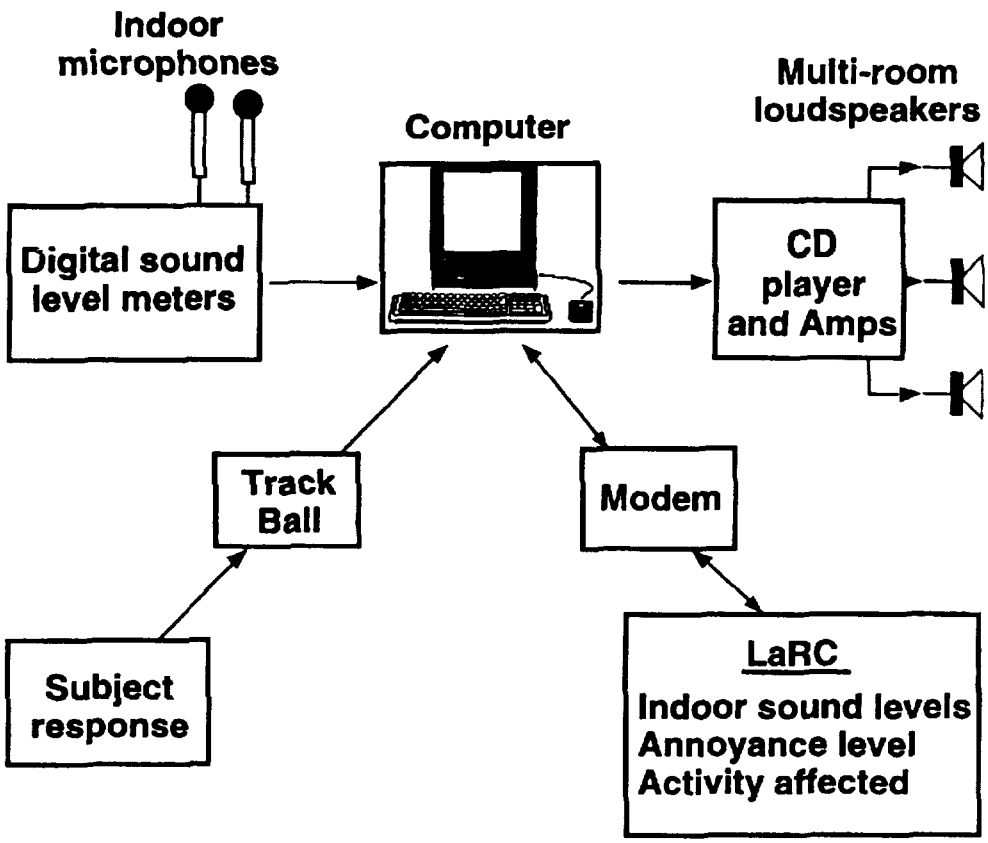

Figure 1.

DEPLOYED IN-HOME NOISE GENERATION/RESPONSE SYSTEM

Figure 2 shows the actual components as deployed in a test subject's home. Selected homes were limited to single family detached dwellings so that the simulated sonic booms would not penetrate the walls into neighbors homes as might be the case in apartments or townhouses. The range of homes selected covered the economic range from lower middle class to upper middle class. The computer, compact disc player, trackball, and monitor were placed on the shelves of a microwave oven cart. The preamplifier, amplifiers, and sound level meters were placed inside the lower cabinet of the cart. The cart was placed in a position that was convenient for the test subject and that simplified the installation of cables. Three or four loudspeakers were placed in the rooms that the test subject indicated he or she most used during the 14 hour boom period each day. The two microphones were placed in two of the rooms with loudspeakers. The system components blended in well with the existing decor in most cases and were often decorated with bric-a-brac by the test subject.

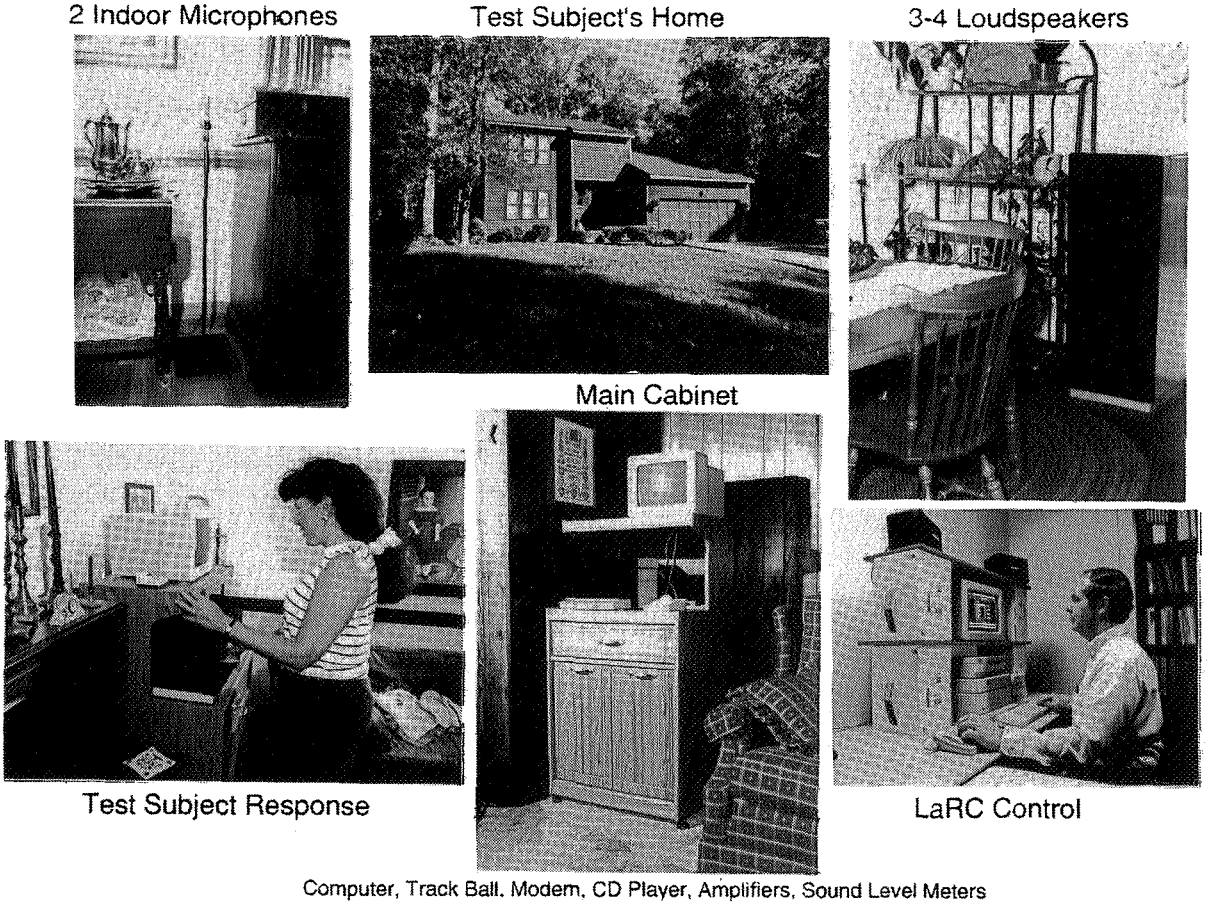

Figure 2.

TEST PLAN

The final test plan is outlined in figure 3. Eight IHONORS systems were used to conduct the in-home study of subjective response to simulated sonic booms. A system was deployed for eight weeks in each of 33 homes. Each day the system played simulated sonic booms during a 14 hour period as the test subject went about his or her normal activities. At the end of the 14 hours the test subject rated his or her annoyance to the sonic booms heard during the day. A total of 264 weeks of data including over 1800 subjective annoyance responses to daily sonic boom exposures were collected; the equivalent of five years of sonic boom exposures in realistic environments.

- February 1993 to December 1993
- 33 homes
- 8 weeks per home
- 14 hour test day (no booms during normal sleep period)
- 1848 total exposure days
- 58,443 total sonic booms

Figure 3.

EXPERIMENT DESIGN

As shown in figure 4, the sonic booms presented each day represented combinations of three sonic boom pressure signatures or waveforms, three A-weighted sound exposure levels (SEL(A)), and seven sonic boom occurrence rates. The SEL(A) levels used were nominally 66, 70, and 74 dB. These values covered the range of indoor sonic boom levels estimated for a variety of second-generation supersonic transport designs. The pressure waveforms represented an outdoor N-wave, an indoor N-wave, and an outdoor "shaped" wave. All the sonic booms had a rise time (τ) of four msec and a duration of 300 msec. The occurrence rates were 4, 10, 13, 25, 33, 44, and 63 booms per 14 hour period. Only one sonic boom waveform was presented each day. On most days the sonic boom was presented at only one SEL(A) level. On a few days the sonic boom was presented at two or three of the SEL(A) levels.

- 3 pressure signatures
  - N-wave, outdoor, τ = 4 msec
  - N-wave, indoor, τ = 4 msec
  - shaped, outdoor, τ = 4 msec

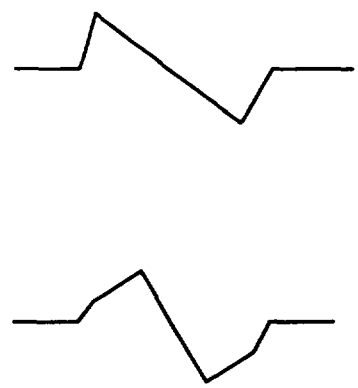

- 3 levels - 66, 70, 74 dB - SEL(A)
- 7 boom occurrence rates - 4, 10, 13, 25, 33 ,44, 63 booms per day

Figure 4.

TEST SUBJECT RESPONSES

The information obtained from the test subjects is outlined in figure 5. The computer-generated questions answered by the test subject at the end of each day are summarized as follows: (1) when were you not inside your house, (2) what activities did you do while inside your house, (3) how annoying were the sonic booms you heard today on a 0 to 10 scale, and (4) were you startled by any of the sonic booms today?

- Daily computer-generated questions
  - When were you not inside the house?
  - What activities did you do while in the house?
  - How annoying were the sonic booms you heard today? (0 to 10)
  - Were you startled by any of the sonic booms today? (Yes or no)

Figure 5.

EFFECT OF ADAPTATION ON TEST SUBJECT ANNOYANCE

As mentioned previously, the first eight days of each testing period consisted of eight introductory exposures that were repeated on randomly selected days later in the testing period. These introductory exposures were included to determine if the test subjects adapted to the new noise environment during the first few days of the testing period.

In order to calculate an exposure level for a day in which more than one boom is heard, it is necessary to determine the effect of number of sonic booms occurrences. Based on energy addition theory and initial analyses of all the data collected (ref. 1-3), the effect of number was modeled by adding "10*log(number of occurrences)" to the individual boom noise level. (The model is discussed and confirmed in a following section.)

Since the number of booms actually heard each day by a test subject could vary, it was not possible to directly compare the response to an introductory day with the response to its repeated day. Therefore, indicator (dummy) variable regression analysis was used to compare the responses to the introductory exposures with the responses to their repeats. The exposures were defined in terms of SEL(A). Since the order of the eight introductory days was varied across test subjects, each of the first eight test days included each of the introductory exposures. For each test day, 1 through 8, the introductory exposures and subjective responses were compared with the repeated exposures and responses. The resulting regression equations for each day found no significant differences in slope between the regression lines for the introductory exposures and the repeat exposures. Each day's difference in subjective response between the introductory and repeated exposures was determined from the regression equation (line intercepts) and converted into equivalent SEL(A) decibels. These subjective differences are plotted against test day in figure 6. The regression analysis indicated that the introductory exposures were more annoying than the repeated exposures for each of the first eight test days. The difference in annoyance was statistically significant for test days 1 and 3. Although the difference for the other six days was not significant, the trend in figure 6 is clear. The test subjects were more annoyed by a given sonic boom exposure occurring in the first few days of the test period than the same exposure occurring later in the test period.

As a result of this adaptation effect, the eight introductory days were removed from the data set. Analyses of the reduced data set are presented in the following sections. Eliminating the introductory days did not significantly affect the results and conclusions of the original analyses using all the days. The use of "10*log(number of occurrences)" to model the effect of number of sonic boom occurrences was confirmed in the re-analysis of the data

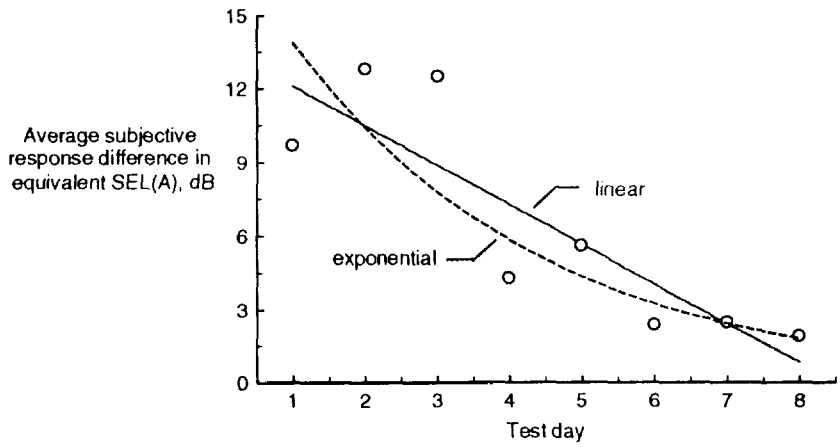

Figure 6.

EFFECT OF NUMBER OF SONIC BOOM OCCURRENCES ON ANNOYANCE

Figures 7 and 8 illustrate the effect of number of booms heard. Figure 7 shows subjective annoyance ratings versus the SEL(A) level of the individual sonic boom repeated during the day. The number of occurrences (n) of the boom is divided into five intervals, each having roughly the same number of data points. The linear regression lines for each interval are plotted in the figure. As illustrated in the figure, the subjective annoyance response increases as the number of occurrences of a sonic boom increases.

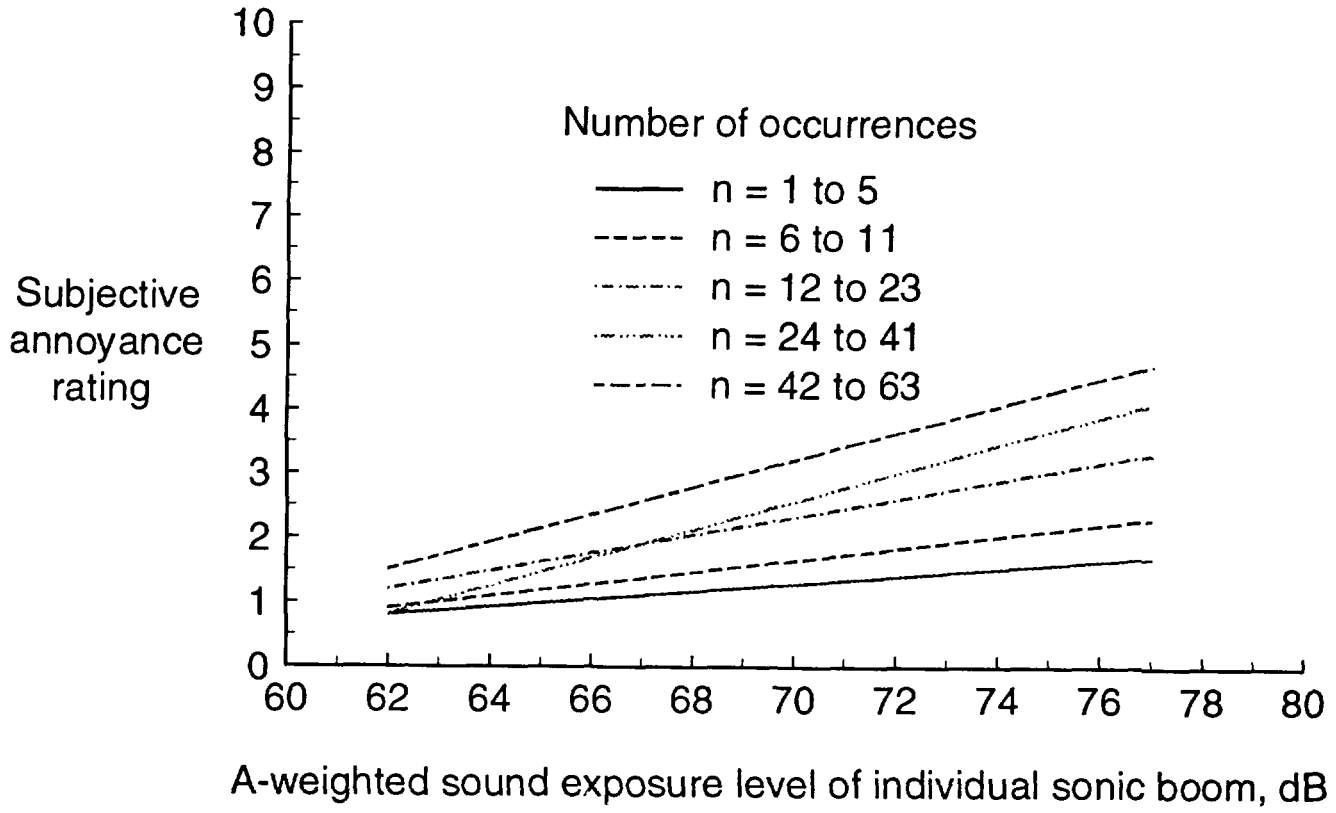

Figure 7.

This effect of number of occurrences can be modeled by the addition of the term *"k * log(number of occurrences)"* to the measured sonic boom level. Figure 8 shows the values of *"k"* and the corresponding 95% confidence intervals determined from regression analyses for each of several noise metrics. The metrics were perceived level (PL), two versions of Zwicker's loudness level (LL_Zd and LL_Zf), perceived noise level (PNL), A-weighted sound exposure level (SEL(A)), C-weighted sound exposure level (SEL(C)), and unweighted sound exposure level (SEL(U)). The metrics represent different ways of modeling the frequency response of the ear (ref. 4,5). As shown in figure 8, analyses of the data indicate that the calculated value of *"k"* ranged from 10 to 15 depending on the noise metric considered. However, for almost all the metrics, the 95% confidence interval about the calculated value includes the value of 10. Therefore, in those cases, the value of *"k"* cannot, statistically, be said to be significantly different from 10, the predicted value based on energy addition.

The two metrics whose 95% confidence intervals on *"k"* did not include the value of 10 were examined further. The value of *"k"* was calculated from the regression coefficients a_1 and a_2 for each metric. Comparison of a_2, the *"log(number of occurrences)"* coefficient, across all metrics found that the value of a_2 was constant across all metrics, indicating that the differences in *"k"* for SEL(U) and SEL(C) were due to the metric and not the effect of number of occurrences.

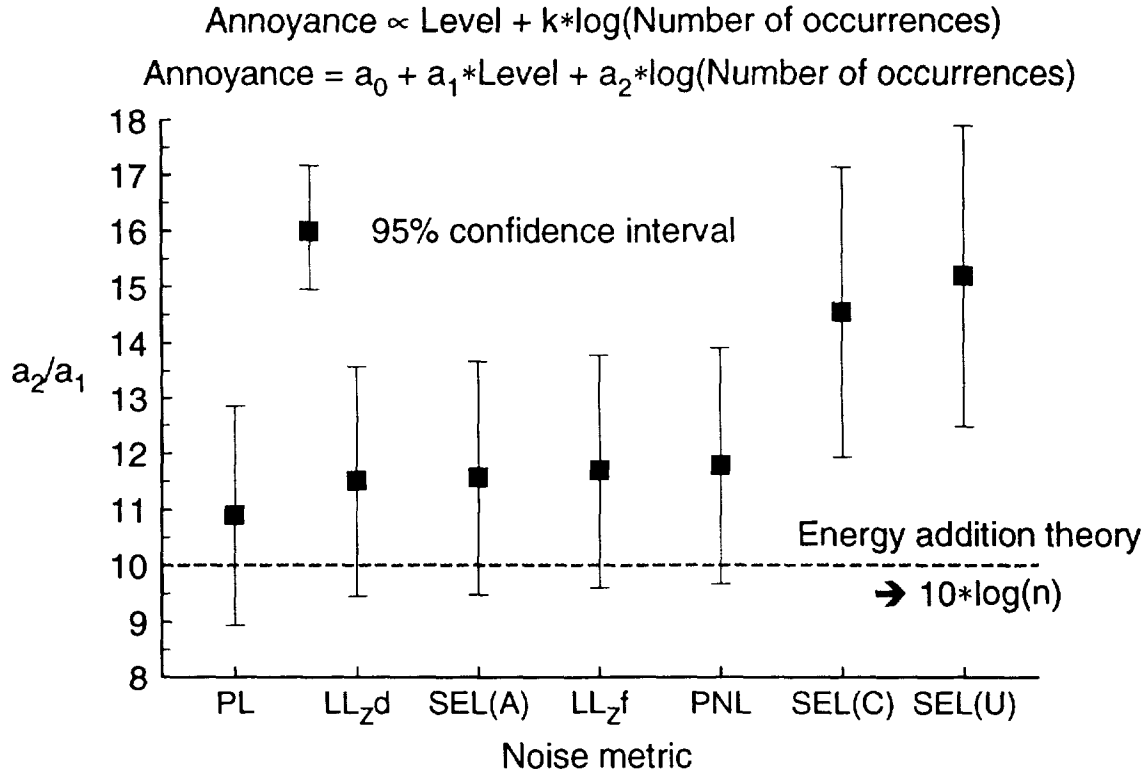

Figure 8.

COMPARISON OF NOISE METRICS

Having confirmed the model for summing the effect of multiple sonic booms, the total daily sonic boom exposure was calculated in terms of each of the noise metrics for comparison with the test subjects' daily annoyance judgments. Daily exposure is commonly expressed in terms of Day-Night Level (DNL). Day-Night Level uses "10*log(number of occurrences)" to sum multiple events and then averages the noise energy across 24 hours (ref. 5). (No late night penalties were assessed.) Although DNL is usually associated with A-weighted sound pressure level, for the purpose of this study, a DNL was calculated using each of the noise metrics.

The predictive ability of the noise metrics was then compared based on the correlation coefficients between the subjective annoyance ratings and the different DNL's. The resulting rank order of metrics is shown in figure 9. Perceived level was a significantly better predictor of annoyance to the simulated sonic booms than the other metrics. Figure 9 also illustrates the subjective annoyance ratings as a function of DNL(PL) and as a function of the more commonly used DNL(A) and DNL(C). A best-fit regression line is drawn through the data in each plot.

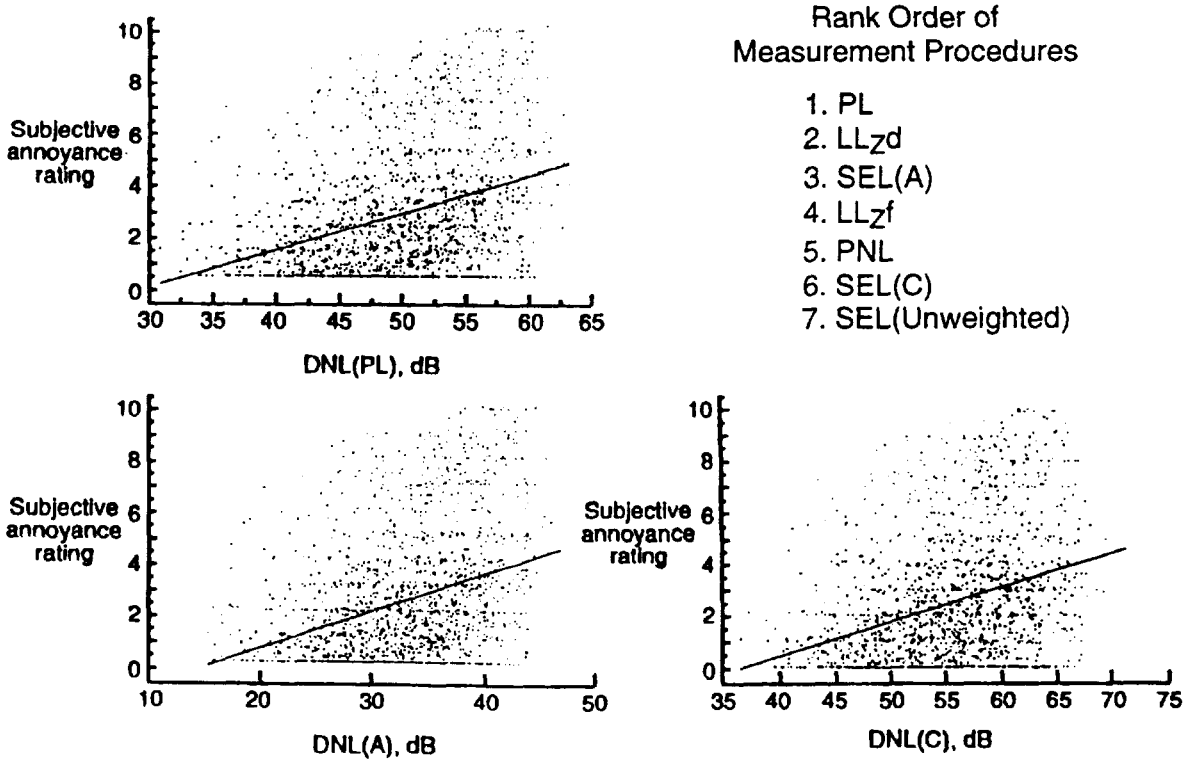

Figure 9.

Figure 10 shows the effect of sonic boom waveform on annoyance for noise measurements based on perceived level. The figure shows the regression line of subjective annoyance rating on day-night level based on perceived level for each of the three sonic boom waveforms used in the study. Indicator (dummy) variable analyses found no difference in either slope or intercept between the three different sonic boom waveforms. This result was the same for all the noise metrics considered.

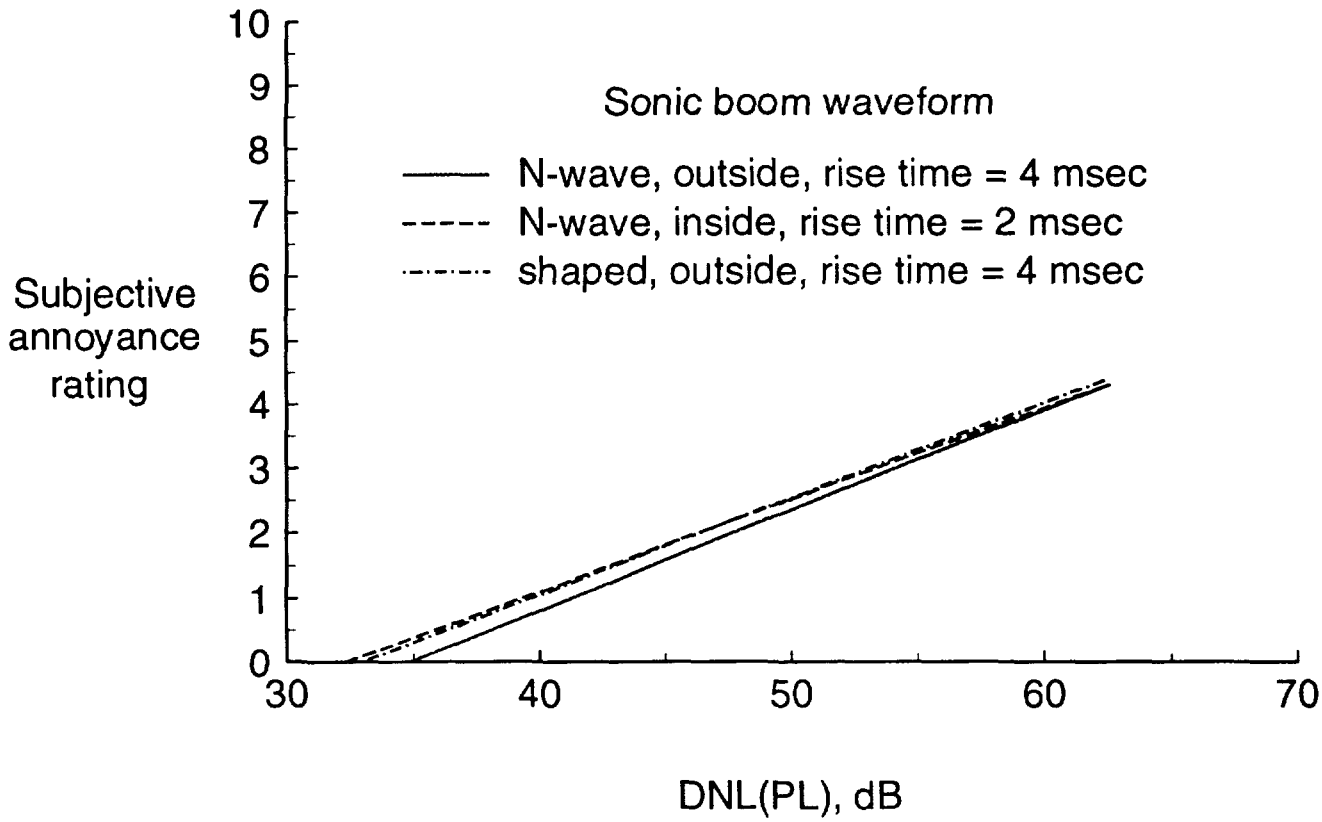

Figure 10.

EFFECT OF STARTLE ON ANNOYANCE TO SONIC BOOMS

Figure 11 shows the effect of startle on annoyance for noise measurements based on perceived level. The regression lines for both startled and not startled are shown for subjective annoyance rating plotted against day-night level based on perceived level. Indicator (dummy) variable analyses indicated a significant difference in both slope and intercept between startled and not startled by a sonic boom. Annoyance is greater when the test subject is startled and the magnitude of the increase in annoyance increases as the sonic boom exposure increases. This effect was the same for all the noise metrics considered.

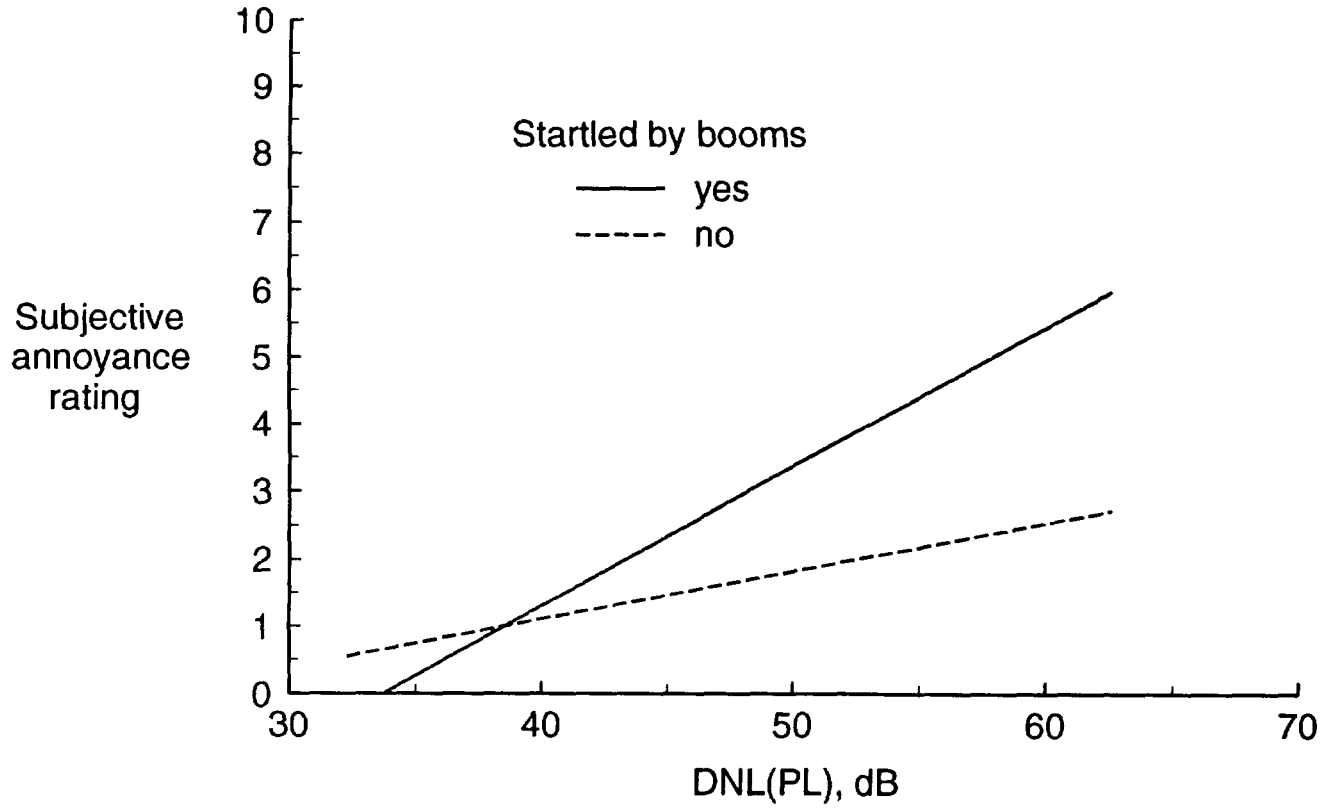

Figure 11.

PERCENTAGE OF SONIC BOOM EXPOSURES CAUSING STARTLE

The daily exposures in which sonic booms were presented at just one noise level were used to determine how often startle occurred as a function of PL. At the end of each day, the test subjects were asked if they were startled by any of the sonic booms heard that day. Figure 12 shows the percentage of exposures causing startle as a function of the PL of the individual sonic boom repeated during the day. Each data point represents at least 20 daily exposures.

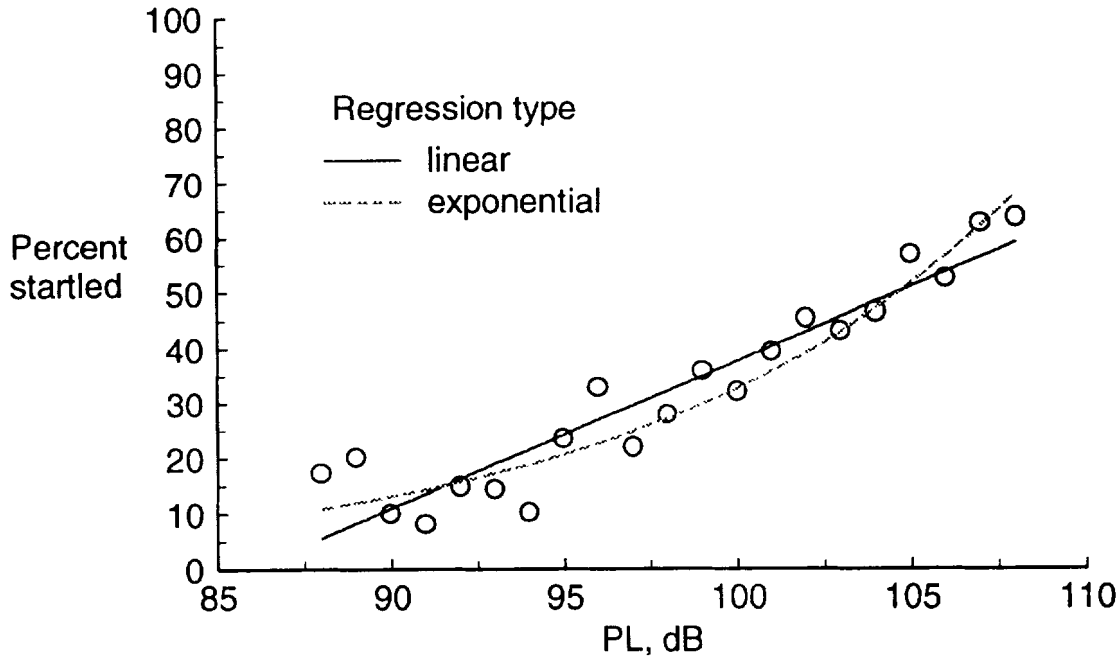

Figure 12.

EFFECT OF INDOOR AMBIENT NOISE LEVEL ON ANNOYANCE

Indoor ambient noise SEL(A) levels were collected 24 hours a day from each of two microphones located in different rooms in each home. Ambient measurements were made between sonic boom presentations and at the end of each hour. This resulted in from 56 to 174 ambient measurements per day per home.

In order to reduce the complexity of the calculation of daily indoor ambient noise levels from this massive amount of data, only those ambient measurements representing at least 50 continuous minutes were included in calculating the daily ambient noise level. Furthermore, the ambient measurements were limited to the fourteen hour testing period during which the sonic booms occurred. This resulted in 623 exposure days for which a daily indoor ambient SEL(A) level was determined. The analyses of the effect of indoor ambient noise level were based on these 623 days, which did represent a wide range of the test conditions in the experiment design.

The daily ambient indoor levels were included in a multiple regression equation with DNL(PL). The resulting coefficient for the ambient level was not significantly different from zero. The multiple regression was repeated using the difference between the ambient levels and the DNL(PL) levels in place of the ambient levels. Again the resulting coefficient for the ambient term was not significantly different from zero. Therefore, annoyance was not significantly affected by indoor ambient noise level.

Annoyance was not significantly affected by:

- **Indoor ambient noise level**
- **The difference between indoor ambient noise level and sonic boom level**

Figure 13.

EFFECT OF ACTIVITY ON ANNOYANCE TO SONIC BOOMS

As part of the subjective response questions presented at the end of each day, the test subjects were asked to indicate, to the best of their memories, what type of activities they were engaged in and when during the 14 hour test period. The six types of activities were defined as:

1. Sleeping, napping, resting, ...
2. Talking with other people
3. Listening to TV, radio, music ...
4. Playing ... hobby, reading, etc.
5. Working ... chores, job, etc.
6. Other ...

Subjects were instructed to choose the lowest numbered activity if engaged in two or more activities at the same time. Subjects were instructed to provide the information based on their recollections of the day and to not to keep a log during the day.

Since each daily annoyance response almost always covered more than one activity, the activities could not be compared directly. Instead the amount of time engaged in each activity each day was calculated and then included in a multiple regression analysis with DNL(PL). The regression coefficients for activities 1, 2, and 3 were significantly different from zero, indicating significant effects on the annoyance response (fig. 14). Annoyance increased on average an equivalent of 1.5 dB per hour of activity related to sleeping, napping, or resting. Annoyance decreased on average an equivalent of 0.75 dB and 0.5 dB per hour of activity related to, respectively, talking with other people and listening to TV, radio, and music. The other activities had no significant effects on annoyance response.

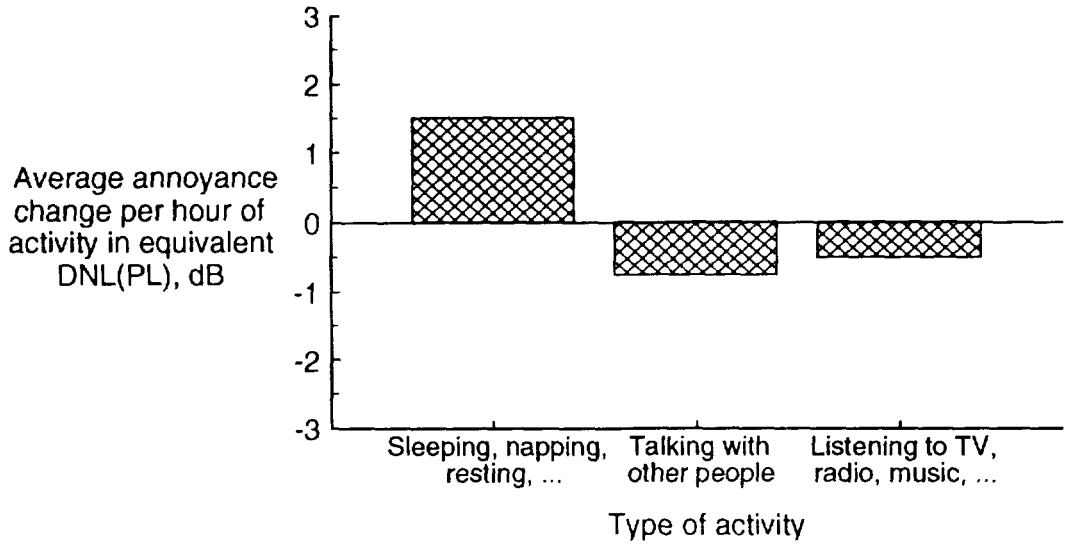

Figure 14.

EFFECTS OF OTHER TEST SUBJECT AND HOUSEHOLD PARAMETERS

Gender. - The 33 test subjects included 25 females and 8 males. No significant effect of gender on annoyance was found using indicator (dummy) variable analysis with DNL(PL) as the noise metric.

Age. - The age of the test subjects at the beginning of the test period ranged from 32 to 71 with a mean of 50.6 and a median of 53. To determine if age had a significant effect on annoyance, it was included in a multiple regression analysis with DNL(PL). The resulting equation was

$$\text{Annoyance} = 0.141 * \text{DNL(PL)} + 0.034 * \text{Age} - 6.373 \quad (1)$$

Both coefficients and the constant were significant. Comparing the two coefficients indicates that the increase in annoyance with one year of age was equivalent to an increase in DNL(PL) of 0.25 dB.

Occupation. - Of the 33 test subjects, 19 were homemakers, 9 were retired, and 5 either worked out of the home or were temporarily unemployed. The effects on annoyance of this limited range of occupation categories were determined using indicator variable analysis with DNL(PL) as the noise metric. No significant effect on annoyance of occupation was found.

Spouse. - Of the 33 test subjects, 26 had spouses living in the household. Indicator variable analysis using DNL(PL) as the noise metric found no significant effect on annoyance of the presence of a spouse.

Number of household members. - Of the 33 households in the experiment, 3 had only one member, 13 had two members, 5 had three members, 11 had four members, and 1 had five members. The number of people in the household was included in a multiple regression equation with DNL(PL). The resulting coefficient for the number of household members was not significantly different from zero. Therefore, annoyance was not significantly affected by the number of people living in a household.

Children. - Eleven of the 33 households in the experiment included children under the age of 18. To determine if the presence of children affected annoyance response, it was included in an indicator variable analysis with DNL(PL). No interaction between DNL(PL) and the presence of children was found, but the presence of children did have a significant effect on the annoyance response. The resulting equation was

$$\text{Annoyance} = 0.149 * \text{DNL(PL)} - 0.817 * \text{Children} - 4.686 \quad (2)$$

where Children = 1 if children under 18 were members of the household and 0 otherwise. The effect of children being presence on the test subjects' annoyance response was equivalent to a decrease in DNL(PL) of 5.5 dB.

Parameter	Effect on Annoyance	Magnitude of effect in equivalent DNL(PL) dB
Gender	no	---
Age	yes	0.25 dB increase per year of age
Occupation	no	---
Spouse	no	---
No. of household members	no	---
Children	yes	5.5 dB decrease in household with children

Figure 15.

PERCENTAGE OF TEST SUBJECTS HIGHLY ANNOYED AS A FUNCTION OF A-WEIGHTED DAY-NIGHT LEVEL

The impact of aircraft flyover noise has usually been examined in terms of the percent of people highly annoyed versus the outdoor A-weighted day night level. Figure 16 illustrates this dose-response relationship for the results from this study. A subjective response rating greater than seven was considered a highly annoyed response. The circles in the plot represent the results of this study using the measured indoor levels. The shaded area represents the range of data when the indoor levels are transformed to outdoor levels by the addition of a 10 to 20 dB correction for house attenuation (ref. 6). Comparison of the sonic boom data with the Federal Aviation Administration (FAA) guideline (Schultz curve, ref. 7) indicates that a greater percentage of the test subjects were highly annoyed by the simulated sonic booms than would be expected for aircraft flyover noise at a given level.

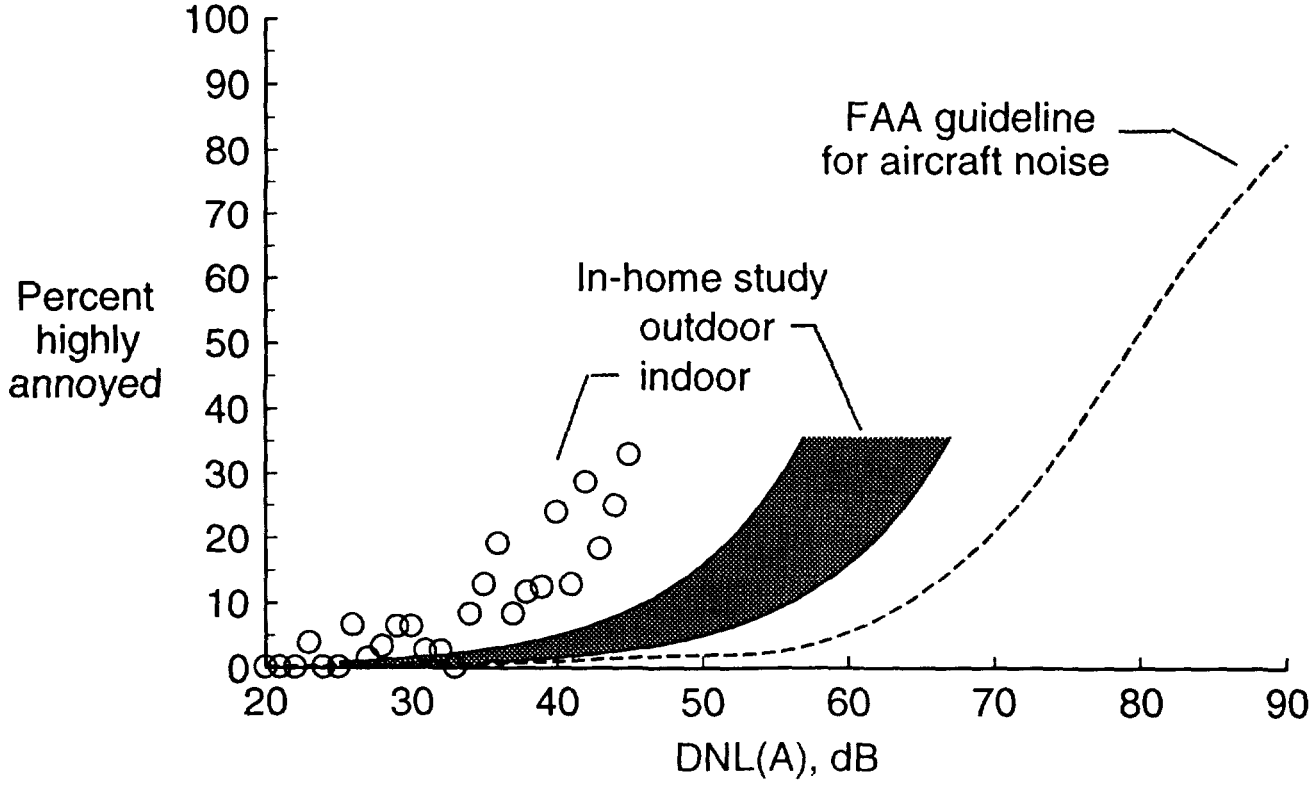

Figure 16.

PERCENTAGE OF TEST SUBJECTS HIGHLY ANNOYED AS A FUNCTION OF C-WEIGHTED DAY-NIGHT LEVEL

The impact of impulse noise has usually been examined in terms of the percent of people highly annoyed versus the outdoor C-weighted day night level. Figure 17 illustrates this dose-response relationship for the results from this study. A subjective response rating greater than seven was considered a highly annoyed response. The circles in the plot represent the results of this study using the measured indoor levels. The shaded area represents the range of data when the indoor levels are transformed to outdoor levels by the addition of a calculated 3 to 11 dB correction for house attenuation. Comparison of the sonic boom data with the Committee on Hearing, Bioacoustics, and Biomechanics (CHABA) recommended curve (ref. 8) indicates that a smaller percentage of the test subjects were highly annoyed by the simulated sonic booms than would be expected by other impulse noises at a given level.

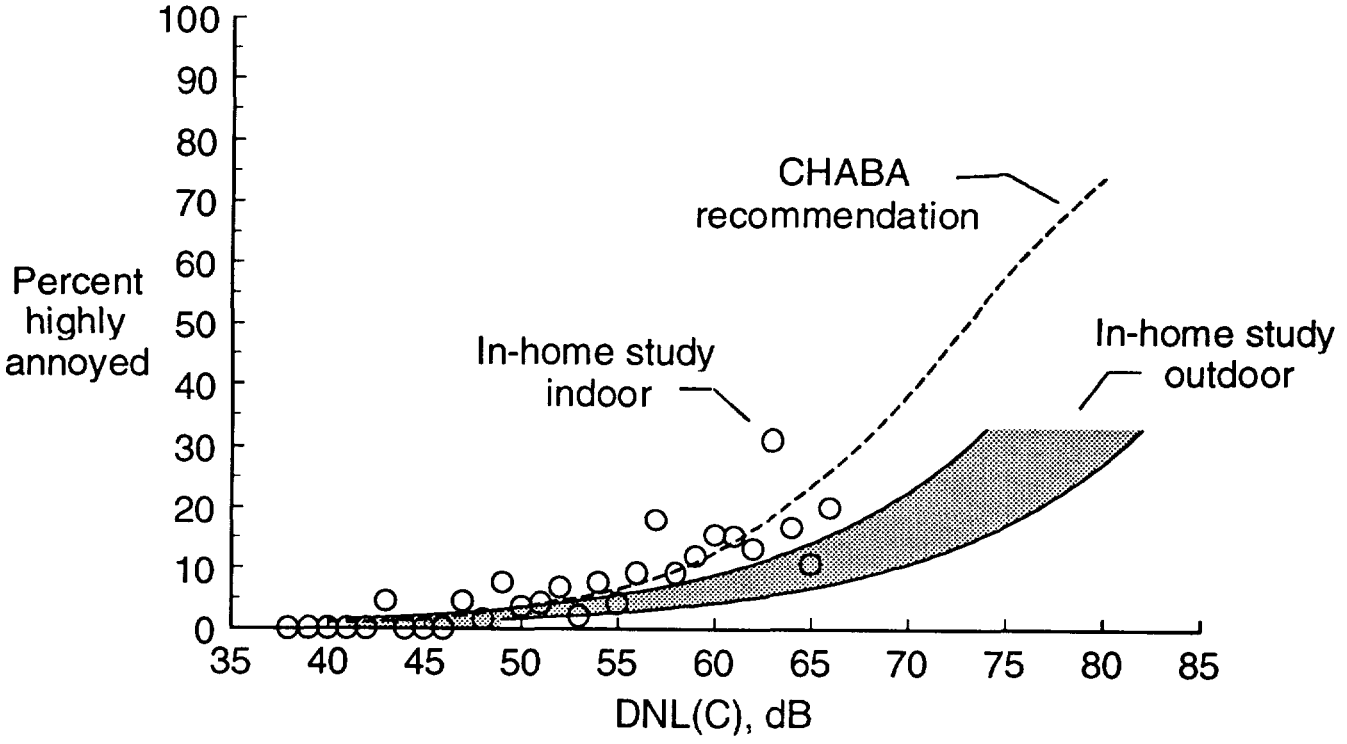

Figure 17.

CONCLUSIONS

Figure 18 summarizes the conclusions from the in-home study of subjective response to simulated sonic booms.

- **Annoyance decreased as subjects adapted during first few days**
- **"Level + 10 * log(n)" confirmed for multiple occurrences**
- **Perceived level was best annoyance predictor**
- **Startle increases annoyance**
- **Indoor ambient noise level did not affect annoyance**
- **Annoyance increases if subject sleeps or rests**
- **Annoyance decreases if subject talks with people or listens to TV, radio, or music**
- **Annoyance increases with age**
- **Annoyance decreases if children in household**

Figure 18.

REFERENCES

1. McCurdy, David A.; Hilliard, R. David; and Brown, Sherilyn A.: Studying the Effects of Simulated Sonic Booms on People in Their Homes. Symposium on Aircraft Noise Abatement Receiver Technology, Volume 1. North Atlantic Treaty Organization, Baltimore, Maryland, May 16-20, 1994.

2. McCurdy, David A.; Brown, Sherilyn A.; and Hilliard, R. David: An In-Home Study of Subjective Response to Simulated Sonic Booms. High-Speed Research: 1994 Sonic Boom Workshop --- Atmospheric Propagation and Acceptability Studies, NASA CP-3279, October 1994, pp. 193-208.

3. McCurdy, David A.; Brown, Sherilyn A.; and Hilliard, R. David: The Effects of Simulated Sonic Booms on People in Their Homes. AIAA Paper No. 95-0834, January 9-12, 1995.

4. Pearsons, Karl S.; and Bennett, Ricarda L.: Handbook of Noise Ratings. NASA CR-2376, 1974.

5. Bennett, Ricarda L.; and Pearsons, Karl S.: Handbook of Aircraft Noise Metrics. NASA CR-3406, 1981.

6. Shepherd, Kevin P.; and Sullivan, Brenda M.: A Loudness Calculation Procedure Applied to Shaped Sonic Booms. NASA TP-3134, 1991.

7. Schultz, Theodore J.: Synthesis of Social Surveys on Noise Annoyance. Journal of the Acoustical Society of America, vol. 64, no. 2, August 1978, pp. 377-405. (Erratum, vol. 65, no. 3, March 1979. p. 849.)

8. National Research Council (1981) : Assessment of Community Response to High Energy Impulsive Sounds. Report of Working Group 84, Committee on Hearing, Bioacoustics, and Biomechanics, Assembly of Behavioral and Social Sciences, Washington, DC : National Academy of Sciences.

COMPARISON OF NEW METHODS FOR ASSESSING COMMUNITY RESPONSE TO HIGH ENERGY IMPULSIVE SOUNDS

Sanford Fidell and Karl S. Pearsons
BBN Acoustic Technologies Divsion
21120 Vanowen Street
Canoga Park, CA 91303

Sonic Boom Workshop, NASA Langley Research Center
Hampton, VA
12-13 September, 1995

ABSTRACT

The latest CHABA Working Group to have reviewed published information about the effects of high energy impulsive sounds (such as sonic booms) on communities has recommended abandonment of the dosage-response relationship identified by its predecessor in favor of two alternate prediction methods. Both of the new assessment methods continue to rely on C-weighted measurements of impulsive sounds.

One of the two assessment methods retains the standard assumptions of the "equal energy hypothesis" (the notion that annoyance is governed simply by the product of level, duration, and number of noise events), and further assumes that the rate of growth of the prevalence of annoyance is proportional to the rate of growth of loudness with level. The other assessment method, however, assumes a level-dependent (non-equal energy) summation of the C-weighted sound exposure levels of individual impulsive events. Since predictions of the second method are distribution-dependent, they are not readily represented graphically in the form of a single dosage-response function. The effects on annoyance predictions of variance in distributions of CSEL values of impulsive sounds are explored in this presentation.

Predicting the prevalence of annoyance caused in communities by sonic booms and other high energy impulsive sounds has never been as straightforward as predicting the prevalence of annoyance associated with non-impulsive noise. The difficulty is not merely that measurement and prediction of long range acoustic propagation for sonic booms is more uncertain than for short range propagation of common neighborhood noise sources; nor that the findings of field studies on the annoyance to sonic booms vary widely. The physical uncertainties are well understood as inherent properties of propagation of acoustic energy through an inhomogeneous atmosphere, and of the great sensitivity of boom shapes and levels to aircraft maneuvering. By the same token, variability in the annoyance of sonic booms, although considerable, is not very different in degree from variability in annoyance due to routine transportation noise.

In fact, the greater problem is not one of measurement at all, but rather a lack of sufficient theoretical understanding of the annoyance of impulsive sounds. This problem is exacerbated by a scarcity of well designed and well conducted field studies of the annoyance of high energy impulsive sounds.[1] Figure 1 illustrates the problem: how should a dosage-response relationship, even an interim one, be inferred for this data set? A draft report produced by CHABA Working Group 102 that is now under review identifies two methods for estimating the prevalence of a consequential degree of annoyance in communities exposed to high energy impulsive sounds.

The first of these methods (as described by Fidell and Pearsons, 1994) preserves the equal energy hypothesis[2], such that the CSEL values of individual impulsive noise events are simply summed logarithmically regardless of their magnitude. The second method relies upon a level-dependent summation of the C-weighted sound exposure levels (CSEL) of individual high energy impulses as a predictor variable. Figure 2 shows a dosage-response relationship inferred by the first of the two CHABA methods. Some of the variability in the data set is accounted for in this approach by attributing it to nonacoustic factors. Figure 3 shows the same dosage-response relationship with respect to the 1981 recommendation of CHABA Working Group 84.

Recent U.S. Army-sponsored studies of the comparative annoyance of explosive sounds and the sounds of tracked and wheeled vehicles (*e.g.*, Schomer, 1994) suggest that the annoyance of impulsive sounds grows much more rapidly with sound exposure level than the annoyance of non-impulsive sounds. Schomer's studies established points of subjective equality of annoyance for A-weighted SEL values of non-impulsive sounds with the C-weighted SEL values of impulsive sounds. Over the range of levels presented for these noise sources, it was observed that the slope of the regression line relating judgments of the annoyance of impulsive sounds to the annoyance of non-impulsive sounds was about two to one.

The second assessment method recognized by the CHABA Working Group therefore requires a level-dependent summation of the C-weighted sound exposure levels (CSEL) of individual high energy impulses as a predictor variable. In effect, the second method is a direct challenge to the equal energy hypothesis, since it violates the standard assumption about the direct interchangeability of the level, duration, and number of noise events.

The level-dependent summation process is accomplished by transforming CSEL values of impulsive

noises into equivalent numbers of "annoyance units," then summing these annoyance units linearly so that they may be transformed into an equivalent (A-weighted) DNL value. The number of "annoyance units" doubles for a 3 dB increase in SEL of A-weighted sounds, but quadruples for a 3 dB increase in CSEL values, as shown in Table 1. The point of equal annoyance in terms of annoyance units of A-weighted (non-impulsive(sounds and C-weighted (impulsive sounds) is 103 dB.

Table 1 Annoyance units (AU) as a function of A-weighted and C-weighted SEL values.

SEL (dB)	ANNOYANCE UNITS (AU)	
	A-weighted sounds	***C-weighted sounds***
88	0.25	0.0078
91	0.5	0.031
94	1	0.125
97	2	0.5
100	4	2
103	**8**	**8**
106	16	32
109	32	128
112	64	512
115	128	2,048
118	256	8,192

The transformation of CSEL values into equivalent annoyance units permits use of the (A-weighted) FICON (1992) dosage-response relationship to predict the prevalence of annoyance with high energy impulses. In practice, the level-dependent summation procedure is accomplished by transforming CSEL values of high energy impulses into annoyance units as shown in Equation 1.

$$L'_{\chi E} = L_{C-A} + (1/\beta)(L_{(50)CE} - L_{A-C}) + 0.115(1/\beta)^2 \sigma^2 \quad (1)$$

where $L_{(50)CE}$ is the arithmetic mean CSEL, σ is the standard deviation, $L'_{\chi E}$ is the mean-square annoyance exposure level, β is the slope of the relation between the CSEL of a high amplitude impulse sound and an equivalently annoying control sound, and $L_{A=C}$ is the point of subjective equality of annoyance (at which the

annoyance of the impulse sound CSEL and a non-impulsive comparison sound ASEL are judged equal). The relationship between percent highly-annoyed and AUDNL is shown in Figure 4 for a variety of standard deviations.

The CHABA Working Group draft report identifies several conditions under which the level-dependent annoyance prediction method should be adopted. These include situations in which detailed knowledge is available of the levels of each individual high energy impulse sound; circumstances in which the standard deviation of the distribution of high energy impulsive sound exposure levels exceeds 5 dB; and in highly variable noise environments composed of a combination of impulsive and non-impulsive sounds.

Figures 5 and 6 show the practical consequences for dosage-response relationships of the level-dependent summation method, for 10 and 100 high energy impulsive sounds per day. Because the standard deviation of the distribution of impulsive sounds is used (in conjunction with an assumption of normality of distribution) to approximate the effect of the level-dependent summation process, the curves are parametric in the standard deviation of the distribution of impulsive sound levels. The standard deviations of actual distributions of sonic booms propagating over long ranges at different times of day are probably closer to the higher values plotted than to the lower values. Figure 7 shows the relationship between the available social survey data points and the dosage-response relationships for the level-dependent summation method. A comparison of the data points with the dosage response curves suggests standard deviations greater than 10 dB for much of the survey noise levels.

Several complications are encountered when an effort is made to prepare a dosage-response relationship for the second method identified by CHABA Working Group 102. Since the summation of CSEL values of (for example) individual sonic booms is level dependent, one can not simply sum the CSEL values logarithmically and subtract 49.4 dB to yield a CDNL value. Instead, one must first convert each CSEL value into an annoyance unit in a level-dependent manner.

A basic complication in applying the second of CHABA's methods to predicting the prevalence of annoyance with sonic booms is therefore that an exact calculation of the effective impulsive sound exposure requires information about the value of each and every boom.[3] In other words, it does not suffice to simply measure CDNL for a day's worth of sonic booms. One must instead record the CSEL of each individual boom and translate them into annoyance units. This conversion into annoyance units is tantamount to performing the integration of the cumulative effect of multiple impulsive exposures on the ordinate, rather than the abscissa of the dosage-response relationship.

The net effect of applying Equation 1 to a distribution of sonic boom sound exposure levels is to compute a corresponding value of Day-Night Average Sound level that can be interpreted by means of a standard dosage-response relationship, such as that recommended by the Federal Interagency Committee on Noise to estimate the prevalence of annoyance. The effect of the standard deviation of the distribution of CSEL values on the percent highly annoyed may be seen in Figure 7. As the standard deviation increases from values of 1 or 2 dB to 5 or 10 dB, the percent highly annoyed increases for the same CDNL. For example at 70 dB CDNL and 10 events per day, the percent highly annoyed rises from 25% for a 1 or 2 dB standard deviation to 40% and 85% for standard deviations of 5 dB and 10 dB respectively.

In summary, much remains to be done before confident and accurate predictions can be made about the prevalence of annoyance produced by sonic booms in communities. The most basic lack is of reliable social survey findings and appropriate impulsive noise measurements. Such information is scarce precisely because it is difficult and expensive to collect. Continued analytic effort is of value, however, to compare predictions produced by the two recognized assessment methods under a variety of noise exposure conditions, and to understand the likely errors of estimate associated with their use.

ENDNOTES

1. CHABA Working Group 69 considered an individual impulse with a C-weighted sound exposure level (CSEL) value in excess of 85 dB (75 dB at night) to be a "high energy" impulse. Sonic booms, artillery, and blasting are examples of high energy impulsive sounds. The term "artillery" includes all large bore (direct and indirect fire) ordnance and bombs, but specifically excludes small arms fire. The term "blasting" includes all explosives such as mining and quarrying explosions, demolition and oil exploration charges, explosive circuit breakers, *etc.* High energy impulsive sounds share two further characteristics: Most (nominally, 75 percent) of the energy of such a sound is concentrated within one second, and virtually all of its sound energy is concentrated within three seconds. If the source of high energy impulsive sound exposure is multiple explosions, then the sound produced by each individual explosion must meet the above criteria.

2. Loosely speaking, the equal energy hypothesis is the notion that the level, duration, and number of individual sounds are freely interchangeable determinants of annoyance as long as their logarithmic sum remains constant.

3. Alternatively, a set of simplifying assumptions such as those embodied in Equation 1 can yield an estimate of the effective exposure, but one which could under some conditions include a substantial error term.

REFERENCES

Fidell, Sanford and Pearsons, Karl S.: "Deriving a Dosage-Response Relationship for Community Response to High-Energy Impulsive Noise," 1994.

Schomer, P.D.: "New Descriptor for High-Energy Impulsive Sounds," Noise Control Engineering Journal, 42(5), pp 179-191, 1994.

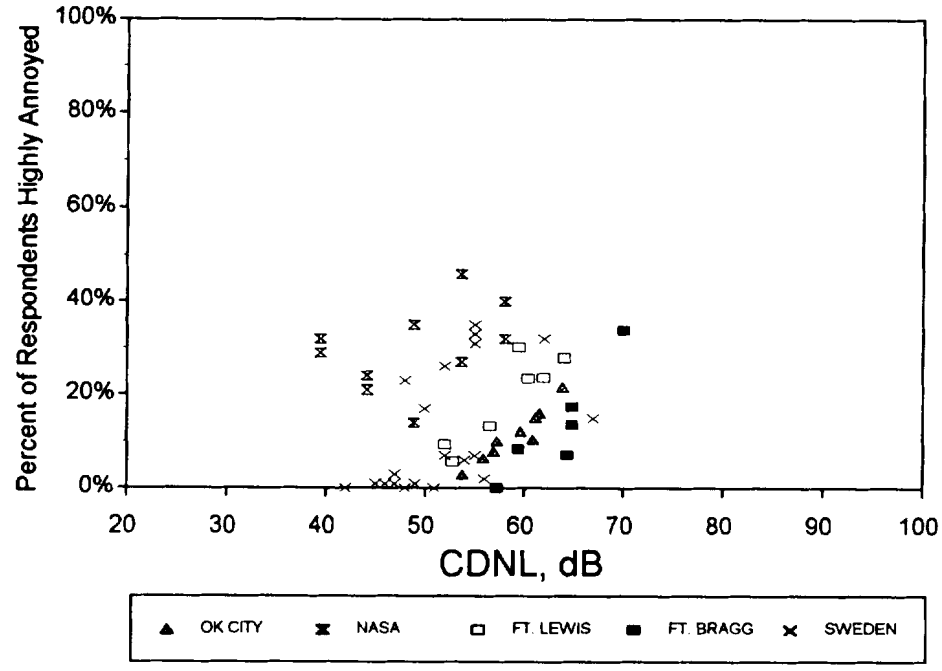

Figure 1 Social survey results for high energy impulsive sounds.

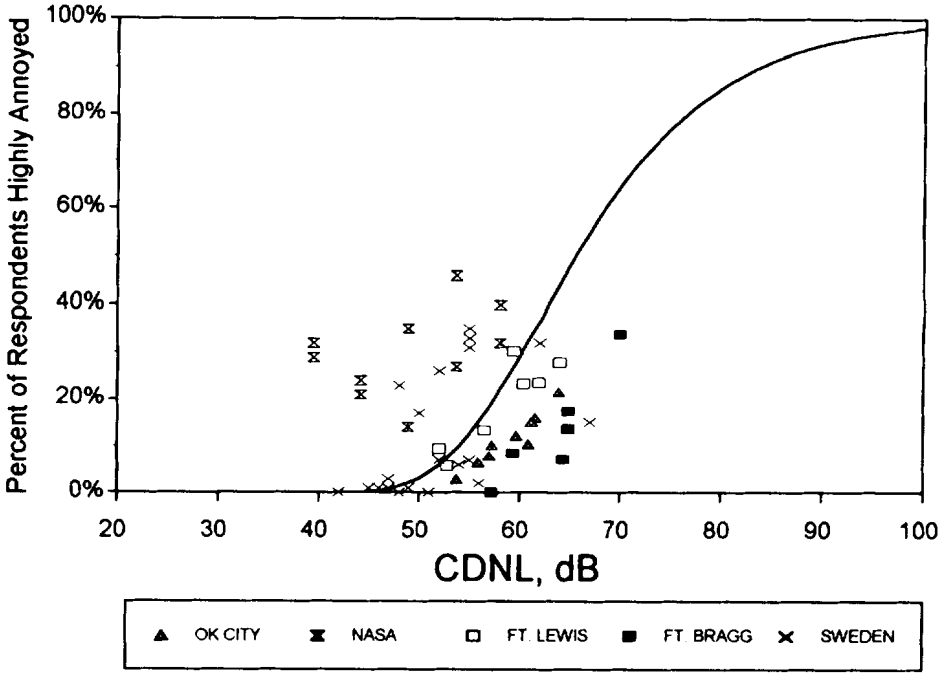

Figure 2 Dosage-response relationship for impulse noises produced by CHABA Method 1.

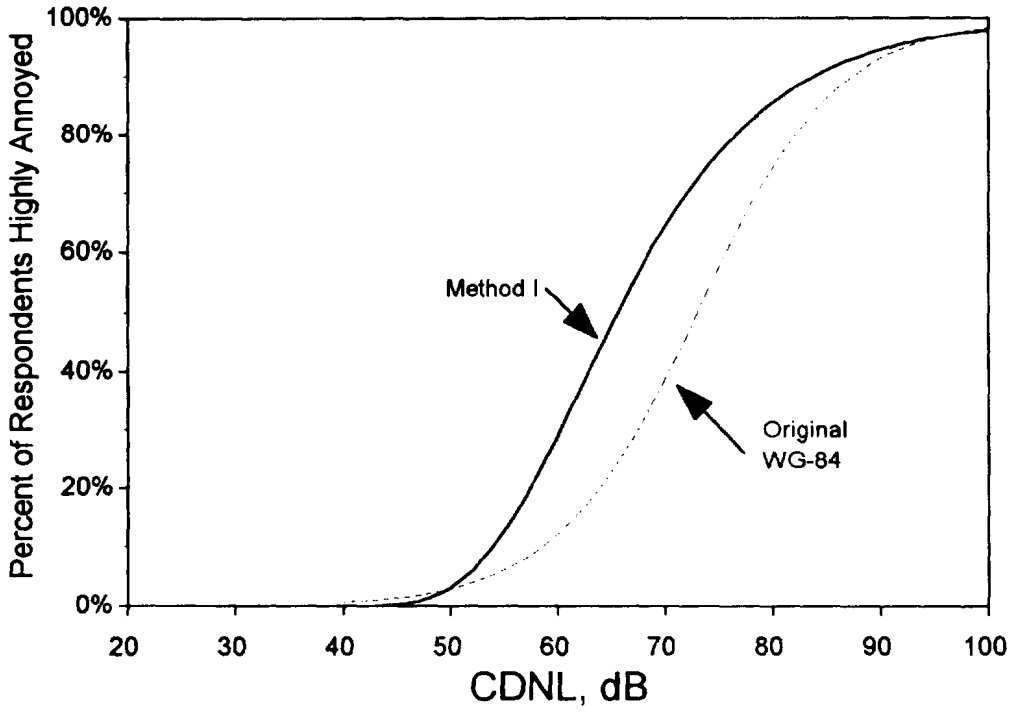

Figure 3 Comparison of impulse noise assessment using CHABA Working Group 102 Method 1 and Working Group 84 models.

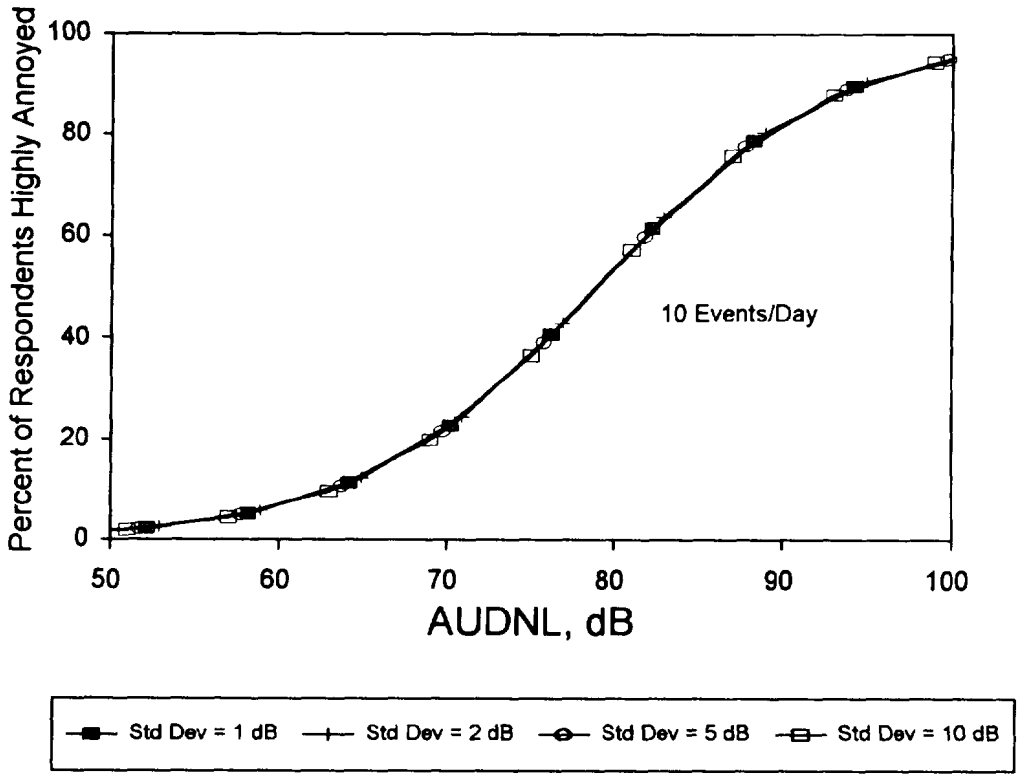

Figure 4 Dosage-response relationship of Method 2 using AUDNL for 10 events per day.

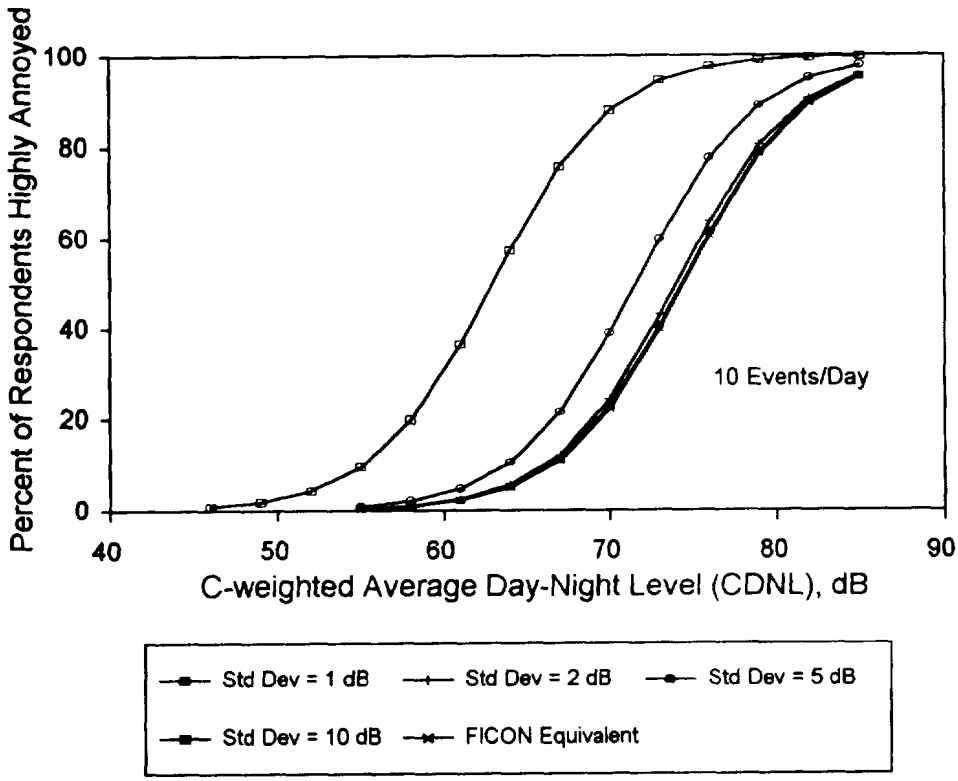

Figure 5 Dosage-response relationship of Method 2 using CDNL for 10 events per day.

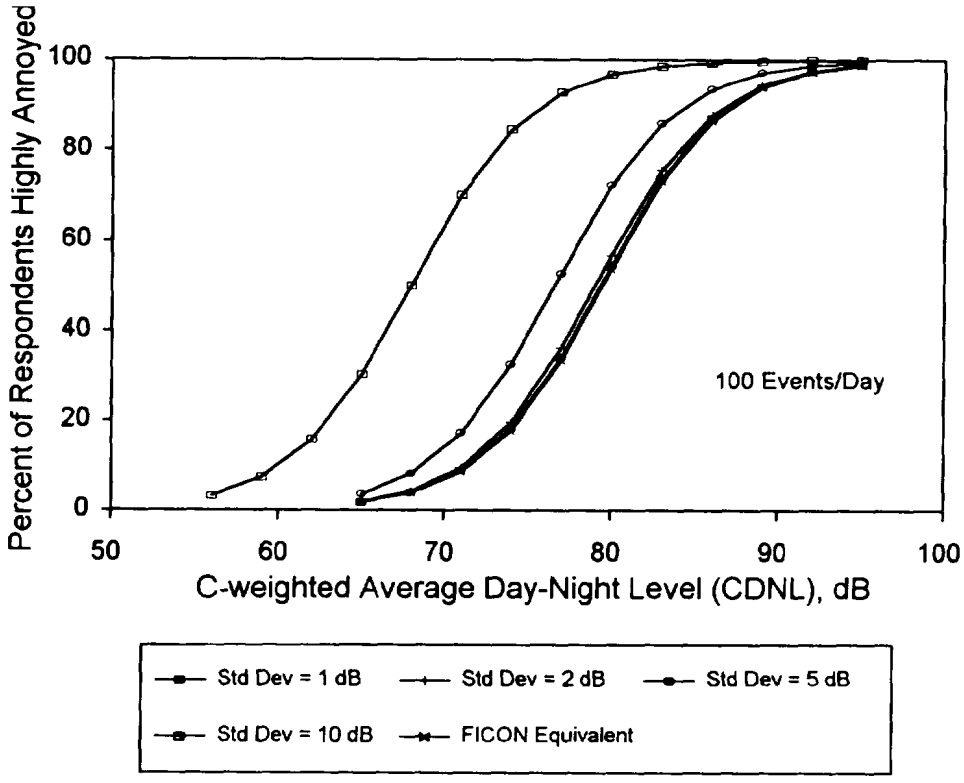

Figure 6 Dosage-response relationship for Method 2 using CDNL for 100 events per day.

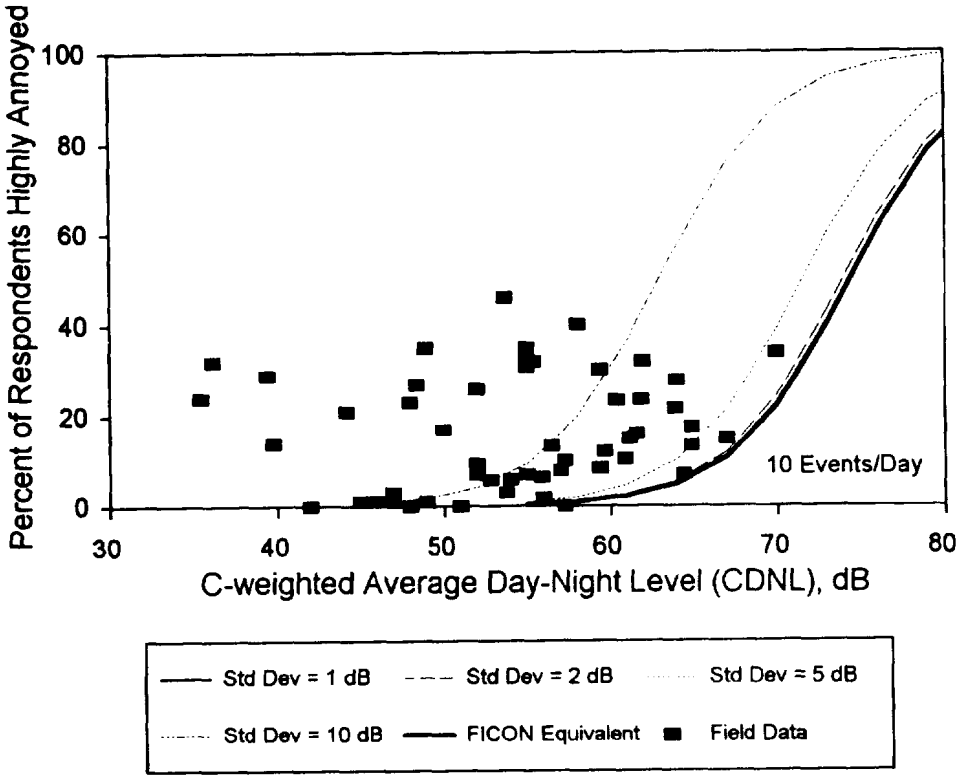

Figure 7 Method 2 fit to social survey results for impulse noises.

THE USE OF STRUCTURAL-ACOUSTIC TECHNIQUES TO ASSESS POTENTIAL STRUCTURAL DAMAGE FROM SONIC BOOMS

Joel Garrelick and Kyle Martini
Cambridge Acoustical Associates, Inc.
200 Boston Avenue, Suite 2500
Medford, Massachusetts, 02155-4243

ABSTRACT

The potential impact of supersonic operations includes structural damage from the sonic boom overpressure. This paper describes a study of how structural-acoustic modeling and testing techniques may be used to assess the potential for such damage in the absence of actual flyovers. Procedures are described whereby transfer functions relating structural response to sonic boom signature may be obtained with a stationary acoustic source and appropriate data processing. Further, by invoking structural-acoustic reciprocity, these transfer functions may also be acquired by measuring the radiated sound from the structure under a mechanical drive. The approach is based on the fundamental assumption of linearity, both with regard to the (acoustic) propagation of the boom in the vicinity of the structure and to the structure's response. Practical issues revolve around acoustic far field and source directivity requirements. The technique was implemented on a specially fabricated test structure at Edwards AFB, CA with the support of Wyle Laboratories, Inc. Blank shots from a cannon served as our acoustic source and taps from an instrumented hammer generated the mechanical drive. Simulated response functions were constructed. Results of comparisons with corresponding measurements recorded during dedicated supersonic flyovers with F-15 aircraft are presented for a number of sensor placements. [Work sponsored by the Armstrong Laboratory, Wright Patterson AFB, OH]

I. INTRODUCTION

The potential impact of supersonic operations includes damage to structures from the sonic boom overpressure. The harm is typically cosmetic, window breakage, plaster cracking etc. For a particular damage assessment one may of course actually subject a vulnerable structure to the supersonic operations envisioned. This is costly at a minimum and in the case of irreplaceable, e.g., historic, structures, quite risky. The alternative is simulation based predictions. In this context, this paper discusses the use of structural-acoustic methods. Specifically, these methods are employed to construct structural-acoustic transfer functions that allow one to predict the response of a structure to any specified boom signature. Predicted levels may then be compared with failure values which must be obtained independently[1]. For example predictions of peak stress in a window pane may be compared with design values for window glass.

Under the fundamental assumption of linearity, both with regard to the (acoustic) propagation of the boom in the vicinity of the structure and to the structure's response, the above problem may be posed as one of structural-acoustics. The boom is represented by an acoustic plane wave. Its spectrum is that of the boom signature, for example the classic N-wave. It impinges on the ground topography and structures (Fig 1) with a propagation vector having an elevation angle measured from the vertical of $\beta_i = \sin^{-1}(1/M)$ with the local Mach number M=U/c, where U is the effective flight speed and c the local air sound speed[2]. Its azimuthal angle, ϕ_i, is given by the flight heading. The response of a structure to any given boom signature may now be formulated in terms of an impulse response function in the time domain, or transfer function in the frequency domain.

Specifically, the time response of a structure at location $\bar{x}$, $a_b(t;\bar{x})$, representing acceleration, displacement, strain, etc., may be expressed as the inverse transform of the product of the frequency transformed boom signature and impulse response function, or spectral transfer function. In equation form

$$a_b(t;\bar{x}) = \pi^{-1} Re \left\{ \int_0^\infty \tilde{a}_b(\omega;\bar{x}) \exp(-i\omega t)\, d\omega \right\} \tag{1}$$

with

$$\tilde{a}_b(\omega;\bar{x}) = \tilde{G}(\omega;\bar{x},\bar{r}_i)\,\tilde{p}_b(\omega;\bar{x},\bar{r}_i) \tag{2}$$

where

$\tilde{a}_b(\omega;\bar{x})$ = boom induced response spectrum; Fourier transform of response time history,

$\tilde{p}_b(\omega;\bar{x},\bar{r}_i)$ = boom spectrum incident along $\bar{r}_i$ at $\bar{x}$; Fourier transform of boom signature, and

$\tilde{G}(\omega;\bar{x},\bar{r}_i)$ = spectral transfer function; Fourier transform of impulse response function.

II. STRUCTURAL-ACOUSTIC FORMULATION

With our plane acoustic wave representation of the boom the transfer function $\tilde{G}(\omega;\bar{x},\bar{r}_i)$, or equivalently its transform, may be obtained with a stationary acoustic source[3]. Specifically, consider a simple acoustic source placed along $\bar{r}_i$ at a range (R) sufficiently long to produce a plane wave at and near $\bar{x}$ (Fig 2a). The spectral transfer function now becomes

$$\tilde{G}(\omega;\bar{x},\bar{r}_i) = \tilde{a}_d(\omega;\bar{x})/\tilde{p}_d(\omega;R\bar{r}_i-\bar{x}) \tag{3}$$

with

$\tilde{a}_d(\omega\,;\bar{x})$ = response spectrum at $\bar{x}$ due to acoustic source at $R\bar{r}_i$, and

$\tilde{p}_d(\omega\,;R\bar{r}_i-\bar{x})$ = free field pressure spectrum at $\bar{x}$ due to acoustic source at $R\bar{r}_i$ and

$$\tilde{p}_d(\omega\,;R\bar{r}_i-\bar{x}) = (\rho\ddot{Q}_d/4\pi\,|R\bar{r}_i-\bar{x}|)\exp(ik|R\bar{r}_i-\bar{x}|) \tag{4}$$

where $k(=\omega/c)$ is the acoustic wavenumber and $\ddot{Q}_d$ is the acoustic source strength (volume acceleration). We will refer to Eq. 4 as our "direct" structural-acoustic simulation, thus the subscript "d".

Within the realm of structural-acoustics certain reciprocal relationships may be exploited[4] to develop a "reciprocal" method for obtaining $\tilde{G}(\omega\,;\bar{x},\bar{r}_i)$. First, for purposes of discussion we confine our attention to the acceleration response of our structure at $\bar{x}$, $\tilde{a}_d(\omega\,;\bar{x})$. Next consider the problem of a force applied to our structure at $\bar{x}$ and oriented along $\tilde{a}_d$. The structure vibrates in response and radiates sound (Fig 2b). This situation is "reciprocal" to our direct problem in that the following relation holds

$$p_r(\omega\,;R\bar{r}_i)/F(\omega\,;\bar{x}) = \tilde{a}_d(\omega\,;\bar{x})/\ddot{Q}(\omega\,;R\bar{r}) \tag{5}$$

and therefore

$$\tilde{G}(\omega\,;\bar{x},\bar{r}_i) = [4\pi\,|R\bar{r}_i-\bar{x}|\exp(-ik|R\bar{r}_i-\bar{x}|)/\rho]\;p_r(\omega\,;R\bar{r}_i)/F(\omega\,;\bar{x}) \tag{6}$$

where

$F(\omega\,;\bar{x})$ = force spectrum of applied force at $\bar{x}$ oriented with $\tilde{a}_d(\omega\,;\bar{x})$

$p_r(\omega\,;\bar{x},R\bar{r}_i)$ = spectrum of pressure radiated to $R\bar{r}_i$.

III. IMPLEMENTATION ISSUES

In this section we outline a few of the implementation issues one confronts with the proposed structural-acoustic simulation.

A. Direct Simulation

1. Plane Wave Incidence

With a direct simulation, structures and ground areas that influence the response function of interest must be in the far field of the acoustic source. Otherwise near field effects introduce errors owing to both phase and level differences with the planar wave front of the boom. This imposes a minimum stand-off distance for the source[5].

2. Replication of Sonic Boom Incidence

Having achieved an effectively plane wave for our simulation it must be incident from the appropriate direction. Matching the required elevation angle is of particular concern for high Mach numbers where the associated source height may not be practical.

3. Source Level Requirements

The requirement on our acoustic source levels is that over the frequency band of concern, they provide adequate signal to noise (S/N) for the structural response sensor suite. There is no other requirement with regard to the spectrum, again under the assumption of system linearity. For a given source, this criterion leads one to shorter ranges in conflict with the above plane wave requirement[5].

4. Source Directivity Requirements

For a direct simulation there is actually no separate requirement on the directivity of the acoustic source. By separate is meant independent of achieving effective plane wave incidence over the required solid angle.

5. Scattering From Adjacent Structures

For all practical purposes the open parameters for our simulation are defined by the above considerations. Consequently there is little additional flexibility remaining to address "secondary" influences such as the effect of scattering from other nearby structures or obstacles.

B. Reciprocal Simulation

For our reciprocal test, there are no separate plane wave requirements to be imposed on the radiated field. A plane wave is not required to satisfy reciprocity but rather to simulate a boom, which has been addressed in specifying the direct acoustic test geometry. The reciprocal equivalent of source directivity is the receiving directivity of the microphone that monitors the radiated sound. Source strength requirements are as described for the direct simulation.

V. MEASUREMENTS

A. Overview

In this section we present measurements on a specially fabricated test structure (Fig. 3) that are part of a larger test program to validate the structural-acoustic techniques described above. The tests were performed on the grounds of Phillips Laboratory at Edwards AFB, CA by the team of Cambridge Acoustical Associates and Wyle Laboratories under the guidance of Dr. Micah Downing (WPAFB). The responses of various components of this structure to dedicated booms and booms of opportunity were recorded and compared with predictions based on our simulations. We focus on a subset of these measurements, principally the acceleration of a glass panel embedded in an exterior wall to six booms from dedicated flyovers, three nominally identical passes by each of two F-15 aircraft flying at approximately 30,000 ft. All six booms occurred over a time interval of less than thirty minutes. Additional comparisons are presented for other accelerometers mounted on the walls of the structure and, in response to a boom of opportunity, a strain gage mounted on the panel. With our direct

simulations blank cannon shots served as an acoustic source and an instrumented hammer was the source of vibrations for our reciprocal tests.

B. Test Structure and Sensor Suite

The test structure is a wood shed of standard studded plywood construction with overall dimensions 8'x9'x10'. The interior is unfinished with the exception of 8'x4' sheetrock partitions in the middle of two opposite walls. There is one exterior window, or test panel, an interior test panel supported by a wood frame and an exterior door. All exterior joints/seams were caulked and the door and window gasketed to minimize the airborne path to the interior space. The lateral dimensions of the test panels were 3'x4' and for the measurements described here they were made of 1/4" thick glass. Also, the subset of sensors on the structure that we will consider here are shown in Fig 4. They consist of accelerometers placed on, and oriented normal to, the interior and exterior test panels, the North and South walls on sheetrock and the East wall directly on the plywood. In addition a single (horizontal) axis strain gage is located at the center of the exterior window. These placements were held constant for all three types of excitation, the flyovers, the direct simulation with a cannon and the reciprocal simulation with our hammer. In contrast for various practical considerations, the microphones were moved depending on the excitation, as indicated in the figure

C. Instrumentation and Processing

A variety of microphones, accelerometers, strain gages, and a force gage was employed to measure source levels and monitor the response of the structure. During flyovers and cannon shots, Endevco type 2242C and 2213 accelerometers with Endevco type 2735 charge amplifiers and Measurement Group type EA-06-10CBE-120 and EA-06-250YA-120 strain gages coupled with type 2310 bridge amplifiers measured structural response. The accelerometers exhibit a flat response down to 4 Hz and may detect signals above 0.002g. The high pressure levels created by the booms and cannon shots were measured using PCB type 106B50 pressure transducers. Their response is flat down to 0.5 Hz. with a level range from 85 to 170 dB re 20 μPa. For the direct simulations a yachting cannon loaded with blank 10 gauge shotgun shells served as our acoustic source.

The vibration source required with our reciprocal tests was a PCB model 086C03 calibrated impulse force hammer. A B&K type 2230 condenser microphone measured the acoustic response. Its response is flat down to 2.6 Hz and it has a dynamic range from 15-146 dB re 20 μPa.

The sensor data were stored on a 16 channel Sony PC216A digital tape recorder. This recorder has a 2.5 kHz low pass filter. Individual gain controls were used to maximize dynamic range. The data were subsequently down loaded to a Dolch personal computer using a Data Translation model DT2821-F-16SE A-D board. Each channel of data was down loaded at 12,500 samples per second. The processing of the data on the PC was performed using the signal analysis software package SIGNAL created by Engineering Design (Belmont, MA). For example the direct and reciprocal simulated transfer functions given by Eq. 3 and Eq. 6 respectively were computed using SIGNAL's complex fast Fourier transform (FFT) software. A rectangular window, 16,384 points, and 1.31 seconds of data were used to create each transform with a frequency resolution of 0.76 Hz and a bandwidth of 5000 Hz. Averaging was used to reduce the random error in the measured transfer functions. With our direct simulations transfer functions were averaged over a minimum of three cannon shots and they were constructed from an average of ten or more hammer blows with our reciprocal tests. With the prevailing wind conditions and the strength of our simulation sources, transfer functions were contaminated by noise below approximately 6 Hz. Consequently computed transfer functions were high pass filtered at 6 Hz. with only minor repercussions, at least with respect to response peaks. Finally, structural response predictions were obtained by multiplying simulated transfer functions by the boom spectra and inverse transforming the product.

D. Measurements With Flyovers

Measurements with the supersonic flyovers consisted of signals from the test structure sensors and three microphones making up a triangulation system to obtain the local sound speed and in turn the effective Mach number and azimuthal flight heading for each event. The pressure-time history for one of the flights is shown in Fig 5a. Gross characteristics for all six flights are summarized in Table I. In Table II, for a subset of the accelerometer

placements, we show the extent to which the peak values collapse when normalized first to the peak boom pressure and then to the boom CSEL.

E. Simulations: Direct

For our direct simulations the cannon was placed at azimuthal angle $\phi_i \sim 35^o$ and at an elevation angle of $\beta_i \sim 26^o$. The latter corresponds to a cannon positioned roughly 25 ft. above the panel center (30 ft. from the ground) at a stand-off distance of 50 ft.

The short pulse lengths of our cannon shots, which are O(10 ms.) is shown in Fig 5b, in stark contrast to the much longer boom. The effects of this disparity on their respective spectra are indicated in Fig 6 for a typically boom and shot. The reader is reminded however that there is no requirement for these spectra to correspond. Rather we require only that our acoustic source provide adequate signal.

We compare the simulated response time history of one of our sensors to that measured during a single flyover in Fig 7. The sensor is an accelerometer affixed to the external glass panel. The correlation coefficient between the simulated and measured signals is indicated as well as the measured and simulated response peaks. The comparison in Fig 7 along with those for a number of other accelerometers mounted elsewhere are summarized in Table III.

In Table III a total of twenty four comparisons of peak acceleration are shown (six booms, four sensors). Over this ensemble the mean of the percent errors is -4% and the standard deviation is 18%. This translates to variations between -39% and +32% for a simulation with a $\pm 2\sigma$ level of confidence. (The maximum discrepancies shown are -46% and +35%). Unfortunately at this time there are inadequate data to similarly analyze the strain gage comparisons.

F. Simulations: Reciprocal

For our reciprocal simulations the structure was struck by our instrumented hammer at the approximate accelerometer locations and the radiated pressure was recorded by microphone M1, positioned at $\varphi \sim 35^o$, 30 ft. above ground, as shown in Fig 4. Results are

summarized in Table IV similar to the presentation given above for our direct simulations in Table III.

Over an ensemble of thirty peak acceleration comparisons (six booms, five sensors) the mean percent error is -26% and the standard deviation is 15%. This translates to $\pm 2\sigma$ confidence level limits between -56% and +4%. The maximum measured discrepancies were -55% and +8%. The larger difference in the mean than was observed with our direct tests might indicate a systematic bias in our predictions, for example arising from an inaccurate calibration. However no such error could be identified at this time.

REFERENCES

1. A review of this data base as of 1990 may be found in Sutherland, Louis C.; Brown, R; and Goerner, D.: Evaluation of Potential Damage to Unconventional Structures by Sonic Booms. Report No. HSD-TR-90-021, U.S. Air Force, Human Systems Division, Noise & Sonic Boom Impact Technology Program, Wright-Patterson AFB, OH, May 1990.
2. Maglieri, Domenic J.; and Plotkin, Kenneth J.: Sonic Boom, Aeroacoustics of Flight Vehicles, Theory and Practice. Edited by Harvey Hubbard. *Amer. Inst. Phys.*, ch. 10. Also, Carlson, Harry W.: Simplified Sonic Boom Prediction, NASA Technical Paper 1122, March 1978.
3. Garrelick, J.M.; and Martini, K.: The Use of Structural-Acoustic Reciprocity Techniques to Assess Potential Environmental (Structural) Damage From Sonic Booms. CAA Final Rept. to Armstrong Laboratory, AL/OEBN, WPAFB, OH under Contract F41624-93-C-9004, Dec. 1993.

4. ten Wolde, T.: On the Validity and Application of Reciprocity in Acoustical, Mechano-Acoustical and Other Dynamical Systems. *Acustica*, vol. 28, 23-32, 1973. Also, Belousov, Y.I.; and Rimskii-Korsakov, A.V.: The Reciprocity Principle in Acoustics and Its Application to the Calculation of Sound Fields of Bodies. *Sov. Phys. Acoust.*, vol. 21, 2, 103-109, 1975.
5. Garrelick, J.M.; and Martini, K.: Source Requirements for Structural-Acoustic Boom Simulations. CAA Tech. Memo TM/U-266-397, prepared for Armstrong Lab., AL/OEBN, WPAFB, OH under Contract F41624-94-C-9007, Oct. 19, 1994.

Table 1 Gross Boom Characteristics for Six Dedicated F-15 Flyovers

Boom Number	5	6	7	8	9	10	Avg.
Peak Pressure* (psf)M3	2.87	1.62	3.10	1.81	2.18	2.53	2.35
CSEL (dB re 20 μPa) M3	107.8	104.4	111.3	104.9	107.0	109.4	107.8
Duration (sec)	0.146	0.160	0.143	0.153	0.156	0.150	0.151
Local Mach No. (M=U/c)	1.08	1.07	1.12	1.09	1.08	1.04	1.08
Elevation Angle (β_i°)	67.5	68.5	66.4	67.0	68.0	73.8	68.1
Azimuthal Angle (ϕ_i°)	40.2	36.2	36.7	35.6	37.7	40.1	37.8

*Assumed to be twice the free field pressure.

Table II Normalized Response Statistics Over Ensemble of Six Booms

Sensor	Peak Acceleration (g)			Peak Accelertion/Peak Boom Pressure* (g/psf)			Peak Acceleration/CSEL Boom Pressure* (g/psf)		
	Mean	Std. Dev.	Dev. as % of Mean for ± 2 σ Level of Confidence	Mean	Std. Dev.	Dev. as % of Mean for ± 2 σ Level of Confidence	Mean	Std. Dev.	Dev. as % of Mean for ± 2 σ Level of Confidence
A1	2.78	0.67	48	1.19	.17	29	27.4	3.3	24
A2	1.86	0.44	47	0.79	.07	18	18.2	1.3	14
A3	1.95	0.38	39	0.85	.12	29	19.5	2.4	24
A5	0.86	0.23	53	0.37	.04	23	8.5	0.9	21
A8	0.90	0.26	58	0.39	.08	42	8.9	1.3	29

*As measured on the ground and taken to be twice the free field pressure.

Table III Comparison of Measured and Simulated Peak Structural Responses: Direct

Sensor	Boom Number	Correlation Coefficient	Peak Acceleration		
			Measured (g)	Simulated (g)	Diff. (%)
A1 Ext. Glass Panel (center)	5	.48	2.64	3.35	27.
	6	.59	1.71	2.33	37.
	7	.39	3.60	3.90	8.
	8	.53	2.22	2.12	-5.
	9	.54	3.11	3.34	8.
	10	.62	3.42	3.91	14.
	Six Boom Avg.	.52	2.78	3.16	15.
A2 Ext. Glass Panel (off-center)	5	.53	1.95	1.90	-2.
	6	.63	1.24	1.35	9.
	7	.64	2.48	2.25	-9.
	8	.40	1.34	1.23	-8.
	9	.57	1.92	1.85	-4.
	10	.69	2.21	2.06	-7.
	Six Boom Avg.	.58	1.86	1.77	-4.
A3 East Wall on Plywood	5	.50	1.80	1.78	-1.
	6	.41	1.45	1.43	-2.
	7	.39	2.35	2.68	14.
	8	.36	1.64	1.35	-18.
	9	.44	1.96	2.12	8.
	10	.41	2.52	2.09	-17.
	Six Boom Avg.	.42	1.95	1.91	-3.
A5 Interior Glass Panel (center)	5	.40	0.88	0.52	-41.
	6	.44	0.56	0.40	-28.
	7	.54	1.30	1.00	-23.
	8	.52	0.68	0.64	-5.
	9	.49	0.91	0.58	-36.
	10	.61	0.86	0.80	-7.
	Six Boom Avg.	.50	0.86	0.66	-23.
Sensor	Boom Number	Correlation Coefficient	Peak Strain (stress)		
			Measured (ϵ E, psi)	Simulated (ϵ E, psi)	Diff. (%)
S1: Ext. Glass Panel (Horiz.)	13	.86	638.	795.	25.
S2: Ext. Glass Panel (Vert.)		.87	428.	703.	64.
S3: Ext. Glass Panel (Diag.)		.85	428.	558.	30.

Table IV Comparison of Measured and Simulated Peak Structural Responses: Reciprocal

Sensor	Boom Number	Correlation Coefficient	Peak Acceleration		
			Measured (g)	Simulated (g)	Diff. (%)
A1 Ext. Glass Panel (center)	5	.51	2.64	2.59	-2.
	6	.59	1.71	1.84	8.
	7	.54	3.60	2.62	-27.
	8	.41	2.22	1.33	-40.
	9	.57	3.11	2.55	-18.
	10	.60	3.42	2.32	-32.
	Six Boom Avg.	.54	2.78	2.21	-19.
A2 Ext. Glass Panel (off-center)	5	.45	1.95	1.42	-27.
	6	.53	1.24	1.13	-8.
	7	.45	2.48	2.18	-12.
	8	.34	1.34	1.16	-14.
	9	.52	1.92	1.77	-8.
	10	.56	2.21	1.95	-12.
	Six Boom Avg.	.48	1.86	1.60	-14.
A3 East Wall on Plywood	5	.38	1.80	1.08	-40.
	6	.41	1.45	0.87	-40.
	7	.35	2.35	1.75	-25.
	8	.25	1.64	0.73	-55.
	9	.30	1.96	1.14	-42.
	10	.26	2.52	1.57	-38.
	Six Boom Avg.	.33	1.95	1.19	-40.
A5 Interior Glass Panel (on-center)	5	.49	0.88	.46	-47.
	6	.52	0.56	.36	-36.
	7	.64	1.30	.79	-39.
	8	.55	0.68	.50	-26.
	9	.65	0.91	.53	-41.
	10	.55	0.86	.67	22.
	Six Boom Avg.	.57	0.86	.55	-35.
A8 North Wall on Sheetrock	5	.77	0.82	.69	-16.
	6	.70	0.64	.50	-22.
	7	.60	1.07	1.01	-6.
	8	.44	0.63	.47	-24.
	9	.71	0.88	.73	-17.
	10	.56	1.39	.77	-44.
	Six Boom Avg.	.53	0.90	.70	-22.

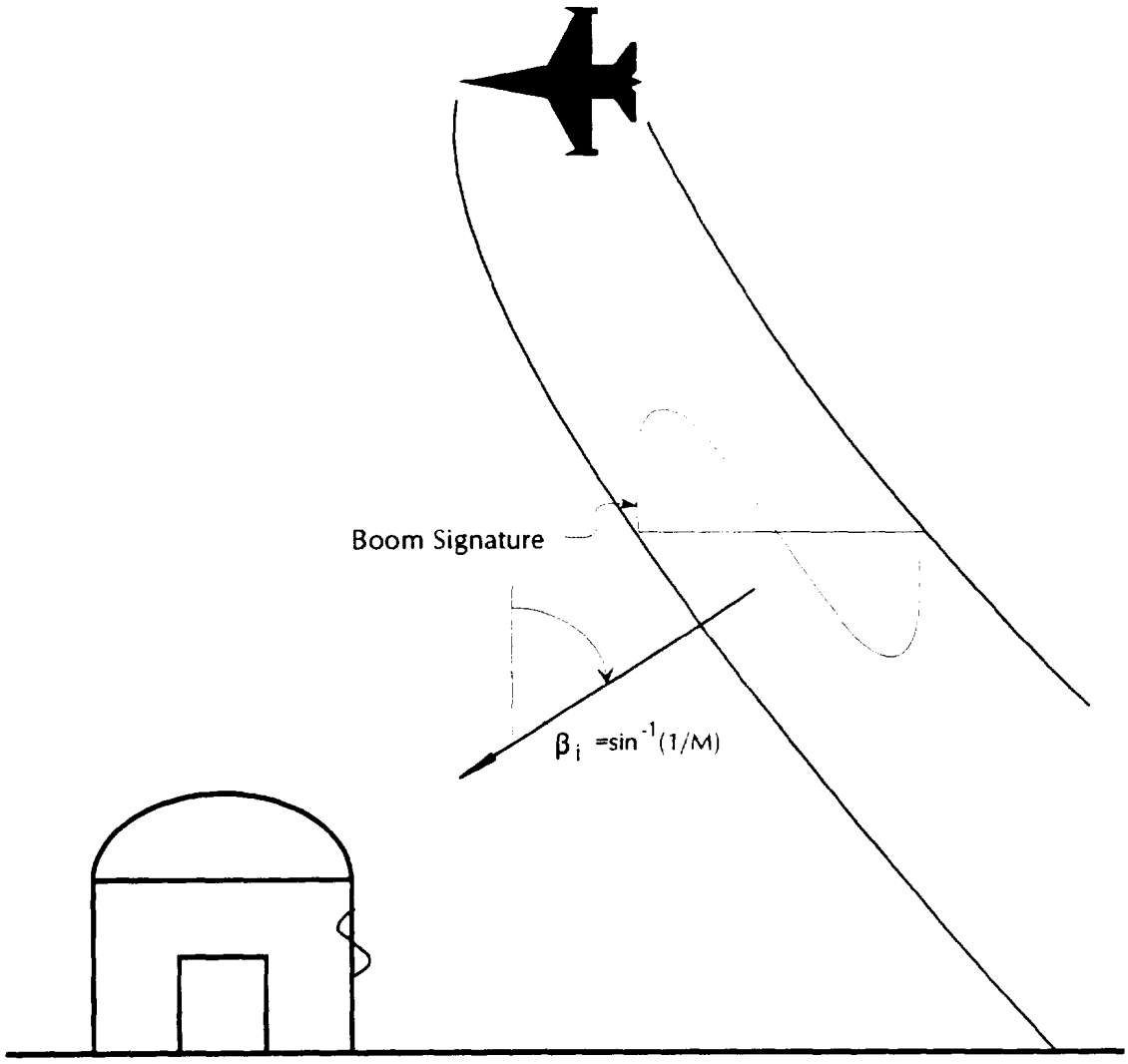

Fig 1. Boom From Supersonic Flyover Vibrates Structure, Potentially Causing Damage (Glass Breakage, Plaster Cracking, Etc.)

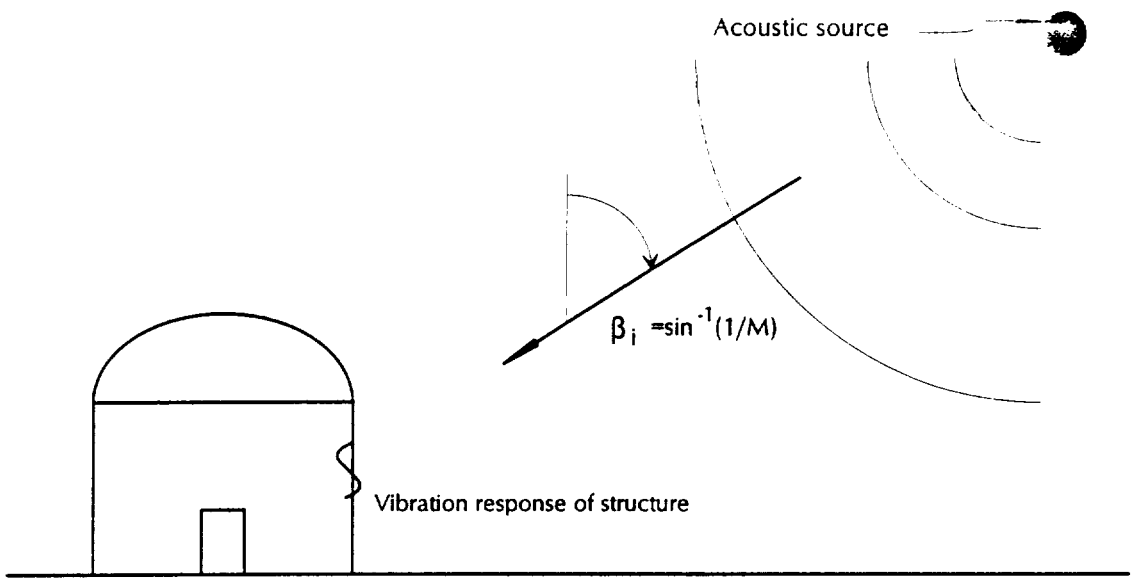

Fig 2a. Direct Structural-Acoustic Simulation of Sonic Boom Impulse Response Function

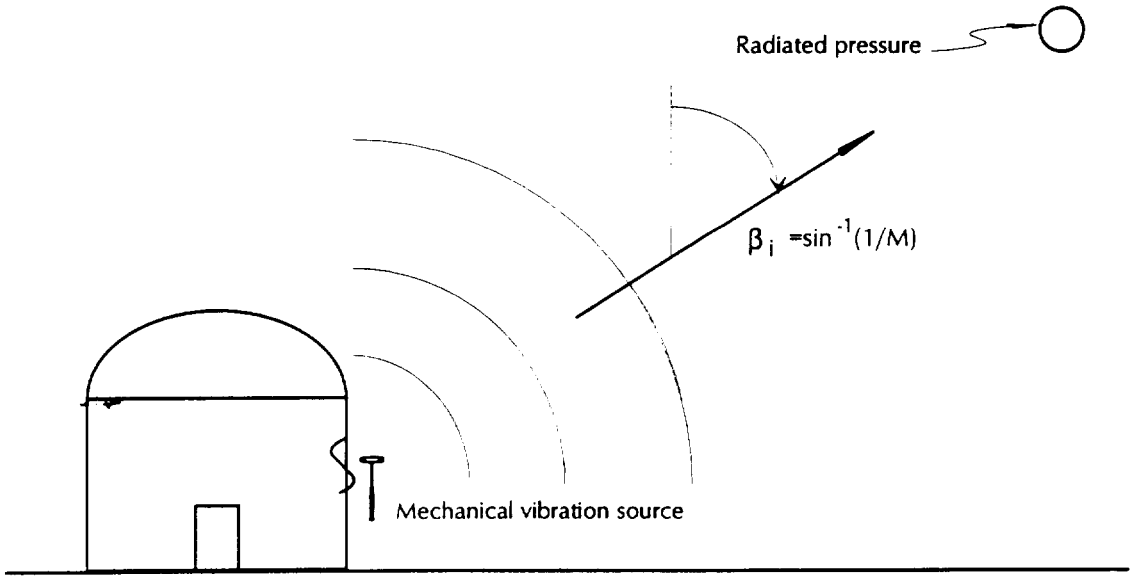

Fig 2b. Reciprocal Structural-Acoustic Simulation of Sonic Boom Impulse Response Function

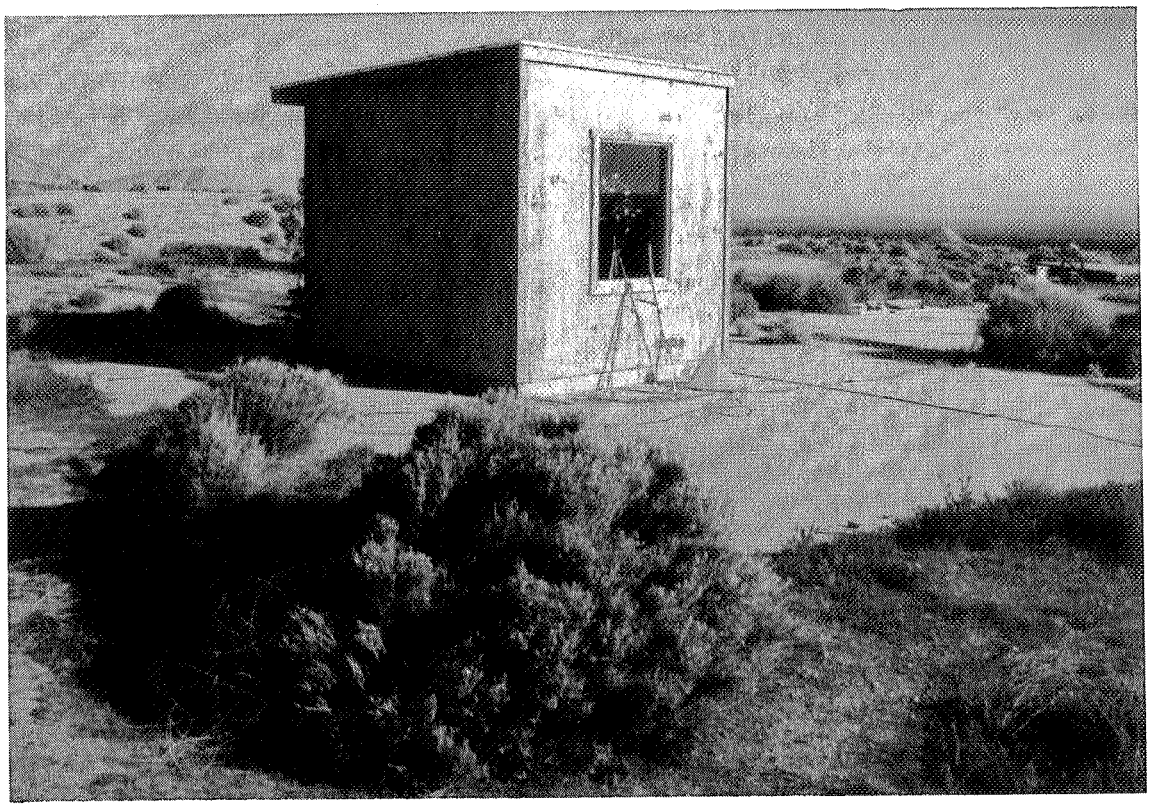

Fig. 3a. Instrumented glass panel on special test structure.

Fig. 3b. Equipment used for elevating acoustic source (cannon) and receiver (microphone) for structural acoustic simulations.

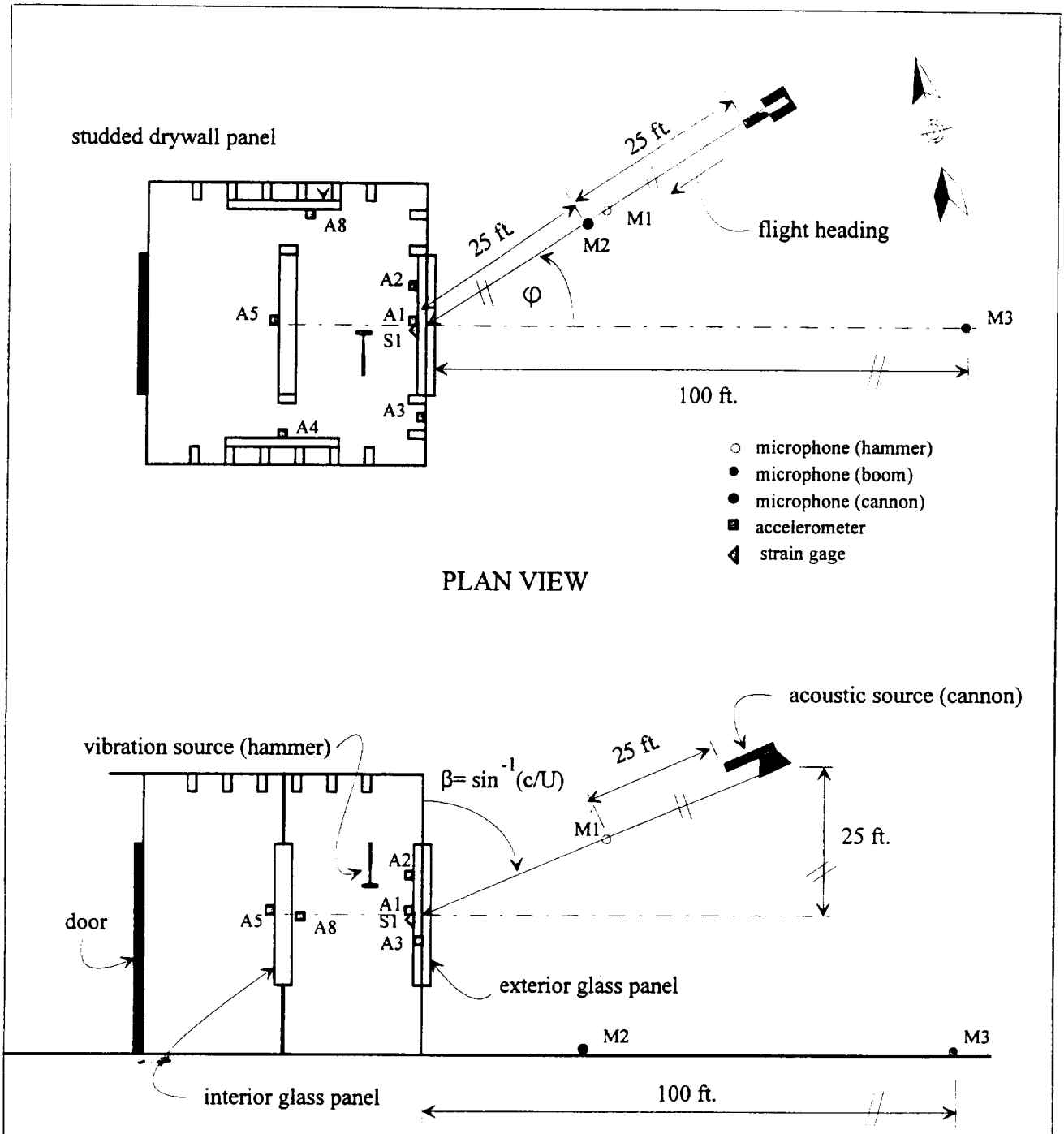

Fig 4. Sketch of Test Structure and Source/Sensor Geometry

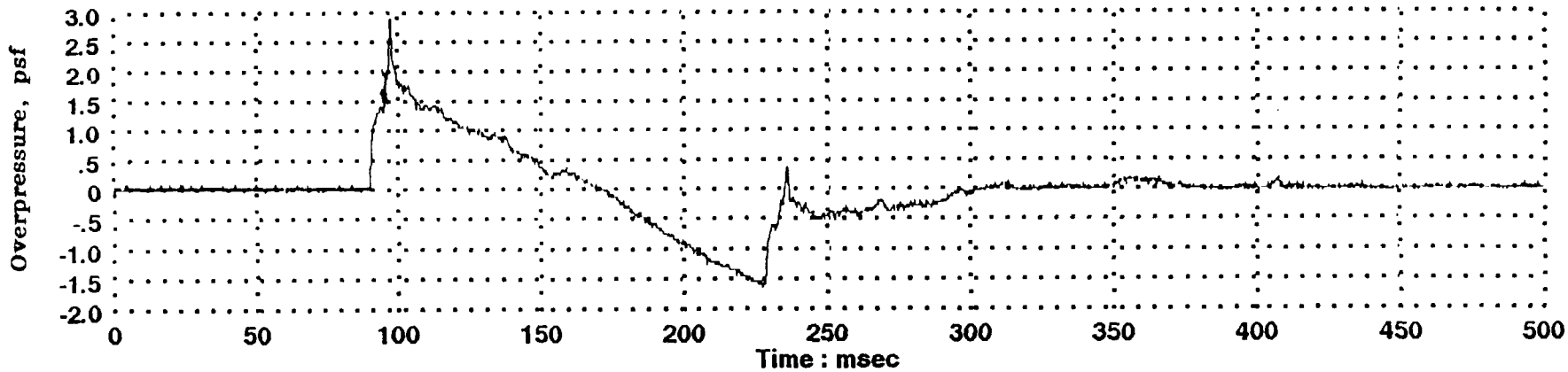

Fig. 5a. Boom Signature from F-15 Flyover (Dedicated Flight as Monitored at Microphone M3).

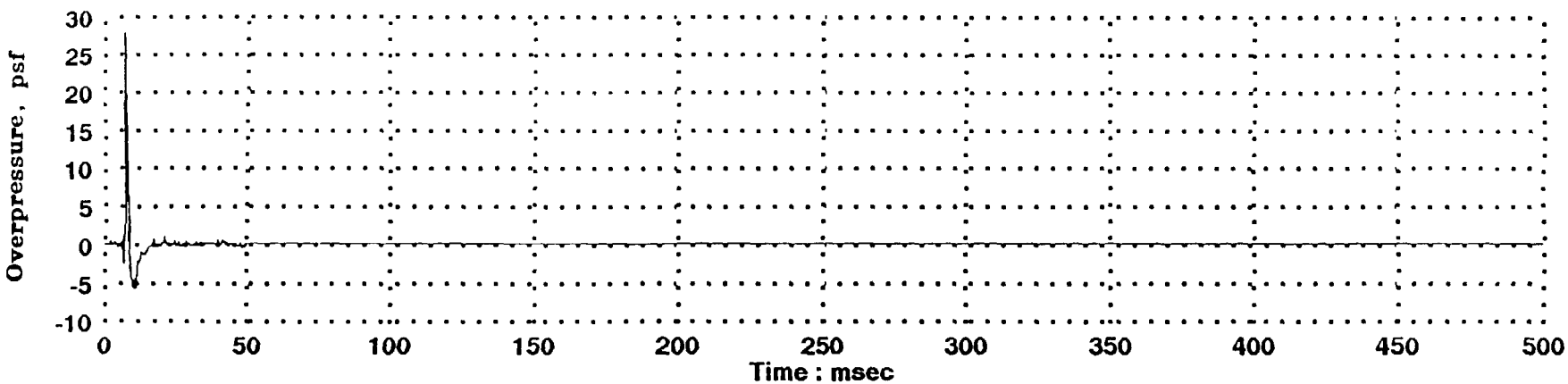

Fig. 5b. Cannon Shot Signature (at 50 ft. as Monitored by Microphone M2).

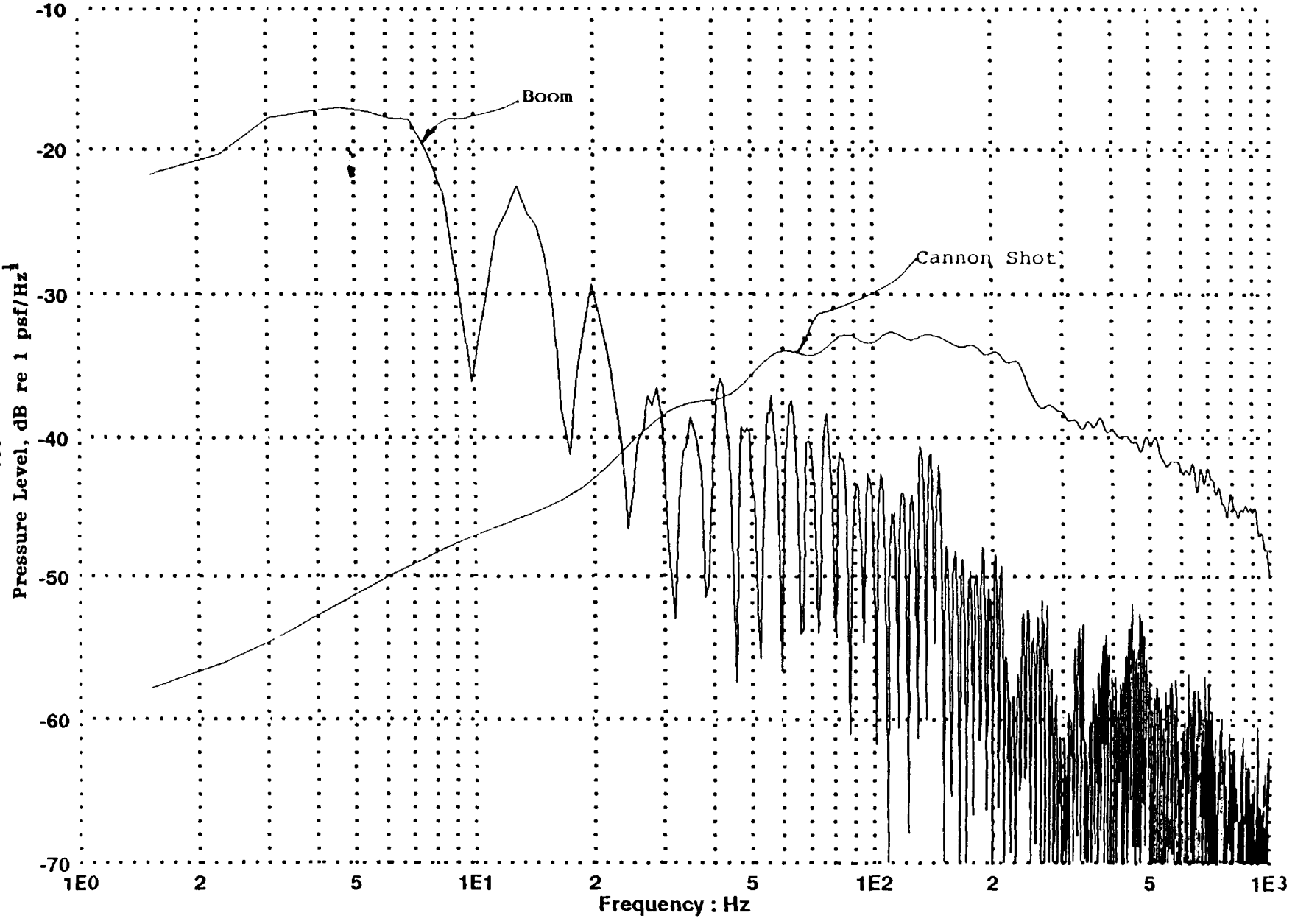

Fig. 6. Typical Auto Spectra of Cannon Shot (at 50 ft.) and Boom as Monitored by Microphones No. 2 and 3 Respectively.

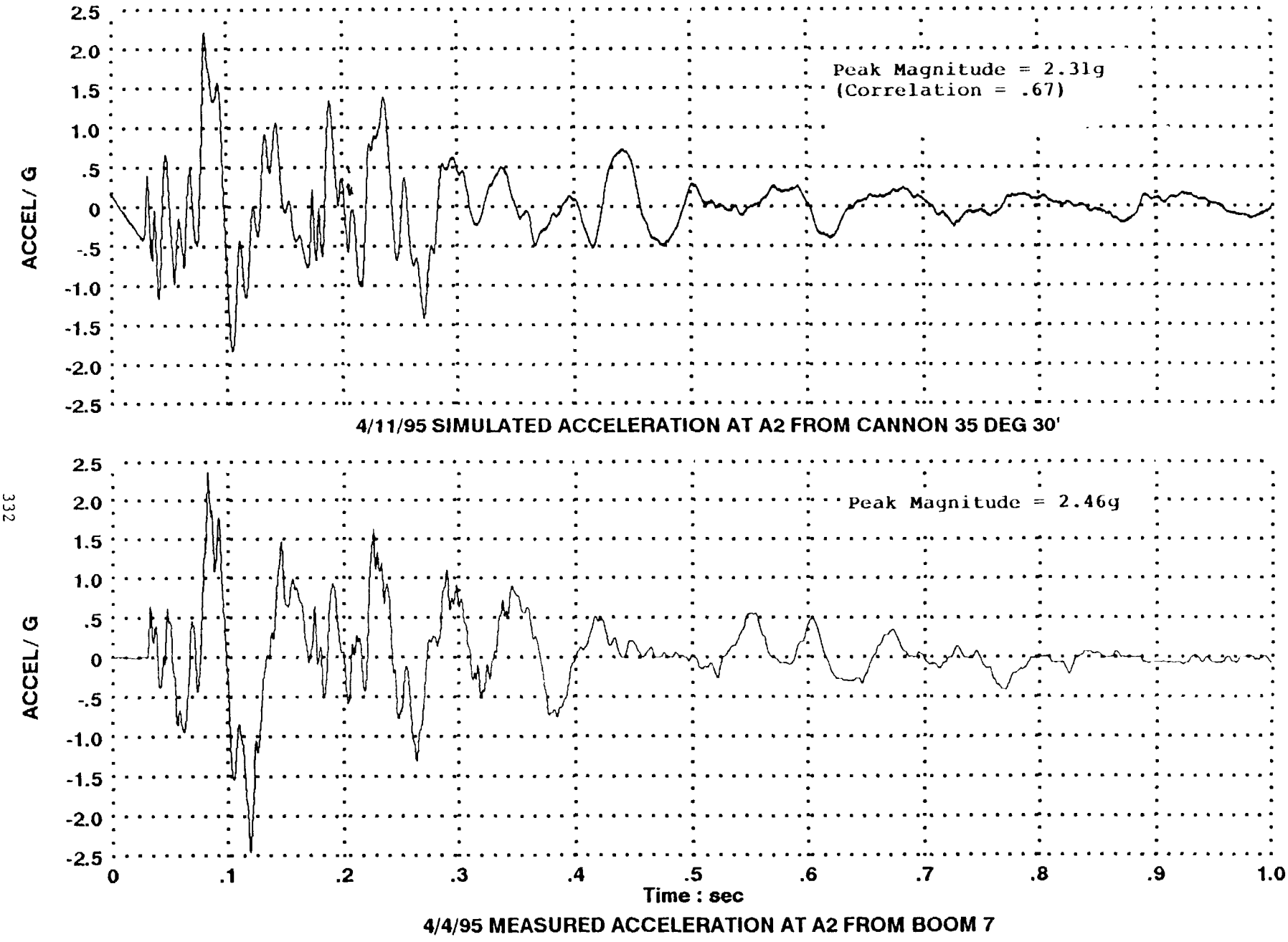

Fig. 7. Comparison of Measured and Simulated Responses of External Glass Panel (A2) to a Single Flyover: Direct Simulation.

SONIC BOOM OCEAN PENETRATION: NOISE METRIC COMPARISON AND INITIAL FOCUSING RESULTS*

Victor W. Sparrow
The Pennsylvania State University
157 Hammond Building
University Park, PA 16802

ABSTRACT

The purpose of the present research is to determine the impact by sonic boom noise penetration into the ocean. Since the 1994 LaRC High Speed Research Program Sonic Boom Workshop several new results have been obtained. This talk reviews these results, and emphasizes the two most important findings.

The first major result is an improved understanding of the noise spectra of the penetrating sonic boom. It was determined that *weighted* sound exposure levels decrease with deeper ocean depths significantly faster than *unweighted* sound exposure levels. This is because low frequencies penetrate the ocean deeper than high frequencies. Several noise metrics were used including peak, SEL, C-SEL, A-SEL, and PLdB, and results are given for all. These results are important because they show that the sonic boom noise impact on marine life a few meters below the ocean surface may be significantly lower using weighted sound levels than if one were to measure the impact using unweighted levels.

The other major finding is the first estimate of the worst case peak levels produced by a penetrating sonic boom being focused by a sinusoidal ocean surface. The method of analysis chosen was computational, a time domain finite difference algorithm. The method is outlined and then example results are presented.

For rounded sonic boom waveforms incident on a sinusoidal ocean surface, it is shown that the percentage increase or decrease in pressure is only occasionally larger than 10%, rarely 25%. These fluctuations indicate, under the assumptions already given, that any increase or decrease in sound level underwater due to focusing or defocusing should be small, less than 3 dB.

* Work supported by NASA LaRC Grant NAG 1 – 1638

INTRODUCTION

The project "Sonic boom noise penetration into the ocean" began on August 15, 1994. The overall goal of this research is to determine the underwater sound levels that a High Speed Civil Transport (HSCT) might produce. One emphasis in the research is to determine quantitatively how realistic ocean surfaces focus and defocus the sound waves.

About the Project

- Began August 15, 1994.
- Overall goal: determine the underwater sound levels due to HSCT in the ocean environment.

REVIEW

In 1968 Sawyers showed that evanescent sonic boom sounds penetrate the air – ocean interface. In 1970 Cook elaborated on this finding. These theoretical studies were verified experimentally by the work of Waters (1971) and Intrieri and Malcolm (1973). Thus, there is clear and convincing evidence that sonic boom noise from a HSCT will penetrate the surface of the air – ocean interface.

In addition, it is known that low frequency sound penetrates further than high frequencies. Later in this talk this will become an important point. Additionally, Sparrow (1995) has shown that a faster flying HSCT will produce a sonic boom that penetrates deeper into the ocean.

Brief Review

- Evanescent sonic boom sound always penetrates the air – ocean interface for HSCT — no way to avoid.
- Low frequencies penetrate further than high frequencies.
- Faster flying HSCT in steady flight $\Longrightarrow$ more sound penetration.

The depth dependence of the penetrating sonic boom sound is easily seen in an example. In the figure an N-wave shaped sonic boom is incident at a mach number of 2.4 upon a perfectly flat ocean which is assumed to be very deep so that bottom reflections can be ignored. The values along the vertical axes are acoustic pressure scaled to the acoustic pressure at the surface. The acoustic pressure at the surface is same on both sides of the air – water interface. The horizontal axes are time scaled by the duration of the N wave at the surface. Three graphs are shown for depths of 1, 10, and 100 m. One notices that the waveforms do persist even to 100 m. Further, at deeper depths the waveforms are smoothed compared to those at a shallower depth.

Typical N Wave Penetration

- Perfectly flat surface and deep ocean assumed.
- Pressure nondimensionalized to values at the surface.
- Time nondimensionalized to boom duration at the surface.
- Notice:
  - waveforms persist to over 100 meters depth
  - waveforms at deeper depths are considerably smoothed

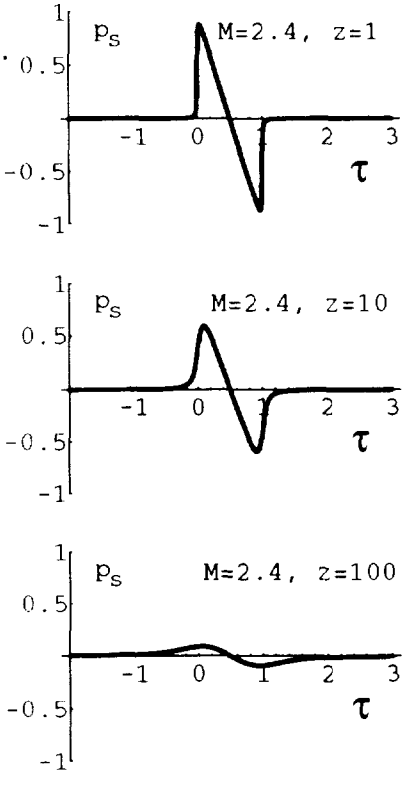

PRIMARY ACCOMPLISHMENTS

This year two significant achievements came from the present research. The first result is a comparison of appropriate noise metrics for the penetration of N waves. This research was presented at Inter–Noise 95, during July of 1995. The second achievement is the first set of results of sonic boom evanescent noise focusing due to the ocean surface. The computational methods for producing these focusing results were presented at the Second International Conference on Theoretical and Computational Acoustics in August of 1995. These accomplishments will now be described.

This Year's Primary Accomplishments

(in addition to reading lots of papers)

A. Noise metric comparison for penetration of N waves.

- Presented at InterNoise 95, July 1995.

B. Initial results for focusing of sonic boom evanescent noise by ocean surface.

- Presented at 2nd Intl. Conf. Theo. Comp. Acoust., August 1995.

NOISE METRIC COMPARISON

As noted earlier, peak sonic boom levels persist to depths of over 100 m. One may ask, however, whether peak levels are the best indicator of the effects of sonic boom noise. The answer is no. There are many other descriptors of sonic boom noise, many of which are described in the work of Brown and Sutherland, for example.

A question which must be answered, then, is will other measures of the sonic boom noise persist to such depths? In addition, which measures should be used?

Noise Metric Comparison

- Peak levels persist to over 100 meters.
- Will other measures of noise persist this far?

Since one wishes to know the effects or noneffects of sonic boom noise on marine mammals and other underwater wildlife, it makes sense that one would pick noise measures appropriate for such animals. However, no such measures are presently available, although they are under development. (Today there is no W weighting for whales!)

Given that marine mammal noise metrics do not exist, one is left with trying a variety of sonic boom noise measures appropriate for humans. Thus, human measures were compared in the present study.

Noise Weightings for Marine Mammals?

- Unfortunately, these are only under development.
- For now, use most common noise metrics for humans.

Brown and Sutherland have shown that one can measure a sonic boom either subjectively or physically. The common subjective metrics are Stevens' Mark VII perceived level in PLdB and sound exposure level. Physically one can measure flat, C-weighted, and A-weighted sound exposure levels, as well as peak levels. The Stevens' perceived level is almost always the best predictor of human annoyance. C-weighted and unweighted sound exposure levels are the next best predictors, followed lastly by A-weighted sound exposure level.

To provide a broad sampling of the available metrics, the following were used in this study: peak level, unweighted sound exposure level (flat SEL), L_{UE}; C-weighted sound exposure level (C-SEL), L_{CE}; A-weighted sound exposure level (A-SEL), L_{AE}; and Stevens' Mark VII perceived level, PLdB.

Sonic Boom Metrics

- Subjective description
  - Mark VII Perceived Level of Stevens (PLdB)
  - Sound Exposure Levels (L_E)
- Physical description
  - Unweighted (Flat) or C-weighted Sound Exposure Levels
  - A-weighted Sound Exposure Level

$\Rightarrow$ We used:

dB peak, L_{UE}, L_{CE}, L_{AE}, PLdB

In making the metric comparison, sonic boom waveforms for an incident N wave were predicted using the symbolic manipulation program *Mathematica* for depths of 1, 2, 4, 8, 16, 32, 64, and 128 m. The Sawyers' theory is used directly in finding the appropriate waveforms. *Mathematica* then calculated the peak, unweighted, A-weighted, and C-weighted noise measures, as well as produced datafiles containing a sampled waveform for each depth. These datafiles were then used as input to a Fortran program developed by Kevin Shepherd and Brenda Sullivan of NASA Langley Research Center. The Fortran program then calculated the Stevens' perceived level of sound. The present author and his graduate assistant, Judy Rochat, particularly thank Shepherd and Sullivan for the use of this program.

Numerical Analysis of Predicted Waveforms

Programs for calculations:

- *Mathematica*
  - finds pressure as a function of time, depth, and sonic boom parameters
  - applies A- and C-weighted filters
  - calculates sound pressure levels and sound exposure levels
- Fortran (Thank you, Shepherd and Sullivan of NASA LaRC.)
  - finds perceived level of sound

The parameters used for the noise metric comparison are those envisioned for a HSCT, and they are given below. Using these parameters, the corresponding decibel levels in air at the surface of the ocean are given in Table I, also shown below. One sees that for the same sonic boom waveform, the peak level is highest in value and the A-weighted level is lowest. Note also that the C-weighted sound exposure level is closest to the Stevens' Mark VII metric.

Parameters used for hypothetical HSCT:

- speed = Mach 2.4
- N-wave duration = 300 ms
- N-wave peak pressure = 50 Pa ($\approx$ 1 lb/ft^2)

  $\Longrightarrow$ peak pressure = 100 Pa at ocean surface

Corresponding decibel levels at surface of water: Table I.

depth (meters)	dB peak	L_{UE} (dB)	L_{CE} (dB)	L_{AE} (dB)	PLdB (dB)
0	131.0	118.0	108.0	94.4	106.1

reference pressure = 20 μPa, reference time = 1 second

The results seen in Table I are relatively easy to calculate in the Fourier domain since the N-wave pulse shape is band limited in time. The underwater waveforms, however, are theoretically predicted by the Sawyers' theory to have infinitely long tails, and are not band limited in time. Thus, in the calculations it was necessary to apply a nonlinear filter to the underwater waveforms to force the tails to zero. This is because the calculations were performed on desktop computers which could not handle more than 16,384 samples in the fast fourier transforms required in calculating the weighted sound exposure levels.

Computational limits:

- greater depth $\Longrightarrow$ longer tails on waveform
- longer tails on waveform $\Longrightarrow$ increased window size
- increased window size $\Longrightarrow$ more samples needed

  $>$ 16,384 samples $\Longrightarrow$ too much computation time

  (for our computer)
- solution:

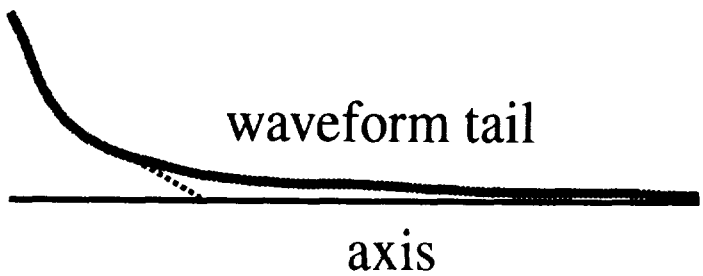

This table shows the results of the noise metric comparison. The decibel levels shown are those relative to the levels at the surface, i.e., the levels presented in Table I. It is clear that the peak and unweighted sound exposure level decay the least with increasing depth, while the A-weighted sound exposure level decays the most. It makes sense that the A-weighted SEL decays the most because this noise measure penalizes low frequencies more than the others. Note that the decrease in the levels with depth is not uniform. For example at a depth of 8 m, the difference in decay between the C-weighted level and the Stevens' Mark VII perceived level is 9.6 dB, while at 128 m the difference is only 0.4 dB.

Overall, one can see that the weighed levels show much greater decay with depth than the unweighted levels.

Noise Metric Comparison Results

Decibel levels as a function of depth relative to those in Table I.

depth (meters)	dB peak	L_{UE} (dB)	L_{CE} (dB)	L_{AE} (dB)	PLdB (dB)
0	0.0	0.0	0.0	0.0	0.0
1	-0.9	-0.3	-6.8	-18.6	-7.9
2	-1.4	-0.5	-8.6	-25.1	-11.7
4	-2.0	-0.9	-11.3	-33.3	-17.5
8	-3.0	-1.6	-15.1	-43.6	-24.7
16	-4.6	-2.7	-20.1	-56.2	-30.7
32	-7.2	-4.7	-26.1	-71.0	-35.0
64	-11.6	-8.1	-33.0	-84.8	-38.7
128	-18.4	-13.4	-42.0	-91.5	-42.4

One can conclude from this study that the metrics most associated with human response to sonic booms, Stevens' Mark VII perceived level and C-weighted sound exposure level, decayed with depth significantly faster than the unweighted metrics. Thus, the noise impact which marine mammals may experience due to sonic booms may be significantly diminished compared to the impact one would predict using unweighted levels. Also it was shown that there is significant variability in the predicted sound levels depending on which weighting is used. In this study weightings for humans were used because these were available, and they may provide some prediction of marine mammal annoyance. It is clear, however, that weightings should be developed specifically for pinnipeds, such as seals, and cetaceans, such as whales and dolphin. As indicated by Dr. Ann Bowles [personal communication] weightings involving startle response would be most appropriate.

Conclusions: Noise Metric Comparison

- Examined several sound descriptors as a function of depth.
- Perceived levels decrease rapidly with depth.
  - Impact experienced may be significantly diminished, compared to unweighted levels.
- Human weightings may give prediction of marine mammal annoyance.
  - However, weightings should be developed for pinnipeds and cetaceans, including those involving startle response (A. Bowles).

SONIC BOOM FOCUSING BY THE OCEAN SURFACE

One now turns to the second investigation of the present project, initial results for the focusing of the evanescent sonic boom noise penetrating the air – ocean interface. At last year's workshop, it was predicted that the focusing of this noise would produce hot and cold spots of sound under the ocean surface. The goal of the investigation was to determine the magnitude of this focusing and defocusing; is this a strong or weak effect?

Focusing of Sonic Boom Noise by Ocean Surface

From last year's workshop:

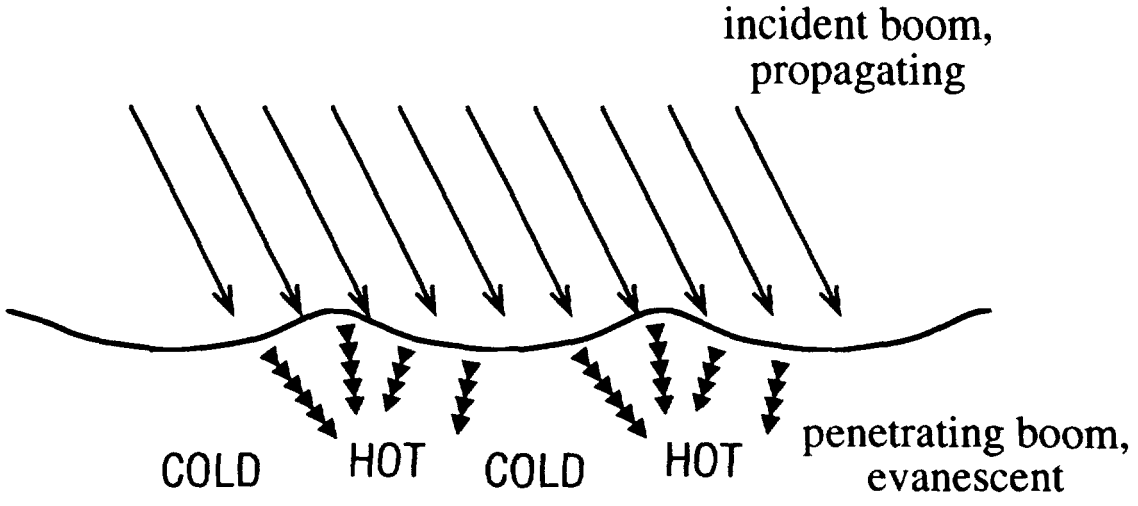

Our goal: determine the magnitude of this focusing.

Several avenues are open for determining the penetrating sonic boom noise: analytical approaches, the T-matrix method, direct approximations of the Kirchhoff-Helmholtz Integral Theorem (KHIT), and finite difference methods. The analytical methods such as perturbation methods could be implemented via symbolic manipulation programs such as *Mathematica*. T-matrix is a frequency domain method, just as is the common boundary element approximations of the KHIT. Because of the difficulty of the perturbation methods, and because of the many frequencies that would have to be superimposed to get realistically shaped sonic booms for the frequency domain methods, finite difference methods were chosen for the initial study. The finite difference solutions are already in the time domain, and in the future one may easily modify them to model both nonlinear propagation, appropriate for very loud sound booms, and inhomogeneous media, appropriate for turbulence in the air and bubbles in the water. The other methods are not easily extensible to include nonlinearities and inhomogeneities.

Methods of Analysis

- Analytical — *Mathematica*, perturbation methods
- T-matrix — frequency domain
- Kirchhoff-Helmholtz Integral Theorem
  - — frequency domain boundary elements
- Finite Difference *(today)*
  - time domain
  - upgradeable to — nonlinear propagation
    - — inhomogeneous media

In computational acoustics one usually never needs to model sound waves getting through an air – water interface. From the air, usually a hard surface suffices as a boundary condition. Similarly from the water, the air is usually modeled as a pressure release surface.

For finite differences one can easily handle the sound speed change, a factor of 4.4, between air and water. The difficulty is that there is a huge ambient density change between air and water, a factor of approximately 827. Most finite difference schemes will go unstable with this large of a change in ambient density.

Here sound waves get THROUGH an air-water interface.

- Tough problem:
  - Usually from air . . . see a hard interface.
  - Usually from water . . . see a pressure release interface.

Why tough?

- Sound speed change, factor of 4.4 — no problem:

$$c_{\text{air}} \longrightarrow c_{\text{water}}$$

- Huge ambient density change, factor of 827 — very big problem:

$$\rho_{0,\text{air}} \longrightarrow \rho_{0,\text{water}}$$

To handle the large density contrast one cannot use an off the shelf CFD code, or poor results will be obtained. Many numerical methods were attempted by the present author, but all failed to give the analytically predicted reflection and transmission coefficients for an air – water interface. After an extensive literature search, a method was found in seismology that can account for such an interface. What is required is to explicitly integrate the wave equation across the interface. Using such a method will insure the proper reflection and transmission coefficients.

How to Handle Large Density Contrast?

- Considered many methods

  — easy to find methods which won't work.

- Can't use an off the shelf CFD code.

- Finally modified a method used in seismology.
  - Similar to Sochacki *et al.*
  - Uses integral form of acoustic equations at air – water interface.

$$\int (\text{wave equation})\, dx$$

The method used is similar to that of Sochacki *et al.* Their method could not be used directly because their equation of state is incorrect. Starting with the inhomogeneous wave equation from the work of Pierce, valid for both air and water, one first rewrites the equation into a compact form using two functions of space a and b. Here standard acoustic notation is used, *viz.*, ρ_0 is the ambient density, c is the speed of sound, and p is the acoustic pressure.

Method:

(similar to Sochacki *et al.* [Geophysics **56**, 168–181 (1991)], although their equation of state is wrong)

Inhomogeneous WE (Pierce's book):

$$\frac{1}{\rho_0(\bar{x})c^2(\bar{x})}\frac{\partial^2 p}{\partial t^2} - \nabla \cdot \left(\frac{1}{\rho_0(\bar{x})}\nabla p\right) = 0$$

Rewrite as

$$a(\bar{x})\frac{\partial^2 p}{\partial t^2} - \nabla \cdot (b(\bar{x})\nabla p) = 0$$

where

$$a(\bar{x}) = \frac{1}{\rho_0(\bar{x})c^2(\bar{x})} \quad \text{and} \quad b(\bar{x}) = \frac{1}{\rho_0(\bar{x})}$$

Considering a one-dimensional spatial integral over the rewritten inhomogeneous wave equation over the interval $-\epsilon$ to ϵ, one can quickly find an approximate finite difference version by letting ϵ equal half of the grid spacing. Using the resulting finite difference equation at the interface and second order in time and space central differences elsewhere works well: the method is both stable and numerically accurate.

1-D interface formulation:

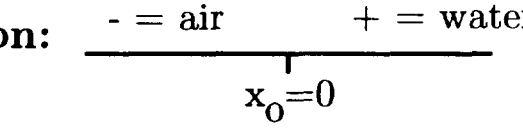

$$\int_{-\epsilon}^{\epsilon} a\, p_{tt} dx = \int_{-\epsilon}^{\epsilon} (b\, p_x)_x dx = b\, p_x|_{-\epsilon}^{\epsilon} = b(\epsilon)p_x(\epsilon,t) - b(-\epsilon)p_x(-\epsilon,t)$$

$$a^- \int_{-\epsilon}^{0} p_{tt} dx + a^+ \int_{0}^{\epsilon} p_{tt} dx = b^+ p_x(\epsilon,t) - b^- p_x(-\epsilon,t)$$

Let $\epsilon \rightarrow \Delta x/2$ and approximate:

$$\frac{\Delta x}{2}(a^+ + a^-)p_{tt} = b^+ p_x(\epsilon,t) - b^- p_x(-\epsilon,t)$$

Finite difference version:

$$\left(\frac{(a^+ + a^-)\Delta x}{2\Delta t^2}\right)(p_0^{n+1} - 2p_0^n + p_0^{n-1}) = \frac{b^+}{\Delta x}(p_1^n - p_0^n) - \frac{b^-}{\Delta x}(p_0^n - p_{-1}^n)$$

Use 2nd order central differences elsewhere. . . works great!

One can go through a similar derivation for a two-dimensional interface between two media and develop a similar finite difference formula to apply along the interface. The equation is slightly more complicated than the one-dimensional equation just derived. This is because the a and b functions now must be evaluated along a possibly curved surface.

For the present work, staircase approximations to the height variations in the ocean surface are used. Eventually one would like to use finite difference grids which warp or conform to the interface surface.

Similar interface formulation for 2-D, trickier due to curved surfaces:

$$\frac{a_{j,k}}{\Delta t^2}(p_{j,k}^{n+1} - 2p_{j,k}^{n} + p_{j,k}^{n-1})$$

$$= \frac{1}{\Delta x^2}\left[b_{j+1/2,k}\, p_{j+1,k}^{n} - (b_{j+1/2,k} + b_{j-1/2,k})\, p_{j,k}^{n} + b_{j-1/2,k}\, p_{j-1,k}^{n}\right]$$

$$+ \frac{1}{\Delta z^2}\left[b_{j,k+1/2}\, p_{j,k+1}^{n} - (b_{j,k+1/2} + b_{j,k-1/2})\, p_{j,k}^{n} + b_{j,k-1/2}\, p_{j,k-1}^{n}\right]$$

where $a_{j,k} = \alpha a_1 + \beta a_2$.

One could use warped grids . . .

. . . but for now we use staircase approximation for curved interfaces.

The two-dimensional calculations that were run to obtain the focusing results are described in the figure below. An initial condition is prescribed in the computational domain, and then the finite difference scheme is marched forward in time. A typical calculation will take approximately 30 minutes on a modern workstation.

The Calculations

Domain: 800 m long by 900 m deep (340 m air, 560 m water)

I.C.: Very rounded sonic boom wave in air with 300 ms duration.

Grid: $\Delta x = \Delta z = 1$ m (coarse)

B.C.: top, right, left = rigid bottom = absorbing*

interface = flat or sinusoidal

* modified from

[V. Sparrow and R. Raspet, J. Acoust. Soc. Am. **87**, 2422–2427 (1990).]

As an example calculation the two snapshots seen below are at time t = 0.7 s of simulated time after the initial condition is given at t = 0. The snapshots show a mach 2.4 rounded sonic boom wave incident on both a flat ocean surface and an ocean surface where the crest to trough wind wave height is 2.3 m, corresponding to a 20 knot wind. On both plots the vertical axes give depth z in meters where the air – water interface is at z = -340. The horizontal axes give range in meters. Minimal differences can be seen in these grayscale plots of acoustic pressure where the darker pixel values indicate positive acoustic pressures and lighter pixel values indicate negative acoustic pressures. (0 acoustic pressure on the pixel value scale is 127.) One can discern, however, interference effects in the reflected wave for the wave height of 2.3 m. Focusing and defocusing is taking place, but it is just too small an effect in magnitude to be clearly seen on the right hand plot.

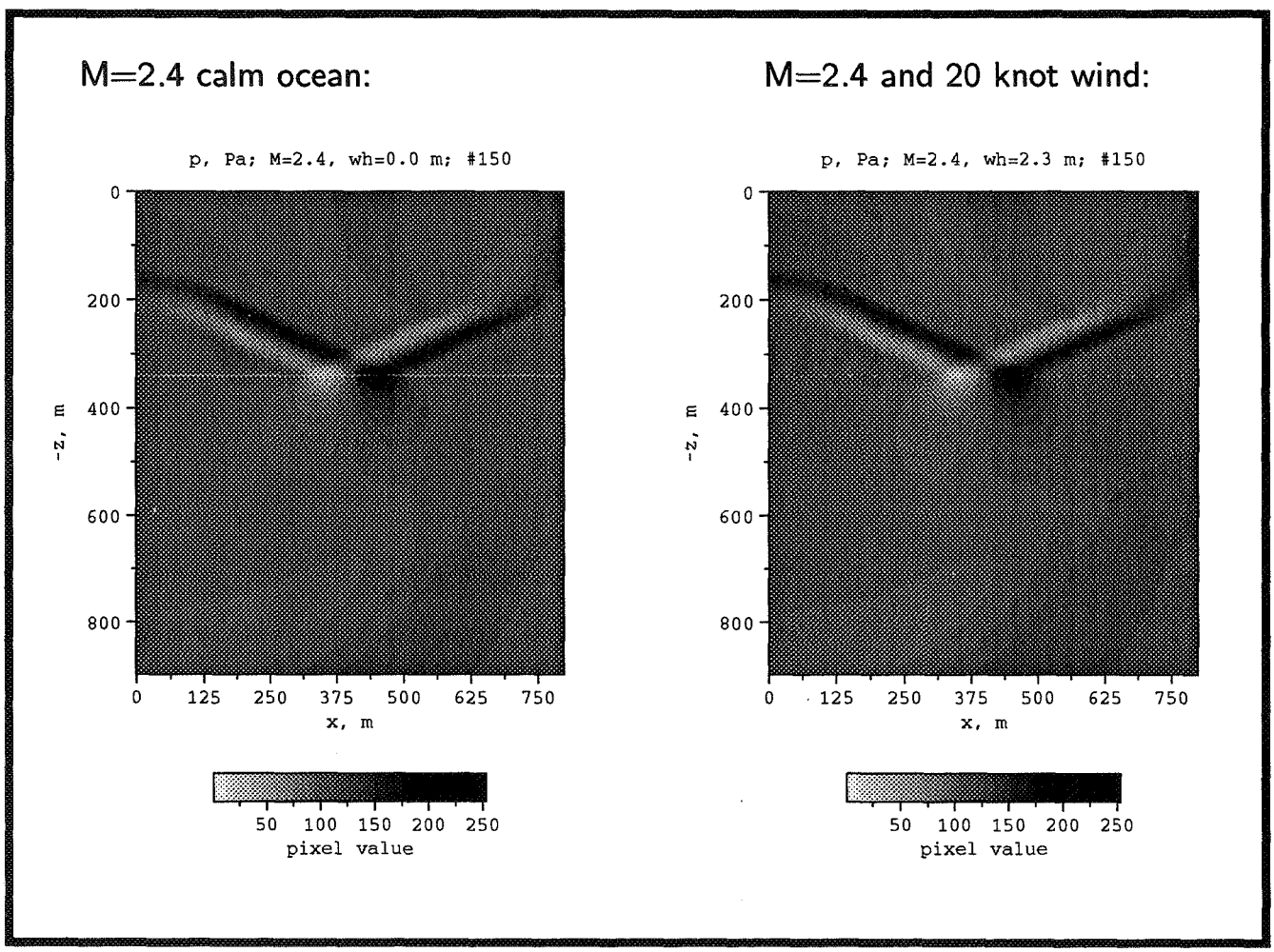

Shown in the table below are some typical focusing and defocusing results of the finite difference investigations for rounded sonic boom waves and sinusoidally shaped ocean surfaces. Positive or negative percentage changes in the positive and negative peaks of the penetrating sonic boom waves are plotted for various wind wave heights for the mach numbers of 1.4 and 2.4. The nonzero wind wave heights selected, 1.4, 2.3, and 3.75 m, roughly correspond to 10, 20, and 30 knot winds. The wavelengths of the wind waves are taken as 20 times the wind wave heights, which is a common ocean engineering approximation.

It is seen that larger focusing or defocusing generally occurs for the larger mach number. The percentage changes are often less than 10% and they are rarely greater than 25%, with seemingly equal probability of focusing or defocusing. Two typical values are shown for mach 1.4 and a wind wave height of 3.75 m, for example. On a dB scale these percentage changes would be small, always less than 3 dB.

Typical Focusing Results

Wind wave height,* (m)	Change in +/− peaks of penetrating sonic boom due to focusing	
	M=1.4	M=2.4
0	0 / 0	0 / 0
1.4	2.5% / 3.4%	6.1% / 11.0%
2.3	0.3% / −2.4%	6.1% / 13.0%
3.75	3.6% / 2.2% −3.8% / −3.6%	9.1% / 25.0%

* (crest to trough)

From this initial study for rounded sound boom waves and sinusoidal ocean surfaces one can make a number of conclusions. First the huge density contrast problem for finite difference modeling can be overcome by using an explicit integration across the interface. Using this method, it is shown that focusing and defocusing of the penetrating sonic boom noise does take place because of the curvature of the air – ocean interface. The percentage changes associated with this focusing and defocusing are small, and on a decibel scale the noise levels are unlikely to increase or decrease by more than 3 dB. While performing the research it was determined that finer grids and possibly warped grids will be needed for improved predictions. Other sonic boom signatures and wind wave shapes should be investigated, and these studies are currently underway.

Initial Conclusions: Boom Focusing

- Integrating across the interface overcomes the huge density contrast problem for finite differences.
- Evanescent waves created by sonic booms penetrating an air–water interface do focus and defocus due to wind waves.
- Percentage changes in peaks of rounded sonic boom waveforms are small — peak levels never changed by more than 3 dB.
- What is needed (in progress): comparisons with other methods, finer grids, other boom signatures and wind wave shapes.

REFERENCES

1. Brown, D.; and Sutherland, L.: Evaluation of outdoor-to-indoor response to minimized sonic booms. NASA CR-189643, 1992.

2. Cook, R.: Penetration of a Sonic Boom into Water. *J. Acoust. Soc. Am.*, vol. 47, no. 5, pt. 2, 1970, pp. 1430–1436.

3. Intrieri, P.; and Malcolm, G.: Ballistic Range Investigation of Sonic-Boom Overpressures in Water. *AIAA J.*, vol. 11, no. 4, 1973, pp. 510–516.

4. Pierce, A.: *Acoustics: An Introduction to Its Physical Principles and Applications.* Acoustical Society of America, Woodbury, NY, 1989.

5. Rochat, J.; and Sparrow, V.: Sound Levels Under the Ocean Surface Due to Sonic Boom Penetration, in *Proceedings of Inter–Noise 95.* Noise Control Foundation, New York, 1995, pp. 967–970.

6. Sawyers, K.: Underwater Sound Pressure from Sonic Booms. *J. Acoust. Soc. Am.*, vol. 44, no. 2, 1968, pp. 523–524.

7. Shepherd, K.; and Sullivan, B.: A Loudness Calculation Procedure Applied to Shaped Sonic Booms. NASA TP-3134, 1991.

8. Sochacki, J.; *et al.*: Interface Conditions for Acoustic and Elastic Wave Propagation. *Geophysics*, vol. 56, no. 2, 1991, pp. 168–181.

9. Sparrow, V.: The Effect of Supersonic Aircraft Speed on the Penetration of Sonic Boom Noise into the Ocean. *J. Acoust. Soc. Am.*, vol. 97, no. 1, 1995, pp. 159–162.

10. Waters, J.: Penetration of Sonic Boom Energy into the Ocean: an Experimental Simulation. in *Noise and Vibration Control Engineering,* M. Crocker, Ed., Proc. of the Purdue Noise Control Conference, Purdue Univ., Lafayette, IN, July 14-16, 1971, pp. 554–557.

11. Wolfram Research Inc.: *Mathematica,* Ver. 2.2. Wolfram Research, Inc., Champaign, IL, 1993.

EFFECTS OF SONIC BOOMS ON MARINE MAMMALS: PROBLEM REVIEW AND RECOMMENDED RESEARCH

Ann E. Bowles
Hubbs-Sea World Research Institute
2595 Ingraham Street
San Diego, CA

INTRODUCTION

By flying the High-Speed Civil Transport (HSCT) exclusively over uninhabited areas and mostly over water, human annoyance will be reduced to acceptable levels. However, this strategy will force HSCT proponents to contend with the potential effects of sonic booms on animals, particularly marine mammals. What follows is a summary of the environmental regulations that must be addressed, the scientific community's concerns about the potential effects of the HSCT, and recommendations for research to address the most important concerns.

The recommendations included herein are based both on existing scientific evidence and regulatory needs. One cannot overemphasize the importance of obtaining the appropriate information prior to substantial public exposure (*e.g.*, public hearings, press coverage). Recent controversies over other human-made acoustic sources in the ocean (*e.g.*, ref. 1-3) suggest that the HSCT will receive intense scrutiny. It seems certain that an Environmental Impact Statement (EIS) and Incidental Harassment Authorization (IHA) under the Marine Mammal Protection Act (MMPA) or its equivalent will be necessary.

Three acts govern projects that may affect marine mammals, the Endangered Species Act (ESA) of 1973 (P.L. 93-205, 87 Stat. 884, 16 U.S.C. 1531-1543; 50 C.F.R. 17, 220-222), the Marine Mammal Protection Act (MMPA) of 1972 (P.L. 92-522, 86 Stat. 1027, 16 U.S.C. 1361-1407; 50 C.F.R. 18, 216), and the Fur Seal Act (FSA; P.L. 89-702, 80 Stat. 1091, 16 U.S.C. 1151-1175; 50 C.F.R. 215). The regulation of these acts is the responsibility of two agencies, the U.S. Fish and Wildlife Service (manatees, dugongs, sea otters, polar bears, and walruses) and the National Marine Fisheries Service (all other marine mammals; also marine and anadromous fishes). Sea turtles are the responsibility of the two agencies jointly (ref. 4).

The ESA is part of the National Environmental Policy Act (NEPA), and applies to both domestic and foreign activities by U.S. citizens. It prohibits the taking of any threatened or endangered marine species within U.S. territorial waters or on the high seas. Permits to violate the ESA for endangered species are authorized (50 C.F.R. 17.21, 17.61, 222.21) for scientific research, enhancement of populations, or incidental takes that have no significant impact on the survival of the species. Permits

for threatened species are authorized (50 C.F.R. 17.31, 17.71) for scientific research, enhancement, incidental takes, and exhibition for educational purposes.

Under NEPA, proponents of an activity may file an Environmental Assessment (EA) demonstrating that their proposed activity will have no significant impact on endangered marine mammals. They must estimate the number of individuals to be taken and the area over which they will be affected. The onus of proof is on the proponent, but the evaluation and final EA are submitted by NMFS/OPR. From a scientific point of view, the resulting "Finding of No Significant Impact" (FONSI) is something of a misnomer, as it is not possible to prove that there will be no significant effect under all possible future conditions (hence the term "Fallacy of FONSI"). By applying a mixture of legal and scientific common sense, regulators arrive at an interpretation of the available information; often, they recommend mitigation measures, research, or a monitoring effort. In the case of the HSCT, obtaining satisfactory estimates of potential takes is likely to be a complex effort, as the number of species involved is large and the research needed to predict impact is largely unavailable. Under NEPA, proponents of an activity cannot be required to conduct research that is unreasonably expensive (>10% of the value of the activity), but large and publicly-visible activities, like the eventual flight of the HSCT, are likely to be adversely affected by a trial in the court of public opinion if adequate research effort is not initiated early.

The Marine Mammal Protection Act applies only to marine mammals; its governance is overseen by a commission appointed by the Executive Branch, the Marine Mammal Commission. It is the only such commission to oversee the protection of wild animals, which are otherwise the responsibility of the Departments of Interior and Commerce. This places marine mammals in a uniquely-powerful position relative to other animals, including endangered species. Although the evaluation of potential risks under the MMPA is somewhat similar to the environmental impact assessment process under NEPA, the MMPA places more emphasis on individual welfare.

In common parlance, the term "take" refers to killing, capturing, or seriously injuring an animal. The MMPA (50 C.F.R. 18.11, 216.11) defines the term as follows: "[to] harass, hunt, collect, capture, kill, or attempt to harass, hunt, capture, collect, or kill". This includes restraint or detention, negligent or intentional operation of an aircraft or vessel in the vicinity of marine mammals and any negligent or intentional act that results in disturbing or molesting marine mammals. "Harassment" is defined as pursuit, torment, or annoyance that has the potential to injure a marine mammal in the wild, or that has the potential to disturb individuals by disrupting migration, breathing, nursing, breeding, feeding, sheltering, or other behavior patterns. In essence, any human action that causes a detectable change in behavior constitutes a take.

Any activity in U.S. waters or international waters that takes marine mammals is in violation of the MMPA. If activity proponents, the public, or NMFS suspect that takes may occur, a permit or letter of authorization (LOA) exempting the activity from MMPA regulations must be requested. If proponents believe that their activity will have no effect, but wish formal confirmation, they may request a letter of opinion from the Office of Protected Resources at NMFS. However, in situations where there is concern that legal action might be taken, a permit is always required.

Permits to violate the terms of the Marine Mammal Protection Act are issued for scientific research *on marine mammals*, pubic display, and enhancement of the survival or recovery of a species or stock. Marine mammal research sponsored by the High Speed Research Program (HSRP) and its cooperators will be authorized by a scientific research permit. Other activities, including commercial

flights of the HSCT, will require an LOA or formal regulation exempting the activity from compliance with the MMPA. Currently, regulations cover captures or incidental mortality caused by specific industries (*e.g.*, zoological parks, the fishing industry), whereas noise-producing activities (*e.g.*, oil industry seismic surveys, large vehicle launches) obtain letters of authorization for specified periods (usually 3-5 yr).

Scientific research permits have been issued in the past to harass large numbers of animals in cases where no effect is expected, but such permits are an embarrassment to proponents and regulators alike. As a result, MMPA regulations have been changed recently (April 1994) to recognize two levels of take for scientific research:

Level A: *Requires a full permit request and publication in the Federal Register; the process may take 4-12 months; includes any activity that has the potential to injure a marine mammal or marine mammal stock.*

Level B: *Requires only a letter of authorization, without public announcement; it is issued quickly, in 1-2 mo; it includes any act of pursuit, torment, or annoyance that has the potential to harass but not injure.*

In actual flight, the HSCT will almost certainly "take" large numbers of animals in the strictest sense of the term, but these takes will be incidental to the activity, rather than the result of an experimental procedure Incidental takes that do not have the potential to affect individuals or species significantly must be authorized by an LOA commonly referred to as the "Small Take Authorization" or "Small Take Exemption". A small take exemption can be obtained for any activity that may take marine mammals as long as (a) it does not fall into the categories of fishing, public display and education, population enhancement, or scientific research on marine mammals, and (b) the estimate of the number of takes is "small". Small take exemptions can take 1-2 years to issue. They often include a requirement for monitoring, to insure that takes actually have no important effect.

Because many incidental takes pose no risk to marine mammals, NMFS has recently proposed a new set of regulations for issuing authorizations for non-damaging incidental takes, taking advantage of the tiered system (Level A, B) now used for marine mammal research. If the proposed Incidental Harassment Authorization (IHA) is included in MMPA regulations (60 CFR Part 228) by the time the HSCT begins to fly, it will simplify the process of obtaining an authorization, but it will probably continue to require some form of monitoring program. As currently written, the modified regulations do not contain a definition of "small" take. As take estimates for the HSCT are likely to be quite large, some clarification will be needed.

A number of written guidelines govern specific implementation of MMPA regulations. For example, no vessel may approach a marine mammal within 100 yds, and no aircraft may come within 1000 ft AGL without violating the law. There are also informal, unwritten guidelines used by NMFS/OPR to calculate take estimates and to determine whether permits are needed. These are particularly important in the case of noise exposure, as no standards for defining acceptable levels of noise are available for any animal. In the past, NMFS/OPR has occasionally used a limit for continuous noise exposure of 120 dB re 1 μPa, and for impulsive sources, 160 dB re 1 μPa, but without proper technical specifications. Controversial activities have been required to include every animal that might hear the proposed sound in their estimate of "take" - for example, the research permit issued for the Heard Island Feasibility Test was required to include every marine mammal in the Indian Ocean

south of the Antarctic Convergence (~186,000 animals). NMFS has recognized the need for consistent and appropriately-specified guidelines and is now in the process of preparing them. Such guidelines, when accepted, will certainly apply to the HSCT.

POTENTIAL EFFECTS ON MARINE MAMMALS: PUBLISHED RECOMMENDATIONS

Although activities are required to show they will have no significant impact on animals, they are not responsible for conducting research that will cost more than a small proportion of the project value (≤10%). Usually, projects fund applied research targeting the particular species and area of concern. They rarely fund basic long-term research into the biology of noise effects. On the other hand, granting agencies like the National Science Foundation usually consider disturbance effects to be too 'applied'. In effect, there is no reliable, long-term source of funding that promotes basic biological studies of response to human disturbance. Most investigators conduct basic research into disturbance effects as an adjunct to NEPA-mandated applied research or as a part of small pro-active research efforts funded by the DoD and other agencies (*e.g.*, the Office of Naval Research [ONR], the USAF's Noise and Sonic Boom Impact Technology Program, and NASA). Not surprisingly, there is a great paucity basic information about most of the species likely to be affected by the HSCT.

Several recent efforts have recommended research to determine the potential effects of various noise sources on marine mammals, much of which falls into the gray area between applied and basic research. The Ocean Studies Board of the National Academy of Sciences established a Committee on Low-frequency Sound and Marine Mammals, which issued a report in 1994 (ref. 5) reviewing the potential effects of low frequency noise on marine mammals and recommending research. This effort concentrated on low-frequency (< 300 Hz) sources used by the Navy, geophysical survey industry, and oceanographic research community to probe the ocean, but some of its recommendations apply to other noise sources as well. Its chief recommendations were:

- Determine normal behavior of marine mammals in the wild and their behavioral responses to anthropogenic acoustic signals.
- Determine how marine mammals use natural sounds for communication and for maintaining their normal behavioral repertoire.
- Determine how animals adapt to the presence of anthropogenic sounds, either by altering their natural behavior or by habituating.
- Determine how different sound types and levels affect migration and other movement patterns of marine mammals.
- Determine the responses of deep-diving marine mammals to low-frequency sounds whose characteristics duplicate or approximate anthropogenic sources (source level, frequency, bandwidth, duty cycle, intermittency, variability, onset rate, *etc.*)
- Determine the structure and capabilities of the auditory system in a variety of species of marine mammals.

- Determine the hearing capabilities of larger marine mammals. In particular, develop procedures for rapid determination of hearing capabilities of beached or ensnared marine mammals.
- Determine inter- and intra-specific variability in hearing capabilities, particularly as a result of factors such as age, disease, parasitism and population genetics.
- Determine sound pressure levels that produce temporary and permanent hearing loss in marine mammals.
- Determine the anatomy of the auditory system in various marine mammals.
- Develop technology to protect animals from intense anthropogenic sounds.
- Develop acoustic-monitoring devices and other recorders that can be placed on animals to study animal movement and behavior on a large scale in relation to natural and anthropogenic sounds.
- Determine whether natural avoidance mechanisms can be used to keep animals away from intense sound sources.

In addition to the Ocean Studies Board Report, NASA commissioned a review of sonic boom noise effects on marine mammals that included recommended research (ref. 6) specifically for the HSCT program. These were:

- Ascertain the gross non-auditory and auditory physiological effects of sonic booms on marine mammals in the laboratory using a sonic boom simulation system.
- Investigate accommodation and habituation to sonic booms in a laboratory setting, preferably using recently-captured animals.

NMFS/OPR has also expressed an interest in research on habituation processes.

All the research recommended would be valuable in preparing the EIS for a large scale, noise-producing activity like the HSCT, but the HSRP could not possibly accomplish all these tasks for all the species that are likely to hear the HSCT. Some priorities will be decided by NMFS regulators and public debate when the project enters its final stages, but many potential concerns can be eliminated by some well-planned research in advance. In order to understand the specific recommendations included here, a brief review of the literature on sonic boom impacts is needed.

POTENTIAL EFFECTS OF SONIC BOOMS ON MARINE ANIMALS

Risk of Traumatic Injury

Animals exposed to surprising events, such as gunshots, low-altitude aircraft overflights, and sonic booms, can panic, resulting in acute traumatic injuries in collisions, falls and other accidents. Traumatic losses have been observed after exposure to transients in confined domestic mammals and birds. Panics capable of producing traumatic injuries disappeared within < 5 exposures in poultry (ref.

7), cattle, and horses (ref. 8). Wild caribou in areas receiving repeated exposures to aircraft overflights do not engage in dangerous running, but run readily in remote areas where there is little opportunity to habituate to disturbance (see review in ref. 9). Richardson *et al.* (ref. 3) reviewed the literature on marine mammals and found no evidence of traumatic injuries from sonic boom-induced panics. Unfortunately, all the experiments and observations of responses and have been conducted on pinnipeds and in areas where booms are common (ref. 10-11, Stewart pers. comm). Therefore, the probability of accidents cannot be predicted for remote areas and other species.

Experimental studies of domestic animals have revealed the danger of making conclusions from an absence of evidence - repeated experimental effort has failed to produce lethal panics in poultry and large stock under experimental conditions, but clinical accounts of lethal panics caused by sonic booms indicate that a combination of factors - dangerous housing, inclement weather, and naïve individuals - can cause losses that would never occur in an experimental setting (ref. 9). In addition, individuals receiving minor injuries in panics can die later, *e.g.*, from an infected wound, an effect that would not be detected without longitudinal monitoring of exposed individuals.

The available behavioral observations suggest that the incidence of losses in panics will normally be low because animals control themselves, even in panic, in order to avoid injury. Risk of trauma varies based on species-typical defensive responses (*e.g.*, flight), group size, and the capacity for behavioral adaptation.

All species are expected to exhibit some habituation. Even the skittish harbor seal is capable of adapting to anthropogenic disturbances as long as it is not approached closely (ref. 12). Therefore, risks will be greatest during the first flights of the HSCT over remote areas. HSCT planners will try to eliminate risk by avoiding areas with large concentrations of marine mammals, but some routes will inevitably overfly sparsely distributed populations of polar bears, ice seals, fur seals, walruses, threatened Steller sea lions and other high-latitude species. Areas with large populations of marine mammals and birds include the Gulf of Alaska, Aleutian Islands, Bering Sea, Chukchi Sea, Alaskan and Canadian Beaufort, the so-called Northwest Passage, Baffin Bay, Labrador Sea, Greenland Sea, Norwegian Sea, coastal waters of northern Europe and Siberia, and the Arctic Ocean. In these areas, the risk of injuries in panics is the most significant risk posed by the HSCT.

Other Potentially Harmful Behavioral Responses

Among terrestrial mammals and birds, dangerous or energetically-expensive behaviors such as panic flight occur only at high stimulus levels and in naïve animals. Less energetic behaviors, such as alerting or brief flights can occur persistently at relatively low stimulus levels. Some species of birds do not appear to lose the flight response completely, at least at sound levels in excess of about 90 dB (*e.g.*, gulls, terns, and migratory waterfowl). California sea lions and harbor seals in areas where sonic booms occur regularly respond to boom overpressures in excess of 1 psf by walking, running, diving into the water, or swimming away, but their movements are controlled, often leading to normal activities such as foraging trips.

Quantified data on the thresholds of various behavioral responses to subsonic aircraft overflights and sonic booms are available for birds and, to a lesser extent, for terrestrial animals (the best example is given in Figure 1; ref. 13). Unfortunately, studies of marine mammals have generally quantified only one behavior as an indicator of response, usually any detectable change in direction of movement or activity. These changes are usually selected specifically because they are sensitive indicators, not because they pose a risk to the exposed individuals. Such behaviors must be correlated with a potential impact before they can be treated as evidence of risk.

Behaviors that can result directly in proven negative effects are more useful measures. For example, moderate movements are important if young are exposed to predators or inclement weather after a parent leaves them. Egg predators like gulls and crows attack nests when parents fly up (ref. 14-15) and carnivores may attack moving calves (ref. 16). In addition, mammals separated from their young during the first few hours after birth, when the mother-offspring bond is weak, may not reunite - there is at least one account of large losses occurring after a low flying aircraft disturbed a harbor seal

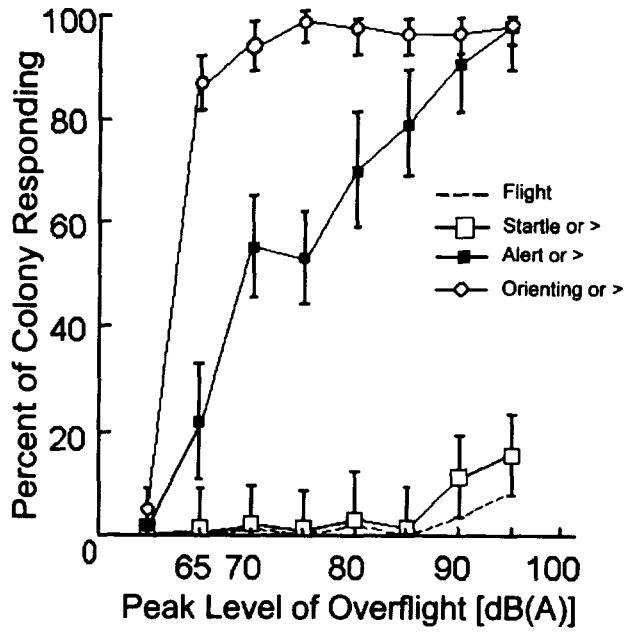

Figure 1: Proportion of crested terns responding to approach by light aircraft. Peak A-weighted sound pressure level was used as the measure of exposure, but terns were also exposed to sight of the aircraft. The terns were somewhat habituated to aircraft (data from ref. 13).

colony (ref. 17).

Subtle effects on behavior resulting from non-auditory physiological responses are seen in domestic birds and laboratory mammals. These responses include irritability, increases in agonistic (conflict) interactions, and changes in parent-offspring interactions. Such changes in behavior may or may not have serious consequences, depending on the species and conditions. Long-term observations of individuals will be needed to demonstrate significant effects resulting from such changes.

Habituation

Laboratory studies and field observations indicate persistent movements after exposure to subsonic aircraft noise in excess of about 90-100 dB, A-weighted SPL in air (colonial gulls, ref. 14), impulses in excess of 100 dB (peak SPL; laboratory rats; ref. 18), sonic booms of unspecified level (the sooty tern; ref. 19), and sonic booms in excess of 1 psf (pinnipeds; ref. 10-11). Figure 2 suggests the reason for these observations - neurophysiological and behavioral studies of laboratory animals and humans (ref. 20) have shown that reflexive responses (cardiac responses, muscular flinch, galvanic skin response) habituate rapidly at low sound levels, but that at higher levels, sensitization is possible (at least during the first few exposures) and habituation is slow and incomplete. Reflexive responses are not universal in mammals - for example, the chinchilla has no detectable muscular flinch response to transients at levels as high as 130 dB (peak SPL; Ison, pers. comm).

In some species, previous exposure to a stimulus at low amplitude reduces the probability of large muscular movements, including dangerous panics, after exposure at higher levels. These observations suggest that it may be possible to mitigate the consequences of panics by habituating animals to lower-amplitude exposures in advance.

Risk of Hearing Loss

There is some agreement that the inner ear and the ossicular chain in the middle ear of humans (and laboratory animals that are used as models for humans) begin to exhibit non-linear responses to impulses at peak sound levels (A-weighted) above 130-140 dB. These responses can lead to catastrophic hearing losses in small proportions of the population and constitute a threshold for PTS in larger proportions. However, it is not at all clear that terrestrial animals are good models for marine mammals, which are specialized for underwater sound perception (ref. 21), and adapted to withstand the large changes in static pressure associated with diving. Hearing loss can occur, as it has been detected in small odontocetes in captivity (ref. 22), and free-ranging mysticetes (ref. 23) and pinnipeds (ref. 24), but none of the available cases resulted from noise exposure *per se* (detonations were the most probable cause of hearing losses detected in pinnipeds and mysticetes). Therefore, the potential for noise-induced hearing loss in marine mammals is unknown.

In addition, almost nothing is known about hearing loss or the natural variation of auditory capacities in any wild mammal. Wild animals experience parasite load, disease, malnutrition, injuries, and the stresses of maintaining territory, raising young, fighting for mates, and avoiding predators. All these can produce physical conditions that could potentiate or aggravate hearing loss. Because the

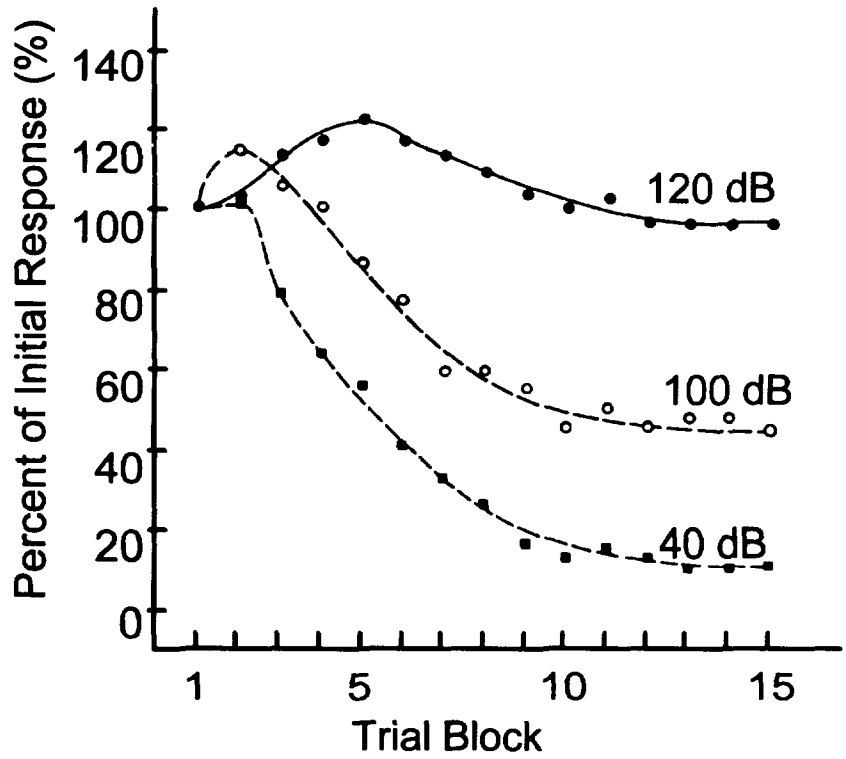

Figure 2. Relationship between sound pressure level of a stimulus and galvanic skin response as a function of the initial response (data from studies of human subjects; ref. 20).

potential for hearing losses is completely unknown, some research will undoubtedly be necessary to satisfy NEPA requirements. In addition, models now available for predicting hearing loss due to transient exposures in terrestrial mammals will have to be tested to determine their applicability to marine mammals. Since such models are still the subject of debate, even for well-studied species like humans and laboratory animals, this process is likely to take time. Peak overpressure and onset time are the features most likely to affect the potential for damage after sonic boom exposures.

Risk of Non-auditory Physiological Effects

The possibility of sonic boom-induced effects non-auditory physiology have not been investigated often in wild animals. The non-auditory physiological effects for which there is some evidence include hypertension, cardiac arrest (among individuals at risk), stress-induced myopathy, immune suppression, slowed growth, energetic expenditure resulting from increased activity, interruption of hormonal cycles, and psychological depression. Years of persistent effort have failed to find incontrovertible evidence of such physiological effects in humans and laboratory animals exposed to intermittent transients, although the evidence for some of these effects after protracted exposure to continuous noise is strong (ref. 25).

In the absence of good models for non-auditory physiological effects resulting from exposures to transients, it is difficult to know how to approach the study of non-auditory physiological effects in marine mammals. Increases in activity are often observed in wild terrestrial mammals, resulting when animals are aroused (wakened, stimulated to rise, stimulated to walk) by subsonic overflights or sonic booms. The significance of increased activity depends on the overall energy budget for the animal, its capacity for behavioral adaptation, and the rate at which it is exposed. In those studies that measured the energetic costs of exposure to occasional intense transients, effects have not been significant (*e.g.*, ref. 26), although small increases in distance traveled could be detected (ref. 27).

Energetic costs to marine mammals have not been examined. "Regular" exposure to sonic booms in previous studies has meant once or twice a week, rather than many times a day. At this exposure rate, increases in energy expenditure will not be measurable.

Energetic effects on migratory waterfowl exposed to subsonic, low-altitude aircraft overflights have been predicted by extrapolation from short-term observations (ref. 28-29), but without measuring habituation - if birds altered their behavior to maintain their energetic reserves after repeated exposure, the predictions would be invalidated.

The potential for changes in circulating levels of reproductive steroids or other blood factors has not received adequate attention - the literature is sparse, weak, and almost totally devoted to laboratory mammals. Chronic experimental exposure to transients (tens or hundreds of exposures per day) can cause adrenal hypertrophy in small mammals (ref. 30-31), but not detectable changes in functional measures, such as growth or reproduction (ref. 32-33). Domestic stock exposed to low-altitude overflights, which are more disturbing than sonic booms, have not experienced significant long-term changes in heart rate or circulating levels of reproductive hormones, although increases in levels of adrenal products (catecholamines, glucocorticoids) lasting several hours were documented (see ref. 9).

The dose-response function that characterizes the range from "infrequent" to "too frequent" is likely to be complex - intermediate levels of exposure can enhance reproduction or growth in domestic animals, whereas high levels can suppress both. Because effects are difficult to detect with infrequent exposures, a study of sonic-boom effects on health, reproduction, and growth would have to be conducted in areas with heavy exposure (*e.g.*, under the flight path of a major airport) or using sonic boom simulators. In addition, only longitudinal studies (long-term monitoring of individuals) with large samples of subjects will have sufficient sensitivity to detect effects.

Acute panic reactions are supposed to interrupt reproduction. Clinical accounts indicate that abortions can occur after exposure to aircraft when the mother is injured, but established pregnancies of healthy animals are not interrupted. However, panic may be able to interrupt the earliest stages of reproduction - gametogenesis, fertilization, and early development (before the placenta becomes functional) - because rapid increases in catecholamine and corticosteroid levels can alter the release of blood factors controlling early reproduction. Convincing evidence for such effects from exposure to transient noise is lacking, however, and, in its absence, applied studies in support of the HSCT program would not be justified. However, some effort to determine how such measurements could be made would be worthwhile.

The Sooty Tern Incident

In 1969, a colony of 50,000 pairs of sooty terns (*Sterna fuscata*) on the Dry Tortugas suffered a catastrophic reproductive failure, in which 99% of the eggs laid failed to hatch (ref. 34). The loss was linked by a process of elimination to high-amplitude sonic booms, but there were no direct observations of the event(s) that caused the failure. Eggs were laid normally at the start of the season, but were found 3 months later containing partially developed, dead embryos in eggshells that were cracked but not crushed. The original verbal presentation about the incident suggested that sonic booms cracked eggs, causing death. The physical forces needed to crack an egg argue against this hypothesis, as do experimental studies with real and simulated sonic booms (ref. 9, 35-36), but an extended manuscript by the field team (ref. 19) suggested a more plausible mechanism, that sonic booms scared birds off the nest repeatedly, resulting in loss of eggs to exposure.

The authors eliminated all the natural factors they could think of as possible causes (*e.g.*, contamination by DDT, failure of the colony's food supply). This left only a series of sonic booms in March of 1969 as an explanation. The authors cited cracking plaster on buildings at neighboring historic Fort Jefferson National Monument and the accounts of rangers at the station as evidence for the unusual intensity of the sonic booms. Unfortunately, these observations provide little information about the components of the sonic booms heard by birds.

Although the cause of the catastrophe in the spring of 1969 will never be known, the evidence linking sonic booms to the catastrophic failure is circumstantial and unconvincing in the face of observations and experimental evidence to the contrary. Noddy terns (*Anous stolidus*) breeding on the Dry Tortugas at the time of the 1969 incident suffered no losses. Eyewitness accounts before and after the incident indicated that the sooty terns were exposed to sonic booms regularly, responding with brief flights off their nests, but not for long enough to cause losses. Experimental exposures of experienced brown pelicans (*Pelecanus occidentalis*) to repeated impulses with peak sound pressure levels exceeding 148 dB (flat weighted SPL) failed to elicit repeated flight (ref. 37). In cases where losses due to repeated subsonic aircraft noise have been observed, losses were small, mostly due to predator attacks on the nest (ref. 14). Flight times for birds disturbed from the nest by assorted human-made sources are uniformly short (median flight time < 2 minutes, ref. 9), suggesting that birds are reluctant to leave their nests, even when surprised.

Naïve, remote colonies of marine birds may be more subject to losses. Bunnell *et al.* (ref. 38) reported failure of 80% of newly-laid eggs in a remote colony of white pelicans (*Pelecanus occidentalis*) within a few days of being overflown at low altitude by a light aircraft. There was no eyewitness account of the disturbance in this case either, but the pelican colony was inspected within days of the event and the eggs were crushed, as if parents had stepped on them after being startled into flight. In this case, the relationship between the overflights and the losses was much more plausible; however, the birds were unaccustomed to aircraft noise and were also exposed to the added visual stimulus of the low-flying aircraft. Small losses due to egg breakage or accidental ejection of eggs from nests have been observed in accounts of aircraft approaches elsewhere (*e.g.*, ref. 39).

The available evidence is sufficient to suggest that large losses are possible if naïve colonies are exposed to close approach by aircraft, but not sufficient to show that sonic booms alone can have this effect. Nonetheless, the Sooty Tern Incident will certainly be a subject of debate when public hearings about the HSCT are held - the account published in 1972 (ref. 34) was raised frequently during the

public debate over the SST in the 1970's, and most reviewers since have quoted the Sooty Tern Incident as evidence that sonic booms can cause catastrophic reproductive losses, but without critical comment (*e.g.*, ref. 40). The original authors of the incident report, who are well-recognized ornithologists, are still of the opinion that the incident could have been caused by sonic booms. Experimental studies in remote areas would go a long way to diffuse this potential controversy.

Potential Effects on Fish and Marine Turtles

Although many marine fish do not hear well, they often hear better at low frequencies (<100 Hz) than marine birds and mammals (ref. 41). They respond to very low frequency impulses with species-specific predator avoidance behaviors, but the levels required to produce avoidance are high. Some species have habituated slowly to high-amplitude impulses, but large differences between species may be expected.

Fishermen in areas exposed to other noise-producing human activities (*e.g.*, seismic surveys) have expressed concern over reduced catchability. However, the poor penetration of sonic booms into deep water is likely to eliminate any significant effect on most fisheries. Commercial fish farms, which hold fish close to the surface, are more vulnerable. By the time the HSCT flies, these farms will produce a large proportion of the fish consumed world-wide. Therefore, effects on farm-reared fish should be the focus of any effort to measure impact. The only available experimental evidence suggests that farm-raised fish will not experience any detectable impact.

Aquatic turtles have best sensitivities of approximately 50 dB (peak SPL in air; ref. 42); their best sensitivity in water is approximatly 20 dB better. Absolute thresholds of marine turtles have not been measured either in air or in water, but results of electrophysiological measurements do not suggest great sensitivity. Unfortunately, testudinate hearing is highly sensitive to temperature and the available experiments were not designed to determine best auditory sensitivity in the optimal temperature range. Therefore, very little can be inferred about marine turtle best sensitivities in water *a priori*. Marine turtles also spend variable amounts of time at the surface, depending on species and season. Therefore, although the risk to marine turtles is considered small, there is little adequate evidence to support this conclusion. Marine turtles respond at ranges of several kilometers to significant sounds, such as the noise from a pursuing boat.

RECOMMENDED STUDIES

The following list of studies is recommended to address concerns about the HSCT and to prepare for the environmental impact assessment process. They fall into major categories, (1) studies needed to detect or mitigate potential effects on marine mammals, (2) technology development needed to support these studies, (3) studies needed to prepare requests for an Incidental Harassment Authorization, LOA, or permits, and (4) studies needed to respond to NEPA requirements. Studies are assigned priorities (L=low, M=intermediate, H=high).

Studies of Behavioral Responses of Marine Mammals

Habituation of startle responses in cetaceans and pinnipeds (H)

Although it would be ideal (at least from the perspective of developing models for responses) to measure habituation by conducting field experiments, exposing large numbers of animals to a variety of sonic booms, no such experiments will ever be practical. However, laboratory study of the startle reflex and orienting response may provide a useful indication of thresholds of response for use in planning a small number of critical field trials.

Sonic boom sound level, onset rate, and frequency affect the perception of boom loudness in humans (ref. 43), and are likely to affect responses of marine mammals as well. In humans, A-weighting, an idealized version of the 40 dB equal-loudness contour, is used to calculate predictors of annoyance and other psychological responses. Although a rough equivalent of the equal-loudness contour might be measurable in animals (on laboratory rats, ref. 44), accepted versions will not be available for applied studies in the near future. Startle responses (measured by muscle flinches and changes in heart rate) are likely to provide a more useful measure for sonic boom-induced effects in any event - startles are part of the sequence leading to panic flight.

The recommended study should consist of stages, (1) methods development, (2) actual measurements of startle responses with varying stimulus features, and (3) measurements of habituation with repeated exposure. Equal-response contours should be estimated using the resulting data.

The study should target as many as possible of the major groups that are likely to be exposed to the HSCT at the surface. Otariids, phocids, sea otters, walruses and small surface-dwelling cetaceans are commonly held in captivity and would be excellent subjects for such a study. Models developed from this effort can be used to design a small number of field trials with worst-case exposures. Ultimately, such methods could be used to measure responses of the species that are of great concern but difficult to work on, such as mysticetes and large odontocetes.

Mitigating flight responses of pinnipeds (H)

While the results of the above study will provide estimates of the threshold for strong responses, they will not document panic responses directly. Direct, experimental studies of panic responses in remote areas will not be sanctioned by any Institutional Animal Care and Use Committee, nor would NMFS/OPR issue permits to conduct such studies. The only way to obtain information about the potential for panic is to make observations opportunistically during incidents that cannot be avoided, or through a study of mitigation methods. The second is the more practical approach.

Pinnipeds familiar with sonic booms startle and run when exposed to overpressures in excess of ~1 psf, but do not damage themselves or abandon their young. Mitigation of dangerous responses is therefore theoretically possible. The results of the laboratory studies on habituation could be used to design stimuli to "pre-habituate" pinnipeds, after which controlled exposures to aircraft carpet booms could be conducted to prove the effectiveness of the mitigation technique.

First, measurements made during laboratory experiments should be used to design stimuli adequate to habituate panic responses. Second, a rookery or hauling site in an area where pinnipeds are unlikely to experience dangerous panics should be exposed to the mitigating stimulus, followed by worst-case sonic booms (*e.g.*, an experienced rookery on a wide beach outside the pupping season).

Finally, a similar experiment should be conducted in a remote area. Species, season, colony size, and habitat type will have to be selected carefully to minimize the risks if animals panic, while still conducting a realistic trial.

Any tests of this sort are likely to engender controversy in and of themselves, and should not be attempted until every strategy for avoiding rookeries has been adopted. Even if mitigation trials are successful, it is unclear how low-amplitude sonic booms might be delivered as "pre-habituating" stimuli over all the planned flight routes. However, if polar routes cannot be avoided, mitigating experiments may be the only alternative.

Even if the field tests of mitigation measures are never completed, crucial naïve colonies under the flight path of the HSCT should be monitored several seasons before and after the first overflights. Observers and sonic boom monitoring equipment should be placed on such rookeries, and a sample of individuals should be tracked using satellite packages equipped with dive monitors. This effort will be needed (1) to determine whether panics occur and (2) to insure that unexpected incidents can be explained by eyewitness accounts.

***Detecting flight and diving responses of small cetaceans* (L)**

Small cetaceans could scatter and dive when exposed to sonic booms at the surface. They hear poorly at low frequencies, but will be able to hear 1-4 psf booms when at the surface. In confined areas, small cetaceans are capable of injuring themselves by running into barriers after a startle. Their natural defensive response to attack includes porpoising (leaping out of the water) and darting with abrupt changes in direction, behaviors that can easily bring them into contact with obstructions. In open water, the opportunity for such injuries is small. However, there are areas where startled flight may bring them into contact with dangers, either human-made or natural, such as nets, canyon walls, or predators. Gillnets, which are not always detected even when animals are undisturbed, present a particular risk in some areas.

If devices can be developed capable of monitoring movements and diving patterns for several months, they should be deployed on small cetaceans before and during the first overflights of the HSCT in any area where potential concerns are identified. Ideally, they should be equipped to quantify sonic boom exposures. At present, the possibility of effects on small cetaceans is a matter of speculation, but a monitoring study would forestall any controversy.

***Avoidance and changes in diving behavior of large mysticetes* (M)**

Large mysticetes are the most likely to hear the HSCT because they typically feed at shallow depths, because they travel widely in the open ocean, and because they hear well at low frequencies based on anatomical studies and examination of their social signals. Previous studies have documented brief, local deviations from migratory pathways when mysticetes are exposed to seismic survey impulses, but responses to sonic booms have not been documented (ref. 3). Brief deviations from their path of travel are unlikely to have lasting consequences, and it is difficult to envision how occasional brief exposures will affect these animals (in the absence of auditory injury; see below). If the effects on large whales are to be determined, observations lasting days or weeks must be obtained in areas where the probability of exposure to sonic booms is high. If these criteria could be met, measurements of vocal behavior and long-term diving patterns would be very valuable.

Ideally, whales should be equipped with devices that record sonic boom exposures, whale vocalizations, and short samples of ambient noise. The cost of deploying these instruments will be high, not only because the instruments are still in the developmental stages, but because support to deploy them is expensive and the reliability of the instruments is still low. An effort to improve remote monitoring devices should precede any effort to measure whale responses. In addition, the devices should be made available commercially so that biologists world-wide can deploy them under a variety of programs - the HSRP cannot support research in all the areas that will be exposed.

Long-range acoustic tracking of mysticetes in an area with high incidence of sonic booms could be conducted using arrays such as the US Navy's SOSUS network. Most of the energy in sonic booms attenuates within the top 100 m, most existing DoD assets are deployed on the ocean floor, and whales will only be detectable by these arrays when they are vocalizing, so detection of responses to sonic booms may be difficult. Nevertheless, other tracking arrays are likely to be available by the time the HSCT begins to fly, and large-scale, long-range acoustic surveys are a powerful tool when combined with tracks from a small number of instrumented individuals. These studies should be conducted at the time the HSCT begins to fly.

Effects of chronic exposure on breeding pinnipeds **(M)**

Pinniped rookeries occur in areas exposed frequently to sonic booms in excess of 1 psf, for example areas under the flight path of the Concorde or areas overflown by large launch vehicles (Space Shuttle, Titan IV, *etc.*) A long-term study in one of these areas would show whether pinniped cows and pups exposed to sonic booms experience lower success than those that are not exposed. However, the study would lack a point of comparison unless (1) the exposure conditions changed (addition of a flight route, closing of a flight route), or (2) planned overflights were conducted. The initial flights of the HSCT are ideal candidates for such a study, of course, if pinniped rookeries are overflown unavoidably.

In order to detect effects, longitudinal observations on individuals must be conducted. A large sample of cows should be equipped with satellite tracking devices with, at minimum, a diving monitor and a radio-transmitter to assist in localizing the animal on the rookery. Such devices commonly measure physiological parameters (*e.g.*, heart-rate and temperature). Movements and mother-pup interactions while on the rookery should be monitored for long enough to obtain adequate data to detect differences of < 10% before and after the HSCT begins to fly. Population counts in the few years before and after the initial flights would be beneficial as well.

In the absence of experimental manipulations (planned sonic boom exposures), measurements of responses to aircraft such as the Concorde will provide essential information for writing an EIS. These efforts will show what may be expected in colonies exposed daily over long periods to carpet booms from the HSCT. However, studies of colonies that are already exposed will not put to rest suspicions about subtle effects on reproductive success; this question must be addressed by experimental manipulation and longitudinal monitoring of individuals.

Changes in the acoustic behavior of sperm whales **(M)**

Sperm whales often cease vocalizing when exposed to anthropogenic noise (*e.g.*, ref. 45-46). The change in behavior is robust and lasts as long as exposure continues (exposures of hours or days have been observed). Other responses may accompany silences, or the silences may have secondary

consequences (*e.g.*, loss of feeding time). Since sperm whales seem to be particularly responsive to anthropogenic noise, since they are the only odontocetes known to have reasonably good low-frequency hearing (ref. 47), and since they are very likely to be found in open water, they will undoubtedly be a species of concern. However, they are deep divers, spending little time in the top 100 m of water, where exposures are likely to occur. Therefore, experimental exposures of this species would be necessary.

There are already a number of studies planned to document sperm whale responses to playback of continuous noise sources underwater. These studies are dependent on acoustic tracking techniques, which are limited to small areas and periods when whales are vocalizing, because sperm whales have proven difficult to equip with implanted transmitters. Therefore, HSCT proponents should support a technology development program to improve remote tracking devices - studies of sperm whale responses to the HSCT are not recommended until they can be tracked independently of their acoustic behavior.

Effects on Hearing

***Thresholds for temporary auditory threshold shift in pinnipeds and small cetaceans* (H)**

The HSCT is not expected to produce sonic booms intense enough to cause significant hearing damage in pinnipeds and small cetaceans, but the fact that no models are available for predicting effects will make it difficult to defend this prediction, particularly if there is controversy about the program as a whole. Experiments should be conducted to measure the potential for auditory damage, particularly in animals compromised by physical conditions characteristic of wild animals such as age, starvation, physiological stress, parasite infestation, and disease. This question could be addressed relatively easily in pinnipeds, first in the laboratory, and then in the wild. There are facilities already in existence for presenting the appropriate sonic boom exposures. These measurements should be made in air initially, but should be conducted underwater as soon as techniques for underwater exposures are developed.

No one has measured temporary or permanent noise-induced changes in auditory function of small cetaceans; therefore, even laboratory studies on healthy captives would provide crucial information. Any such study is likely to present a number of important technical challenges. Normally, the hearing of small cetaceans is measured using behavioral conditioning because they are intelligent enough to accept conditioning quickly and because they cannot be anaesthetized without great risk. However, in this case small cetaceans are likely to find the most intense test exposures aversive, making them more difficult to condition. In addition, facilities for producing exposures do not exist as yet. It is possible that studies on stranded animals held briefly for rehabilitation could be conducted successfully using impulses emitted by high-intensity transducers such as the J-15 (NRL).

If mild temporary threshold shifts are found at sonic boom overpressures typical of the HSCT, it will still be necessary to determine whether the shifts can be tolerated without long term effect. If the methods tested in the laboratory will allow an animal's hearing to be assessed in the field, preferably with a minimum of chemical restraint, the hearing of a large sample of wild pinnipeds could be measured before and after HSCT overflights. This procedure would have two advantages - species-typical incidence of hearing deficits would be characterized, and, if any animals with deficits are discovered, their long-term success could be monitored by tagging and tracking them. Results of such

a study will be most convincing if the study is conducted in conjunction with initial HSCT flights or other similarly intense sonic boom exposures.

***Comparative anatomy of the inner ear of cetaceans* (H)**

At present, the only data available on mysticete hearing is based on anatomical measurements of bullae taken from stranded specimens. Although it may be possible to apply electrophysiological methods to great whales stranded or trapped in fishing gear (see below), many species may only become available as dead specimens, particularly elusive, deep-diving species such as beaked whales. Ongoing efforts to make anatomical measurements of ears from stranded whales should continue to receive support.

***Auditory thresholds of large cetaceans* (H)**

In order to estimate the range at which mysticetes may be disturbed, it will be necessary to estimate their auditory threshold function. There is a program already underway through the Naval Research and Development Laboratory in San Diego (ref. 48) to estimate the mysticete auditory threshold function using a portable system for measuring electrophysiological responses (ABR). The system is designed to make measurements on stranded or entrapped individuals before release. Improvements to allow remote collection of evoked responses are needed, and the system must be deployed as opportunity permits in the next few years. This or a similar effort should continue under the auspices of the HSCT program.

Supporting Studies

***Calibrate non-behavioral techniques for measuring animal auditory threshold* (M)**

Several techniques are available for measuring hearing thresholds that do not require time-consuming training. These must be calibrated against behavioral measures, the "gold-standard" for estimating auditory threshold, and they must be modified for use in the field on wild animals.

Auditory evoked responses: Clicks and tone-pips are used routinely to collect auditory evoked electrophysiological responses from the brainstem (ABR) using surface-mounted or implanted electrodes. The most accurate evoked response measurements are made with electrodes placed in the auditory brainstem, but this method is considered unethical in the U.S. and would never be used. Measurements with surface-mounted electrodes are used routinely to obtain information about hearing loss in unresponsive humans and to measure auditory threshold functions of species that are difficult to train. Evoked responses are not perfectly concordant with behavioral measures - they vary with age and state of consciousness, regardless of the animals' sensitivity, they underestimate best sensitivity by 5-10 dB even under the best conditions, and they are increasingly unreliable at the extremes of the auditory range. Therefore, calibration of the method against behavioral measures should be conducted using as many species as possible.

Low frequency sensitivity of several species of small cetacean has been measured using the envelope following response (EFR), an evoked response stimulated by the envelope of an amplitude-modulated tone having a high frequency carrier (ref. 49). The technique holds promise, but has not been accepted widely for measuring low frequency thresholds as yet. Only one laboratory is using the technique routinely. The HSRP should continue to support development of the technique.

Both of these methods can be used to estimate auditory thresholds at many frequencies in the course of a few days, as opposed to the months required to collect behavioral thresholds. Even with their limitations, they can be used to detect threshold shifts precisely and quickly in an unresponsive animal. Therefore, they are the weapon of choice for conducting hearing studies in the field. These techniques should be improved by (1) calibrating them against behavioral measures for representative taxa, (2) developing methods for detecting evoked responses with electrodes placed outside the skull even when the signal strength is poor (*e.g.*, in presence of interfering electrical noise, or when the animal has a thick skull), and (3) developing the EFR technique for routine use.

Distortion-product otoacoustic emissions: Otoacoustic emissions, faint acoustic signals returned by the outer hair cells in the cochlea when an animal hears a sound, can be used to estimate animal auditory thresholds as well. Like the ABR, this technique yields results not perfectly concordant with behavioral measures. The technique has been tested recently with some success on pinnipeds (Stewart unpub. data), but has not been tested on small cetaceans. In pinnipeds, the auditory meatus is sometimes long and invested with a mix of wax and dead epithelium. In these species and in small cetaceans, good DPOAE returns have proven difficult to obtain. Further trials are needed to determine the full potential of the technique.

Reflex modification: A tone or air puff presented within a few milliseconds of a startling stimulus alters the startle response as measured by muscular flinch (reflex modification), a change that can be used to determine whether an animal has heard the tone. Reflex modification has been used to measure the auditory threshold functions of a variety of laboratory rodents and has been tested preliminarily on one wild carnivore, the desert kit fox (ref. 50-51). Because the startle response is controlled primarily by structures in the brainstem, the technique is not equivalent to conditioning experiments using positive reinforcement, but it is somewhat more sensitive than ABR, yielding estimates of absolute threshold within a few dB of standard behavioral measures. In addition, it can be used to estimate auditory thresholds at low frequencies and it does not require sedation. The technique is not widely to measure absolute thresholds, but it is frequently used to determine the effects of ototoxic drugs on hearing. The startle reflex is not universal in mammals, so the technique must be assessed species by species, but if pinnipeds exhibit reflex inhibition, the technique should be explored for use in field studies.

***Develop remote tracking devices to monitor movements and received sonic boom levels* (H)**

There is widespread agreement among bioacousticians that the best way to measure noise exposure is to collect received level directly at the animal, preferably with a device comparable to the personal noise monitors designed for humans. Animal noise monitors will provide the only really reliable estimates of exposure to booms, to be correlated with changes in diving behavior. Such devices must have the following properties: (1) small size, (2) design for long-term placement, (3) high density storage media, (4) long battery life, (5) retrievability. Several initiatives to develop such devices for the marine environment are underway, but the devices under development have poor data storage capacity and are not capable of recording adequate data when animals are swimming steadily. Rare events like sonic booms would be easily missed. The development effort should be stimulated further until adequate devices are available that can be used by a number of researchers. Ideally, data would be uploaded immediately to a satellite; existing satellite systems available to biologists have low data bandwidth, but improvements are expected by the time the HSCT begins to fly.

Studies in Support of MMPA Requirements

Measure transmission of sonic booms into water (H)

There is still considerable discussion about the transmission of sonic booms from air into water. At the anticipated flight velocity of the HSCT, direct transmission into water is not expected, but surface sound waves (evanescent energy) will produce significant exposures in the top few meters. For typical carpet booms from high-altitude overflights, peak overpressures of ≤3-4 psf are likely to be observed, (≤163-166 dB re 1 μPa). Recent modeling efforts (ref. 52, H.K. Cheng, pers comm.) have shown that levels and rise times close to the surface will be similar to those immediately above the surface in-air, but attenuation and loss of the high-frequency component is rapid with depth.

Empirical studies of sonic boom transmission into water are likely to be costly, and in some respects lie outside the scope of a marine mammal research effort. However, NASA and the aerospace industry would be well-served to conduct the appropriate studies. The environmental community and NMFS/OPR are unlikely to find theoretical models believable without empirical verification. The key issues are (1) peak sound pressure level and onset time of sonic booms transmitted through the air-water interface into the top 10 m, (2) the rate of attenuation, particularly of the low-frequency component of the signal with depth, and (3) estimates of variability in transmission resulting from varying atmospheric conditions, stratification, ice, and bottom topography.

Distribution and abundance of marine mammals under the flight path of the HSCT (M)

To minimize impacts on marine mammals, HSCT flights will be routed to avoid concentrations of marine mammals as much as possible. This strategy depends on good knowledge of the distribution, size, and movements of concentrations of marine mammals. Unfortunately, the available information is often inadequate, and it is not easily accessed, even by experts. Although surveys are usually required in cases where activities occur in restricted areas, adequate surveys for marine mammals along HSCT flight routes would take many years of effort and millions in funding, an effort that HSRP cannot be asked to undertake. However, the High Speed Research Program (HSRP) could develop an accessible and easily-maintained information retrieval system for the data that are being collected under their own and other initiatives, including efforts conducted overseas. HSRP contractors would be responsible for archiving survey data and for providing adequate quality control. Such a system should allow, at minimum (1) integrated representations of survey data on a GIS platform as soon as reports are published; (2) access to raw data and descriptions of survey design as soon as they are released by individual investigators; (3) an indication effort invested by period and area; (4) a review process that allows quality of data to be represented. If the system is sufficiently accessible and easy to use, contributions will be submitted readily by investigators in many countries.

Studies in Support of NEPA Requirements

Mitigation of effects on bird colonies (H)

The Sooty Tern Incident will be brought forth as evidence for impact when the HSCT EIS is released. There is adequate information available to demonstrate that sonic booms will not crack bird eggs or cause any of the other direct physical effects that were suspected at the time of the Sooty Tern Incident in 1969. However, Dr. Glen Woolfenden (Archbold Biological Station), one of the most

respected ornithologists in the country, still believes that sonic booms could have driven adult sooty terns off the nest for long enough to expose eggs fatally. The empirical data available are not adequate to address this concern because (1) all the experiments have been done in areas already heavily exposed to anthropogenic noise, and (2) because the process of habituation has not been documented adequately.

The HSRP should support an experimental study of mitigation methods similar to the one suggested for pinnipeds. It should be designed to test the hypothesis that colonial birds could be habituated to sonic booms in advance of the HSCT, eliminating the risk of significant losses. Examples of locations where such experiments could be accomplished are Johnston Island, Adak Island, Ascension Island, and colonies along the American and Canadian coast of the Bering, Chukchi, and Beaufort seas.

Responses of schooling fish (L)

In some areas, particularly off the west coast of the U.S. and in Europe, fishermen are very concerned about the potential impact of anthropogenic noise on fish. The HSRP should be prepared to address this concern. If trends in fish farming continue, most fish protein will be obtained from farms by the time the HSCT begins to fly; this means that concerns about stress in captive fish will be the most important consideration. Responses of naïve fish on large fish farms should be measured after exposure to experimental sonic booms and habituation rates documented. A combination of sonar tracking and individual marking using small pingers could be used to document responses.

Audition and responses of marine turtles (L)

It is likely that marine turtles will be able to detect HSCT sonic booms near the surface and on nesting beaches. There is some consensus that marine turtles are unlikely to have negative responses to HSCT impulses, but the EIS would be strengthened if this opinion were supported by empirical data, as all species of marine turtles are either threatened or endangered. The auditory thresholds of marine turtles have been measured in-air using electrophysiological techniques, but absolute thresholds were not obtained, and their sensitivity underwater is still largely unknown. Absolute thresholds should be estimated using evoked responses in air and underwater for several species in appropriate temperature regimes. If they turn out to have greater sensitivity than anticipated, studies of their behavioral responses to experimental impulses should be conducted.

REFERENCES

1. Herman, L. M.: Hawaiian Humpback Whales and ATOC: a Conflict of Interests. *Journal of Environment and Development*, vol. 3, 1994, pp. 63-76.

2. Potter, J. R.: ATOC: Sound Policy or Enviro-Vandalism? Aspects of a Modern Media-Fueled Policy Issue. *Journal of Environment and Development*, vol. 3, 1994, pp. 47-62.

3. Richardson, W. J., Greene, C. R., Jr., Malme, C. I., and Thomson, D. H.: *Marine Mammals and Noise*. Academic Press, Inc., 1995.

4. Smithsonian Institution: *A Primer to Endangered Species Law*. 3rd Ed. Smithsonian Institution, Washington, D.C., 1993.

5. Green, D. M., H. A. DeFerrari, D. McFadden, J. S. Pearse, A. N. Popper, W.J. Richardson, S.H. Ridgway, and P. L. Tyack 1994. Low-Frequency Sound and Marine Mammals: Current Knowledge and Research Needs. Report by Committee on Low-frequency Sound and Marine Mammals, Ocean Studies Board, Commission on Geosciences, Environment, and Resources, National Research Council. National Research Council, Washington, D.C.

6. Cummings, W.C. 1993. Sonic Booms and Marine Mammals: Informational Status and Recommendations. Report by Oceanographic Consultants, San Diego, CA to National Aeronautics and Space Administration, Langley Research Center, Hampton, VA. NASA Contract L 26228D. Aug., 1993.

7. Bradley, F., Book, C., and Bowles, A. E.: Effects of Low-altitude Aircraft Overflights on Domestic Turkey Poults. Final Report for Period December 1989 - June 1990. Report by BBN Laboratories, Inc. for Noise and Sonic Boom Impact Technology Program, Brooks Air Force Base. Technical Report No. HSD-TR-90-034, 1990.

8. Stephan, E.: Behavioral Patterns of Domestic Animals as Induced by Different Qualities and Quantities of Aircraft Noise. *Actes INRETS*, vol 34, no. 3, 1993, pp. 487-495.

9. Bowles, A.E.: Responses of Wildlife to Noise. Chapter 8, in Knight, R.L., and Gutzwiller, K.J., eds. *Wildlife and Recreationists: Coexistence through Management and Research,* Island Press, Washington, D.C., 1994, pp. 154-213.

10. Bowles, A. E., and Stewart, B. S.: Disturbances to the Pinnipeds and Birds of San Miguel Island, 1979-1980. In Jehl, J. R., Jr. and Cooper, C. F., *eds.* Potential Effects of Space Shuttle Sonic Booms on the Biota and Geology of the California Channel Islands: Research Reports. San Diego State University Foundation Technical Report Number 80-1, 1980, pp. 99-137.

11. Stewart, B. S.: Studies on the Pinnipeds of the Southern California Channel Islands, 1980-1981. Report by Hubbs-Sea World Research Institute for U.S. Air Force, Space & Missile Systems; HSWRI. Technical Report No. 82-137, 1982.

12. Brasseur, S. M.: Tolerance of Harbor Seals to Human Related Disturbance Sources During Haulout. Presented at the Tenth Biennial Conference on the Biology of Marine Mammals, November 11-15, Galveston, TX. Society for Marine Mammalogy, November, 1993.

13. Brown, A. L.: Measuring the Effect of Aircraft Noise on Sea Birds. *Environment International*, vol. 16, 1990, pp. 587-592.

14. Burger, J.: Behavioral Responses of Herring Gulls *Larus argentatus* to Aircraft Noise. *Environmental Pollution,* vol. 24, 1981, 177-184.

15. Emlen, J. T., Miller, D. E.. Evans R. M and Thompson, D.H.: Predator-Induced Parental Neglect in a Ring-Billed Gull Colony. *Auk*, vol. 83, 1966, pp. 677-679.

16. Harrington, F. H., and Veitch, A. M.: Calving Success of Woodland Caribou Exposed to Low-level Jet Fighter Overflights. *Arctic*, vol. 45, no. 3, 1992, pp. 213-218.

17. Johnson, B.: The Effects of Human Disturbance on a Population of Harbor Seals. *Environmental Assessment of the Alaskan Continental Shelf Annual Reports of Principal Investigators for the Year Ending March 1977. Vol. 1. Receptors - Mammals*, 1977, NOAA, Boulder, NTIS PB-280934/1, pp. 422-431.

18. Hoffman, H. S., and Searle, J. L.: Acoustic and Temporal Factors in the Evocation of Startle. *Journal of the Acoustical Society of America,* vol. 43, no. 2, 1968, pp. 269-282.

19. Austin, O. L., Jr., Robertson, W. B., Jr., and Woolfenden, G. E.: Mass Hatching Failure in Dry Tortugas Sooty Terns *(Sterna fuscata)*. Manuscript on file with the Van Tyne Library of Ornithology, University of Maryland, 1972a, unpub. ms.

20. Thompson, R. F., Groves, P. M., Teyler, T. J., and Roemer, R. A.: A Dual-Process Theory of Habituation: Theory and Behavior. Chapter 7 in Peeke, H. V. S. and Herz, M. J., eds. *Habituation, Volume I: Behavioral Studies,* Academic Press, Inc., New York, 1973, pp. 239-271.

21. Ketten, D. R.: The Marine Mammal Ear: Specialization for Aquatic Audition and Echolocation. in D. B. Webster, R. R. Fay, and A. N. Popper (eds) The Evolutionary Biology of Hearing. Springer-Verlag, 1992, pp. 717-750.

22. Ridgway, S. H., and. Carder, D. A:. High-frequency Hearing Loss in Old (25+ year old) Male Dolphins. *Journal of the Acoustical Society of America,* vol. 94. no. 3, pt. 2, 1993, p. 1830.

23. Ketten, D. R.: Blast Injury in Humpback Whale Ears. Journal of the Acoustical Society of America vol. 94, 1993, pp. 1849.

24. Bohne, B. A., Thomas, J. A., Yohe, E. R., and Stone, S. H.: Examination of Potential Hearing Damage in Weddell Seals (*Leptonychotes weddelli*) in McMurdo Sound, Antarctica. *Antarctic Journal of the United States*, vol. 19, no. 5, 1985, pp. 174-176.

25. Kryter, K. D.: *The Handbook of Hearing and the Effects of Noise*. Academic Press, 1994.

26. White, R. G., Murphy, S. M., Kugler, B. A., Kitchens, J. A., Luick, B. R., Smith, M. D., and Barber, D. S.: Energy Expenditure Responses of Caribou to Low-Altitude Jet Aircraft. Report by Institute for Arctic Biology for U.S. Air Force Noise and Sonic Boom Impact Technology Program, Wright-Patterson Air Force Base, Ohio. 1994.

27. Murphy, S. M., Smith, D. M., White, R. G., Kitchens, J. A., Kugler, B. A., and Barber, D. S.: Behavioral Responses of Caribou to Low-Altitude Jet Aircraft. Report Prepared by Alaska Biological Research, Inc., Institute of Arctic Biology, and BBN Systems and Technologies for Armstrong Laboratory, Wright-Patterson Air Force Base. Armstrong Laboratory Report AL/OE-TR-1994-0117, December, 1993.

28. Bélanger, L. and Bédard, J.: Responses of Staging Snow Geese to Human Disturbance. *Journal of Wildlife Management*, vol. 53, 1989, pp. 713-719.

29. Bélanger, L. and Bédard, J.: Energetic Cost of Man-induced Disturbance to Staging Snow Geese. *Journal of Wildlife Management,* vol. 54, 1990, pp. 36-41.

30. Chesser, R. K., Caldwell, R. S., and Harvey, M. J.: Effects of Noise on Feral Populations of *Mus musculus*. *Physiological Zoology*, vol. 48, 1975, pp. 323-325.

31. Anthony, A. and Ackerman, E.: Effects of Noise on the Blood Eosinophil Levels and Adrenals of Mice. *Journal of the Acoustical Society of America*, vol. 27, pp. 1144-1149.

32. Borg, E.: Physiological and Pathogenic Effects of Sound. *Acta Oto-Laryngologica*, vol. 381, Suppl., 7-68.

33. Gamble, M. R.: Sound and its Significance for Laboratory Animals. *Biological Review*, vol. 57, 1982, pp. 395-421.

34. Austin, O. L. Jr., Robertson, W. B, Jr., and Woolfenden, G. E.: Mass Hatching Failure in Dry Tortugas Sooty Terns (*Sterna fuscata*). In Vous, K. H., ed. *Proceedings of the XVth International Ornithological Congress, The Hague, Netherlands, 30 August - 5 September*, E.J. Brill, Leiden, 1972b, p. 627.

35. Bowles, A. E., Awbrey, F. T., and Jehl, J. R., Jr.: The Efects of High-amplitude Impulsive Noise on Hatching Success: a Reanalysis of the "Sooty Tern Incident". Report by Hubbs-Sea World Research Institute for the U.S. Air Force Noise and Sonic Boom Impact Technology Program, Wright-Patterson Air Force Base. Technical Report Number HSD-TP-91-0006, 1991

36. Bowles, A. E., Knobler, M. K., Sneddon, M. D., and Kugler, B. A.: Effects of Simulated Sonic Booms on the Hatchability of White Leghorn Chicken Eggs. Report by BBN Systems and Technologies and Hubbs-Sea World Research Institute for Systems Research Laboratories, Dayton, OH, under contract to U.S. Air Force, Noise and Sonic Boom Impact Technology Program, Wright-Patterson Air Force Base, Ohio, 29 August, 1994a.

37. Schreiber, E. A., and Schreiber, R. W.: Effects of Impulse Noise on Seabirds of the Channel Islands. *in* J. R. Jehl, Jr,. and C. F. Cooper, *eds*. Potential Effects of Space Shuttle Sonic Booms on the Biota and Geology of the California Channel Islands: Research Reports. San Diego State University Foundation Technical Report No. 80-1, 1980, pp. 138-162.

38. Bunnell, F. L., Dunbar, D., Koza, L., and Ryder, G.: Effects of Disturbance on the Productivity and Numbers of White Pelicans in British Columbia - Observations and Models. *Colonial Waterbirds,* vol. 4, 1981, pp. 2-11.

39. Hunt, G. L. Jr.: Offshore oil development and seabirds: The Present Status of Knowledge and Long-Term Research Needs. I*n* Boesch, D. F. and Rabalais, N. N. *(eds.) Long-term Environmental Effects of Offshore Oil and Gas Development,* 1985, pp. 539-586, Elsevier Applied Science, New York.

40. Haynes, A. M.: Human Exploitation of Seabirds in Jamaica. *Biological Conservation*, vol. 41, 1987, pp. 99-124.

41. Enger, P. S., Karlsen, H. E., Knudsen, F. R., and Sand. O.: Detection and Reaction of Fish to Infrasound. *ICES Marine Sciences Symposia,* vol. 196, 1993, pp. 108-112.

42. Patterson, W.C.: Hearing in the turtle. *Journal of Auditory Research*, vol. 6, 1966, pp. 453-464.

43. Shepherd, K. P. and Sullivan, B. M.: A Loudness Calculation Procedure Applied to Shaped Sonic Booms. NASA Technical Paper 3134, 1991, 10 p.

44. Johnen, M., and Schnitzler, H.-U.: Effects of Change in Tone Frequency on the Habituated Orienting Response of the Sleeping Rat. *Psychobiology*, vol. 26, 1989, pp. 343-351.

45. Watkins, W. A., and Schevill, W. E.: Sperm Whales (*Physeter catodon*) React to Pingers. *Deep-Sea Research*, vol. 22, 1975, 123-129

46. Bowles, A. E., M. Smultea, B. Würsig, D. P. DeMaster, and D. Palka. Relative Abundance and Behavior of Marine Mammals Exposed to Transmissions from the Heard Island Feasibility Test. *Journal of the Acoustical Society of America*, vol. 96, no. 4, 1994b, pp. 2469-2484.

47. Carder, D. A., and Ridgway, S. H.: Auditory Brainstem Responses in a Neonatal Sperm Whale, *Physeter* spp. *Journal of the Acoustical Society of America*, vol. 88, Suppl. 1, 1990, pp. S4.

48. Ridgway, S. H., and. Carder, D. A.: Audiograms for Large Cetaceans: a Proposed Field Method for Field Studies. *Journal of the Acoustical Society of America*, vol. 74, 1983, p. S53.

49. Dolphin, W. F.: Steady-state Auditory Evoked Potentials in Three Cetacean Species Elicited Using Amplitude-Modulated Stimuli. In Kastelein, R. A., Thomas, J. A., and Nachtigall, P. E. (eds), *Sensory Systems of Aquatic Mammals*, 1995, De Spil: Woerden, pp. 25-49.

50. Young, J. S., and Fechter, L. D.: Reflex Inhibition Procedures for Animal Audiometry: A Technique for Assessing Ototoxicity. Journal of the Acoustical Society of America, vol. 73, 1989, pp. 1686-1693.

51. Bowles, A. E., Francine, J. Wisely, S. , and McClenaghan, L..: The Effects of Low-Altitude Aircraft Overflights on Predator- Prey Relations Between the Desert Kit Fox (*Vulpes macrotis arsipus*) and its Small Mammal Prey on the Barry M. Goldwater Gunnery Range. Final Report by BBN Systems and Technologies for U.S. Air Force, Noise and Sonic Boom Impact Technology Program, Wright-Patterson Air Force Base. Contract F33615-90-D-0653, Delivery Order 2, BBN Report Number 8090, 1995.

52. Sparrow, V. W.: The Effect of Supersonic Aircraft Speed on the Penetration of Sonic Boom Noise into the Ocean. *Journal of the Acoustical Society of America*, vol. 97, 1995, pp. 159-162.

REPORT DOCUMENTATION PAGE

Form Approved
OMB No. 0704-0188

1. AGENCY USE ONLY *(Leave blank)*	2. REPORT DATE	3. REPORT TYPE AND DATES COVERED
	July 1996	Conference Publication

4. TITLE AND SUBTITLE
1995 NASA High-Speed Research Program Sonic Boom Workshop
Volume I

5. FUNDING NUMBERS
537-07-21-21

6. AUTHOR(S)
Daniel G. Baize, Compiler

7. PERFORMING ORGANIZATION NAME(S) AND ADDRESS(ES)
NASA Langley Research Center
Hampton, VA 23681-0001

8. PERFORMING ORGANIZATION REPORT NUMBER
L-17572

9. SPONSORING/MONITORING AGENCY NAME(S) AND ADDRESS(ES)
National Aeronautics and Space Administration
Washington, DC 20546-0001

10. SPONSORING/MONITORING AGENCY REPORT NUMBER
NASA CP-3335

11. SUPPLEMENTARY NOTES

12a. DISTRIBUTION/AVAILABILITY STATEMENT
Unclassified–Unlimited
Subject Category 01

12b. DISTRIBUTION CODE

13. ABSTRACT *(Maximum 200 words)*

The High-Speed Research Program and NASA Langley Research Center sponsored the NASA High-Speed Research Program Sonic Boom Workshop on September 12-13, 1995. The workshop was designed to bring together NASA's scientists and engineers and their counterparts in industry, other Government agencies, and academia working together in the sonic boom element of NASA'S High-Speed Research Program. Specific objectives of this workshop were to (1) report the progress and status of research in sonic boom propagation, acceptability, and design; (2) promote and disseminate this technology within the appropriate technical communities; (3) help promote synergy among the scientists working in the Program; and (4) identify technology pacing the development of viable reduced-boom High-Speed Civil Transport concepts. The Workshop included these sessions: Session I – Sonic Boom Propagation (Theoretical); Session II – Sonic Boom Propagation (Experimental); and Session III – Acceptability Studies – Human and Animal.

14. SUBJECT TERMS
High-speed research; High-speed civil transport; Sonic boom propagation (theoretical and experimental)

15. NUMBER OF PAGES
393

16. PRICE CODE
A17

17. SECURITY CLASSIFICATION OF REPORT	18. SECURITY CLASSIFICATION OF THIS PAGE	19. SECURITY CLASSIFICATION OF ABSTRACT	20. LIMITATION OF ABSTRACT
Unclassified	Unclassified	Unclassified	